Synthesis and Application of Nanocomposites for Adsorption Heat Transformation and Storage

Lead Guest Editor: Debabrata Barik
Guest Editors: Cherif F. Matta

Synthesis and Application of Nanocomposites for Adsorption Heat Transformation and Storage

Synthesis and Application of Nanocomposites for Adsorption Heat Transformation and Storage

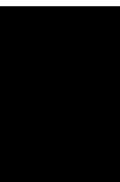Lead Guest Editor: Debabrata Barik
Guest Editors: Cherif F. Matta

Chief Editor

Advisory Board Member(s)

Contents

Contents

Retraction

Retracted: Implementation of Solar Heat Energy and Adsorption Cooling Mechanism for Milk Pasteurization Application

Adsorption Science and Technology

This article has been retracted by Hindawi following an investigation undertaken by the publisher [1]. This investigation has uncovered evidence of one or more of the following indicators of systematic manipulation of the publication process:

(1) Discrepancies in scope

(2) Discrepancies in the description of the research reported

(3) Discrepancies between the availability of data and the research described

(4) Inappropriate citations

(5) Incoherent, meaningless and/or irrelevant content included in the article

(6) Peer-review manipulation

The presence of these indicators undermines our confidence in the integrity of the article's content and we cannot, therefore, vouch for its reliability. Please note that this notice is intended solely to alert readers that the content of this article is unreliable. We have not investigated whether authors were aware of or involved in the systematic manipulation of the publication process.

Wiley and Hindawi regrets that the usual quality checks did not identify these issues before publication and have since put additional measures in place to safeguard research integrity.

We wish to credit our own Research Integrity and Research Publishing teams and anonymous and named external researchers and research integrity experts for contributing to this investigation.

The corresponding author, as the representative of all authors, has been given the opportunity to register their agreement or disagreement to this retraction. We have kept a record of any response received.

References

[1] G. Ramkumar, B. Arthi, S. D. S. Jebaseelan et al., "Implementation of Solar Heat Energy and Adsorption Cooling Mechanism for Milk Pasteurization Application," *Adsorption Science & Technology*, vol. 2022, Article ID 5125931, 13 pages, 2022.

Research Article

Predicting the Adsorption Efficiency Using Machine Learning Framework on a Carbon-Activated Nanomaterial

Kalapala Prasad,[1] **V. Ravi Kumar,**[2] **R. Suresh Kumar,**[3] **A. S. Rajesh,**[4] **Anjani Kumar Rai,**[5] **Essam A. Al-Ammar,**[6] **Saikh Mohammad Wabaidur,**[7] **Amjad Iqbal,**[8] **and Dawit Kefyalew** [9]

[1]*Department of Mechanical Engineering, UCEK, JNTUK Kakinada, Andhra Pradesh 533003, India*
[2]*Department of Mechanical Engineering, Amrita School of Engineering, Amrita Vishwa Vidyapeetham, Bengaluru 560035, India*
[3]*Department of Mechanical Engineering, B.M.S. College of Engineering, Bengaluru, Karnataka 560019, India*
[4]*Department of Mechanical Engineering, JSS Science & Technology University, Mysuru, Karnataka 570006, India*
[5]*Department of Computer Engineering and Applications, GLA University, Mathura 281406, India*
[6]*Department of Electrical Engineering, College of Engineering, King Saud University, P.O. Box 800, Riyadh 11421, Saudi Arabia*
[7]*Chemistry Department, College of Science, King Saud University, Riyadh 11451, Saudi Arabia*
[8]*Department of Advanced Materials & Technologies, Faculty of Materials Engineering, Silesian University of Technology, 44-100 Gliwice, Poland*
[9]*Department of Automotive Engineering, Arba Minch Institute of Technology (AMIT), Arba Minch University, Ethiopia*

Correspondence should be addressed to Dawit Kefyalew; dawit.kefyalew@amu.edu.et

Due to the excessive use of paracetamol (PCM), a significant amount of its metabolite has been released into the surroundings, and its removal from the surroundings must happen quickly and sustainably. Multicomponent adsorption modelling is difficult because it is challenging to anticipate the relationships among the adsorbates in this artificial intelligence-based modelling, a choice among different algorithms. Utilizing various algorithms, many studies assessed the single and binary adsorption of paracetamol on activated carbon. The present study implements that the effectiveness of PCM adsorption on a carbon-activated nanomaterial was predicted using an artificial neural network, a machine learning technology. As a factor of adsorbent particle size, adsorbent dosage, training time, and starting concentrations, the adsorption capacity for each medicinal ingredient was examined. SEM was used to analyze a nanomaterial that had been chemically altered with orthophosphoric acid (FTIR). To determine the residual proportion of PCM in solvent, batch adsorption of PCM was then carried out at various operation conditions, including contact time, temperatures, and initial dosage. The adsorption effectiveness of paracetamol on carbon-activated nanoparticle was calculated using experimental results. Thus, by using machine learning framework, the adsorption efficiency of paracetamol on a carbon-activated nanomaterial was predicted.

1. Introduction

Pharmaceutical substances are now understood to be developing contaminants with detrimental effects on both the surroundings and public health. Pharmaceutical contaminants are quickly emerging as new contaminants and are accumulated in sewage and aquatic systems. As a result, 300 million tons of industrial and medicinal chemicals are released into the environment annually. These contaminants are dangerous for the ecosystem because they are nonbiodegradable and extremely poisonous and have a unique molecular size. In order to prevent medicines' negative impacts on the ecosystem, people, and aquatic environments, it is imperative that they are removed from sewage. The research states that paracetamol and nimesulide bioactive chemicals were found in small amounts in the waterways of South American countries. For example, due to its hepatotoxic consequences and gastrointestinal harms, the promotion

and intake of nimesulide were forbidden in various nations [1], while 4-aminophenol, an extremely dangerous and carcinogenic chemical that causes genetic defects and cellular deaths, could be produced when paracetamol is broken down. In the United States and Europe, paracetamol is the most typical cause of acute liver failure (ALF). A hyperacute structure governs both injury and recovery, with maximum hepatocyte damage occurring 72 hours after a single consumption and possible recovery occurring at a similarly rapid pace. The rapidity and magnitude of the disease, the possibility of recovering without LT, and the existence of complex psychosocial factors in the majority of patients make organ transplants for acetaminophen-induced acute liver failure frequently present considerable challenges and issues despite sensible renal transplant recipient results [2]. Regarding nanomaterial structures, characteristics, adsorption, and catalysis, this viewpoint illustrates and discusses the problems of general interest for the implementations and viewpoints of ML in the field of NM. NMs have created new opportunities for nanomedicine and healthcare development. Comprehending the nanomaterial foundation for use in biomedical application is their interfacial interactions with life. ML offers significant advantages in precisely determining and anticipating biochemical functions to the characteristics of both known and unknown molecules, which aid in the discovery of new functional nanomaterials and the prevention of negative consequences. Machine learning techniques lack comprehensibility (i.e., are ambiguous in their physical, chemical, or biological meaning), particularly deep learning systems with high prediction performance comparing to chemical, pharmaceutical, and biological molecular. Likewise, machine learning databases are still in their development. Additionally, they go over how to encourage the use of learning algorithm, create datasets in the realm of commodities, and create open to interpretation algorithms (e.g., white box models). Additional facets of the application of ML to advance nanotechnology are offered towards the conclusion of this viewpoint, for example, nano-pattern image classification [3].

Although modelling techniques like multilinear regression models and linear correlativity are frequently used to describe the adsorption process, they are only somewhat accurate and applicable. In contrast, data-driven machine learning techniques are an effective tool that might be utilized to investigate the intricate connection among adsorption capacities and biochar characteristics. Methods can be classified, predicted, optimized, and clustered using ML. To hasten the completion of pharmaceutical adsorption processes using biochar, ML has been employed. Nevertheless, given this field's relative youth, there is not much information now available. A component is moved from the liquid stage to the interface of a solid through the charge transport procedure termed as adsorption, where it is subsequently bound by either physical, chemical, or a combination of the two. Studies have concentrated on using inexpensive, environmentally acceptable compounds to remove MPs, such as chitosan and bentonite. Chitosan's glucose molecules contain several hydroxyl groups, making it more hydrophilic and technically excellent for inorganic and

organic adsorption. Hydrogel structures have a great deal of interest in chitosan, a natural cationic copolymer. This polymer is biocompatible and biodegradable due to its hydrophilic nature and the capacity of degradation via human enzymes, two biological qualities typically required for biological devices. The main component of bentonite is the clay mineral montmorillonite. Pollutant removal from water has frequently employed low-cost adsorption as a criterion. Upgraded organ bentonite absorbed about 81% of the AMX [4]. Adsorbent architectures, fluid characteristics, impurity frameworks, operational circumstances, and system control are only a few of the variables that play a role in the adsorption mechanism. Silica gel, alumina, clays, composites, zeolites, activated carbon, biomasses, and biological and polymeric substances are just a few of the elements that have been utilized as adsorbents to remove toxins from aquatic environment. So over the last ten years, work on the use of carbon-based nanomaterials as adsorbents has grown quickly. The distinctive qualities and variety of carbon-based nanostructures, as well as the emergence of new possibilities in numerous subspecialties of chemical, economics, and construction, are the primary driving forces behind the development of this discipline. The capacity of carbon-based product to adsorb a wide range of water contaminants, including hazardous metallic ions, medications, insecticides, transition metals, and other both inorganic and organic chemicals, could be achieved using a number of processes [5]. The usual pollutants are simply concentrated and moved to other stages when using absorbance as a water treatment process.

The connections among adsorbed molecules and adsorbent are what define and rely on the adsorption phenomenon. The kind of the adsorptive (protein kinase, polarization, functioning, diameter, and molecular mass), the adsorption (chemical bonding and pore size and composition), and the solution circumstances all affect how well a carbon-based adsorbent absorbs chemical substances (ionic strength, pH, and temperature). Van der Waals, induced-dipole, dipole-dipole, and hydrogen bonding donor-acceptor interactions, as well as the liquid phase, are what cause different chemicals to bind to different adsorbents and accumulate there. Hydrogen and other chemical bonds, together with covalent and electrostatic contacts, the hydrophobic action, and other interactions, all play crucial parts in the adsorption process. AC, carbon nanofibers, carbon nanotubes, graphene, biochar, and carbon aerogels are all components of CBMs. A variety of CBMs utilized in the adsorption process are shown in Figure 1 [6].

With its benefits of high effectiveness, reduced energy usage, and broad scalability for various pressure and heat ranges, adsorption with adsorbent material to transiently collect carbon dioxide from flue gas generated in the coal combustion of fossil fuels has attracted immense attention. Zeolites, porous polymers, covalent organic frameworks, metal organic frameworks, and porous carbon materials are some of the commonly researched solid adsorbents for carbon dioxide collection. Porous carbon materials (PCMs) stand out among the others because of their copious and adaptable porous architectures, simple manufacturing and

rejuvenation, excellent good thermal stability, cheap and accessible raw ingredients, and superior resistance to water vapor. The kind and quantity of activating agents, the thermochemical transformation techniques, and the process temperature all had a significant impact on the final physicochemical attributes of PCMs. The stimulation processes sped up the breakdown of carbon antecedents and helped rearrange transitional byproducts to create porous carbon frameworks. Numerous investigations have shown that this family of porous carbons has outstanding carbon dioxide adsorption capacity [7].

According to the investigator, more research is needed on continuous flow studies to comprehend the adsorption capability and to take into account the adsorption of several pollutants. According to a new analysis, the effectiveness of medication elimination by biochar adsorption differs and depends substantially on a number of variables, including the physicochemical qualities of biochar, the reaction environment, and the kind of medicines involved. These difficulties have made it necessary to create various methods and data-driven techniques to comprehend the adsorption capability and forecast the effectiveness of pharmacological removal, particularly for complicated pollutants. Due to their beneficial morphological, biochemical, electrical, and optical properties, nanoparticles have received a lot of research attention in a variety of sectors, including food technology, power, technology, and pharmaceuticals [8]. Metal organic structures have attracted interest recently in contrast to other rigid nanoparticle transports because of their well-structured organization, exceptionally large surface area, high porosity, variable pore size, and simple chemical functionalization. A repetitive, hollow architecture resembling a cage is created in a metal by the linking of ions or ions in clusters by organic compounds. The examination of preclinical nanocomposite safety and risk management has made extensive use of intelligence approaches. Adverse effects of nanoparticles on living things, such as people, animals, algae, plants, and the ecosystem at various points along the food chain, could be mitigated by proper nanomaterial engineering. Evaluations before product release (presymptomatic) are necessary to forestall the use of dangerous nanoparticles (nanotechnology). An index case can spread the disease to close contacts without showing symptoms at the time of exposure. The main factor still preventing the widespread application of nanomaterials in consumer goods, particularly in healthcare, is higher nanotoxicity in environmental compartments and during clinical studies [9].

Utilizing ANN, multiple studies have modelled the adsorption effectiveness of various pollutants. For the purpose of predicting the effectiveness of activated carbon powder in eliminating chromium (VI) from wastewater, investigation created a three-layer feed-forward neural network. Adsorbent dosage, solution pH, contact period, and beginning concentration are among the attribute values. The ideal number of invisible neurons for the hidden layer was determined to be 10, which also produced the least mean square error result. In the first version of their investigation, the backpropagation technique altered the activation functions of tansig, satlin, and poslin at the hidden units.
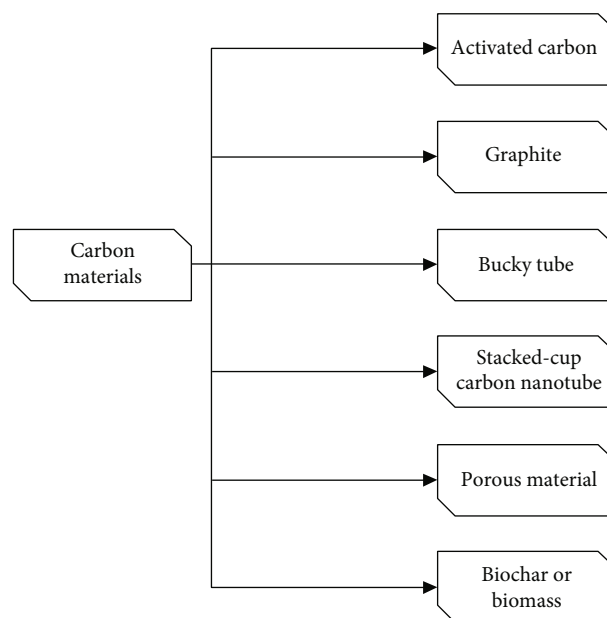
FIGURE 1: Several CBMs that can be used in adsorption techniques.

This is an example of a neural transfer function. Transfer functions are functions that determine the output of a layer based on the net input of that layer. At the output nodes, purelin activation function was utilized. Based on R^2 and mean square error values, the optimal method, activation function, and number of hidden neurons were chosen. When contrasting several forecasting systems for the efficacy of walnut, azo dyes [10]. In this research, a three-layer structure with a tansig converter at the concealed layer and endorphin transfer function at the output nodes was built. Size of the particles, beginning pH, dye concentration, training time, and temperatures are the five input factors that make up the material's input neurons. The quantity of dye deposited serves as the output neuron. Using trial and error, the researchers were able to choose the 25 hidden neurons that best suited the model for the adsorption mechanism. Nevertheless, a three-layered architecture with a 5-25-1 network arrangement was produced as a result. Composite adsorption is difficult to simulate since, in contrast to reactions among the adsorbent and the many adsorbents, operating factors significantly affect the adsorption mechanism. In this regard, multiphase network prediction has been achieved successfully using artificial neural networks (ANN). ANN seems to be more flexible than other traditional processes and has been utilized to anticipate isotherms, kinetic breakthrough curves, and operational efficiencies because it adjusts instantly from empirical observations without imposing assumptions about the thermodynamic framework that impacts the adsorption process [11].

This study looked into how paracetamol adsorbs on activated carbon in both single and binary aqueous environments. At various operational situations, the multicomponent state's antagonism and synergic impacts were demonstrated. For artificial neural network improvement of adsorption capability, independent parameters such as initial concentration,

adsorbent dose, adsorbent particle size, and starting intensity were employed as input data (output data). To find the best ANN, other network architectures and training procedures were also tested.

2. Related Works

In this research, a unique activated carbon with built-in capacities to really remove acetaminophen and ketoprofen from fluids was created using the endocarp of the Butia capitata species as a precursor material. The activated carbon showed a mostly microporous structure with a median pore diameter of 1.23 nanometer, a considerable pore capacities of $0.449 \, cm^3 \, g^{-1}$, and a significant particular contact region of $820 \, m^2/g$. In accordance with the adsorption kinetics of both medications, the combination reached equilibrium after 120 minutes for ketoprofen and 170 minutes for acetaminophen. The best matches for the substance were provided by the Elovich concept and the pseudo-second-order framework, correspondingly. According to the findings from the adsorption equilibrium, the maximal adsorption capacities for the drugs ketoprofen and paracetamol were determined to be $108.79 \, mg \, g^1$ and $100.60 \, mg \, g^1$, correspondingly. The Freundlich and Langmuir theories, in turn, offered the most appropriate statistical adjustments for the adsorption of ketoprofen and paracetamol, respectively. The Langmuir isotherm is used for monolayer adsorption on homogeneous surfaces, while the Freundlich isotherm suites are used for multilayer adsorption on heterogeneous sites. The thermal study verified that the processes for given parameter were exothermic and endothermic, respectively. The results of the recycling tests showed that the average reduction for elimination proportion for ketoprofen and paracetamol for the adsorbent was only 1.88% and 1.57%, respectively. According to cost estimates, the cost of 1 kilogram of activated carbon is 2.39 USD at the very least. Finally, the substance demonstrated extremely effective adsorptive action, removing 84.82% of a synthetic combination combining various salts and medicinal chemicals [12].

Concomitant adsorption of medicinal drugs is difficult to achieve for the purpose of water and wastewater treatment in a practical setting. Activated carbon was utilized in this examination in the role of an adsorbent so that researchers could look into the possibility of paracetamol and nimesulide being adsorbed at the same time. The findings of the study demonstrated that CSH can serve as a reliable, cost-effective, and environmentally friendly feedstock for the production of AC, which can then be utilized for the effective removal of paracetamol from an aqueous environment. In order to assess the variations in adsorption behavior, single adsorption tests were also carried out. For example, nimesulide ($196.32 \, mg \, g^1$) has a larger single adsorption capacity in AC than paracetamol ($58.21 \, mg \, g^1$). It is worth noting that nimesulide atoms were adsorbed into active sites that had earlier been inhabited by paracetamol particles during binary adsorption. This displacement effect, caused by the competing of drug molecules at increasing drug dosages, severely inhibited the adsorption of paracetamol on AC while promoting the adsorption of nimesulide. Since nimesulide is more hydrophobic than paracetamol (log Kow =

0.49), the AC and nimesulide have a stronger attraction for one another. In addition, it seemed from Fourier transform spectra taken both prior to and after adsorption that nimesulide was adsorbed by H bonding, whereas paracetamol was adsorbed by different hydrogen bonding and other dispersion connections. The single equilibrium isotherm models for both medicines were transformed by the Langmuir equation. To forecast the binary adsorption of paracetamol and nimesulide on AC, the expanded Langmuir model was employed. Finally, exothermic, advantageous, impulsive adsorption with lower adsorption vitalities that favoured physisorption was predicted by the dynamic simulation [13].

Due to their minuscule size, pharmaceuticals in wastewater are quickly evolving into new emergent contaminants that threaten both humans and the aquatic ecology. Due to its low affordability, adaptability, and recyclability, adsorption is proving to be a viable method for the extraction of pharmaceuticals from untreated wastewater. Adsorbents are porous substances that are frequently employed to eliminate medicinal contaminants via adsorption. Examples of adsorbents include silicon, kaolin, resinous, and carbon-based substances including charcoal, carbon nanotubes, and activated carbon. Among these, biochar is a newly developed, economical, and environmentally beneficial sorbent. Although modelling techniques like multilinear regressions and linear correlativity are frequently used to describe the adsorption behavior, they are only somewhat accurate and applicable. On the other hand, machine learning techniques are a potent tool that might be utilized to investigate the intricate connection among adsorption capacities and biochar characteristics. This paper offers a summary of current achievements in the study of drug adsorption onto biochar using machine learning techniques. An overview to various ML techniques is given, along with information on their benefits and drawbacks. The difficulties and potential outcomes of applying machine learning to the investigation of the adsorption mechanism are also discussed. In order to evaluate the elimination of medical products from wastewater utilizing charcoal or carbon black, the approach on assessing the potential of machine learning methods was developed by [1].

A category of porous carbons formed from biomass waste was created in recent years as an outcome of the creation of sophisticated materials. These carbons are employed for carbon capture and environmentally friendly waste treatment. Studying the adsorption process of carbon dioxide into the atmosphere is challenging due to the wide variety of characteristics it possesses due to its various textures, functional group existence, pressure, and temperature ranges. These characteristics have a variety of effects on the adsorption of carbon dioxide and provide significant difficulties in the procedure. To meet this numerous goal requirement, researchers use a machine learning forecasting models, carefully modelling the carbon dioxide absorption as a consequence of constituent and texturing aspects as well as adsorbed factors. The ML classification assists in the classification of various porous carbon materials throughout testing and validation. The results of the simulation show that the suggested method is more effective to previous methods for classifying the general porous nature of carbon

dioxide-adsorbed compounds. Therefore, Soft Computing Methods for Predicting Carbon Residue in Biomass Wastes [14]. With the development of nanotech, researchers are witnessing a shift in the global economy and deep infiltration of synthetic chemicals ranging from essentials to cutting-edge electronics, healthcare, and pharmaceuticals. Nanoproducts should be closely controlled to prevent undesirable consequences as they may produce undesirable adverse effects. The shortcomings of conventional safety assessment techniques are highlighted by the toxicological and safety measures that would arise in relation to the rapid integration of nanoparticles with various functions and properties into consumer items. The simulations and modelling of nano-bio relations are presently expected to benefit from artificial intelligence and machine learning algorithms, and this extends to the postmarketing monitoring of nanotechnology in the actual life. In order to gain unique insights on the perturbations of sensitive bioactivities following integration with nanoparticles, ML could be combined with biology and nanoparticles. The possibility of integrating integrative omics with learning algorithms in assessing nanoparticles security and threats evaluation is discussed in this paper, along with the advice for regulatory bodies. As a result, omics with computational integration were used to evaluate the danger and toxicity of nanoparticles [4].

The computation complexity of using molecular computation for adsorbent screening makes it impractical for the new material development. Techniques for machine learning (ML) that have been trained on the essential characteristics of a material may be able to offer fast and accurate testing techniques. Prior work concentrated on developing structural characteristics for machine learning. In this work, architectural properties and the usage of pharmacological descriptions for adsorption evaluation were combined. To forecast methane ingestion on fictitious metal organic architectures, assessments of the structural and chemical characteristics along with different ML methods, such as decision tree, support vector machine, Poisson's regression, and random forest, were conducted. Machine learning models were compared on the residual 92% of the given database, which included 130,398 MOFs, after being trained on 8% of it to demonstrate their predictive power. With an R^2 of 0.98 as well as a mean absolute percentage inaccuracy of about 7%, the random forest technique with cross validation of tenfold beats the other Ml techniques if both mechanical and chemical parameters were used as inputs. On a single personal computer, the training and forecasting employing random forest approach for estimating the adsorption capacity of all 130,398 MOFs took about 2 hours, which is a considerable amount faster than actual chemical computations on powerful computational complexes. As a result, the metal organic framework (MOF) methane adsorption efficiency forecast method using machine learning utilizing combined structural and chemical descriptors was developed by [15].

3. Methodology

3.1. Absorbates.
Dermapele offered paracetamol ($C_8H_9NO_2$) in high purity (99%). To make work preparations, specific

TABLE 1: Paracetamol molecular characteristic.

Property	Paracetamol	
Size of particle	Pore volume ($cm^3 \cdot g^{-1}$)	Average pore size (nanometer)
150	0.205	3.635
300	0.163	3.639
500	0.158	3.654
850	0.145	3.622

quantities of each pharmaceutical ingredient were dissolved in deionized saline and ethyl alcohol (10% v/v). To adequately depict medicinal pollutants, ethyl alcohol was employed. Table 1 lists the molecular weight, acid dissociation logarithmic constants, and octanol/water partitioning ratios of every synthesized medication in addition to the three-dimensional chemical equation. Labor fluids were created using distilled water. Add both ethanol and water to enhance absorption. Analytical grade chemicals were the remaining ones.

3.2. Activated Carbon Nanomaterial Preparation.
The precursor material chosen for activated carbon manufacture is determined by numerous variables, such as accessibility, hazardous and nonhazardous character, and manufacturing costs. Many investigations have found that composites with a high fixed carbon content and low ash content have superior structural and textural properties. Because of their high carbon content, plant-based substances have become widely used in the synthesis of activated carbon. Various parts of this plant have indeed been employed in various dimensions and manufacturing procedures, including the core, seed, flowers, branches, peels, fruits, shells, leaves, husks, and stones. Activated carbon from date beads was generated by pyrolysis at 300 degrees Celsius for 3 hours and tested for lead nitrate adsorption from aqueous systems, yielding an adsorption ability of 76.8 mg/g. Carbonization is typically employed prior to activation chosen antecedent substance, in which it endures a thermal treatment called as pyrolysis to enhance carbon content. Moisture and low molecule weight aromatics, light flavorings, and ultimately H_2 gas are released during the catalytic pyrolysis, producing a fixed carbonaceous framework [16]. The majority of the pores in the pyrolyzed carbonaceous substances are filled by tarry chemicals, which results in the substances having a low porosity. Tarry oxidation products are the name given to the byproducts that are created when nitric acid reacts with aniline in an oxidation reaction. As a result, an activation step is necessary to generate the nanocarbon's unique properties. According to studies, the choice of carbonization variables, particularly temperatures, heating duration, and dwelling duration, has a considerable impact on the permeability and adsorption efficiency of the finished piece. Thermal treatment processing has been utilized to transform the precursor material's saccharides into graphite discs with low particular surface region. Carbon materials generated in this manner need not milling prior to activated processing and often have a minimal ash concentration. Subsequent

physical, chemical, or physicochemical procedures are required to activate the carbonaceous material and enhance the amount of functional containing oxygen on the interfaces of the activated charcoal. Figure 2 summarizes the biomass transformation into activated carbon [17].

The activated carbons were produced from lignocellulosic materials in four phases. The approach is as follows: (i) Hempseed oil slurry and activation reagent concentrations (K_2CO_3 or KOH) were combined for 24 hours at 1000 rpm continual agitation. (ii) To produce the impregnated material, this solution was heated at 110°C for 24 hours. (iii) The impregnated material was placed in a stainless rigid bed furnace with a 6 cm diameter and a 21 cm height. The impregnated material was pyrolyzed for 1 hour at temperatures of 600 and 800°C with a nitrogen flow rate of 30 mL min[1] and a heating time of 5°C min^{-1}. (iv) The carbonized sample was then rinsed multiple times using hot distilled water and then with cold distilled water until the pH of the filtrate reached neutral. To produce the activated carbons, the cleaned materials were heated at 110 degrees Celsius for 24 hours. Following that, the activated carbons were cooked in a hydrogen chloride solution on reflux to remove the contaminants and decrease the ash content of the activated carbons. They were again rinsed numerous times in hot distilled water and lastly with distilled cold water till no contaminants were identified. To produce the activated carbons, the rinsed particles were dried at 110 degrees Celsius for one day [18].

Biochars produced from soybean oil cake without chemical activation were identified as BC1 and BC2, correspondingly. SAC1 and SAC2 are the activated carbons generated through chemical treatment with K_2CO_3 at 600 and 800 degrees Celsius, correspondingly. SAC3 and SAC4 are the activated carbons generated through chemical treatment with KOH at 600 and 800 degrees Celsius, respectively.

The empirical procreation ratio was calculated using the following equation:

Procreation ratio

$$= \frac{(\text{wt of sample after procreation}) - (\text{wt of waste biomass})}{\text{wt of waste biomass}}. \tag{1}$$

In Equation (1), the procreation (impregnation) ratio is estimated by taking the difference of weight of impregnation and weight of waste biomass by weight of waste biomass in which "wt" denotes the weight.

The amount of activated carbon was calculated using the following equation:

$$\text{Yield} = \frac{\text{wt of activated carbon}}{\text{wt of waste biomass}} \times 100. \tag{2}$$

Using a surface analyzer and nitrogen gas adsorption, the precise surface areas of activated carbons made from soybean oil cake were determined (at 77 K). Novawin 2 software was used to compile data, and the t-plot method was employed to determine micropore volume. The micropo-
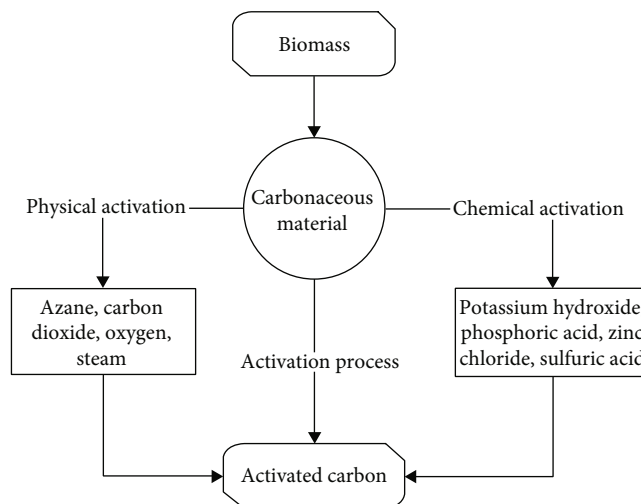
Figure 2: Carbon activation technique.

rous volumes and specific surface area of a sample can be calculated using the well-known t-plot approach by comparing the adsorption isotherm of the test to that of a benchmark nonporous material that has the exact surface chemistry.

Superficial function classes of AC were detected utilizing Fourier spectra taken on a spectroscopy with 32 scans and a sensitivity of 4 cm[1] inside the region 5000 to 500 cm[1], after the substance had been dispersed in potassium bromide. X-ray diffraction (XRD) utilizing copper-K monochromatic light in the 5° to 100° range confirmed the crystalline structures of AC. The primary application of the fast analytical technique known as X-ray powder diffraction (XRD) determines the phase of a crystalline material, and this approach can also reveal information on the unit cell dimensions. The outer layer and textural properties of AC were determined utilizing nitrogen gas adsorption behavior at 77 K done in a volumetric adsorption analyzer utilizing the Brunauer-Emmett-Teller and Barrett-Joyner-Halenda methods. The surface morphology was acquired using a scanning electron microscope after the samples were earlier metalized with gold. At varying pH value, the determination of point of zero charge is processed utilizing the adsorbent agent at the quantity of 1 gram·L^{-1} combined at 150 rpm and 298 Kelvin for one day. Using the Boehm titration, the oxygenated function groups of the adsorbent surface were generated with combination of adsorbent 1 g combined with 50 mL of hydrochloric acid, sodium hydroxide and sodium hydrogen carbonate with 0.1 molarity and sodium carbonate with 0.05 molarity.

3.3. Adsorbent Chemical Modification. 50 g of the previously prepared dry material was weighted with an analytical balance and moved to a glass vial. 600 cm³ of 0.3 mol/dm³ orthophosphoric acid was applied to the glass specimen; it was well stirred with a stirrer and cooked on a medium heat till the slush in the form of paste was created. Then, it was placed in a crucible. The material was therefore moved to a desiccator, which has been inserted in an oven that was heated to 500°C for one hour, until charcoal emerged. The
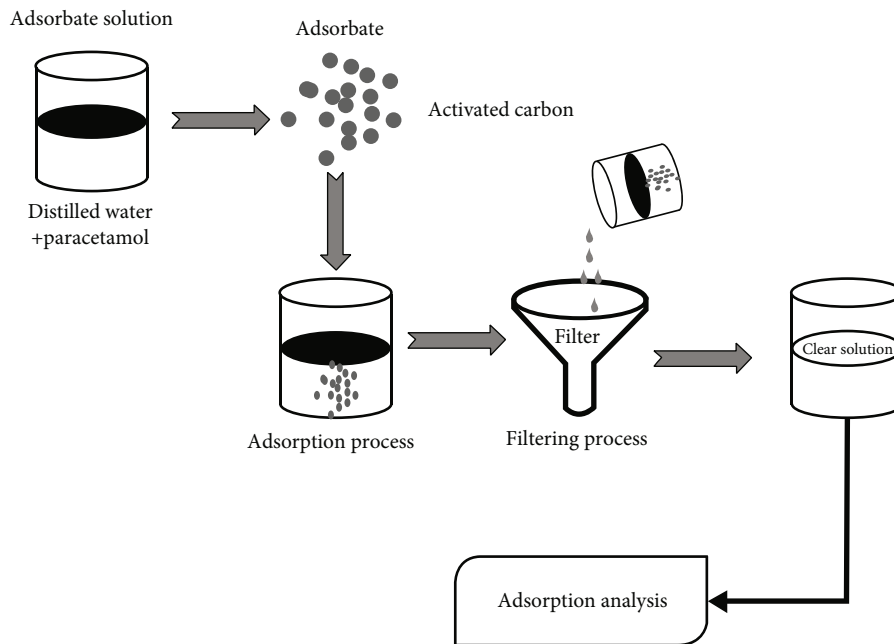
FIGURE 3: Adsorption process.

resulting charcoal was allowed to cool at room heating rate before being rinsed multiple times using distilled water till it reached a neutral pH. The cleaned charcoal was stored in an oven at 1050 degrees Celsius for four hours until it reached a consistent weight. After that, the charcoal was stored in an impermeable vessel for description and further adsorption investigations [19].

3.4. Adsorbate Solution Preparation. Adsorption is a surface phenomenon that affects only the adsorbent surface, and adsorbate must not enter the adsorbent's core. The adsorption process is depicted in Figure 3.

One gram of PCM was dissolved in one liter of filtered water to make a solution containing. To produce workable solution with concentrations of 10, 20, 30, 40, and 50 milligrams per liter, serial dilutions were performed. Because porous carbon materials are accessible in polar solvents, the experimental solutions were created with filtered water. A constant amount of adsorbent (0.1 g) was introduced to a series of 250 milliliter Erlenmeyer vials holding 100 milliliter of porous carbon material liquid with varying starting levels. The vials were shaken in an adiabatic liquid bath mixer at 200 revolutions per minute and at distinct temperature (30, 40, and 50 degree Celsius) until equilibrium was established. To measure the residual percentages, standard solutions were drained at periodically with a microfilter needle until homeostasis was attained. To avoid the interference of carbon particles, the solution was strained before examination. The test was permitted to continue until it achieved equilibrium [20].

At 298 Kelvin and 150 rpm, adsorption studies were carried out in a thermostat agitation. Activated carbon C with varying particle sizes between 15 and 800 μm and doses around 0.5 to 2.0 grams per liter was employed to neutralize paracetamol at a starting quantity of 0.1 mmol·L^{-1} and at the

acidity level of 8. The samples were extracted at predefined intervals of 5 min, 1 hour, 2 hours, and 5 hours; the stationary material was filtered out. The residual proportion in the liquid phase was determined using spectrophotometry at paracetamol's maximum wavelength ($\mu_{\max} = 244$ nm). All procedures were conducted out in triplicate ($x = 3$), and void checks were performed to ensure data repeatability and reliability. The standard deviation was no more than 3%. Equation (3) was used to compute the concentrations of paracetamol in the binary system. Lastly, Equation (5) was used to calculate the adsorption capability of each medicinal component (y):

$$C_U = \frac{k_{U2} U g_1 - k_{U1} U g_2}{k_{U2} - k_{U1}}, \qquad (3)$$

where k_{U2} and k_{U1} are the paracetamol's calibrating variables (B) at 393 nm (1) and 244 nm (2) wavelengths, correspondingly, and $U g_1$ and $U g_2$ are the comparable acetaminophen absorbency readings.

Equation (4) could be employed to calculate the quantity of adsorbed compound at optimized conditions, which corresponds to the adsorption capacity, Q_a and Q_b, which is the proportion of adsorbed component at random period b:

$$Q_a = \frac{(C_x - C_y) \cdot V_l}{W_t}, \qquad (4)$$

$$Q_b = \frac{(C_x - C_b) \cdot V_l}{W_t}, \qquad (5)$$

where C_x, C_y, and C_b (mg/L) are the absorbate contents at the start, time b, and equilibrium, accordingly, V_l is the volume of solution (L), and W_t is the adsorbent weight (g).

3.5. Artificial Neural Network. In order to mimic the empirical findings in an effort to forecast the extraction efficiency of PCM using a neural network classifier, a feed-forward backpropagation train approach was selected as the appropriate method to use. It is important to remember that backpropagation (BP) is a feed-forward neural network, which means that it uses error propagation in the opposite way to update the weights of hidden layers. The deviation between actual output and the desired output, as calculated using the gradient descent algorithm, is the error. The research technique in this study was predicated on a component, i.e., one X variable at a period. This has been accomplished by holding the other two factors constant and varying a single input variable. 495 prototype examples were created from experiments conducted in this paper. The information was arbitrarily partitioned between the testing and training sets. 330 real numbers were utilized for training and the remainder for testing. Using Equation (6), the training and testing data were adjusted to decrease error.

$$X_i = \frac{A_i - A_{\min}}{A_{\max} - A_{\min}} \times (v_{\max} - v_{\min}) + v_{\min}, \tag{6}$$

where A_i is an input or output parameter and X_i is the normalized quantity of A_i, while $A_{\min}$ and $A_{\max}$ are the extreme values of A_i. In the research, A_i is adjusted to a ranging restriction defined by $v_{\max}$ and $v_{\min}$. The input information and output information in this research were standardized among 0 and 1. After modelling, the results were reset to their original value. As illustrated in Figure 4, the experimental information was modelled in a three-layer artificial neural network (the network configuration contains input, hidden, and output layers).

Artificial neural network is commonly employed as a modelling tool to estimate complicated systems that cannot be modelled using traditional modelling techniques. They are commonly employed in categorization, pattern matching, and function approximation. There is no clear method for determining the artificial neural network structure and training procedure in tackling a specific problem. The structure and technique to be used in tackling a certain challenge are chosen through trial and error. This choice may, nevertheless, begin with a simple communication network and progress to a complicated network until an adequate compromise with tolerable minimum error is obtained. There are various network topologies in artificial neural network modelling [21]. The basic design is an MLP feed-forward neural network that uses a backpropagation training technique to train input data. If there is difference in the sequence of stages in the organization, the quantity of neurons within each layer, and/or transmission ratios at the source and destination nodes, there may be variability in the design. In this research, a three-layer ANN was developed, with an input layer (independent factor) having three synapses (interaction duration, operating temperature, and early dosage), a hidden units including seventeen neurons, and an outcome unit (dependent parameter) containing one neuron as in Figure 4. At the output and hidden layers
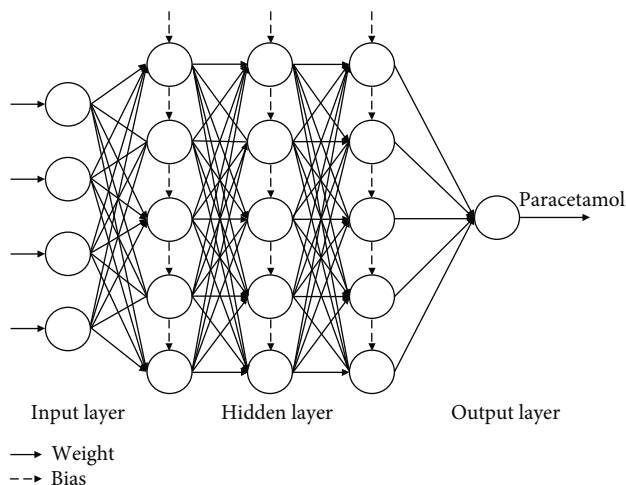
FIGURE 4: ANN processing.

of the neural system, a linear and nonlinear activation function was utilized in the topology. There were 495 experimental observation instances created. The database was randomly partitioned into training (70%) and testing (30%) subdatasets [9].

In order to correctly forecast data, it is crucial to determine how many hidden units and layers to employ in the artificial neural network modelling process. Optimal structures for artificial neural networks were found through exploration of varying numbers of hidden units and layers. The most significant positive Pearson linear correlation coefficient and the smallest mean square error were utilized to pick the best building design. One typical method of assessing linear relationships is the Pearson correlation coefficient (r). A coefficient measures the intensity and direction of a link between two variables and takes on a value between -1 and 1. For any given change in a given variable, there is an inverse and complementary shift in the other variable. Equations (7) and (8) were utilized to calculate the mean square error and the R^2, respectively:

$$\text{Mean square error} = \frac{1}{N} \sum_{i=1}^{N} \left(x_i^{\text{AN}} - x_i^{ex} \right)^2, \tag{7}$$

$$R^2 = \frac{\sum_{i=1}^{N} \left(x_i^{ex} - \bar{x}_i^{ex} \right) \left(x_i^{\text{AN}} - \bar{x}_i^{\text{AN}} \right)}{\sqrt{\sum_{i=1}^{N} \left(x_i^{ex} - \bar{x}_i^{ex} \right) \sum_{i=1}^{N} \left(x_i^{\text{AN}} - \bar{x}_i^{\text{AN}} \right)}}, \tag{8}$$

where the normalized x_i^{ex} value is obtained, x_i^{AN} is the ANN prediction, $\bar{x}_i^{\text{AN}}$ is the average values, and the quantity of empirical observations is N.

4. Result and Discussion

To determine the primary functional units contained in AC, the FTIR spectra were produced. Figure 5 shows a spectrum with bands about 3431 cm^{-1}, 2912 cm^{-1}, 1634 cm^{-1}, 1570 cm^{-1}, and 1112 cm^{-1}. The wave at 3430 cm^{-1} could be attributed to the bending frequencies of OH from C_6H_6O, C_2H_2O, and
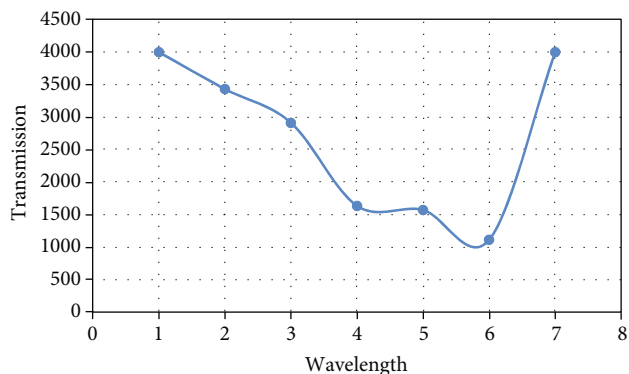
FIGURE 5: Activated carbon spectrum.
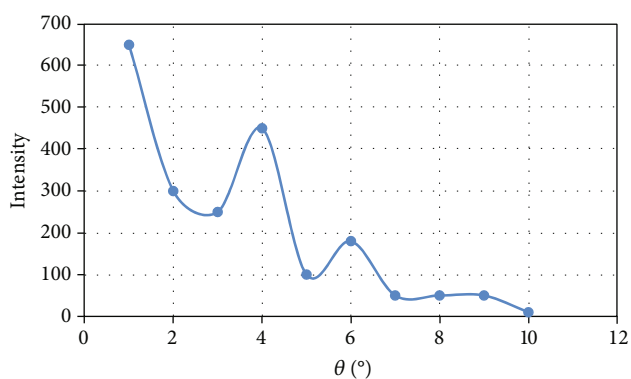
FIGURE 6: Diffraction pattern.

R-COOH existing as functional units of the activated carbon, or it could be explained by the occurrence of aquatic adsorption in the absorbent. The bond found about $2912\,cm^1$ might be attributed to CH_2 and C-H asymmetrical stretching vibrations. The C=O asymmetric stretching vibrations of R-COOH are responsible for the wave at $1634\,cm^{-1}$. The aromatic ring of the AC structure's C=C stretching vibrations may be verified at $1568\,cm^1$. Furthermore, the band at $1112\,cm^{-1}$ can be attributable to hydroxyl CO bending vibration in C_6H_6O, C_2H_2O, and R-COOH.

Figure 6 depicts the diffraction patterns generated for AC. A very broad reflect similar to the reflect may be seen, with the peak location approximately $4 = 26°$. Additionally, a reduced broad peak with an absorption peak of around $2 = 42°$ was found to fit the planes. Figure 6 depicts an ordinary diffraction signal with disordered carbon network, demonstrating that activated carbon is crystalline. An oxidized form is often sufficient for adsorption applications because it contains more vacant spaces that enable medicinal compounds to enter the adsorbent.

0.1 gram of chemically modified orange peel was agitated with 150 mL of porous carbon material solution at various dosages between 15 milligrams per liter and 55 milligrams per liter during the research of the control of paracetamol adsorption on CMOP. The proportion of paracetamol removed in interaction with the improved adsorbent increased steadily in analyzed batch adsorption. The rise in proportion went from 56.66% at 10 milligrams per liter to

TABLE 2: Adsorption efficiency at 35 mg/L.

Period (seconds)	Performance	AN forecasting
240	80.15	4.74
600	83.58	77.58
1500	91.46	96.33
2400	98.97	96.58
3600	98.97	96.75
5400	98.97	96.99
7200	98.97	97.14
9900	98.97	97.29
12600	98.97	99.84
15300	98.97	99.97
18000	98.97	91.25

TABLE 3: Adsorption efficiency at 45 mg/L.

Period (seconds)	Performance	AN forecasting
240	89.93	0
600	92.34	69.14
1500	93.12	97.64
2400	93.22	97.70
3600	95.19	98.88
5400	95.46	99.94
7200	96.94	99.92
9900	99.36	97.71
12600	99.36	97.73
15300	99.36	98.96
18000	99.36	98.96
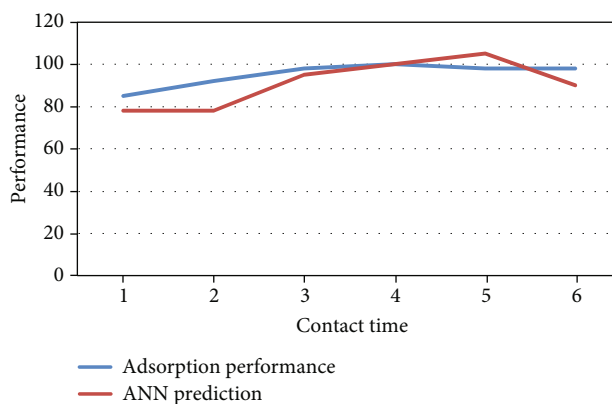
FIGURE 7: Adsorption performance at 15 mg/L.

99.36% at 45 milligrams per liter. At 55 milligrams per liter, there was a small drop to 98.5%. This may be owing to the adsorbent's accessible unoccupied pores leading in adsorption at lower amounts, as opposed to higher doses where adsorption might be determined by the amount of adsorbate diffusion along the adsorbent. The adsorption mechanism reached a steady as quickly as half an hour of adsorbate-adsorbent interaction at doses ranging from 10 to 30 mg/L, with the greatest inhibition efficiency at 35 mg/L and a
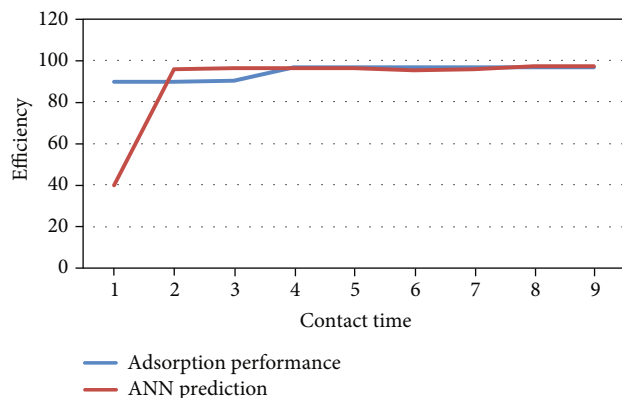
FIGURE 8: Adsorption performance at 45 mg/L.

reasonably stable removal number at all of these concentrations after the optimized conditions.

The adsorption mechanism, however, reaches homeostasis at 3 hours for porous carbon material concentrations of 40 mg/L with 99.35% clearance. With adsorption performance as a top concern, 40 milligrams per liter was determined to be the best dosage for the adsorption mechanism. Given the cost-effectiveness, 30 milligrams per liter was chosen as the appropriate dosage for the adsorption mechanism since it reached a steady in half an hour, implying that a lower temperature would be needed for the adsorption mechanism, as shown in Tables 2 and 3. The link among the testing outcome and the projected ANN result is depicted in Figures 7 and 8.

5. Conclusion

A large majority of current research studies have shown a considerable improvement in the adsorption process of all altered activated carbons when compared to nonmodified, suggesting a tremendous promise for transformed activated carbon in eliminating heavy metals in the industry. Activated carbon has evolved from an intriguing alternative antecedent to a strong particular configuration, with cost-effectiveness and industrialization in consideration. Numerous physiological remodelling approaches for activated carbons have enormous commercial viability. In this research, ANN factors along with hidden neurons, training techniques, and backpropagation were investigated in order to build an ideal ANN structure for predicting adsorption performance. The effects of absorbent particle diameter, adsorbent dosages, and training duration were evaluated on every pharmaceutical reactor core adsorbed efficiency. The optimum adsorption efficiency for acetaminophen was found to be 98 percentage elimination for binary paracetamol adsorption, accordingly. As a consequence, nimesulide particles were linked with acetaminophen molecules throughout binary adsorption to lessen acetaminophen adsorption. As a result, even with the presence of simultaneous and antagonistic relationships, ANN could be utilized to ensure the smooth operation to forecast the adsorption capacity of these medicinal compounds.

Data Availability

The data used to support the findings of this study are included within the article. Further data or information is available from the corresponding author upon request.

Conflicts of Interest

The authors declare that there are no conflicts of interest regarding the publication of this paper.

Acknowledgments

References

[1] J. A. Okolie, S. Savage, C. C. Ogbaga, and B. Gunes, "Assessing the potential of machine learning methods to study the removal of pharmaceuticals from wastewater using biochar or activated carbon," *Total Environment Research Themes*, vol. 1-2, article 100001, 2022.

[2] J. L. Speiser, C. J. Karvellas, B. J. Wolf, D. Chung, D. G. Koch, and V. L. Durkalski, "Predicting daily outcomes in acetaminophen-induced acute liver failure patients with machine learning techniques," *Computer Methods and Programs in Biomedicine*, vol. 175, pp. 111–120, 2019.

[3] A. Spaltro, M. N. Pila, D. D. Colasurdo et al., "Removal of paracetamol from aqueous solution by activated carbon and silica. Experimental and computational study," *Journal of Contaminant Hydrology*, vol. 236, article 103739, 2021.

[4] F. Ahmad, A. Mahmood, and T. Muhmood, "Machine learning-integrated omics for the risk and safety assessment of nanomaterials," *Biomaterials Science*, vol. 9, no. 5, pp. 1598–1608, 2021.

[5] M. M. Sabzehmeidani, S. Mahnaee, M. Ghaedi, H. Heidari, and V. A. L. Roy, "Carbon based materials: a review of adsorbents for inorganic and organic compounds," *Materials Advances*, vol. 2, no. 2, pp. 598–627, 2021.

[6] L. Spessato, K. C. Bedin, A. L. Cazetta et al., "KOH-super activated carbon from biomass waste: insights into the paracetamol adsorption mechanism and thermal regeneration cycles," *Journal of Hazardous Materials*, vol. 371, pp. 499–505, 2019.

[7] X. C. Nguyen, Q. V. Ly, T. T. H. Nguyen, H. T. T. Ngo, Y. Hu, and Z. Zhang, "Potential application of machine learning for exploring adsorption mechanisms of pharmaceuticals onto biochars," *Chemosphere*, vol. 287, article 132203, Part 2, 2022.

[8] A. Almuntashiri, A. Hosseinzadeh, U. Badeti et al., "Removal of pharmaceutical compounds from synthetic hydrolysed urine using granular activated carbon: column study and predictive modelling," *Journal of Water Process Engineering*, vol. 45, article 102480, 2022.

[9] J. L. S. Fagundez and N. P. G. Salau, "Optimization-based artificial neural networks to fit the isotherm models parameters of

aqueous-phase adsorption systems," *Environmental Science and Pollution Research*, vol. 29, no. 53, pp. 79798–79807, 2022.

[10] G. Alam, I. Ihsanullah, M. Naushad, and M. Sillanpää, "Applications of artificial intelligence in water treatment for optimization and automation of adsorption processes: recent advances and prospects," *Chemical Engineering Journal*, vol. 427, article 130011, 2022.

[11] W. Guo, J. Liu, F. Dong et al., "Deep learning models for predicting gas adsorption capacity of nanomaterials," *Nanomaterials*, vol. 12, no. 19, p. 3376, 2022.

[12] C. M. Kerkhoff, K. . Boit Martinello, D. S. P. Franco et al., "Adsorption of ketoprofen and paracetamol and treatment of a synthetic mixture by novel porous carbon derived from Butia capitata endocarp," *Journal of Molecular Liquids*, vol. 339, article 117184, 2021.

[13] P. S. Pauletto, S. F. Lütke, G. L. Dotto, and N. P. G. Salau, "Adsorption mechanisms of single and simultaneous removal of pharmaceutical compounds onto activated carbon: isotherm and thermodynamic modeling," *Journal of Molecular Liquids*, vol. 336, article 116203, 2021.

[14] P. Verma, J. Godwin Ponsam, R. Shrivastava et al., "Predicting carbon residual in biomass wastes using soft computing techniques," *Adsorption Science and Technology*, vol. 2022, article 8107196, pp. 1–8, 2022.

[15] M. Pardakhti, E. Moharreri, D. Wanik, S. L. Suib, and R. Srivastava, "Machine learning using combined structural and chemical descriptors for prediction of methane adsorption performance of metal organic frameworks (MOFs)," *ACS Combinatorial Science*, vol. 19, no. 10, pp. 640–645, 2017.

[16] A. Abdolali, H. H. Ngo, W. Guo et al., "Characterization of a multi-metal binding biosorbent: chemical modification and desorption studies," *Bioresource Technology*, vol. 193, pp. 477–487, 2015.

[17] X.-Y. Huang, X.-Y. Mao, H.-T. Bu, X.-Y. Yu, G.-B. Jiang, and M.-H. Zeng, "Chemical modification of chitosan by tetraethylenepentamine and adsorption study for anionic dye removal," *Carbohydrate Research*, vol. 346, no. 10, pp. 1232–1240, 2011.

[18] M. Haroon, L. Wang, H. Yu et al., "Chemical modification of starch and its application as an adsorbent material," *RSC Advances*, vol. 6, no. 82, pp. 78264–78285, 2016.

[19] Q. Chen, X. Zheng, L. Zhou, and M. Kang, "Chemical modification of starch microcrystals and their application as an adsorbent for metals in aqueous solutions," *BioResources*, vol. 14, no. 1, pp. 302–312, 2019.

[20] D. Schwantes, A. C. Gonçalves, G. F. Coelho et al., "Chemical modifications of cassava peel as adsorbent material for metals ions from wastewater," *Journal of Chemistry*, vol. 2016, Article ID 3694174, 15 pages, 2016.

[21] P. S. Pauletto, S. F. Lütke, G. L. Dotto, and N. P. G. Salau, "Forecasting the multicomponent adsorption of nimesulide and paracetamol through artificial neural network," *Chemical Engineering Journal*, vol. 412, article 127527, 2021.

Research Article

Bar Adsorbent Microextraction with Carbon-Based Sorbent Layers for the Identification of Pharmaceutic Substances

S. Thenmozhi,[1] V. Gowri,[1] K. S. Vinayaka,[2] Ravindra Pratap Singh,[3] V. M. Vel,[4] Kareem Yusuf,[5] Ahmed muteb Aljuwayid,[5] Md Ataul Islam,[6] and Abdi Diriba [7]

[1]*Department of Civil Engineering, St. Joseph's College of Engineering, OMR, Chennai, 600119 Tamil Nadu, India*
[2]*Department of Botany, Sri Venkataramana Swamy College, Bantwal, Dakshina Kannada, Karnataka 574211, India*
[3]*Department of Mechanical Engineering, GLA University, Mathura 281406, India*
[4]*Department of Mechanical Engineering, School of Technology, Glocal University, Delhi-Yamunotri Marg, Uttar Pradesh 247121, India*
[5]*Department of Chemistry, College of Science, King Saud University, Riyadh 11451, Saudi Arabia*
[6]*School of Health Sciences, Faculty of Biology, Medicine and Health, University of Manchester, Manchester, UK*
[7]*Department of Mechanical Engineering, Mizan–Tepi University, Ethiopia*

Correspondence should be addressed to Abdi Diriba; abdi@mtu.edu.et

Thirteen carbon materials were tested as sorbent layers in bar adsorbent microextraction (BAμE) to monitor hint amounts of 10 common pharmaceutical compounds (PhCs) in surface and groundwater matrices such as surface and groundwater, saltwater, spring water, and sewage. The persistence of trace amounts of three organophosphate insect repellent and cis and trans permethrin (PERM) in water quality matrices is suggested using bar adsorptive microextraction in conjunction with microliquid dissolution accompanied by significant volume injection-gas chromatography-mass spectroscopic analysis able to operate in the particular ion monitoring acquisition mode. Using BAμE to compare several sorbent coatings (five porous carbon and six polymers), it was discovered that activated carbon (AC2) was the optimum compromise among specificity and effectiveness. 17-estradiol, estrone, sulfamethoxazole, diclofenac, triclosan, gemfibrozil, 17-ethinylestradiol, mefenamic acid, and clofibric acid were chosen as system drugs to represent different treatment groups. Despite their lower porosity, statistics revealed that low-T-activated hydrochars, made from carbohydrates and a eutectic salt mixture at constant temperature (e.g., 180°C) and autogenerated pressures, could compete at the top level commercially carbonaceous materials in this purpose. These L-T-activated hydrochars had the best overall recovery (between 21.8 and 83.5 percent) for the simultaneous analysis of ten targeted PhCs with very different physical and chemical possessions, utilizing higher-efficiency liquid chromatography diode array identification.

1. Introduction

In recent decades, the main focus of the research has changed away from traditional pollutants and toward emerging pollutants, which pose a threat to the aquatic environment and health. Pharmaceutical and personal service goods (PPCPs) are a type of developing contaminant that has turned into a global environmental issue. Human and veterinary medications were used to treat or prevent diseases in humans, as well as antiseptics and perfumes for personal care products like lotion, body cleansers, and sun protection, which are all found in pharmaceutical compounds. Most PPCPs can persist in sewage treatment plants if they are very slightly altered or even unaltered. Because of the continual discharge, they are semipersistent in the ecosystem and could be hazardous to nontarget creatures [1]. Environmentalists have a tough time analyzing PPCPs in various environmental specimens because of their low amounts in the environment and the complexity of the sample matrices. Empirical methodologies and approaches frequently stymie

research on the occurrence and distribution of PPCPs. For the removal of PPCPs, qualitative evaluation procedures, such as liquid-phase microextraction (LPME), solid-phase microextraction (SPME), and solid-phase extraction (SPE), have already been used. Automated analysis chemical sample collection procedures have been characterized by reduction and high throughput in recent years to improve selectivity and sensitivity, particularly for the determination of traces. Sorptive analytical techniques have already been widely developed and employed to identify the highest range of organic solute molecules in a variety of matrices. Solid-phase extraction, solid-phase microextraction (SPME), and, more lately, in the process of getting ready for phase separation, one of the most popular sorptive enrichment procedures utilized is called stir bar sorptive extraction, or SBSE for short. Sorptive extraction is the foundation of this technology. During this process, the solutes are extracted into a polymer, such as polydimethylsiloxane (PDMS), which is coated on a stir bar. It was created as a one-of-a-kind separation and purification analysis focusing on another principle such as SPME, and it is currently a widely utilized filter for leftovers of important organic pollutants in wastewater and a range of matrix [2].

In research applications, carbon-based nanoparticles have already been widely employed. Fullerenes, nanohorns, carbon nanofibers, nanotubes, and graphene, as well as their chemically processed equivalents, have all been explored as sorbents in sample processing. Noncovalent connections, such as stacking, hydrogen bonding, van der Waals' forces, hydrophobic interactions, and electrostatic forces, are possible thanks to the unique architectures of carbon-based nanoparticles. Carbon-based nanoparticles offer wide numerous applications in various sample preparation procedures, according to the aforementioned capabilities [3]. Although the rationale for selecting one allotrope over the other is always being debated, there is a vast range of carbon-based compounds that can be used in analytical techniques. Carbon nanotubes (CNTs) have shown considerable promise in a wide range of processes and applications since their first announcement in 1991. Physical and chemical qualities that are unmatched by almost all metal elements have been achieved by combining architectures, sizes, and topology. CNTs are indeed being recognized as an effective formulation in matrix-assisted laser dissolution ionization, as stationary phases in separation processes (capillary electrochromatography, high-efficiency liquid chromatography, gas chromatography, and capillary electrophoresis), and as new SPE materials in chemical analysis. In terms of this last use, the amount of research has expanded dramatically during the last two decades [4]. Ketamine (KET) was created in 1962 as a less hazardous alternative to phencyclidine (PCP), an anesthetic that had established a reputation for causing illusions and insanity. KET is an ideal drug for short-term medical processes in animals and in human medical treatment, particularly in children, advantages of fast onset and short sustained release with only subtle aerobic and resistance depressive episodes in contrast to other general anesthetics and the ability to inhale to maintain the anesthetic state [5]. The most significant drawback of KET is that it

has the potential to induce visual hallucinations that are analogous to those brought on by the use of lysergic acid diethylamide (LSD). Memory loss and ulcerative cystitis are two of the most serious side effects of using ketamine for recreational purposes. Memory loss, mood changes, respiratory distress, trouble with the bladder and urination, high heart rate, seizures, overdose, and other adverse effects may occur in the long term as a result of this medication. As a consequence, it was overused by medical workers at first, but it gradually gained popularity among youthful users during dance and rave gatherings.

Because of the widespread use of medications, their existence in the atmosphere has been documented in recent decades becoming a serious concern. Pharmaceuticals are discharged into the atmosphere in either their unmetabolized or metabolized form, mostly by homes, sewage treatment plants, institutions, industrial sites, and veterinary services. Based on the chemical features of each medicine, they all have polar features that make them easier to introduce into the water habitats, resulting in the poisoning of freshwater environments. Nonsteroidal anti-inflammatory drugs (NSAIDs), such as diclofenac (DIC), ketoprofen (KET), naproxen (NAP), and mefenamic acid (MEF), are one of the most widely used classifications of pharmaceutical drugs because they have a wide range of therapeutic characteristics, including antipyretic, analgesic, and anti-inflammatory characteristics [6]. Diuretics are still another category of pharmaceutical medications that are used to treat cardiovascular disease, high blood pressure, and edema, in addition to the purposes of doping, such as furosemide (FUR), despite the fact that the use of these drugs is prohibited in athletic competition. Because diuretics can produce rapid weight loss and can operate as masking agents both during and outside of competition, they are prohibited in all sports. Diuretics can also cause rapid weight loss. Mebeverine (MEB) is a musculotropic chemical element that operates on the smooth muscle cells of the digestive organs and is particularly effective against colonic spasms. Although the potential for these substances to cause harm to the ecosystem is unknown, endocrine disruption and the development of drug-resistant bacteria have indeed been described. Concerns about pharmaceutical abuse, forensic and sports doping instances, and drugs not being entirely removed by wastewater treatment plants (WWTPs) abound [7]. Moreover, urine is an underlying genetic structure to be analyzed for toxicants and therapeutic approach measurement reasons in biology and medicine, for a precise clinical explanation of metabolomic data in humans and other animals and technical fault of endocrine glands and crucial identification of pituitary tumors, that could be affiliated with many illnesses such as anorexia nervosa, breast cancer, and pseudohermaphroditism. The steroid hormones are produced in the human body by endocrine glands in free or conjugated form, and their primary method of metabolism of dietary in the human body is glucuronidation in the liver and excretion in urine; however, sulfated compounds have been reported in other instances [8]. Bioreactors, such as the enzyme-linked immunosorbent assay (ELISA), are quick and inexpensive for testing anabolic hormones, but they lack

specificity for the determination of trace and frequently produce a false-positive result. Because physiological tests lack sensitivities and efficiency, extraction methods became the analytical methods of choice, as they allow for the precise selection of relevant compounds of interest and are known to be particularly sensitive analytic methods. Bar adsorptive extraction (BAE), a new spontaneous emulsification technology that works in the static floating sample method, was launched in recent years. BAE has the benefit of being adjustable to more appropriate nanostructured adsorbents (e.g., polymers (Ps) and activated carbons (ACs)) depending on the nature of the operation. This innovative analytical approach has proven to be a wonderful alternative to the traditional sorption-based approaches for determining the concentration of medium polar-to-polar chemicals in aqueous fluids with good efficacy in various types of matrices [9]. New enhancements to the BAE methodology have recently been made, including shrinking the analysis equipment, reducing the liquids desorption quantity to the L level, and removing the solution switch phase. Furthermore, miniaturization of the BAE device utilizing a less sorptive stage produced excellent analytical results, while reducing the solvent enables a more environmentally responsible approach while maintaining high efficacy, making the analysis technique faster and more efficient.

Within that respect, and given the importance of carbonaceous materials as micropollutant adsorption process, it is worth considering the ability of different sources of carbon substances, such as carbohydrate-derived hydro chars and their enabled compadres, as coating stages for efficient removal of a variety of PhCs. Hydrochars are made by hydrothermally carbonizing carbohydrate precursors with water as the medium during mild process parameters. Hydrochars are essentially nonporous solids with a chemical nature rich in oxygen functional groups, as opposed to carbonaceous materials made using traditional activation methods. Before gas or liquid chromatographic, most methodological approaches described for minimal level measurement of PhCs in surface and groundwater matrix have included a sample preliminary design. Miniaturized passively sorption-based technologies, such as stir bar sorptive extraction (SBSE), bar adsorptive microextraction (BAE), and solid-phase microextraction (SPME), have recently emerged as perhaps the most relevant for determining polar to nonpolar chemicals in an aqueous medium. BAE is based on the implementation of this method of floating sampling technique, which allows for the selection of the optimal sorbent coating to ensure high effectiveness just on targeted PhCs [10]. The assessment of trace compounds in complicated construction collections has become increasingly significant in recent years because of the possible damaging consequences of trace components of the environment, food, drugs, and other environments on humans, animals, and ecosystems. These materials, nevertheless, are exceedingly complicated, and the solutes are present at minute levels, making analysis extremely challenging. As a result, the basic premise of this methodology procedure has become a significant aspect of the analysis to enrich trace components, increase method sensitivities, and remove interference compounds [11]. PE is among the most widely utilized specimen processing techniques for preconcentrating analytes in a wide range of samples because of its characteristics of high enriched uranium component, low organic solvent consumption, high recovery, low cost, rapid phase separation, and the capacity to couple with various identification techniques in either an online or offline mode. It is common knowledge that the two most important considerations to make when utilizing SPE are the development of an effective technique and the selection of an adequate sorbent. In recent years, the key problems in terms of SPE techniques have been reducing the amount of experimental solvent used and the formation of toxic waste, saving employees' time and labour, bringing down expenses, and improving the efficiency of analyte separation. Verifying that the analytical system is operating appropriately is the first stage in the process of resolving issues relating to recovery or reproducibility in an experiment. Many residual constituents have indeed been extracted from various complicated samples employing innovations such as solid-phase microextraction (SPME), magnetic solid-phase extraction (MSPE), and dispersive solid-phase extraction (DSPE) using CNTs as sorbent materials [12].

Multiresidue research using gas chromatography is the most comprehensive chromatography approach for analyzing contaminants from water in samples collected (GC). Many of the chemicals of focus on environmental materials are likely to be absorbed and degraded on the column or injection, necessitating the use of volatile, high thermal stability molecules. As a result, investors can trade reactions that are required. Ultra-high-performance liquid chromatography (UHPLC) and liquid chromatography (LC) are currently being employed in conjunction with spectrometry (MS) to detect nontarget species solutes that are extremely polar and nonvolatile and have high molecular masses, rendering them incompatible with GC. As a result, a single research run can be used to evaluate or identify both targeted and nontargeted solutes. The use of a liquid chromatography-mass spectrometer, also known as an LC-MS, in conjunction with a sample preconcentration and clean-up stage is recommended due to the LC-high MS's specificity and sensitivity. In comparison to HPLC, the LC-MS method that was presented was more rapid, sensitive, and specific. In contrast to HPLC, LC-MS can be utilized in the analysis of mixtures that are only partially resolved. Exhaustive conventional pretreatment procedures such as liquid-liquid extraction (LLE) and solid-phase extraction (SPE) are being utilized to separate and preconcentrate diverse families of analytes from aquatic and terrestrial ecosystems [13]. Due to the necessity to reduce solution quantities and avoid utilizing harmful organic solvents throughout LLE and SPE, existing preconcentration techniques have been modified to develop innovative methodologies. As a result, nanotechnology becomes a critical component in achieving these goals, and new approaches have been created. Microextraction procedures are nonexhaustive preconcentration techniques that use a very small quantity of the extraction stage (in the order of a few liters) in comparison to the sample. Solid-phase microextraction (SPME) or solvent microextraction is used to recover particles from a

slight quantity of a solid or semisolid polymeric material (SME). Due to their significant structural variations, both procedures have a lot in common because they are both spontaneous emulsification methods. Due to their simplicity, efficiency, low cost, minimum extraction temperature, and outstanding ability to clean up specimens, both procedures are viable options for sample processing [14].

In the development of computational techniques, the preconcentration stage is critical. Typically, this stage takes up the majority of the time inside the investigation, with the accuracy and quality of the results being highly reliant on the procedure used to prepare the samples. Some traditional procedures, such as liquid-liquid extraction (LLE) and solid-liquid extraction (SLE), have certainly been frequently used for regular investigations with excellent results. However, there are several drawbacks, such as the usage of massive quantities of toxic organic liquids and the amount of time it takes for the extraction methods [15]. Furthermore, in LLE, achieving restricted sample preparation parameters and the likelihood of emulsion is a critical barrier to achieving the extraction accuracy and effectiveness of the assessment. Obtaining ecologically responsible analytical techniques becomes a key priority in a lot of labs, in addition to all these important challenges. As a result of this tendency, various spontaneous emulsification technologies have already been presented as viable "green" alternatives to the previously mentioned traditional approaches. These methods are useless organic substances and materials, and they enable the accurate and consistent identification of many analytes in a range of matrices utilizing an appropriate and efficient methodology.

2. Related Works

The advancement, efficiency, verification, and implementation of a novel methodical technique for the perseverance of the six most common tricyclic antidepressant drugs (TCAs; trimipramine, mianserin, amitriptyline, imipramine, mirtazapine, and dosulepin) in urine matrix were determined, utilizing bar adsorptive microextraction technique (BAμE). For the first time, researchers combined the latest generation spontaneous emulsification gadgets encased with suitable polymers, sorbent phases, and novel carbon materials compiled from biodegradable polymer squandering with large-volume injection-gas chromatography-mass spectroscopic analysis functioning in selected ion monitoring mode. Preliminary tests on sorbent coverings revealed that the polymeric phases function far better than the studied biosorbents, which were ineffective for use in spontaneous emulsification procedures. The limit of detection obtained for the six TCAs varied from 0.3 to $1.5\,g\,L^{1}$ utilizing BAμE covered with C_{18} polymers under optimum experimental parameters, and weighted linear regression analysis yielded outstanding linearity ($r^2 > 0.9961$) between 10.00 and $1000.00\,g\,L^{-1}$. The proposed mathematical scientific method produced appropriate matrix effects (90.4–112.9 percent, RSD 13.8 percent), high recovery (92.4–111.6 percent, standard deviation 12.4 percent), and phenomenal overarching operational efficiencies (ranging from 84.8 percent to 124.4

percent, standard deviation 13.8 percent). The six TCAs were successfully screened in real urine samples using the designed and verified technique. In comparison to existing microextraction-based approaches, the suggested investigation system demonstrated to be an environmentally responsible and user-friendly way of monitoring trace amounts of TCAs in complicated urine composites. The major drawback of the research is only a limited amount of samples could be analyzed in the bar adsorptive microextraction application on determining the tricyclic antidepressants in a urine sample which is proposed by [1]. Pesticides are widely used in various fields to increase crop productivity by preventing pests from wreaking havoc. Triazine insecticides are a class of compounds that are applied frequently. They are distinguished by the presence of a modified C3H3N3 heterocyclic ring. Triazine pesticides can be harmful to both persons and the aquatic resources they come into contact with as a result of their high level of toxicity and the toxic effect they generate. Triazines can be moderately irritating to the eyes and cause only slight irritation to the skin. The amount of these chemical components in samples collected, on the other hand, is very low. Furthermore, additional substances present in water specimens could obstruct the detection of triazine herbicides. For this reason, it is critical to establish preconcentration methodologies for the preconcentration of the target molecule as well as appropriate sample cleanup. Liquid-phase and solid-phase microabstraction, dispersive solid-phase abstraction, stir bar fabric phase sorbtive extraction, magnetic solid-phase extraction, and sorbtive abstraction are only a few of the new extraction methods and miniaturized extraction methods that have recently been made. Researchers hope to address current developments in the separation of triazine pesticides from environmental water samples in this study. Novel preconcentration procedures and novel reducing agents developed for sorbent-based separation processes will be highlighted. The precision and sensitivity are very low when compared to other methods, and this is the major limitation of advanced extraction of triazine herbicides from a specimen of water [16].

The determination of this literature review is to expose readers to several ways of extracting vitamins using composites of detailed way levels. The most creative and fascinating preconcentration procedures dedicated to vitamin separation are critically described in research papers published in the recent five years. Only 40% of research in the last five years on vitamin assessment in the clinical and pharmaceutical sectors used some new or green specimen processing techniques. The lowering of solvent amounts and specimen turnaround times is, nevertheless, a widespread tendency. In the medical and pharmacological domains, the massive potential of spontaneous emulsification methods depending on nanostructures and esoteric solvents is yet to be completely realized. In light of the high cost of carbon-based nanoparticles, approaches for the separation of liquids using membranes that are based on neoteric liquids are likely to become more efficient for specimen preparation in the near future. When two liquids or gases that are miscible are separated by a thin gas or liquid film in a liquid membrane, the barrier that is generated by this film determines

the amount of mass transfer that occurs between the two phases. These extraction methods are very important for vitamin research because of their low cost, simplicity, environmental friendliness, speed, and high intangible resources. The major drawback of the research is that it is time-consuming when compared to other methods [10]. Safety-related researchers have very few alternatives for analyzing and processing the hazards due to the usage of a substance that has been recognized as a particular kind of explosive proliferation by the Yoshida association. To estimate explosive speed while necessitating further experimental results, oxygen equilibrium computations, the rule of 6, and an exploding carbonyl groups list are routinely used as sustainable solutions and statistically valid techniques. A full UN Movement of Carriage Of Goods testing regime, on the other hand, necessitates at least 2 kg of materials for the first experimental series, an exorbitant quantity that is also rarely available in starting pharmaceutics. The O.R.E.O.S. approach, which integrates the three classic techniques for testing explosive characteristics with the onset of disintegration estimated by differential scanning, has indeed been created. The Yoshida association has indicated recognized energy substances as possibly capable of explosion proliferation, and this new assessment has indeed been demonstrated to be useful at categorizing substances in a scale-dependent approach. The tool can be tailored to any organization's current guidelines for dealing with functional materials. This evaluation must be useful to both pharmaceutical property developers and research institutions as a way to define substances that may require significant testing before being scaled up or to guide teamwork to better options. To simplify the process of obtaining such essential data, a brief discussion of the challenges connected with the transportation for the UN Series Assessment is also provided. Thus, the volatile hazard detection in the medicinal procedure based on the novel screening method and workflow failed to provide a proper accuracy rate and also consumes a large amount of time [1].

Solid-phase microextraction (SPME) is a preparative technology that is constantly evolving and has a broad array of applications. The type of fiber coating used in this process is critical for removal efficiencies. Commercial coatings now on the market have some limitations that have been overwhelmed by the creation of new coatings based on innovative materials, which have enhanced extraction selectivity, competence, and constancy. Medicinal and personal care products (PPCPs) are among the most common developing pollutants, yet some research suggests that these substances can have negative health effects. Because there are presently no formal monitoring guidelines for these chemicals, analytical techniques that allow their detection in organic pollutants must be developed. Because of the intricacy of samples collected and the small concentration values of these substances, preparative procedures effective in eliminating disruptions and preconcentrated present in the sample are required, and SPME is a potential option for doing so. The latest breakthroughs in SPME with traditional and innovative coatings, as well as its application for PPCP measurement in the samples collected, are reviewed in this chapter. However, more investigation into the detection and characterization of these molecules is necessary for the implementation of solid-phase microextraction for the extraction of environmental pharmaceuticals [7].

3. Material and Methods

AnalaR NORMAPUR provided glucose, fructose, and sucrose and provided 99 percent lithium chloride (LiCl), and Acros Organics provided 98 percent zinc chloride (ZnCl), carbamazepine (99.0%), triclosan (97.0%), mefenamic acid (98.5 percent), and diclofenac sodium salt (99.0%). Sigma-Aldrich provided 17-estradiol (98.0 percent), estrone (99.0 percent), clofibric acid (98.0 percent), sulfamethoxazole (98.0 percent), gemfibrozil (98.5 percent), and potassium carbonate (K_2CO_3, 99 percent). Riedel-de Haen provided 17-ethinylestradiol (98.0 percent) [17]. The chemical compositions of the PhCs investigated, as well as their solubility ratios, log KO/W, and pKa, are shown in Figure 1. The solvents employed were HPLC-grade alcohol (MeOH, 99.9%) and acetonitrile (Acetone, 99.9%) procured. Merck Millipore provided 99.5 percent sodium chloride (NaCl), while AnalaR (BDH chemicals) provided 98.0 percent sodium hydroxide (NaOH) pellets. Pancreatic provided 37 percent hydrochloric acid (HCl), 99.5 percent acetic acid, and 85 percent potassium hydroxide (KOH). Merck supplied the acrylic acid (AA, which has a purity of 99 percent). All of the different chemicals and volatile compounds were employed without further purifying, and the Milli-Q water yielded an ultrapure water process of filtration.

3.1. Characterization and Synthesis of Carbon Factor. Varied synthesis techniques were employed to create nonporous hydrochars, along with reactivated hydrochars and stimulated carbons with medium, acidic/basic surface composition and higher surface areas, and various topologies, to achieve substances with a distinct texture and surface morphology. Hydrothermal carbonization (HTC) of carbohydrates was used to make the carbon hydrochars: 16 mL of 1.6 mol L^{-1} glucose or sucrose concentrations were placed in a sterilizer and warmed at 190°C for 5 hours. As per the carbohydrate precursor (glucose or sucrose, accordingly) and HTC temperatures, these specimens are classified as HG/190 or HS/190 [18]. A similar process was used to make enhanced sucrose-derived hydrochars, but acrylamide (i.e., 27.14 and 7 wt.%) was added to the sucrose aqueous medium. The improved hydrochars were given the designation HSAAx/190, with x denoting the proportion of acrylic acid present. Chemical activation of the high-T-activated hydrochars was done as previously stated. HS/H800 and HS/C800 high-T-activated hydrochars were made by activating 2 g of sucrose-derived hydrochars with 5 g of K_2CO_3 and potassium hydroxide for 1 hour at 900°C, respecively.

The investigation on glucose has an impact on the production of low-T-activated hydrochars. In a nutshell, 11.26 grams of eutectic zinc chloride/lithium chloride salt mixture was ground and homogenized in an agate filling; then, 4.6 grams of a cellulose precursor (F—fructose, S—sucrose, and G—glucose,) was introduced, and the combination was
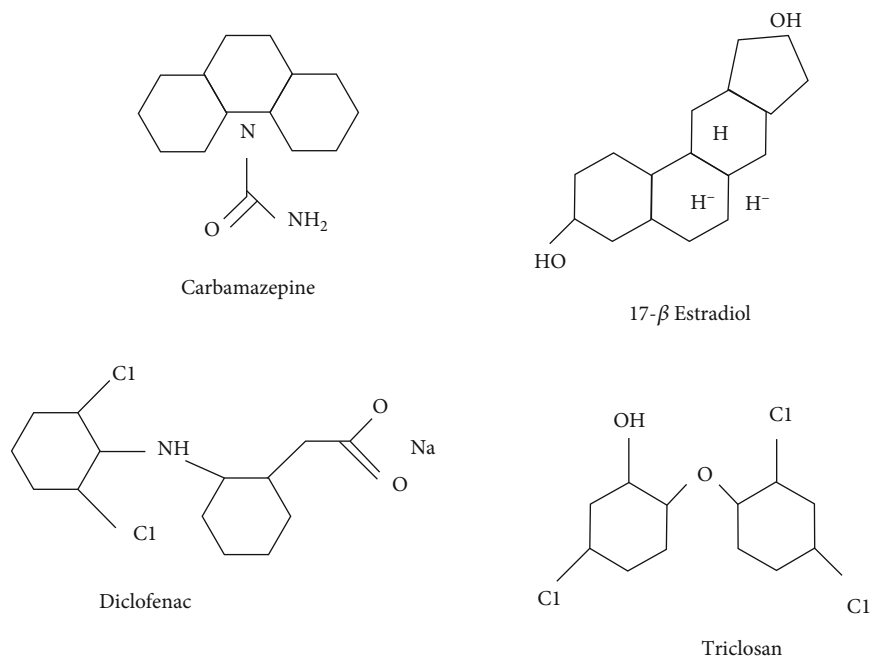
FIGURE 1: Different chemical structures utilized.

ground until a homogeneous sample was obtained in a Teflon-lined stainless steel sterilizer, the carbohydrate:eutectic salt mixture was injected (35 mL). The sterilizer was locked, agitated forcefully, and positioned in an oven at 180°C for 17 hours after adding 2.3 mL of ultrapure liquid [19]. After evaporation to ambient conditions, the low-T-enabled hydrochars were thoroughly soaked in purified liquid until no sodium hypochlorite anions could be detected (i.e., silver chloride is added, and there is no rainfall). The materials were washed, dehydrated at ambient pressure, crushed, and sieved to retain particulates with diameters of less than 0.148 mm (mesh 100). The low-T-activated hydrochars were designated as Hy/LiZn180, with y denoting the carbohydrate precursors (HF/lithium and zinc180, HG/lithiumzinc180, and HS/lithiumzicn180, respectively) and "lithiumzinc180" denoting the eutectic mixture and synthesis temperatures. Using saccharides rather than biomass alone as a source of precursors for carbon compounds has many benefits, including the absence of emissions, the repeatability of the compounds, and the command over the morphology of the product. Monosaccharides are the simplest form of carbohydrates since they cannot be broken down by hydrolysis into lesser forms of carbohydrates. All of these are important factors in the production of high-purity carbon adsorbent materials, which are necessary for efficient chemical microextraction [19]. Steam activation of enlarged corkboard grains at a semi-industrial level was carried out as per the methodology used to produce the activated carbon material Cork/S800. In contrast, the profitable ground-activated carbon (PAC) products CN1 from Cabot-Norit (Com/CN1, provided) and R from Riedel-de Haen were evaluated. Chemical activation with H_3PO_4 was used to make the commercial activated carbon Com/CN1. Particle diameters in all carbon compounds

examined are below 0.149 mm on (mesh 100) average [20]. Additional information on the production and description of several of these carbon-based compounds has before been published, and it is included in Table 1 for comparability.

3.2. Carbon Particle Characterization.

Nitrogen gas adsorbents at -196°C in an autonomous volume device from micromeritics were used to analyze the geometric characteristics of carbon-based composites (model ASAP 2010). The materials (60–100 mg) were caused by trauma at 120°C overnight (16 hrs) under suction (compression 10-2 Pa) before Nitrogen adsorption [21]. The A_{BET}, apparent surface area, was calculated from nitrogen gas adsorbate in the p/p0 region of the adsorbent plot, which guarantees an optimistic intercept on the BET plot's ordinates (C greater than zero) and a linear rise of $n^{ads}(2\text{-}p/p^0)$ with p/p^0. The entire pore volume, V^{Total}, was calculated using the Gurvich rule. The isotherm was utilized to determine the micropores utilizing the s technique. The total small pore size, $V^{\alpha Total}$, relates to apertures with a breadth of 2.0 nm; the ultramicropore quantity, $V^{\alpha ultra}$, to holes with a diameter of 0.8 nm; and the super-micropore volume, $V^{\alpha super}$, to holes with a width of 0.8 nm to 2.1 nm.

The surface modification of the substances was evaluated utilizing reversed mass analytical balance and a sympHony SP70P pH meter to determine the pH at zero charges and point of zero charges. The compounds' diffused reflection infra-Fourier transform (DRIFT) spectra were acquired using a Nicolet Magna-IR 560 spectrophotometer equipped with a very sensitive mercury cadmium telluride detectors (MCT-A) operating under cryogenic conditions. The DRIFT technique is a sort of spectroscopy that involves measuring the diffuse reflection of a single pulse of infrared radiation

TABLE 1: Exterior assets of carbon sorbent.

Categories	Carbon particles	Structural assets	External assets (pH point of zero charge)
Hydrochar	Acrylic acid-modified hydrochars[c] (i) HSAA7/190 (ii) HSAA27/190 (iii) HSAA14/190	NP	≈3
	HC[b] (i) HS/190 (ii) HG/190	NP	3
Stimulated carbon	Commercial (i) Com/CN1 (ii) Com/R	Apparent surface area ≈1000 m^2	5.2
	SAC[a]	Area = 750 m^2/g	≥2
Activated hydrochar	High-T-activated hydrochars[d] (i) HS/C800 (ii) HS/H800	Apparent surface area = 1352 m^2/g	≈5
	Low-T-activated hydro chars (i) HG/LiZn180 (ii) HF/LiZn180 (iii) HS/LiZn180	Apparent surface area (HG/LiZn180) = 528 m^2/g Apparent surface area (HF/LiZn180) = 408 m^2/g Apparent surface area (HS/LiZn180) = 488 m^2/g	2.8-3.2

by a sample and then applying a Fourier transform to the spectrum that is acquired from this measurement. Each spectrum was acquired by accumulating 256 scans with a resolution of spectrum range of 2 cm^{-1} in the mid-IR (4000-700 cm^{-1}) spectral band utilizing dusted materials with no KBr additions [22]. The thermal assessment was conducted on 14 mg of material at a constant rate pass-through of mL min^{-1} of nitrogen gas up to 900°C. After 3 hours of exposure to 600°C in the air (50 mL min^{-1}), the quantity of the low-T-reactivated hydrochars was evaluated utilizing a similar apparatus (constant mass).

Monthly, the standard solution combination and individual security solution of each PhC (1,000.0 mg L^{-1}) were individually produced in methanol and maintained at 5°C. In most experiments, the working standard mixture (1.0 mg L^{-1}) utilized for confounding was generated daily in the very same organic liquid. For optical verification, methanol-diluted standard combination solutions were utilized. Samples were gathered around the urban region [23]. Seawater measurements were extracted along the shore, and lake samples of water from an underground lake and tap water specimens were gathered from the public water distribution system. The water samples were taken for the initial solvent evaporation, filtering is done, and the waste-water samples were also collected from different plants. All the specimens are gathered in amber glass vials that are screened with screening paper and stored at -20°C.

4. Bar Absorption Methodology

The BAE gadgets (diameter of 3 mm and length of 7.6 mm) were made internally, as previously stated. The gadgets were incubated at ambient temperature after being constructed in a closed container flask. Before usage, the BAμE electronics were washed with methanal and ultrapure water [24]. Because microextraction bars are comparatively cheap, quick to make, and use very minor quantities of sorbent material coatings, they were thrown after each usage to eliminate any potential contamination. In the BAμE-LD process, a 26 mL volume of a water specimen was placed in a matching glass flask, accompanied by a BAμE device covered with carbon-based material sorbent covering and a traditional Teflon constant agitation bar. The tests were carried out in a multiple access constant agitation plate at ambient temperature for 16 hours at 1,000 rpm (pH 2.0). The gadgets were taken from the specimens with clean tweezers after the extraction method, dehydrated for a few minutes with a lint-free paper, and inserted into a glass vial insertion containing 100 L of ACN before ultrasonic treatment at ambient temperature for one hour [25].

Following LD, the gadgets were withdrawn, 100 L of distilled water was introduced, the vials were mixed thoroughly for 6 s and sealed, and the HPLC-DAD study was applied. The sample preparation technique (SAM) was used to analyze real water specimens, with four stimulation scales reaching from 7.0 g L^{-1} to 105.0 g L^{-1} for all PhCs under investigation and blank tests (no spiking—"zero-point" assays) [26]. Unless otherwise stated, all BAμE-LD tests were repeated three times. The HPLC-DAD samples were analyzed using the same apparatus and technique as previously mentioned in the literature review, with the accompanying alterations [27]. Apparatus stability was determined by infusing different stock keys with concentrations ranging from 10.0 to 30.0 g L^{-1} (according to the chemical) to 5,000.0 g L^{-1}, where correlation ratios (r^2) of more than 0.98 were obtained for the active compounds. Peak areas

TABLE 2: Porous carbon textural properties.

Specimen	V^{total}	A_{BET}	$V^{meso a}$	α_s method			pH
				$V^{\alpha total b}$	$V^{\alpha super d}$	$V^{\alpha ultra c}$	
HS/LiZn180	0.48	488	0.34	0.13	0.13	0	3.2
HG/LiZn180	0.59	530	0.48	0.12	0.12	0	3.1
HF/LiZn180	0.29	406	0.15	0.13	0.13	0	2.8
HS/H800	1.11	1376	0.05	1.09	1.09	0	4.1
HS/C800	0.63	2432	0.02	0.63	0.28	0.34	4.4
Com/R	0.65	965	0.38	0.29	0.19	0.11	6.4
Cork/S800	0.44	618	0.29	0.18	0.08	0	5.2
Com/CN1	0.45	1180	0.69	0.29	0.31	0.11	≥12

[a] denotes the mesopore volume, [b] denotes the overall micropore volume, [c] denotes the ultra-microscope volume, and [d] denotes the super-micropore volume.
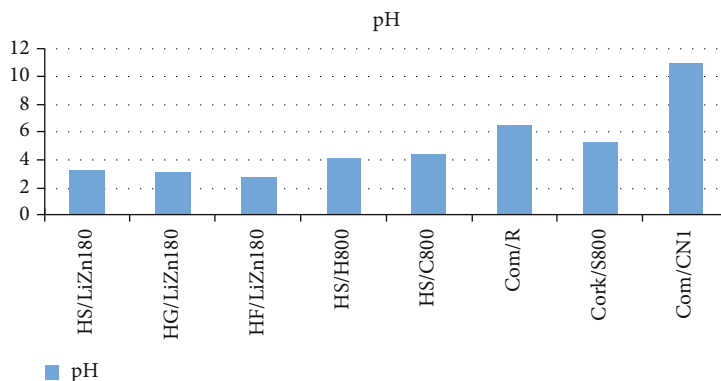
FIGURE 2: pH value of various specimens.

from each test were matched to the top regions of the procedure utilized for the spike to calculate restoration. The susceptibility of the experimental method is demonstrated using detection limits (LODs) and quantitation (LOQs) determined with signal-to-noise ratios (S/N) of 3/1 and 10/1, correspondingly, for all the PhCs under research, which varied at a different range. The accuracy of the equipment was tested by injecting a standard combination ($n = 7$, $01.2\,mg\,L^{-1}$), which resulted in comparative standard deviations of less than 2.8 percent [28].

5. Result and Discussion

Thirteen carbon-based materials were investigated as sorbent coverings again for the extraction of PhCs utilizing 17-estradiol, triclosan, 17-ethinylestradiol, carbamazepine, and diclofenac, as inclusion complexes to maximize the microextraction effectiveness by the BAμE-LD method. As shown in Table 2, these carbon elements are available to describe a broad range of image characteristics (from nonporous to high porosity specimens with A_{BET} up to 2400 m^2/g), surface characteristics (neutral, acidified, or basic, with pH$_{PZC}$ varying from 2 to 11), and morphological characteristics (e.g., pointed, circular, and spongelike). Carbon-based coverings have very different sizes and shapes on the micro-nanoscale, as shown by micrographs [17]. The assessment experiments were performed in triplicate with ultra-pure samples collected and treated at a concentration of

$15.0\,gL^{-1}$. The recovered rates were utilized to monitor the effectiveness of the thirteen carbon-related sorbent substances, which were characterized as the quantity of PhC measured after and back removal with bar adsorptive microextraction equipment. pH value of various specimens is shown in Figure 2.

In Table 2, the extraction effectiveness of the ceramic materials for x PhCs is extremely reliant on either the sort of product or the targeted pharmacological molecule.

In Figure 3, utilizing commercial and lab-made heterogeneous catalysts, the effect of adsorptive selection on the recovered rates of the five PhCs was investigated. In this, C1 to C5 represent the five types of carbon materials such as carbamazepine, 17α-ethinylestradiol, 17β-estradiol, diclofenac, and triclosan.

The nonporous hydrochars in the figure managed to recuperate diclofenac, and though the specimens HG/190 and HS/190 were intelligent to retrieve around 50% of the residual PhCs, the acrylic effects on the chemical hydrochars (HSAAx/190) failed to recover 17-estradiol and 17-ethinylestradiol. The acid low-T-stimulated hydrochars shown in Figure 4 with micro-/mesopore network and medium surface energy, on the other hand, enabled the recovery of the five targeted PhCs. Additionally, with the exception of carbamazepine, the strip that was manufactured using specimen HS/LiZn180 as a coating enabled a recovery that was comparable to that of the finest activated carbon for all PhCs (range from 43 to 80 percent). The advertising
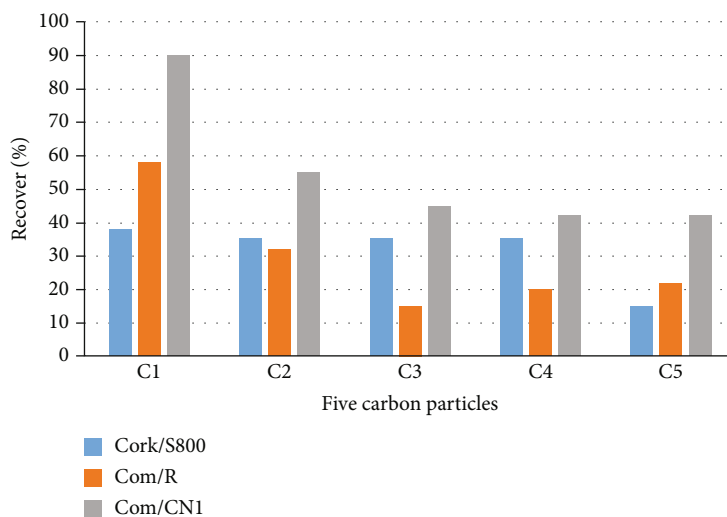
FIGURE 3: Hydrochars based on lab-made carbon materials.
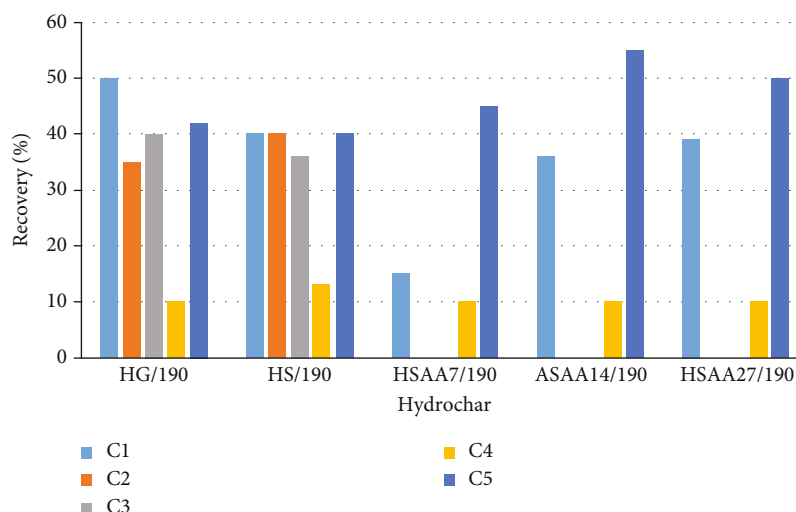
FIGURE 4: High-T-activated hydrochars based on lab-made carbon materials.

specimen Com/CN1 with an adsorbent region greater than 1000 m^2/g, a micro+mesopore framework, and a slightly acidic identity significantly outperforms the steam-enabled cork carbon with a reduced surface region and basic identity, along with the elevated stimulated hydrochars mentioned in Figure 5.

Figures 6–9 show how the qualities of the thirteen composites discussed above affect their effectiveness as sorbent coverings. The four graphs show the relationship among specified carbon characteristics (pH$_{PZC}$ against A_{BET}, V^{micro}, V^{total}, and percent V^{meso}) and the percentage of PhCs removed (17-ethinylestradiol, carbamazepine, 17-estradiol, diclofenac, and triclosan). At small pH$_{PZC}$ attributes related to the proportions of micropores around 20% and 60%, and hence the occurrence of a micro- and mesopore system, the frequency of instances related to deletions in the first quadrant is consistently larger.

The percentage frequency elimination (in quartiles) attuned for the elimination variety of each PhC is shown by circles, with S1 equating to the top 25% deletion and S4

corresponding to the lowest 25% elimination, and circle diameters are directly proportionate to the proportion of occurrence.

It was reasonable to infer that (i) entirely microporous-stimulated carbon atoms with just an acidified exterior perform badly in the recovery of many PhCs, most likely due to irrevocable (good separation with poor back extraction) adsorbent. (ii) Basic stimulated carbons with a micro-mesopore system effectively reduce healing efficiency improvements than acidic contemporaries. (iii) Basic photo-catalysts with a micro-mesopore system produce low retrieval efficiency improvements than acidic contemporaries. To summarize, these findings suggest that when selecting an appropriate carbon coated for BAμE-LD/HPLC-DAD to guarantee good recovery, reducing agents with a well porous assembly in the micro- to mesopore region, as well as acidic functional group, must be considered (i.e., phenol and a carboxylic acid, see DRIFT spectra information in sympathetic data). These carbon-based
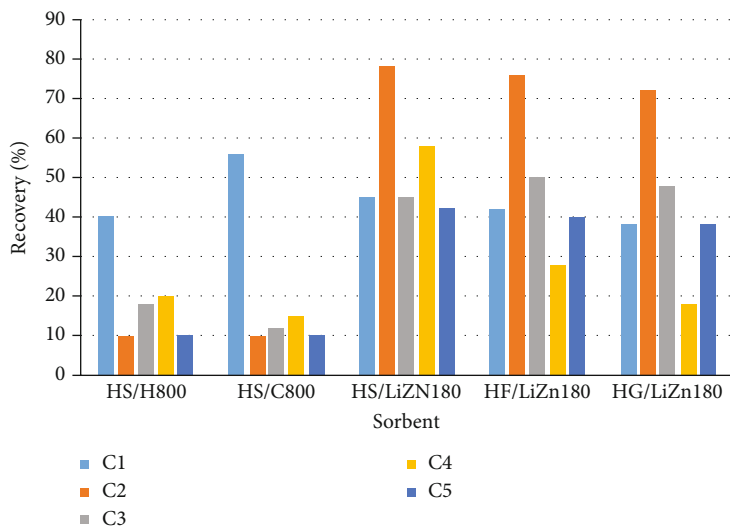
FIGURE 5: Sorbent Coating obtained by BAμE.
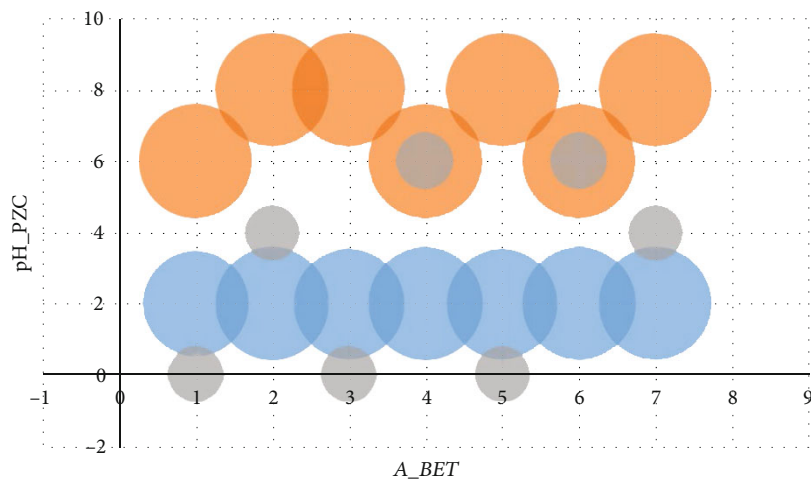
FIGURE 6: Point-of-zero charge vs. BET.
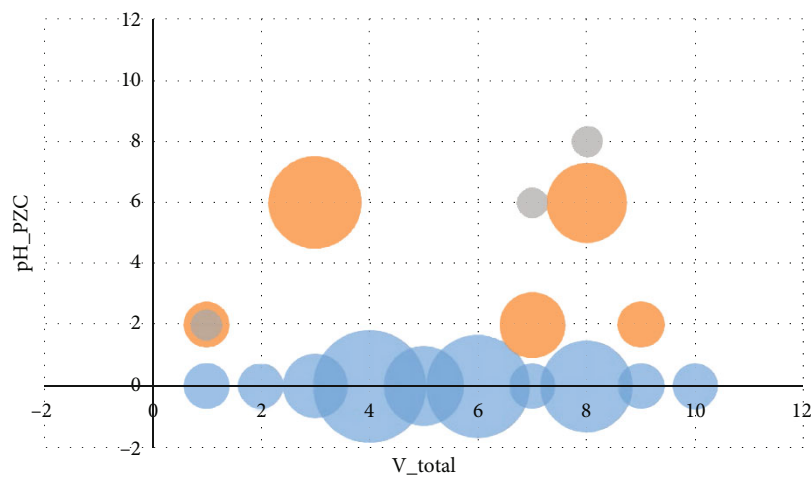
FIGURE 7: Total pore volume.
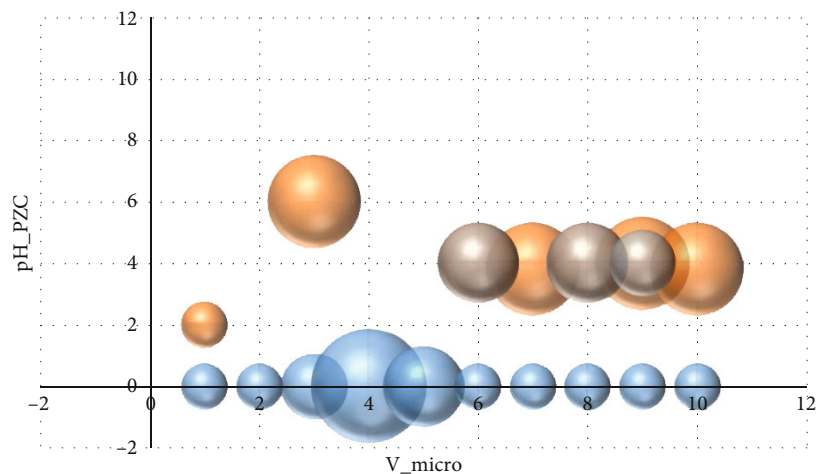
FIGURE 8: Micropore volume percentage.
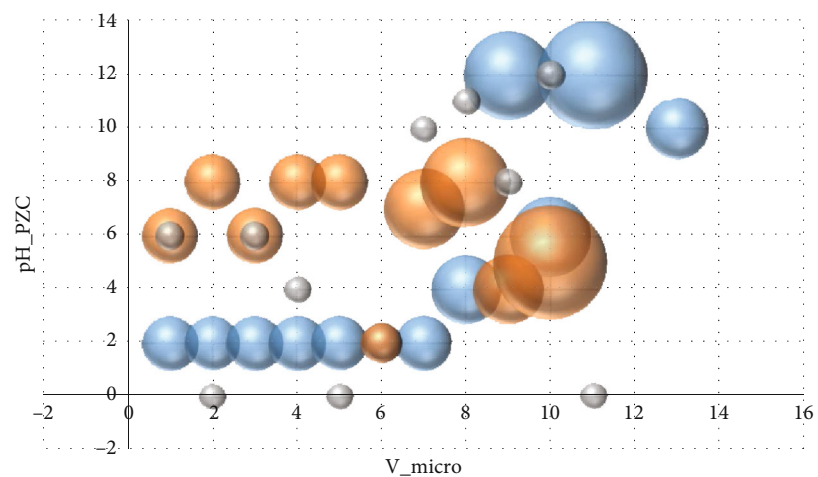
FIGURE 9: Mesopore volume percentage.
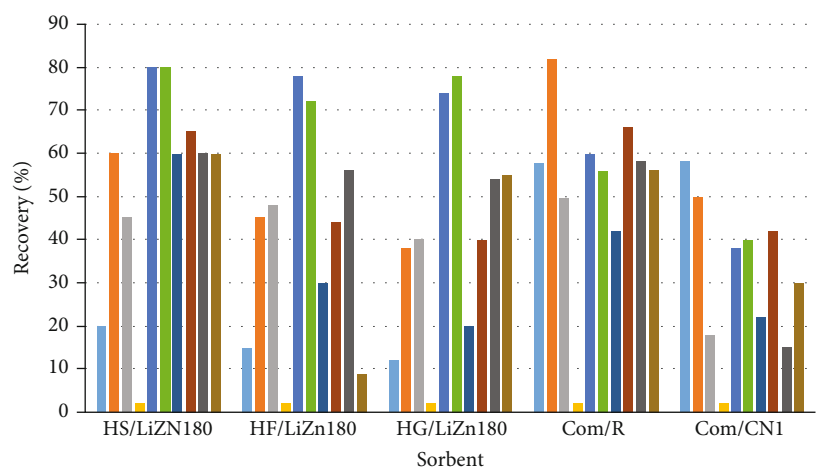
FIGURE 10: Sorbent selective effect.

materials were subsequently investigated as sorbtive coverings for the extraction of ten PhCs and compared against commercial PACs given these partial estimates for the low-T-activated hydrochars with a total of five objectives mentioned in Figure 10. As can be shown, neither of the composites was able to restore clofibric acid underneath the evaluated laboratory conditions, despite the recovery of close to 50% for the other strong acid chemicals [17].
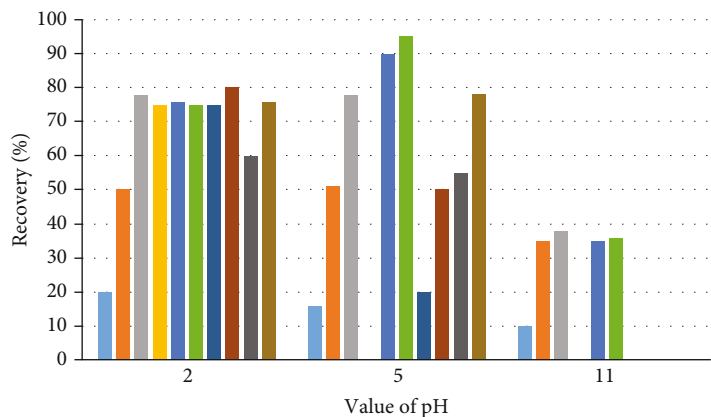
(a)
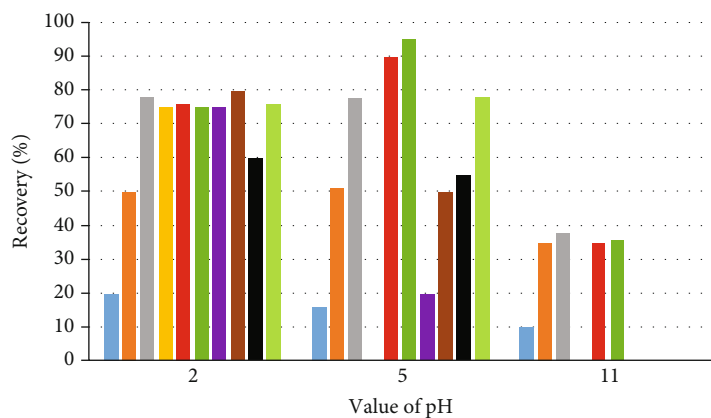
(b)
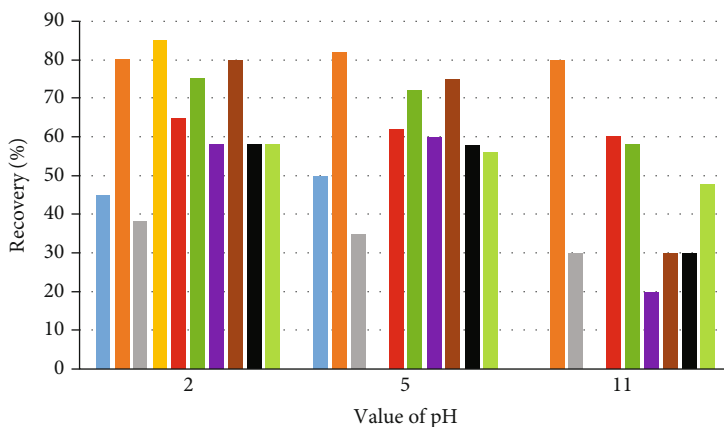
(c)

FIGURE 11: (a) HF/LiZN180. (b) Com/CN1. (c) Sorbtive layer.

Clofibric acid and sulfamethoxazole get one solubility than the other targeting PhCs, and they have the lowest log D readings (log D 0.7-0.8) at pH 5.5, making them the most hydrophobic molecules in the set. Moreover, because clofibric acid is produced in the elemental state at pH 5.5, it has stronger hydrophilicity, limiting the possibility of contact with the high sorption substance and subsequent removal. The bulk of PhCs performed poorly in Com/R, except for sulfamethoxazole and carbamazepine. The LD variables, ionic strength, balance time, stirring speed, matrix orienta-

tion, and samples pH were examined after picking the best efficiency activated carbon via BAμE for the measurement of the desired PhCs from aqueous solutions. All of the improvement findings, excluding the former, which would be described later, may be found in SI. In the testing methods, optimum time is important, and while one hour of back-removal time is sufficient to ensure optimal recovery, the supreme retrieval rates are only achieved after 16 hrs of removal time [19]. The aqueous matrix's chemical compositions were also evaluated, including initial

concentration, initial concentration, and polarization. The recovered rates for the BAμE systems at varying solution pH among 2.1 and 11.1 for the three chosen carbon coverings are shown in Figures 11(a)–11(c). The recoveries of all the targeted means that exist were influenced heavily by the solution pH, apart from carbamazepine recoveries with specimen Com/CN1.

This was partly anticipated, given that the ion or neutrality states of PhCs in water, or the net charge density of carbon-based compounds, are all affected by this variable. Clofibric acid, the component with the lowest pKa value, was recovered with rates ranging from 80 to 95% for all of the sorbtive phases that were assessed in an environment with a pH that was acidic. The extent of acid dissociation can be predicted based on the numerical value of the constant Ka. In addition, the value of the pKa is inversely proportional to the strength of the acid. The pH change between 2.0 and 11.0 did not allow considerable recovery augmentation for sulfamethoxazole, which, like clofibric acid, is hydrophobic and extremely fluid permeable. This could be owing to its complicated fractionation. The findings, nevertheless, unambiguously revealed that the concentration of the anion exchange sulfamethoxazole speciation (pH > 5.5) has a deleterious influence on its recuperation, similar to what has been observed with clofibric acid. Mefenamic acid, gemfibrozil, and diclofenac, all of which have negative log D values at pH 11.0, are also unrecoverable at the extraction's basic pH.

In the figure each colour bar represents 10 carbon material where blue represents C1, orange represents C2, grey represents C3, yellow represents C4, red represents C5, green represents C6, violet represents C7, brown represents C8, black represents C9, and light green represents C10. To recapitulate, the BAμE(HS/LiZn180)/HPLC-DAD system outclasses well-developed pretreatment enhancement methodologies and powerful quantitative methodologies because it achieves good rehabilitation for a significant number of PhCs with distinguishable hydrophobic/hydrophilic characteristics, when HPLC-DAD quantitative measurements are used. The combination of the optimized BAμE (HS/LiZn180) approach with more influential measurement techniques is predicted to the chosen PhCs; the impressive outcomes of this proof-of-concept portend promising outcomes for extra courses of contamination, such as the difficult polar groups.

6. Conclusion

Thirteen carbon substances have been evaluated as sorbent coating materials for bar adsorbent microextraction accompanied by microliquid extraction and high-efficiency liquid chromatography-diode array discovery procedure for the concurrent analysis of suggestions of different PhCs from profitable and lab-made carbon materials, H-T-activated hydrochars, hydrochars, and L-T-activated hydrochars. Due to a hierarchy porous structure in the full micro-mesopore spectrum associated with a rich chemical nature constituted of acid O groups that favored both accumulation (separation) and desorption (back extraction) of the active

compounds, the carbon, made at the lab, low-T-activated hydrochars demonstrated to contend with promotional activated carbon sorbent materials for the richness of PhCs, contributing to the exceptional productivity at the trace concentrations. The analytical and numerical approach was shown to be both ecologically friendly and simple to adopt. It also had great sensitivity and robustness, as well as a short surface area/volume requirement. Moreover, the new microextraction-based approach appears to be acceptable for compliance with EU Decision 2015/495 and USEPA requirements for PhC tracking, particularly when integrated with tandem mass spectrometry instruments, which could offer additional information.

Data Availability

The data used to support the findings of this study are included within the article. Further data or information is available from the corresponding author upon request.

Conflicts of Interest

The authors declare that there are no conflicts of interest regarding the publication of this paper.

Acknowledgments

References

[1] M. N. Oliveira, O. C. Gonçalves, S. M. Ahmad et al., "Application of bar adsorptive microextraction for the determination of levels of tricyclic antidepressants in urine samples," *Molecules*, vol. 26, no. 11, p. 3101, 2021.

[2] S. M. Ahmad, B. B. Calado, M. N. Oliveira, N. R. Neng, and J. Nogueira, "Bar adsorptive microextraction coated with carbon-based phase mixtures for performance-enhancement to monitor selected benzotriazoles, benzothiazoles, and benzenesulfonamides in environmental water matrices," *Molecules*, vol. 25, no. 9, p. 2133, 2020.

[3] P. Jõul, M. Vaher, and M. Kuhtinskaja, "Carbon aerogel-based solid-phase microextraction coating for the analysis of organophosphorus pesticides," *Analytical Methods*, vol. 13, no. 1, pp. 69–76, 2021.

[4] S. Xu, H. Liu, A. Long et al., "Carbon dot-decorated graphite carbon nitride composites for enhanced solid-phase microextraction of chlorobenzenes from water," *Nanomaterials*, vol. 12, no. 3, p. 335, 2022.

[5] B. Hashemi and S. Rezania, "Carbon-based sorbents and their nanocomposites for the enrichment of heavy metal ions: a review," *Microchimica Acta*, vol. 186, no. 8, 2019.

[6] N. J. Waleng, S. K. Selahle, A. Mpupa, and P. N. Nomngongo, "Development of dispersive solid-phase microextraction coupled with high-pressure liquid chromatography for the preconcentration and determination of the selected

neonicotinoid insecticides," *Journal of Analytical Science and Technology*, vol. 13, no. 1, pp. 1–15, 2022.

[7] O. J. Portillo-Castillo, R. Castro-Ríos, A. Chávez-Montes et al., "Developments of solid-phase microextraction fiber coatings for environmental pharmaceutical and personal care products analysis," *Reviews in Analytical Chemistry*, vol. 37, no. 2, 2018.

[8] J. B. Sperry, M. Azuma, and S. Stone, "Explosive hazard identification in pharmaceutical process development: a novel screening method and workflow for shipping potentially explosive materials," *Organic Process Research & Development*, vol. 25, no. 2, pp. 212–224, 2021.

[9] P. Mohammadi, M. Masrournia, Z. Es'haghi, and M. Pordel, "Hollow fiber coated Fe3O4@ maleamic acid-functionalized graphene oxide as a sorbent for stir bar sorptive extraction of ibuprofen, aspirin, and venlafaxine in human urine samples before determining by gas chromatography–mass spectrometry," *Journal of the Iranian Chemical Society*, vol. 18, no. 9, pp. 2249–2259, 2021.

[10] G. D'Orazio, A. Gentili, S. Fanali, C. Fanali, and C. Dal Bosco, "Innovative solutions for the extraction of vitamins from pharmaceutical and biological samples," *Current Analytical Chemistry*, vol. 17, no. 8, pp. 1114–1132, 2021.

[11] N. N. AL-Hashimi, H. A. Aleih, I. I. Fasfous, and H. S. AlKhatib, "Multi-walled carbon nanotubes as efficient sorbent for the solid bar microextraction of non-steroidal anti-inflammatory drugs from human urine samples," *Current Pharmaceutical Analysis*, vol. 14, no. 3, pp. 239–246, 2018.

[12] H. Sereshti, O. Duman, S. Tunç, N. Nouri, and P. Khorram, "Nanosorbent-based solid phase microextraction techniques for the monitoring of emerging organic contaminants in water and wastewater samples," *Microchimica Acta*, vol. 187, no. 9, 2020.

[13] N. Manousi, O.-E. Plastiras, N. P. Kalogiouri, C. K. Zacharis, and G. A. Zachariadis, "Metal-organic frameworks in bioanalysis: extraction of small organic molecules," *Separations*, vol. 8, no. 5, p. 60, 2021.

[14] M. J. Santoyo Treviño, S. Zarazúa, and J. Płotka-Wasylka, "Nanosorbents as materials for extraction processes of environmental contaminants and others," *Molecules*, vol. 27, no. 3, p. 1067, 2022.

[15] A. Speltini, F. Merlo, F. Maraschi, G. Marrubini, A. Faravelli, and A. Profumo, "Magnetic micro-solid-phase extraction using a novel carbon-based composite coupled with HPLC–MS/MS for steroid multiclass determination in human plasma," *Molecules*, vol. 26, no. 7, p. 2061, 2021.

[16] N. Manousi, A. Kabir, and G. A. Zachariadis, "Recent advances in the extraction of triazine herbicides from water samples," *Journal of Separation Science*, vol. 45, no. 1, pp. 113–133, 2022.

[17] J.-W. Liu, K. Murtada, N. Reyes-Garcés, and J. Pawliszyn, "Systematic evaluation of different coating chemistries used in thin-film microextraction," *Molecules*, vol. 25, no. 15, p. 3448, 2020.

[18] S. Hamidi, N. Alipour-Ghorbani, and A. Hamidi, "Solid phase microextraction techniques in determination of biomarkers," *Critical Reviews in Analytical Chemistry*, vol. 48, no. 4, pp. 239–251, 2018.

[19] G. Mafra, M. T. García-Valverde, J. Millán-Santiago, E. Carasek, R. Lucena, and S. Cárdenas, "Returning to nature for the design of sorptive phases in solid-phase microextraction," *Separations*, vol. 7, no. 1, p. 2, 2020.

[20] M. He, B. Chen, and B. Hu, "Recent developments in stir bar sorptive extraction," *Analytical and Bioanalytical Chemistry*, vol. 406, no. 8, pp. 2001–2026, 2014.

[21] S. M. Daryanavard, H. Zolfaghari, A. Abdel-Rehim, and M. Abdel-Rehim, "Recent applications of microextraction sample preparation techniques in biological samples analysis," *Biomedical Chromatography*, vol. 35, no. 7, article e5105, 2021.

[22] J. An, X. Wang, Y. Li, W. Kang, and K. Lian, "Polystyrene nanofibers as an effective sorbent for the adsorption of clonazepam: kinetic and thermodynamic studies," *RSC Advances*, vol. 12, no. 6, pp. 3394–3401, 2022.

[23] S. Peng, X. Huang, Y. Huang et al., "Novel solid-phase microextraction fiber coatings: a review," *Journal of Separation Science*, vol. 45, no. 1, pp. 282–304, 2022.

[24] N. Rastkari, R. Ahmadkhaniha, M. Yunesian, L. J. Baleh, and A. Mesdaghinia, "Sensitive determination of bisphenol A and bisphenol F in canned food using a solid-phase microextraction fibre coated with single-walled carbon nanotubes before GC/MS," *Food Additives and Contaminants*, vol. 27, no. 10, pp. 1460–1468, 2010.

[25] R. V. Emmons, R. Tajali, and E. Gionfriddo, "Development, optimization and applications of thin film solid phase microextraction (TF-SPME) devices for thermal desorption: a comprehensive review," *Separations*, vol. 6, no. 3, p. 39, 2019.

[26] N. Fontanals, R. M. Marcé, and F. Borrull, "Materials for solid-phase extraction of organic compounds," *Separations*, vol. 6, no. 4, p. 56, 2019.

[27] M. Szultka, P. Pomastowski, V. Railean-Plugaru, and B. Buszewski, "Microextraction sample preparation techniques in biomedical analysis," *Journal of Separation Science*, vol. 37, no. 21, pp. 3094–3105, 2014.

[28] X. Hou, L. Wang, and Y. Guo, "Recent developments in solid-phase microextraction coatings for environmental and biological analysis," *Chemistry Letters*, vol. 46, no. 10, pp. 1444–1455, 2017.

SSAGE Publishing

Research Article

Optimization of Activated Carbon Fiber Preparation from Hemp Fiber through Dipotassium Hydrogen Phosphate for Application of Thermal Storage System

L. Natrayan [iD],[1] **S. Kaliappan** [iD],[2] **S. Chinnasamy Subramanian,**[3] **Pravin P. Patil,**[4] **S. D. Sekar,**[5] **Y. Sesha Rao,**[6] **and Melkamu Beyene Bayu** [iD][7]

[1]*Department of Mechanical Engineering, Saveetha School of Engineering, SIMATS, 602 105, Chennai, Tamil Nadu, India*
[2]*Department of Mechanical Engineering, Velammal Institute of Technology, Chennai, 601204 Tamil Nadu, India*
[3]*Department of Mechanical Engineering, Velammal Engineering College, Chennai, 66 Tamil Nadu, India*
[4]*Department of Mechanical Engineering, Graphic Era Deemed to be University, Bell Road, Clement Town, 248002 Dehradun, Uttarakhand, India*
[5]*R. M. K. Engineering College, R. S. M. Nagar, Kavaraipettai 601206, Gummidipoondi Taluk, Thiruvallur District, Tamil Nadu, India*
[6]*Department of Mechanical Engineering, QIS College of Engineering and Technology, Ongole, Andhra Pradesh, India*
[7]*Department of Mechanical Engineering, Ambo Institute of Technology-19, Ambo University, Ethiopia*

Correspondence should be addressed to Melkamu Beyene Bayu; melkamu.beyene@ambou.edu.et

With significant benefits over many other commercialised thermal storage methods, activated carbon fiber (ACF) is believed to be among the finest biosorbents for adsorbent purposes. If correctly made, it is an outstanding mesoporous lightweight material with micropores and, in most cases, no micropores. ACF's higher bulk densities and great dynamic capacity demonstrate its value and are used in adsorbent technologies. The present study's primary goal is to create active carbon fiber from organic hemp fiber. The following parameters were selected: (i) activating temperatures, (ii) activating timing, (iii) carbonization temperature, (iv) activating ingredient %ages, and (v) speed of activation temperature, all with four levels to achieve the goal. Taguchi optimization techniques were used to optimize the adsorbent characteristics. The current study used an L16 orthogonal array to accomplish that improvement. According to the previous Taguchi, the optimal conditions were 300°C combustions, insemination with 22.5% w/v K_2HPO_4 solution, and activating at 800°C for 3 hours at 20°C/min. The greatest contribution is 54.75%, followed by the rate of temperature activation at 23.35%, carbonated temperature at 10.14%, duration of stimulation at 8.82%, and H_3PO_4 concentrations at 2.94%. The results show that the activation temperature and rate of the temperature of activations are the essential elements in the current study's accomplishment of the best adsorption capacities.

1. Introduction

Environmental contamination is a severe adverse effect of the modern country's fast economic expansion. Industrial effluent, in particular, poses significant problems, if not a catastrophe, due to its massive flow, increased nutrient concentration, intense hue, and complex breakdown [1, 2]. As a result, eliminating dye effluent is a critical challenge for industrialization. Membrane filtration, electrodynamics, and photocatalyst innovation have all been shown to be effective for sophisticated wastewater purification. Furthermore, the above procedures have certain limitations, including complexity, high price, and limited purifying effectiveness [3, 4]. Apart from the strategies mentioned previously, the physiological adsorption process has received increasing attention in the use of dyeing for sewage decontamination due to its high sorption performance and low technological hurdles. Because of their rich porous structure, high surface area, and diversity of established groups, active carbon fibers (ACFs) are regarded as effective adsorbents [5].

As a result, various ACFs were documented to be used in the filtration of printed and dyed effluent. In earlier studies, synthetic fibers such as PAN (polyacrylonitrile) and cellulosic were used as precursor materials to produce active carbon fibers with outstanding adsorption efficiency for metal ions and specific molecular pigments. Furthermore, undesired deterioration has hampered the progress of such chemically bonded ACFs [6, 7].

Biocomposite substances have lately gained popularity as a response to the disposal site crisis, the depletion of oil supplies and worries about emissions produced by their use. These comprise sustainable agricultural production fuel sources such as timber, agricultural residues, and plant-origin fibers [8, 9]. Hence, the need to create activated carbon adsorbent materials with low-cost, high-efficiency alternative antecedents. As a result of their minimal price, recyclability, and willingness to contract, natural fabrics are among the different scenarios [10]. Activated carbons were prepared using natural materials like hemp fiber, oil palm fiber, linen, and kenaf. Natural materials are divided into three groups based on their source within the tree: the thickest, leaves, and germ fibers. Bast fibers include cotton, jute, wheat, and flax. Bast fibers are widely used in the production of cables and monumental manufacturing textiles [11, 12]. Hemp fiber is commonly used for membranifaciens, specialised textile materials like mainsail and napkins, and specialised printing like tea paper and Starbucks filtration. Leaf fibers include jute, bananas, coconut, and pineapple [13, 14].

Due to its cost-effectiveness, limited technological obstacles, and long-term benefits, considerable effort has been made to manufacture active carbon fibers from biomasses, particularly biological residuals like lemon peel, stems, and disposal residuals from extraction minerals [15, 16]. Furthermore, active carbon fibers from renewable sources opened up a new avenue for the elevated exploitation of biowaste. Moreover, the adsorption rate of activated charcoal fiber biorenewable resources varies greatly, with consternation carbon fiber exhibiting the highest adsorption capability (165210 mg/g for methylene blue), implying that the microhardness of organic matter fiber has a significant effect on carbon fiber achievement [17, 18]. Moreover, the reaction mechanism in the production of carbon fiber is an essential factor that affects carbon composite sorption capacity; additionally, comprehensive activation, supplementary initiation, and surface coating consolidated reaction mechanisms are all helpful for increasing carbon fiber adsorption efficiency [19].

Adsorbents utilising heterogeneous catalysts are a simple and effective strategy to remove a wide range of natural and artificial contaminants from sewage. There are three techniques for producing activated charcoal. The catalytic cracking of a precursor in an innocuous flow at temperatures up from 500 to 1000 degrees Celsius results in char creation [20, 21]. The charcoal is then ignited in an oxidising gas like carbon dioxide and vapour at temperatures ranging from 700 to 1300 degrees Celsius. Enzymatic hydrolysis entails impregnating a prelude with oxidising reagents like K_2CO_3, $ZnCl_2$, H_3PO_4, $AlCl_3$, and Na_2HPO4 and burning them in a neutral gas like nitrogen or argon gas [22, 23]. The bio-physical activating approach combines physiochemical activating methods. The Taguchi optimization approach could be used to optimize active carbon generation. Taguchi, a simple and effective statistical and analytical strategy, conducts continuous testing to identify near-optimal choices for compensation and efficiency. A high number of parameters may be explored with a minimal number of experimental runs in this manner [3, 4].

The synthesis of active carbon fiber utilising natural hemp materials employing a chemical activation technique was studied in this work. It determined the optimal quantity of every variable in manufacturing activated carbon fiber. The Taguchi design analysis was used to measure the impact of process variables like carbonization temperature, dipotassium hydrogen phosphate composition in the authentication solvent, activation temperature, and activation process on the adsorption capacities of rehearsed adsorbent fiber. The properties and adsorption capabilities of activated carbon fiber produced under optimal circumstances were also studied.

2. Experimental Works

2.1. Materials. Rithu Natural Fiber Industry in Vellore, Tamil Nadu, India, supplied the hemp fiber. Naga Chemical Industry in Chennai, Tamil Nadu, India, supplied the dipotassium hydrogen phosphate. Other compounds have been of analytical quality. All needed formulations were prepared using double-filtered water.

2.2. Activated Carbon Preparations. The primary material for producing active carbon fibers is hemp fiber-based fabric. Cannabis was cleaned with double purified water to eliminate dirt before drying. Dried cannabis specimens weighing 5 g were put in a steel longitudinal tubular furnace. A neutral nitrogen flow was forced through the combustion chamber at a fluid velocity of 75 cm^3/min for 30 min. The oven temperature was increased at an average rate of 20°C/min throughout the combustion process to obtain the different carbonization temperatures indicated by a Taguchi technique [24]. Hemp specimens were maintained at these temperatures for 1 hour. In an N_2 atmosphere, carbonized cannabis samples were washed to ambient temperature. In addition, many hemp specimens were tested without activated carbon. Activated carbon hemp was immersed in a 50 mL K_2HPO_4 solution and left overnight to attain maximal immersion during the chemical transformation [25]. The Taguchi technique suggested the examined %ages of K_2HPO_4 mixtures with different proportions. The soaking carbonized hemp was then dried in a hot air oven at 110°C before being inserted in furnaces. It held for 30 min at room temperature below a nitrogen environment with a fluid velocity of 75 cm^3/min. Following that, the burner was warmed with varying rates of temperature increase and maintained at this level for different periods. The Taguchi approach suggested the activating temperatures, activation process, and probability of obtaining the activating temp. Subsequently, the activated carbon was chilled in an anaerobic environment before being rinsed using solvent and

Table 1: Parameters and their levels.

Sl. No	Parameters	Symbols	Levels			
			L1	L2	L3	L4
1	Temperature of activation (°C)	A	600	700	800	900
2	Rate of temperature activation (°C/min)	B	40	30	20	10
3	H_3PO_4 concentration (w/v)	C	7.5	15	22.5	30
4	Carbonization temperature (°C)	D	Without	200	300	400
5	Time of activation (hrs)	E	1	2	3	4

Table 2: Iodine values of different process parameters on the adsorption.

Sl. No	A	B	C	D	E	Iodine values		Mean values	S/N values
						X_1	X_2		
1	600	40	7.5	Without	1	42.05	51.59	46.82	33.41
2	600	30	15	200	2	134.68	144.22	139.45	42.89
3	600	20	22.5	300	3	193.91	203.45	198.68	45.96
4	600	10	30	400	4	141.86	151.4	146.63	43.32
5	700	40	15	300	4	133.67	143.27	138.47	42.83
6	700	30	7.5	400	3	101.76	111.3	106.53	40.55
7	700	20	30	Without	2	240.6	238.96	239.78	47.60
8	700	10	22.5	200	1	214.95	225.68	220.315	46.86
9	800	40	22.5	400	2	253.1	262.64	257.87	48.23
10	800	30	30	300	1	260.19	259.14	259.665	48.29
11	800	20	7.5	200	4	294.72	304.26	299.49	49.53
12	800	10	15	Without	3	234.47	244.01	239.24	47.58
13	900	40	30	200	3	229.11	238.65	233.88	47.38
14	900	30	22.5	Without	4	181.19	186.54	183.865	45.29
15	900	20	15	400	1	242.34	245.89	244.115	47.75
16	900	10	7.5	300	2	335.59	331.57	333.58	50.46

Table 3: S/N values of adsorption for storage system.

Levels	A	B	C	D	E
1	41.40	47.06	43.49	43.47	44.08
2	44.46	47.71	45.26	46.66	47.29
3	48.41	44.25	46.59	46.89	45.37
4	47.72	42.96	46.65	44.96	45.24
Delta	7.01	4.72	3.16	3.42	3.22
Rank	1	2	5	3	4

afterwards twice filtered water till the pH of a cleaning discharge was achieved.

2.3. Optimization of ACF Preparation Conditions. The Taguchi design approach was utilised to optimize the ACF processibility. An L16 factorial design containing five process variables in four stages was employed to determine the best frequencies. The four stages of every studied operation variable would be as follows: Table 1 displays the different parameters and respective ranges.

Table 1 shows the preparation of 16 distinct ACF specimens using the Taguchi array design concept. The iodine value of every produced ACF specimen was evaluated in double in specified tests as a criterion of the material's adsorption ability. The optimisation criteria were the iodine value of the specimens. To study the effect of operating settings on the adsorption capacities of the produced ACF, the signal-to-noise ratios (S/N ratios) of recorded iodine concentrations were studied using the variance test (ANOVA) approach. Because the improved circumstances correspond to the adsorbent's higher adsorption capabilities, the

TABLE 4: ANOVA analysis of adsorptions of iodine in phenolic acid.

Source	DF	SOS	Contribution (%)	Adj SS	Adj MS
A	3	45743	54.75	45743	15247.7
B	3	19514	23.35	19514	6504.7
C	3	2453	2.94	2453	817.7
D	3	8472	10.14	8472	2824.1
E	3	7372	8.82	7372	2457.5
Error	0	0	0	0	0
Total	15	83555	100	—	—
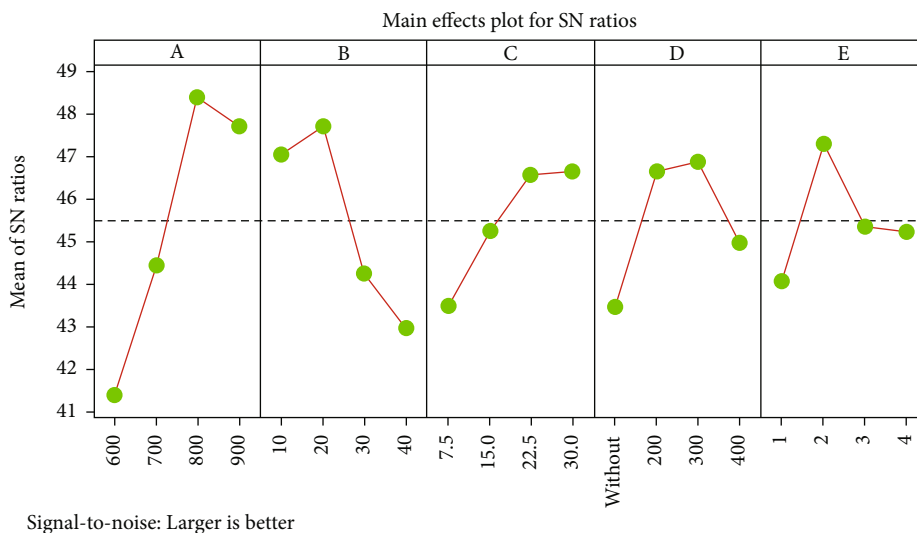
FIGURE 1: The iodine values of adsorptions based on various input factors.

"bigger-is-better" approach for calculating the S/N ratios was used [3, 8]. The S/N ratio is determined as follows:

$$S/N\,ratio = -10\,\log_{10} \frac{1}{e} \sum_{a=i}^{e} \frac{1}{X_i}, \qquad (1)$$

where e represents the size of replicas and x_i is the iodine value of created ACF specimen in every replicate. Due to the obvious "larger is good" approach, raising the S/N ratio corresponds to raising the adsorption properties of the ACF samples produced. ASTM D4607-94 was used to estimate the iodine value of ACF specimens.

3. Result and Discussion

3.1. Regression-Based Analysis. Based on the different combinations, 16 distinct ACF specimens were generated using the Taguchi technique's L16 array, and the iodine value of every specimen was calculated. Table 2 displays the iodine values and their accompanying S/N combinations. Table 3 shows the delta rank and its accompanying values. Table 4 displays the results of the *F*-test for S/N proportions. Improving the S/N proportion corresponds to enhancing the adsorption
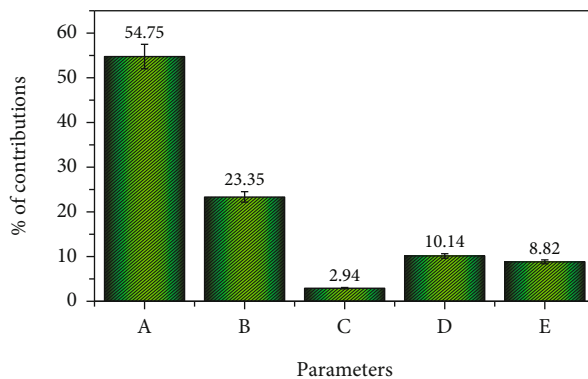
FIGURE 2: Error plots of percent contributions of various influencing parameters of iodine adsorptions.

capability of ACF samples generated. Figure 1 shows the iodine values of adsorptions based on various input factors.

3.2. Analysis of Variance. An ANOVA was used to determine the significance of interrupted processing elements. Table 4 provides the %age of contribution for each processing parameter. The process parameter known as the *F*-test is hypothesised to affect adsorption characteristics. Figure 2
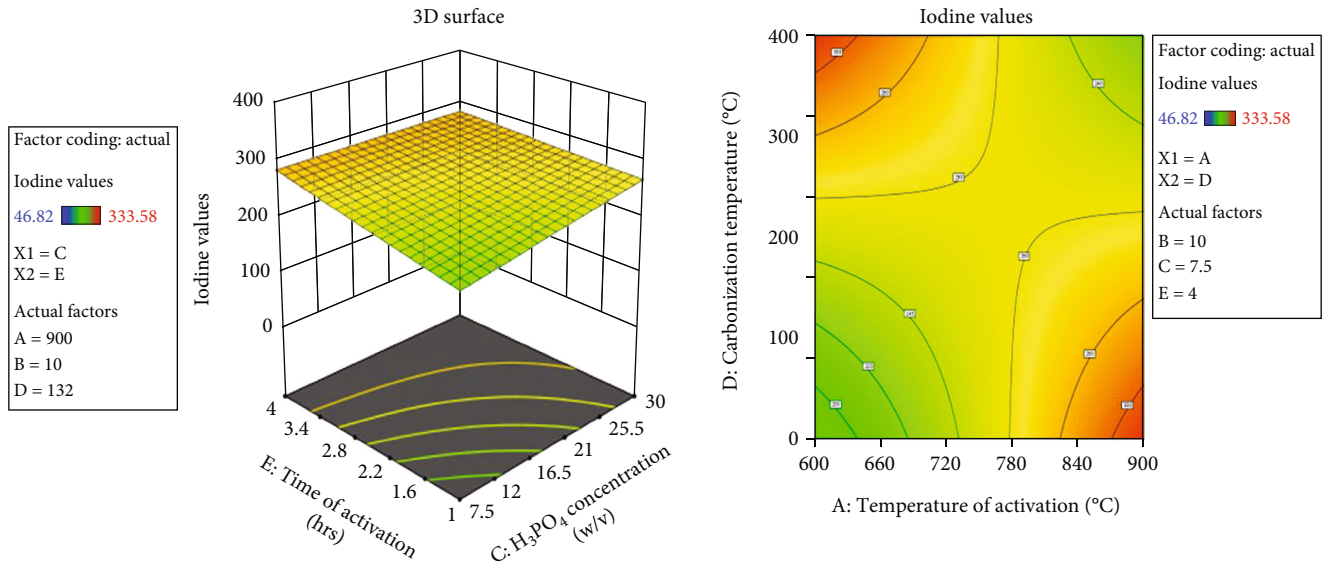
FIGURE 3: Surface and contour plots of activation temperature based on input parameters.
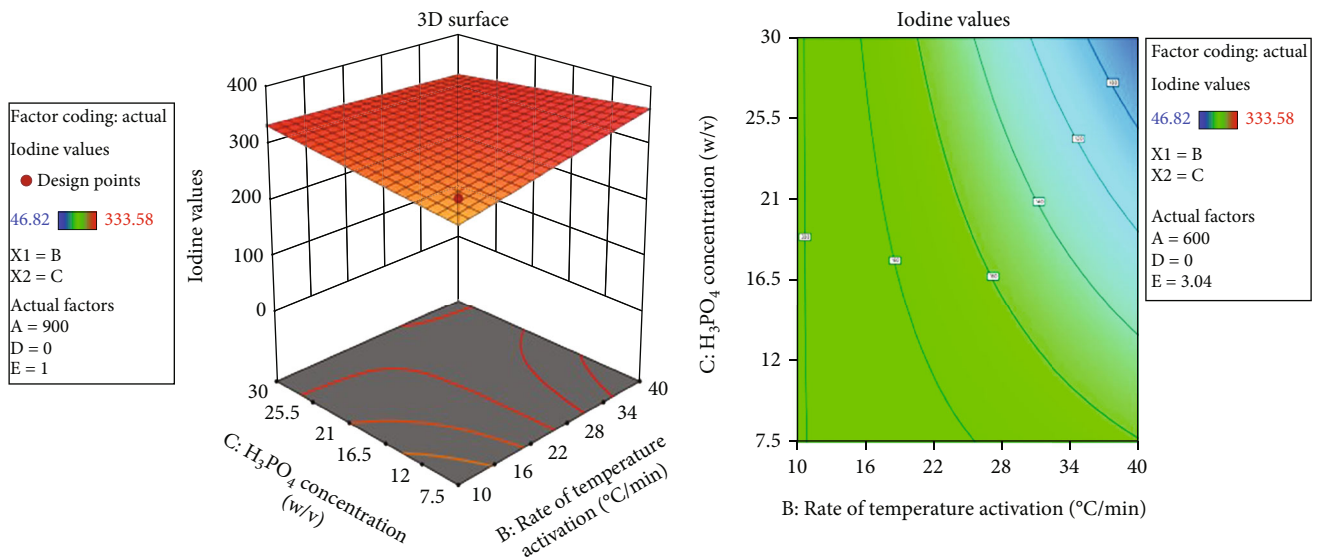
FIGURE 4: Surface and contour plots of rate of activation temperature based on input parameters.

depicts the %age contribution of each ingredient. The contributory %age is the fraction of the sentencing hearing total variance that considers each meaningful impact [4]. The regressions of current adsorption characteristics are expressed by equation (2).

$$
\begin{aligned}
\text{Iodine values} = {} & 205.5 - 72.63A1 - 29.25A2 + 58.54A3 \\
& + 43.34A4 + 29.42B1 + 39.99B2 \\
& - 33.15B3 - 36.26B4 - 8.919C1 \\
& - 15.21C2 + 9.659C3 + 14.47C4 \\
& - 28.10D1 + 17.76D2 + 27.07\,D3 \\
& - 16.74D4 - 12.80E1 + 37.15E2 \\
& - 10.94E3 - 1.41E4.
\end{aligned} \tag{2}
$$

Figure 2 depicts the contribution of processing parameters to adsorption characteristics. Table 4's percent contribution is a controlling factor to attain the highest iodine. The P value specifies the probability of recurrent factors. The most significant contribution is 54.75%, followed by the rate of temperature activation at 23.35%, carbonated temperature at 10.14%, duration of stimulation at 8.82%, and H_3PO_4 concentrations at 2.94%. The results show that the activation temperature and rate of the temperature of activations are the essential elements in the current study's accomplishment of the best adsorption capacities.

4. Impact of Processing Parameters

4.1. Result of Activation Temperature. Raising the activating temperatures to 800°C improves the S/N ratio, implying that
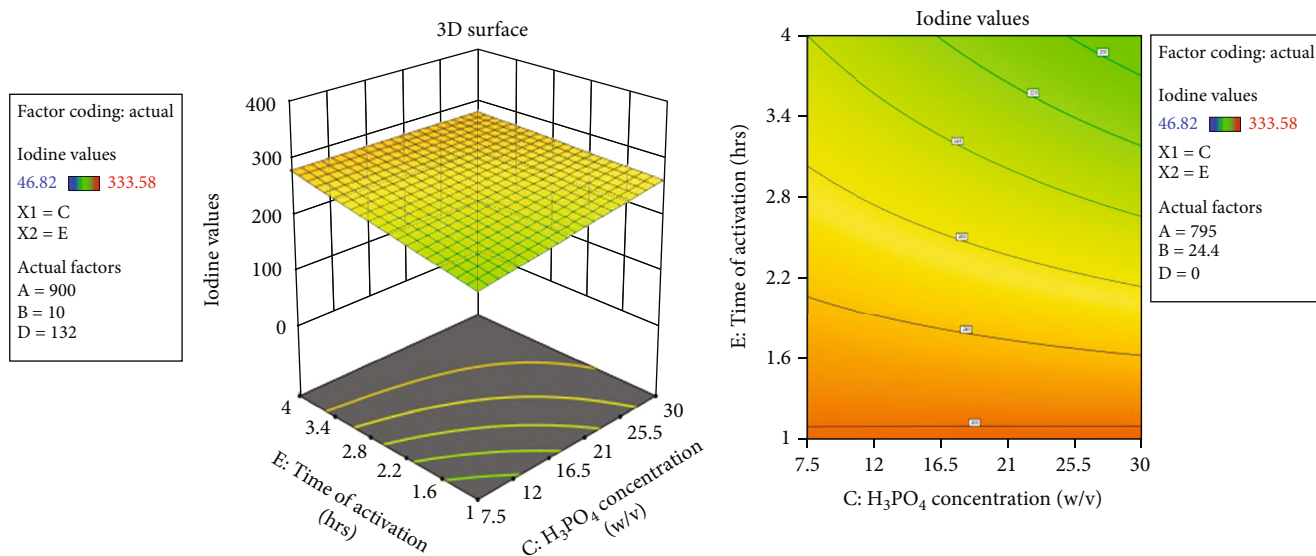
FIGURE 5: Surface and contour plots of effect of K_2HPO_4 concentration based on input parameters.
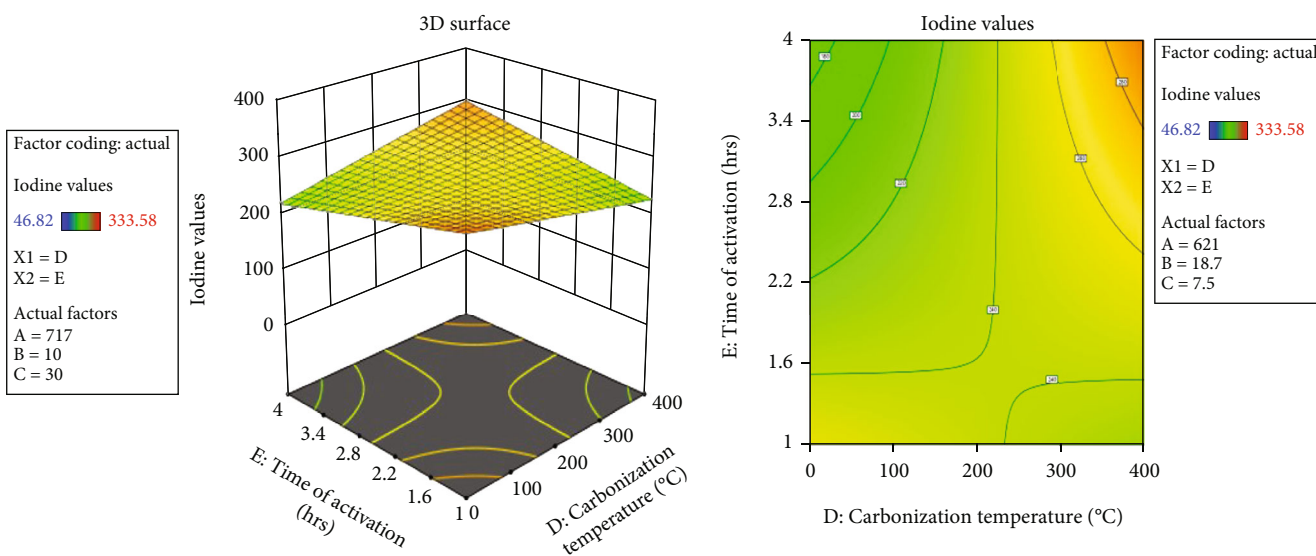
FIGURE 6: Surface and contour plots of the effect of carbonation temperature based on input parameters.

the adsorption efficiency of ACF specimens improves as the activating temperature increases. This might be attributed to increased activation and small pore creation throughout the processed ACF. Several studies have found similar findings. An elevation in reaction temperature up to 900˚C reduces the ACF's adsorption capability. This is most likely due to the loss of the porous structure and the formation of bigger pores that limit the adsorption capability [24, 26]. Figure 3 demonstrates the above findings.

4.2. Consequence of the Level of Attaining the Activation Temperature. Figure 4 indicates that increasing the activating temperature level between 10 and 20˚C/min improves

the S/N ratio of the generated ACF specimens. This leads to a rise in ACF adsorption, which may be due to decreased degradation of ACF molecules. The ACF structure is most likely destroyed and transformed at excessive temperature increase levels to charcoal [27, 28].

4.3. Effect of K_2HPO_4 Concentration. As shown in Figure 5, increasing the phosphorus potassium dihydrogen level from 7.5 to 22.5% w/v increases the S/N ratio of the iodine values in the activated carbon fiber specimens produced. This might be attributed to a rise in the creation of small pores, as in ACF, that are more efficient in the adsorption mechanism and boost absorbent adsorption properties. Surpassing
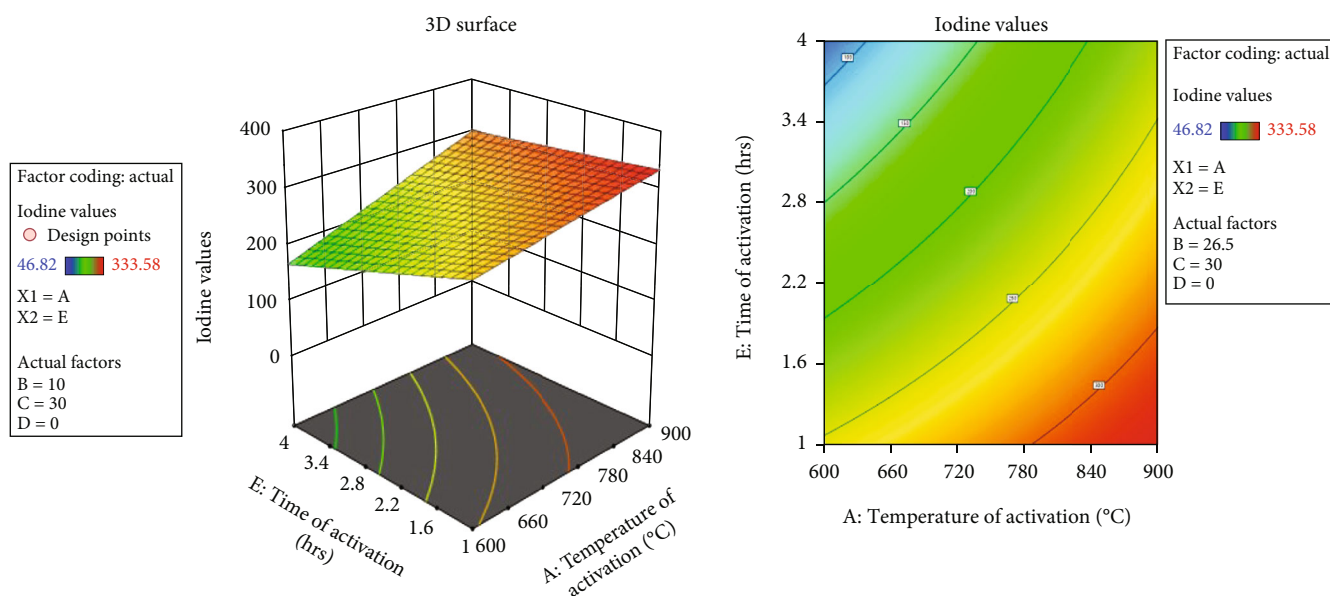
FIGURE 7: Surface and contour plots of the effect of pulse duration based on input parameters.

the phosphorus-potassium dihydrogen level by up to 30% w/v reduces or maintains the S/N proportion [25, 29]. Increased activating agents may cause increased drying and the dissolution of activated carbon fiber small pores, resulting in bigger pores with lower adsorption effectiveness. Similar findings have been reported in the research.

4.4. Effect of Carbonization Temperature.
Figure 6 shows that more of the activated carbon fiber obtained by carbonizing hemp at 300°C is greater than that of activated carbon fiber generated without such a phase. Dissociating volatile substances from hemp structures could allow additional places for the activating chemical to deposit and provide more activation spots on the particle surface, enhancing activated carbon fiber adsorption [17, 30]. Carbonization at 400°C reduces the adsorption properties of activated carbon fiber, most likely owing to the shrinking of the carbonized charred molecule. Several investigators achieved consistent outcomes.

4.5. Effect of Activation Time.
The findings of such an analysis of variance for the influence of pulse duration on the S/N proportions of the iodide values are shown in Figure 7. The experimental findings show that ACF's adsorption rate steadily rises after increasing pulse duration up to 3 h. A rise in pulse duration of up to 4 h reduces adsorption ability. Processing for 3 hours undoubtedly enhances the development of small pores that are more efficient in the adsorption mechanism. However, with longer activating durations, the walls of the small pores may break, and they become shiny and porous [31, 32].

4.6. Description of the Augmented Settings.
According to the previous segment, the optimal conditions were 300°C combustions, insemination with 22.5% w/v K_2HPO_4 solution, and activating at 800°C for 3 hours at 20°C/min. Figure 8
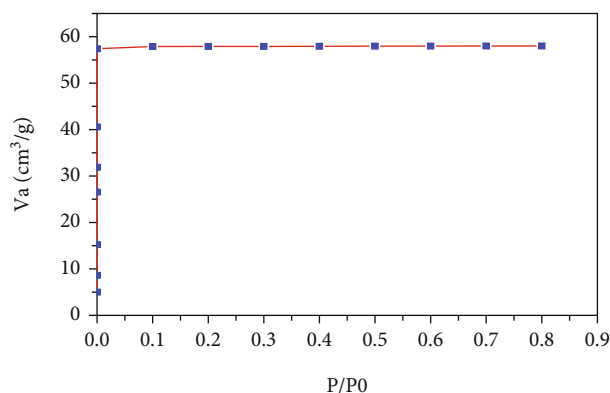
FIGURE 8: Nitrogen adsorption at -196°C on the activated carbon fiber prepared at optimal conditions.

depicts the nitrogen adsorbent equilibrium adsorption curves obtained at -196°C under optimum circumstances. As per the IUPAC, the resulting equilibrium adsorption curves support a category I adsorbent where most activated carbon fiber's permeability seems to be in microporous sizes [20, 33]. The MP techniques yielded the following outcomes: an appropriate surface region of 469 m^2/g, a small pore surface of 461 m^2/g, a micropore surface of 10.7 m^2/g, small pore volumes of 0.15 m^3/g, and a microporous volume of 1.24×10^2 m^3/g. When specific surface area volume data were compared, it was discovered that the majority of the permeability of a produced surface would be in the microporous range, indicating that activated carbon fiber created under optimal conditions has a very high porosity structure and is composed of small pores [34].

Figure 9 shows the microstructural images of pure and activated hemp fibers. A comparison of SEM micrographs of the ACF surface generated under optimal circumstances
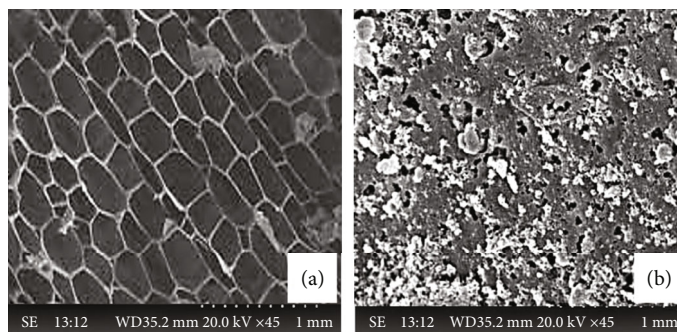
FIGURE 9: Microstructural images of (a) pure hemp and (b) activated carbon-based hemp.

with pure hemp shows that a significant amount of permeability is formed throughout the carbonization phases. The ACF's uneven porosity suggests a much greater surface area than created under optimum ACF processing conditions.

5. Conclusion

The activated carbon from hemp-based natural fibers was successfully formed using dipotassium hydrogen phosphate's chemical solvent, and the results were optimized through the Taguchi optimization tool. The following results were obtained.

(i) According to the previous Taguchi, the optimal conditions were 300°C combustions, insemination with 22.5% w/v K_2HPO_4 solution, and activating at 800°C for 3 hours at a rate of 20°C/min

(ii) The most significant contribution is 54.75%, followed by the rate of temperature activation at 23.35%, carbonated temperature at 10.14%, duration of stimulation at 8.82%, and H_3PO_4 concentrations at 2.94%. The results show that the activation temperature and rate of the temperature of activations are the most important elements in the current study's accomplishment of the best adsorption capacities

(iii) As per the IUPAC, the resulting equilibrium adsorption curves support a category I adsorbent where most activated carbon fiber's permeability seems to be in microporous sizes

(iv) The MP techniques yielded the following outcomes: an appropriate surface region of $469 \, m^2/g$, a small pore surface of $461 \, m^2/g$; a micropore surface of $10.7 \, m^2/g$; small pore volumes of $0.15 \, m^3/g$; and a microporous volume of $1.24 \times 10^2 \, m^3/g$

(v) Dissociating volatile substances from hemp structures could allow additional places for the activating chemical to deposit and provide more activation spots on the particle surface, enhancing the adsorption of activated carbon fiber

(vi) The experimental findings show that ACF's adsorption rate steadily rises after increasing pulse dura-

tion up to 3 h. A rise in pulse duration of up to 4 h reduces adsorption ability. Processing for 3 hours undoubtedly enhances the development of small pores that are more efficient in the adsorption mechanism

Data Availability

The data used to support the findings of this study are included within the article.

Conflicts of Interest

The authors declare that there are no conflicts of interest regarding the publication of this paper.

Acknowledgments

References

[1] S. Ouajai and R. A. Shanks, "Composition, structure and thermal degradation of hemp cellulose after chemical treatments," *Polymer Degradation and Stability*, vol. 89, no. 2, pp. 327–335, 2005.

[2] N. Saba, M. T. Paridah, K. Abdan, and N. A. Ibrahim, "Effect of oil palm nano filler on mechanical and morphological properties of kenaf reinforced epoxy composites," *Construction and Building Materials*, vol. 123, pp. 15–26, 2016.

[3] V. Ganesan and B. Kaliyamoorthy, "Utilization of Taguchi technique to enhance the interlaminar shear strength of wood dust filled woven jute fiber reinforced polyester composites in cryogenic environment," *Journal of Natural Fibers*, vol. 19, no. 6, pp. 1990–2001, 2022.

[4] G. Velmurugan and K. Babu, "Statistical analysis of mechanical properties of wood dust filled jute fiber based hybrid composites under cryogenic atmosphere using Grey-Taguchi method," *Materials Research Express*, vol. 7, no. 6, 2020.

[5] M. Anbia, F. M. Nejati, M. Jahangiri, A. Eskandari, and V. Garshasbi, "Optimization of synthesis procedure for NaX zeolite by Taguchi experimental design and its application in CO_2 adsorption," *Islamic Republic of Iran*, vol. 26, pp. 213–222, 2015.

[6] A. Sharafian, K. Fayazmanesh, C. McCague, and M. Bahrami, "Thermal conductivity and contact resistance of mesoporous silica gel adsorbents bound with polyvinylpyrrolidone in contact with a metallic substrate for adsorption cooling system applications," *International Journal of Heat and Mass Transfer*, vol. 79, pp. 64–71, 2014.

[7] J. Sarkar and S. Bhattacharyya, "Application of graphene and graphene-based materials in clean energy-related devices Minghui," *Archives of Thermodynamics*, vol. 33, pp. 23–40, 2012.

[8] M. Meikandan, M. Karthick, L. Natrayan et al., "Experimental investigation on tribological behaviour of various processes of anodized coated piston for engine application," *Journal of Nanomaterials*, vol. 2022, Article ID 7983390, 8 pages, 2022.

[9] K. Renugadevi, P. K. Devan, and T. Thomas, "Fabrication of Calotropis gigantea fibre reinforced compression spring for light weight applications," *Composites Part B, Engineering*, vol. 172, pp. 281–289, 2019.

[10] V. Paranthaman, K. Shanmuga Sundaram, and L. Natrayan, "Influence of SiC particles on mechanical and microstructural properties of modified interlock friction stir weld lap joint for automotive grade aluminium alloy," *Silicon*, vol. 14, no. 4, pp. 1617–1627, 2022.

[11] S. Mishra, A. K. Mohanty, L. T. Drzal, M. Misra, and G. Hinrichsen, "A review on pineapple leaf fibers, sisal fibers and their biocomposites," *Macromolecular Materials and Engineering*, vol. 289, no. 11, pp. 955–974, 2004.

[12] J. C. dos Santos, R. L. Siqueira, L. M. G. Vieira, R. T. S. Freire, V. Mano, and T. H. Panzera, "Effects of sodium carbonate on the performance of epoxy and polyester coir- reinforced composites," *Polymer Testing*, vol. 67, pp. 533–544, 2018.

[13] R. del Rey, R. Serrat, J. Alba, I. Perez, P. Mutje, and F. X. Espinach, "Effect of sodium hydroxide treatments on the tensile strength and the interphase quality of hemp core fiber-reinforced polypropylene composites," *Polymers*, vol. 9, no. 8, pp. 6–8, 2017.

[14] A. S. Negi, J. K. Katiyar, S. Kumar, N. Kumar, and V. K. Patel, "Physicomechanical and abrasive wear properties of hemp/ Kevlar/carbon reinforced hybrid epoxy composites," *Materials Research Express*, vol. 6, no. 11, 2019.

[15] L. Yan, N. Chouw, and K. Jayaraman, "Flax fibre and its composites - a review," *Composites Part B, Engineering*, vol. 56, pp. 296–317, 2014.

[16] S. J. Muthiya, L. Natrayan, S. Kaliappan et al., "Experimental investigation to utilize adsorption and absorption technique to reduce CO_2 emissions in diesel engine exhaust using amine solutions," *Adsorption Science & Technology*, vol. 2022, article 9621423, pp. 1–11, 2022.

[17] J. M. Pinheiro, S. Salústio, A. A. Valente, and C. M. Silva, "Adsorption heat pump optimization by experimental design and response surface methodology," *Applied Thermal Engineering*, vol. 138, pp. 849–860, 2018.

[18] K. R. Sumesh and K. Kanthavel, "Synergy of fiber content, Al_2O_3 nanopowder, NaOH treatment and compression pressure on free vibration and damping behavior of natural hybrid-based epoxy composites," *Polymer Bulletin*, vol. 77, no. 3, pp. 1581–1604, 2020.

[19] K. Lim, J. Kim, and J. Lee, "Comparative study on adsorbent characteristics for adsorption thermal energy storage system," *International Journal of Energy Research*, vol. 43, no. 9, pp. 4281–4294, 2019.

[20] S. Aber, A. Khataee, and M. Sheydaei, "Optimization of activated carbon fiber preparation from Kenaf using K_2HPO_4 as chemical activator for adsorption of phenolic compounds," *Bioresource Technology*, vol. 100, no. 24, pp. 6586–6591, 2009.

[21] A. Frazzica and V. Brancato, "Verification of hydrothermal stability of adsorbent materials for thermal energy storage," *International Journal of Energy Research*, vol. 43, no. 12, pp. 6161–6170, 2019.

[22] X. Du, T. Wu, F. Sun et al., "Adsorption equilibrium and thermodynamic analysis of CO_2 and CH_4 on Qinshui Basin anthracite," *Geofluids*, vol. 2019, Article ID 8268050, 14 pages, 2019.

[23] P. G. Youssef, H. Dakkama, S. M. Mahmoud, and R. K. AL-Dadah, "Experimental investigation of adsorption water desalination/cooling system using CPO-27Ni MOF," *Desalination*, vol. 404, pp. 192–199, 2017.

[24] F. Tadayon, T. Branch, S. Motahar, N. T. Branch, and O. Branch, "Application of Taguchi method for optimizing the adsorption of lead ions on nanocomposite silica aerogel," *Academic Research International*, vol. 2, pp. 42–48, 2012.

[25] K. Lim, J. Che, and J. Lee, "Experimental study on adsorption characteristics of a water and silica-gel based thermal energy storage (TES) system," *Applied Thermal Engineering*, vol. 110, pp. 80–88, 2017.

[26] K. E. N'Tsoukpoe, H. Liu, N. Le Pierrès, and L. Luo, "A review on long-term sorption solar energy storage," *Renewable and Sustainable Energy Reviews*, vol. 13, no. 9, pp. 2385–2396, 2009.

[27] J. Jänchen and H. Stach, "Adsorption properties of porous materials for solar thermal energy storage and heat pump applications," *Energy Procedia*, vol. 30, pp. 289–293, 2012.

[28] K. Linnow, M. Niermann, D. Bonatz, K. Posern, and M. Steiger, "Experimental studies of the mechanism and kinetics of hydration reactions," *Energy Procedia*, vol. 48, pp. 394–404, 2014.

[29] U. Pathak, S. Kumari, A. Kumar, and T. Mandal, "Process parametric optimization toward augmentation of silica yield using Taguchi technique and artificial neural network approach," *Ecology and Environment*, vol. 5, no. 4, pp. 294–312, 2020.

[30] K. C. Ng, H. T. Chua, C. Y. Chung et al., "Experimental investigation of the silica gel-water adsorption isotherm characteristics," *Applied Thermal Engineering*, vol. 21, no. 16, pp. 1631–1642, 2001.

[31] N. Yu, R. Z. Wang, and L. W. Wang, "Sorption thermal storage for solar energy," *Progress in Energy and Combustion Science*, vol. 39, no. 5, pp. 489–514, 2013.

[32] S. Vasta, V. Brancato, D. La Rosa et al., "Adsorption heat storage: state-of-the-art and future perspectives," *Nanomaterials*, vol. 8, no. 7, p. 522, 2018.

[33] A. S. Kaliappan, S. Mohanamurugan, and P. K. Nagarajan, "Numerical investigation of sinusoidal and trapezoidal piston profiles for an IC engine," *Journal of Applied Fluid Mechanics*, vol. 13, no. 1, pp. 287–298, 2020.

[34] L. Wang, L. Chen, H. L. Wang, and D. L. Liao, "The adsorption refrigeration characteristics of alkaline-earth metal chlorides and its composite adsorbents," *Renewable Energy*, vol. 34, no. 4, pp. 1016–1023, 2009.

Research Article

Thermal Adsorption and Mechanical Behaviour of Polypropylene Hybrid Composite Synthesized by Glass/Hemp Fibre via an Injection Moulding Process

R. Venkatesh,[1] I. Kantharaj,[2] R. Sasikumar,[3] C. Ramesh Kannan,[4] Anupam Yadav,[5] M. Karthigairajan,[6] P. Vivekanandan,[7] and Arundeep Murugan [8]

[1]Department of Mechanical Engineering, Saveetha School of Engineering, SIMATS, Chennai, 602105 Tamil Nadu, India
[2]Department Mechanical Engineering, JAIN (Deemed-to-be University), Bengaluru, India
[3]Department of Mechanical Engineering, Erode Sengunthar Engineering College, Erode-, -638 057 Tamil Nadu, India
[4]Department of Mechanical Engineering, SRM TRP Engineering College, Trichy, 621105 Tamil Nadu, India
[5]Department of Computer Engineering & Applications, GLA University, Mathura 281406, India
[6]Department of Mechanical Engineering, Gojan School of Business and Technology, Chennai, 600052 Tamil Nadu, India
[7]Department of Mechatronics Engineering, SNS College of Technology, Coimbatore, 641035 Tamil Nadu, India
[8]School of Mechanical and Industrial Engineering, Institute of Technology, Debre Markos University, Debre Markos, Ethiopia

Correspondence should be addressed to Arundeep Murugan; arundeepmurugan@gmail.com

Thermoplastic-based polymers are gathering importance in several engineering fields like electrical, electronic, automotive, aerospace, and structural. The additions of secondary phase reinforcements such as natural and synthetic fibre improve thermoplastic-based polymer's properties. The thermoplastic and natural fibre combinations are found to have low mechanical strength and incompatibility and need special treatment for synthesizing the natural fibre. The present experimental investigation deals with the enhancement of polypropylene hybrid composite by using the combinations of glass (synthetic)/ hemp (natural) fibre for the ratio of $0:35$, $5:30$, $10:25$, and $15:20$ reinforced with $5\,wt\%$ compatibilizer through injection moulding. The revealed test results of polypropylene hybrid composite showed improved mechanical impact and flexural and tensile strength of 37.5%, 14.2%, and 21.1%, respectively. The thermal adsorption characteristics were evaluated by thermogravimetric analysis apparatus. It showed the decomposition of composite limited by hemp fibre at $27^\circ C$ to $700^\circ C$.

1. Introduction

Recently, automotive industries are expanding their demand for new lightweight materials with good corrosion resistance, higher strength, and good thermal behaviour at low cost. To meet the above demands, industries are interested in natural fibre-based polymer matrix composite as the best alternative material, which is reinforced to the filament, nanofiller, and fabric, which leads to increased composite performance [1, 2]. In the past decades, natural fibre-reinforced thermo-/thermoset plastic composites improved tremendously in the automobile industries. It could make an environmentally user-friendly, economic, reduced weight, and renewable composite, resulting in increased strength and fuel economy [3–5]. Most common natural fibres like kenaf, flax, hemp, and jute have less density, are easy to process, and are low cost compared to synthetic fibre [6–9]. So, polymer matrix composites bonded with natural fibre gained awareness in various engineering fields, researchers, and industries. However, the main drawback of natural fibre-reinforced polymer composite was reduced compatibility, poor elongation, and lower impact strength [10, 11]. It was essential to adjoin a minor amount of synthetic fibre added into natural fibre-reinforced polymer composite via physical or chemical, which resulted in increased compatibility [12].

Similarly, the combined weight could be reduced with increased performance of composite that leads an economic operation at applications of the automobile, structural, and aerospace [13, 14]. The current choice of polypropylene (PP), polyvinyl chloride, and polythene has been considered as matrix material due to their extreme performance of robust, reliable, easy to process, economic, and good thermal stability compared to conventional thermoplastics. So it was used for lining materials for automotive applications [15–17]. The polypropylene-based polymer was enhanced via natural hemp fibre for automotive components via various techniques like compression moulding, resin transfer moulding, vacuum impregnation, and hand layup [18, 19]. The polypropylene composite was developed using 40 wt% of hemp fibre through a compression mould assisted with the film stacking route.

The result found high stiffness and strength compared with all other natural fibres [20, 21]. The carbonized bone ash particulate-reinforced compression mould route results in synthesized polypropylene composite showed good wear resistance [22, 23]. The biopolymer composites were synthesized with chopped hemp by extrusion setup injection mould technique. The experimental results found that the presence of chopped hemp fibre enhanced the stiffness and flexural strength of the composite [24]. Similarly, bioplastic composites were developed from hemp fibre [25]. The author investigated the effect of fibre loading on the mechanical and thermal performance of hemp-reinforced polypropylene composite [26]. They found that the presence of natural hemp fibre has good thermal stability and enhanced mechanical strength compared to unreinforced polymer composites. Recently, polymer coating techniques on conventional steel materials were increased on low-cost fabrication with increased corrosion resistance [27]. One of the researchers found good tribological performance on the polypropylene composite reinforced with basalt fibre [28]. However, the hybridization of natural fibre composite is an excellent choice to overcome the composite's poor compatibility and strength. It facilitates reducing the process cost, increasing the thermal performance, limiting the wear, and enhancing the composite's mechanical properties. Therefore, the current research focuses on fabricating the polypropylene hybrid composite, and their thermomechanical characteristics are enhanced with the secondary reinforcement fibres like glass/hemp. The additions of 5 wt% compatibilizer increase the polypropylene/glass/hemp fibre combination adhesive properties. The developed polypropylene hybrid composite thermomechanical properties are evaluated through ASTM test standards.

2. Materials and Processing Details

2.1. Materials. The PP6331 grade polypropylene is chosen as matrix material, which has a density of 0.90 g/cc and 1.71 g/10 min melt flow index during hybrid composite processing at 230°C. The selected PP6331 grade polypropylene has enhanced properties like high stiffness, good heat deflection, and good compatibility and is suitable for food and medical product storage with microwavable reheating [2].

The natural hemp fibres are chopped to -12 mm size, and the polypropylene composite with hemp fibre is enriched with a minor amount of E-glass fibre (10 mm) to hybridize polypropylene resulting in increased mechanical and thermal performance. Among the various natural fibres, hemp fibre is very cheap, strong, and durable.

2.2. Synthesis of PP6331 Hybrid Composite. Polypropylene hybrid composite is prepared with the constitutions of glass/hemp fibre hybridization by using compatibilizer as mentioned in Table 1. Initial stage, the required quantity of polypropylene (PP6331) and glass/hemp fibres are weighted by digital balancing machining configured with ±0.01 g accuracy. The weighted polypropylene and glass/hemp fibres were blended with the help of an electronic-assisted mechanical stirrer operated at 80-100 rpm speed for 10 min durations at 180°C temperature. After delicate blending of both polypropylenes, glass and hemp fibres were mixed with 5 wt% of compatibilizer to enhance the adhesive properties between the polypropylene matrix and fibre [22].

The thoroughly blended matrix and fibre constitutions are fed into the injection mould via a hopper, continued with screw-type drive motor pass granules into the injection nozzle. Finally, the molten mixture is injected into preheated mould die to form the desired shape like $200 \times 20 \times 20$ mm. The developed composites are cooled by natural convection at elevated temperatures. The prepared polypropylene hybrid composite samples are shown in Figure 1.

2.3. Evaluation Procedure for Testing of Developed Polypropylene (PP6331) Hybrid Composites

2.3.1. Thermal Adsorption Behaviour of PP6331 Hybrid Composites. The thermal adsorption performance on the degradation of PP6331 hybrid composite is evaluated by thermogravimetric analysis (TGA) configured with the maximum temperature range of 1000°C. The Q500 series TGA is used to find the effect of thermal radiation on the degradation of composite weight loss during 27°C to 700°C at 25°C/min heat flow rate.

2.3.2. Heat Deflection Temperature Studies on Developed PP6331 Hybrid Composites. The heat deflection effects on developed polypropylene hybrid composite samples are estimated by the ASTM D648 standard. A three-jaw point fixes the test sample, and the heat is supplied by 23°C/min.

2.3.3. Mechanical Properties of Developed PP6331 Hybrid Composites. The mechanical properties of developed PP6331 hybrid composite samples are experimentally tested by the ASTM test standard. The Izod impact toughness of polypropylene hybrid composite was tested by an impact tester configured with 0-300 J capacity pursued via ASTM D256 (63.5 mm × 12.7 mm × 12.7 mm). The universal tensile test equipment was utilized to evaluate the tensile and flexural strength composite under the cross-slide speed of 10 mm/min. It was estimated by the standard of D638 (165 mm×19 mm×13 mm) and D790 followed ASTM.

TABLE 1: Constitution of polypropylene (PP6331) hybrid composite.

Sample	Weight percentages in wt%			
	PP6331	Compatibilizer	E-glass fibre	Hemp fibre
1			0	35
2			5	30
3	60	5	10	25
4			15	20
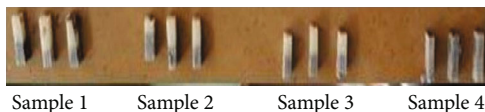
FIGURE 1: Developed polypropylene (PP6331) hybrid composite samples.

3. Results and Discussions

3.1. Thermal Adsorption Studies. The thermal adsorption properties of developed (PP6331) polypropylene hybrid composite samples are estimated by the thermogravimetric apparatus. The effect of glass/hemp fibre on the polypropylene composite decomposition range is evaluated by the constant heat flow rate of 25°C/min with a temperature span of 27°C to 700°C. Figure 2 illustrates the thermal adsorption properties of E-glass/hemp fibre-reinforced polypropylene hybrid composite with their decomposition weight.

During the starting stage, the composite temperature was 27°C at 25°C/min heat flow rate, showing 100% weight, while the increase in the temperature of more than 27°C represents progressive weight loss. It was due to the degradation of polypropylene structure with redistricted fibre movement at a higher temperature. The decomposition initiated by more than 220°C showed a two-step degradation curve up to 310°C. It was because incorporating compatibilizer in the polypropylene hybrid composite increases the adhesive properties, resulting in the decomposition rate on two stages mentioned in the two-step curve. It was found in minor physical changes. This physical change may be varied due to interfacial bonding between fibre and matrix. However, the interfacial bonding strength was increased by adding a 5 wt% compatibilizer which gives better adhesive properties. The management of thermal adsorption and its steady state flow may change the phase during steam generation applications [29]. The primary decomposition rate was observed from 296° to 302°C, but the composite containing 15 wt% glass showed better thermal ability than all others. The glass fibre has good thermal and mechanical properties, while the fibres combined with natural hemp fibre found good thermal stability. Similarly, the weight loss of 75%, 50%, and 25% percentage of the composite was valued in Table 2. Moreover, the presence of glass fibre has enhanced thermal stability with reduced degradation of composite values referred from Table 2, and the 75% weight loss occurred by the temperature range from 272°C to 324°C. Similarly, 50% and 25% of weight were found at 325°C-412°C and 427°C-471°C. More than 550°C found 10-14% weight loss due to the decomposed

layers on polypropylene composite. It may lead to a significant physical change in the structure of the composite.

3.2. Heat Deflection Temperature Studies. The influences of heat deflection temperature on glass/hemp fibre-reinforced polypropylene composites are evaluated by the ASTM D648 standard. It is the fundamental data that has been considered during designing a product that needs dimensional stability and can withstand the specific temperature span. Similarly, the materials can maintain the elastic limit and retain their stiffness at room temperature. Figure 3 indicates the heat deflection temperature of polypropylene and its hybrid composite contained glass/hemp fibre.

The heat deflection temperature of PP6331 is 58°C, while adding glass fibre content in PP6331 matrix/hemp fibre increases the deflection temperature from 58°C to 121°C in sample 1 as identified in Figure 3. Similarly, samples 2, 3, and 4 illustrate improved composite heat deflection temperature. The maximum heat deflection temperature of 141°C is found on 60 wt% PP6331/15 wt% glass fibre/20 hemp/5 wt% compatibilizer. It was because their E-glass fibre can withstand the maximum temperature of 324°C with 75% weight loss, which is proved above the thermal adsorption performance curve from Figure 2. Normally, the heat deflection temperature of the composite was enhanced by the inclusion of filler materials [15, 26]. However, the hemp/polypropylene composite is hybridized with E-glass fibre to attain maximum thermal characteristics and retain the stiffness with a reduction of the material's volume. The developed composites are dimensionally stable and are used for automotive door frame, rooftop, and frame applications.

3.3. Impact Strength of PP6331 Hybrid Composites. Figure 4 represents the Izod impact strength histogram illustration of the PP6331 hybrid composite containing glass/hemp fibre. The composite material measurement can resist the high impact force that may damage the structure, like fracture or bending. It is directly connected with material toughness. Here, the minor amount of E-Glass fibre plays a vital role in PP6331 hybrid composite that is able to withstand the high impact load, resulting in the integration of crack propagation without a break of composite. The PP6331 matrix has a low impact strength of 21 J/m. At the same time, the addition of 35% hemp fibre in PP6331 shows 90% improved impact strength.

Further increase in hemp fibre in PP6331 matrix hybridization with 0 wt%, 5 wt%, 10 wt%, and 15 wt% E-glass fibre enhanced the impact strength of PP6331 hybrid composite. The maximum impact strength is 55 J/m, found in sample 4. It is improved 1.6 times of PP6331 and 37.5% of sample 1. However, a small amount of E-glass fibre enhances the resistance against the impact load, and 5 wt% compatibilizer augments suitable adhesive between matrix and fibre. The glass fibres have good fracture toughness properties [22].

3.4. Flexural Strength of PP6331 Hybrid Composites. The effect of E-glass fibre content on the flexural strength of hemp/PP6331 composites is shown in Figure 5. It is observed from Figure 5 that the flexural strength of the PP6331 hybrid
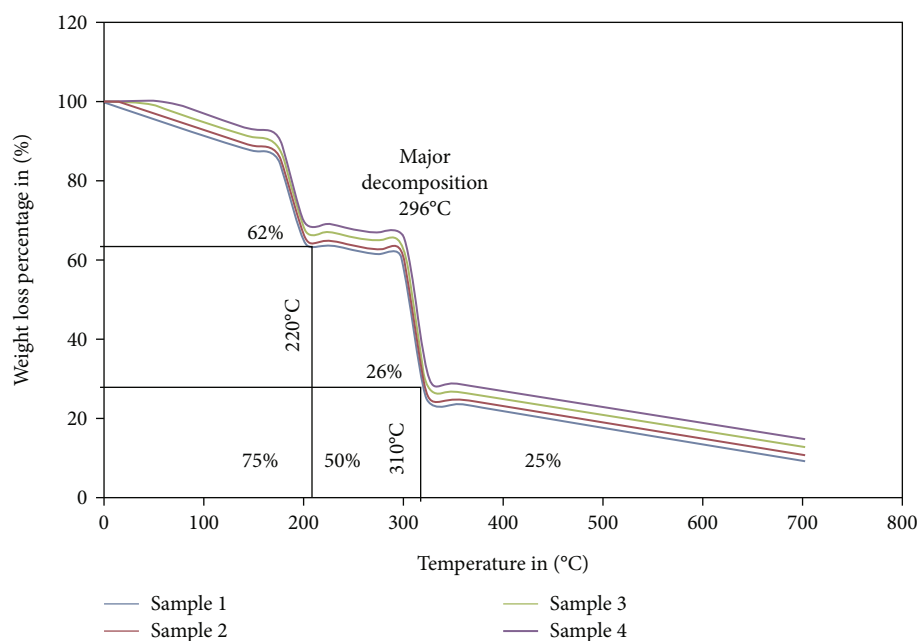
FIGURE 2: Thermal adsorption curves of PP6331 hybrid composites.

TABLE 2: Thermal adsorption behaviour of polypropylene hybrid composites.

Sample no.	The temperature range in °C			Weight loss % More than 550°C
	75%	50%	25%	
1	272	325	427	10
2	291	354	440	11
3	315	371	451	13
4	324	412	471	15

composite is increased significantly with the additions of E-glass/hemp fibre. The flexural strength of the PP6331 matrix is 44.1 MPa, and its property is significantly improved by the incorporation of hemp at 35 wt% maximum which shows 91 MPa. Its strength is improved by 1.06 times of PP6331 matrix strength. At the same time, adding E-glass fibre into the hemp/PP6331 matrix has higher flexural strength than the unhybridized PP6331 matrix. The composite containing 5 wt%, 10 wt%, and 15 wt% of E-glass fibre shows a superior flexural strength of 95 MPa, 98 MPa, and 104 MPa. Sample 4 is found to have maximum flexural strength and improved by 1.4 times of PP6331 material and 14.2% compared to sample 1. The increased flexural strength is due to their adequate bonding of shot fibre, which can make good strength and resist fibre movement. One of the authors reported a similar statement during the evaluation of natural fibre-reinforced polypropylene biocomposite [10]. The presence of both synthetic and natural fibre can withstand the maximum tensile load and resist internal movement.

3.5. Tensile Strength of PP6331 Hybrid Composites. The tensile strength variations of the E-glass/hemp fibre-reinforced PP6331 hybrid composite are represented in Figure 6. The overall contribution of fibre is 35 wt%, and the content of E-glass fibre varies from 0 wt% to 15 wt% with an interval of 5 wt%. Similarly, 5 wt% of compatibilizer is added with the PP6331/glass/hemp fibre hybrid composite, increasing the adhesive behaviour of the composite. The tensile strength of developed composites is tested by universal tensile testing apparatus built up manual controller assisted by an electronic plotter. The cross-slide movement is limited to 10 mm/min. Correspondingly, every reaction to physical changes of composite is noted.

The tensile strength of PP6331 is found to be 30.3 MPa, and the incorporation of a glass/hemp fibre ratio of 0 : 35 showed that 52 MPa and 58 MPa are noted on a 5 : 30 fibre ratio (sample 2), which improved by 11.53% compared to sample 1. So, from this, PP6331's hybridization with E-glass fibre is proven. Further increases in E-glass fibre in PP6331 composite found increased tensile strength of composites. It was due to the reaction-free polypropylene matrix that has been perfectly bonded with chopped fibre filler [2, 10]. The higher tensile strength identified from Figure 6 shows that the composite containing 15 wt% of glass fibre/20 wt% of hemp fibre added
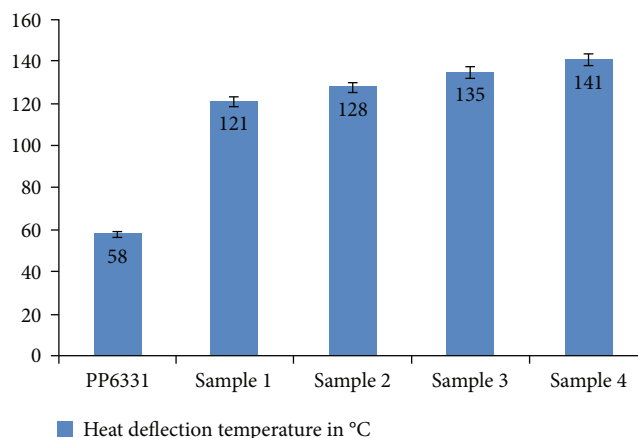
FIGURE 3: Heat deflection temperature histogram of PP6331 and its hybrid composites.
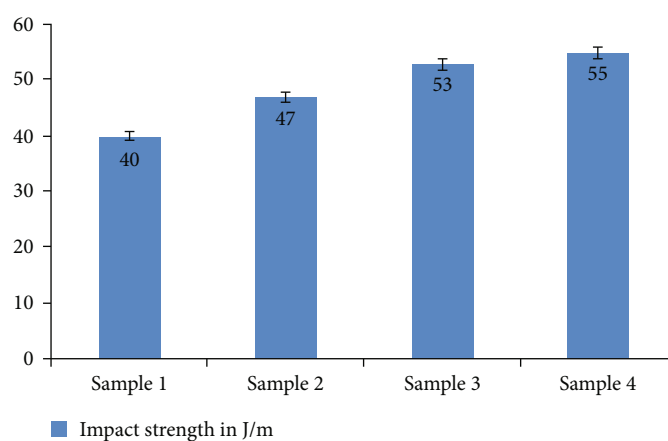
FIGURE 4: Impact strength of PP6331 hybrid composites.
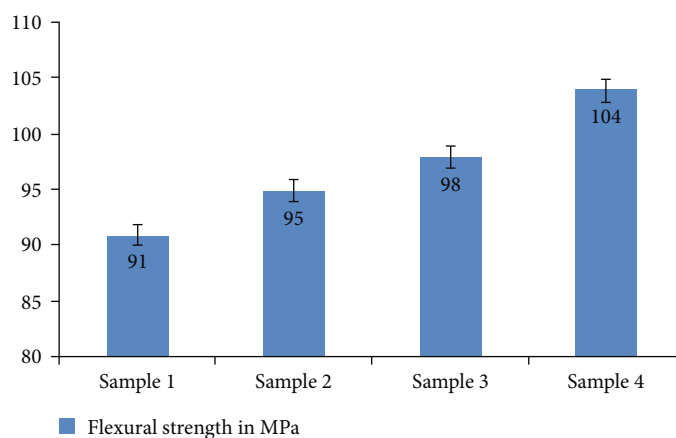
FIGURE 5: Flexural strength of PP6331 hybrid composites.

with constant weight percentages of compatibilizer (5 wt%) is 63 MPa and improved by 1.07 times of PP6331 matrix and 21.1% of sample 1. The maximum enhancement of the composite was due to the incorporation of hemp, limiting the tensile fracture against the high tensile load.

3.6. SEM Micrograph of Sample 4 Polypropylene Hybrid Composite.
Figure 7 illustrates the SEM micrograph of sample 4 polypropylene hybrid composite containing 15 wt% of E-glass fibre and 20 wt% of hemp blended by 5 wt% of compatibilizer. This composite attained maximum tensile, impact,
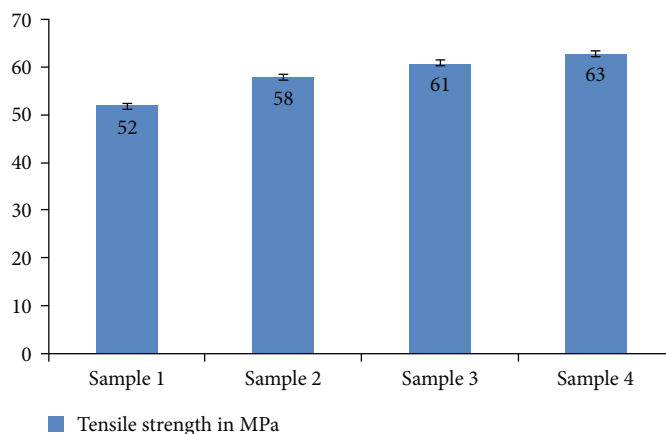
FIGURE 6: Tensile strength of PP6331 hybrid composites.
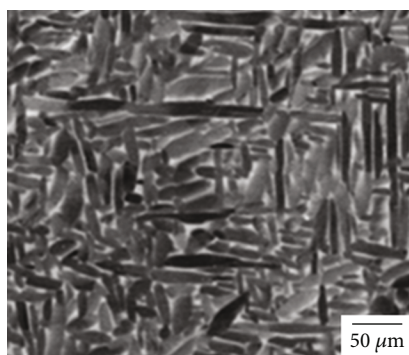
FIGURE 7: SEM micrograph of (sample 4) polypropylene hybrid composite.

and flexural strength compared to other compositions. The micrograph's dark and light field image represents the hemp and E-glass fibre. It was revealed from Figure 7 that both E-glass and hemp fibres interacted with the base matrix. Both fibres were uniformly bonded with a polypropylene matrix phase with increased adhesive properties. It is proof of good interfacial bonding and enhances mechanical and thermal properties.

4. Conclusions

The current investigation of polypropylene hybrid composite thermal and mechanical properties was successfully enriched by using the different weight percentage ratios of $0:35$, $5:30$, $10:25$, and $15:20$ glass/hemp fibre hybridization with the utilization of 5 wt% compatibilizer via injection moulding technique. The evaluated experimental ASTM test results showed that the thermogravimetric analysis of thermal adsorption properties of PP6331 hybrid composite found that 75% of weight loss occurred at 272°C to 324°C, and 50% and 25% of weight loss were found at 325°C-412°C and 427°C-471°C, respectively. The heat deflection temperature on 60 wt% PP6331/15 wt% glass fibre/20 hemp/5 wt% compatibilizer is 141°C. Therefore, the developed composite with 15 wt% E-glass fibre can be dimensionally stable at higher temperatures for automotive door frames, rooftop, and frame applications. The mechanical properties like the impact, tensile, and flexural strength of sample 4 were found to have a maximum strength of 55 J/m, 63 MPa, and 104 MPa and improved 1.6 times, 1.4 times, and 1.07 times of PP6331 of sample 1.

Data Availability

All the data required are available within the manuscript.

Conflicts of Interest

Authors declare no conflicts of interest.

References

[1] K. G. Satyanarayana, G. G. C. Arizaga, and F. Wypych, "Biodegradable composites based on lignocellulosic fibers–an overview," *Progress in Polymer Science*, vol. 34, no. 9, pp. 982–1021, 2009.

[2] S. Mukhopadhyaya and R. Srikanta, "Effect of ageing of sisal fibres on properties of sisal - polypropylene composites," *Polymer Degradation and Stability*, vol. 93, no. 11, pp. 2048–2051, 2008.

[3] S. Armioun, S. Panthapulakkal, J. Tjong, and M. Sain, "Renewable, recyclable, and lightweight structural prototype for greener automotive interior panels," in *65th Canadian Chemical Engineering Conference Canada(CSCHE2015)*, Calgary, 2015.

[4] C. Dineshbabu and R. Venkatesh, "Investigation of aspect ratio and friction on barrelling in billets of aluminium upset forging," *Materials Today: Proceedings*, vol. 21, no. 1, pp. 601–611, 2020.

[5] S. Sudhagar, S. Sathees Kumar, V. Vijayan, and R. Venkatesh, "UV- and visible-light-driven TiO2/La2O3 and TiO2/Al2O3 nanocatalysts: synthesis and enhanced photocatalytic activity," *Applied Physics A*, vol. 128, no. 4, p. 282, 2022.

[6] K. Friedrich, "Polymer composites for tribological applications," *Advanced Industrial and Engineering Polymer Research*, vol. 1, no. 1, pp. 3–39, 2018.

[7] J. Broge, "Natural fibres in automotive components," *Automotive Engineering International*, vol. 1, p. 120, 2000.

[8] S. Baskar, T. Maridurai, R. Arivazhagan, S. SivaChandran, and R. Venkatesh, "Thermal management of solar thermoelectric power generation," *AIP Conference Proceedings*, vol. 2473, no. 1, 2002.

[9] H. N. Yu, S. S. Kim, I. U. Hwang, and D. G. Lee, "Application of natural fiber reinforced composites to trenchless rehabilitation of underground pipes," *Composite Structures*, vol. 86, no. 1-3, pp. 285–290, 2008.

[10] H. S. Lee, D. Cho, and S. O. Han, "Effect of natural fiber surface treatments on the interfacial and mechanical properties of henequen/polypropylene biocomposites," *Macromolecular Research*, vol. 16, no. 5, pp. 411–417, 2008.

[11] M. Taşdemır, H. Biltekin, and G. T. Caneba, "Preparation and characterization of LDPE and PP—wood fiber composites," *Journal of Applied Polymer Science*, vol. 112, no. 5, pp. 3095–3102, 2009.

[12] K. Bledzki, S. Reihmane, and J. Gassan, "Properties and modification methods for vegetable fibers for natural fiber composites," *Journal of Applied Polymer Science*, vol. 59, no. 8, pp. 1329–1336, 1996.

[13] B. Dahlke, H. Larbig, H. D. Scherzer, and R. Poltrock, "Natural Fiber reinforced foams based on renewable resources for automotive interior applications," *Journal of Cellular Plastics*, vol. 34, no. 4, pp. 361–379, 1998.

[14] A. M. Eleiche and G. M. Amin, "The effect of unidirectional cotton fibre reinforcement on the friction and wear characteristics of polyester," *Wear*, vol. 112, no. 1, pp. 67–78, 1986.

[15] U. Nirmal, B. F. Yousif, D. Rilling, and P. V. Brevern, "Effect of betelnut fibres treatment and contact conditions on adhesive wear and frictional performance of polyester composites," *Wear*, vol. 268, no. 11-12, pp. 1354–1370, 2010.

[16] N. S. M. El-Tayeb, "A study on the potential of sugarcane fibers/polyester composite for tribological applications," *Wear*, vol. 265, no. 1-2, pp. 223–235, 2008.

[17] N. Chand and U. K. Dwived, "Effect of coupling agent on abrasive wear behaviour of chopped jute fibre- reinforced polypropylene composites," *Wear*, vol. 261, no. 10, pp. 1057–1063, 2006.

[18] G. Mehta, L. T. Drzal, A. K. Mohanty, and M. Misra, "Effect of fiber surface treatment on the properties of biocomposites from nonwoven industrial hemp fiber mats and unsaturated polyester resin," *Journal of Applied Polymer Science*, vol. 99, no. 3, pp. 1055–1068, 2006.

[19] T. Behzad and M. Sain, "Cure simulation of hemp fiber acrylic based composites during sheet molding process," *Polymers and Polymer Composites*, vol. 13, no. 3, pp. 235–244, 2005.

[20] M. Sain, P. Suhara, S. Law, and A. Bouilloux, "Interface modification and mechanical properties of natural fiber-polyolefin composite products," *Journal of Reinforced Plastics and Composites*, vol. 24, no. 2, pp. 121–130, 2005.

[21] G. I. Williams and R. P. Wool, "Composites from natural fibres and soy oil resins," *Applied Composite Materials*, vol. 7, no. 5/6, pp. 421–432, 2000.

[22] P. Wambua, J. Ivens, and I. Verpoest, "Natural fibres: can they replace glass in fibre reinforced plastics?," *Composites Science and Technology*, vol. 63, no. 9, pp. 1259–1264, 2003.

[23] F. Asuke, M. Abdulwahab, V. S. Aigbodion, O. S. I. Fayomi, and O. Aponbiede, "Effect of load on the wear behaviour of polypropylene/carbonized bone ash particulate composite," *Egyptian Journal of Basic and Applied Sciences*, vol. 1, no. 1, pp. 67–70, 2014.

[24] A. K. Mohanty, P. Tummala, W. Liu, M. Misra, P. V. Mulukutla, and L. T. Drzal, "Injection molded biocomposites from soy protein based bioplastic and short industrial hemp fiber," *Journal of Polymers and the Environment*, vol. 13, no. 3, pp. 279–285, 2005.

[25] A. K. Mohanty, A. Wibowo, M. Misra, and L. T. Drzal, "Effect of process engineering on the performance of natural fiber reinforced cellulose acetate biocomposites," *Composites Part A: Applied Science and Manufacturing*, vol. 35, no. 3, pp. 363–370, 2004.

[26] M. C. Khoathane, O. C. Vorster, and E. R. Sadiku, "Hemp fiber-reinforced 1-pentene/polypropylene copolymer: the effect of fiber loading on the mechanical and thermal characteristics of the composites," *Journal of Reinforced Plastics and Composites*, vol. 27, no. 14, pp. 1533–1544, 2008.

[27] R. Venkatesh, S. Manivannan, P. Sakthivel, V. Vijayan, and S. Jidesh, "The investigation on newly developed of hydrophobic coating on cast AZ91D magnesium alloy under 3.5 wt% NaCl solutions," *Journal of Inorganic and Organometallic Polymers and Materials*, vol. 32, no. 4, pp. 1246–1258, 2022.

[28] M. Krishnaraj, T. Thirugnana Sambandha, R. Arun, and T. Vaitheeswaran, "Fabrication and wear characteristics basalt fiber reinforced polypropylene matrix composites," in *SAE Technical Paper Series*, United States, 2019.

[29] S. Marimuthu, P. Lakshmanan, K. Raju, A. Mohana Krishnan, R. Venkatesh, and M. Dineshkumar, "Performance study on glazzed solar air heater for agri products," *Materials Today: Proceedings*, vol. 69, pp. 633–636, 2022.

Research Article

Evaluation of Thermal Adsorption and Mechanical Behaviour of Intralaminar Jute/Sisal/E-Glass Fibre-Bonded Epoxy Hybrid Composite as an Insulator

R. Venkatesh,[1] S. Raghuvaran,[2] M. Vivekanandan,[3] C. Ramesh Kannan,[4] T. Thirugnanasambandham,[5] and Arundeep Murugan [6]

[1]Department of Design, Saveetha School of Engineering, SIMATS, Chennai, 602105 Tamil Nadu, India

[2]Department of Mechanical Engineering, K. Ramakrishnan College of Engineering, Trichy, 621112 Tamil Nadu, India

[3]Department of Mechanical Engineering, Kongunadu College of Engineering and Technology, Trichy, 621215 Tamil Nadu, India

[4]Department of Mechanical Engineering, SRM TRP Engineering College, Trichy, 621105 Tamil Nadu, India

[5]Department of Mechanical Engineering, Ponnaiyah Ramajayam Institute of Science and Technology, Thanjavur, 613203 Tamil Nadu, India

[6]School of Mechanical and Industrial Engineering, Institute of Technology, Debre Markos University, Debre Markos, Ethiopia

Correspondence should be addressed to Arundeep Murugan; arundeepmurugan@gmail.com

A thermal gravimetric analyzer analyzed the thermal adsorption properties of developed composites with the temperature range of 28°C–650°C at a 20°C/min constant heat flow rate. The epoxy hybrid composites were synthesized using natural jute/sisal fibre hybridized with the addition of synthetic E-glass fibres at 0-degree, 0/90-degree, and intralaminar orientations through the wet filament-winding process. The effects of orientations on tensile, flexural, and impact strengths of epoxy hybrid composites were studied using ASTM D3039, D790, and D6110. The evaluated results were compared, and the epoxy hybrid composite containing intralaminar orientations found better thermal stability with reduced weight loss at 650°C. Similarly, the test result for mechanical studies of the hybrid composite showed superior tensile, flexural, and impact strengths. The epoxy hybrid composite with intralaminar orientation was found to have a maximum tensile, impact, and flexural strength of 61.91 MPa, 770.61 J/m, and 83.90 MPa, respectively.

1. Introduction

The polymer matrix hybrid composites are prepared with natural and synthetic fibre grouping, facilitating good toughness, high strength, better thermal stability, and high corrosion resistance compared to conventional plastic materials. The interfacial bonding strength between the fibre and matrix mainly depends on the enhancement of the composite. More than one reinforcement fibre makes an effective hybrid composite with superior performance applied to various engineering applications [1–6]. The hybrid composites are cheaply prepared with natural and synthetic fibres [7, 8]. The hybridization composite can achieve the desired specific properties with the appropriate selection of natural and synthetic fibres. The applications of hybrid composites have increased in recent years in the fields of structural engineering, construction, sports, and defence [9–15].

Natural fibres are the best alternative for conventional artificial fabric fibres bonded with a poly material that is high strength, nontoxic, renewable, and eco-friendly [16, 17]. Moreover, the ecological behaviour of natural fibres facilitates low density and better damping capability in combination with glass fibres [18]. The epoxy composite was hybridized with jute/sisal fibre via the conventional technique to find the composite's increased tensile strength which had an increase of 77% when compared to the nonreinforced jute composite [19]. The water absorption and mechanical performance of the sisal/stalk fibre hybrid

composite were evaluated based on ASTM standards. The results found that the tensile and flexural strengths of the composite were enhanced by 20% and 49.5%, respectively. The effect of water absorption was limited by adding sisal fibre [20]. The hybridization effect of the hybrid composite was enhanced using different jute/banana fibres that showed high flexural, tensile, and impact strengths and good thermal stability at 50 wt% of jute/epoxy [21].

The polymer composite was developed with jute and glass fibres via the conventional technique. The results showed that jute and glass fibre combinations showed better mechanical characteristics and good thermal behaviour [22]. The different volumes (30–50) of a banana/pineapple/glass fibre-reinforced hybrid composite were studied for their mechanical and thermal characteristics. The composite composed of 40 vol% showed better mechanical performance, and TGA analysis revealed that the composite has optimum thermal adsorption compared to others [23]. The effect of sisal fibre on jute-reinforced thermal and mechanical properties of the epoxy hybrid composite was evaluated. The experimental results showed that the presence of the sisal fibre in the epoxy composite results in superior thermal properties like high-storage modulus and limited weight loss. The mechanical strength is higher than in the ordinary jute fibre-reinforced epoxy composites [24]. The polypropylene composite was prepared with glass/sisal fibre, and its thermal characteristics were studied via TGA. The decomposition ratio at higher temperatures limits the thermal adsorption properties of the polypropylene composite. This is due to the incorporation of the glass fibre as part of hybridization with the composite [25]. Researchers synthesized the hemp fibre-bonded polymer matrix composite via the conventional technique. Hemp fibre in the polymer matrix resulted in good thermal properties compared to the polymer matrix composite without hemp fibre [26].

Similarly, other researchers reported that the thermal conductivity of the polymer matrix composite was enhanced by the presence of hemp fibre [27]. Moreover, the E-glass fibre-reinforced epoxy composite showed better thermal behaviour and enhanced thermal stability between 25°C and 1000°C [28]. The present research investigates enhancing the thermal adsorption and mechanical properties of epoxy hybrid composites bonded with different orientations of natural jute/sisal/E-Glass fibres. The impacts of the experimental results of different orientations on thermal adsorption and mechanical performance are compared. Finally, the enhanced value of the composite sample is recommended for insulator applications.

2. Materials and Methods

Epoxy resin and hardener are chosen as the base polymer resin matrix. The continuous natural jute/sisal is considered the reinforcement fibre, and synthetic E-glass fibre is the choice for hybridizing the epoxy/jut/sisal fibre composite. However, natural jute/sisal fibres have higher stiffness, low density, and good thermal properties [21, 22]. The sisal fibre constitutions in the epoxy composite hybridized with E-glass fibre result in increased mechanical and thermal adsorption

Table 1: Physical, mechanical, and thermal properties of jute/sisal/ and E-glass fibre.

Fibre	Density	Tensile strength	Elastic modulus	Thermal conductivity
	g/cc	MPa	GPa	W/mK
Jute	1.5	390–770	15	427.3
Sisal	1.29	570–710	22	0.205
E-glass	2.54	3400	72	0.03

characteristics [5, 9, 16]. The physical, mechanical, and thermal properties of jute, sisal, and E-glass fibres are mentioned in Table 1.

2.1. Fabrication of Jute/Sisal/E-Glass Fibre-Bonded Epoxy Hybrid Composites. Figures 1(a)–1(c) illustrate the fabrication setup with a fibre mandrel wrap, epoxy resin pool, and filament-winding robot arm. The continuous jute/sisal/ E-glass fibres were held separately using the fibre mandrel wrap configured with a stepper motor. Similarly, the 60 : 40 volume fractions of the epoxy resin and hardness were mixed uniformly in the wet filament resin pool container. The individually wrapped continuous jute, sisal, and E-glass fibres were dipped into an epoxy resin pool. The tipped continuous fibres have been winded with the help of a robot. Based on the specified orientations, epoxy hybrid composites were developed.

Finally, the prepared epoxy composite was naturally dried at ambient temperature. ASTM test standards shaped the synthesized composites. All the fibres are formed via a shuttle and part filament-winding axle as per (a) zero orientation, (b) 0- and 90-degree cross-orientation, and (c) intra-laminar model block diagram as shown in Figure 2.

2.2. Evaluations of Developed Composite Samples. The epoxy hybrid composite was contained in a thermal gravimetric analyzer that experimentally measured the jute/sisal/E-glass fibre's thermal adsorption and heat deflection properties at a constant heat flow rate of 20°C/min. The developed composite samples were evaluated based on ASTM standards. The tensile and flexural strengths of the composite were evaluated via an FIE-made UTM machine with a cross-slide speed of 5 mm/min according to ASTM D3039 and ASTM D790. The IT-made Charpy impact tester measured the impact toughness of the composite based on the ASTM D6110 standard.

3. Results and Discussions

3.1. Thermal Characteristics Study

3.1.1. Thermal Adsorption Characteristics Study. The thermal adsorption performance of hybrid composites is studied with different fabric orientations, following Figure 2. The composite was a 5 mm × 5 mm sample and kept in the thermal gravimetric analyzer apparatus. During the thermal gravimetric analysis, the temperature is varied from 28°C to 650°C at a 20°C/min constant heat flow rate. Figure 3(a) indicates the thermal adsorption-mass loss curve of a hybrid composite with different laminates. The 0-degree orientations
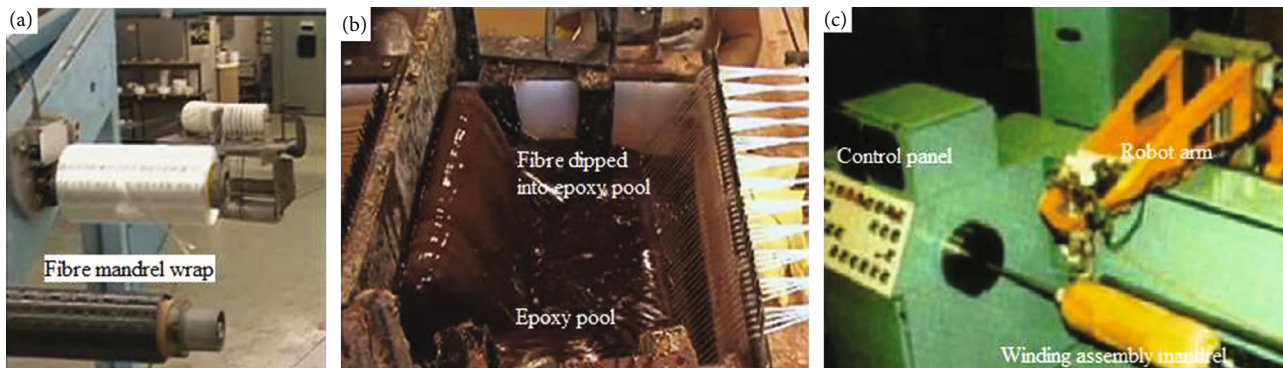
FIGURE 1: Actual fabrication setup of wet winding machine. (a) Fibres are placed in roving roller, (b) resin bath, and (c) filament-winding robot arm with a fabric mat.
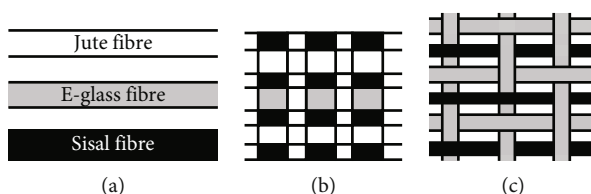
FIGURE 2: Different arrangements of fibre in epoxy composite: (a) zero orientation, (b) 0- and 90-degree cross-orientation, and (c) intralaminar.
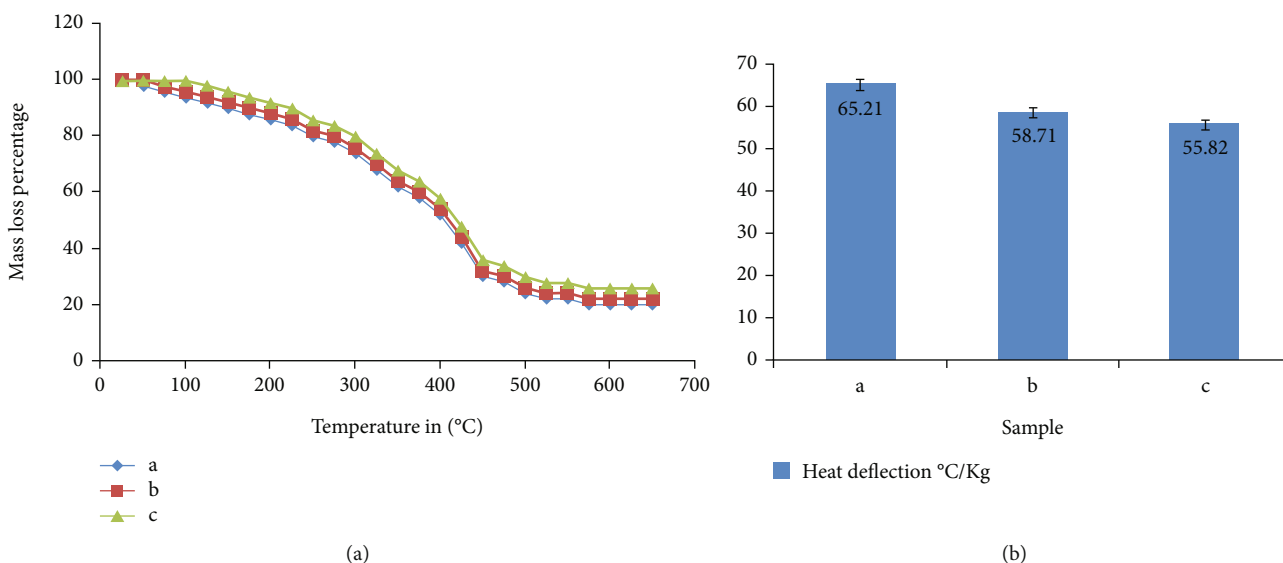
FIGURE 3: (a) Thermal adsorption behaviour on mass loss of epoxy hybrid composites. (b) Heat deflection temperature of epoxy hybrid composites.

of the jute/sisal/E-glass fibre-bonded epoxy hybrid composite sample a show a significant decomposition rate with 20% mass loss on more than 400°C, and the sample b (0/90-degree orientation) epoxy hybrid composite shows a similar trend of the decomposition rate with improved thermal stability at 25% mass loss during examination at high temperature (more than 400°C). The materials degrade at high temperatures via mass loss due to the volatility of the fabric material in epoxy [23, 24]. It is observed from Figure 3 that the epoxy hybrid composite with intralaminar orientation of sample c shows a minimum mass loss during the high thermal adsorption stud-

ies as compared to that of sample b. The decomposition due to mass loss of the glass fibre is more significant than the decomposition of natural fibre. However, all the composites are shown with a downtrend inclination curve. The maximum thermal stability was observed on the intralaminar composite that is used as a good insulator for energy storage applications.

3.1.2. Heat Deflection Temperature. Figure 3(b) represents the heat deflection temperatures of epoxy hybrid composites using various fibre orientations of jute/sisal/E-glass fibre. The heat deflection of the epoxy hybrid composite sample

a has a higher value of $65.21 \pm .09 \circ$ C/kg. The higher heat deflection is due to the 0-degree orientations of the jute/sisal/E-glass fibre being able to transfer a large amount of heat, resulting in variations of the internal structure like decomposition. The heat deflection of sample b is limited by 11% compared to that of the epoxy hybrid composite sample b. The most negligible heat deflection is $55.82 \pm 1.02 \circ$ C/kg found on epoxy hybrid composite sample c, which is limited by 17% compared to sample a. The 0- and 90-degree cross-positioned fibre has to delay the heat transfer and be stable at varied temperatures. However, the epoxy laminate's heat deflection depends on the selection of fibre, orientations, and processing [24, 27]. Control of the thermal behaviour is the primary reason for the thermal stability of the E-glass fibre's intraorientation. It may depend on thermal aging and reinforced fibre processing [28].

3.2. Tensile Strength of Hybrid Composites.

The $300 \, mm \times 25 \, mm \times 4 \, mm$ test samples were evaluated based on the ASTM D3039 standard using the UTM tensile test machine with a $5 \, mm/min$ cross-slide speed. The tensile strength of the developed epoxy hybrid composite using different fibre orientations of jute/sisal/E-glass fibre is shown in Figure 4. The three trials from each sample (a, b, and c) are considered for the tensile strength evaluation, and their mean value is taken. It is noted from Figure 4 that the tensile strength of the hybrid composite significantly varies due to the orientations of the fibre in the epoxy matrix. However, the fibre orientations are one reason for enhancing mechanical properties [7–9]. The tensile strength of sample a is found to be $48.12 \pm 1.78 \, MPa$, and the tensile strength of the composite is increased by 15.8% on the 0- and 90-degree orientations of the fibre (sample b). The improvement in tensile strength of the composite is due to the orientations of the fibre and processing of the composite [24]. The maximum tensile strength of $61.91 \pm 2.1 \, MPa$ is measured on the intralaminar composite (sample c) fabricated with the jute/sisal/E-glass fibre-bonded epoxy. It was the intrafabric combinations that resist the maximum tensile load and the tensile fracture. The maximum tensile strength was enhanced by 28.65% compared to that of the sample a epoxy hybrid composites as shown in Figure 4.

3.3. Flexural Strength of Hybrid Composites.

Figure 5 depicts an epoxy hybrid composite's flexural strength with different jute/sisal/E-glass fibre orientations. The flexural strength of the epoxy hybrid composite sample a is $56.91 \pm 1.44 \, MPa$, and $77.85 \pm 1.40 \, MPa$ is obtained by the 0- and 90-degree orientations of the jute/sisal/E-glass fibre-bonded epoxy hybrid composite sample b. The improvement of flexural strength is due to the adequate bonding strength between the matrix and fibre, thus resisting the high tensile force. The composite's flexural strength may vary due to fibre compositions, laying method, and the second phase reinforcement selection [11–13]. However, the flexural strength of the composite has been related to the selection fibre and its sequence [15, 16]. The flexural strength of the epoxy hybrid composite sample c synthesized using the jute/sisal/E-glass fibre as the intralayer is found at a maximum strength of
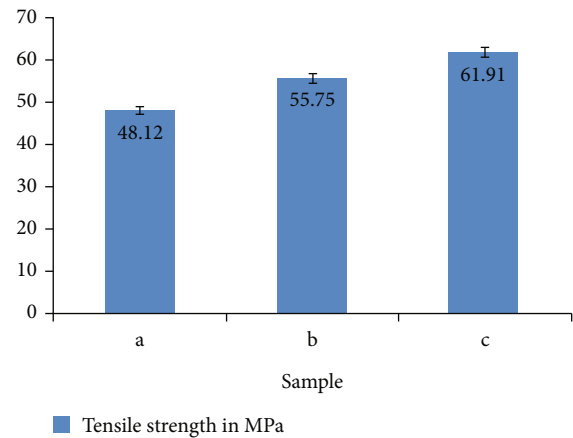
Figure 4: Tensile strength of epoxy hybrid composites.
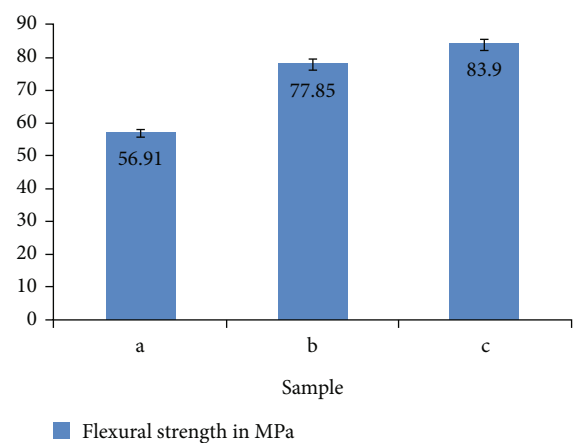
Figure 5: Flexural strength of epoxy hybrid composites.

$83.9 \pm 1.21 \, MPa$. Flexural strength enhancement is mainly attributed to the content of E-glass fibre presence in the jute/sisal laminate. The intralaminate is one of the primary reasons for the increased flexural strength of the composite. One of the researchers reported a similar report while evaluating a polymer composite bonded by natural fibre/E-glass fibre [18, 19]. The highest flexural strength is found on the intralaminar composite with good bonded structure. The results revealed that the intralaminar composite flexural strength is higher than the value of others. The flexural strength of the intralaminar composite is increased by 47% compared to that of the sample a epoxy hybrid composites.

3.4. Impact Strength of Hybrid Composites.

The impact strengths of the different orientations of the jute/sisal/E-glass fibre-bonded epoxy hybrid composite are represented Figure 6. Similar mechanical behaviour is observed in the impact strength of the epoxy hybrid composite. The impact toughness of the epoxy hybrid composite sample a is evaluated as $560.78 \, J/m$, while the that of the epoxy hybrid composite sample b is increased by 18.22%. The presence of natural jute and sisal fibre is the primary reason for increased impact strength, because natural fibres have naturally good toughness, high energy-absorbing capacities, and high stiffness compared to synthetic fibres [18–24]. The highest impact strength is
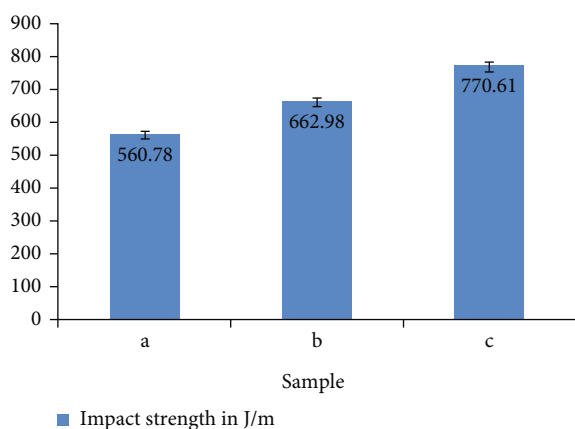
FIGURE 6: Impact strength of epoxy hybrid composites.
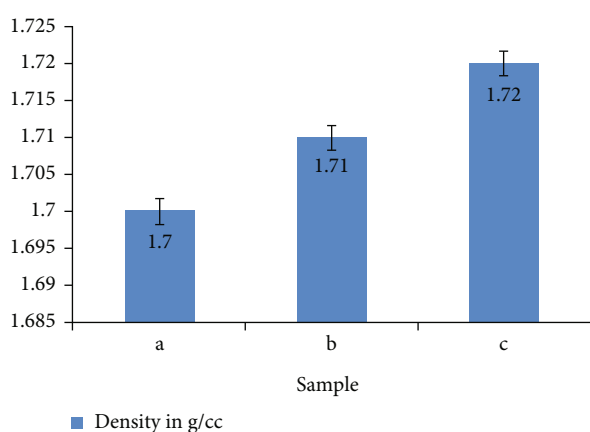
FIGURE 7: Density of epoxy hybrid composites.

observed in Figure 6, in which the composite contains intralaminar orientations resulting in good impact strength of 770.61 ± 1.31 J/m and improved energy-absorbing capability of 37.41% compared to those of sample a. This is due to the effective layer having been enhanced in the laminar fabric. Thus, the intralaminar-fabricated hybrid composite can withstand high-impact energy during the high-impact loading.

3.5. Density of Hybrid Composites. The densities of the different orientations of jute/sisal/E-glass fibre-bonded epoxy hybrid composite are represented in Figure 7. It is observed from Figure 7 that there are no significant variations found on the epoxy hybrid composite. The density of the epoxy hybrid composite sample a is found to be 1.7 ± 0.81 g/cc, and 1.71 ± 0.78 g/cc is measured for the 0- and 90-degree orientations of the jute/sisal/E-glass fibre-bonded epoxy hybrid composite sample b. For sample c, minor variations of 1.11% in its density were observed compared to sample a. The minor variations in density are due to similar constitutions but with changes in orientations.

4. Conclusions

The epoxy hybrid composite was successfully synthesized via the wet filament-winding process using different orientations of the jute/sisal/E-Glass fibre, and its thermomechanical behaviour was studied. The following conclusions are mentioned:

(i) Consistent among the fabric orientations of the epoxy hybrid composites, the intralaminar composite enhanced thermal adsorption and mechanical properties

(ii) The density of the sample c epoxy hybrid composite is the least (1.72 g/cc)

(iii) The thermal gravimetric analysis of the thermal adsorption properties of sample c found that the reduced decomposition rate due to mass loss of the epoxy hybrid composite was less than 20% at more than 400°C

(iv) The sample c showed that the minimum heat deflection is $55.82 \pm 1.02 \circ$ C/kg and is limited by 17% compared to sample a

(v) The tensile, flexural, and impact strengths of the epoxy hybrid composite sample c is higher than those of sample a and sample b. They were improved by 28.65%, 47%, and 37.41%, respectively, compared to the sample a epoxy hybrid composite

(vi) The enhanced sample c epoxy hybrid composite is recommended for thermal insulator applications

Data Availability

All the data required are available within the manuscript.

Conflicts of Interest

The authors declare that there are no conflicts of interest regarding the publication of this paper.

References

[1] R. Z. A. A. Ramadhan, A. R. Abu Talib, A. S. Mohd Rafie, and R. Zahari, "High velocity impact response of Kevlar-29/epoxy and 6061-T6 aluminum laminated panels," *Materials and Design*, vol. 43, pp. 307–321, 2013.

[2] R. Higuchi, T. Okabe, A. Yoshimura, and T. E. Tay, "Progressive failure under high-velocity impact on composite laminates: experiment and phenomenological mesomodeling," *Engineering Fracture Mechanics*, vol. 178, pp. 346–361, 2017.

[3] R. Venkatesh and S. Siva Chandran, "Magnesium alloy machining and its methodology: a systematic review and analyses," *AIP Conference Proceedings*, vol. 2473, no. 1, 2022.

[4] O. Faruk, A. K. Bledzki, H.-P. Fink, and M. Sain, "Biocomposites reinforced with natural fibers: 2000-2010," *Progress in Polymer Science*, vol. 37, no. 11, pp. 1552–1596, 2012.

[5] P. Sahu and M. Gupta, "Sisal (Agave sisalana) fibre and its polymer-based composites: a review on current developments," *Journal of Reinforced Plastics and Composites*, vol. 36, no. 24, pp. 1759–1780, 2017.

[6] S. Baskar and R. Venkatesh, "Thermal management of solar thermoelectric power generation," *AIP Conference Proceedings*, vol. 2473, no. 1, 2022.

[7] Y. Swolfs, L. Gorbatikh, and I. Verpoest, "Fibre hybridisation in polymer composites: a review," *Composites. Part A, Applied Science and Manufacturing*, vol. 67, pp. 181–200, 2014.

[8] T. Gurunathan, S. Mohanty, and S. K. Nayak, "A review of the recent developments in biocomposites based on natural fibres and their application perspectives," *Composites. Part A, Applied Science and Manufacturing*, vol. 77, pp. 1–25, 2015.

[9] Y. Li, Y.-W. Mai, and L. Ye, "Sisal fibre and its composites: a review of recent developments," *Composites Science and Technology*, vol. 60, no. 11, pp. 2037–2055, 2000.

[10] R. Zah, R. Hischier, A. L. Leão, and I. Braun, "Curaua fibers in the automobile industry - a sustainability assessment," *Journal of Cleaner Production*, vol. 15, no. 11-12, pp. 1032–1040, 2007.

[11] J. Isaac Premkumar, A. Prabhu, V. Vijayan, and R. Venkatesh, "Combustion analysis of biodiesel blends with different piston geometries," *Journal of Thermal Analysis and Calorimetry*, vol. 142, no. 4, pp. 1457–1467, 2020.

[12] A. Ramzy, D. Beermann, L. Steuernagel, D. Meiners, and G. Ziegmann, "Developing a new generation of sisal composite fibres for use in industrial applications," *Composites. Part B, Engineering*, vol. 66, pp. 287–298, 2014.

[13] S. N. A. Safri, M. T. H. Sultan, M. Jawaid, and K. Jayakrishna, "Impact behaviour of hybrid composites for structural applications: a review," *Composites. Part B, Engineering*, vol. 133, pp. 112–121, 2018.

[14] R. Eslami-Farsani, S. M. Reza Khalili, and M. Najafi, "Effect of thermal cycling on hardness and impact properties of polymer composites reinforced by basalt and carbon fibers," *Journal of Thermal Stresses*, vol. 36, no. 7, pp. 684–698, 2013.

[15] M. Najafi, S. M. R. Khalili, and R. Eslami-Farsani, "Hybridization effect of basalt and carbon fibers on impact and flexural properties of phenolic composites," *Iranian Polymer Journal*, vol. 23, no. 10, pp. 767–773, 2014.

[16] R. A. Braga and P. A. A. Magalhaes Jr., "Analysis of the mechanical and thermal properties of jute and glass fiber as reinforcement epoxy hybrid composites," *Materials Science and Engineering: C*, vol. 56, pp. 269–273, 2015.

[17] M. Shamsuyeva, O. Hansen, and H. Endres, "Review on Hybrid Carbon/Flax Composites and Their Properties," *International Journal of Polymer Science*, vol. 2019, Article ID 9624670, 17 pages, 2019.

[18] D. Cavalcanti, M. D. Banea, J. Neto, R. Lima, L. F. M. da Silva, and R. Carbas, "Mechanical characterization of intralaminar natural fibre-reinforced hybrid composites," *Composites. Part B, Engineering*, vol. 175, article 107149, 2019.

[19] B. T. Ferreira, L. J. da Silva, T. H. Panzera, J. C. Santos, R. T. S. Freire, and F. Scarpa, "Sisal-glass hybrid composites reinforced with silica microparticles," *Polymer Testing*, vol. 74, pp. 57–62, 2019.

[20] T. Maridurai and R. Venkatesh, "Review on direct steam generation using concentrated solar collectors," *AIP Conference Proceedings*, vol. 2473, no. 1, 2022.

[21] M. Boopalan, M. Niranjanaa, and M. Umapathy, "Study on the mechanical properties and thermal properties of jute and banana fiber reinforced epoxy hybrid composites," *Composites. Part B, Engineering*, vol. 51, pp. 54–57, 2013.

[22] R. Venkatesh and N. Karthi, "Synthesis and Adsorbent Performance of Modified Biochar with Ag/MgO Nanocomposites for Heat Storage Application," *Adsorption Science & Technology*, vol. 2022, Article ID 7423102, pp. 1–14, 2022.

[23] M. H. Zin, K. Abdan, and M. N. Norizan, "The effect of different fibre loading on flexural and thermal properties of banana/pineapple leaf (PALF)/glass hybrid composite," in *In Structural Health Monitoring of Biocomposites, Fibre-Reinforced Composites and Hybrid Composites*, Elsevier, Amsterdam, The Netherlands, 2019.

[24] M. Gupta, "Thermal and dynamic mechanical analysis of hybrid jute/sisal fibre reinforced epoxy composite," *Proceedings of the Institution of Mechanical Engineers, Part L: Journal of Materials: Design and Applications*, vol. 232, pp. 743–748, 2018.

[25] R. Venkatesh, S. Manivannan, P. Sakthivel, V. Vijayan, and S. Jidesh, "The investigation on newly developed of hydrophobic coating on cast AZ91D magnesium alloy under 3.5 wt% NaCl solutions," *Journal of Inorganic and Organometallic Polymers and Materials*, vol. 32, pp. 1246–1258, 2022.

[26] T. Behzad and M. Sain, "Measurement and prediction of thermal conductivity for hemp fiber reinforced composites," *Polymer Engineering Science*, vol. 12, pp. 977–983, 2007.

[27] A. Sayyidmousavi, H. Bougherara, S. R. Falahatgar, and Z. Fawaz, "Prediction of the effective thermal conductivity of fiber reinforced composites using a micromechanical approach," *Journal of Mechanics*, vol. 35, no. 2, pp. 179–185, 2019.

[28] C. Atasand and A. Dogan, "An experimental investigation on the repeated impact response of glass/epoxy composites subjected to thermal ageing," *Engineering*, vol. 75, pp. 127–134, 2015.

SAGE
Publishing

Research Article

Synthesis and Experimental Thermal Adsorption Characteristics of Epoxy Hybrid Composite for Energy Storage Applications

R. Venkatesh,[1] **Roshita David,**[2] **C. B. Priya,**[3] **M. Aruna** [iD]**,**[4] **Gopal Kaliyaperumal** [iD]**,**[5] **N. Mukilarasan** [iD]**,**[6] **Avinash Malladi** [iD]**,**[7] **and M. Karthikeyan** [iD][8]

[1]*Department of Design, Saveetha School of Engineering, SIMATS, Chennai, 602105 Tamil Nadu, India*
[2]*Department of Mechanical Engineering, Faculty of Engineering and Technology, JAIN (Deemed-to-be University), Karnataka-562112, India*
[3]*Department of Mechanical Engineering, OASYS Institute of Technology, Trichy, 621006 Tamil Nadu, India*
[4]*Faculty of Mechanical and Industrial Engineering, Liwa College of Technology, Abudhabi, UAE*
[5]*Department of Mechanical Engineering, New Horizon College of Engineering, Bengaluru, Karnataka 560103, India*
[6]*Department of Mechanical Engineering, Jeppiaar Institute of Technology, Chennai, 631604 Tamil Nadu, India*
[7]*Department of Mechatronics Engineering, ICFAI Tech, ICFAI Foundation for Higher Education, Hyderabad, 501203 Telangana, India*
[8]*Department of Electrical and Computer Engineering, Wolaita Sodo University, Sodo, Ethiopia*

Correspondence should be addressed to M. Karthikeyan; karthikeyan.m@wsu.edu.et

Polymer-based matrix hybrid composites meet their demand in various engineering applications and food industries due to their excellent mechanical, thermal, corrosion, and biodegradable performance. The polymer-based hybrid composites have been a better choice for high thermal insulation at low cost. This experiment attempted to find the thermal adsorption characteristics, heat deflection temperature, linear thermal expansion, and thermal conductivity of epoxy hybrid composites, which contained four different layers of Kevlar and basalt fiber fabricated via a low-cost conventional hand mold layup technique. This experiment revealed that the effect of basalt/Kevlar fiber on epoxy increased thermal performance. The results noted that the hybrid composite consists of less Kevlar fiber with the maximum basalt fiber of sample 4, showed excellent thermal adsorption effect on weight loss limited at 70.98%, and a better heat deflection temperature and 11.78×10^{-6} per °C linear thermal expansion were obtained. Sample 3 exhibited a maximum thermal conductivity of 0.251 W/mK. However, the thermal adsorption of hybrid composite has been limited by more basalt fiber, leading to a 1 wt%/°C decomposition rate.

1. Introduction

Great potential with lightweight polymer matrix composites is considered the best alternative for replacing conventional plastic material in several engineering, food, and medical industries. Polymer matrix composites are invented by polymer resin bonded with secondary phase material like fibers. It has been produced quickly using conventional techniques at a reasonable cost. Epoxy resin is mainly used for polymer matrix fabrication to obtain a high feature of mechanical, thermal, and chemical resistance [1, 2]. The polymer composite consists of various laminate fibers and dramatically impacts engineering manufacturing. It engages more percentage of the total production volume in various automotive applications [3]. The advanced grouping of natural and synthetic fiber composites is a better substitution for conventional composites due to their enhanced compatibility with resin [4–6]. More research investigation is done relevant to polymer matrix composite with various combinations of natural and synthetic fibers. The Kevlar/

(a)

(b)
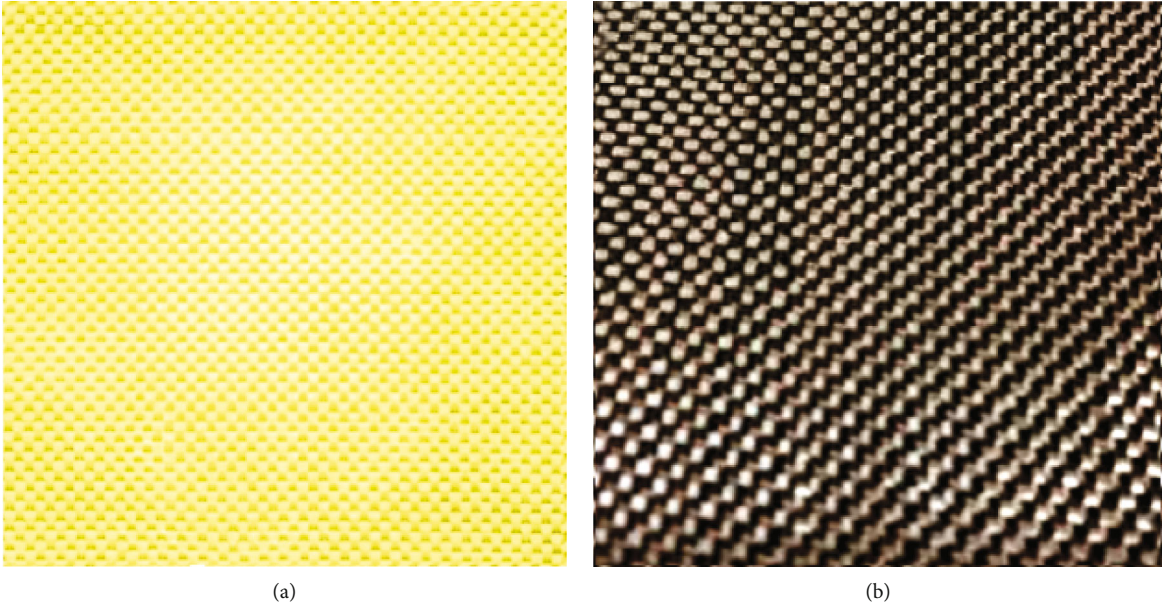
FIGURE 1: Fabric mat (a) Kevlar fiber and (b) basalt fiber.

TABLE 1: Mechanical and thermal properties of the fabric mat.

Fiber/properties	Density in g/cc	Tensile strength in MPa	Elastic modulus in GPa	Thermal conductivity (W/mK)
Kevlar	1.44	3620	62	0.04
Basalt	2.65	4800	110	1.62

basalt fiber combinations play a vital role in various industrial applications due to their enhanced thermal characteristics compared to other combinations [7–9]. The sandwich-configured Kevlar-flax-epoxy hybrid composite found superior impact and tensile strength [10].

Similarly, the epoxy/basalt fiber composite laminate with various graphene nanopellets (GNP) showed increased tensile, flexural, and impact strength of the composite [11]. Recently, Kevlar has been grouped with aramid fiber, resulting in low density, good thermal behavior, high thermal stability, and high strength. It is used to replace steel material in various applications, like bicycle frames and racing cars [12]. The mixed vinyl ester composite grouping with flax/basalt fiber showed higher tensile strength with limited brittleness and stiffness behavior [13]. The thermal conductivity of hemp-reinforced polymer composite is studied and experimentally measured and compared with that of the poly matrix. It showed good relation between theoretical to actual [14, 15]. The granite/basalt fiber/sandstone-reinforced polymer composite found better thermal stability at 25°C and 1000°C [16]. The E-glass-reinforced epoxy composite was developed via a conventional method to find increased thermal behavior [17]. The impact strength of glass fiber-reinforced polymer laminates shows a better resistive force on high-impact load [18]. The Kevlar-basalt fiber-mapping polymer composite with three layers thick showed better mechanical strength. It is impacted with 40-60 m/sec velocity, increasing the bonding strength [19]. The thermal conductivity of composite varies for the following reasons:

fiber orientation, base material, number of layers, and method of composite fabrication [20]. Incorporating fiber content in large volumes can increase thermal characteristics and provide good mechanical strength [21]. The thermal gravimetric analysis of the glass/carbon/Kevlar/polymer matrix hybrid composite showed minimum weight loss during high-temperature evaluation [22]. The following factors may affect the thermal characteristics of the composite fiber: length, diameter, mixing ratio, and defects [23]. The main aim of the experimental work is to evaluate the thermal adsorption characteristics of epoxy composite hybridization with Kevlar/basalt fiber via the conventional hand layup technique. The thermal behavior, like thermal conductivity, heat deflection temperature, and linear thermal expansion of composite, is also evaluated by different thermal conditions.

2. Experimental Details

2.1. Materials. The 400 GSM synthetic basalt and natural Kevlar fibers are chosen as reinforcement, as shown in Figures 1(a) and 1(b). Epoxy resin and hardener were chosen as adhesive materials. Kevlar and basalt fiber combinations improve the composite's thermal stability and impact strength [7–9]. The mechanical and thermal properties of both fibers are listed in Table 1.

2.2. Synthesis of Hybrid Composite. The epoxy resin and hardener mix at a ratio of 15 : 1 through manual stir action. The dimensions of 300 mm × 100 mm × 2 prepare the Kevlar
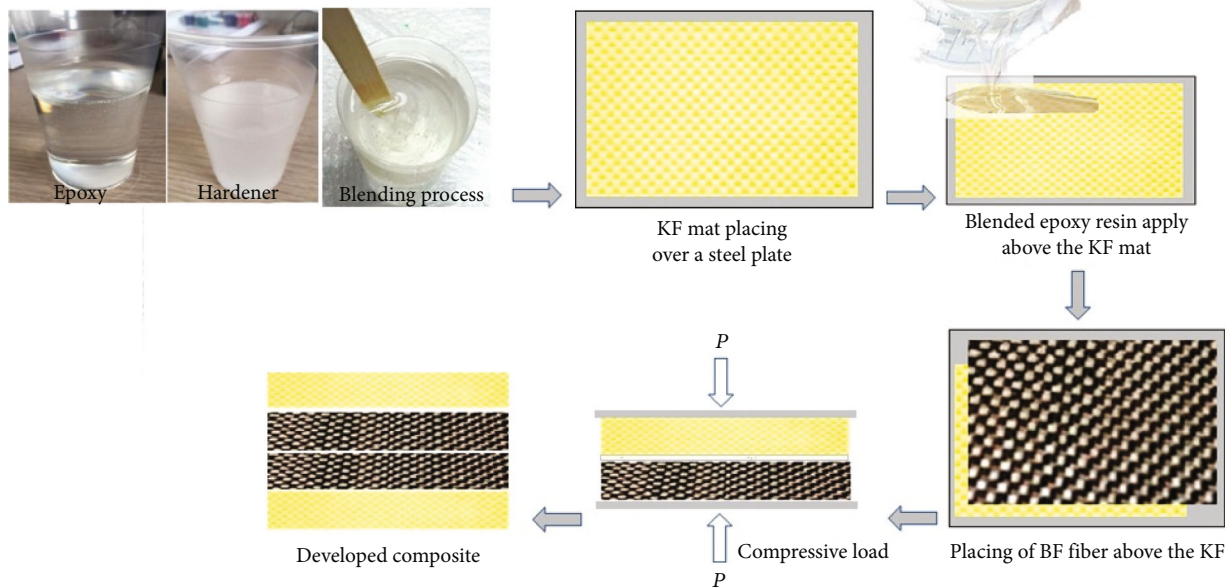
FIGURE 2: Flow process layout for epoxy hybrid composite fabrication.
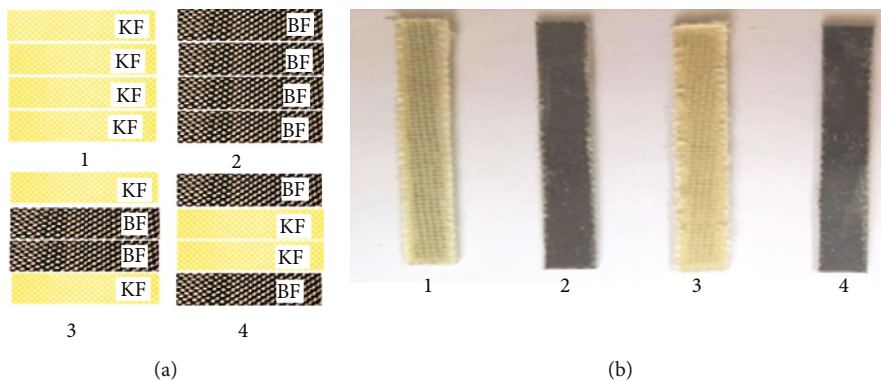
FIGURE 3: Epoxy hybrid composite. (a) Different stacking sequences of KF/BF on epoxy composite. (b) Developed hybrid composite samples.

and basalt fiber mat mm. The sample 3 hybrid composite fabrication details are shown in Figure 2. Initially, the Kevlar fiber (KF) mat is placed over the flat steel plate, and blended epoxy resin is uniformly laid over the KF mat at 0.5 mm thickness via a hand-operated roller. Similarly, the next basalt fiber (BF) layer is placed perpendicular to the Kevlar fiber over the epoxy layer. The KF and BF with intermediate epoxy resin are compacted by a 1 KN compressive load at 20 mins and cured by an electric oven at 40-55°C. A similar procedure is repeated for the next BF and KF layer of intermediate epoxy resin. The various sequences of Kevlar fiber KF and basalt fiber (BF) with intermediate epoxy resin are illustrated in Figure 3(a), and their developed composites are illustrated in Figure 3(b). The prepared KF/BF/BF/KF composite mat was kept in a hydraulic compression machine configured with a 1-ton capacity. The composite was compressed with an applied compressive force of 1 KN maintained for the next 1 hr. It helps increase adhesive properties [8, 9]. Finally, the developed composites are shaped as per test standards.

3. Results and Discussions

3.1. Thermal Adsorption Properties of Hybrid Composites. The effects of Kevlar and basalt finer on the thermal adsorption behavior of epoxy hybrid composites were evaluated by thermal gravimetric analysis. Figures 4(a)–4(d) depict the thermal adsorption behavior on weight loss during high-temperature decomposition of hybrid composite with different stacking sequences as mentioned in Figure 3(a) (samples 1, 2, 3, and 4).

The decomposition rate of the hybrid composite was measured by its composition, pyrolysis, and material volatility. The composite's thermal adsorption on mass loss decomposition percentage was examined from 25°C to 670°C at a 27°C/min heat flow rate. Normal airflow may lead to material decomposition during inert atmospheric conditions, whereas increased temperature may prevent this [23–25]. The various stacking sequences of KF and BF layer results showed lower weight loss (less than 40%) at higher temperatures (more than 240°C). The thermal adsorption
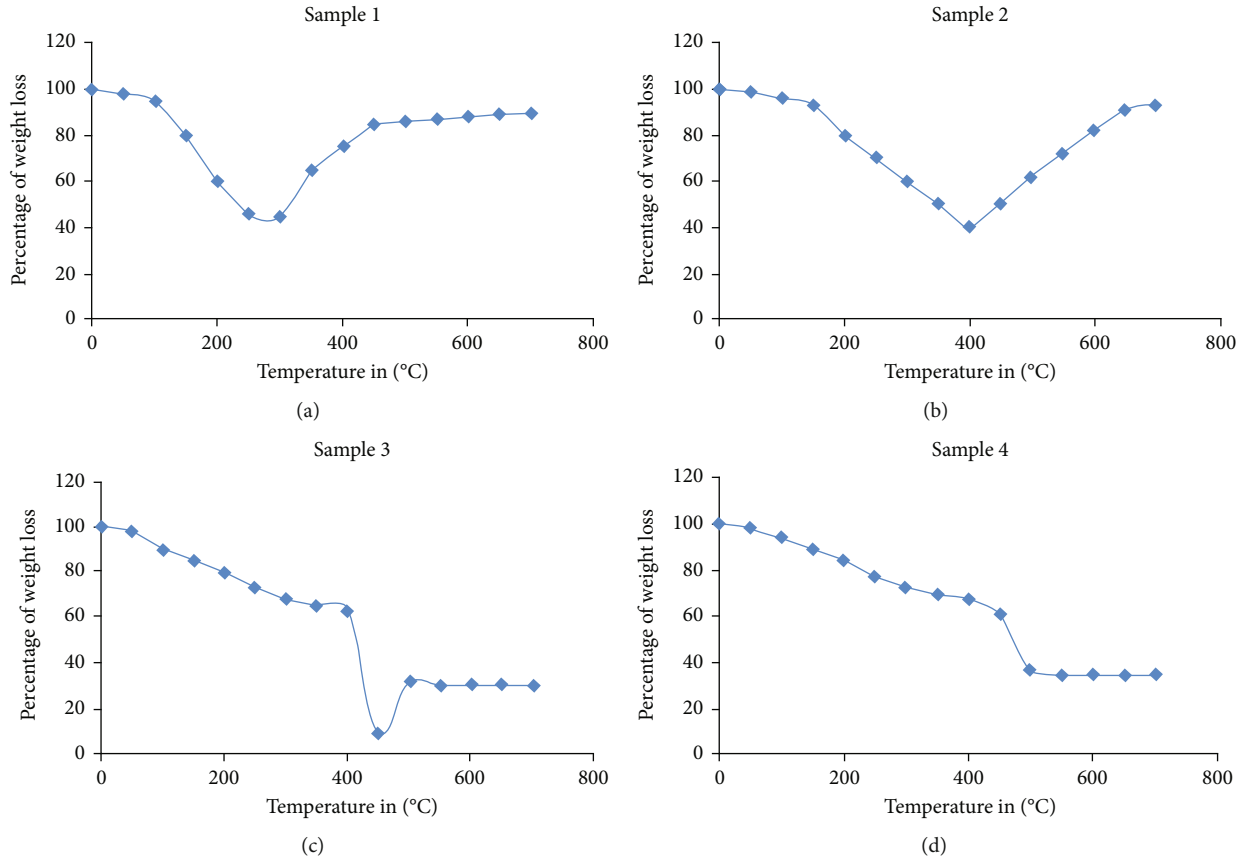
Figure 4: (a) Thermal adsorption on weight loss percentage of hybrid composite sample 1. (b) Thermal adsorption on weight loss percentage of hybrid composite sample 2. (c) Thermal adsorption on weight loss percentage of hybrid composite sample 3. (d) Thermal adsorption on weight loss percentage of hybrid composite sample 4.

behavior varied based on KF and BF stacking sequences. Table 2 depicts the weight loss of a hybrid composite with various stacking sequences, which results in superior thermal adsorption properties. It is observed from Figure 4 and the corresponding Table 2 that the percentage of weight loss due to high-temperature decomposition is 58% related to sequences of hybrid composites. The thermal reactions were observed during the evaluation of thermal adsorption behavior, and the effect of KF/BF on hybrid composite showed an exothermic effect of heat able to decompose the structure. However, stacking different sequences could resist the decomposition rate during high temperatures. It forms V and U curves related to the exothermic effects of Kevlar and basalt fiber. Samples 1 and 2 found as U and V exothermic curves represent the effect of exothermic during the higher temperature of decomposition, and their percentages are mentioned in Table 2. The decomposition rate of sample 4 was limited by 1% as compared to sample 1.

3.2. Heat Deflection Temperature.
Figure 5 illustrates the effect of KF/BF on the heat deflection temperature of an epoxy hybrid composite evaluated by different stacking positions of KF/BF, as shown in Figure 3(a). It is observed from Figure 5 that the heat deflection of epoxy hybrid composite samples 1–4 found a variation value with increased thermal conductivity. The higher heat deflection temperature of

Table 2: Weight-loss percentage of various thermal adsorption conditions.

| Sample no. | Weight loss percentage | | |
	Decomposition	Medium temperature	Residue
1	65.23	75.91	32.81
2	50.29	50.78	30.23
3	66.98	63.7	29.18
4	70.98	67.01	28.78

$105.74 \pm 1.56°C/Kg$ was identified in sample 1 with its thermal conductivity range of 0.198 W/mK. While compared to sample 1, the heat deflection temperatures of samples 2, 3, and 4 were noted as the decreased value of $66.91 \pm 1.29°C/Kg$, $71.18 \pm 1.72°C/Kg$, and 69.23 ± 1.57, respectively. However, the basalt fiber-faced epoxy hybrid composite has a low heat deflection temperature compared to the Kevlar fiber-faced epoxy hybrid composite. The basalt fiber laminates with epoxy resin have performed extreme thermal stability behavior [11].

Sample 2 was noted by a minor heat deflection temperature of $66.91 \pm 1.29°C/Kg$. It was due to the effect of basalt fiber effectively bonded with epoxy material by an applied compressive load of 1 KN. The basalt fiber exhibited good mechanical and thermal characteristics [24]. The heat
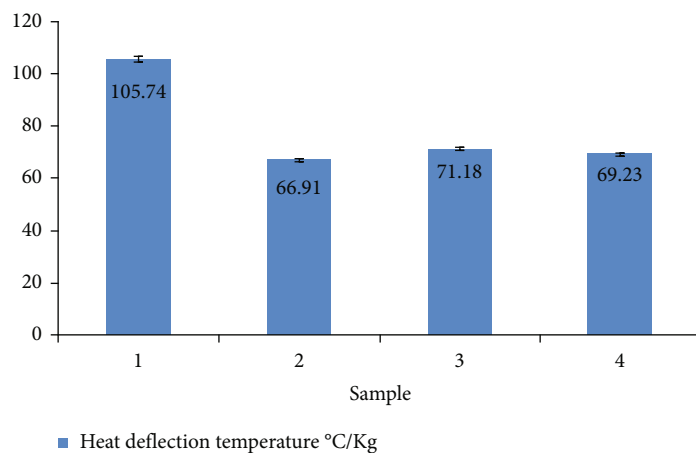
FIGURE 5: Heat deflection temperature of hybrid composites.
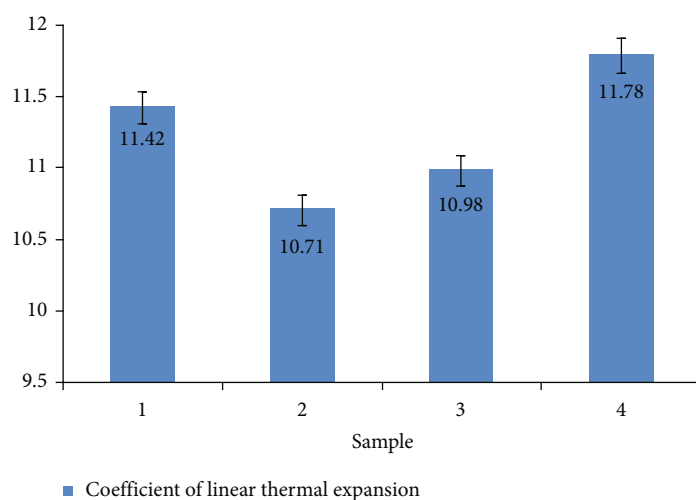
FIGURE 6: Coefficient of linear thermal expansion of hybrid composites.
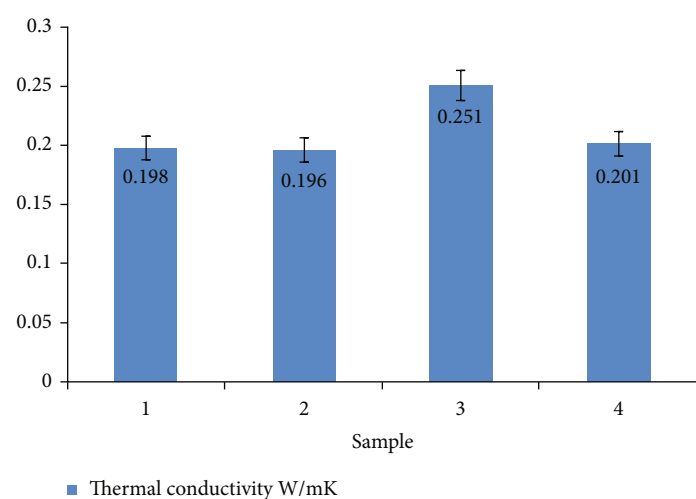
FIGURE 7: Thermal conductivity of hybrid composites.

deflection evaluation of the composite helps find the thermal stability of the composite [26]. Moreover, the coated ceramic material has to lead to good mechanical and thermal charac- teristics [27]. Both sample 2 and sample showed the least heat deflection temperature. So these samples may promote good insulation for energy storage applications.

3.3. Coefficient of Linear Thermal Expansion. The coefficient of thermal expansion of various stacking sequences of a developed KF/BF hybrid composite bonded with epoxy was evaluated by the relations between heat supplied and temperature difference. Figure 6 presents the coefficient of thermal expansion of hybrid composites (samples 1, 2, 3, and 4). It is evidenced in Figure 6 that the composite, which contained a multilayer of KF and BF, shows a good coefficient of thermal expansion compared to a similar fiber-fabric hybrid composite. The coefficient of thermal expansion of samples 1 and 2 is found to be 11.42×10^{-6} per °C and 10.71×10^{-6} per °C. Heat transformation is separated by a multilayer fabric mat composite with different sequences. The multifabric arrangement with 0° and 90° orientations makes a perfect heat transfer during the isotropic process [28]. Sample 4 has an excellent thermal expansion coefficient of 11.78×10^{-6} per °C, and effective heat transfer was found between the fabric mats via an epoxy matrix. Kevlar and basalt fiber contribute to thermal expansion with limited effective binding performance. Sample 4 represents that the coefficient of thermal expansion of hybrid composite with basalt fiber-faced epoxy hybrid composites (BF/KF/KF/BF) reduces the effect of maximum heat transformation.

3.4. Thermal Conductivity. Figure 7 depicts the effect of KF/BF on the thermal conductivity of epoxy hybrid composites with different stacking sequences. It is noted from Figure 7 that the hybrid composite with similar layers like KF/KF/KF/KF and BF/BF/BF/BF epoxy hybrid composite samples 1 and 2 showed the most negligible thermal conductivity of 0.198 ± 0.18 and 0.196 ± 0.11 W/mK, respectively. At the same time, the multilayer KF/BF combinations of samples 3 and 4 of the epoxy hybrid composite were found to have good thermal conductivity compared to samples 1 and 2. The composite grouping with KF/BF/BF/KF (sample 3) showed a higher thermal conductivity of 0.251 W/mK. The thermal conductivity of sample 3 was 26.6% higher than that of sample 1. It was due to the effective basalt fiber layer occupied between Kevlar fibers. However, the thermal conductivity of epoxy composites was enriched by Kevlar fiber bonded with epoxy with a BF interlayer. The Kevlar fiber has good thermal conductivity [14, 15, 17].

The stacking thermal gravimetric curve of Kevlar and basalt fibers has a low thermal conductivity compared to other multilayer KF/BF fiber hybrid composites. The Kevlar fiber facilitates good heat transfer between the layers more than once. However, the basalt fiber leads to enhanced thermal conductivity in composites.

4. Conclusions

The effect of Kevlar and basalt fiber on thermal adsorption, heat deflection temperature, coefficient of linear thermal expansion, and thermal conductivity of epoxy hybrid composite was studied experimentally, and their results were compared to obtain optimum properties. A low-cost conventional hand layup technique successfully fabricated the epoxy hybrid composite. Samples 3 and 4 of multilayer (KF/BF with epoxy) composites performed good thermal performance compared to the monolayer (KF and BF with epoxy) samples 1 and 2. Sample 4 (BF/KF/KF/BF) had an excellent thermal adsorption effect and a reduced mass loss during decomposition of 70.98%. Similarly, the heat deflection temperature and coefficient of linear thermal expansion are offered with basalt fiber at 69.23°C/Kg and 11.78×10^{-6} per °C. The multilayer sample 3 epoxy hybrid composite found good thermal conductivity, with a value of 0.251 W/mk, and has improved by 26.6% compared to sample 1. However, the basalt fiber-faced sample 4 epoxy hybrid composite observed good thermal adsorption behavior and limited mass loss with controlled decomposition with reduced heat deflection temperature acting as better insulation for heat energy storage applications in power plant sectors.

Data Availability

All the data required are available within the manuscript.

Conflicts of Interest

The authors declare that there are no conflicts of interest regarding the publication of this paper.

References

[1] R. M. Christensen, *Mechanics of Composite Materials*, Courier Corporation, North Chelmsford', MA, 2012.

[2] P. K. Mallick, *Fiber-Reinforced Composites: Materials, Manufacturing, and Design*, CRC press, Boca Raton', FL, 2007.

[3] P. V. Straznicky, J. F. Laliberté, C. Poon, and A. Fahr, "Applications of fiber-metal laminates," *Polymer Composites*, vol. 21, no. 4, pp. 558–567, 2000.

[4] A. Elmarakbi, *Advanced Composite Materials for Automotive Applications: Structural Integrity and Crashworthiness*, John Wiley & Sons, Hoboken, NJ, USA, 2013.

[5] O. M. L. Asumani, R. G. Reid, and R. Paskaramoorthy, "The effects of alkali-silane treatment on the tensile and flexural properties of short fibre non-woven kenaf reinforced polypropylene composites," *Part A Applied science manufacturing*, vol. 43, no. 9, pp. 1431–1440, 2012.

[6] G. R. Arpitha and B. Yogesha, "An overview on mechanical property evaluation of natural fiber reinforced polymers," *Material Today Proceeding*, vol. 4, no. 2, pp. 2755–2760, 2017.

[7] S. Biswas, S. Shahinur, M. Hasan, and Q. Ahsan, "Physical, mechanical and thermal properties of jute and bamboo fiber reinforced unidirectional epoxy composites," *Procedia Engineering*, vol. 105, pp. 933–939, 2015.

[8] R. Venkatesh, P. R. Sekaran, K. Udayakumar et al., "Adsorption and photocatalytic degradation properties of bimetallic ag/MgO/biochar nanocomposites," *Adsorption Science & Technology*, vol. 2022, article 3631584, pp. 1–14, 2022.

[9] M. Ramasamy, A. Arul Daniel, M. Nithya, S. Sathees Kumar, and R. Pugazhenthi, "Characterization of natural - Synthetic fiber reinforced epoxy based composite - Hybridization of kenaf fiber and kevlar fiber," *Materials Today: Proceedings*, vol. 37, pp. 1699–1705, 2021.

[10] A. Sarwar, Z. Mahboob, R. Zdero, and H. Bougherara, "Mechanical characterization of a new kevlar/flax/epoxy hybrid composite in a sandwich structure," *Polymer Testing*, vol. 90, article 106680, 2020.

[11] M. Bulut, "Mechanical characterization of basalt/epoxy composite laminates containing graphene nanopellets," *Composites Part B: Engineering*, vol. 122, pp. 71–78, 2017.

[12] S. Rajesh, B. V. Ramnath, C. Elanchezhian, M. Abhijith, R. D. Riju, and K. K. Kishan, "Investigation of tensile behavior of Kevlar composite," *Material today proceeding*, vol. 5, no. 1, pp. 1156–1161, 2018.

[13] C. Fragassa, A. Pavlovic, and C. Santulli, "Mechanical and impact characterisation of flax and basalt fibre vinylester composites and their hybrids," *Composites Part B: Engineering*, vol. 137, pp. 247–259, 2018.

[14] T. Behzad and M. Sain, "Measurement and prediction of thermal conductivity for hemp fiber reinforced composites," *Polymer Engineering and Science*, vol. 47, no. 7, pp. 977–983, 2007.

[15] A. Sayyidmousavi, H. Bougherara, S. R. Falahatgar, and Z. Fawaz, "Prediction of the effective thermal conductivity of fiber reinforced composites using a micromechanical approach," *Journal of Mechanics*, vol. 35, no. 2, pp. 179–185, 2019.

[16] R. Venkatesh, N. Karthi, N. Kawin et al., "Synthesis and adsorbent performance of modified biochar with ag/MgO nanocomposites for heat storage application," *Adsorption Science & Technology*, vol. 2022, article 7423102, pp. 1–14, 2022.

[17] C. Atasand and A. Dogan, "An experimental investigation on the repeated impact response of glass/epoxy composites subjected to thermal ageing," *Composite Part B Engineering*, vol. 75, pp. 127–134, 2015.

[18] B. Schrauwen and T. Peijs, "Influence of matrix ductility and fibre architecture on the repeated impact response of glass-fibre-reinforced laminated composites," *Applied Composite Materials*, vol. 9, no. 6, pp. 331–352, 2002.

[19] M. Khazaie, R. Eslami-Farsani, and A. Saeedi, "Evaluation of repeated high velocity impact on polymer-based composites reinforced with basalt and Kevlar fibers," *Materials Today Communications*, vol. 17, pp. 76–81, 2018.

[20] R. D. Sweeting and X. L. Liu, "Measurement of thermal conductivity for fibre-reinforced composites," *Composites Part A: Applied Science and Manufacturing*, vol. 35, no. 7-8, pp. 933–938, 2004.

[21] Z. Javanbakht, W. Hall, and A. Öchsner, "Effective thermal conductivity of fiber reinforced composites under orientation clustering," *Advanced Structured Materials, Springer International Publishing*, vol. 92, pp. 507–519, 2019.

[22] C. Ramesh Kannan, R. Venkatesh, M. Vivekanandan et al., "Synthesis and characterization of mechanical properties of AA8014 + Si3N4/ ZrO2 hybrid composites by stir casting process," *Journal of Advances in Materials Science and Engineering*, vol. 2022, article 9150442, pp. 1–11, 2022.

[23] S. Ghasemi, M. Tajvidi, D. W. Bousfield, and D. J. Gardner, "Reinforcement of natural fiber yarns by cellulose nanomaterials: a multi-scale study," *Industrial Crops and Products*, vol. 111, pp. 471–481, 2018.

[24] M. Krishnaraj, R. Arun, and T. Vaitheeswaran, *Fabrication and wear characteristics basalt fiber reinforced polypropylene matrix composites*, SAE Technical Paper, 2019.

[25] J. Isaac Premkumar, A. Prabhu, V. Vijayan, and R. Venkatesh, "Combustion analysis of biodiesel blends with different piston geometries," *Journal of Thermal Analysis and Calorimetry*, vol. 142, no. 4, pp. 1457–1467, 2020.

[26] N. B. Karthik Babu, S. Muthukumaran, S. Arokiasamy, and T. Ramesh, "Thermal and mechanical behavior of the coir powder filled polyester micro-composites," *Journal of Natural Fibers*, vol. 17, no. 7, pp. 1058–1068, 2020.

[27] G. Mittal, K. Y. Rhee, V. Mišković-Stanković, and D. Hui, "Reinforcements in multi-scale polymer composites: processing, properties, and applications," *Composites Part B: Engineering*, vol. 138, pp. 122–139, 2018.

[28] R. Venkatesh, S. Manivannan, P. Sakthivel, V. Vijayan, and S. Jidesh, "The investigation on newly developed of hydrophobic coating on cast AZ91D magnesium alloy under 3.5 wt% NaCl solutions," *Journal of Inorganic and Organometallic Polymers and Materials*, vol. 32, no. 4, pp. 1246–1258, 2022.

Research Article

Optimization Process of Potassium Carbonate Activated Carbon through Jute-Based Core Materials by Using Artificial Neural Network with Response Surface Methodology

L. Natrayan [iD],[1] **V. R. Niveditha,**[2] **S. Kaliappan,**[3] **Pravin P. Patil,**[4] **C. K. Arvinda Pandian** [iD],[5] **Y. Sesha Rao,**[6] **and P. Murugan** [iD][7]

[1]*Department of Mechanical Engineering, Saveetha School of Engineering, SIMATS, Chennai, Tamil Nadu 602105, India*
[2]*Department of Computer Science and Engineering, Sathyabama Institute of Science and Technology, Chennai, 600119 Tamil Nadu, India*
[3]*Department of Mechanical Engineering, Velammal Institute of Technology, Chennai, 601204 Tamil Nadu, India*
[4]*Department of Mechanical Engineering, Graphic Era Deemed to be University, Bell Road, Clement Town, 248002 Dehradun, Uttarakhand, India*
[5]*Department of Automobile Engineering, School of Mechanical Sciences, B. S. Abdur Rahman Crescent Institute of Science & Technology, Vandalur, Chennai, 600048 Tamil Nadu, India*
[6]*Department of Mechanical Engineering, QIS College of Engineering and Technology, Ongole, Andra Pradesh, India*
[7]*Department of Mechanical Engineering, Jimma Institute of Technology, Jimma University, Ethiopia*

Correspondence should be addressed to P. Murugan; murugan.ponnusamy@ju.edu.et

Potassium carbonate was tested as novel information for producing carbonaceous materials from jute cores. Two quadratic models have been developed for both answers to link the preparatory parameters: activating temperatures, molar ratio, and incubation time. The RSM and ANN models were used to improve the processing conditions to maximise the quantities of iodine and methylene blue penetration. The best charcoal was obtained using 900°C activating temperatures, a 1.5 molar ratio, and a 4-hour activating time. This resulted in iodine and methylene blue absorption of 1260.07 mg/g and 369.21 mg/g, respectively. It was discovered that the K_2CO_3-based pyrolysis process might be anticipated to become a safe yet incredibly efficient process of making activated carbons with a very well-defined and monocultural porous structure. Even though the precise emphasis given to K_2CO_3 is unknown at the moment, given the creation of $K_2C_3O_4$ just after evolvement with one additional molarity of CO at approximately 870°C, these same porous and papule responses begun by K_2CO_3 stimulation might be temporarily posited to be quite comparable to an initiation action needed to make progress by $K_2C_3O_4$. The influence of control parameters was examined in this study using variance analysis like the ANOVA test. Furthermore, the response surface (RSM) and artificial neural networks (ANN) are employed to improve the output results while optimising the methylene blue and iodine qualities. Consequently, the experimental findings correlate well with the statistics.

1. Introduction

Activated carbon is a flexible, highly porous concept widely used as an adsorbent in fluid and gas processes and heterogeneous catalysis. As contamination has become a much more significant issue, the demand for carbonaceous materials grows. The characteristics of carbonaceous materials are determined by the activating agent's quality and activating techniques [1, 2]. In practice, anthracite, hardwood, and coconut husks are the historical documents of commercially carbonaceous materials. Owing to their cheap cost, durability, and ease of handling, several agricultural wastes have subsequently gained a lot of interest as alternate materials for manufacturing carbonaceous materials [3, 4].

Pollutants encircled humans, which appears to be a significant threat to all life forms. Developed countries attempt to reduce pollution by adopting drastic measures to substitute polluting resources with sustainable alternatives [5]. Scientists have developed an organic biobased alternative to the existing composite polymers. Composites are regarded as essential components in a wide range of large-scale operations [6]. Substantial expenditures were invested in developing synthetic composites that have functioned admirably in various uses. However, with increasing global warming and risks, significant attention has shifted to creating biological and nanocomposite materials [7]. Consequently, the production of such hybrids has received considerable attention in recent history. Biocomposites were already being researched to replicate the success of synthetic fibre. Such biocomposites are recyclable, and various natural fibres were employed in their creation to make them sustainable and environmentally friendly in origin, with fewer emissions [8, 9]. Compared to proprietary brands, the composite material has also gained popularity due to its excellent compressive and flexural qualities. Biocomposites are organic, compact, lightweight, emitting little CO2, and having minimal material and production costs. Above everything, the fibres employed in the production of biocomposites are plentiful in the environment. Because of their numerous practical uses, biocomposites are now on the verge of being intrinsic community members [10, 11].

Furthermore, jute fibres are environmentally benign, recyclable, inexpensive, and disposable. Jute fibres are mainly composed of lignocellulosic materials [12]. Cellulose is a polymer that aids in the presence of hydrogen among substrates with fibres, hence increasing interface contractures. Jute fibre is in significant demand outside the composites and biopolymer sectors [13]. Jute fibre qualities are often influenced by the tree's age, fibre content, and hybrid production procedures. Jute fibre is now employed in various industries, including fabrics, cars, and many uses [14]. Jute plant, also known as ligno, was used in the automotive industry to make a variety of components such as side panels, hatchback linings, and centre consoles. In particular, large automakers like Daimler, as well as numerous European and American automakers, are eager to incorporate increasingly sustainable composite and polymeric materials. Jute-based biocomposites comprising natural substances have evolved in recent years with excellent tensile qualities over native jute-based hybrids [15, 16].

Because jute core fibre has a considerably large lignin concentration but little coal ash, it is a suitable substrate for commercially generating quality charcoal filters to increase financial benefit [17]. Munawar et al. [8] reported the combustion accompanied by potassium iodide activation of jute matting to produce active carbon fibre (ACF) with the most excellent permeability of $582 \, m^2/g$. To the aim of contributing, published studies on the use of discarded jute cores for the generation of chemical activation are scarce [18]. Various activating processes are used in synthesising carbonaceous materials: physiological, chemical, and biophysical engagement. Carbonization has unique benefits, including solitary activation, higher production, and

TABLE 1: BBD constraints and their levels.

Sl. no	Parameters	L1	L2	L3
1	Impregnation ratio	1	1.5	2
2	Time (hrs)	3	3.5	4
3	Temperature (°C)	800	850	900

improved micropores [19]. The more powerful and successful molecular enhancers in manufacturing high surface energy carbonaceous materials are phosphoric acid, zinc chloride, potassium hydroxide, and potassium carbonate [20]. Potassium salts were discovered to be more effective activation chemicals than most in producing activated charcoal materials of high porosity and permeability values. Nonetheless, our understanding of carbonization pathways is far from complete [21, 22].

The Box-Behnken experimental setup for RSM and ANN ware was used to analyse the impact of important evaluation factors using potassium iodide and methylene blue adsorbent value systems as reactions to identify the most appropriate initiation method for creating jute-based charcoal filters to preferred adsorbent performance this season by K_2CO_3 stimulation. In the proposed investigation, potassium carbonate has been used as an alternate efficient activating agent to manufacture jute-based chemical activation. This is because the iodine amount and adsorption isotherm values are the most commonly used metrics for accurately measuring the adsorption ability of the porous structure architectures of the carbon materials generated. On the other hand, the iodine number can be roughly comparable to the absorber plate area of a charcoal molecule in m^2/g. As a result, the iodine number and the sorbent grade are commonly employed as adsorbed species indicators, exhibiting excellent significant associations with the adsorption process of sorbent material in small and medium-scale molecules separately. The outcomes of this study help generate a prospective new pharmacological activation and produce good use of jute to make charcoal filters have desirable characteristics by determining the ideal operating settings using RSM and ANN approaches.

2. Investigational Works

2.1. Materials.
The jute came from the Jute Research Farm Salam in Tamil Nadu, India. That production's chemical products were of analytical reagents. Before any additional interventions, the viscose cores were cleaned with water to eliminate impurities, dry at 110°C for 48 hours, and crushed; then, samples were filtered to 100-212 mesh size.

2.2. Creation of Activated Carbon.
The research was conducted at various K_2CO_3/forerunner insemination concentrations. The 25 g of dried precursors were steeped in a 25% K_2CO_3 mixture at ambient atmospheric conditions for 14 hours, with periodic mixing. The mixture was then continuously dried in a hot oven at 110 degrees Celsius. This solvent temperature was increased to the specified ultimate heat in a burner at a fluid velocity of 350 mL/min of nitrogen. In addition, jute core carbon was made at 900°C for 3
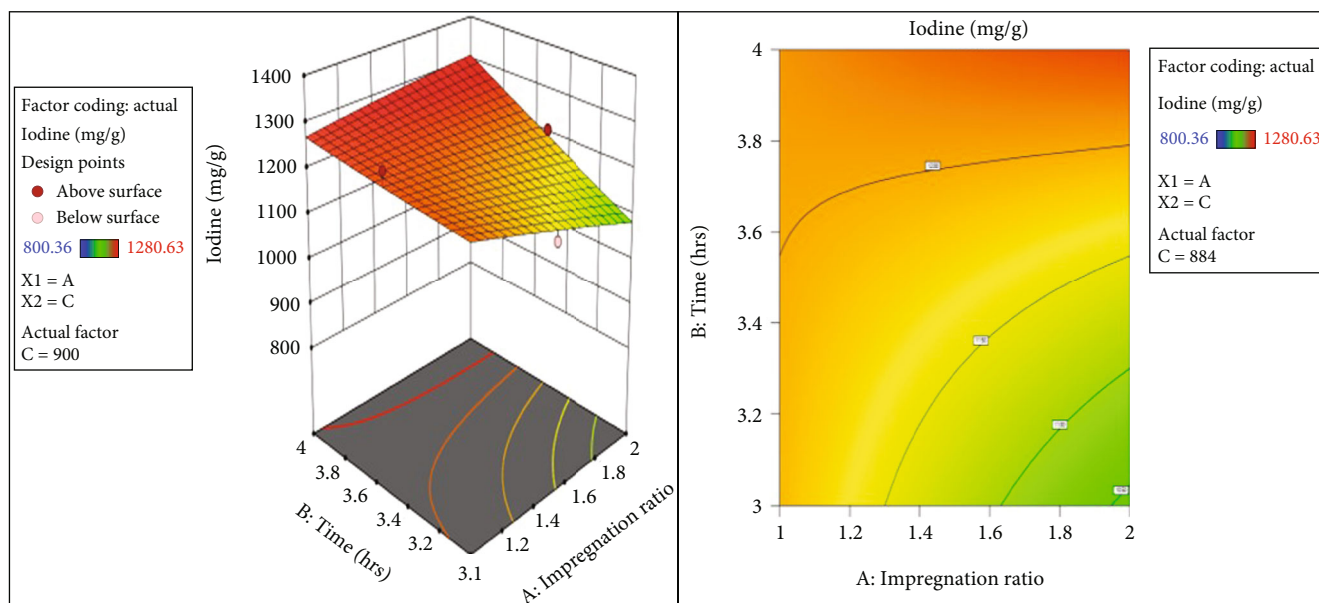
(a)
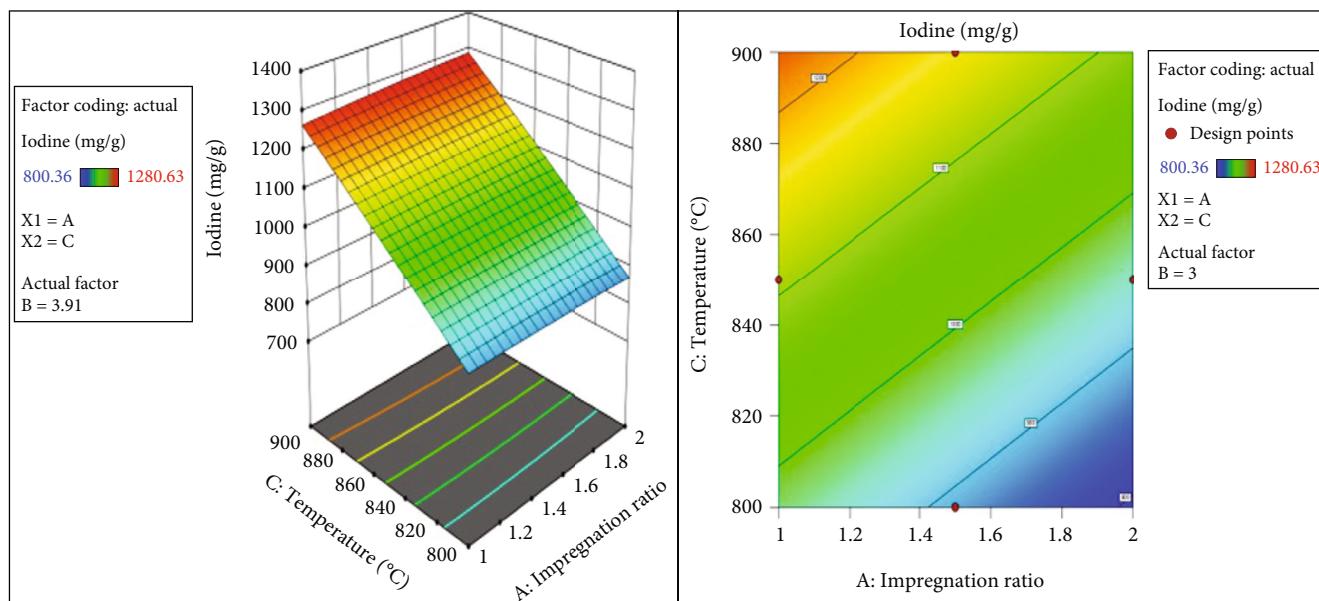
(b)

Figure 1: Continued.

(c)
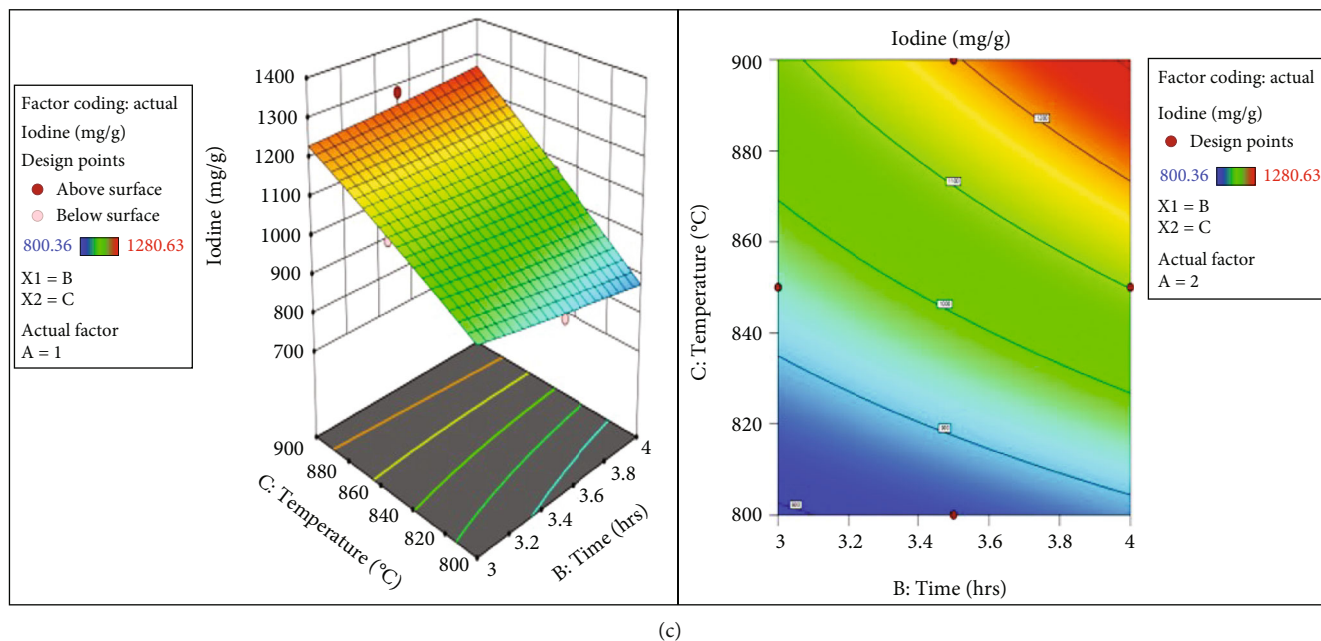
FIGURE 1: Response 3D surface and contour plots of iodine number based on the input parameters.

hours before implantation using K_2CO_3 solutions. The compounds were washed several times using 0.5 ml of hydrochloric acid with rubbing alcohol till the pH of a supernatant approached about 6.0, dried over 24 hours at 110°C, and then measured.

2.3. Adsorption Characteristics.

Both the iodine amount and methylene blue adsorption have been measured in accordance with GB/T 12496.8-1999 and GB/T 12496.10-1999, respectively. Iodine is a typical absorption coefficient probing chemical, representing small pores with diameters greater than 1.0 nanometers. On the other hand, methylene blue is the most widely used modelling structure for evaluating an adsorbent's most significant potential to reduce soluble compounds with molecular sizes greater than 1.5 nanometers. The adsorbent capabilities of iodine and MB are provided in milligrammes of adsorbent surface captured by 1 gramme of charcoal. Nitrogen desorption at 77 K has been used to characterise the texture of the indicated activated specimen.

2.4. Response Surface Methodology.

The Box-Behnken design includes specified placement of input parameters and has 3 dimensions for every element labelled as 1, 0, and +1. It was designed to predict a statistical approach and deliver high empirical results at the centre of a design project and lower at the frame's extremities. This is a rotational polynomial pattern with part of what makes up the centre point at the centre of the sides and even in the middle [23]. A Box-Behnken statistically exploratory approach using the RSM was employed to study the impacts of three variables: period, molar ratio, and temperatures. The responsive factors were selected as the iodine amount with methylene blue adsorbed. The Box-Behnken design was selected owing to its low cost and high efficiency [24, 25]. Experimentation results were recorded and then matched towards the two multiple regres-

sions utilising the Design Expert 13 programme to assess the importance of a dependent dimension.

$$Z = A_o + \sum_{i=1}^{n} AiYi + \sum_{i=1}^{n} AiiYi2 + \sum_{i=1}^{n=1} AijYiYj + e. \quad (1)$$

Z would be the appropriate reaction, Yi and Yj are the relevant factors, A_0, Ai, Aii, and Aij were predicted values for the interception, linearity, exponential, and interaction components, e is the errors, where n is the number of possibilities analysed. The F test was used to analyse the relevance of a functional form and its resulting consequences. The coefficient of determination R^2 and modified R^2 were used to measure the experience of the polynomial system of equations. The statistically significant correlation of a design was determined using variance analysis (ANOVA). The ideal parameters were determined using the following linear relationship; then, contours were utilised to examine every variable's interaction influence [26].

3. Result and Discussions

3.1. RSM Models.

The Box-Behnken model is a helpful exploratory study using 3D surface methods based on 3 imperfect random effects. It aids in optimising the impacts of many factors, either solitary or interactive, to get the optimum results. The two elements in this concept are at the centre points of the processing satellite's borders and the centre. BBD is more effective for quadratic polynomials than orthogonal arrays (OA) and especially beneficial in preventing excessive control variables [27]. Table 1 shows the three critical parameters and the static loading with observable consequences of iodine. The absolute errors and variability were calculated using the cycle at the correct location. According to the
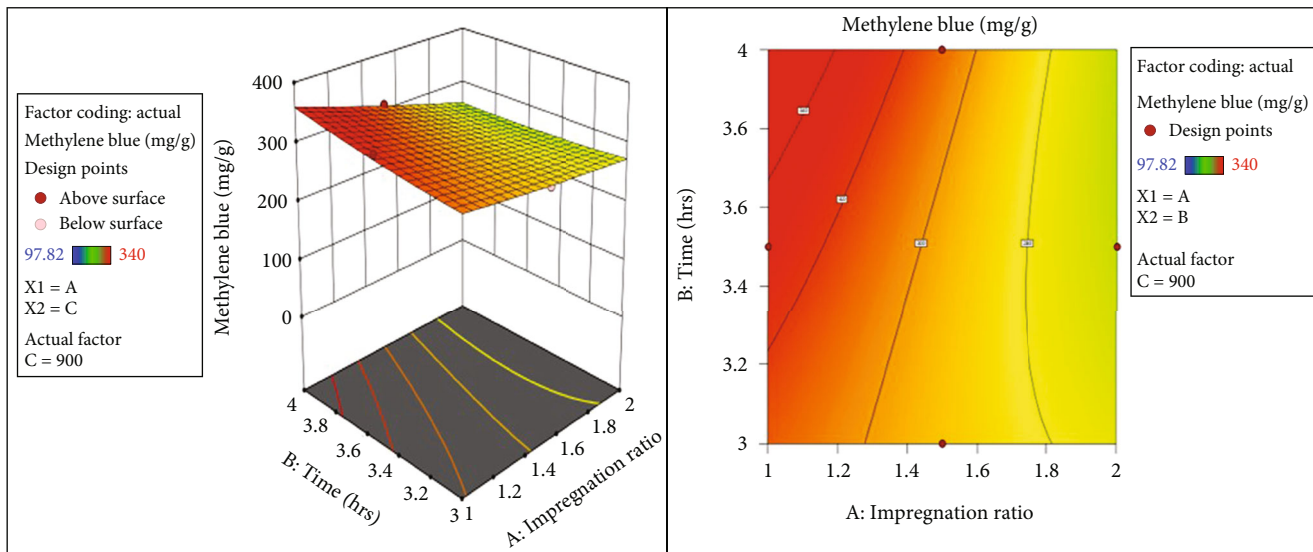
(a)

(b)
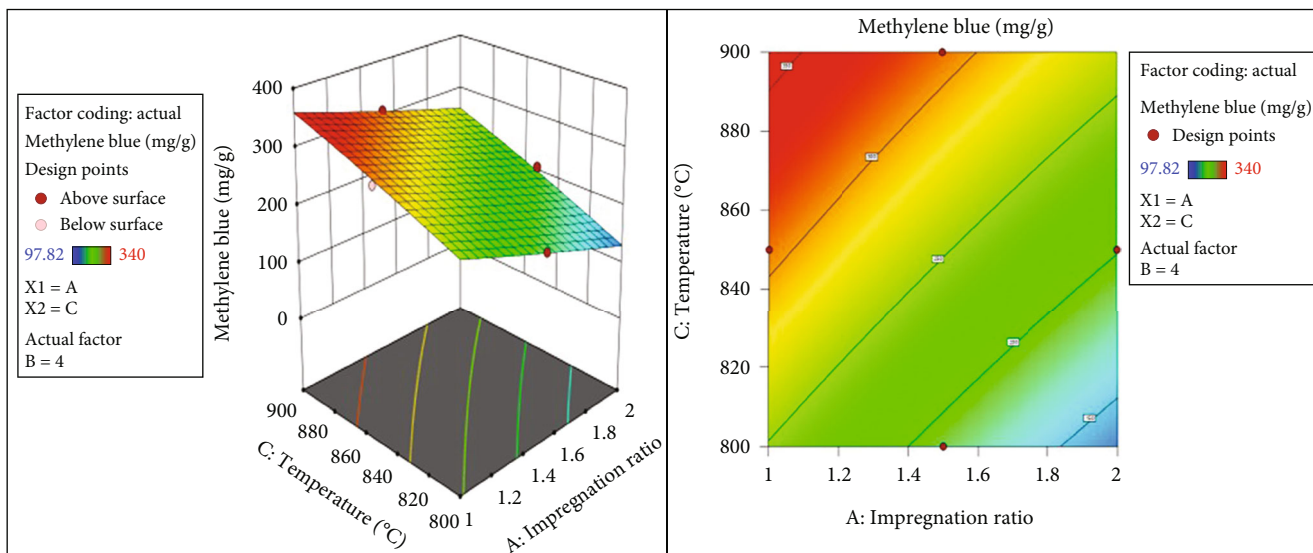
FIGURE 2: Continued.
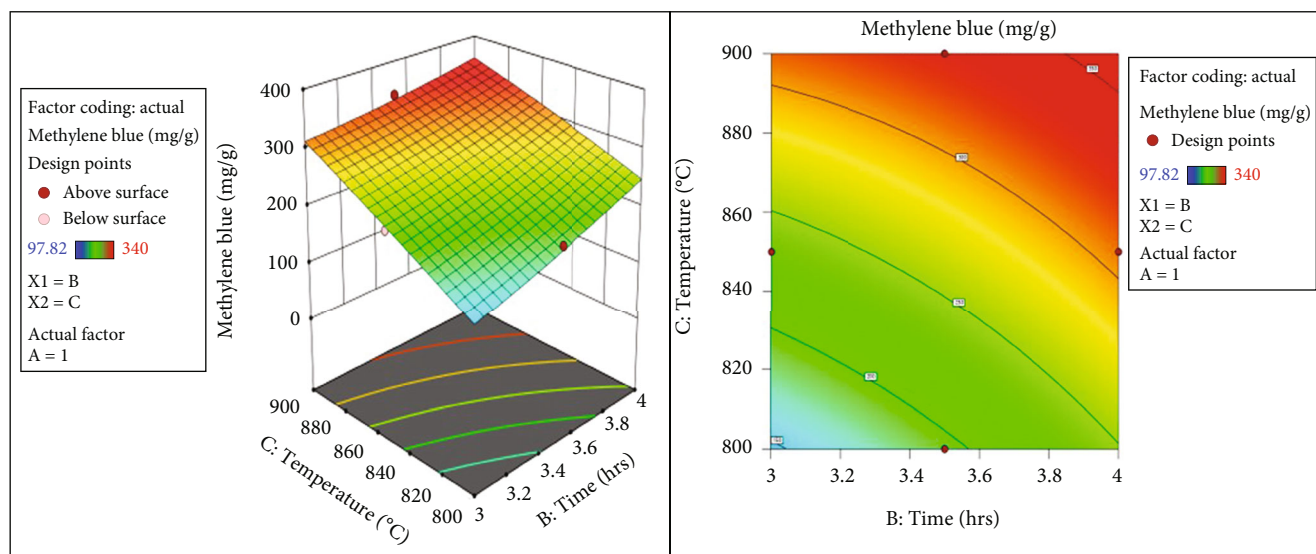
(c)

FIGURE 2: Response 3D surface and contour plots of methylene blue based on the input parameters.

TABLE 2: ANOVA predictions of iodine number.

Source	SOS	Df	MS	F value	P value
Model	266749.359	9	29638.818	20.085	0.001
Impregnation ratio	10222.856	1	10222.856	6.928	0.034
Time	8020.301	1	8020.301	5.435	0.053
Temperature	234646.751	1	234646.751	159.012	0.001
AB	8649.651	1	8649.651	5.862	0.046
AC	339.112	1	339.112	0.230	0.646
BC	4626.040	1	4626.040	3.135	0.120
$\widehat{A}^2$	36.794	1	36.794	0.025	0.879
$\widehat{A}^2$	24.331	1	24.331	0.016	0.901
$\widehat{A}^2$	183.709	1	183.709	0.124	0.735
Residual	10329.579	7	1475.654		
Lack of fit	5049.996	3	1683.332	1.275	0.396
Pure error	5279.583	4	1319.896		
Cor total	277078.938	16			

programme, the model equation was chosen for matching iodine and methylene blue adsorption abilities. After excluding the statistically irrelevant impacts of salt and methylene blue absorption, our final empirical regressors in terms of coding components were just as shown in the following:

$$\text{Iodine} = 1059.26 - 35.75A + 31.66B + 171.26C + 46.50\text{AB}$$
$$+ 9.21\text{AC} + 34.01\text{BC} - 2.96A^2 + 2.96B^2 - 6.61C^2,$$
$$(2)$$

$$\text{Methylene blue} = 225.55 - 38.43A + 22.69B + 74.13C$$
$$- 14.69\text{AB} + 4.82\text{AC} - 13.63\text{BC} \quad (3)$$
$$+ 1.94A^2 + 4.36B^2 - 3.76C^2.$$

The measured results of iodine and methylene blue adsorbed were in excellent accordance with quantities anticipated by equations as shown in Figures 1 and 2. The corrected reliability ratio (R^2) estimates for Equations (2) and (3) of the models remained at 0.9618 and 0.9793, correspondingly. All values of R^2 are near 1.0, suggesting that the constructed regression analysis is very reliable in describing the variances in the empirical observations.

In the instance of iodine absorption values in Figures 1(a)–1(c), every linear regression graph exhibits a distinct peak along with symmetrically filled arcs in the associated contour showing that the peak amount of a reaction (Z1) is achievable inside the design process. Figures 2(a)–2(c) exhibit multiple (3D) linear regression graphs of a predicted quadratic polynomial for methylene blue adsorption, correspondingly. As

TABLE 3: ANOVA prediction of methylene blue.

Source	SOS	Df	MS	F value	P value
Model	61736.363	9	6859.596	41.736	0.001
Impregnation ratio	11812.614	1	11812.614	71.871	0.001
Time	4120.050	1	4120.050	25.068	0.002
Temperature	43956.125	1	43956.125	267.441	0.001
AB	862.891	1	862.891	5.250	0.056
AC	92.930	1	92.930	0.565	0.477
BC	742.563	1	742.563	4.518	0.071
A^2	15.794	1	15.794	0.096	0.766
B^2	80.105	1	80.105	0.487	0.508
C^2	59.550	1	59.550	0.362	0.566
Residual	1150.506	7	164.358		
Lack of fit	561.290	3	187.097	1.270	0.397
Pure error	589.216	4	147.304		
Cor Total	62886.869	16			

shown in Figures 2(a)–2(c), ignition delay has by far the most dramatic influence (F value = 41.73) on methylene blue (Y2) sorption of any three components tested (activating heat, molar ratio, and reaction rate). However, according to Figure 2(a), the combined impact of heating rate on iodine has no substantial effect on the growth of adsorbent values under the circumstances examined [28]. Figures 2(b) and 2(c) show that a prolonged incubation period is beneficial for increasing methylene blue adsorbent dosage.

The design project's desired spot predictions feature was used to figure out how to maximise the absorption coefficients of iodine and methylene blue within the experiment limits investigated. The projected best adhesion values were found by employing an activating temperature of 898.91°C, an impregnation ratio of 1.52, and an active duration of 3.5 hours. Considering the real-time operating procedure, the altered optimal conditions were determined as 900° C, impregnation ratio, and 3.5 hours. Adsorbent uptakes of iodine and methylene blue were determined to be 1247.63 mg/g and 340 mg/g, correspondingly. To validate the projected findings, several desorption specimens were created under the ideal conditions above for further iodine and methylene blue sorption experiments. The mean measurement results for iodine and methylene blue desorption were 1055.89 mg/g and 226.74 mg/g, correspondingly, which are in good accordance with econometric methods' impact on subsequent, having relatively little uncertainties of 1.56% and 1.80%, respectively. The operating parameters for the coagulant are detailed in Table 2.

A descriptive analysis (ANOVA) was used to assess the model's relevance and appropriateness and to discover the complicated link between factors and outcomes. Tables 2 and 3 summarise the presented iodine and methylene blue summary statistics. Due to the absence of fitting rates, estimated F values, and a very low probability for answers and values of P (0.001) as shown in Table 2, the regression has a firm fit and is considerable. Table 3 shows the ANOVA prediction of methylene blue.

Figures 3(a) and 3(b) show the normal probability plots of the outcomes of iodine and methylene blue. All Y12 interaction variables were found to be insignificant to the outcomes of the two experiments. Furthermore, the overall quadratic impacts of Y1 (temperature) and Y3 (time) are optimistic, indicating that these factors have a beneficial or cooperative influence on iodine and methylene blue desorption levels in the studied experimental location. Furthermore, the interaction factors Y1Y3 and Y2Y3, as well as Y2 and all exponential factors, show substantial as well as hostile impacts on reactions, meaning that increasing these variables further than the limitations is likely to lower iodine and methylene blue desorption levels.

For a successful fit, the endpoints must be near the fitting line, with small comfort intervals. Points just on the show's left or right, at the furthest average, have had the most leverage and can successfully drag the directly connected towards the centre [29, 30]. Exceptions are locations that are substantially distant from the line. All sorts of tips can degrade the fitting. The chart depicts an ANOVA analysis, but every piece of data is presented, giving readers far more information than simply the hypothesis. This standard error over the whole model range depicts the F-test, which indicates that almost all variables except for the slope are 0. The hypotheses test is practical when the standard error does not contain the horizontally neutral product lineup [31].

Jute inner carbon has iodine and methylene blue desorption capabilities of 846 mg/g and 98.21 mg/g, correspondingly. Those are all significantly less than all the carbonaceous materials generated under the given circumstances as shown in Figures 1 and 2. It was also found that the entire jute progenitor cell lump charcoal carbonised at 900°C for 3.5 hours had a methylene blue adsorption performance of 340 mg/g. As a result, adding an adequate weight ratio of potash bicarbonate to a substrate substantially influences the growth of the more expanded permeability inside the polymeric network. As the comparative temperature builds, the empirical model of both materials rises slowly, and a residual stress forms, indicating that the significant
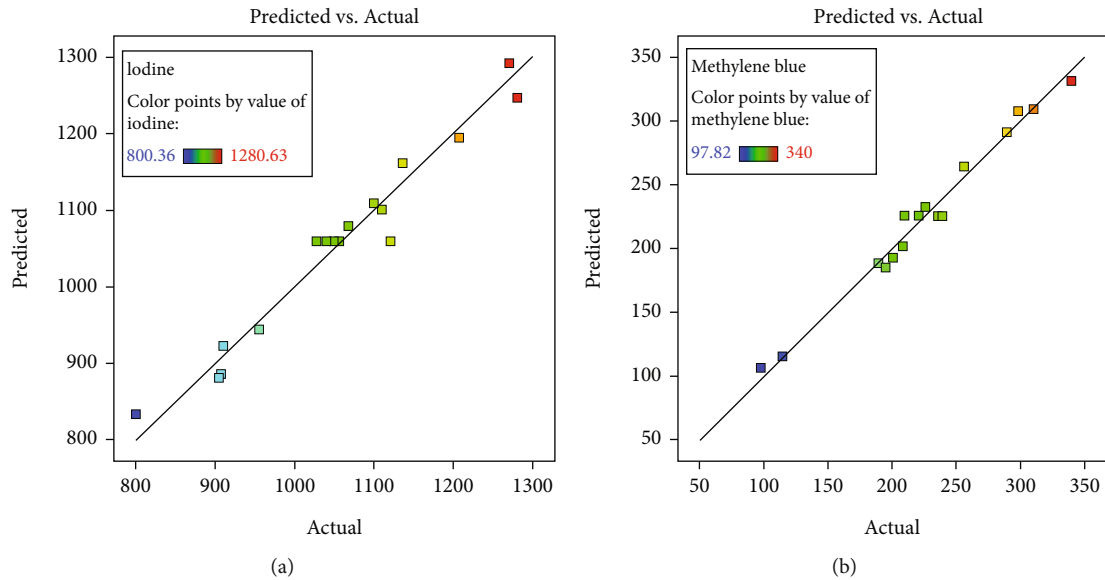
FIGURE 3: Actual vs. predicted plots of (a) iodine number and (b) methylene blue.
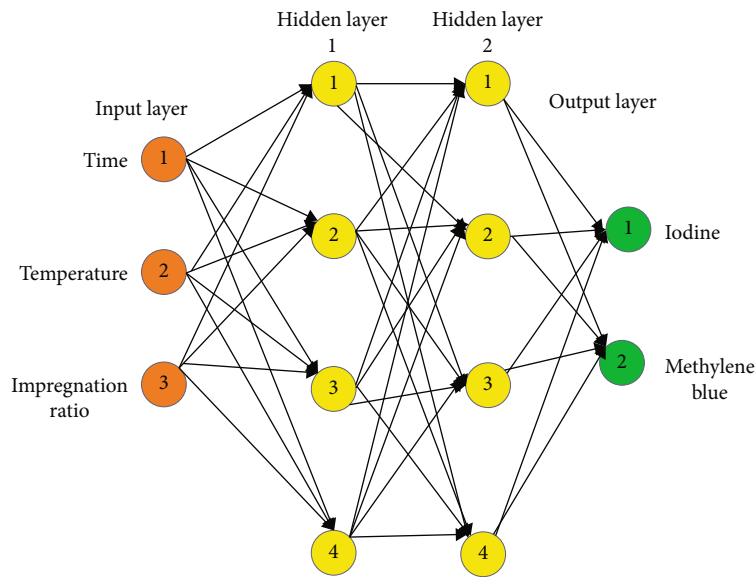
FIGURE 4: ANN structure of present research work.

number of small pores is linked with significant microporosity growth.

3.2. Optimization through ANN Modelling. In recent decades, ANN has emerged as a critical technique in the simulation and management of electrospun operations. As a computer tool, the ANN provides a graphical view with a slew of levels and multiple interacting processor parts that are primarily aware of inputs [32]. However, ANNs may adapt to real-world samples of a situation by utilising different equations among neurons and specialised machine learning built into the architecture of software applications. Figure 4 demonstrates the ANN structure of the current research.

The impregnation ratio, time length, and warmth were selected as input variables for the ANN, and the iodine number and methylene blue were selected as output results. This research explored the parabolic tangential, logistic digression, and linear activation parameters to improve the backpropagation neural network [33, 34]. Backpropagation (BP) has been used as a learning method to calculate performance gradients for weight vector parameter X. All specimens were separated into three subgroups at randomization to conduct an assessment. The supervised learning comprised 60% of specimens, the verification time series comprised 20% of specimens, and the testing data source held 20% of all specimens. The verification dataset is used to reduce the possibility of an over or forgetting [35]. This implies that whenever the inaccuracy of a
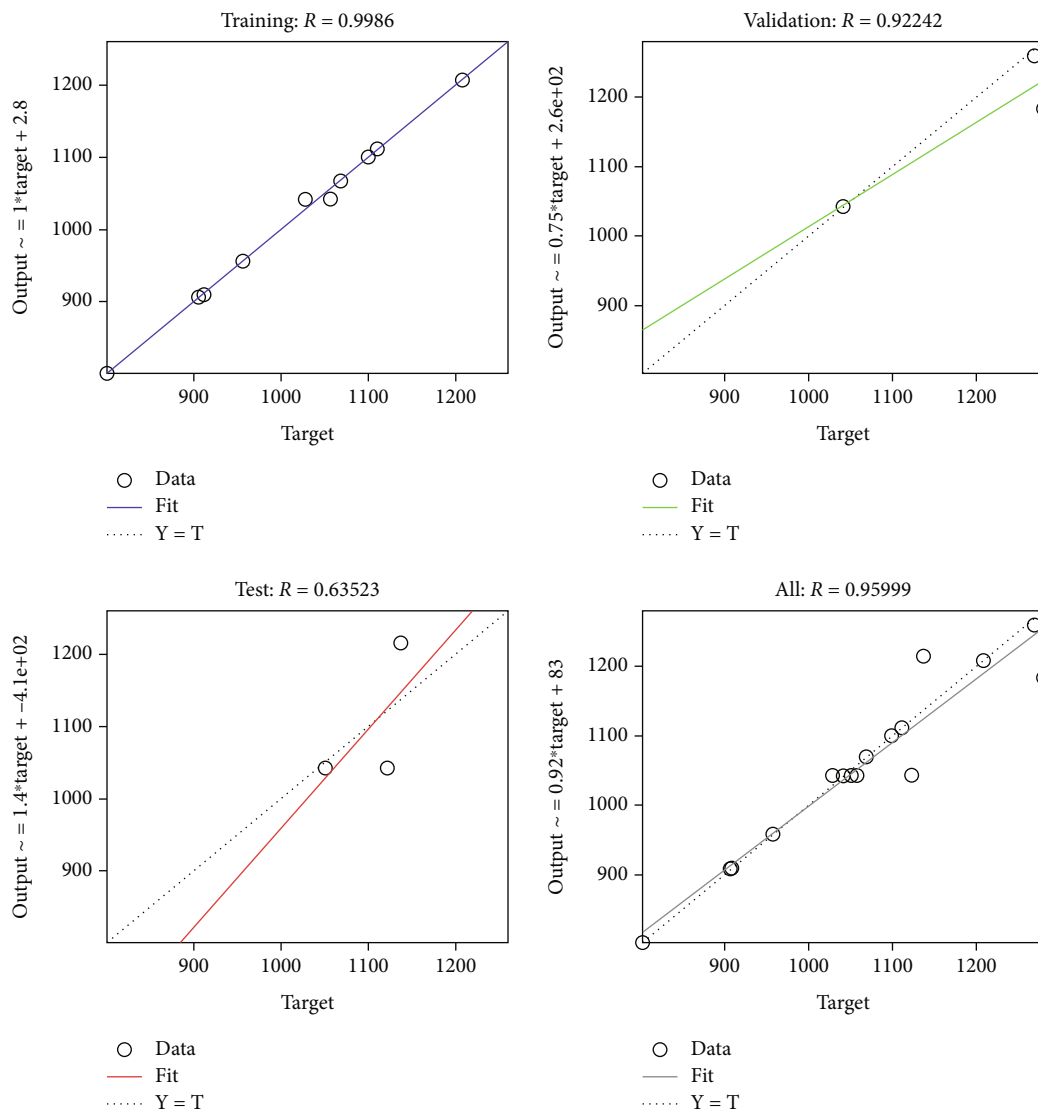
Figure 5: Continued.

(b)
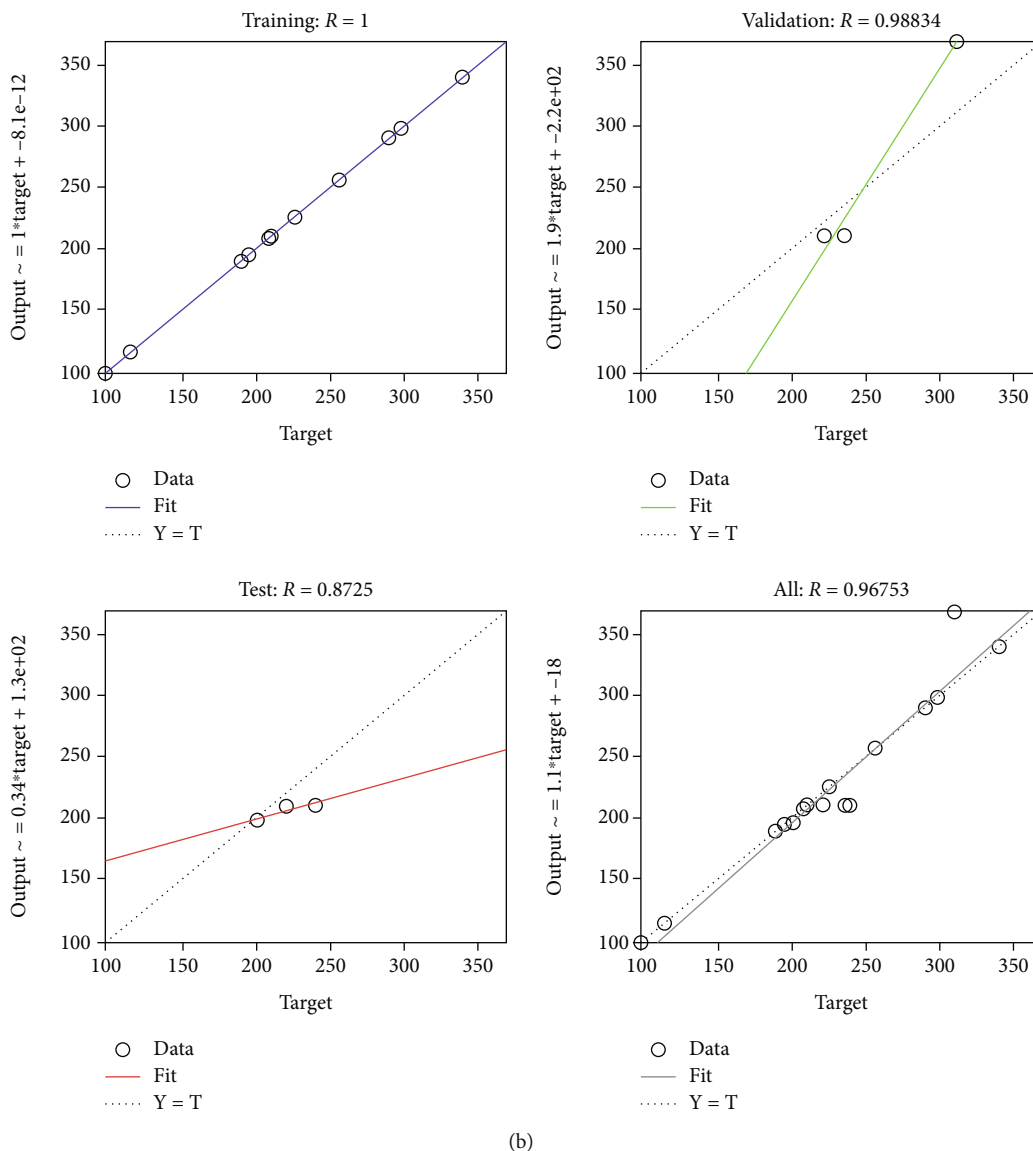
FIGURE 5: ANN performance features of (a) iodine number and (b) methylene blue.

learning test dataset drops while the fault of a testing dataset set grows, then network training is halted, and overtraining is prevented. Figures 5(a) and 5(b) show the predicted features of ANN results of iodine and methylene blue.

ANN can become caught in a minimum of errors, which the velocity factor helps to avoid. As a result, adopting the velocity factor reduces the probability of an under. This network can be trained using the Levenberg-Marquardt (LM) classification model. Although this approach handles general contour issues, its LM may be locked on the shortest path. To prevent the minimum error trapping, a velocity factor is provided. The Levenberg-Marquardt method is much more resilient than other algorithms that, in so many circumstances, result in the greatest network quality [36, 37]. A programme in MATLAB software was supplied to create the architecture of the graze and return network (version R2016). Since there is no predetermined procedure for determining its cortex and levels in the ANN framework,

the network output and stages are determined through experimentation. The number of nodes and levels was raised throughout this experiment to minimise the error function. Still, any growth in the population of neurons and levels did not improve the accuracy.

The assessment subcategories for training, validation, and assessment are shown in Table 4 along with the expected failure rate. Figures 5(a) and 5(b) show how well neurological systems predict what will happen. With values of 0.9599 for iodine and 0.9675 for methylene blue, the average amount of anticipated errors was reduced by less than 3%. Figures 6(a) and 6(b) are excellent instances of that one. Figures 7(a) and 7(b) provide iodine and methylene effectiveness graphs, respectively. The investigation was allowed since the measurement items were within the allowable levels. It can assess the accuracy of experiments conducted [38, 39]. The reliability of investigation, prediction, and artificial neural networks is summarised in Table 4.

TABLE 4: Predicted error based on the comparison of experimental and ANN values.

RUN	Experimental		ANN		Error	
	Iodine	Methylene blue	Iodine	Methylene blue	Iodine	Methylene blue
1	1182.650	340	1212.650	340	-2.53668	$-3.00936E-13$
2	800.360	97.82	800.630	97.82	-0.03373	$8.78917E-12$
3	1042.280	210	1072.280	210	-2.87831	$-1.43462E-12$
4	1207.170	256.21	1201.250	256.21	0.490403	$-1.17587E-12$
5	1068.250	298.19	1098.250	298.19	-2.80833	$-6.67199E-13$
6	1100.287	225.79	1100.270	225.79	0.001545	$-2.21543E-12$
7	1042.280	235.96	1042.000	210	0.026865	11.00186472
8	1042.280	239.65	1023.000	210	1.849791	12.37220947
9	1042.280	220.71	1072.280	210	-2.87831	4.852521408
10	1260.077	310.28	1290.077	369.2163412	-2.38081	-18.99456659
11	907.900	114.78	937.900	114.78	-3.30433	$4.35809E-12$
12	910.650	200.89	910.580	197.0881454	0.007688	1.892505633
13	905.570	189.78	935.570	189.78	-3.31283	$5.24165E-13$
14	956.170	194.89	956.320	194.89	-0.01569	0
15	1214.591	289.78	1248.210	289.78	-2.76793	$-1.03965E-12$
16	1042.280	221.45	1165.320	210	-11.8049	5.170467374
17	1110.140	208.54	1040.140	208.54	6.305511	$-4.77012E-13$
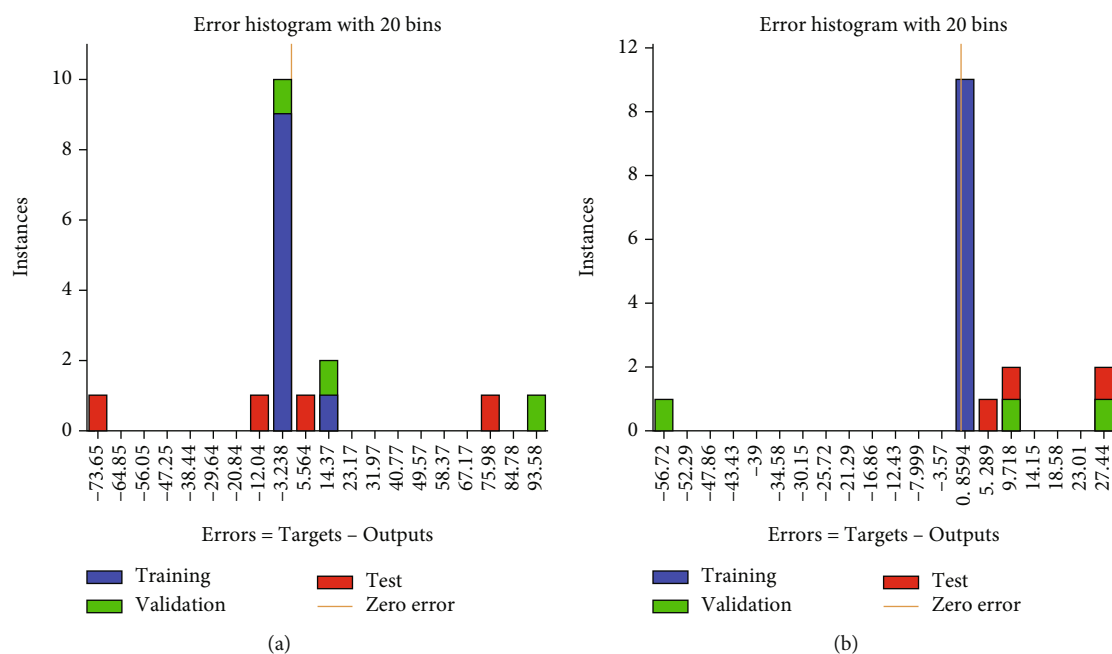
FIGURE 6: Error plots of (a) iodine and (b) methylene blue.

Statistical analysis revealed that the RSM or ANN approaches yield accurate findings.

According to the transmittance finding given in Figure 8, the adsorbed contains considerable microporous and mesoporous, compared with an average pore diameter of 3.16 nm. Comparison of experimental, RSM, and ANN-predicted values of iodine number and methylene blue are shown in Figures 8(a) and 8(b). Even though the precise emphasis given to K_2CO_3 is unknown at the moment, given the crea-tion of $K_2C_3O_4$ just after evolvement with one additional molarity of CO at approximately 870°C, these same porous and papule responses begun by K_2CO_3 stimulation might be temporarily posited to be quite comparable to an initia-tion action needed to make progress by $K_2C_3O_4$ [40]. The additional CO launched during K_2CO_3 dissolution, on either side, could act as a gas phase to aid in the removal of gasifi-cation volatile matter from the carbonaceous mixture to a high likelihood extent and have a moderate beneficial impact

Best validation performance is 3235.8818 at epoch 4

Best validation performance is 1426.1721 at epoch 5

(a)

(b)
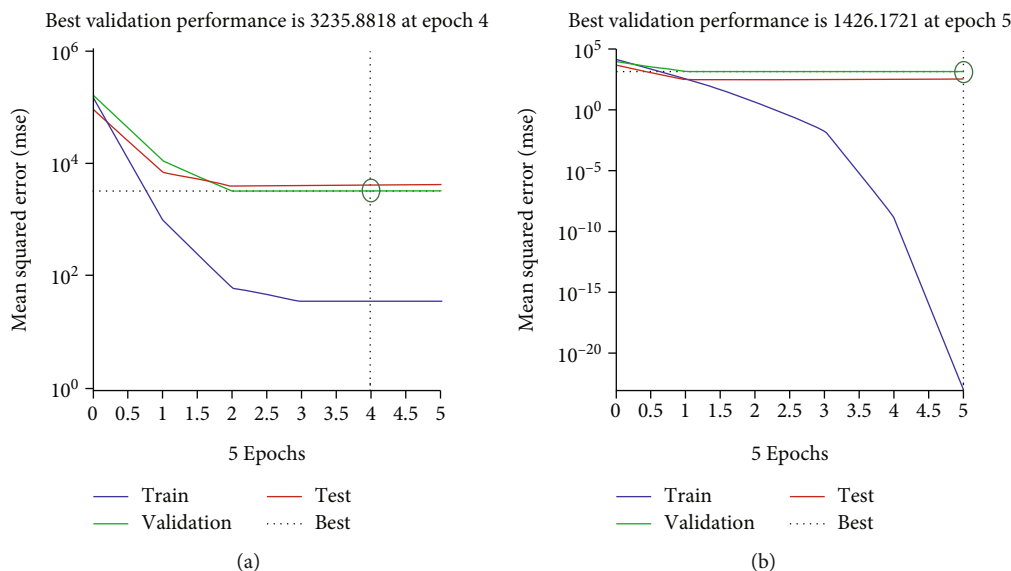
Figure 7: Effectiveness plots of (a) iodine and (b) methylene blue.

(a)

(b)
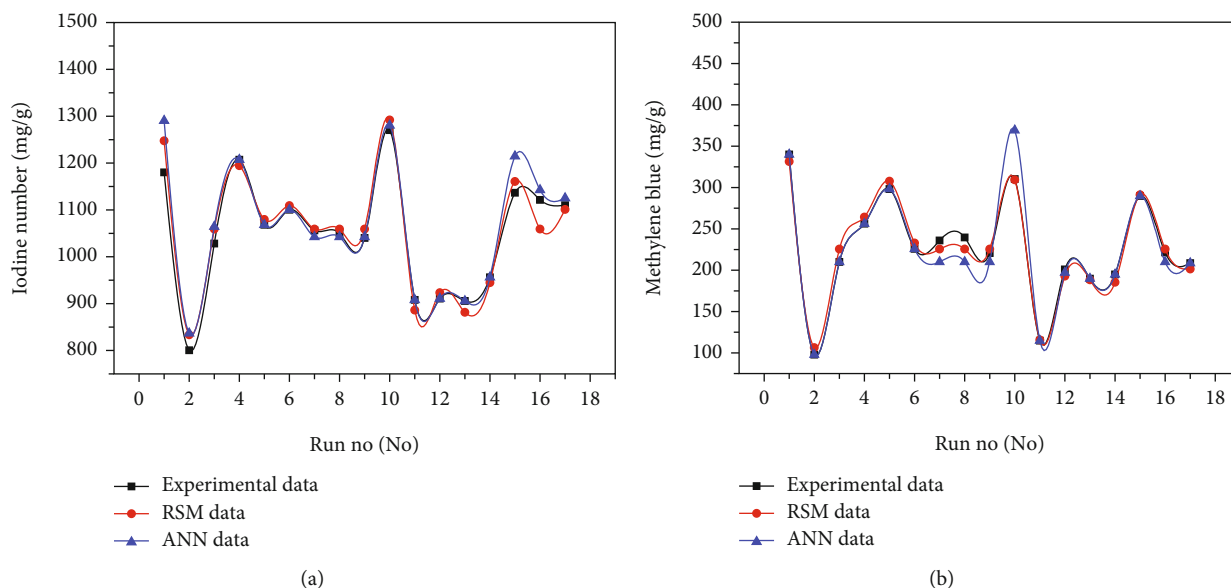
Figure 8: Comparison of experimental, RSM, and ANN-predicted values of (a) iodine number and (b) methylene blue.

on suppressing this same overaggressive porous broadening advancement to accomplish a relatively homogenous porous structure and high return [41]. Future studies should focus on a more in-depth examination of the activating effect of K_2CO_3 and $K_2C_3O_4$ on the pore structure of these carbonaceous materials. The ANN approach produced more future systems with a 95% reliability rate than response surface data. The ANN optimum model helps the user to account for the uncertainty associated with a particular cast combination.

4. Conclusion

BBD effectively optimised the process of producing K_2CO_3-activated carbons from the jute core. RSM and ANN model-ling were used to maximise the findings appropriately. The experimental results for iodine and methylene blue desorption were directly correlated very well with polynomial model predictions. The best charcoal was obtained using 900°C activating temperatures, a 1.5 molar ratio, and a 4-hour activating time. This resulted in iodine and methylene blue absorption of 1260.07 mg/g and 369.21 mg/g, respectively. It was discovered that the K_2CO_3-based pyrolysis process might be anticipated to become a safe yet incredibly efficient process of making activated carbons with a very well-defined and monocultural porous structure. Both the RSM and ANN models have to modify coefficients more significantly than 95%. (i.e., R^2 and adj. R^2). The prediction of ANN values of 0.9599 for iodine and 0.9675 for methylene blue reduced the average amount of anticipated errors by

less than 3%. This clearly demonstrates that the adsorbed contains considerable microporous and mesoporous, compared with an average pore diameter of 3.16 nm. Even though the precise emphasis given to K_2CO_3 is unknown at the moment, given the creation of $K_2C_3O_4$ just after evolvement with one additional molarity of CO at approximately 870°C, these same porous and papule responses begun by K_2CO_3 stimulation might be temporarily posited to be quite comparable to an initiation action needed to make progress by $K_2C_3O_4$.

Data Availability

The data used to support the findings of this study are included within the article. Should further data or information be required, these are available from the corresponding author upon request.

Conflicts of Interest

The authors declare that there are no conflicts of interest regarding the publication of this paper.

References

[1] Y. Li and M. Zhang, "Mechanical properties of activated carbon fibers," *Activated Carbon Fiber and Textiles*, vol. 6, pp. 167–180, 2017.

[2] I. Martin-Gullon and R. Font, "Dynamic pesticide removal with activated carbon fibers," *Water Research*, vol. 35, no. 2, pp. 516–520, 2001.

[3] V. K. Gupta, D. Pathania, and S. Sharma, "Adsorptive remediation of cu(II) and Ni(II) by microwave assisted H_3PO_4 activated carbon," *Arabian Journal of Chemistry*, vol. 10, pp. S2836–S2844, 2017.

[4] J. Zheng, Q. Zhao, and Z. Ye, "Preparation and characterization of activated carbon fiber (ACF) from cotton woven waste," *Applied Surface Science*, vol. 299, pp. 86–91, 2014.

[5] C. Nieto-Delgado, D. Partida-Gutierrez, and J. R. Rangel-Mendez, "Preparation of activated carbon cloths from renewable natural fabrics and their performance during the adsorption of model organic and inorganic pollutants in water," *Journal of Cleaner Production.*, vol. 213, pp. 650–658, 2019.

[6] G. Velmurugan and K. Babu, "Statistical analysis of mechanical properties of wood dust filled jute fiber based hybrid composites under cryogenic atmosphere using Grey-Taguchi method," *Materials Research Express.*, vol. 7, no. 6, 2020.

[7] C. Ye, N. Hu, and Z. Wang, "Experimental investigation of _Luffa cylindrica_ as a natural sorbent material for the removal of a cationic surfactant," *Journal of the Taiwan Institute of Chemical Engineers*, vol. 44, no. 1, pp. 74–80, 2013.

[8] S. S. Munawar, K. Umemura, and S. Kawai, "Characterization of the morphological, physical, and mechanical properties of seven nonwood plant fiber bundles," *Journal of Wood Science.*, vol. 53, no. 2, pp. 108–113, 2007.

[9] M. C. Symington, W. M. Banks, O. D. West, and R. A. Pethrick, "Tensile testing of cellulose based natural fibers for structural composite applications," *Journal of Composite Materials*, vol. 43, no. 9, pp. 1083–1108, 2009.

[10] R. Sudin and N. Swamy, "Bamboo and wood fibre cement composites for sustainable infrastructure regeneration," *Journal of Materials Science*, vol. 41, no. 21, pp. 6917–6924, 2006.

[11] A. Kicińska-Jakubowska, E. Bogacz, and M. Zimniewska, "Review of natural fibers. Part I—vegetable fibers," *Journal of Natural Fibers*, vol. 9, no. 3, pp. 150–167, 2012.

[12] P. Gopinath, P. Murugesan, R. Manjula Devi et al., "Characterization of jute fibre-epoxy reinforced composites," *Materials Today: Proceedings.*, vol. 46, pp. 8858–8863, 2021.

[13] T. B. Yallew, P. Kumar, and I. Singh, "Sliding wear properties of jute fabric reinforced polypropylene composites," *Procedia Engineering.*, vol. 97, pp. 402–411, 2014.

[14] V. Ganesan and B. Kaliyamoorthy, "Utilization of Taguchi technique to enhance the interlaminar shear strength of wood dust filled woven jute fiber reinforced polyester composites in cryogenic environment," *Journal of Natural Fibers*, vol. 19, no. 6, pp. 1990–2001, 2022.

[15] V. S. Chinta, P. Ravinder Reddy, and K. E. Prasad, "The effect of stacking sequence on the tensile properties of jute fibre reinforced hybrid composite material for axial flow fan blades: an experimental and finite element investigation," *Materials Today: Proceedings.*, vol. 59, pp. 747–755, 2022.

[16] A. K. Mohanty and M. Misra, "Studies on jute composites—a literature review," *Polymer-Plastics Technology and Engineering.*, vol. 34, no. 5, pp. 729–792, 1995.

[17] N. Reddy and Y. Yang, "Biofibers from agricultural byproducts for industrial applications," *Trends in Biotechnology.*, vol. 23, no. 1, pp. 22–27, 2005.

[18] A. K. Mohanty, M. A. Khan, and G. Hinrichsen, "Surface modification of jute and its influence on performance of biodegradable jute-fabric/Biopol composites," *Composites Science and Technology*, vol. 60, no. 7, pp. 1115–1124, 2000.

[19] S. Kaliappan, S. Mohanamurugan, and P. K. Nagarajan, "Numerical investigation of sinusoidal and trapezoidal piston profiles for an IC engine," *Journal of Applied Fluid Mechanics*, vol. 13, no. 1, pp. 287–298, 2020.

[20] J. Kazemi and V. Javanbakht, "Alginate beads impregnated with magnetic nanocomposite for cationic methylene blue dye removal from aqueous solution," *International Journal of Biological Macromolecules.*, vol. 154, pp. 1426–1437, 2020.

[21] H. B. Quesada, T. P. de Araújo, L. F. Cusioli, M. A. S. D. de Barros, R. G. Gomes, and R. Bergamasco, "Caffeine removal by chitosan/activated carbon composite beads: adsorption in tap water and synthetic hospital wastewater," *Chemical Engineering Research and Design.*, vol. 184, pp. 1–12, 2022.

[22] B. Debnath, D. Haldar, and M. K. Purkait, "Environmental remediation by tea waste and its derivative products: a review on present status and technological advancements," *Chemosphere*, vol. 300, p. 134480, 2022.

[23] V. Balaji, S. Kaliappan, D. M. Madhuvanesan, D. S. Ezhumalai, S. Boopathi, and S. Mani, "Combustion analysis of biodiesel-powered propeller engine for least environmental concerns in aviation industry," *Aircraft Engineering and Aerospace Technology*, vol. 94, no. 5, pp. 760–769, 2022.

[24] O. S. Onyekwere, C. Odiakaose, and K. A. Uyanga, "Multi response optimization of the functional properties of rubber seed – shear butter based core oil using D-optimal mixture design," *Archives of Foundry Engineering.*, vol. 17, no. 4, pp. 207–223, 2017.

[25] R. Ghelich, M. R. Jahannama, H. Abdizadeh, F. S. Torknik, and M. R. Vaezi, "Central composite design (CCD)-response

surface methodology (RSM) of effective electrospinning parameters on PVP-B-Hf hybrid nanofibrous composites for synthesis of HfB$_2$-based composite nanofibers," *Composites Part B: Engineering.*, vol. 166, pp. 527–541, 2019.

[26] R. Sasidharan and A. Kumar, "Response surface methodology for optimization of heavy metal removal by magnetic biosorbent made from anaerobic sludge," *Journal of the Indian Chemical Society.*, vol. 99, no. 9, article ???, 2022.

[27] M. S. Bhatti, D. Kapoor, R. K. Kalia, A. S. Reddy, and A. K. Thukral, "RSM and ANN modeling for electrocoagulation of copper from simulated wastewater: multi objective optimization using genetic algorithm approach," *Desalination*, vol. 274, no. 1-3, pp. 74–80, 2011.

[28] S. J. Muthiya, L. Natrayan, S. Kaliappan et al., "Experimental investigation to utilize adsorption and absorption technique to reduce CO2 emissions in diesel engine exhaust using amine solutions," *Adsorption Science & Technology*, vol. 2022, article 9621423, pp. 1–11, 2022.

[29] M. M. Matheswaran, T. V. Arjunan, S. Muthusamy et al., "A case study on thermo-hydraulic performance of jet plate solar air heater using response surface methodology," *Case Studies in Thermal Engineering*, vol. 34, article 101983, 2022.

[30] V. Paranthaman, K. Shanmuga Sundaram, and L. Natrayan, "Influence of SiC particles on mechanical and microstructural properties of modified interlock friction stir weld lap joint for automotive grade aluminium alloy," *Silicon*, vol. 14, no. 4, pp. 1617–1627, 2022.

[31] B. Subramanian, N. Lakshmaiya, D. Ramasamy, and Y. Devarajan, "Detailed analysis on engine operating in dual fuel mode with different energy fractions of sustainable HHO gas," *Environmental Progress & Sustainable Energy*, vol. 41, no. 5, article e13850, 2022.

[32] A. E. Rodríguez-Sánchez, E. Ledesma-Orozco, S. Ledesma, and A. Vidal-Lesso, "Application of artificial neural networks to map the mechanical response of a thermoplastic elastomer," *Materials Research Express.*, vol. 6, no. 7, 2019.

[33] G. J. Yun, J. Ghaboussi, and A. S. Elnashai, "A new neural network-based model for hysteretic behavior of materials," *International Journal for Numerical Methods in Engineering.*, vol. 73, no. 4, pp. 447–469, 2008.

[34] D. M. Dimiduk, E. A. Holm, and S. R. Niezgoda, "Perspectives on the impact of machine learning, deep learning, and artificial intelligence on materials, processes, and structures engineering," *Innovations*, vol. 7, no. 3, pp. 157–172, 2018.

[35] D. Wang, Q. Zhu, Z. Wei et al., "Hot deformation behaviors of AZ91 magnesium alloy: constitutive equation, ANN- based prediction, processing map and microstructure evolution," *Journal of Alloys and Compounds.*, vol. 908, p. 164580, 2022.

[36] F. Masi and I. Stefanou, "Multiscale modeling of inelastic materials with thermodynamics-based artificial neural networks (TANN)," *Computer Methods in Applied Mechanics and Engineering*, vol. 398, article 115190, 2022.

[37] A. Habib and U. Yildirim, "Developing a physics-informed and physics-penalized neural network model for preliminary design of multi-stage friction pendulum bearings," *Engineering Applications of Artificial Intelligence.*, vol. 113, p. 104953, 2022.

[38] J. Du, Y. Wu, Z. Dong et al., "Single and competitive adsorption between indigo carmine and methyl orange dyes on quaternized kapok fiber adsorbent prepared by radiation technique," *Separation and Purification Technology.*, vol. 292, p. 121103, 2022.

[39] D. Ghosh and K. G. Bhattacharyya, "Adsorption of methylene blue on kaolinite," *Applied Clay Science.*, vol. 20, no. 6, pp. 295–300, 2002.

[40] M. Rafatullah, O. Sulaiman, R. Hashim, and A. Ahmad, "Adsorption of methylene blue on low-cost adsorbents: a review," *Journal of Hazardous Materials.*, vol. 177, no. 1-3, pp. 70–80, 2010.

[41] V. S. Shankar, G. Velmurugan, S. Kaliappan et al., "Optimization of CO2 concentration on mortality of various stages of Callosobruchus maculatus and development of controlled atmosphere storage structure for black gram grains," *Adsorption Science & Technology*, vol. 2022, pp. 1–12, 2022.

Research Article

Employing a Carbon-Based Nanocomposite as a Diffusive Solid-Phase Extraction Adsorbent for Methamphetamine for Therapeutic Purposes

K. Lakshmi Kala,[1] **G. Anbuchezhiyan,**[2] **Kavitha Pingili,**[3] **Pradeep Kumar Singh,**[4] **V. M. Vel,**[5] **Kareem Yusuf,**[6] **Ahmed Muteb Aljuwayid,**[6] **Md Ataul Islam,**[7] **and David Christopher** [8]

[1]*Department of Mechanical Engineering, Mohanbabu University, Tirupati, Andhra Pradesh, India*
[2]*Department of Mechanical Engineering, Saveetha School of Engineering, Saveetha Institute of Medical and Technical Sciences, Chennai, Tamil Nadu 602105, India*
[3]*Department of Chemistry, Chaitanya (Deemed to be University), Warangal, Telangana 506001, India*
[4]*Department of Mechanical Engineering GLA University, Mathura 281406, India*
[5]*Department of Mechanical Engineering, School of Technology, Glocal University, Delhi-Yamunotri Marg, Uttar Pradesh 247121, India*
[6]*Department of Chemistry, College of Science, King Saud University, Riyadh 11451, Saudi Arabia*
[7]*School of Health Sciences, Faculty of Biology, Medicine and Health, University of Manchester, Manchester, UK*
[8]*Department of Mechanical Engineering, College of Engineering, Wolaita Sodo University, Ethiopia*

Correspondence should be addressed to David Christopher; david.santosh@wsu.edu.et

Due to the obvious minimal doses of drugs in biological matrices as well as the societal difficulties caused by methamphetamine usage, methamphetamine identification is critical in clinical and forensic laboratories. Because of their simple and inexpensive production procedure, as well as their excellent selectivity and sensitivity, polymeric carbon-based nanocomposites are strong contenders for the diffusive solid-phase extraction approach. The diffusive solid-phase extraction absorbent nanographene oxide polypyrrole composite was produced and used to recover methamphetamine from a complicated urine substrate. The generated NGPPC was fully characterized, and the significant extracting parameters have been explored using the one-parameter-at-a-time strategy. NGOPC is being used to extract methamphetamine using a urine medium with high efficiency. The NGPPC synthesizing procedure was easy, and the extraction method will demonstrate good repeatability. Moreover, the practical and efficient synthesis process stimulates the use of carbon-based compounds in various extraction procedures. As for detecting and quantifying equipment, HPLC monitors are being used. 300 mL methanol, 7 min extracting and desorption duration, 5000 mixing frequency, urinary pH value of 20, 40 mg adsorption, and 5 mL amount of urine were the optimal extraction variables. Following tracing the calibration graph, the method's linear ranges were determined to be 40-600 ng/ml. The detection limits (LOD) and quantitation limits (LOQ), correspondingly, were 10 and 35.80 ng/mL. The proposed methodology seemed to have a detection range of 9 ng/mL. The suggested approach's applicability in numerous characterization and medical facilities was proven by the examination of addicted subjects using the proposed technique. For successful extraction of methamphetamine using biological urine samples, the carbon-based adsorbent was being used as diffusive solid-phase extraction adsorption.

1. Introduction

A nanocomposite is comprised of two or perhaps more various materials with different physicochemical characteristics, at least one of which is a nanomaterial. Nanocomposite components are formed to have characteristics that far outweigh, and in some cases vastly outweigh, the capacity of its constituent elements. Components (referred to as the reinforcement phase) were embedded in some other materials in order to create nanocomposites. Nanomaterials could exist in one or both stages [1]. The matrices are frequently stretchy or rougher, while the reinforcement chemicals are fairly strong and have a lower density. If the mixtures are effectively designed and manufactured, they combine the strength of the reinforcement with the hardness of the substrate to provide a unique combination of desirable properties not available in any separate traditional materials. The most difficult aspect of manufacturing nanocomposites is creating a uniform diffusion of nanoparticles [2]. The efficiency of the diffusion must have an impact on the interactions among the stages, which could influence the nanocomposite's properties of the resulting. That becomes feasible to tailor distinctive features (such as biomechanical, electrically, thermodynamic, magnetism, or indeed acoustical) by integrating differential materials, architectures, and concentrations in nanocomposites, enabling the nanocomposite substance ideal for diverse applications. As a result, nanocomposites have spawned the rapidly expanding area of multifunctional materials. Nanoparticle fillings contain a limited number of atoms each particle including, as a result, might also have distinct characteristics and significant connections with the matrix over larger materials. It is characterized by a large nanoparticle-matrix interfacial area, as well as molecular basis interconnections among nanoparticles and matrices, which were thought to make a significant contribution to affecting the physical and mechanical features of nanocomposites [3].

Nanocomposites could be made from a variety of components, including nanostructured materials, biomaterials, and conducting polymers [4]. For example, using genetic engineering, the researchers blended two separate organic elements with distinct and crucial features into a single composite structure. They created a new biomimetic nanocomposite by integrating the properties of silken and biosilica through the design, manufacturing, and characterization of a novel group of chimera proteins. Polymer nanocomposites are two-phase mechanisms made up of polymers and reinforcing fillers having a large surface area [5]. The improvements in mechanical characteristics are with very low contents loadings. Nanocomposites are also possible with standard polymeric manufacturing, eliminating the expensive layup necessary for traditional fiber-reinforced composite manufacture. Nanocomposites, with the exception of enhanced elastomers, really have not met expectations [6]. While assertions of a tenfold increase in rigidity exist, these assertions are contradicted by experiments that demonstrate little or no change. At this time, we are only interested in the effect of nanoscale fillers on composites' modulus. The essential possessions of the matrix and filler, as well as interfaces among the two, have a role in modulus increase. Poor diffusion, poor interfacial deformation, technique defects, poor alignments, reduced load transmission to the interiors of filling strands, and the fractal structure of filler groups have all been blamed for nanocomposites poor performance. Figure 1 depicts the illustration of the nanocomposite.

Industrial and academic sectors have paid close attention to organic/inorganic nanocomposites. To blend the characteristics of diverse materials and obtain regulated characteristics and prospective applicability, many methodologies were used to create and manufacture organic/inorganic nanocomposites. Due to the obvious possible advantages in chemical sensing, catalytic, optics, and electrical equipment, much effort has been devoted to including or decorating metallic nanoparticles in the matrices or on the surfaces of polymer electrolytes. Polypyrrole (PPy), a conductive polymer with strong environmental resilience, high conductivity, and biocompatibility, is of specific importance [7]. By utilizing various nanostructures, such as nanowire, nanotube, and nanoparticles, PPy was being employed as a matrix to integrate or scatter many metal nanoparticles used in electrocatalysis and sensing. A conjugated polymer with unique electrical characteristics, such as conductivity, is PPy. Additionally, due to their favourable chemical and physical properties, PPy has also developed into one of the most researched materials for biological applications. The aggregating of inorganic nanoparticles, on the other hand, will result in a loss of surface area as well as a reduction in predicted attributes as a result of decreasing overall surface tension. Numerous synthesized approaches have developed in recent years to address this problem. Super capacitor electronic interfaces made of graphene/PPy nanofiber combinations were used to improve its faradaic response, resulting in increased resistance. PPy nanotubes, unlike PPy nanofibers, have an interior cavity that is several to thousands of nanometers in diameter, allowing electrolyte transportation not just to the internal sections of the PPy nanotubes but also with the outer surface. PPy nanotubes have a great potentiality for ionic conduction and are accessible, which means they have a lot of capacitance. At ambient temperature, PPy may be readily produced in large quantities using a variety of liquids. It may be made with a variety of porosities and has a high surface area that could be precisely controlled by adding activating chemicals, rendering it more appropriate for biological applications. Corrosion protection, fuel cells, microsurgical instruments, biosensors, brain tissue engineering, and drug delivery systems are just a few of the applications for PPy today.

Throughout the last twenty years, the nanoscience concept has grown into a wide variability of effect types, and the concentration of nanotechnology/nanomaterial is circumfluence in several promising grounds, such as sensing, biomedical, and numerous helpful implementations. The capability to synthesize nanomaterials from varied structural materials, along with turning the specimens into sophisticated nanoarchitectures, has been accelerated research in related domains [8]. Due to this, owing to its large conduction capabilities, the monolayer of two-dimensional graphene substantial having honeycomb lattice construction,
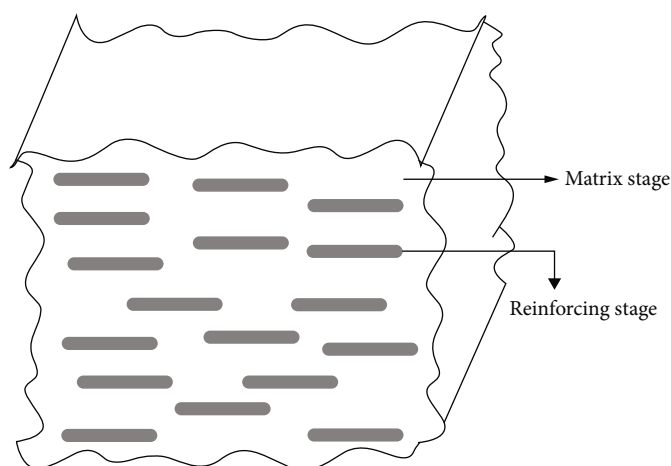
Figure 1: Nanocomposite illustration.

that includes an intercarbon binding affinity of roughly 0.142 nm, is widely used in biomedical and nanomedicine purposes. Biological properties which provide for cellular proliferation as well as development, such as the delivery of drugs and chemotherapeutic therapy, might benefit greatly from graphene-based nanomaterials. Furthermore, the materials could be utilized to engage bioactive molecules (e.g., DNA, membranes, or proteins). Graphene/chitosan films have previously been investigated as an implant material in synthetic biology using the solutions fabrication technique [9]. Graphene oxide (GO) that has not been properly functionalized has been discovered to be a hazardous substance. Functionalized nanographene as well as its composite materials is having increasingly garnered attention in biological applications owing to its special and improved physicochemical characteristics. GO and reduced graphene oxide (rGO), on the other hand, could have been functionalized with biocompatible polymers including PEGylated (PEG), which can be achieved by both covalently and noncovalent techniques to improve physiological environment stability. A sensitivity platform made of graphene is frequently utilized for detecting biological systems in the ability to identify the transition mechanism in addition to the power current of the human cell membrane. The profusion of functionalized nanoscale rGO-based bio-conjugated nanocomposites has already been widely used as drug or gene delivery methods owing to its improved porous structure (single sheet organized with carbon atoms) [10]. Furthermore, due to its strong near-IR (NIR) absorption, its associated compounds of functionalized graphene exhibited remarkable tumor elimination therapeutic benefits. Graphene oxide (GO) is made up of numerous carboxylic, carbonyl, and epoxide structural features and has a higher specific surface area. It was a great biochemical, thermal, and mechanical stability. Furthermore, conductive polymers (CPs), such as polypyrrole, have highly reversible electrochemical activity as well as unique plastic-metal characteristics. Because of their stability and multifunctionality, CPs have gotten a lot of attention in recent decades. Combining different materials can be a good way to make new activated carbons that have the benefits of many of the constituents [11].

Methamphetamine is an extremely addictive amphetamine which generates the consequences. Crystal methamphetamine is a methamphetamine which looks like pieces of glass or shining, bluish-white stones. This has a similar chemical structure to amphetamine, a medication was using to treat ADHD and drowsiness, an insomnia [12]. The United Nations Office on Drugs and Crime reported that 290 tonnes of methamphetamine were produced in 2005, which is equal to 2.9 billion 100 mg doses of antibiotics. Methamphetamine is the two most frequently used illicit substances in the world, with a global prevalence of 0.4 percent. The medicine is most commonly used in Asia, Oceania, and North America. Adult prevalence rates in the Philippines are 14 percent, 3.2 percent in Australia, and 0.8 percent in the United States. Methamphetamine, often known as MA, is a central nervous system stimulant that causes intoxication by enhancing the activity of dopamine and norepinephrine pathways in the brain [13]. To a much lesser extent, it is also used as a treatment for attention deficit hyperactivity disorder and obesity, but recreational usage is by far the more popular application of this substance. The benefits of MA, such as attentiveness, euphoria, and a sensation of well-being, remain significantly longer than those of cocaine, and the drug is processed by the body at a much slower pace. MA is a compound of amphetamine, which had been initially produced in 1887 by a German scientist and researched thoroughly in the early 1930s. Amphetamine is a sympathomimetic medication that activates the compassionate division of the autonomous nervous system, comparable to ephedrine [14].

Muscle breakdown, neurosis, delusions, and seizures are all frequent side consequences through methamphetamine use. Suicide, road accidents, and violence are all important social issues brought on by large doses. In medical and forensic laboratories, organic fluids (urine and plasma) are common samples. Urine is the most useful of these fluids since it is readily available, is intrusive, and can be prepared in huge quantities. Methamphetamine is eliminated in urine at a rate of 37–54 percent in a pH range of 6–8. Because of this, it is quite likely that methamphetamine will be found in the individual's urine [15]. Because of the obvious

complexity and small doses of the analyte in the urine medium, conventional urine analysis is not applicable in the majority of situations; as a result, the development of a technique that combines high sensitivity and selectivity is essential. However, a standard urine test can identify methamphetamine in the system for anywhere from three to five days after the last dose was taken. Because of the composite matrix and low dosages of analytes in varied biochemical media, chemical analysis requires the construction of innovative sample processing techniques. Solid-phase extraction-based (SPEs) approaches being used in analysis methods include solid phase microextraction (SPME), dispersive solid phase extraction (DSPE), magnetic solid phase extraction (MSPE), and microsolid-phase extraction (M-SPE). It has been demonstrated that utilizing these approaches results in high analyte recoveries while using a little number of desorption liquids and achieving optimal preconcentration parameters. Adsorbents were substances that are used in SPE to extract or remove medicines or contaminants from aquatic or biological composites [16]. Solid-phase extraction is a class of alternate extraction procedures (SPE). SPE is a broad field with much applicability that has been the focus of countless articles and research. In most cases, a watery capacity to identify through an immobilized stage is during the distillation process before being extracted with suitable organic solvents. For extremely polar analytes, nevertheless, reduced performances due to poor retention, resulting in low breakthrough volumes, can be seen. Nonetheless, changing the kind of sorbent is among the SPE techniques for overcoming breakthrough quantity [17]. The construction consisting of a polypropylene cartridge with an inserted adsorption stage is the one that is utilized the most frequently in SPE. A high surface area melt-blown polypropylene media is used in the construction of the PP Cartridge. This allows for a minimal initial pressure drop, a high dirt holding capacity, and high-efficiency performance. The substances to be separated are divided into two phases: a solid phase (bed sorbent) and a liquid-liquid phase in SPE (sample). The solid phase should have a higher specificity for such compounds than the chromatographic matrix. Column preparations, specimen load, columns post-wash, and specimen adsorption are the 4 phases of SPE in particular. The stationary phase is conditioned using the abovementioned prewash process. In particular, the post-wash is used to remove unwanted materials. Following washing off the interference chemicals, the targeted analytes are maintained on the suitable bed sorbent. After that, the appropriate elution solvents were utilized to retrieve the data [18].

The differentiation strategy of analytes between the granular packaging and the liquids moving phases is the basis for SPE extraction. A miniaturized extraction (micro-SPE) has many benefits, including the ability to connect directly to high-performance liquid chromatography (HPLC), gas chromatography (GC), or capillary electrophoresis (CE), lower operating costs and time, and the ability to be partially or fully automated, allowing for higher repeatability and hyphenation. SPE's fundamentals entail the separation of substances into two components. Because they should utilize

a higher similarity again for the solid stage than the model matrix, the analytes that need to be extracted are separated between the solids and the liquid phase in the SPE procedure (retention or adsorption step). Solid phase extraction is a technique that takes use of the difference in affinity between an analyte and interferents that are present in a liquid matrix (sorbent). Substances that have remained on the solid matrix could be eluted using a solution that has a higher affinity for such analytes at a later phase (elution or desorption step). Intermolecular interactions among the solution, the adsorption sites on the adsorbent surface, and the dispersion medium or matrix were responsible for the various processes of detention or extraction. The processes underlying in columns column chromatography are about the same. The term HPLC stands for high-performance liquid chromatography. "Chromatography" is a process that separates, "chromatogram" is the chromatography outcome, and "chromatograph" is the chromatography apparatus [19]. Several of the essential aspects of chromatographs include machines designed for molecule isolation termed columns and high-performance compressors for distributing solvents at a steady flow rate, among some of the advanced systems created for chromatography. The technique once known as HPLC was known simply as "LC" as associated technologies were becoming more advanced. Ultrahigh-performance liquid chromatography (UHPLC), that is suitable of incredible examination, is becoming increasingly widely being used now. HPLC could only evaluate chemicals that are immersed in solutions [20]. HPLC isolates chemicals dispersed in a diluted solution, allowing for descriptive and analytical examination of which constituents are exists in the model and how much of every element is present. The nanographene oxide polypyrrole composite (NGPPC) was produced and studied in this study using a simple approach. In order to extract methamphetamine from urine, NGPPC was employed as a DSPE adsorbent. HPLC technique was used to regulate and quantify the amount of MA. The positive relative recuperation analysis indicates that using NGPPC in the DSPE method is a novel sample preparation approach that might be used in effective analysis and medical labs. The remaining sections are arranged as follows. In Section 2, the related work was presented. The materials and methods are in Section 3. Section 4 put the result and discussion to the test in terms of performance and efficiency, with figures and charts displaying the findings. The final section summarises the paper's conclusions.

2. Related Works

A device that extracts amphetamines and methylenedioxyamphetamines from urine is created using a spin column filled using octadecylsilane-bonded monolithic silicon to deal with the challenges of solid-phase extracting. The National Institute of Technology and Evaluation purchased methamphetamine (MA) hydrochloride as well as produced amphetamine (AP) hydrosulfate had been tested for quality. MDMA and MDA (methylenedioxymethamphetamine and methylenedioxyamphetamine) have been acquired. The medicines are digested in 0.01 M HCl and kept at 4°C and

refrigerated to make the standard stock solution volumes (1.0 mg/mL). GL Sciences provided the spinning columns. A normal adult provided drug-free urine, which was kept at 20 degrees Celsius until examination. The preactivated columns were filled with urine (0.5 mL), buffer (0.4 mL), and methoxyphenamine (internal standard). During additional permits and washing, the columns were centrifuged (3000 rpm, 5 min). Despite evaporating, the adsorption analytes are subsequently rinsed and examined using high-performance column chromatography. Limit of detection is 0.1 g/ml, linear curves (drug concentrations of 0.2–20 g/mL), and correlation coefficients >0.99. This suggested technique is also not applicable to medicines composed of organic substances, but it is also very repeatable for toxicology testing in urination. Since both specimens and the solvents move in only one direction, there is no chance of sample contamination. Furthermore, since the samples may be recovered with a tiny amount of solvent, this approach has cost expensive [21]. The research offers an extremely specific stir bar sorptive extraction technique for direct estimation of amphetamines in samples taken employing carbon-coated magnetic nanoparticles like a unique stir bar covering. Satisfactory linearity will be reported in the maximum concentration of 20–2000 ng/mL for amphetamine and 20–2500 ng/mL for methamphetamine, including 30–1500 ng/mL for pseudoephedrine using solvent evaporation circumstances. The created recommended approach tested the affirmative urine specimen with successful results. The proposed stir bar sorptive extraction method was used in a variety of forensics as well as medical facilities, according to the findings. The MNC sol gel-coated stir bar demonstrated good reliability and selectivity while determining mixtures in a complicated urine mixture. In comparison to conventional SPME fibers, the experimentally stir bars had a deeper protective coating that resulted in improved removal efficiencies. Additionally, the suggested technique has a modest training procedure, quick sample preparation duration, and is worthwhile. Furthermore, the good recovery observed for the studies given in this paper confirms the suggested technique's usability in the majority of related different laboratories. Given the continuous creation and innovation of various coverings, other obstacles should be solved, such as liquid desorption efficiency, the difficulty of reanalysis following heating desorption, coated condition monitoring after so much usage, and the blending of old and new twisters. SBSE does not have the best precisions (RSD) when compared to certain other extraction processes because stir-bars are costly and should be recycled for numerous extraction processes as much as the covering is in perfect shape [22].

The utility of solid-phase microextraction (SPME) in the perseverance of a growing number of high volatility, as well as semivolatile samples in biological matrices and components, is being investigated. In spite of the problems posed by minuscule concentration ratios and lengthy absorption coefficient durations, semivolatiles have grown increasingly popular as experimental targets in recent years. Because of these constraints, amphetamines were selected as potential candidates for the semivolatile category, and evaluation methodologies were devised. Amphetamines are routinely tested in matrices that are notoriously difficult to analyze. Solid-phase microextraction has proven to be helpful for these types of investigations since it reduces the amount of interaction between the sample and the fiber. The amphetamines were extracted using human urine that used a 100 mm polydimethylsiloxane- (PDMS-) coated SPME fiber. Gas chromatography (GC) with flame-ionization monitoring has been used to determine the presence of amphetamine (FID). To achieve constant separation, temperature, duration, and sodium concentration have been tuned. A straightforward method for testing amphetamine (AMP), methamphetamine (MA), 3,4-methylenedioxyamphetamine (MDA), 3,4-methylenedioxy-N-methamphetamine (MDMA), and 3,4-methylenedioxy-N-ethylamphetamine (M amphetamine (19.5–47%) and methamphetamine (20–38.1%))) had higher recovery rates than MDA (5.1–6.6%) (5.4–9.6 percent). SPME is a fast, solvent-free extraction method that can be used instead of standard liquid-liquid as well as solid–phase extraction for amphetamine detection in organic resources. The focus of this research is to use the HS-SPME to obtain maximum analyte recoveries. As a result, a simple way of determining AMP and MA in urine samples was devised, as well as a distinct approach for determining MDA, MDMA, and MDEA. However, one of the major disadvantages of SPME approaches is the restricted amount of readily accessible column chromatography (fiber materials), which only comprises the polarities range of targeted analytes to a degree [23].

In the subject of systems biology, there must have subsequently become a surge in the rise in the popularity of Rezaee's dispersive liquid-liquid microextraction (DLLME), which was first created in 2006. DLLME is a compact liquid-liquid extraction method with a much lower acceptor-to-donor stage ratio than conventional systems. The use of DLLME in conjunction with various analysis methods including atomic absorption spectrometry (AAS), inductively coupled plasma-optical emission spectrometry (ICP-OES), gas chromatography (GC), and high-performance liquid chromatography (HPLC) for preconcentration and perseverance of synthetic samples in various kinds of materials is discussed. Through the use of an additional solvent to alter the thickness of the extracting mixture, and through the use of ionic liquid-based DLLME to determine synthetic organisms perhaps in the case of excessive sodium content, the systematic study discusses significant breakthroughs in DLLME, such as displacement-DLLME, through the use of an additional solvent to alter the thickness of the extracting mixture. DLLME is an extraction method that was created during the past decade and involves the dispersion of small droplets of extraction solvent in an aqueous sample. This technique was initially used to extract lipids from aqueous samples. A hazy complex is made when a suitable combination of the extractant as well as the disperser liquid with elevated mixtures including both aqueous and organic stages is quickly infused into the acidic suspension of the specimen, and a fine spatter of such removal liquid dissipates in the liquid sample. The small droplets settle at the bottom of the cylindrical glass beaker after centrifugation of the hazy liquid. The solutes have been retrieved out from exact guess and focused on a small capacity of the

deposited process, where they can be determined using standard methodological approaches. Despite DLLME providing exceptional achievement in the liquid solution, it is still not applicable to various matrixes like bioactive molecules. As a result, additional upgrades are required. The utilization of comparatively massive quantities (i.e., mL) of disperser liquids, that process can be broken down the aqueous solubility of specimen matrices into the extraction solvent stage, is one of the major drawbacks of DLLME [24].

The measurement of methamphetamine as a reference component in biological material was recorded using graphene oxide enhanced two-phase electromembrane extraction (EME) combined with gas chromatography in this research. The inclusion of graphene oxide in the hollow fiber walls could improve the available surface area, chemical contacts, and the polarization of the supporting stream membranes, leading to a rise in sample movement. Comparison research was conducted among graphene oxide and graphene oxide/EME techniques to see how the inclusion of graphene oxide in the supporting liquid membranes affects removal efficiency. The research clearly reveals that immobilizing GO in barriers is an effective way to improve EME performance. This is most likely due to the discovery of a novel channel for bulk transport of METH through the SLM, and as a result, the suggested approach is much more effective and sensitive than traditional EME. The extracting conditions were calculated, including the kind of organic system, supplier stage pH, stirring speed, duration, power, sodium additions, and graphene oxide concentrations. The suggested microextraction approach had a lower detection limit (2.4 ng/mL), significant preconcentration factors (195–198), and a high compared recoveries (95–98.5percent) within optimal circumstances. Ultimately, the approach was used to properly precautions methamphetamine levels in urinary, and samples were taken. Despite separation without agitating being possible, the GC signals remained substantially weaker than many of those obtained with stimulation. As a result, 1000 rpm was chosen for future research. The mixing rate promotes extracting by increasing convective in the liquid sample. Nevertheless, it is possible that SLM was partially diminished at greater agitation rates, and that organic phase leaking from the SLM occurred [25].

3. Materials and Methods

3.1. Compounds and Reagents.
Merck Chemical compounds provided 2-methylimidazole, sodium hydroxide, hydrogen chloride, potassium dihydrogen phosphate, acetonitrile, methanol, and acetone (all HPLC grade) (Darmstadt, Germany). TitraChem provided the zinc nitrate (Tehran, Iran). Sigma-Aldrich provided methamphetamine hydrochloride sample solutions 1000 g/mL in methanol (USA). Milli-Q water system (Darmstadt, Germany) provided ultrapure water.

3.2. Device for Chromatography.
During pressure in an oxygen environment with a gold layer (DST1, Nanostructured coatings co., Tehran, Iran), scanned transmission electron (SEM) (MIRA3 FEG–SEM, Tescan, Czech Republic) has been

used to analyze the diameter of the adsorption (MIRA3 FEG–SEM, Tescan, Czech Republic). The Tensor 27 FTIR equipment (Bruker, Germany) was used to acquire their spectroscopy of the specimens (made as KBr disc). On a D5000 (Siemens, Germany) device, powdered X-ray diffraction patterns (XRD) have been acquired. A Zetasizer (Nanotrac Wave, Microtrac, Germany) was used to determine the zeta potential. HPLC assessment was conducted with the use of a Knauer (Germany) machine with a UV–visible detection. As a chromatographic purification column, a C18 column (5 m particle size, 4.6 mm i. d. 25 cm) (Knauer, Germany) has been used at a flow rate of 1 mL/min, and the mobile stage has been composed of acetonitrile-phosphate buffer (10 mM, pH = 3.5) in a $20:80$ (V/V) ratio. All test subjects were given the opportunity to give their permission from the participants.

3.3. Preparation of NGPPC Compounds.
In a previous paper, nanographene oxides (NGO) were produced by employing an enhanced version of the Hummer process. The modified Hummers method, which is a process that is simple, does not take a lot of time, and does not cost a lot of money, was used to synthesis GO. In addition, utilizing this process results in the introduction of an increased number of hydrophilic groups inside the carbon material, there is no release of hazardous gases, and the conductivity of the material is improved. The following is a summary of the synthesis techniques: 1 gram of graphene was combined with 24 mL of 98 percent H2SO4 and teamed inside a frozen bucket. Then, as an oxidation reaction, 3 g $KMnO_4$ was gently applied. Second, the balloons were placed in an oil tank as well as the temperatures of the reaction were set to 35-40 degrees Celsius. Following that, after approximately 30 minutes of mixing, a light brown colour appeared. The temperature was then increased to 98°C by adding 30 mL H_2O. Mixing was therefore maintained for the next 30 minutes. The brownish brown tint was accomplished by combining 1 mL of H_2O_2 (30%). Dual distilled water and HCl were used to purify and clean the finished version (5 percent). Lastly, water was put into the system and vortexed vigorously to produce a uniform suspension. To generate a nano-GO solution, the mixture was stirred continuously for 40 minutes. Glassware balloons were filled with 50 mL of produced nanographene oxide solution and then stirred for 15 minutes in a nitrogen atmosphere. A total of 0.068 g of pyrrole was combined with the reaction mixture that was then agitated for 20 minutes. The heat of the reaction will therefore be regulated to 0-5°C by utilizing an ice bath continuously stirring for 6 hours, and 20 mL of 2.5 M $FeCl_3.6H_2O$ solutions will be added to the mixture. The resulting dark mixture was centrifuged and then rinsed three times using water and ethanol. The resulting black nanocomposite was placed in the oven to dry at 50°C and used as a DSPE adsorbent [26].

3.4. Acquiring Urine Specimen.
The task requires a normal participant to submit a drug-free urine specimen. The specimens were stored at 4°C in a polyethylene container once they were used. MAHAN treatment clinic promptly gathered appropriate urine specimens (Tabriz, Iran). First, 1 g/mL methamphetamine was combined with 5 mL of urine from a healthy subject. Irresolvable small solid particles have

been collected and later detached by centrifuging at 5000 rpm for 10 minutes at ambient temperature after the pH of the urine specimen was corrected to 10. (uni 320, Pole Ideal Tajhiz Co., Iran). For the remainder of the investigation, the supernatant solution was transferred to a fresh container as well as maintained at 4°C [27].

3.5. Method for Dispersive Solid Phase Extraction.
The following is how the extracting process has been done: the extract was mixed for 5 minutes after 50 mg of the adsorption was introduced to 6 mL of methamphetamine (0.1 g/mL) spiking urinal. The inclusion of hydrophilic functional groups causes the adsorption to disperse properly in the urine medium, resulting in increased contact between the analyzer and the adsorption. The supernatant was removed after centrifuging the material. To the gathered adsorbent materials, 400 liters of methanol was poured as a desorption solution. The samples were centrifuged following 10 minutes of sonication (30 seconds, Farasout, Iran), and then, 20 liters of the supernatant was fed into the HPLC-UV analysis system.

4. Result and Discussions

4.1. Analysis of Nanographene Oxide Polypyrrole Composites.
NGPPC was categorized using Fourier transform infrared spectroscopy (FTIR). The appearance of a spike at 3434 is linked to the hydroxyl group's stretching vibrating band on the NGO porous structure. The carboxylic C=O functional group of NGO is represented by the maximum at 1703 cm^{-1}. In 1634 cm^{-1}, a stretching vibration of C=C emerged. NGPPC's FTIR spectroscopy was investigated. The existence of a spike at 1742 cm^{-1} is linked to the NGO's C=O structural formula. The peak indicates that NGO has been incorporated into the polymeric nanocomposite composition. C-C, C-N, and N-H stretching vibrations of polypyrrole have reached a maximum at 1550, 1460, and 3442 cm-1. The NGO and NGPPC X-ray diffraction patterns (XRD) were studied. The interplanar separation increases of chemical reduction and remaining unoxidized graphene, correspondingly, were represented by the spikes at 2 = 11 and 26°. The existence of a moderately broad peak at 2 = 11.5∘ corresponds to the typical peaking of pyrrole in the NGPPC framework, indicating that pyrrole has been incorporated into the nanographene oxide structure. With just a mean range of 22 nm, the fine complex structures of NGO were clearly visible without any further amorphous structure. The layered structure of NGO is combined with uniformly distributed polypyrrole-covered polymeric on the NGO surfaces including on the NGO sheeting including a mean range of 42 nm, as seen in the SEM image of the NGPPC. The observations of the zeta potential were carried out. The -32.5 mV zeta potential measured demonstrated the existence of strongly negative charging on the NGPPC surfaces, which improved NGPPC interactions with methamphetamine and NGPPC distribution in the medium.

4.2. GO and NGPP Absorption as DSPE.
A comprehensive one-factor-at-a-time experimental method will be used to enhance the extracting characteristics. Significant removal parameters were analyzed, including the quality and number of the extracting solvent system, pH, ionic strength, type and number of adsorption, urine output, mixing speed, extraction time, and desorption time. In a urine sample, the extracting effectiveness of nano-GO and NGPPC in methamphetamine separation were examined. NGPPC had a two-fold better removal efficiency than GO, according to the findings. Following polymerization by pyrrole, the augmentation of phenolic cycles on the NGPPC resulted in the highest association between methamphetamine and NGPPC surface area as shown in Figure 2.

The most effective dosage of NGPPC in methamphetamine removal has been determined through experimenting with new amounts of NGPPC (40-60 mg) in the process of extraction. Once the highest peak regions were reached, 60 mg of NGPPC was administered. The increasing concentration of NGPPC in the maximum absorption wreaked havoc. It could be owing to adsorbent aggregating at greater NGPPC concentrations, which reduces the effectiveness of NGPPC with methamphetamine combinations. Figure 3 shows the graph of the adsorbent's quantity.

4.3. Extraction Solvents and Efficient Volume.
The different compounds remained pushed to its limits to see which one was best in removing methamphetamine from NGPPC porous structure. Multiple types (such as methanol, acetonitrile, and acetone) have been tested for this function. Figure 4 depicts the graph of desorption solvents. The results show that methanol is the most efficient solvent for extracting. Methanol has a greater analysis of interactions and is, therefore, more effective in desorbing methamphetamine from the NGPPC surfaces.

It is critical to adjust the effective volume of methanol. As a result, methanol volumes ranging from 300 to 900 liters have been investigated. A capacity of 300 liters is sufficient to desorb the greatest quantity of methamphetamine from the surfaces of the NGPPC. As a consequence of analyte diluting in the medium, the steady increase of desorption solvents exhibited a reduction. Figure 5 shows the quantity graph of desorption solvents.

4.4. The Efficiency of Urine Volume, pH, and Ionic Strength.
An additional factor impacting removal efficiency is urine quantity. As a result, urine quantities ranging from 1 to 8 mL have been examined. The findings demonstrate how utilizing 5 mL of urine resulted in the highest removal effectiveness. The adsorbent's surface energy is a factor that influences removal efficiency and adsorbent aggregation. The pHs of the solution have been studied in the series of 4–12. The quantity of negative controls on the NGPPC increases as its pH of the medium rises from 4 to 10, resulting in a better connection between the positively charged samples as well as negatively charged chemical adsorption. Figure 6 depicts the graph for urine specimen quantity.

At a pH of 10, the behaviour achieves its pinnacle. The removal rate was reduced when pH = 12 was used. Given that the pKa of methamphetamine is 10.1, it changes back to the normal analyzer at higher pH levels. This has the impact of limiting the effective interactions between the
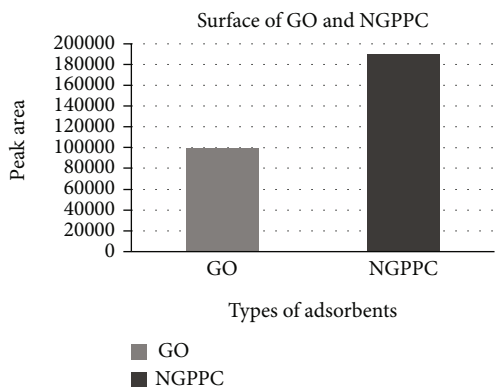
Figure 2: Surface area graph of GO and NGPPC adsorbents.
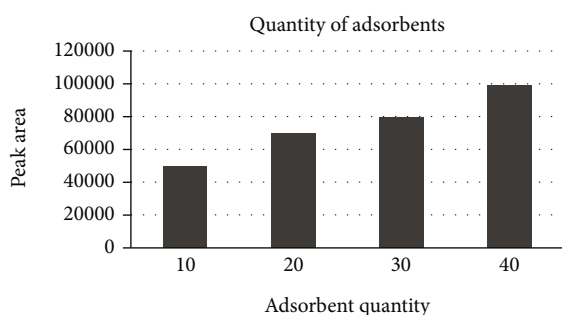
Figure 3: Graph of adsorbent's quantity.
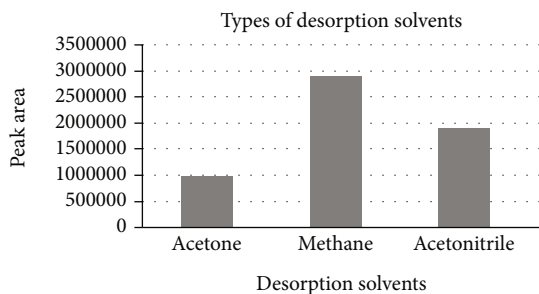
Figure 4: Graph of desorption solvents.
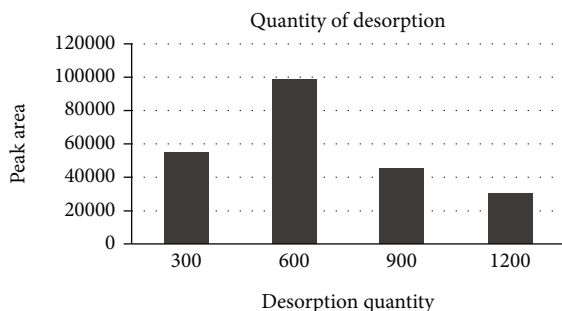
Figure 5: Graph of desorption solvent's quantity.

Figure 6: Graph of urine quantity.
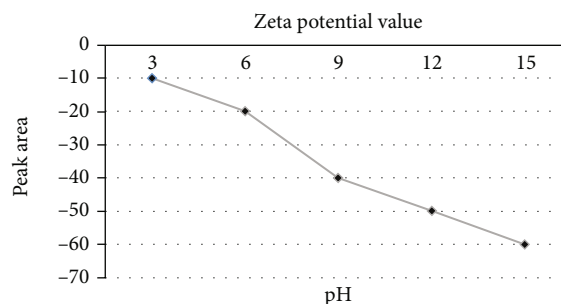
Figure 7: Zeta potential value of pH.
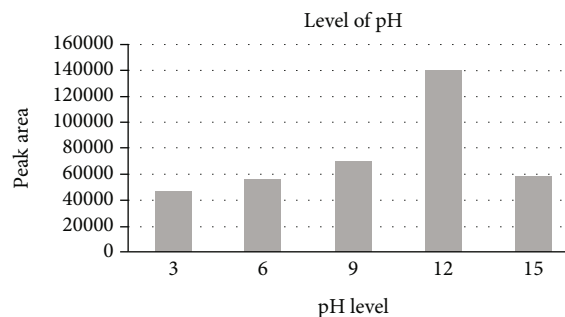
Figure 8: Graph of pH level.

As an outcome, pH = 10 has been selected as the best extracting pH for the separation method.

Plotting zeta potential as a proportion of pH could clarify such behaviour as shown in Figure 7. As can be seen, increasing the pH between 4 and 10 results in a greater number of adverse charging on the NGPPC adsorption, resulting in maximal analysis separation.

Figure 8 shows the graph of pH level. Despite the fact that a continual improvement in pH up to 12 resulted in an increment in negative controls on the NGPCC adsorbent, the removal efficiencies remained unchanged. The outcome is connected to the usual method of methamphetamine, which has a pKarate of 11.1 in a pH of 12, resulting in lower removal efficiencies. By applying 0–7% (W/V) NaCl towards the extracting solvent, the impact of ionic strength has been examined. The research was conducted without putting salt since the removal efficiencies did not vary significantly (data not shown).

analyzer and the adsorption of negative charges. It can be assumed from this fact that the cation form of this molecule will predominate almost totally in the natural environment.
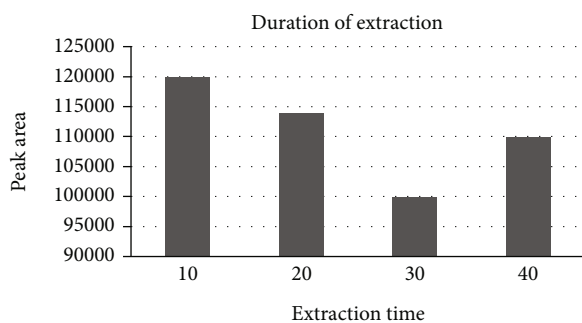
FIGURE 9: Graph of extraction duration.

FIGURE 11: Rate of mixing.

FIGURE 10: Graph of desorption duration.

FIGURE 12: Analyzing NGPCC reusability.

4.5. Extraction and Desorption Duration and Mixing Rate.
Establishing equilibrium in extracting processes is critical, and duration is a changeable variable to accomplish so. The procedures were tested over a time span of 10-40 minutes, with peak removal efficiencies of 10 minutes as shown in Figure 9. Because the process has remained stable, increasing the extracting duration has no effect on the removal efficiencies.

Desorption duration had also been examined in the 10-40 minute range as depicted in Figure 10. The equilibrium was reached in ten minutes, and a gradual increase in desorption duration had no effect on removal efficiencies. Furthermore, mixing speed influences the development of the NGPPC-methamphetamine interactions.

As a result, a stirring frequency of 2000-8000 was calculated as shown in Figure 11. The aggregate of NGPPC is much more likely at greater mixing speeds. Furthermore, the process reaches equilibrium at 6000 rpm, and greater mixing rates have little effect on the methamphetamine maximum absorption.

4.6. Adsorbent Capability and Reusability.
From a cost standpoint, the adsorbent's application programs were critical. As a result, the adsorbent's reusability was evaluated using extraction efficiency conditions as depicted in Figure 12. The outcomes indicated that higher to 6 times reusing of the produced adsorbents, there was no substantial shift in removal efficiencies. The following formula has been used to compute the adsorbent capability in the following equation.

$$E_q = \left(\frac{(b_1 - b_2)u_v}{a_m} \right) \times 100. \tag{1}$$
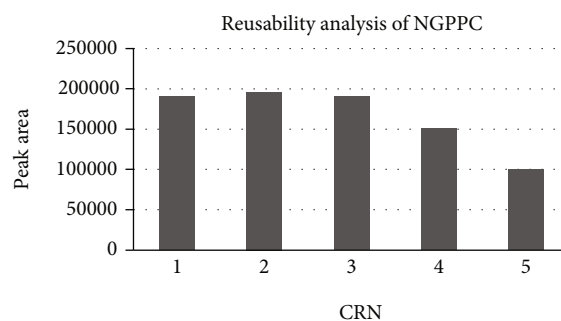
The preliminary and equilibrium quantities of the MA in the urine specimen (g/mL) are b_1 and b_2, correspondingly. a_m is the mass of adsorption, while u_v is the capacity of urine (mL) (g). The adsorbing efficiency measured was 0.3 mg/g.

4.7. Verification of the Methodology.
For demonstrating the technique's suitability for extracting methamphetamine through the urinary medium, certain analysis features of the proposed technique were established. Limit of quantification (LOQ), relative standard deviation (RSD), limits of detection (LOD), coefficient of determination (CO), and linearity have been investigated in three repetitions with five concentrations that covered the calibration graph. Table 1 shows the properties of DSPE analysis for MA.

In the range of concentrations of 50–2500 ng/mL, the technique remained linear. When comparing the suggested method to certain other recently reported approaches, it was discovered that DSPE-derived adsorbents remove pharmaceuticals from biological materials having acceptable and repeatable outcomes due to their great physical elasticity, hydrophilic or hydrophobic characteristics, and configurable pore scope as shown in Table 2 and Figure 13.

The UV detector's experimental restriction, as opposed to fluorescence, mass spectroscopy, or gas chromatography, may account for the relatively greater concentration range. In three different concentrations comprising the calibration graph, Table 3 shows the investigative sensitivity and specificity of the suggested novel DSPE technique. The findings supported the product's repeatability and efficiency.

4.8. Analyzing Real Samples Using the DSPE Approach.
Real samples were tested to demonstrate the usability of the established DSPE approach. As a result, the addicts' urine

TABLE 1: Properties of DSPE analysis for MA.

Sample	CR	CO	Limit of detection	Limit of quantification	Relative standard deviation
MA	40-2400	0.9945	12	40.90	5.40

TABLE 2: Comparison table of proposed and existing methods.

Sample	Technique	Limit of detection	Recovery
Methamphetamine	Solid phase extraction	100	60.6
	Stir bar sorptive extraction	60	82.8
	Solid phase microextraction	30	96.7
	Dispersive liquid-liquid ME	20	98.5
	Proposed-diffusive SPE	10	99.2
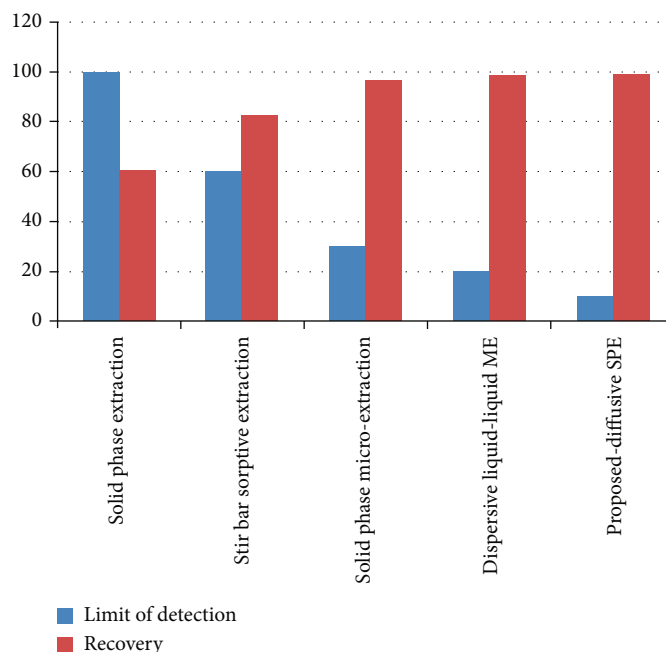
FIGURE 13: Limit of detection and recovery of various models.

TABLE 3: Verification outcomes for the provided DSPE method.

MA solutions (millilitre)	Within the days		Between days	
	Acc	Sen	Acc	Sen
0.08	2.24	0.74	3.27	0.96
0.2	2.19	0.52	3.26	0.82
1.10	5.10	0.92	6.23	0.92

extraction was done using NGPPC absorbent and inserted into the HPLC. Whenever positive urine specimens have been analyzed, the presented procedure yielded satisfactory findings, with a comparative recovery efficiency of 99.76 percent. The optimum condition is for current data to be verified using certified reference materials (CRM). Nevertheless, the current data can be trusted since (a) the high-performance liquid chromatography (HPLC) method can qualitatively and quantitatively analyze what components and how much of each component are present in a sample by separating chemicals that have been dissolved in a liquid.

The gold standard technique for separating in the evaluation of whether or not the limited chromatograms is well-matched with variable absorptions of requirements is the HPLC-UV method; and (b) the comparative recovery findings have been adjusted to account for variations in the spiking drug. Concurrent spikes of 0.1 gmL^{-1} methamphetamines, as well as many associated metabolites, were being used to test the selectivity of the innovative DSPE approach in methamphetamine separation. The findings revealed there were no other substantial spikes that might lead to FP results. The procedure is called selectivity, and it is used to extract methamphetamine from urine. The following equation was used to investigate the matrix effect in the following equation.

$$m_e = \frac{Y}{X} \times 100. \tag{2}$$

Assume X as the peak area of the aqueous mixture, as well as Y as the peak area of the postextraction solvent.

The matrix effects were estimated to be 111 percent, indicating that the matrix impact is dismissible.

5. Conclusion

NGPPC was being used to recover methamphetamine through urine medium with high efficiency. The NGPPC synthesizing procedure was easy, and the extraction technique demonstrated good repeatability. Furthermore, the suggested method's medical usefulness was demonstrated by its quick extracting and desorption durations, selectivity, and capacity sample analysis. The suggested method was validated, as well as the coefficient of correlation is of 0.996 indicated that the technique was linear in the absorption in the range contained by the calibration curve (30-800 g/mL). Furthermore, the suggested DSPE approach for methamphetamine identification demonstrated good precision, accuracy, and durability. Even without the involvement of metabolites, methamphetamine might well be recognized. Furthermore, the suggested DSPE approach for methamphetamine identification demonstrated great precision, accuracy, and robustness. The DSPE-based analytical approach has been suggested for specific methamphetamine measurement in biological urine medium with excellent removal efficiencies and a lower detection limit. Furthermore, the approach is quick and inexpensive, with significant recovery efficiency, making it an ideal analysis technique for clinical and forensic laboratories. Methamphetamine may be identified without any metabolite influence. Moreover, the practical and efficient synthesis process stimulates the use of carbon-based compounds in various extraction procedures.

Data Availability

The data used to support the findings of this study are included within the article. Further data or information is available from the corresponding author upon request.

Conflicts of Interest

The authors declare that there are no conflicts of interest regarding the publication of this paper.

Acknowledgments

References

[1] S. Stankic, S. Suman, F. Haque, and J. Vidic, "Pure and multi metal oxide nanoparticles: synthesis, antibacterial and cytotoxic properties," *Journal of nanobiotechnology*, vol. 14, no. 1, p. 73, 2016.

[2] E. Thostenson, C. Li, and T. Chou, "Nanocomposites in context," *Composites Science and Technology*, vol. 65, no. 3–4, pp. 491–516, 2005.

[3] S. Komarneni, "Feature article. Nanocomposites," *Journal of Materials Chemistry*, vol. 2, no. 12, p. 1219, 1992.

[4] T. A. Rajesh and D. Kumar, "Recent progress in the development of nano-structured conducting polymers/nanocomposites for sensor applications," *Sensors and Actuators B: Chemical*, vol. 136, no. 1, pp. 275–286, 2009.

[5] D. W. Schaefer and R. S. Justice, "How nano are nanocomposites?," *Macromolecules*, vol. 40, no. 24, pp. 8501–8517, 2007.

[6] R. Vaia and J. Baur, "Adaptive composites," *Science*, vol. 319, no. 5862, pp. 420-421, 2008.

[7] F. Liu, Y. Yuan, L. Li et al., "Synthesis of polypyrrole nanocomposites decorated with silver nanoparticles with electrocatalysis and antibacterial property," *Composites. Part B, Engineering*, vol. 69, no. 18, pp. 232–236, 2015.

[8] R. A. Vaia and H. D. Wagner, "Framework for nanocomposites," *Materials Today*, vol. 7, no. 11, pp. 32–37, 2004.

[9] C. Hu, T.-R. Su, T.-J. Lin, C.-W. Chang, and K.-L. Tung, "Yellowish and blue luminescent graphene oxide quantum dots preparedviaa microwave-assisted hydrothermal route using $_{H2O2and}$ KMnO4as oxidizing agents," *New Journal of Chemistry*, vol. 42, no. 6, pp. 3999–4007, 2018.

[10] H.-C. Tian, J. Q. Liu, D. X. Wei et al., "Graphene oxide doped conducting polymer nanocomposite film for electrode- tissue interface," *Biomaterials*, vol. 35, no. 7, pp. 2120–2129, 2014.

[11] S. M. Mousavi, F. W. Low, S. A. Hashemi et al., "Development of graphene based nanocomposites towards medical and biological applications," *Artificial cells, nanomedicine, and biotechnology*, vol. 48, no. 1, pp. 1189–1205, 2020.

[12] C. C. Cruickshank and K. R. Dyer, "A review of the clinical pharmacology of methamphetamine," *Addiction*, vol. 104, no. 7, pp. 1085–1099, 2009.

[13] J. Mendelson, N. Uemura, D. Harris et al., "Human pharmacology of the methamphetamine stereoisomers," *Clinical Pharmacology and Therapeutics*, vol. 80, no. 4, pp. 403–420, 2006.

[14] M. D. Anglin, C. Burke, B. Perrochet, E. Stamper, and S. Dawud-Noursi, "History of the methamphetamine problem," *Journal of Psychoactive Drugs*, vol. 32, no. 2, pp. 137–141, 2000.

[15] T. Kumazawa, C. Hasegawa, X. P. Lee et al., "Simultaneous determination of methamphetamine and amphetamine in human urine using pipette tip solid-phase extraction and gas chromatography-mass spectrometry," *Journal of Pharmaceutical and Biomedical Analysis*, vol. 44, no. 2, pp. 602–607, 2007.

[16] B. Buszewski and M. Szultka, "Past, present, and future of solid phase extraction: a review," *Critical Reviews in Analytical Chemistry*, vol. 42, no. 3, pp. 198–213, 2012.

[17] Q. Wan, H. Liu, Z. Deng et al., "A critical review of molecularly imprinted solid phase extraction technology," *Journal of Polymer Research*, vol. 28, no. 10, p. 401, 2021.

[18] L. A. Berrueta, B. Gallo, and F. Vicente, "A review of solid phase extraction: basic principles and new developments," *Chromatographia*, vol. 40, no. 7–8, pp. 474–483, 1995.

[19] L. Labat, E. Kummer, P. Dallet, and J. P. Dubost, "Comparison of high-performance liquid chromatography and capillary zone electrophoresis for the determination of parabens in a cosmetic product," *Journal of Pharmaceutical and Biomedical Analysis*, vol. 23, no. 4, pp. 763–769, 2000.

[20] X. Hu, J. Pan, Y. Hu, and G. Li, "Preparation and evaluation of propranolol molecularly imprinted solid-phase microextraction fiber for trace analysis of β-blockers in urine and plasma samples," *Journal of Chromatography. A*, vol. 1216, no. 2, pp. 190–197, 2009.

[21] A. Namera, A. Nakamoto, M. Nishida et al., "Extraction of amphetamines and methylenedioxyamphetamines from urine using a monolithic silica disk-packed spin column and high-performance liquid chromatography-diode array detection," *Journal of Chromatography. A*, vol. 1208, no. 1-2, pp. 71–75, 2008.

[22] A. Taghvimi, S. Dastmalchi, and Y. Javadzadeh, "Novel ceramic carbon-coated magnetic nanoparticles as stir bar sorptive extraction coating for simultaneous extraction of amphetamines from urine samples," *Arabian Journal for Science and Engineering*, vol. 44, no. 7, pp. 6373–6380, 2019.

[23] N. Raikos, K. Christopoulou, G. Theodoridis, H. Tsoukali, and D. Psaroulis, "Determination of amphetamines in human urine by headspace solid-phase microextraction and gas chromatography," *Journal of Chromatography B*, vol. 789, no. 1, pp. 59–63, 2003.

[24] H. M. Al-Saidi and A. A. A. Emara, "The recent developments in dispersive liquid-liquid microextraction for preconcentration and determination of inorganic analytes," *Journal of Saudi Chemical Society*, vol. 18, no. 6, pp. 745–761, 2014.

[25] H. Bagheri, A. F. Zavareh, and M. H. Koruni, "Graphene oxide assisted electromembrane extraction with gas chromatography for the determination of methamphetamine as a model analyte in hair and urine samples," *Journal of Separation Science*, vol. 39, no. 6, pp. 1182–1188, 2016.

[26] K. V. Harpale, S. R. Bansode, and M. A. More, "One-pot synthesis, characterization, and field emission investigations of composites of polypyrrole with graphene oxide, reduced graphene oxide, and graphene nanoribbons," *Journal of Applied Polymer Science*, vol. 134, no. 32, p. 45170, 2017.

[27] M. Cruz-Vera, R. Lucena, S. Cárdenas, and M. Valcárcel, "Sorptive microextraction for liquid-chromatographic determination of drugs in urine," *TrAC Trends in Analytical Chemistry*, vol. 28, no. 10, pp. 1164–1173, 2009.

SAGE Publishing

Research Article

Mechanical and Thermal Adsorption Actions on Epoxy Hybrid Composite Layered with Various Sequences of Alkali-Treated Jute and Carbon Fibre

R. Sasikumar,[1] K. Venkadeshwaran,[2] C. Ramesh Kannan,[3] Melvin Victor De Poures [ID],[4] M. Aruna [ID],[5] N. Mukilarasan [ID],[6] Gopal Kaliyaperumal [ID],[7] and Arundeep Murugan [ID][8]

[1]*Department of Mechanical Engineering, Erode Sengunthar Engineering College, Erode, 638 057 Tamil Nadu, India*
[2]*Department Mechanical Engineering, JAIN (Deemed-to-be University), Bengaluru, India*
[3]*Department of Mechanical Engineering, SRM TRP Engineering College, Trichy, 621105 Tamil Nadu, India*
[4]*Department of Thermal Engineering, Saveetha School of Engineering, SIMATS, Chennai, 602105 Tamil Nadu, India*
[5]*Faculty of Mechanical and Industrial Engineering, Liwa College of Technology, Abu Dhabi, UAE*
[6]*Department of Mechanical Engineering, Jeppiaar Institute of Technology, Chennai, 631604 Tamil Nadu, India*
[7]*Department of Mechanical Engineering, New Horizon College of Engineering, Bengaluru, Karnataka 560103, India*
[8]*School of Mechanical and Industrial Engineering, Institute of Technology, Debre Markos University, Debre Markos, Ethiopia*

Correspondence should be addressed to Arundeep Murugan; arundeepmurugan@gmail.com

Structural applications are accomplished by using a lightweight epoxy matrix bonded with natural jute fibre/synthetic carbon fibre to enhance the physical, mechanical, and thermal properties obtained by different sequences of alkali-treated jute fibre (J.F.)/carbon fibre (C.F.) through conventional hand layup technique. The sequences of the sample are named as H1, H2, H3, and H4 layers of JF/JF/JF/JF, CF/CF/CF/CF, JF/CF/CF/JF, and CF/JF/JF/CF. Influences of JF/CF on physical, mechanical, and thermal adsorption properties of the epoxy composite are evaluated and compared. The mechanical tensile performance of the jute fibre-covered (JF/CF/CF/JF) composite H3 sample is augmented by 29% compared to the H4 sample. Similarly, the CF/JF/JF/CF combinations exhibited a higher impact strength of 129.71 KJ/m^2. The maximum hardness of 47.12Hv was found on the four-layered carbon fibre. The thermal adsorption actions on developed composites are evaluated by thermogravimetric apparatus (TGA). It is confirmed that the presence of JF/CF in epoxy composites can endure stability at a higher temperature.

1. Introduction

The requirement of polymer matrix composites is reinforced with natural, synthetic, and combinations of both natural and synthetic fibre, increasing in the application of structural field owing to lightweight, good strength, enhanced wear characteristics, superior corrosion resistance, and good toughness [1–5]. Natural fibres (jute, bamboo, flax, coir, and bagasse) can overcome synthetic fibre drawbacks like cost, short life span, nonbiodegradable, and ecofriendly. Using natural fibres facilitates better alternative reinforcements for the polymer matrix composite, gaining advantages on low cost, lightweight, enhanced stiffness, renewable, and

nonpollutants [6–8]. While compared to the different varieties of natural fibres listed above, the jute fibre has the highest stiffness and reduces the combined weight [9]. However, it has low impact strength and, owing to high water absorption properties, results in poor interfacial bonding strength [10]. The combinations of natural jute and synthetic fibres are familiar in marine, defence, aerospace, and structural applications due to their excellent bonding strength, enhancing mechanical and thermal performance. However, synthetic fibre is costlier than natural fibre [11–13]. The suggestion by most of the reviewers is that the combinations of natural and synthetic fibre in a solo matrix lead to increases in the balancing properties of mechanical as well

as cost [14–16]. The mechanical characteristics of jute and glass fibre-reinforced hybrid composite were studied with different fabric conditions. The glass fibre in the above jute fibre resulted in superior mechanical properties of 121 MPa [17]. The mechanical properties of jute and glass fibre-reinforced hybrid composite may vary due to the stacking positions of fibres. The hybrid composite layer containing glass/jute/jute/glass showed good flexural strength (3.35 GPa) and high mechanical performance compared to other laminates [18]. The flax-reinforced polymer matrix composite is hybridization with carbon fibre and shows a higher tensile strength of 215 MPa [19]. The various jute/glass/carbon composite layers are embedded with epoxy resin. The presence of carbon shows a higher flexural strength, and the glass fibre withstands maximum impact strength [20]. The jute fibre-reinforced polymer matrix composite developed by the vacuum resin technique results in an increased modulus of elasticity (0.06 mm) and strength composite (125 MPa) [21]. The maximum flexural strength has been attained by the lamination of multilayer jute/glass/epoxy [22]. The standard of ASTM results evaluating the prepared polyester/jute fibre composites showed that the presence of jute fibre in polyester matrix owned good tensile strength, stiffness, and thermal adsorption properties [23]. The polyester composite enriched with two different layers of jute/glass and jute/carbon makes a practical impact and tensile strength performance.

Carbon increases tensile strength, and glass fibre shows extreme impact strength compared to monopolyester [24]. The combination of natural bamboo fibre bonded with glass fibre hybrid polypropylene matrix composite has enhanced thermal stability and can carry maximum degradation temperature for more than 500°C with reduced weight loss [25]. Based on the above existing literature reported by many researchers, the multilayer fabric sequence has increased the feasibility of composite life with superior properties, and hybridization with synthetic fibre increases the quality of composite in hybrid. So, the present work is to fabricate the different layer sequences of alkali-treated JF/CF-reinforced epoxy composite via hand layup technique to obtain a hybrid composite with increased mechanical and thermal adsorption performance. Correspondingly, the composite's hardness, impact, and tensile strength are examined by E384, D6110, and D309 of ASTM standard.

2. Materials and Experimental Details

2.1. Selection of Materials.
The favourite epoxy resin (R101) and (H101) hardener are considered the primary adhesive materials to acquire an excellent interfacial between fibres. The combinations of epoxy additives are the right choice for bonding both natural and synthetic fibre in a single mat resulting in balanced mechanical properties [14–16]. The 10 : 1 mixing ratio was followed as R101 and H101, respectively. Epoxy resin is a standard resin available at a low cost and forms any shape easily [22, 26]. The 2×2 fabric plain bidirectional woven jute and twill weave carbon fibre are chosen as secondary materials. The jute fibre owing to the highest stiffness with reduced density results in reduced combined weight. The carbon fibre leads enhance the thermal and mechanical properties [9]. The physical and mechanical properties of the jute/carbon fibre fabric are specified in Table 1.

2.2. Chemical Treatment of Jute Fibre.
The natural jute fibres had good moisture-absorbing capability because of their hydrophilic properties. It may affect the polymer matrix, which results in poor adhesive and mechanical properties [7, 9]. The above fibre has been treated by different processing techniques to overcome the drawbacks. The chemical processing of jute fibre facilitates excellent quality compared to traditional methods. It results in decreased dust particles and impurities. Various chemical treatments like acetylation, alkali, methacrylate, sodium chlorite, and enzyme enhance the compatible action [27, 28]. Among the various processes reported above, the alkali route is practical, economical, and suitable for all types of natural fibre. The alkali treatment offers excellent interaction between polymer matrix and secondary phase fibre, thermally stable, and good thermal resistance [29]. The alkalization process treats the current research chosen jute fibre. Initially, the jute fibres were immersed in 10 wt% of NaOH-based solution for 120 mins, and every 30 mins, it was refreshed by using 5 litres of distilled water. After the alkali treatment, it was kept in an electric oven and maintained at 55°C for 5 hrs to remove the moisture content. Finally, the treated jute fibres are formed by shrinkage-free structure.

2.3. Preparation of Alkali-Treated Jute with Carbon Fibre Epoxy Composites.
The present experimental work follows the basic hand layup technique to prepare the epoxy hybrid composite layering with four varieties of fabric sequences of alkali jute and carbon fibre at an elevated temperature of $25 \pm 3°C$ as mentioned in Table 2.

Figure 1 shows the flow process diagram for the epoxy hybrid composite fabrication. Initially, the alkali-treated jute and carbon fibre fabric mat are sized 350 mm × 350 mm and formed by the different fabric sequences mentioned above in Table 2, the different J.F. and C.F. sequences of (4 layers) layers are formed by using conventional low-cost hand layup technique. The treated jute/carbon fibre mat is kept in an electric oven separately and preheated to 65°C at 10 hrs to eliminate the wettability of fibre. The H1 hybrid composite is prepared by using J.F. as the first layer. The epoxy and hardener are mixed with a ratio of 10 : 1 with manual stirring for 15 mins. To continue, the epoxy is applied over the first jute fibre layer, and layer 2 (J.F.) is placed over layer 1 (J.F.) with an applied compressive load of 50 kg. It helps to increase the adhesive properties and reduce the pores.

Similarly, layer 3 (J.F.) and layer 4 (J.F.) are formed with a thickness of 10 mm, and the final synthesized composite was cured at 25°C for 1 day. Afterward, it is placed in the oven for postcuring treatment at 45°C for 5 hrs. It helps to increase the bonding strength and increase the compact ratio. A similar procedure is repeated for H2, H3, and H4 samples. ASTM test standards shape the developed hybrid composites H1, H2, H3, and H4.

Table 1: Physical and mechanical properties of jute/carbon fibre fabric.

Properties	Unit	Jute fibre	Carbon fibre
Physical			
Density	g/cc	1.5	1.8
Mechanical			
Tensile strength	MPa	390 to 770	3490 to 4990
Young's modulus	GPa	10 to 33	260
Elasticity	%	1.8	1.8

Table 2: Fabric sequences of alkali-treated J.F./C.F. hybrid composites.

Sample code	Fabric sequences (J.F.: jute fibre; C.F.: carbon fibre)			
	Layer 1	Layer 2	Layer 3	Layer 4
H1	J.F.	J.F.	J.F.	J.F.
H2	C.F.	C.F.	C.F.	C.F.
H3	J.F.	C.F.	C.F.	J.F.
H4	C.F.	J.F.	J.F.	C.F.

2.4. Characterization of Hybrid Composite. The developed fibre hybrid composites were subjected to various characteristics study. The ASTM-E384 test standard examines the hybrid composite's micro Vickers hardness number (VHN). The VHN test samples are polished with different emery sheets and fine polish is done by double disc polishing apparatus configured with velvet cloth. The polished test samples are examined by pyramid-type indenter configured with a diamond tip with an angle of 136° at 100 grams load under 10 sec dwell time. The Charpy impact strength of produced hybrid composites is tested by ASTM D6110 standard via an impact tester configured with 300 J capacity. The developed hybrid composite tensile strength is evaluated by UTM tensile machine with 10 mm/min cross-slide speed. The ASTM D3039 standard is followed to estimate the tensile strength of hybrid composites. The dimension of the tensile sample (ASTM D3039) is 300 mm × 25 mm × 4 mm, respectively. The effect of alkali-treated jute and carbon fibre in epoxy composite with degradation is calculated from a thermogravimetric apparatus configured with 22°C to 850°C at a 23°C constant heat flow rate.

3. Results and Discussions

3.1. Micro Vickers Hardness of Hybrid Composites. Figure 2 illustrates the micro Vickers hardness of epoxy hybrid composite layered with various jute and carbon fibre. It is noted that the micro Vickers hardness number of pure jute fibre H1 samples shows a lower hardness value (26.12 ± 1.18) compared to the remaining samples.

Similarly, four layers of carbon fibre with epoxy show $35.69 \pm .34$ Hv. So, the effect of interfacial bonding between J.F. to J.F. and C.F. to C.F. is low. It was due to their similar layer may slip and create a poor interfacial action during

high tensile load, resulting in reduced mechanical properties [17]. The hybrid composites H3 and H4 show good hardness and are much higher than the H1 and H2 samples. The higher hardness of 47.12 ± 1.18 Hv. It improved by 80.3% and 32% compared to H1 and H2 samples. The increase in hardness value mainly depends on the stacking position of jute and carbon fibre, which was placed by bidirection orientations. Moreover, the fabric combinations with CF/JE/JE/CF sequence (bidirectional mat bonding with epoxy) can resist the indentation against the diamond indenter so that the fabric makes an adequate interfacial strength as considerable error variance in hardness of 1.18 Hv.

3.2. Impact Toughness of Hybrid Composites. Figure 3 shows the impact toughness of jute/carbon fibre layered with epoxy matrix hybrid composite. The impact toughness of H1 (JE/JE/JE/JE) is 41.78 ± 1.28 K.J./m^2, and 83.98 ± 2.1 KJ/m^2 is noted on pure carbon fibre laminates. The impact strength of carbon laminate epoxy composite is higher than that of pure J.E. layer composite. It was due to their high elastic modulus and high impact load stability [20, 24]. It is seen in Figure 3 that the addition of multifibre fabrics like J.E. and C.F. layers in epoxy shows higher impact strength as compared to H1 and H2 composites. The composite with both ends of J.E. fibre covered with C.F. shows an adequate impact toughness of 129.71 ± 2.5 KJ/m^2. So, the end layer of carbon fibre can stand the high-impact load without fracture. The various sequences of jute and carbon fibre fabric make good impact strength. The sample H4 is found to have a maximum impact toughness of 129.71 ± 2.5 KJ/m^2. It was due to their carbon fibre leading to enhance the epoxy composite, and its bidirectional stacking sequences may be influenced by the absorb the maximum impact energy. It was related to interfacial bonding strength [10]. So, H4 facilitates good mechanical characteristics in structural applications. The complete break occurred on the top of the portion during high-impact load. However, jute and carbon fibre may absorb the maximum impact energy without failure.

3.3. Tensile Strength of Hybrid Composites. The tensile strength of the hybrid composite with various fabric sequences of alkali-treated jute (J.F.)/carbon fibre (C.F.) is shown in Figure 4. It varied due to the type of fibre, processing, interfacial bond strength, types of matrix, and sequences of fabric arrangements [18–20]. The tensile strength of the jute layer epoxy hybrid composite is 56.97 ± 2.4 MPa, and 161.39 ± 3.1 MPa is identified on pure carbon sequence with epoxy adhesive. The pure carbon stacking sequence is improved 1.83 times of jute fibre sequence. However, the different layer sequence with two-layer jute/carbon has better tensile strength than pure jute fibre and carbon fibre. The H3 sample is noted in Figure 4 as the highest value compared to others. The two outer jute fibre sequences covered with carbon sequence increased by 24% compared to the carbon layer covered with jute fibre. It was due to the arrangements of jute fibre in carbon fibre that gained strong interfacial bonding leading to increased mechanical strength. The results revealed in Figure 4 that the tensile strength of
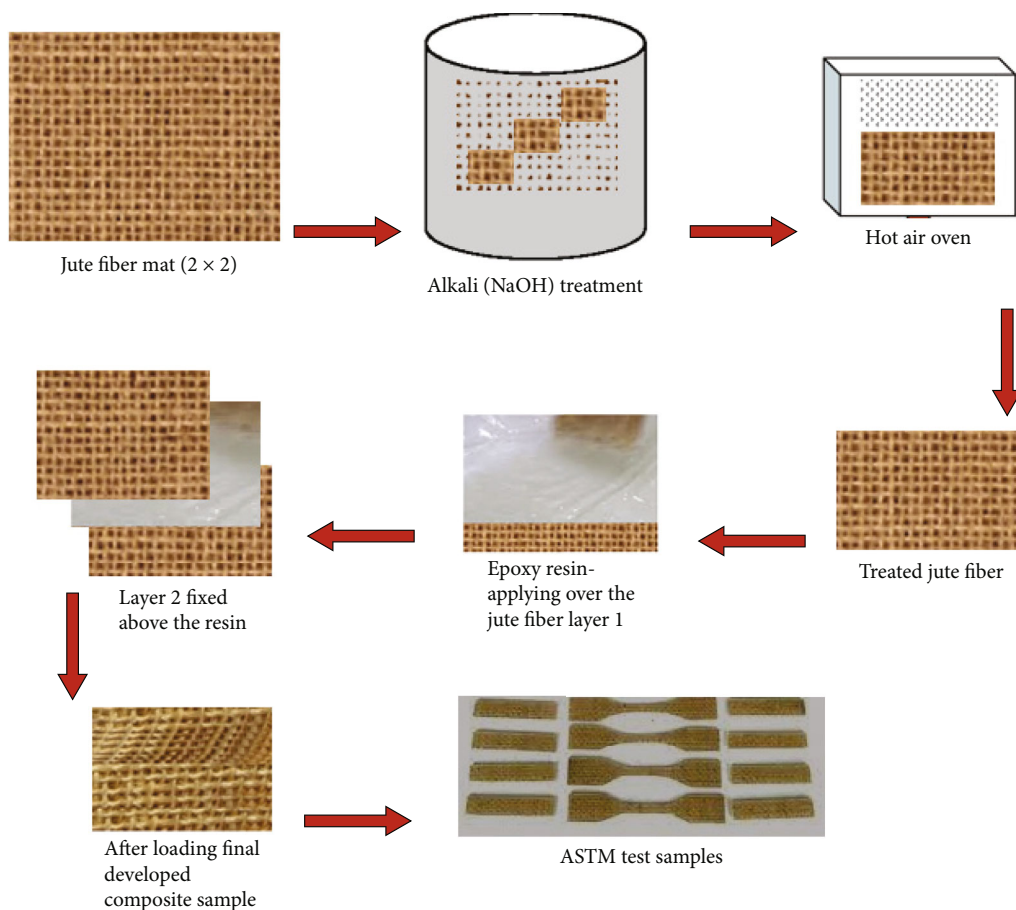
Figure 1: Process layout for epoxy hybrid composite fabrication.
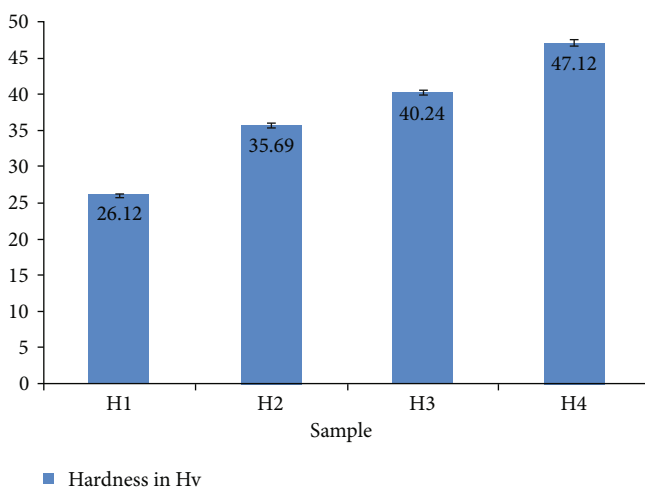
Figure 2: Hardness of hybrid composites.

the composite might differ due to test conditions and natural fibre treatment.

Therefore, the outer layer of the composite leads an essential role in tensile load during the evaluation of tensile strength. The strong J.E. layer perfectly bonded with carbon fibre may increase the tensile strength of composites. The

applied load and curing time was the main reason for increased adhesive between matrix and fibre, which resulted in increased tensile strength. Bidirectional fibre is another reason for higher tensile strength because the layerable resists the internal movement on a higher tensile load. Sample H4 shows a decreased tensile strength of 235.97 ± 1.98 MPa. It was because carbon fibre may be deboned from the jute fibre during high tensile load. Because the outer carbon layer has a chance to break on high tensile load [9].

3.4. Thermal Adsorption Properties of Hybrid Composite. The thermal stability and mass loss due to decomposition during high temperature on thermal adsorption performance of epoxy composite layers with jute and carbon fibre estimated by thermogravimetric apparatus configured with 22°C to 850°C at 23°C constant heat flow rate. Figure 5 represents the thermogravimetric thermal stability analysis related to mass loss of untreated jute fibre, alkali-treated jute fibre, and epoxy hybrid composite. The current experiment on the thermal degradation of composite is estimated with 28°C to 550°C at a 23°C constant heat flow rate. It was noted during the thermogravimetric analysis that the three variants of decomposition, like first stage weight loss, are identified as the temperature range of 28°C to 131°C, the second phase of decomposition on mass loss of composite progressively
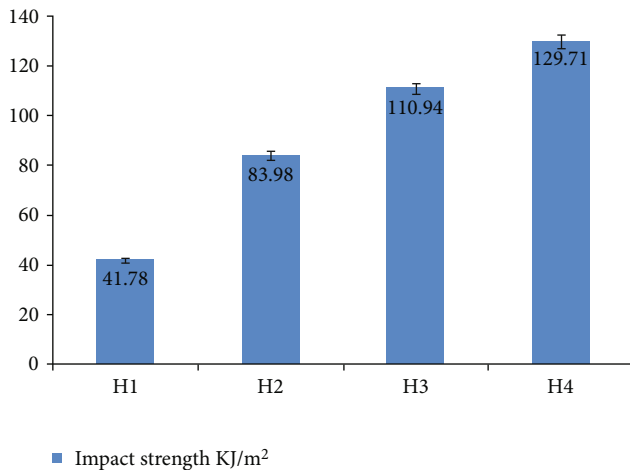
Figure 3: Impact toughness of hybrid composites.

Figure 4: Tensile strength of hybrid composites.

Figure 5: Thermal adsorption effect on thermal stability related to the mass of untreated, treated, and hybrid jute fibre composites.
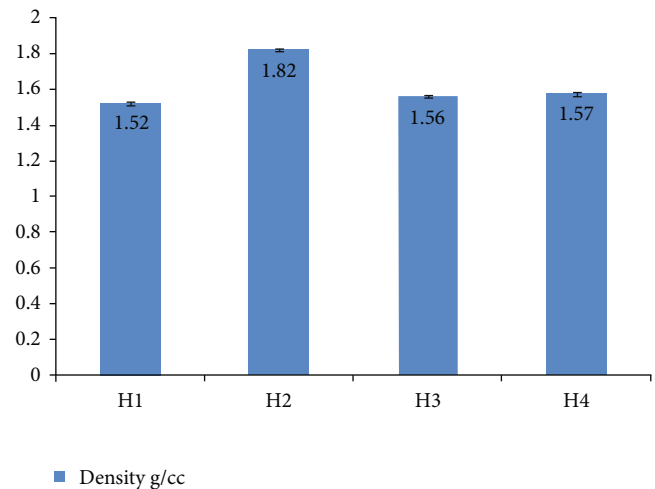
Figure 6: Density of hybrid composites.

reduced with increasing the temperature of 148°C to 286°C, and correspondingly, decomposition of final stage shows a light mass loss. However, Figure 5 illustrates that the mass loss of untreated, treated, and hybrid composite shows progressive mass loss during increased decomposition on increased thermal conditions. The similar mass loss curved profile is followed by stages 1, 2, and 3, respectively. But the initial stage shows fast decompositions on untreated fibre, the next stage shows increased thermal stability with reduced mass loss (24, 28, and 36%) at 550°C compared to the initial stage, and the last stage on hybrid composite shows good thermal stability with reduced decomposition rate and mass loss 78, 82, and 90%. However, the alkali-treated jute fibre with carbon fibre makes higher thermal stability during high-temperature studies. It was improved by 12% as compared to untreated fibre. The weight loss percentage of hybrid composite is much lower than the untreated and treated fibre.

3.5. Density of Hybrid Composite. Figure 6 illustrates the density of an epoxy hybrid composite consisting of different jute/carbon fibre layers. The combinations of jute and carbon fibre vary the density of the composite. However, it has to obey the rule of mixture. In the jute fibre combinations of 4 layers (J.F.), the H1 sample was found as 1.52 ± 1.01 g/cc.

Similarly, in the carbon fibre combinations of 4 layers (C.F.), the H2 sample observed an increased density value of1.82 ± 0.92 g/cc. The increase in composite density was due to the presence of carbon fibre. The intercombinations of H3 and H4 samples are noted as 1.56 ± 0.28 g/cc and 1.57 ± 0.87 g/cc. The optimum properties of the H3 sample are found to be lightweight, and its weight is reduced by 17% as compared to the H2 sample.

4. Conclusions

In the current experimental investigations of alkali-treated jute/carbon fibre fabric, a hybrid composite developed effectively via hand layup technique with various sequences of

J.E. and C.F. The effect of bidirectional fibre orientations with different sequences of J.F. and C.F. on physical, mechanical, and thermal adsorption performance of epoxy hybrid composite was studied by ASTM, and the final decision to the conclusions of results is mentioned below.

(i) The chemical alkali-treated jute fibre enhances the carbon composite with JE/CF/CF/JF (H3) sequences and CF/JF/JF/CF (H4).

(ii) The similar J.F. or C.F. layer shows a low hardness, impact, and tensile strength

(iii) The presence of treated jute fibre in the carbon fibre layer having good mechanical properties like the two-outer layer of carbon fibre circumstance jute fibre hybrid composite (sample H3) found increased hardness and impact strength of 47.12 ± 1.18 Hv and 129.71 ± 2.5 KJ/m^2, respectively

(iv) Similarly, the outer jute layer bonded with internal carbon fabric (sample H3) showed a higher tensile strength of 304.18 ± 5.4 MPa and increased 1.83 times jute fibre and 24% H4 sample

(v) The thermal adsorption on thermal stability related to mass loss percentage of untreated, treated, and hybrid composite was studied, and hybrid composite found superior thermal stability at higher temperatures and increased 12% compared to untreated fibre

(vi) The density of the H3 sample is limited by 17% as compared to the H2 sample

Data Availability

All the data required are available within the manuscript.

Conflicts of Interest

The authors declare that there are no conflicts of interest regarding the publication of this paper.

References

[1] D. Gay, *Composite Materials. Design and Applications*, CRC Press, Boca Raton, FL, 2022.

[2] T. Tang, S. Fang, J. Chen, L. Ma, L. Li, and X. Wu, "Axial compression behavior of recycled-aggregate-concrete-filled GFRP-steel composite tube columns," *Engineering Structures*, vol. 216, article 110676, 2020.

[3] S. Armioun, S. Panthapulakkal, J. Tjong, and M. Sain, "Renewable, recyclable, and lightweight structural prototype for greener automotive interior panels," *SAE World Congress Exposition*, 2004.

[4] M. Jawaid, H. P. S. A. Khalil, A. A. Bakar, and P. N. Khanam, "Chemical resistance, void content and tensile properties of oil palm/jute fibre reinforced polymer hybrid composites," *Material design*, vol. 32, no. 2, pp. 1014–1019, 2011.

[5] S. Marimuthu and R. Venkatesh, "Performance study on glazzed solar air heater for agri products," *Materials Today Proceedings*, vol. 69, pp. 633–636, 2022.

[6] K. Bledzki, S. Reihmane, and J. Gassan, "Properties and modification methods for vegetable fibers for natural fiber composites," *Journal of Applied Polymer Science*, vol. 59, no. 8, pp. 1329–1336, 1996.

[7] R. A. Braga and P. A. Magalhaes, "Analysis of the mechanical and thermal properties of jute and glass fiber as reinforcement epoxy hybrid composites," *Materials science and engineering: C*, vol. 56, pp. 269–273, 2015.

[8] M. Shamsuyeva, O. Hansen, and H. J. Endres, "Review on hybrid carbon/flax composites and their properties," *International journal of polymer science*, vol. 2019, Article ID 9624670, 17 pages, 2019.

[9] M. A. Elbaky and M. A. Attia, "Water absorption effect on the in-plane shear properties of jute–glass–carbon-reinforced composites using Iosipescu test," *Journal of composite material*, vol. 53, no. 21, pp. 3033–3045, 2019.

[10] S. D. Pandita, X. Yuan, M. A. Manan, C. H. Lau, A. S. Subramanian, and J. Wei, "Evaluation of jute/glass hybrid composite sandwich: water resistance, impact properties and life cycle assessment," *Journal of Reinforced Plastics and Composites*, vol. 33, no. 1, pp. 14–25, 2014.

[11] A. Sobhanadri, G. Senthilkumar, M. Vivekanandan, and R. Venkatesh, "A CFD investigation and heat transfer augmentation of double pipe heat exchanger by employing helical baffles on shell and tube side," *Thermal Science*, vol. 26, no. 2A, pp. 991–998, 2022.

[12] P. S. Ramalingam, K. Mayandi, T. Srinivasan, I. J. Leno, R. Ravi, and G. Suresh, "A study on E-Glass fiber reinforced interpenetrating polymer network (vinylester/polyurethane) laminate's flexural analysis," *Materials Today: Proceedings*, vol. 33, pp. 854–858, 2020.

[13] M. Krishnaraj, R. Arun, and T. Vaitheeswaran, *Fabrication and wear characteristics basalt fibre reinforced polypropylene matrix composites*, SAE Technical Paper, 2019.

[14] R. Venkatesh, S. Manivannan, P. Sakthivel, V. Vijayan, and S. Jidesh, "The investigation on newly developed of hydrophobic coating on cast AZ91D magnesium alloy under 3.5 wt% NaCl solutions," *Journal of Inorganic and Organometallic Polymers and Materials*, vol. 32, no. 4, pp. 1246–1258, 2022.

[15] M. A. Khan, J. Ganster, and H. P. Fink, "Hybrid composites of jute and man-made cellulose fibers with polypropylene by injection moulding," *Composite Part A: Applied science and manufacturing*, vol. 40, no. 6-7, pp. 846–851, 2009.

[16] M. Jawaid and H. P. S. Khalil, "Cellulosic/synthetic fibre reinforced polymer hybrid composites: a review," *Carbohydrate polymers*, vol. 86, no. 1, pp. 1–18, 2011.

[17] K. S. Ahmed and S. Vijayarangan, "Tensile, flexural and interlaminar shear properties of woven jute and jute- glass fabric reinforced polyester composites," *Journal of materials processing technology*, vol. 207, no. 1-3, pp. 330–335, 2008.

[18] R. Gujjala, S. Ojha, S. K. Acharya, and S. K. Pal, "Mechanical properties of woven jute-glass hybrid-reinforced epoxy composite," *Journal of Composite Materials*, vol. 48, no. 28, pp. 3445–3455, 2014.

[19] S. Rajkumar, M. Loganathan, and R. Venkatesh, "Optimization of NACL based spray corrosion test process parameters of heat treated hybrid metal matrix composites," *Bulletin of the Chemical Society of Ethiopia*, vol. 36, no. 4, pp. 903–914, 2022.

[20] M. A. Elbaky, "Evaluation of mechanical properties of jute/glass/carbon fibers reinforced hybrid composites," *Fibre polymers*, vol. 18, no. 12, pp. 2417–2432, 2017.

[21] T. M. Gowda, A. C. Naidu, and R. Chhaya, "Some mechanical properties of untreated jute fabric-reinforced polyester composites," *Composite part A: Applied science and manufacturing*, vol. 30, no. 3, pp. 277–284, 1999.

[22] M. Ramesh, K. Palanikumar, and K. H. Reddy, "Comparative evaluation on properties of hybrid glass fiber- sisal/jute reinforced epoxy composites," *Procedia Engineering*, vol. 51, pp. 745–750, 2013.

[23] M. Vivekanandan, M. Premalatha, N. Anantharaman, R. Venkatesh, and V. Vijayan, "Hydrodynamic studies of CFBC boiler with three types of air distributor nozzles: experimental and CFD analysis," *Journal of Thermal Analysis and Calorimetry*, vol. 148, no. 2, pp. 405–415, 2023.

[24] H. Sezgin and O. B. Berkalp, "The effect of hybridization on significant characteristics of jute/glass and jute/carbon reinforced composites," *Journal of Industrial Textiles*, vol. 47, no. 3, pp. 283–296, 2017.

[25] S. K. Nayak, S. Mohanty, and S. K. Samal, "Influence of short bamboo/glass fiber on the thermal, dynamic mechanical and rheological properties of polypropylene hybrid composites," *Material science and engineering part A*, vol. 523, no. 1-2, pp. 32–38, 2009.

[26] D. Chmielewska, M. Barczewski, and T. Sterzynski, "A new method of curing epoxy resin by using bis(heptaphenylaluminosilsesquioxane) as a hardener," *Polimery*, vol. 58, no. 4, pp. 270–275, 2013.

[27] R. Venkatesh and P. R. Sekaran, "Adsorption and photocatalytic degradation properties of bimetallic Ag/MgO/biochar nanocomposites," *Adsorption Science & Technology*, vol. 2022, article 3631584, pp. 1–14, 2022.

[28] A. Gopinath, M. S. Kumar, and A. J. Elayaperumal, "Experimental Investigations on Mechanical Properties Of Jute Fiber Reinforced Composites with Polyester and Epoxy Resin Matrices," *Process Engineering*, vol. 97, pp. 2052–2063, 2014.

[29] D. Ray, M. Das, and D. Mitra, "Influence of alkali treatment on creep properties and crystallinity of jute fibres," *BioResources*, vol. 4, pp. 730–739, 2009.

Research Article

Thermal Adsorption and Corrosion Characteristic Study of Copper Hybrid Nanocomposite Synthesized by Powder Metallurgy Route

V. Senthilkumar,[1] A. Nagadeepan,[1] Melvin Victor De Poures [iD],[2] R. Sasikumar,[3] N. Mukilarasan [iD],[4] M. Aruna,[5] C. B. Priya [iD],[6] Gopal Kaliyaperumal,[7] and Elangomathavan Ramaraj [iD][8]

[1]*Department of Mechanical Engineering, SRM TRP Engineering College, Trichy, 621105 Tamil Nadu, India*
[2]*Department of Thermal Engineering, Saveetha School of Engineering, SIMATS, Chennai, 602105 Tamil Nadu, India*
[3]*Department of Mechanical Engineering, Erode Sengunthar Engineering College, Erode, 638057 Tamil Nadu, India*
[4]*Department of Mechanical Engineering, Jeppiaar Institute of Technology, Chennai, 631604 Tamil Nadu, India*
[5]*Faculty of Mechanical and Industrial Engineering, Liwa College of Technology, Abu Dhabi, UAE*
[6]*Department of Mechanical Engineering, OASYS Institute of Technology, Trichy, 621006 Tamil Nadu, India*
[7]*Department of Mechanical Engineering, New Horizon College of Engineering, Bengaluru, Karnataka 560103, India*
[8]*Department of Biology, College of Natural and Computational Sciences, Debre Tabor University, Amhara Region, Ethiopia*

Correspondence should be addressed to Elangomathavan Ramaraj; elanmath@dtu.edu.et

Novel constitutions of ceramic bond the new opportunity of engineering materials via solid-state process attaining enhanced material characteristics to overcome the drawback of conventional materials used in aquatic applications. The copper-based materials have great potential to explore high corrosion resistance and good thermal performance in the above applications. The main objectives of this research are to develop and enhance the characteristics of the copper-based hybrid nanocomposite containing different weight percentages of alumina and graphite hard ceramics synthesized via solid-state processing (powder metallurgy). The presence of alumina nanoparticles with a good blending process has to improve the corrosion resistance, and graphite nanoparticles may limit the weight loss of the sample during potentiodynamic corrosion analysis. The developed composite's micro Vickers hardness is evaluated by the E384 standard on ASTM value of 69 Hv and is noted by increasing the weight percentages of alumina nanoparticles. The conduction temperature of actual sintering anticipates the thermogravimetric analysis of developed composite samples varied from 400°C to 750°C. The thermogravimetric graph illustration curve of the tested sample found double-step decomposition identified between 427°C and 456°C. The potentiodynamic analyzer is used to evaluate the corrosion behaviour of the sample and the weight loss equation adopted for finding the theoretical weight loss of the composite.

1. Introduction

Copper is one of the best corrosion-free metals in defense and aquatic applications. Naturally, it is ductile, has good fluidity, and exhibits high thermal and electrical conductivity compared to traditional metals [1]. In addition, copper-based composite materials can serve extensive performance in the automotive and electronic industries due to their excellent thermal, tribo-logical, mechanical, electrical, and corrosion characteristics [2–5]. The secondary phase materials based on ceramics are used to create copper composite. It offers the specific desired characteristics with economic [6, 7]. The drawback behind the fabrication of copper/ceramic composite is poor bonding on inferior wetting properties [8, 9]. To solve the above, more than one suitable secondary phase reinforcement has been adopted in a similar composite in the form of nano- or

TABLE 1: Properties of pure copper.

Properties	Density	Vickers hardness	Tensile strength	Elongation at break	Coefficient of thermal expansion	Thermal conductivity	Melting point	Corrosion rate
Units	g/cc	Hv	MPa	%	μm/m$^\circ$C	W/m·K	$^\circ$C	mm/year
Value	7.76	50	210	60	16.4	385	1083	0.001

TABLE 2: Properties of ceramics.

Properties	Density (g/cc)	Hardness (Mohs)	Tensile modulus (GPa)	Coefficient of thermal expansion (μm/m$^\circ$C)	Thermal conductivity (W/m·K)
Alumina	3.96	9	370	0.6	30
Graphite	2.25	1	4.8	0.6-4.30	24

microparticles called hybrid nanocomposite. Recently, the growth hybrid composite materials developed with different matrix materials are incorporated with suitable secondary phase reinforcement materials that can prevent catastrophic and scuffing indemnity [10–13]. Many hybrid composites have been produced for various applications like sports goods, marine, automotive, structural, aviation, and defense [14–17]. However, the investigation results of increases in the tensile strength and hardness and a constrained coefficient of friction show that the composite created with a copper-based matrix and graphite particles can provide a solid lubricant effect. One additional ceramic phase, either aluminium oxide or silicon carbide, is considered to be a reinforcement [18, 19]. The above-referred ceramic has been influenced by copper's inherent conductivity and machinability [20]. The copper matrix with different secondary phase combinations is evaluated by a digital-type thermoanalyzer, resulting in better thermal conductivity. The majority of jet engines now have copper/ceramic combinations with good corrosion resistance [21]. At the earliest, chromium-reinforced copper matrix composite coated with carbon nanotubes found a problem with the wetting of secondary reinforcement [22].

The hybrid composite produced by two different ceramic particles is considered one in nanoscale and micron size via powder metallurgy. It results in superior strength of composite [23]. The corrosion behaviour of 1% carbon-reinforced Fe composite was evaluated by 1% of HNO_3 solution at 25 hours. It reveals that the corrosion rate on pure Fe was inversely higher than Fe/1% carbon composite [24]. The powder metallurgy route was developed with the waste ground nut of shell ash-reinforced Cu-WC hybrid composite. The results of the produced composite containing higher ground shell ash found increased corrosion resistance [25]. A seawater environment tested the corrosion performance of copper and its alloy via an electrochemical corrosion test. It was noticed with high corrosion resistance on both copper and its alloy [26]. The Al-Si alloy composite developed with alumina nanoparticles found increased corrosion resistance compared to cast Al-Si alloy. The corrosion resistance enhancement was mainly attributed to its Si constitutions with hard ceramic [27]. The mechanical alloying method was one of the best routes to obtain pore-free composites [28, 29]. The electrochemical corrosion test of copper-based composites found increased resistance value due

TABLE 3: Constitutions of copper hybrid nanocomposites.

Sample no.	Copper in %	Alumina in %	Graphite in %
1	93	2	5
2	93	4	3
3	93	6	1

to the effective blending of metal powder [30]. According to the recent research literature cited above from a variety of researchers, the development of a copper matrix composite, which is attracting more attention from the nanoscience community, could replace the microparticle size with a nanosize, improving the matrix's ability to resist corrosion. As a result, the current experimental inquiry focuses on heat adsorption, and the thermogravimetric and potentiodynamic analyses were used to examine the corrosion resistance behaviour of a copper hybrid nanocomposite made via powder metallurgy.

2. Materials and Processing Details

2.1. Choice of the Base Matrix. In the present investigation, pure copper (varied particle size) is considered as the matrix material, and its properties are mentioned in Table 1. It consists of 99.5% copper with 0.5% of other constitutions helping to assist the thermal changes during the melting of copper [1, 2]. Pure copper facilities have good thermal, electrical, and wear properties [3–5].

2.2. Choice of Reinforcements. The alumina and graphite particles are considered for reinforcements with a particle size of 50 nm. Both ceramics are thermally stable at a higher temperature, provide good solid lubricant, resist scratch against the frictional force, and have good hardness [18, 20, 21]. The characteristics of nanoalumina and micrographite particles are tabulated in Table 2.

2.3. Processing Details for Copper Hybrid Nanocomposites. The constitutions of copper matrix and ceramic reinforcement details are referred to in Table 3. The required percentages of copper metal powder and its secondary bonding phase elements, such as alumina/graphite nanoparticles, are weighted by a digital weighing machine with the accuracy of ±0.001 grams as shown in Figures 1(a)–1(c).

FIGURE 1: Actual illustrations for (a) copper metal particles, (b) alumina nanoparticles, and (c) graphite nanoparticles.

Figure 2 represents the overall powder metallurgy process. Figure 2(a) shows the process layout for composite fabrication. The measured quantity of copper matrix and its ceramic (alumina/graphite) are blended at 500 rpm for 2 hours via a PM100 ball milling machine configured with a planetary ball setup, shown in Figure 2(b). The PM100 ball mill is easy to use for 8 kg mass and 220 ml for sample material. The blended materials are placed in air-sealed TiC-coated vessels that hold a few TiC-coated balls at a ratio of 10 : 1. (10: metal powder in grams and 1: number of TiC balls). It leads to an increase in particle compactness with uniform and homogenous particle distribution achieved. It helps to limit the micron size aggregation.

The blended metal powders are filled into circular die sizes of 50 mm in diameter. After that, it is compacted via a universal compact testing machine with an applied compressive force of 20 tons to make circular green pellets. Finally, the compacted green pellets are sintered by an induction furnace at the temperature of 700°C under a soaking period of 180 min. However, the sintering temperature of green pellets is lower than the melting point temperature of parent materials.

The mechanical and tribological properties of the sintered metal samples are improved, and oxidation is minimised when they are stored in a boiler to debond the moisture contents in an inert atmosphere [28, 31]. The developed composite samples are shown in Figure 2(c).

2.4. Experimental Test Details. The micro-Vickers hardness of advanced hybrid composites (E384) is estimated using the VM50 model apparatus by the ASTM standard via FIE. The ASTM-E384 standard prepared hybrid nanocomposite samples are tested by 70 grams load at 20-second time duration. The thermal behaviour of the polymer matrix composite is analyzed by thermogravimetric analysis. A potentiodynamic analyzer evaluated the corrosion studies of advanced composites, and the theoretical weight loss of the composite is identified by equation (1).

3. Results and Discussions

3.1. Micro Vickers Hardness. Figure 3 represents the micro Vickers hardness value of a copper hybrid nanocomposite containing alumina and graphite nanoparticles, followed by the ratio of 2 : 5, 4 : 3, and 6 : 1, respectively. The presence of 50 nm size alumina particles occupying a significant por-

tion of the copper matrix results in an increased hardness value of the composite.

The addition of alumina nanoparticles to the copper matrix causes a rise in Vickers hardness number, which is measured as microhardness on the copper matrix [32]. It is revealed from Figure 3 that the Vickers hardness of copper hybrid nanocomposite linearly increases with an increase in alumina content, resulting in 58 ± 0.5 Hv, 64 ± 0.71 Hv, and 69 ± 0.73. The maximum hardness value of 69 ± 0.73 is observed by sample 3 (6 : 1). It was due to the presence of complex alumina nanoparticles that resist the indentation against the applied load. The hardness of sample 3 increased by 38% compared to cast copper. Similarly, the hardness of the hybrid composite was increased by 30% with the presence of Si_3N_4/ZrO_2 [17]. However, the presences of alumina and graphite nanoparticles in the copper matrix resist the indentation against the load applied and limit the dislocation of particle.

3.2. Thermal Performance Studies

3.2.1. Thermogravimetric Analysis on Thermal Adsorption Properties for Copper Hybrid Nanocomposites. The real sintering conduction temperature, which ranges from 400°C to 750°C over a certain time period, is used to evaluate the thermal performance on thermogravimetric analysis for the mass of copper hybrid nanocomposites including various percentages of alumina and graphite nanoparticles. This thermogravimetric estimation offered the physical changes for the composite phase transitions and decomposition during thermal changes. Substantial limits calculate the thermal adsorption on the thermal stability of copper hybrid nanocomposite. However, the insignificant mass loss on copper hybrid nanocomposite is not traced or shows a nonslope trace [33–35]. The differential temperature analysis (DTA), thermal-gravimetric analysis (TGA), and combinations of differential thermogravimetric (DTG) thermograph are used to study the thermal adsorption performance curve of copper hybrid nanocomposite samples 1, 2, and 3. The TGA, DTA, and DTG curves of a copper hybrid nanocomposite comprising ceramics in the ratios of 4 : 3 and 6 : 1 are shown in Figures 4(b) and 4(c). Sample 1 from Figure 4(a) represents the decompositions of copper hybrid nanocomposite containing 2 wt% alumina and 5% graphite nanoparticles lying in the 440°C to 480°C temperature range. Above 520°C temperature found the increased decomposition rate due to the dislocation of particles within the matrix. So

(a)

(b)

(c)
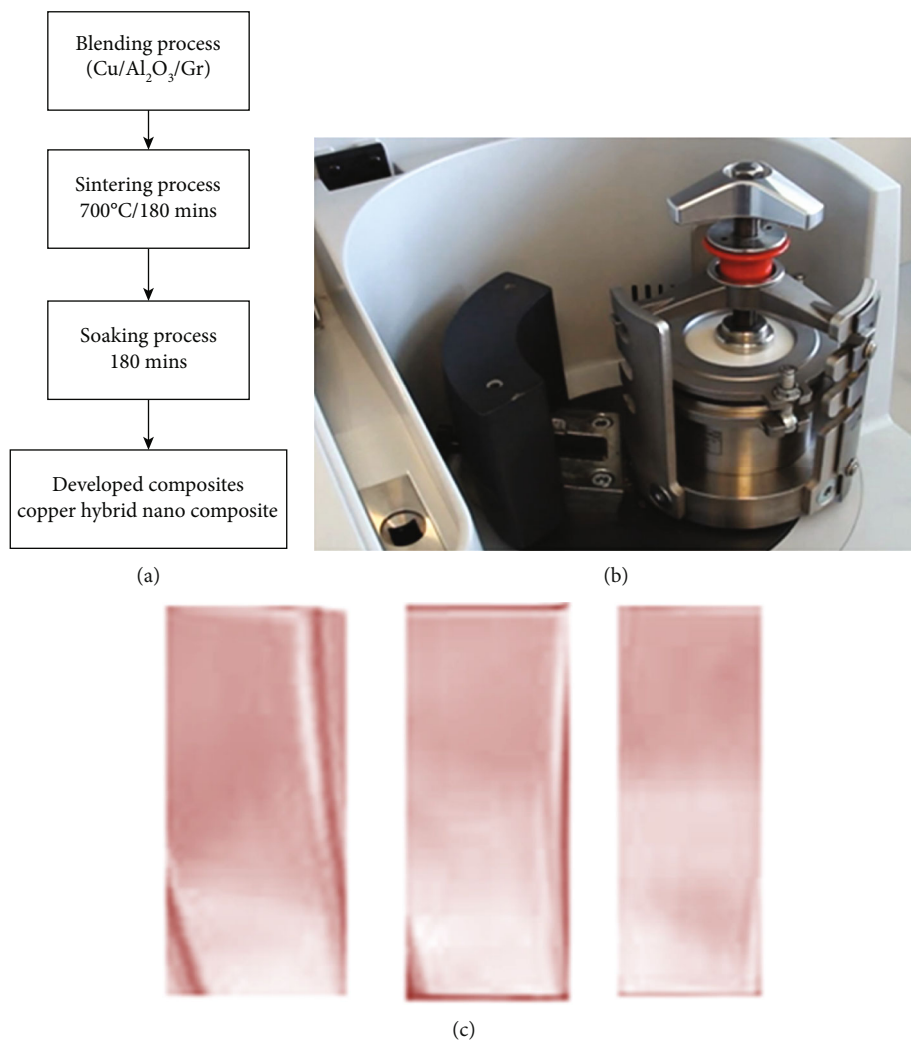
FIGURE 2: Overall powder metallurgy process: (a) process layout, (b) PM100 model planetary ball milling apparatus, and (c) developed composite samples.
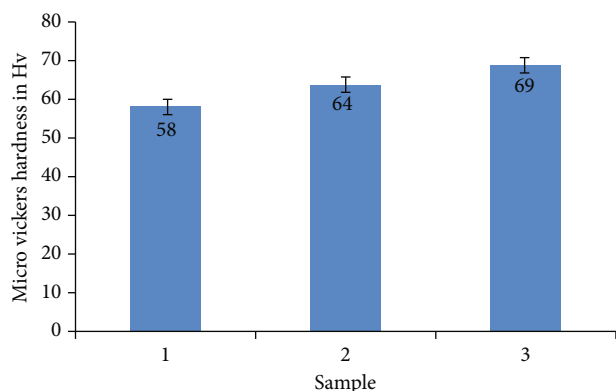
FIGURE 3: Micro Vickers hardness for copper hybrid nanocomposites.

the mass loss of the composite is hiked more than 600 micrograms. Figures 4(b) and 4(c) show the TGA, DTA, and DTG curves of copper hybrid nanocomposite containing the ceramic at ratios 4 : 3 and 6 : 1. Samples 2 and 3 show similar decomposition with minor slope variations due to irreversible ratio of

alumina and graphite nanoparticles in the copper matrix. However, it is revealed from Figures 4(a)–4(c) that the thermograph of copper hybrid nanocomposites is accomplished with higher temperature variations and withstands the working temperature devoid of structural loss or damage. The entire test samples of thermal adsorption on hybrid nanocomposite are stable and show ±42°C adsorption temperature.

The results from Figures 4(a)–4(c) show a similar curve pattern on TGA, DTA, and DTG thermographs. Moreover, the content of 93% copper bonded with 6% alumina and 1% graphite shows optimum mass loss results during thermal adsorption of 5.18 mg at 236°C. Further increase in temperature above 250°C shows the intermediate zone to minimize the mass loss of 5.21 mg between 450°C and 471°C. The minimum mass on the thermal adsorption effect of copper hybrid nanocomposite was 5.39 mg at 723°C. It was a limited 18.78% mass loss compared to copper elements. However, the TGA-developed double-step curve on decomposition was identified between the temperature ranges of 427°C to 456°C. More than 300 micrograms increases the mass loss of the composite at the increased
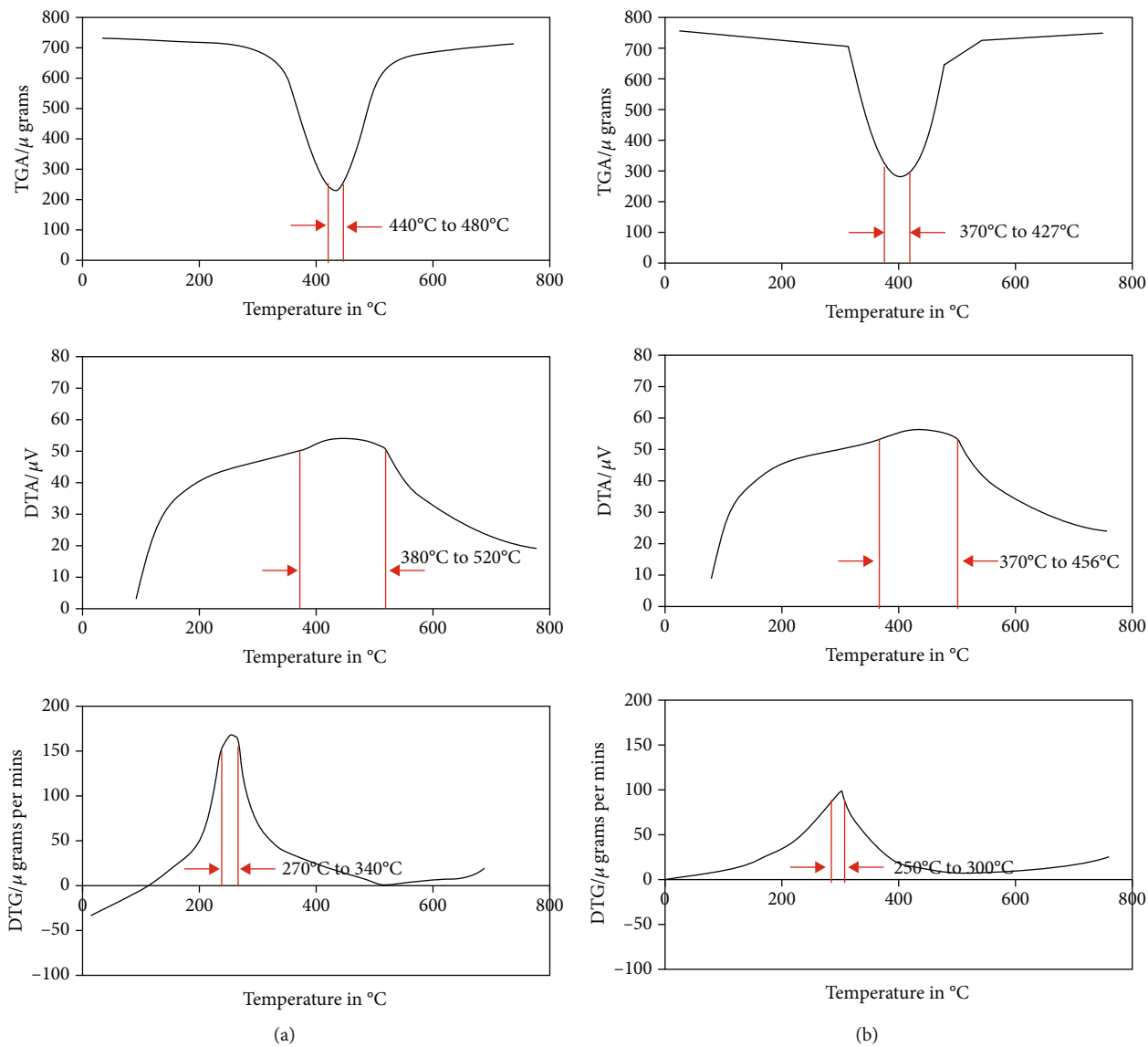
FIGURE 4: Continued.

(c)
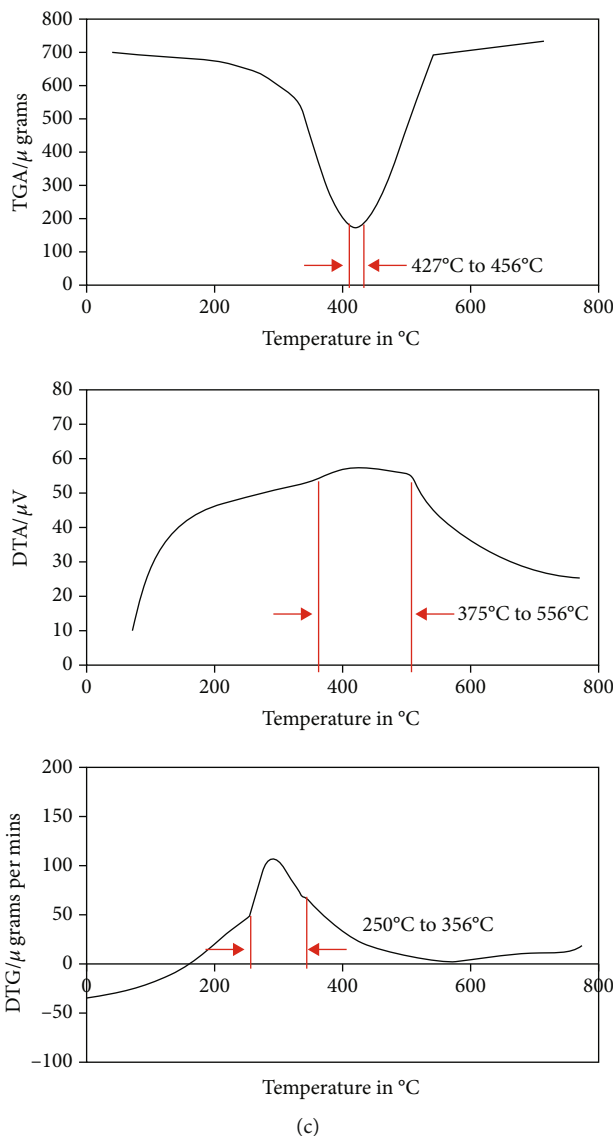
FIGURE 4: (a) Thermal adsorption effect on TGA, DTA, and DTG results for sample 1. (b) Thermal adsorption effect on TGA, DTA, and DTG results for sample 2. (c) Thermal adsorption effect on TGA, DTA, and DTG results for sample 3.

temperature of 427°C, as noted in Figure 4(b). Similarly, the composite contained 6 wt% alumina, and 1% graphite found an increased mass loss from 50 mg to 95 mg on improved temperature rise of 250°C to 356°C.

3.3. Corrosion Performance. In the present study, copper metal is considered a cathode polarity and easily permits the electron to oxidation. A base metal accomplishes the developed composites for aquatic applications. The solution medium of sodium chloride and sodium hydroxide evaluates the corrosion nature of multiceramic-reinforced copper matrix hybrid nanocomposites. The 1.5% of sodium hydroxide solution is diluted for 300 ml solution. It is held in a glass beaker. The copper matrix hybrid nanocomposite of corrosion samples is immersed in the sodium hydroxide solution for 1 day to study the potentiodynamic analysis. Figures 5(a)–5(c) illustrate the potentiodynamic analysis on corrosion studies of copper hybrid nanocomposites containing 2%, 4%, and 6% alumina.

Correspondingly, the graphite nanoparticle incorporated with alumina is 5%, 3%, and 1%, respectively. The digital weighing machine with an accuracy of ±0.001 gram is utilized to measure the weight of the composite sample before ($W1$) and after ($W2$) corrosion study. The theoretical weight loss is calculated by

$$\text{Weight loss of composite} = \frac{W2 - W1}{W2}. \quad (1)$$

Figure 5 shows that a copper hybrid nanocomposite with 6% alumina and 1% graphite had the highest resistance to the development of corrosion. When compared to the anode pole, the cathode polarisation has greater corrosion resistance. Similarly, the prepared corrosion test samples are dipped in sea salt water, and the weight loss method estimates its effect on corrosion formation. The test result of the corrosion study is mentioned in Table 4. It was noted
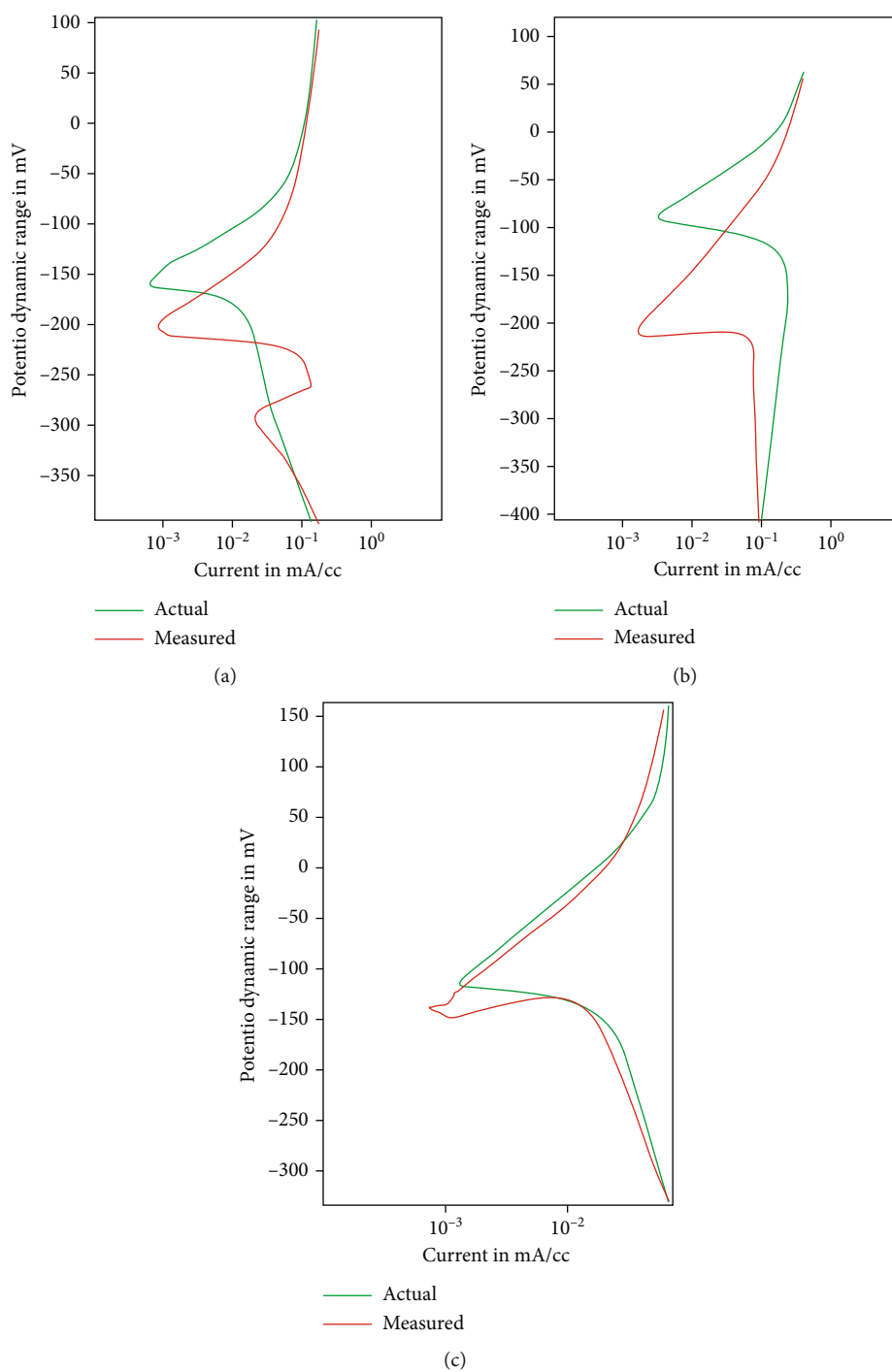
FIGURE 5: (a) Potentiodynamic analysis of corrosion results on sample 1. (b) Potentiodynamic analysis of corrosion results on sample 2. (c) Potentiodynamic analysis of corrosion results on sample 3.

TABLE 4: Corrosion test results.

| Sample | Sodium hydroxide solution | | | | Sea water | |
| | Initial weight (g) | pH concentration in g | | | Initial weight (g) | Loss of weight (g) |
		0.75%	0.50%	0.25%		
1	6	0.19	0.15	0.087	3	0.187
2	6	0.15	0.13	0.031	3	0.181
3	6	0.02	0	0	3	0
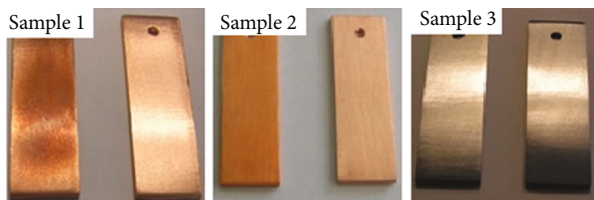
FIGURE 6: Corrosion test samples.

from Table 4 that sample 3 found intensive corrosion resistance with zero weight loss. It was due to the combination of copper/alumina/graphite. The alumina content resists the corrosion support on the copper matrix, and graphite limits weight loss.

It is observed from Figure 5(a) that the potentiodynamic analysis curve for sample 1 is not similar to the actual representation. The line of green represents the actual curve before the corrosion test, and the red curve indicates the curve for corrosion sample 1. There are few changes found in the potential curve. Sample 1 is not suitable for the above applications. It has some minor corrosion-affected areas to be deflected.

Figure 5(b) represents the potentiodynamic analysis of corrosion results on sample 2 copper hybrid nanocomposites. The potential pattern for both actual and measured values shows a similar pattern, but the measured corrosion value deviates from the actual value. It has represented some corrosion-affected places during the evaluation of sodium hydroxide solution for 1 day. It may lead to damage to the copper matrix hybrid nanocomposites. The proof of pH concentration is mentioned in Table 4.

Figure 5(c) shows the potentiodynamic analysis curve on corrosion results on sample 3 hybrid nanocomposite. The actual and measured corrosion curves match similarly with a few variations. This demonstrates that sample 3's corrosion analysis resulted in no material loss. The measured corrosion value of sample 3 is represented in Table 4 with varied pH concentrations. The tested samples are shown in Figure 6.

4. Conclusions

The copper-based hybrid nanocomposite is effectively developed with alumina and graphite nanoparticles through the powder metallurgy route. The developed hybrid nanocomposites are subjected to hardness; thermal adsorption behaviour on TGA, DTA, and DTG routes; and corrosion studies. The following conclusions are made as follows:

(i) The presence of nanoalumina and graphite ceramics enhances the characteristics of hybrid nanocomposite, and its experimental results are proven

(ii) There is a progressive improvement in hardness, effective thermal performance, and good corrosion resistance

(iii) Sample 3 (Cu/6% Al_2O_3/1% graphite) found a superior hardness of 69 ± 0.73 and increased 38% of cast copper material

(iv) The intermediate thermal stability of the composite (sample 3) was identified as 5.21 mg between 450°C and 471°C

(v) The corrosion studies found that the increased alumina content in the copper matrix shows an exhibited corrosion resistance value. There is no significant loss of composite during the potentiodynamic analysis

Data Availability

All the data required are available within the manuscript.

Conflicts of Interest

The authors declare no conflicts of interest.

References

[1] C. A. Loto, "Electrochemical noise evaluation and data statistical analysis of stressed aluminium alloy in NaCl solution," *Journal of Alexandria Engineering Journal*, vol. 57, no. 3, pp. 1313–1321, 2018.

[2] S. Mallik, N. Ekere, C. Best, and R. Bhatti, "Investigation of thermal management materials for automotive electronic control units," *Applied Thermal Engineering*, vol. 31, no. 2-3, pp. 355–362, 2011.

[3] R. Zitoune, M. el Mansori, and V. Krishnaraj, "Tribo-functional design of double cone drill implications in tool wear during drilling of copper mesh/CFRP/woven ply," *Wear*, vol. 302, no. 1-2, pp. 1560–1567, 2013.

[4] S. Kumari, A. Kumar, P. R. Sengupta, P. K. Dutta, and R. B. Mathur, "Improving the mechanical and thermal properties of semi-coke based carbon/copper composites reinforced using carbon nanotubes," *Journal of Advanced Material Letter*, vol. 5, no. 5, pp. 265–271, 2014.

[5] M. Vivekanandan, M. Premalatha, N. Anantharaman, and R. Venkatesh, "Hydrodynamic studies of CFBC boiler with three types of air distributor nozzles: experimental and CFD analysis," *Journal of Thermal Analysis and Calorimetry*, vol. 148, no. 2, pp. 405–415, 2023.

[6] M. Yusoff, R. Othman, and Z. Hussain, "Mechanical alloying and sintering of nanostructured tungsten carbide- reinforced copper composite and its characterization," *Material Design*, vol. 32, no. 6, pp. 3293–3298, 2011.

[7] A. A. Thakre and S. Soni, "Modeling of burr size in drilling of aluminum silicon carbide composites using response surface methodology," *Engineering Science and Technology*, vol. 19, no. 3, pp. 1199–1205, 2016.

[8] S. F. Moustafa, Z. Abdel-Hamid, and A. M. Abd-Elhay, "Copper matrix SiC and Al_2O_3 particulate composites by powder metallurgy technique," *Material Letter*, vol. 53, no. 4-5, pp. 244–249, 2002.

[9] R. K. Gautam, S. Ray, S. C. Sharma, S. C. Jain, and R. Tyagi, "Dry sliding wear behavior of hot forged and annealed Cu-Cr-graphite in-situ composites," *Wear*, vol. 271, no. 5-6, pp. 658–664, 2011.

[10] J. Sankar, S. S. Kumar, P. Balamurugan, S. Kumar, S. A. Saleem, and S. V. Krishna, "Fabrication and corrosion studies of bronze based composite prepared through powder metallurgy route," *Material Today Proceeding*, vol. 50, no. 5, pp. 1067–1070, 2022.

[11] R. Venkatesh, C. R. Kannan, S. Manivannan et al., "Synthesis and experimental investigations of tribological and corrosion performance of AZ61 magnesium alloy hybrid composites," *Journal of Nanomaterials*, vol. 2022, Article ID 6012518, 12 pages, 2022.

[12] S. Priya Karjala, V. K. K. Rajammal, S. Gopi, R. Ravi, D. Chockalingam, and M. C. Muthukaruppan, "Influence of IPNS (vinylester/epoxy/polyurethane) on the mechanical properties of glass/carbon fiber reinforced hybrid composites," *IIUM Engineering Journal*, vol. 23, no. 1, pp. 339–348, 2022.

[13] R. Venkatesh, N. Karthi, N. Kawin et al., "Synthesis and adsorbent performance of modified biochar with ag/MgO nanocomposites for heat storage application," *Adsorption Science & Technology*, vol. 2022, article 7423102, pp. 1–14, 2022.

[14] K. Karthikeyan, V. Mariappan, P. Kalidoss et al., "Preparation and thermal characterization of capric-myristic acid binary eutectic mixture with silver-antimony tin oxide and silver-graphane nanoplatelets hybrid-nanoparticles as phase change material for building applications," *Materials Letter*, vol. 328, article 133086, 2022.

[15] A. M. Kovalchenko, O. I. Fushchich, and S. Danyluk, "The tribological properties and mechanism of wear of Cu-based sintered powder materials containing molybdenum disulfide and molybdenum diselenite under unlubricated sliding against copper," *Wear*, vol. 290-291, pp. 106–123, 2012.

[16] M. Vamsi Krishna and M. Xavior Anthony, "An investigation on the mechanical properties of hybrid metal matrix composites," *Procedia Engineering*, vol. 97, pp. 918–924, 2014.

[17] P. S. Reddy, R. Kesavan, and B. Vijaya Ramnath, "Investigation of mechanical properties of aluminium 6061-silicon carbide, boron carbide metal matrix composite," *Silicon*, vol. 10, no. 2, pp. 495–502, 2018.

[18] C. Ramesh Kannan, R. Venkatesh, M. Vivekanandan et al., "Synthesis and characterization of mechanical properties of AA8014 + Si_3N_4/ ZrO_2 hybrid composites by stir casting process," *Advances in Materials Science and Engineering*, vol. 2022, Article ID 9150442, 11 pages, 2022.

[19] A. Mohan and S. Poobal, "Crack detection using image processing: a critical review and analysis," *Alexandria Engineering Journal*, vol. 57, no. 2, pp. 787–798, 2018.

[20] M. Uthayakumar, V. Manikandan, N. Rajini, and P. Jeyaraj, "Influence of redmud on the mechanical, damping and chemical resistance properties of banana/polyester hybrid composites," *Material Design*, vol. 64, pp. 270–279, 2014.

[21] C. S. Ramesh, R. Noor Ahmed, M. A. Mujeebu, and M. Z. Abdullah, "Development and performance analysis of novel cast copper-SiC-Gr hybrid composites," *Material Design*, vol. 30, no. 6, pp. 1957–1965, 2009.

[22] A. K. Kanayo and O. B. Ufuoma, "Mechanical properties, wear and corrosion behavior of copper matrix composites reinforced with steel machining chips," *International Journal of Engineering Science and Technology*, vol. 19, no. 3, pp. 1593–1599, 2016.

[23] K. Chu, C. C. Jia, L. K. Jiang, and W. S. Li, "Improvement of interface and mechanical properties in carbon nanotube reinforced Cu-Cr matrix composites," *Material Design*, vol. 45, pp. 407–411, 2013.

[24] T. Rajmohan and K. Palanikumar, "Application of the central composite design in optimization of machining parameters in drilling hybrid metal matrix composites," *Measurement*, vol. 46, no. 4, pp. 1470–1481, 2013.

[25] R. Chandramouli, T. K. Kandavel, D. Shanmugasundaram, and T. Ashok Kumar, "Deformation, densification, and corrosion studies of sintered powder metallurgy plain carbon steel preforms," *Material Design*, vol. 28, no. 7, pp. 2260–2264, 2007.

[26] R. Venkatesh, P. R. Sekaran, K. Udayakumar, D. Jagadeesh, K. Raju, and M. B. Bayu, "Adsorption and photocatalytic degradation properties of bimetallic Ag/MgO/biochar nanocomposites," *Adsorption Science & Technology*, vol. 2022, article 3631584, pp. 1–14, 2022.

[27] R. Orozco-Cruz, "In situ corrosion study of copper and copper-alloys exposed to natural seawater of the Veracruz port (Gulf of Mexico)," *International Journal of Electrochemical Science*, vol. 12, pp. 3133–3152, 2017.

[28] D. Saber, R. Abdel-Karim, A. A. Kandel, and K. A. el-Aziz, "Corrosive wear of alumina particles reinforced Al–Si alloy composites," *Physics of Metals and Metallography*, vol. 121, no. 2, pp. 188–194, 2020.

[29] C. Suryanarayana and A. A. Nasser, "Mechanically alloyed composites," *Progress in Material Science*, vol. 58, pp. 383–502, 2013.

[30] A. Mohana Krishnan, P. Laxmanan, and R. Venkatesh, "Salt spray corrosion study on aluminium metal matrix composites (AMMCs) prepared by powder metallurgy route," *Materials Today Proceedings*, vol. 62, no. 2022, pp. 1954–1957, 2022.

[31] J. I. Iribarren, F. Liesa, C. Alemán, and E. Armelin, "Corrosion rate evaluation by gravimetric and electrochemical techniques applied to the metallic reinforcing structures of a historic building," *Journal of Cultural Heritage*, vol. 27, pp. 153–163, 2017.

[32] A. Sobhanadri, G. Senthilkumar, M. Vivekanandan, and R. Venkatesh, "A CFD investigation and heat transfer augmentation of double pipe heat exchanger by employing helical baffles on shell and tube side," *Thermal Science*, vol. 26, no. 2A, pp. 991–998, 2022.

[33] A. Fathy, F. Shehata, M. Abdelhameed, and M. Elmahdy, "Compressive and wear resistance of nanometric alumina reinforced copper matrix composites," *Material Design*, vol. 36, pp. 100–107, 2012.

[34] A. W. Coats and J. P. Redfern, "Thermogravimetric analysis: a review," *Analyst (Cambridge, UK)*, vol. 88, no. 1053, pp. 906–924, 1963.

[35] A. Mohana Krishnan, M. Dineshkumar, and R. Venkatesh, "Evaluation of mechanical strength of the stir casted aluminium metal matrix composites (AMMCs) using Taguchi method," *Materials Today Proceedings*, vol. 62, no. 2022, pp. 1943–1946, 2022.

Research Article

Synthesis and Thermal Adsorption Characteristics of Silver-Based Hybrid Nanocomposites for Automotive Friction Material Application

R. Venkatesh,[1] P. Sakthivel [ID],[2] M. Vivekanandan,[3] C. Ramesh Kannan,[4] J. Phani Krishna,[5] S. Dhanabalan,[6] T. Thirugnanasambandham,[7] and Manaye Majora [ID][8]

[1]*Department of Mechanical Engineering, Saveetha School of Engineering (SIMATS), Chennai, 602105 Tamil Nadu, India*
[2]*Department of Mechanical Engineering, Sri Krishna College of Technology, Coimbatore, 641042 Tamil Nadu, India*
[3]*Department of Mechanical Engineering, Kongunadu College of Engineering and Technology, Trichy, 621215 Tamil Nadu, India*
[4]*Department of Mechanical Engineering, SRM TRP Engineering College, Trichy, 621105 Tamil Nadu, India*
[5]*Design Engineering, Powder Handling Solutions, RIECO industries Ltd. Pune, 411005, India*
[6]*Department of Mechanical Engineering, M.Kumarasamy College of Engineering, 639113 Tamil Nadu, India*
[7]*Department of Mechanical Engineering, Ponnaiyah Ramajayam Institute of Science and Technology, Thanjavur, Tamil Nadu 613203, India*
[8]*Department of Mechanical Engineering, Faculty of Manufacturing, Institute of Technology, Hawassa University, Ethiopia*

Correspondence should be addressed to Manaye Majora; man-buy@hu.edu.et

Advances in friction materials are imposed on developing multiceramic reinforced hybrid nanocomposites with superior tribomechanical properties. The silver-based matrix metals are gained significance in various applications like bearing, ratchet, and electrical contacts due to their high frictional resistance and good thermal and chemical stability compared to traditional metals. The present research is to develop silver-based hybrid nanocomposites containing alumina (Al_2O_3) and silicon carbide (SiC) nanoparticles of 50 nm mixing with the ratio of 0 wt% Al_2O_3/0 wt% SiC, 5 wt% Al_2O_3/0 wt% SiC, and 5 wt% Al_2O_3/5 wt% SiC via the semisolid vacuum stir-cast technique. The vacuum technology minimizes casting defects and increases composite properties. The casted composite samples are subjected to study the effect of reinforcement on thermal adsorption, conductivity, diffusivity, and frictional resistance. The composite containing 5 wt% Al_2O_{3np}/5 wt% SiC_{np} is to find optimum thermal and frictional behaviour. The thermal adsorption and frictional resistance are increased by 30% and 27% compared to unreinforced cast silver. The Ag/5 wt% Al_2O_{3np}/5 wt% SiC_{np} hybrid nanocomposite is recommended for automotive friction-bearing applications.

1. Introduction

In modern research, the world is forced to search the new advanced material to meet the industrial requirement and fulfill the following qualities: high strength, good thermal stability, enhanced corrosion resistance, ability to withstand high frictional force with reduced wear loss, and increased coefficient of friction. Many researchers have experimentally studied the aluminium alloy-based matrix composite [1–4] due to their lower density, high ductility, good strength, and stiffness compared to conventional materials [5–8]. However, the characteristics of composite with their hybrid systems may be varied due to the particle shape and size, mixing ratio, casting process parameters, and method of processing of composite [9–11]. The particulate-reinforced composite can perform high strength and friction resistance [12]. Specifically, silicon carbide, aluminium oxide, tungsten carbide, boron carbide, and zirconium dioxide-based ceramics to metal matrix result in high hardness, resistance to high frictional force, and high thermal stability [13]. The

zinc/lead and nickel-based matrix composite is adopted in aviation and space applications due to its high frictional resistance, anticorrosion, and thermal proof [14, 15]. In the future, silver-based metal matrix composites (SMMCs) will perform extraordinary (solid) lubrication effect and withstand the high thermal stress during high frictional force applied in aerospace motor applications, high friction bearing, and electrical contact applications [16–20]. However, few studies are available on silver matrix composite for automotive friction material applications [21]. Pure silver is characterized by low wear resistance and superior thermoelectrical conductivity. Due to these properties, it was accomplished by several industries alloying with Zn, Cu, Mn, Ni, and aluminium alloy to obtain a specific performance [22]. In the past decades, the frictional properties for different constitutions of aluminium/mica and copper/coated ground mica have been studied for bearing applications. The facilitation of mica influences higher frictional strength [23]. The CSM tribotester estimated the silver-copper-based composite's dry sliding wear characteristics. The result reveals that the composite's worn surface is directly impacted by the friction coefficient and rate of wear [24]. Most matrix materials are bonded with suitable reinforcements via solid-state processing (powder metallurgy), liquid-state processing (gravity, centrifugal, stir, and vacuum stir casting), and vapour-state processing (vapour and spray deposition process) techniques [25, 26]. Among various fabrication techniques listed above, the liquid-state processing distinctively improves physical-chemical properties between matrix and reinforcements resulting in increased product quality and suitability for mass production. Most researchers reported that the liquid-state stir processing is apposite for complex shape production at massive and economical production [27–31]. Based on the above literature, various matrix alloying materials, reinforcements, and their processing methods are discussed with their enhanced properties. The present research is to develop a silver matrix hybrid nanocomposite containing Al_2O_3/SiC nanoparticles via the vacuum sir cast technology. The fabricated samples were studied for their thermal and friction characteristics. The influences of both ceramics on the silver matrix found enhanced thermal adsorption with reduced mass loss, better conductivity, diffusivity, and rate of wear. The ASTM G99-05 standard evaluates the wear rate of advanced composites. Finally, all the test results were compared, and the best constitution having enhanced properties to fulfil the automotive friction material applications was recommended.

2. Experimental Details

2.1. Selection of Primary Matrix Material.
The present study chose the silver-based alloy as the primary matrix material. The properties of silver are mentioned in Table 1.

2.2. Selection of Secondary Phase Reinforcements.
The complex ceramic aluminium oxide and silicon carbide particle (50 nm) with an average size of 50 nm is chosen as secondary phase reinforcement to obtain better composite performance

[28, 30, 31]. The properties of both ceramic phases are represented in Table 2.

2.3. The Mixing Ratio of Composite.
Table 3 illustrates the phase constitution of a silver matrix concerning weight percentages of reinforcement used by the production of silver matrix hybrid nanocomposite.

2.4. Method and Processing of Composites.
Figures 1(a) and 1(b) represent the silver matrix composite fabrication full setup with vacuum pump assembly. The different-sized silver round bar was preheated at 400°C for 30 min and melted via an electrical furnace with an applied temperature range of 1000°C to 1200°C under an inert atmosphere (supply of argon gas at a constant level of 3 l/h) to avoid the thermal oxidation. The higher temperature may increase the oxidation resulting in an increased porosity [27, 28]. According to the phase constitutions (mixing ratio) reported in Table 3, the preheated reinforcements (Al_2O_3/SiC) are added into a silver molten pool stirred with 500 rpm stir speed. Here, the graphite mechanical stirrer is used to improve the fluidity for surface preparation. A similar concept was reported by silver composite [20]. Thoroughly stirred molten state mixed silver matrix hybrid nanocomposite is developed with an applied vacuum pressure of 1×10^5 bar, resulting in minimized casting defects with increased composite performance. Table 4 represents the processing parameters of silver matrix composites.

2.5. Evaluation of Thermal Characteristics.
The thermal characteristics of silver matrix MMCs are evaluated by STA Jupiter make 449/F3 model differential thermal analysis equipment configured with -150°C to 2400°C under argon atmosphere. The laser flash technique is accomplished to find the thermal conductivity ($ʎ$) and its diffusivity as referred follows [20].

$$ʎ(T) = \rho(T)x\alpha(T)xCp(T). \quad (1)$$

Here $ʎ$ is the thermal conductivity, T the temperature, ρ the density of material, α the thermal diffusivity, and Cp the specific heat coefficient.

The NETZSCH-made DIL 402C and LFA 427 models are considered for evaluating linear thermal expansion and its diffusivity of ϕ8 mm and 25 mm length sample under the ambient temperature of 27°C to 1000°C with 7°C/min heat flow.

2.6. Evaluation of Frictional Characteristics.
The dry sliding frictional characteristics of cast silver, nanocomposite, and hybrid nanocomposite were evaluated by rotating pin on disc tribotester configured with a hardened steel disc with an applied load of 10 N, 20 N, and 30 N under the constant sliding velocity of 0.75 m/sec. The above conditions estimated the effect of reinforcement on frictional resistance of the silver matrix. The top view of the wear tester is shown in Figure 1(c).

TABLE 1: Properties of silver matrix.

Properties	Density	Elastic modulus	Tensile strength	Melting temperature	Thermal conductivity	Emissivity	Specific heat capacity
Ag	10.49 g/cc	76 GPa	140 MPa	962°C	419 W/mK	0.055	0.234 J/g°C

TABLE 2: Properties of reinforcements.

Reinforcements	Density g/cc	Hardness VHN	Modulus of elasticity GPa	Melting point °C	Thermal conductivity W/mK
Al_2O_3	3.96	1366	375	2055	30.12
SiC	3.1	14450	412	2799	77.54

TABLE 3: Phase constitutions of silver matrix composite.

Sample	Descriptions	Phase constitutions in wt%		
		Ag	Al_2O_3	SiC
1	Alloy	100	0	0
2	Nanocomposite	95	5	0
3	Hybrid nanocomposite	90	5	5

3. Result and Discussions

3.1. Differential Thermal Effect on Mass Loss of Silver Matrix Composites.

Figures 2(a)–2(c) illustrate the differential thermal effect on mass loss of cast silver correlated with Al_2O_3- and SiC-reinforced silver nano- and hybrid nanocomposites evaluated under the thermal region of 27°C to 1000°C. The temperature-to-mass loss of each test sample is explained in detail. When the temperature increases from ambient temperature to high temperature, it shows solid to semisolid phase and liquid phase at the higher temperature (phase transformations—solid/liquid and liquid/solid) of heating and cooling phase during the evaluation of thermal studies. It is revealed from Figure 2(a) that the mass loss of cast silver (Ag) alloy is gradually decreased from $0.02\,\mu$V/mg to $0.0098\,\mu$V/mg with an increase in temperature of 27° to 825°C under an inert atmosphere. At the same time, increasing the temperature of cast silver by more than 825°C results to the formation of the plastic region with improved mass loss of $0.0302\,\mu$V/mg. It was due to the reaction of intermetallic coarse fine grain structure and dissolution of the Ag phase. Similar conditions have been reported by Jakub et al. [20] during the evaluation of silver matrix MMCs. The wettability of the composite was limited by the volume fraction SiC [22].

Figure 2(b) represents the variations in weight loss of cast Ag alloy nanocomposite consisting 5 wt% alumina nanoparticles during differential thermal analysis. The red and blue curve represents the heat and cooling phase of Ag matrix composite processing as per the condition mentioned in Table 2. The heating curve in Figure 2(b) shows a gradually sloping from $0.0213\,\mu$V/mg to $0.0086\,\mu$V/mg for a semisolid phase temperature of 760°C. In-reversal effect of the heating curve shows that the maximum temperature of 840°C reduces the mass loss on the phase of bonded

matrix—reinforcement by an applied stir speed of 500 rpm results in the formation of a homogenous uniform structure. The constant stir speed may reduce the composite's casting defect (weight loss). The selection of stir-cast processing parameters was necessary for the quality of the composite. The discontinued stir action increases the cavity of the composite, resulting in increased porosity [27].

Figure 2(c) represents the phase transformation during the heat and cooling phase of silver matrix hybrid nanocomposite with a varied temperature range of 27°C to 1200°C. The intermediate transition zone (820°C) for both the heat and cooling phases shows a minimum mass loss of less than $0.009\,\mu$V/mg. Here, the thermal effect of silver matrix composite varied due to the chemical constitutions and bonding strength between matrix and alumina/silicon carbide nanoparticles.

A similar scenario was reported by Mata and Alcala [9] during the performance friction material. However, both reinforcements are thermally stable at higher temperature (1000°C) for melting silver. The intermediate phase for silver, silver nanocomposite, and silver hybrid nanocomposite was found by differential thermal effect analysis, and the values are tabulated in Table 5.

3.2. Effect of Reinforcement on Thermal Adsorption and Thermal Diffusivity of Silver Matrix Composites.

Figure 3 graph describes the detailed heat wave circulation (linear expansion and adsorption) of unreinforced Ag alloy and Al_2O_3/SiC-reinforced composites. The unreinforced Ag alloy is found 18×10^{-6} per K (1.70%). The inclusion of alumina nanoparticle (5 wt%) into Ag alloy shows a 4.8×10^{-6} per K. It was due to the rigid ceramic particles leading to increase hardness and withstand the higher temperature [18]. The circulation of the thermal wave to

(a)

(b)

(c)
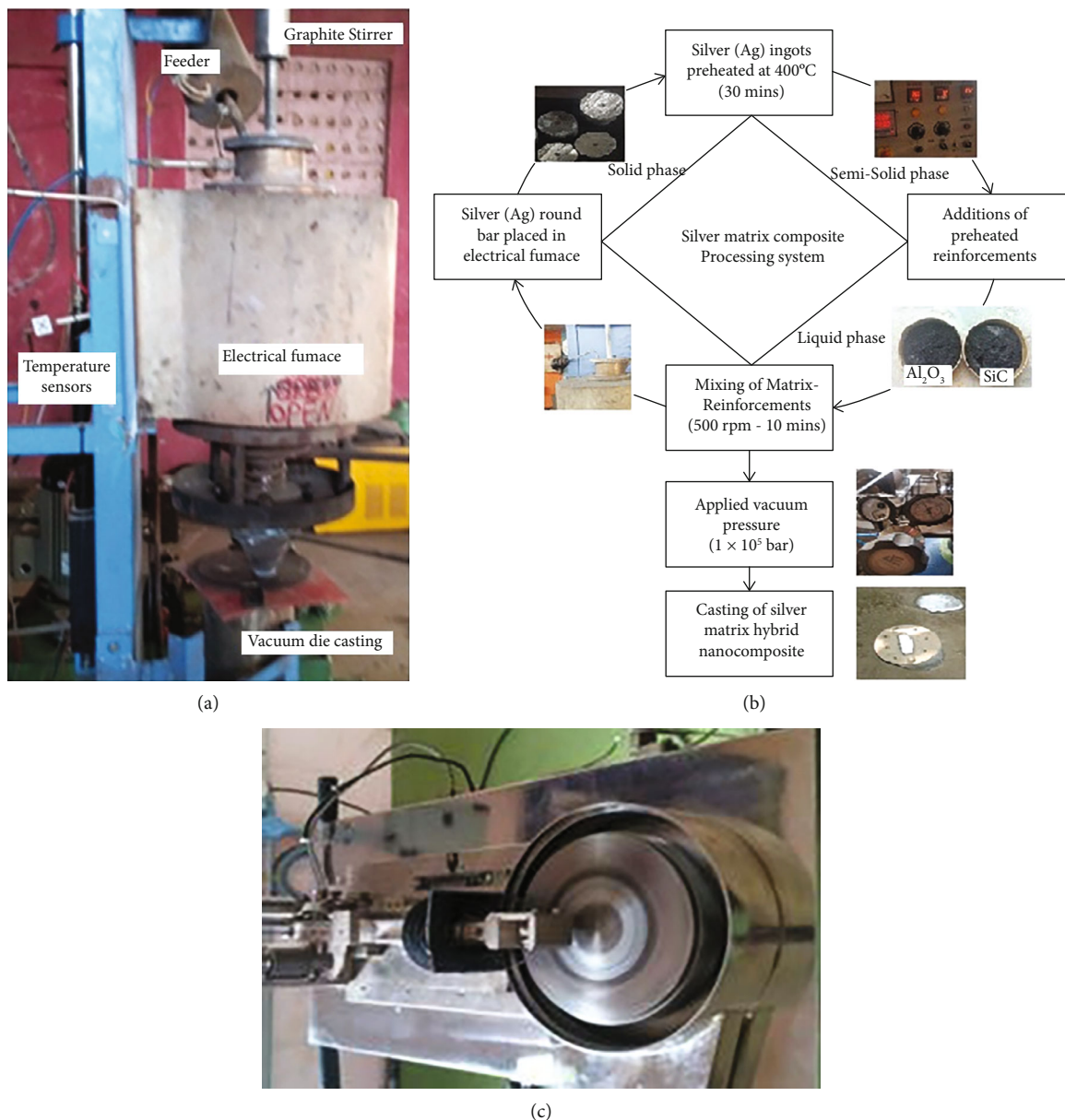
FIGURE 1: Actual fabrication setup for silver matrix composite. (a) Actual setup. (b) Processing chain with different thermal phase. (c) Pin on disc wear apparatus.

TABLE 4: Process parameter for silver matrix composites.

Descriptions	Preheating temperature Matrix	Rotational speed (stir) Reinforcements	Impeller type	Stir time	Feed rate	Die preheat temperature	Vacuum pressure
Units	400°C	500 rpm	Graphite	10 min	0.9 g/sec	350°C	1×10^5 bar

Ag nanocomposite is decreased to 12% compared to unreinforced Ag alloy. The composite contained 5 wt% alumina and silicon carbide nanoparticle is found at 1.42%. Generally, both reinforcements are complex, and high melting temperature reduces linear expansion. The various phase transformation during the evaluation is noted in Figure 3, and its intermediate zone for optimum thermal effect temperature tangent lines is drawn. However, the physical presence of both Al_2O_3 and SiC nanoparticles leads to decreased thermal coefficient and increased composite adsorption. The higher temperature withstand capacity was increased by over 30% compared to Ag alloy at 1000°C.

The experimental results for thermal diffusivity of (a) Ag/0 wt% Al_2O_{3np}/0 wt% SiC_{np}, (b) Ag/5 wt% Al_2O_{3np}/
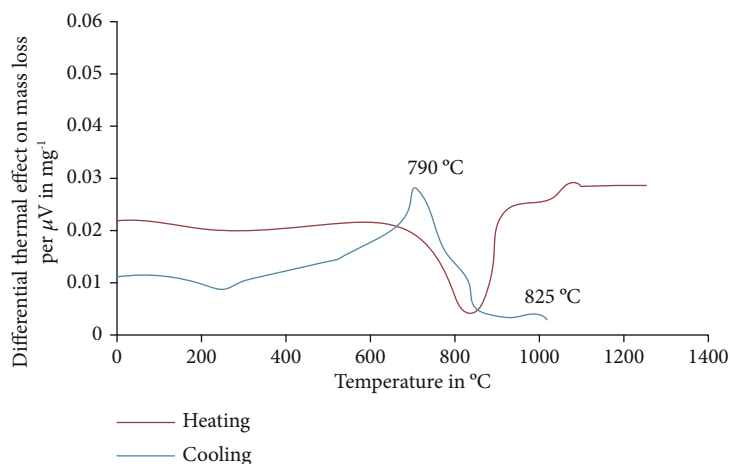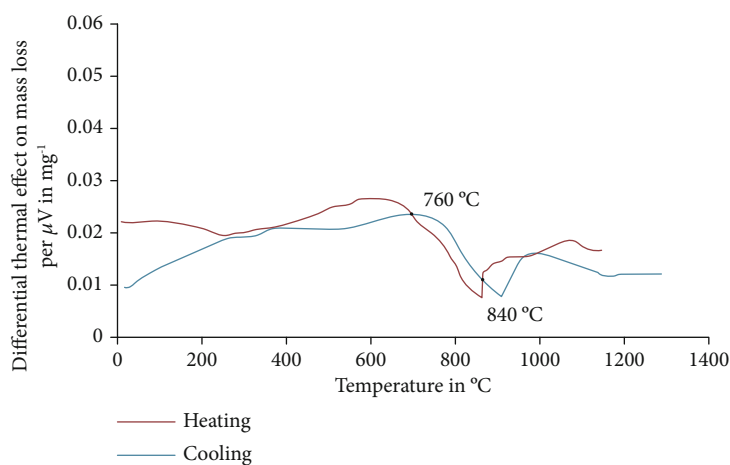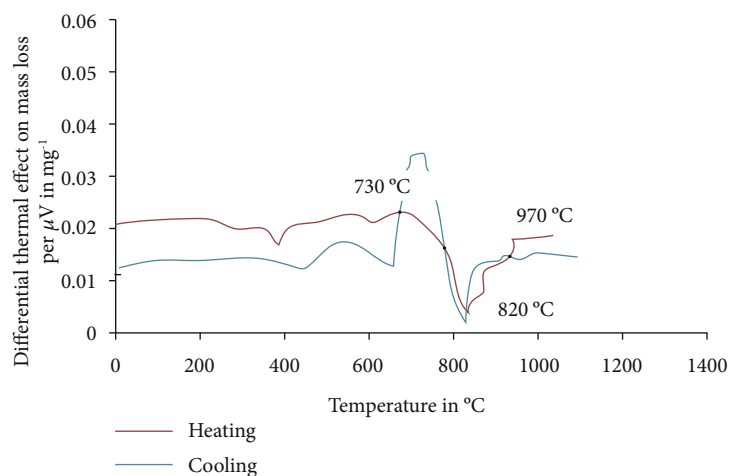
FIGURE 2: Differential thermal effect on mass loss of silver matrix hybrid nanocomposite. (a) Ag/0 wt% Al_2O_{3np}/0 wt% SiC_{np}, (b) Ag/5 wt% Al_2O_{3np}/0 wt% SiC_{np}, and (c) Ag/5 wt% Al_2O_{3np}/5 wt% SiC_{np}.

0 wt% SiC_{np}, and (c) Ag/5 wt% Al_2O_{3np}/5 wt% SiC_{np} composites are shown in Figure 4. The variations in thermal diffusivity of pure Ag is shown in gradual increase with the increase in the temperature from ambient degree (27° C to 1200°C). The highest thermal diffusivity of 24 mm^2/sec is found on pure Ag. However, the thermal diffusivity of hybrid nanocomposite shows the most negligible value compared to all others. It was due to the effect of phase transformation during high temperatures. It was decided as silver and reinforcement atomic structure [21]. It is distinct

TABLE 5: Intermediate transition zone for unreinforced and reinforced silver matrix composite by differential thermal analysis.

Sample	Descriptions	Intermediate zone temperature °C	Mass loss μV/mg
1	Alloy	850	0.0098
2	Nanocomposite	840	0.0086
3	Hybrid nanocomposite	820	0.0009
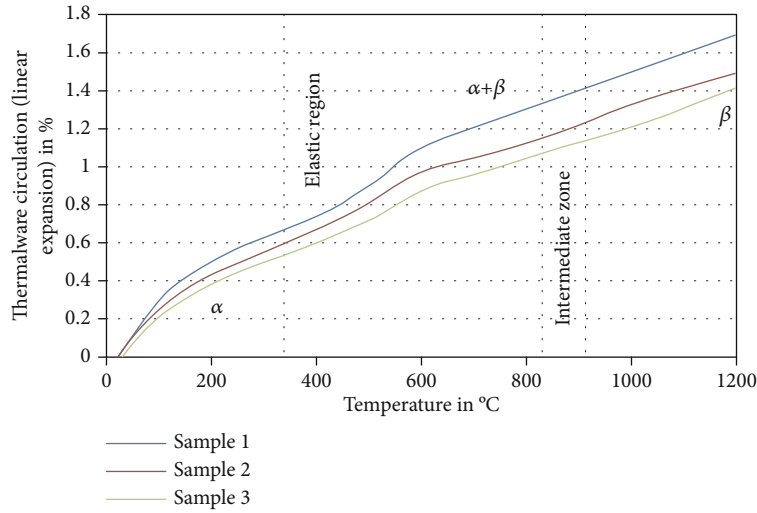
FIGURE 3: Thermal wave circulation (linear expansion and adsorption) phase transformation of silver matrix hybrid nanocomposite.
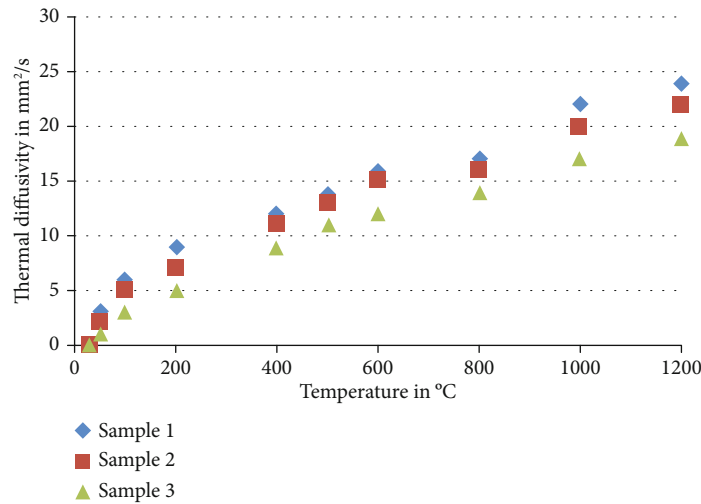
FIGURE 4: Thermal diffusivity of silver matrix hybrid nanocomposite.

to 820°C of the intermediate phase and gets an effective thermal diffusivity of 15 mm^2/sec. While the temperature increases, it has increased in thermal diffusion to 1000°C. It may be varied due to the bonding of the matrix and reinforcements [20, 21].

3.3. Effect of Reinforcements on Frictional Characteristics of Silver Matrix Composites.
The frictional wear loss of unreinforced silver and its composites are shown in Figure 5. The wear loss of silver and its composites are increased linearly with an increase in an applied average load of 10-30 N, respectively. The wear loss of unreinforced silver composite is 10.2 mg on 40 N load under a constant sliding velocity of 0.75 m/sec. At the same time, adding Al$_2$O$_3$ nanoparticles in silver shows a minimum wear loss of 7.1 mg on high load and high sliding speed. The reduced wear loss of the
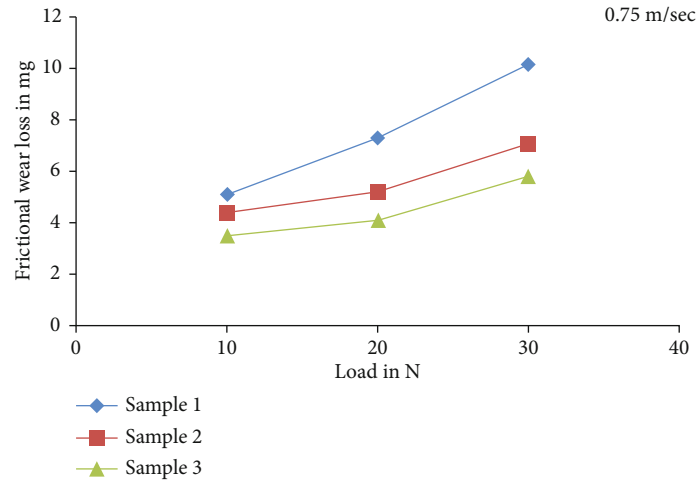
FIGURE 5: Frictional wear loss of silver hybrid nanocomposite.
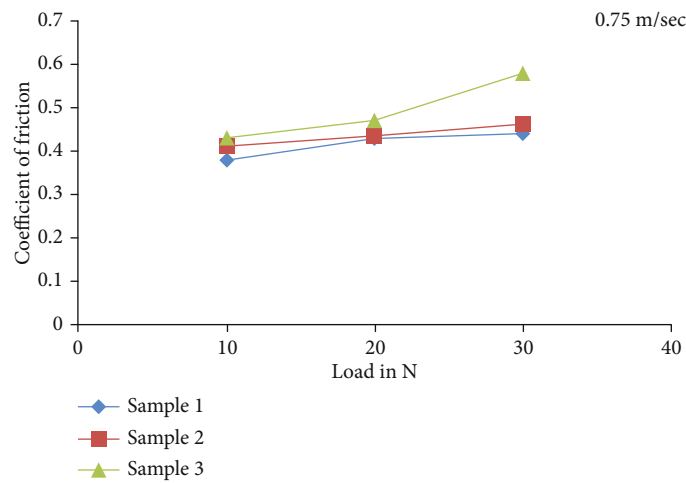
FIGURE 6: Coefficient of friction (COF) of silver hybrid nanocomposite.

composite is mainly attributed to alumina nanoparticles that resist the indentation against the frictional force during high sliding velocity. The alumina and silicon carbide particle combination in the silver matrix has low wear loss compared to all others [30, 31]. The composite contained 5 wt% Al_2O_3/5 wt% SiC 5.8 mg on a 40 N applied load with the frictional force of 23.4 N under 0.75 m/sec. The wear resistance against frictional composite was increased by 56.86% compared to unreinforced silver.

The friction coefficient for silver composites is represented in Figure 6 with different load conditions of 10-30 N at 0.75 m/sec sliding velocity. Sample 1 shows that the COF increases linearly with an increase in load under high sliding velocity. Sample 2 varied from 0.41 to 0.46 with increased content of reinforcements. However, all the test samples were shown increased COF value on the high frictional force. Sample 3 has a maximum COF of 0.58 and improved by 32% compared to sample 1 at 30 N load. It was due to the rigid ceramic particles being diffused within the matrix during high frictional force.
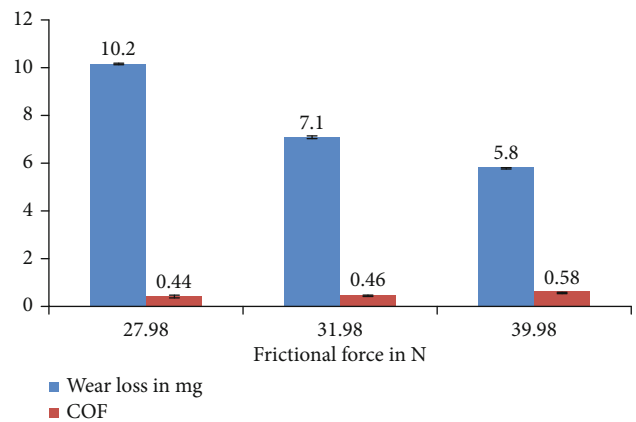
FIGURE 7: Comparisons and effect of the frictional force on wear loss and COF of silver matrix hybrid composite.

Figure 7 illustrates the friction-forced effect on wear loss and coefficient friction of unreinforced and reinforced silver matrix composite. It indicates that composite wear loss decreases gradually with increased frictional force from 27.98 N to 39.98 N. Similarly, the COF curve in Figure 7 represents the improved COF trend on the increased frictional force. However, sample 3 has tribological performance on a 30 N load under 0.75 m/sec sliding speed with 39.98 N frictional force.

4. Conclusions

The silver-based matrix hybrid nanocomposite developed with 5 wt% alumina and 5 wt% silicon carbide nanoparticle via vacuum stir-casting techniques to minimize the casting defect and increase the thermal adsorption composite of the following results are concluded.

(i) The silver matrix hybrid nanocomposite (sample 3) is found to have good thermal characteristics compared to others

(ii) Its intermediate transition zone temperature of 820°C has been adopted for both the heat and cooling phases with a minimum mass loss of 0.009 μV/mg. It saved 16.5% compared to unreinforced cast silver

(iii) The adsorption of hybrid nanocomposite is increased by 30% and thermally stable at higher temperatures, 1000° C

(iv) The adequate thermal wave circulation (linear expansion) of hybrid nanocomposite is 1.42%

(v) The thermal diffusivity of hybrid nanocomposite may be varied due to the bonding strength between the matrix and reinforcements

(vi) Sample 3 is identified as having good wear resistance, and COF has improved by 56.86% and 32% compared to unreinforced silver composite

(vii) It is recommended for automotive friction-bearing applications based on thermal and frictional characteristics

Data Availability

All the data required are available within the manuscript.

Conflicts of Interest

The authors declare no conflicts of interest.

Authors' Contributions

All authors contributed to the study's conception and design. P. Sakthivel is responsible for investigation and validation. J. Phani Krishna is responsible for data collections and executions. R. Venkatesh is responsible for original draft preparations. C. Ramesh Kannan is responsible for methodology and concept. M. Vivekanandan is responsible for for-

mal analysis and review. S. Dhanabalan is responsible for the collection of test results. T. Thirugnanasambandham is responsible for writing and review. Manaye Majora is responsible for supervision and execution of investigation outline. All authors provided language help, writing assistance, and proofreading of the manuscript. All authors read and approved the final manuscript.

References

[1] J. Rodríguez, M. A. Garrido-Maneiro, P. Poza, and M. T. Gómez-del Río, "Determination of mechanical properties of aluminium matrix composites constituents," *Materials Science and Engineering: A*, vol. 437, no. 2, pp. 406–412, 2006.

[2] C. H. Gireesh, K. D. Prasad, and K. Ramji, "Experimental investigation on mechanical properties of an Al6061 hybrid metal matrix composite," *Journal of Composites Science*, vol. 2, no. 3, p. 49, 2018.

[3] C. R. Kannan, R. Venkatesh, M. Vivekanandan et al., "Synthesis and Characterization of Mechanical Properties of AA8014 + Si_3N_4/ ZrO_2 Hybrid Composites by Stir Casting Process," *Advances in Materials Science and Engineering*, vol. 2022, Article ID 9150442, 11 pages, 2022.

[4] M. O. Bodunrin, K. K. Alaneme, and L. H. Chown, "Aluminium matrix hybrid composites: a review of reinforcement philosophies; mechanical, corrosion and tribological characteristics," *Journal of Materials Research and Technology*, vol. 4, no. 4, pp. 434–445, 2015.

[5] S. V. Prasad and R. Asthana, "Aluminum metal-matrix composites for automotive applications: tribological considerations," *Tribology Letters*, vol. 17, no. 3, pp. 445–453, 2004.

[6] P. K. Rohatgi, "Metal matrix composites," *Defence Science Journal*, vol. 43, no. 4, pp. 323–349, 1993.

[7] D. B. Miracle, "Metal matrix composites - from science to technological significance," *Composites Science and Technology*, vol. 65, no. 15-16, pp. 2526–2540, 2005.

[8] A. Macke, B. F. Schultz, and P. Rohatgi, "Metal matrix composites," *Advanced Materials and Processes*, vol. 170, no. 3, pp. 19–23, 2012.

[9] M. Mata and J. Alcalá, "The role of friction on sharp indentation," *Journal of the Mechanics and Physics of Solids*, vol. 52, no. 1, pp. 145–165, 2004.

[10] R. Karthik, K. Gopalakrishnan, R. Venkatesh, A. Mohana Krishnan, and S. Marimuthu, "Influence of Stir Casting Parameters in Mechanical Strength Analysis of Aluminium Metal Matrix Composites (AMMCs)," *Materials Today: Proceedings*, vol. 62, pp. 1965–1968, 2022.

[11] P. Mohanty, R. Mahapatra, P. Padhi, C. H. V. V. Ramana, and D. K. Mishra, "Ultrasonic cavitation: An approach to synthesize uniformly dispersed metal matrix nanocomposites–A review," *Nano-Structures & Nano-Objects*, vol. 23, article 100475, 2020.

[12] Y. Zhan and G. Zhang, "Graphite and SiC hybrid particles reinforced copper composite and its tribological characteristic," *Journal of Mater Science Letters*, vol. 22, no. 15, pp. 1087–1089, 2003.

[13] Y. H. Liang, H. Y. Wang, Y. F. Yang, Y. Y. Wang, and Q. C. Jiang, "Evolution process of the synthesis of TiC in the Cu-Ti-C system," *Journal of Alloys and Compounds*, vol. 452, no. 2, pp. 298–303, 2008.

[14] R. J. Smith, G. J. Lewi, and D. H. Yates, "Development and application of nickel alloys in aerospace engineering," *Aircraft Engineering and Aerospace Technology*, vol. 73, no. 2, pp. 138–147, 2001.

[15] S. P. Rawal, "Metal-matrix composites for space applications," *Journal of Materials Science*, vol. 53, no. 4, pp. 14–17, 2001.

[16] D. H. He and R. Manory, "A novel electrical contact material with improved self-lubrication for railway current collectors," *Wear*, vol. 249, no. 7, pp. 626–636, 2001.

[17] E. W. Roberts, *Space Tribology Handbook*, AEA Technology Plc, Warrington, UK, 3rd edition, 2002.

[18] F. Findik and H. Uzun, "Microstructure, hardness and electrical properties of silver-based refractory contact materials," *Materials and Design*, vol. 24, no. 7, pp. 489–492, 2003.

[19] B. C. Windom, W. G. Sawyer, and D. W. Hahn, "A Raman spectroscopic study of MoS_2 and MoO_3: applications to tribological systems," *Tribology Letters*, vol. 42, no. 3, pp. 301–310, 2011.

[20] J. Wieczorek, T. Maciąg, K. Kowalczyk, and D. Migas, "Evaluation of thermal properties of MMCp composites with silver alloy matrix," *Journal of Thermal Analysis and Calorimetry*, vol. 142, no. 1, pp. 175–182, 2020.

[21] J. Wieczorek, B. Oleksiak, J. Łabaj, B. Węcki, and M. Mańka, "Silver matrix composites structure and properties," *Archives of Metallurgy and Materials*, vol. 61, no. 1, pp. 323–328, 2016.

[22] L. Jian-Guo, "Wettability of silicon carbide by liquid silver and binary silver-silicon alloy," *Materials Letters*, vol. 18, no. 5-6, pp. 291–298, 1994.

[23] Deona and P. K. Rohatgi, "Cast aluminium alloy composites containing copper-coated ground mica particles," *Journal of Materials Science*, vol. 16, no. 6, pp. 1599–1606, 1981.

[24] J. S. Wu, J. F. Li, L. Zhang, and Z. Y. Qian, "Effects of environment on dry sliding wear behavior of silver-copper based composites containing tungsten disulfide," *Transactions of Nonferrous Metals Society of China*, vol. 27, no. 10, pp. 2202–2213, 2017.

[25] Y. Waku and T. Nagasawa, "Future trends and recent developments of fabrication technology for advanced metal matrix composites," *Materials and Manufacturing Processes*, vol. 9, no. 5, pp. 937–963, 1994.

[26] P. S. Bains, S. S. Sidhu, and H. S. Payal, "Fabrication and machining of metal matrix composites: a review," *Materials and Manufacturing Processes*, vol. 31, no. 5, pp. 553–573, 2015.

[27] M. Rashad, F. Pan, Y. Liu et al., "High temperature formability of graphene nanoplatelets-AZ31 composites fabricated by stir-casting method," *Journal of Magnesium and Alloys*, vol. 4, no. 4, pp. 270–277, 2016.

[28] T. Thirugnanasambandham, J. Chandradass, P. B. Sethupathi, and L. J. Martin, "Fabrication and mechanical properties of alumina nanoparticle reinforced magnesium metal matrix composite by stir casting method," in *SAE Technical Paper*, USA, July 2018.

[29] M. O. Shabani, A. A. Tofigh, F. Heydari, and A. Mazahery, "Superior tribological properties of particulate aluminum matrix nano composites," *Protection of Metals and Physical Chemistry of Surfaces*, vol. 52, no. 2, pp. 244–248, 2016.

[30] M. T. Sijo and K. R. Jayadevan, "Analysis of stir cast aluminium silicon carbide metal matrix composite: a comprehensive review," *Procedia Technology*, vol. 24, pp. 379–385, 2016.

[31] A. Mohana Krishnan, M. Dineshkumar, S. Marimuthu, N. Mohan, and R. Venkatesh, "Evaluation of mechanical strength of the stir casted aluminium metal matrix composites (AMMCs) using Taguchi method," *Materials Today: Proceedings*, vol. 62, pp. 1943–1946, 2022.

Research Article

Synthesis, Thermal Adsorption, and Energy Storage Calibration of Polysulfone Nanocomposite Developed with GNP/ CNT Nanofillers

L. Prabhu,[1] R. Saravanan,[2] A. Anderson,[3] A. Senthilkumar ⓘ,[1] V. N. Aneesh,[4] Avinash Malladi ⓘ,[5] A. Mohana Krishnan,[6] and Manaye Majora ⓘ[7]

[1]*Department of Mechanical Engineering, Aarupadai Veedu Institute of Technology, Chennai, 603104 Tamilnadu, India*
[2]*Department of Mechanical Engineering, Saveetha School of Engineering, SIMATS, Chennai, 602105 Tamilnadu, India*
[3]*School of Mechanical Engineering, Sathyabama Institute of Science and Technology, Chennai, 600119 Tamilnadu, India*
[4]*Department of Mechanical Engineering, UKF College of Engineering and Technology, Parippally, 691302 Kerala, India*
[5]*Department of Mechatronics Engineering, ICFAI Tech, ICFAI Foundation for Higher Education, Hyderabad, 501203 Telangana, India*
[6]*Department of Mechanical Engineering, K. Ramakrishnan College of Engineering, Trichy, 621112 Tamilnadu, India*
[7]*Department of Mechanical Engineering, Faculty of Manufacturing, Institute of Technology, Hawassa University, Ethiopia*

Correspondence should be addressed to Manaye Majora; man-buy@hu.edu.et

The growth of polymer-based materials is becoming requisite in various industrial applications like energy storage, automobile, membrane, and orthopaedics, due to advantages over conventional metallic metal, such as less weight, superior corrosion resistance, ease of the process, and good chemical stability. The current research work is to synthesize the polysulfone (PSU) nanocomposite consisting of 2 wt%, 4 wt%, and 6 wt% of graphene nanoplatelets (GNP) and 3 wt%, 5 wt%, and 7 wt% of carbon nanotube (CNT) nanofillers via cast solution technique. The synthesized composite microstructural, heat storage, and thermal adsorption characteristics are studied. The scanning electron microscopic examination for both PSU/GNP and PSU/CNT composites illustrates good interfacial bonded PSU structure with the uniform distribution of GNP and CNT nanofillers. Due to the effect of percolation, the thermal adsorption characteristics and heat storage of PSU nanocomposite were increased progressively with the additions of GNP/CNT. The PSU composite contained 6 wt% GNP and 7 wt% CNT nanofillers, which showed effective thermal conductivity of 1.23 W/m.K and 1.52 W/m.K, which is 1.7 times larger than the unreinforced polysulfone. Interestingly, the increased temperature of the glass transition decreased the thermal expansion of the nanocomposite.

1. Introduction

Generally, polymers are employed broadly in various applications due to their suitability for low cost, lightweight, and good corrosion resistance but have deprived mechanical and thermal properties compared to metallic compounds [1]. At the earliest, In 1990's, traditional filler-reinforced clay compounds and polymer-laid silicate composites have applied in various industry (low load) applications [2, 3]. However, the addition of multiple nanofillers into the polymer layer has good thermal conductivity as well as it has good mechanical properties [4]. Recently, the demand for polysulfone material increased in membrane applications like bioreactors, fuel cells, and food processing and storage due to its superior thermal conductivity [5, 6]. Sohail et al. [7] developed and studied the thermal conductivity effect of ceramic nanofiller bonded polymer nanocomposite. They found the increased thermal on the presence of aluminium nitrides. Weidenfeller et al. [8] synthesized

TABLE 1: Characteristics of polysulfones.

Properties	Density	Hardness	Tensile modulus	Tensile strength	Linear thermal expansion coefficient	Service temperature-air	Deflection temperature at 1.8 MPa	Transmission-visible
Units	g/cc	Hv	GPa	MPa	μm/m$^\circ$C	$^\circ$C	$^\circ$C	%
	1.25	120	2.48	70.3	55.8	141	174	90

TABLE 2: Characteristics of GNP and CNT nanofiller.

Material/ properties	Particle size nm	Density g/cc	Tensile strength GPa	Elastic modulus TPa	Thermal conductivity W/mK
GNP	10-50	0.1	125	1.1	500-600
CNT	10-50	1.74	200	1.7	3000

magnetite (Fe_3O_4) filled polymers for electrical applications. They found increased thermal conductivity on 44 vol% of Fe_3O_4. The polymer-based materials are bonded with copper, magnetite, barite [9], titanium dioxide (TiO_2) and boron nitride [10], CNT/TiO_2 [11], and modified graphene oxide [12, 13]. Among the various investigations, the carbon nanotube (CNT) and graphene nanoplatelet (GNP) bonded polymer systems have good adhesive, enhanced thermal properties, and reliability. It has been used in electronic devices [14–16]. Hu et al. [17] developed GNP/CNT layered polylactic acid nanocomposite for electronic sensing (strain) devices. They reported that both layers in polylactic nanocomposite have good thermal stability. Takenaka and Ichigo [18] reported that the negative or lower thermal expansion of material was estimated easily, and the zero thermal effect of GNP and CNT sensing has been found at an ambient temperature of 25°C. So, the presence of GNP/CNT in a polymer matrix has good thermal sensitivity and is recommended by thermal energy storage applications. However, adding a larger filler in the polymer matrix affected the agglomerate structure and minimized the aspect ratio of surface volume. So, the present study evaluates the microstructure, thermal adsorption, and heat energy storage of polysulfone (PSU) nanocomposite containing 2 wt% to 6 wt% of graphene nanoplatelets (GNPs) and 3 wt% to 7 wt% of carbon nanotube nanofillers with an interval of 2 wt%.

1.1. Selection and Processing of PSU Nanocomposites

1.1.1. Selection of Polymer. The present research polysulfone material is chosen as the primary material due to its transparency, high strength, superior heat resistance, and stability on repeated steam sterilization cycles [19]. It has a suitable glass transition temperature span from 180°C to 250°C. Their characteristics are specified in Table 1.

1.1.2. Selection of Secondary Phase Materials. The graphene nanoplatelets (GNPs) and carbon nanotubes (CNT) were selected as secondary phase materials, and their characteristics are valued in Table 2. Among the various epoxy materials, both effective GNPs and CNT are reinforcements for

improving the material properties like biological and mechanical, thermal, tribological, and electrical [20].

1.2. Processing of PSU Nanocomposites. Figure 1 illustrates the detailed flow processing diagram explaining the concept of pre- and postprocessing of polysulfone nanocomposites containing different weight percentages of GNP/CNT nanofillers.

1.3. Pre- and Postprocessing of PSU Nanocomposites. Based on Stokes' law (equation (1), the essential quantity of polysulfones is bonding on (2 wt%, 4 wt%, and 6 wt %) of GNP along with varying weight percentages (3 wt%, 5 wt%, and 7 wt %) of CNT nanofillers developed via cast solution technique. The combinations of PSU and its reinforcements are mentioned in Table 3. Initially, GNP and CNT are weighted according to Table 2 composition via a digital weighing machine with an accuracy of ±0.001 grams. Similarly, polysulfones are dipped in methyl-2-pyrrolidone solution. Correspondingly, the GNP and CNT are blended with the above matrix. The combinations of polymers with reinforcements are solidified for 120 mins via a probe-type solidifier and continued stirrer action for 1 hour to obtain a homogenous mixture. It helps to minimize the defects on PSU nanocomposites [19]. The stirred PSU/GNP/CNT is mixed with the solution mentioned above to get a homogenous mixture. The solution phase PSU/GNP/CNT is moulded into a desired specific shape. The temperature flow on PSU/GNP/CNT/solution is maintained at 75°C/min, which leads to the evaporation of the solution phase converted into a solid phase. After dry conditions, the prepared nanocomposites' outer thin film layer (less than 2 mm) is detached for further studies.

$$F_d = 6\pi\mu Rv, \tag{1}$$

where F_d is the frictional forced (Stokes drag), μ is the dynamic viscosity, R is the radius of the sphere, and v is the flow velocity.

2. Results and Discussions

2.1. Influences of GNP/CNT on Microstructure Characteristics of PSU Nanocomposite. Figures 2(a)–2(g) represent the SEM micrograph of pure PSU and GNP/CNT bonded PSU nanocomposites. Figure 2(a) shows the slag-free micrograph of a pure PSU matrix. It was observed from Figures 2(b)–2(d) that the detailed constructional view of GNP and its bonding quality of the PSU matrix had enhanced the composite characteristics. The reason for continuous stir action obtained it for
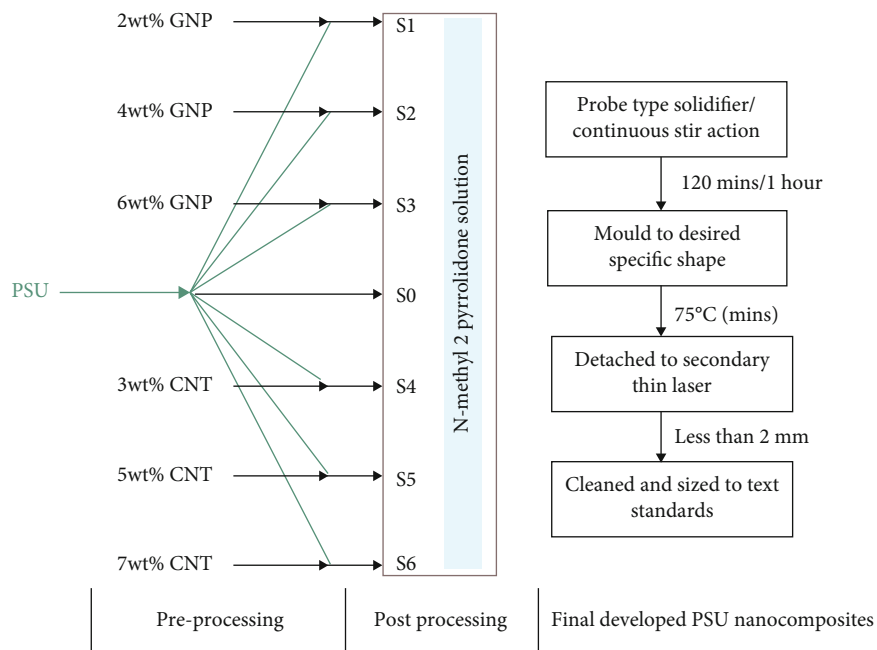
FIGURE 1: Flow processing diagram for PSU nanocomposite fabrication.

TABLE 3: Compositions of PSU nanocomposites.

Elements/sample no.	Units	S0	S1	S2	S3	S4	S5	S6
Composition ratio	wt%	Pure PSU 100/0/0	2 GNP 98/2/0	4 GNP 96/4/0	6 GNP 94/6/0	3CNT 97/0/3	5CNT 95/0/5	7CNT 93/0/7
PSU	Grams	100	98	96	94	97	95	93
GNP/CNT	Grams	0	2	4	6	3	5	7

more than 5 hrs. Similarly, Zhang et al. [13] obtained a fine crystal graphene oxide structure on a PET matrix.

Figure 2(a) indicates the quality connection between PSU and GNP. The fine mesh connection on GNP bonded in the PSU matrix is uniformed. The structure leads to enhance thermal performance as well as reduces the mass during heat storage. Similarly, Figures 2(c) and 2(d) illustrate that the wire mesh connection with good interfacial bonding results in increased thermal conductivity and reduced composite mass loss.

Figure 2(e) shows an effective mesh with PSU composite that resulted in a unique thermal effect on high-temperature storage [5, 6]. Figures 2(e)–(g) show the detailed multilayer mesh connection between PSU and CNT at approximately 15 nm. The fine, coarse multimesh connection was obtained using methyl-2-pyrrolidone solvent at 75°C for 1 hr. The homogenous mixing of the second phase into the primary PSU phase on the solvent medium of methyl-2-pyrrolidone was successfully obtained by continuous stir action under 1 hr at 75°C.

The CNT nanofillers make good interfacial strength and lead to a better conduction path with the enhanced thermal stability of the energy storage system. The multidirectional PSU and CNT network formation was closely observed and illustrated in Figure 2(g). The firm matrix surfaces were attracted between the PSU and CNT filler on lower rate dispersion during high thermal conductivity [21].

2.2. Effect of PSU/GNP and PSU/CNT on Thermal Properties of PSU Nanocomposites

2.2.1. Thermal Conductivity.
Figures 3(a) and 3(b) illustrate the thermal conductivity variations of PSU/GNP and PSU/CNT nanocomposites with their nanofiller concentration. The actual thermal conductivity of PSU nanocomposites was evaluated by a thermocouple-based sensor system configured with digital indication. The measured thermocouple results were compared with the theoretical result to identify the enhancement of thermal conductivity [22, 23]. The effective temperature flow was applied for mono and hybrid filler bonded polymer composite. It was observed from Figure 3 graph that filler concentration's effect on PSU nanocomposite thermal conductivity was closer to the theoretical value. However, the thermal conductivity of PSU/GNP and PSU/CNT nanocomposite was gradually increased with an increase in filler concentration. It was due to the reason that a multiphase interconnection network may lead to enhancing the filler concentration, resulting in increased thermal conductivity. However, the PSU nanocomposite containing 0, 2, 4, and 6 wt% of GNP showed an increased thermal conductivity of 0.45 W/

(a)

(b)

(c)

(d)

(e)

(f)
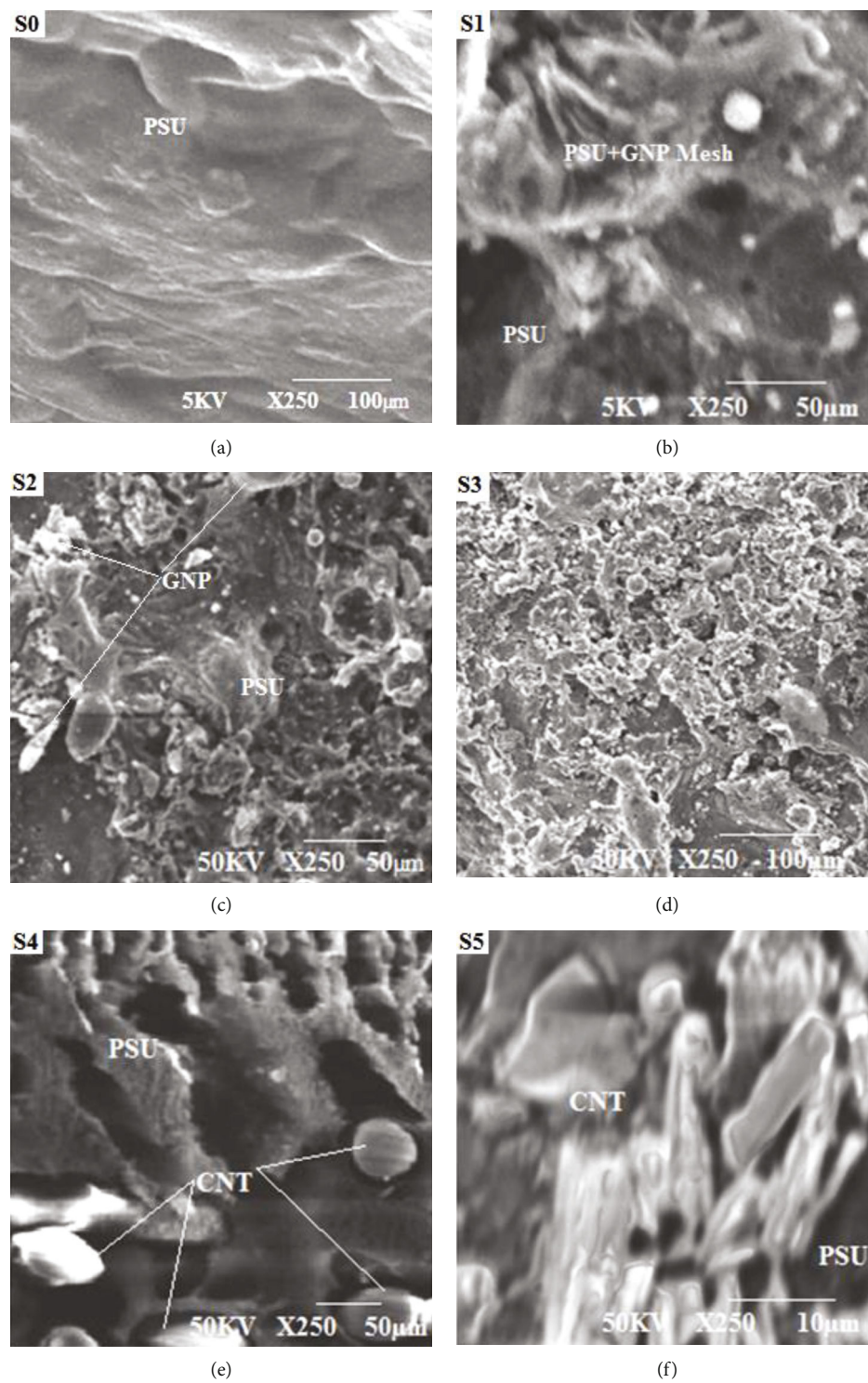
Figure 2: Continued.
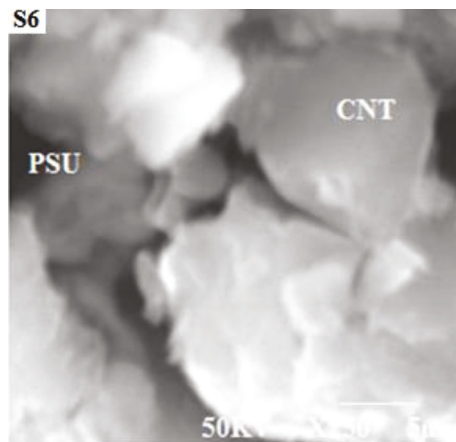
(g)

Figure 2: (a) SEM micrograph of pure PSU. (b) SEM micrograph of PSU/2 wt% GNP. (c) SEM micrograph of PSU/4 wt% GNP. (d) SEM micrograph of PSU/6 wt% GNP. (e) SEM micrograph of PSU/3 wt% CNT. (f) SEM micrograph of PSU/5 wt% CNT. (g) SEM micrograph of PSU/7 wt% CNT.
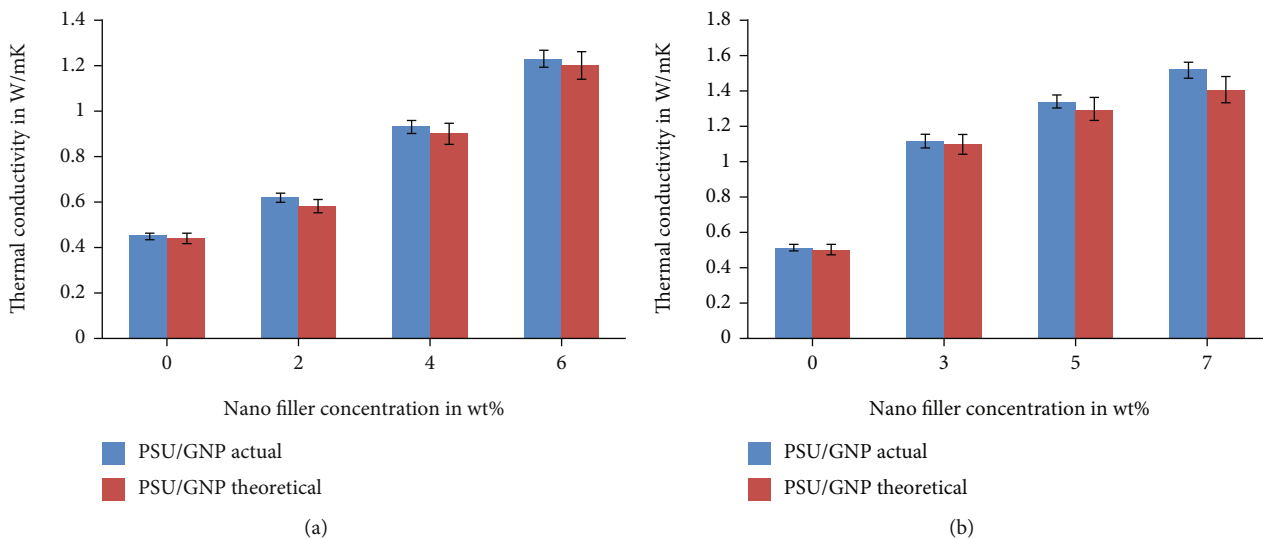
Figure 3: (a) Effect of GNP nanofiller concentration on thermal conductivity of PSU composite compared with the theoretical value. (b) Effect of CNT nanofiller concentration on thermal conductivity of PSU composite compared with the theoretical value.

mK, 0.62 W/mK, 0.93 W/mK, and 1.23 W/mK, respectively. It was because GNP can withstand high temperatures [12, 17].

It was observed from Figure 3(a) that the thermal conductivity of PSU/GNP nanocomposite gradually increased with an increase in GNP nanofiller. The transmission of higher heat energy requires good interfacial connection [20, 23]. The maximum thermal transient effect of 1.23 W/mK was found on 6 wt% GNP bonded PSU nanocomposite. It was 1.7 times higher than the thermal conductivity of the pure PSU matrix. It happened due to the uniform distribution of GNP connection in the PSU matrix, and effective interfacial bonding may be stable in higher temperatures. The proof of multi-interfacial connection is illustrated in Figures 2(b)–2(d).

The thermal conductivity of PSU/CNT nanocomposite was increased by 12.5% approximately as compared to

PSU/GNP composite. It was due to their combination of PSU and CNT. Generally, PSU is stable on repeated seam sterilization and has high heat resistance with a glass transition temperature span from 180°C to 250°C, and CNT has good thermal conductivity in different modes [24]. It is noted in Figure 3(b) that the composite's thermal conductivity increased from 0.52 W/mK to 1.52 W/mK on 0, 3, 5, and 7 wt% of CNT. The effective connection of CNT in the PSU matrix accumulated the heat energy effectively. A similar trend was reported by the researcher [22]. The effective connections of PSU and CNT are evidenced in Figures 2(e)–2(g).

2.2.2. Thermal Effusivity. Figure 4 shows the thermal effusivity of PSU/GNP and PSU/CNT nanocomposite. The GNP and CNT represent a gradual improvement in thermal effusivity on the PSU matrix. The additions of GNP in the PSU
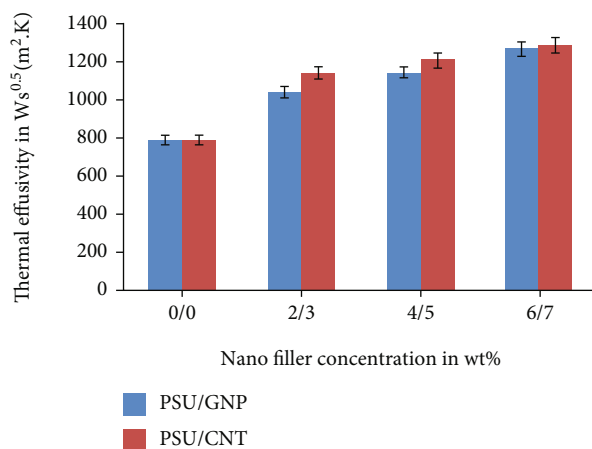
FIGURE 4: Effect of GNP and CNT nanofiller concentration on thermal effusivity of PSU composite.
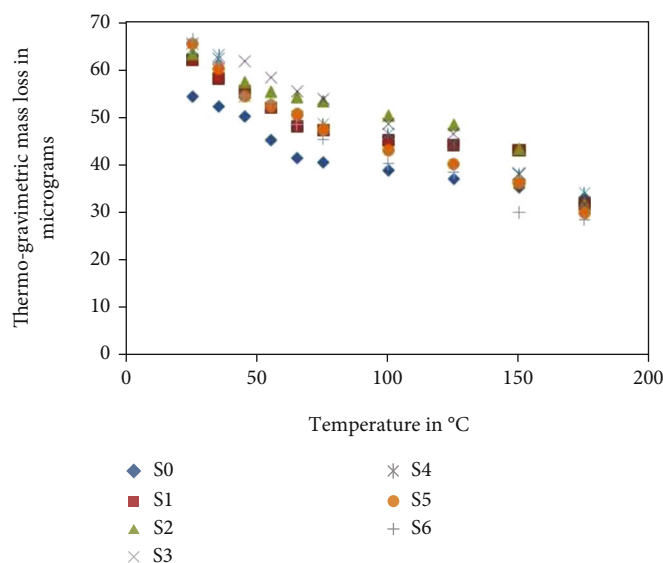
FIGURE 5: Mass loss during thermal adsorption effect of PSU nanocomposite.

matrix increased progressively from 790, 1041, 1145, and 1273 $Ws^{0.5}/m^2.K$. The heat flow path of PSU/GNP nanocomposite compared with PSU/CNT nanocomposite exposed a superior effusivity value of 1290 $Ws^{0.5}/m^2.K$ on 7 wt% of CNT nanofiller. It was due to the number of CNT nanofiller links increased in the PSU matrix. Kim et al. [25] reported that the increased interaction between the polymer matrix and secondary phase leads to enhanced thermal properties. Adding a higher nanofiller in the PSU matrix increases the thermal storage and transfer of charge electrons. So, it was proved that the thermal performance of composites was decided by the secondary phase volume, adhesion characteristics, and aspect ratio. The GNP and CNT are talented in high mixing ratios, resulting in high energy storage and good thermal conductivity. However, the concentration of both GNP and CNT in the PSU matrix increased by 61% and 63%, respectively.

2.3. Effect of Thermal Adsorption. The thermal behaviour of GNP/CNT with their composition effect for thermal adsorption properties of PSU nanocomposites were evaluated by thermo-gravimetric apparatus configured with the temperature range from 25°C to 700°C. The present work on the thermal adsorption effect on mass loss on PSU nanocomposites was estimated by 25°C to 175°C at 30 mins, which is shown in Figure 5. During this period, each stage of temperature adsorption behaviour on mass loss of PSU nanocomposite was measure via thermocouple sensor assisted with a digital system. It helps to identify the physical change of the composite [26]. The developed PSU nanocomposite (S0, S1, S2, S3, S4, S5, and S6) mass loss effect during the thermal adsorption study result is shown in Figure 5. It was observed in Figure 5 that the mass loss of PSU and its nanocomposites is showed downtrend with increased temperature. However, the mass loss curve of PSU and its

GNP/CNT nanocomposite shows minor decomposition that occurs during the high temperature of 175° at 25°C/min constant heat flow. The PSU composite contains 6 wt% GNP and 7 wt% CNT, showing enhanced thermal stability with minor mass loss of 31.8 μg and 28.4 μg, so that composite may damage the PSU matrix at low-level decomposition which may not be directed to reduce the properties of composite that are proved.

3. Conclusions

The effort of the current research work is forced to successfully develop the polysulfone nanocomposites containing 2 wt%, 4 wt%, and 6 wt% of GNP and 3 wt%, 5 wt%, and 7 wt% of CNT via cast solution technique to obey Stokes' law. The following conclusions are made below.

(1) The scanning electron microscope micrograph of both PSU/GNP and PSU/CNT composites was studied, and their micrographs are illustrated in Figures 2(a)–2(g). It reveals that the GNP and CNT nanofillers were uniformly distributed and made good interfacial bonding between PSU/GNP and PSU/CNT

(2) The CNT: the various/multiple links identified between GNP/PSU and CNT/PSU nanocomposite. PSU found good thermal behaviour as compared to GNP/PSU and PSU

(3) The composite containing 7 wt% of CNT nanofiller found superior thermal conductivity of 1.41 W/m K and high thermal effusivity of 1290 Ws$^{0.5}$/m^2.K. It increased 1.7 times and 23.5% of the heat storage system compared to the PSU matrix and PSU/ 6 wt% GNP nanocomposite

(4) The mass loss during the effect of thermal adsorption during the evaluation of PSU and its nanocomposite under 25°C-175°C at 25°C heat flow showed a minimum decomposition rate with little physical change. The composite contained 6 wt% of GNP and 7 wt% of CNT, showing 31.8 μg and 28.4 μg

(5) Hence, the experimental research on PSU nanocomposite found that CNT has good thermal stability and may be applied to energy storage applications like food storage

Data Availability

All the data required are available within the manuscript.

Conflicts of Interest

The authors declare no conflicts of interest.

References

[1] H. Chen, V. V. Ginzburg, J. Yang et al., "Thermal conductivity of polymer-based composites: fundamentals and applications," *Progress in Polymer Science*, vol. 59, pp. 41–85, 2016.

[2] M. Galimberti, *Rubber Clay Nanocomposites: Science, Technology and Applications*, John Wiley &Sons, Hoboken, 1st edition, 2011.

[3] D. E. Kherroub, M. Belbachir, and S. Lamouri, "Nylon 6/clay nanocomposites prepared with Algerian modified clay (12-maghnite)," *Research on Chemical Intermediates*, vol. 41, no. 8, pp. 5217–5228, 2015.

[4] N. Saba and M. Jawaid, "A review on thermomechanical properties of polymers and fibers reinforced polymer composites," *Journal of Industrial and Engineering Chemistry*, vol. 67, pp. 1–11, 2018.

[5] S. Bose, T. Kuila, T. X. H. Nguyen, N. H. Kim, K. T. Lau, and J. H. Lee, "Polymer membranes for high temperature proton exchange membrane fuel cell: recent advances and challenges," *Progress in Polymer Science*, vol. 36, no. 6, pp. 813–843, 2011.

[6] A. Davis, "Thermal stability of polysulphone," *Macromolecular Chemistry and Physics*, vol. 128, no. 1, pp. 242–251, 1969.

[7] O. B. Sohail, P. Sreekumar, S. De et al., "Thermal effect of ceramic nanofiller aluminium nitride on polyethylene properties," *Journal of Nanomaterials*, vol. 2012, Article ID 250364, 7 pages, 2012.

[8] B. Weidenfeller, M. Höfer, and F. R. Schilling, "Thermal and electrical properties of magnetite filled polymers," *Composites. Part A, Applied Science and Manufacturing*, vol. 33, no. 8, pp. 1041–1053, 2002.

[9] B. Weidenfeller, M. Höfer, and F. R. Schilling, "Thermal conductivity, thermal diffusivity, and specific heat capacity of particle filled polypropylene," *Composites. Part A, Applied Science and Manufacturing*, vol. 35, no. 4, pp. 423–429, 2004.

[10] Y. Yang, P. Wang, and Q. Zheng, "Preparation and properties of polysulfone/TiO$_2$ composite ultrafiltration membranes," *Journal of Polymer Science Part B: Polymer Physics*, vol. 44, no. 5, pp. 879–887, 2006.

[11] T. An, L. Sun, G. Li, and S. Wan, "Gas-phase photocatalytic degradation and detoxification of *o* -toluidine: Degradation mechanism and Salmonella mutagenicity assessment of mixed gaseous intermediates," *Journal of Molecular Catalysis A: Chemical*, vol. 333, pp. 128–135, 2010.

[12] L. Xing, Y. Wang, S. Wang et al., "Effects of modified graphene oxide on thermal and crystallization properties of PET," *Polymers*, vol. 10, no. 6, p. 613, 2018.

[13] Y. Zhang, Y. Wang, H. Li et al., "Fluorescent SiO2@Tb3+(PET-TEG)3phen hybrids as nucleating additive for enhancement of crystallinity of PET," *Polymers*, vol. 12, no. 3, p. 568, 2020.

[14] C. Wong and R. S. Bollampally, "Thermal conductivity, elastic modulus, and coefficient of thermal expansion of polymer composites filled with ceramic particles for electronic packaging," *Journal of Applied Polymer Science*, vol. 74, no. 14, pp. 3396–3403, 1999.

[15] X. Lu and G. Xu, "Thermally conductive polymer composites for electronic packaging," *Journal of Applied Polymer Science*, vol. 65, no. 13, pp. 2733–2738, 1997.

[16] A. Rakita, N. Nikolić, M. Mildner, J. Matiasek, and A. Elbe-Bürger, "Re-epithelialization and immune cell behaviour in an *ex vivo* human skin model," *Scientific Reports*, vol. 10, no. 1, pp. 1–14, 2020.

[17] C. Hu, C. Z. Li, Y. Wang et al., "Comparative assessment of the strain sensing behaviors of polylactic acid nanocomposites: reduced graphene oxide or carbon nanotubes," *Journal of Materials Chemistry C*, vol. 5, no. 9, pp. 2318–2328, 2017.

[18] K. Takenaka and M. Ichigo, "Thermal expansion adjustable polymer matrix composites with giant negative thermal expansion filler," *Composites Science and Technology*, vol. 104, pp. 47–51, 2014.

[19] F. Parodi, *'Polysulfones - an Overview - Comprehensive Polymer Science and Supplements', Polysulfones (PS) constitute a large family of biomaterials*, Science direct, 2018.

[20] C. Ramesh Kannan, R. Venkatesh, and M. Vivekanandan, "Synthesis and characterization of mechanical properties of AA8014 + Si3N4/ZrO2 hybrid composites by stir casting process," *Journal of Advances in Materials Science and Engineering*, vol. 2022, article 9150442, 11 pages, 2022.

[21] N. A. Kotov, "Carbon sheet solutions," *Nature*, vol. 442, no. 7100, pp. 254-255, 2006.

[22] K. Raza, M. U. Siddiqui, A. F. M. Arif, S. S. Akhtar, and A. S. Hakeem, "Design and development of thermally conductive hybrid nano-composites in polysulfone matrix," *Polymer Composites*, vol. 40, no. 4, pp. 1419–1432, 2019.

[23] H. M. Irshad, A. S. Hakeem, K. Raza, M. A. TurkiNabiehBaroud, S. A. Ehsan, and M. S. Tahir, "Design, development and evaluation of thermal properties of polysulphone–CNT/GNP nanocomposites," *Nanomaterials*, vol. 11, no. 8, p. 2080, 2021.

[24] R. Arivazhagan and S. Baskar, "Performance analysis of steam generators in thermal power plant," in *AIP Conference Proceedings*, vol. 2473, Ariyalur, Tamilnadu, India, 2022.

[25] H. S. Kim, J. U. Jang, J. Yu, and S. Y. Kim, "Thermal conductivity of polymer composites based on the length of multi-walled carbon nanotubes," *Composite Part B Engineering*, vol. 79, pp. 505–512, 2015.

[26] J. Isaac Premkumar, A. Prabhu, V. Vijayan, A. Godwin Antony, and R. Venkatesh, "Combustion analysis of biodiesel blends with different piston geometries," *Journal of Thermal Analysis and Calorimetry*, vol. 142, no. 4, pp. 1457–1467, 2020.

$\mathcal{S}$SAGE
Publishing

Research Article

Inorganic Adsorption on Thermal Response and Wear Properties of Nanosilicon Nitride-Developed AA6061 Alloy Nanocomposite

F. Mary Anjalin,[1] A. Mohana Krishnan,[2] G. Arunkumar,[3] K. Raju ⓘ,[4] M. Vivekanandan,[5] S. Somasundaram,[6] T. Thirugnanasambandham ⓘ,[7] and Elangomathavan Ramaraj ⓘ[8]

[1]Department of Physics, Saveetha School of Engineering, SIMATS, Chennai, 602105 Tamilnadu, India

[2]Department of Mechanical Engineering, K.Ramakrishnan College of Engineering, Trichy, 621112 Tamilnadu, India

[3]Department of Mechanical Engineering, K.Ramakrishnan College of Technology, Trichy, 621112 Tamilnadu, India

[4]Department of Mechanical Engineering, M.Kumarasamy College of Engineering, Karur, 639113 Tamilnadu, India

[5]Department of Mechanical Engineering, Kongunadu College of Engineering and Technology, Trichy, 621215 Tamilnadu, India

[6]Department of Mechanical Engineering, Sri Venkateswara Institute of science and technology, Thiruvallur, 631203 Tamil Nadu, India

[7]Department of Mechanical Engineering, Ponnaiyah Ramajayam Institute of Science and Technology, Thanjavur, 613203 Tamil Nadu, India

[8]Department of Biology, College of Natural and Computational sciences, Debre Tabor University, Amhara region, Ethiopia

Correspondence should be addressed to Elangomathavan Ramaraj; elanmath@dtu.edu.et

Inorganic-based ceramic reinforcements are promising superior thermal behaviour and are lightweight and developed with aluminium alloy matrix for automobile applications. The AA6061 alloy nanocomposite containing 0 wt%, 4 wt%, 8 wt%, and 12 wt% of silicon nitride nanoparticles(50 nm) was synthesized by stir cast. The influences of thermal adsorption on silicon nitride (nano) additions, density, thermal response, hardness, and wear characteristics of AA6061 matrix nanocomposites are studied. Based on the rule of mixture, the density of nanocomposites is evaluated. The differential thermal and thermogravimetric analysis techniques are used to find the thermal response nanocomposite. The differential scanning calorimeter is used to find the heat flow between 400°C and 700°C. The micro Vickers hardness and wear characteristics of AA6061 nanocomposite were experimentally investigated by ASTM E384 and ASTM G99-05 standards. The adsorption of inorganic nanosilicon nitride particles (12 wt%) in AA6061 alloy showed a decreased mass loss with increased temperatures 0° to 700°C. The differential thermal analysis of nanocomposite reveals the transformation of solid-to-liquid phase under high temperature (528°C).

1. Introduction

A matrix material is becoming essential in Metal Matrix Composites (MMCs) bonded with different reinforcements like organic and inorganic to obtain specific thermal, mechanical, and tribological characteristics. According to the past fifty years survey by Pradeep et al. [1], the demand for MMC's cast increased from 0 to 10 mega kilograms yearly. Commonly, the MMCs are divided into three categories like Aluminium Matrix Composite (AMC), Titanium Matrix Composite (TMC), and Magnesium Matrix Composite (MMC). Mainly, various researchers designated and investigated aluminium and its alloy-based matrix materials due to its exhibited mechanical, electrical, thermal, and corrosion resistance properties, which have been prominent substitutions of conventional matrix materials as listed above. However, it has reduced wear and thermal stability in the applications of high-temperature circumstances.

Based on previous literature reported by Sharma [2] and Shalaby et al. [3], the aluminium alloy materials were retained by aerospace and automotive (engine piston) applications and the materials undergone high thermal stress. While improving the thermal stability and withstanding high thermal stress, it could be added with secondary reinforcement phases like borides (SiB_3 and TiB_2), carbides (SiC and TiC), nitrides (Si_3N_4 and BN), and oxides (Al_2O_3 and TiO_2) grant to higher isotropic characteristics [4–8]. Based on the above literature review, it was identified by nitride-based ceramic-reinforced developed AMC has good thermal stability and is suitable for high-temperature applications. Ramesh et al. [9, 10] studied the physical and mechanical performance of sintered AA6061/Si_3N_4 composite. They reported that the increased weight percentages of Si_3N_4 (10 wt%) in AA6061 alloy showed an excellent tensile strength of 217 Mpa. Bai et al. [11] developed AMC with Al_2O_3/25wt% Si_3N_4 composite and found more pores on grain boundary and increased density due to increased wt% of (25 wt%) Si_3N_4. Fayomi et al. [12] fabricated and studied the microstructural, mechanical, and electrical properties of ZrB_2/Si_3N_4-reinforced aluminium alloy (AA8011) hybrid composite via the double-step stir cast technique. The optical microscope showed uniform distribution of multireinforcement in the AA8081 matrix. It has helped to improve the performance of the composite.

Similarly, the double-step stir cast technique increases wettability, and particle distribution may vary due to the selection of input process parameters. Among the various combinations, silicon nitride owing excellent thermal stability under elevated temperatures (27°C) reported by Zhu et al. [13]. Silicon nitride-bonded aluminium alloy composites were prominently used in high friction and temperature applications like bearings, turbine blades, and heat exchangers [14]. The abovementioned processing techniques and their effect on reinforcement in aluminium alloy matrix properties were explained in detail. It was found that the AMCs are developed by liquid state stir cast technique to facilitate lightweight with complex shape components on low processing cost. Han et al. [15] found that the Si_3N_4 reinforced with an aluminium alloy matrix resulted in good thermal shock resistance, superior thermal conductivity, and excellent wear resistance properties. It has been noted from various kinds of literature that there have few reports available on AMCs with Si_3N_4 nanocomposite manufacturing by liquid state stir cast. The present research is to develop AA6061/Si_3N_4 nanocomposite with improved density, hardness, wear resistance, and thermal adsorption properties.

2. Experimental Details

2.1. Choice of Matrix and Reinforcements.
Aluminium alloy (AA6061) was chosen as the matrix material. It contains 1% magnesium and 0.6% silicon as major constitution having low density (2.70 g/cc), high strength, good thermal conductivity (160 W/m.K), and excellent corrosion resistance [16]. The chemical constitutions of AA6061 alloy are mentioned in Table 1.

The inorganic 50 nm silicon nitride (Si_3N_4) particles were chosen as reinforcement to obtain a better thermal response and wear properties [15]. The physical, mechanical and thermal characteristics of AA6061 and Si_3N_4 are shown in Table 2.

2.2. Processing Techniques of AA6061 Alloy Nanocomposite.
Figures 1(a) and 1(b)illustrate the fabrication setup and flow processing chart for AA6061 alloy nanocomposite fabrication. Initially, the prepared AA6061 alloys are placed in a vortex crucible connected to an electrical furnace. The placed aluminium alloy was preheated to a red hardness temperature of 350°C for 20 mins and then the electrical furnace temperature was hiked to 750°C. It results in the AA6061 alloys melting at the liquid stage. After the temperature of the furnace was reduced to 550°C at 30 mins like semisolid condition and the molten metal was stirred with a graphite twin blade at 600 rpm revealed that the moisture content of the metal was removed. It may lead to a decrease in the porosity of the composite. The externally muffle furnace-preheated (300°C) Si_3N_4 nanoparticles are fed manually via feeder arrangement into a crucible chamber and mixed with molten AA6061 alloy via continuous mechanical stirrer action with an applied stir speed of 600 rpm at 30 mins. It resulted in increased uniform particle distribution and decreased voids [17]. Finally, the mixed molten AA6061 alloy and silicon nitrides were supplied to the casting die at 600°C. The developed composites are cooled by natural convection. The weight percentages of AA6061/Si_3N_4 nanocomposites are mentioned in Table 3. The developed AA6061 nanocomposite is sized as per test standards. A detailed phase transformation diagram for aluminium alloy (AA6061) nanocomposites is presented in Figure 2.

2.3. Discussions of Test Results.
The advanced cast aluminium alloy (AA6061) and silicon nitride nanoparticle-reinforced ASTM test standards evaluated AA6061 alloy nanocomposites and their values were mentioned in Table 4. It was found that the density, micro Vickers hardness, and thermal performance of composites were increased. The porosity and wear rate were decreased with improved content of silicon nitride particles.

2.4. Effect of Si_3N_4 on Density and Porosity of AA6061 Alloy Nanocomposites.
Figure 3 represents the density and porosity level for liquid state stir cast-developed AA6061 alloy and its AA6061/Si_3N_4 nanocomposite. It was noted from Figure 3 that the density of composites was increased and the porosity of the composite was decreased by the additions of Si_3N_4 on the AA6061 alloy matrix. So the density of the composite was inversely proportional to the porosity of the composite. The density of cast AA6061 alloy was 2.67 g/cc and 4 wt% Si_3N_4 showed 2.785 g/cc. While the inclusions of reinforcement may increase the density of the composite, meantime, the porosity of the composite was reduced from 1.15% to 1.03%.

Further inclusions of (8 wt% and 12 wt%) silicon nitrides into aluminium alloy (AA6061) matrix resulted in improvement in (2.804 g/cc and 2.832 g/cc) density of nanocomposite and obeyed the rule of mixture. The porosity of AA6061 alloy and its Si_3N_4-reinforced nanocomposites is measured by the

TABLE 1: Chemical constitutions of AA6061 alloy.

Constitutions	Al	Mg	Si	Fe	Cu	Cr	Zn	Ti	Mn
Percentage	96.20	1.00	0.80	0.70	0.40	0.35	0.25	0.15	0.15

TABLE 2: Properties of AA6061 alloy and Si_3N_4.

Properties	Density	Young's modulus	Tensile strength	Melting temperature	Thermal conductivity	Linear thermal expansion coefficient	Specific heat capacity
	g/cc	GPa	MPa	°C	W/m.K	—	—
AA6061	2.7	68	124-290	585	151-202	2.32×10^{-5}	897 J/kg.K
Si_3N_4	3.21	310	—	1600 (inert)	21	4.3	0.7 J/g°C
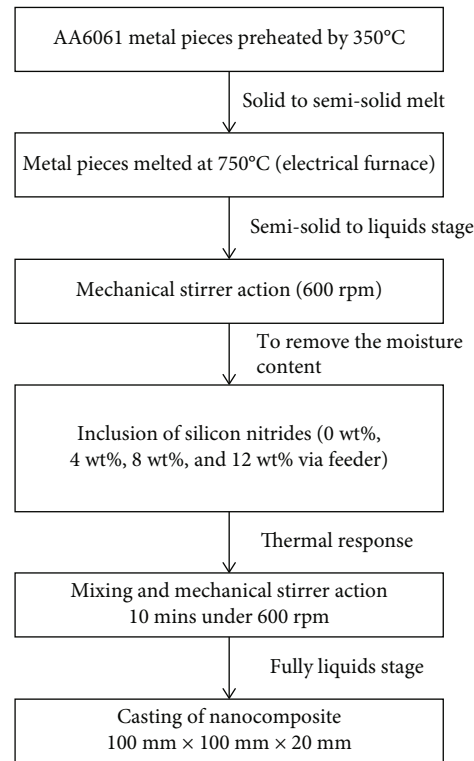
FIGURE 1: Aluminium-melting furnace (a) actual fabrication setup and (b) flow process chart for AA6061 alloy nanocomposites.

TABLE 3: Weight percentages of matrix and reinforcements.

Sample	Constitutions of composites in weight percentages (wt%)	
	AA6061	Si_3N_4
A	100	0
B	96	4
C	92	8
D	88	12

principle of Archimedes as referred from Equation (1). Its values are represented in Figure 3 bar chart-coloured red. It has been observed from Figure 3 bar chart that the level of porosity was decreased with increased content of reinforcement. It was due to continuous stir action during the semisolid

stage with a maintained temperature of 300°C to 528°C. Similarly, Fayomi et al. [12] reported that the constant stir speed developed by aluminium alloy composite has less porosity and enhanced mechanical properties. The nanocomposite contained 12 wt% of silicon nitrides and was found at the minor porosity level of 0.88%. It was identified that the porosity of the composite decreased by 23.47% compared to cast AA6061 alloy.

$$\text{Level of porosity in\%} = (1) - \left\{ \frac{\text{Actual density}}{\text{Theoretical density}} \right\} \times 100.$$

(1)

2.5. Effect of Si_3N_4 and Constant Stir Action on the Microstructure of AA6061 Alloy Nanocomposites.
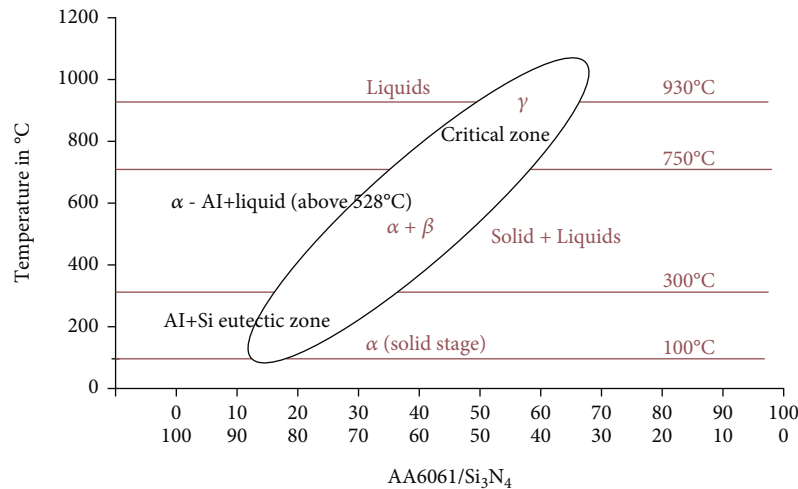
FIGURE 2: Phase transformation diagram for AA6061/Si$_3$N$_4$ nanocomposites with their various phase zone.

TABLE 4: Experimental test results for AA6061 alloy nanocomposite.

Sample	Density in g/cc		Porosity In %	Weight loss at 700°C In mg	Heat flow at 700°C In mW	Micro Vickers hardness In Hv	Wear rate (80 N) In $\times 10^{-5}$ m^3/nm
	Theoretical	Actual					
A	2.701	2.67	1.15	45.12	4	29	13.5
B	2.813	2.784	1.03	123.76	5	38	12.8
C	2.832	2.804	0.99	115.29	7	42	11.6
D	2.857	2.832	0.88	84.62	9	46	10.7
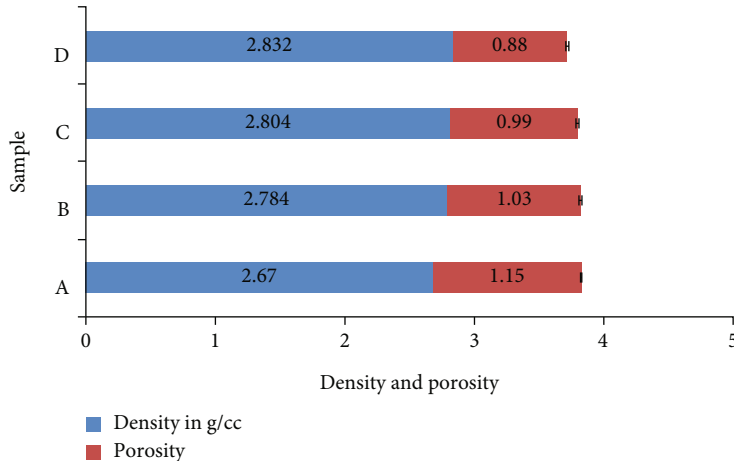
FIGURE 3: Density and porosity of AA6061/Si$_3$N$_4$ nanocomposite.

Figures 4(a)–4(d) illustrate the scanning electron microscope image of AA6061 alloy and 4 wt%, 8 wt%, and 12 wt% Si$_3$N$_4$-reinforced AA6061 alloy nanocomposites. Figure 4(a) shows a clear view of the microstructure with microspores. It was evidenced by the experimental test results mentioned in Table 4 and its level was represented in Figure 3. The composite contained 4 wt% and 8 wt% of Si$_3$N$_4$ showing uniform nanoparticle distribution in the AA6061 matrix as indicated by a white dot. The enlarged view of Si$_3$N$_4$ nanoparticle presence in the AA6061 alloy matrix is shown in Figure 4(d). It shows good interfacial bonding between AA6061 alloy and Si$_3$N$_4$, resulting in increased mechanical, thermal, and wear resistance proper-

ties. It was due to the applied continuous stir speed of 600 rpm. A similar trend was reported by Fayomi et al. [12] and Chandradass et al. [17] during the evaluation of aluminium alloy (AA8011 and AA6061) composites.

2.6. Effect of Si$_3$N$_4$ on the Thermal Response of AA6061 Nanocomposite. The effect of silicon nitrides on the thermal behaviour of AA6061 alloy and 4 wt%, 8 wt%, and 12 wt% Si$_3$N$_4$-reinforced AA6061 alloy nanocomposite was proficient by using differential thermal and thermogravimetric analysis apparatus. It was evaluated by the temperature range of 0°C to 700°C, as shown in Figures 5(a)–5(d). It

(a)

(b)

(c)

(d)
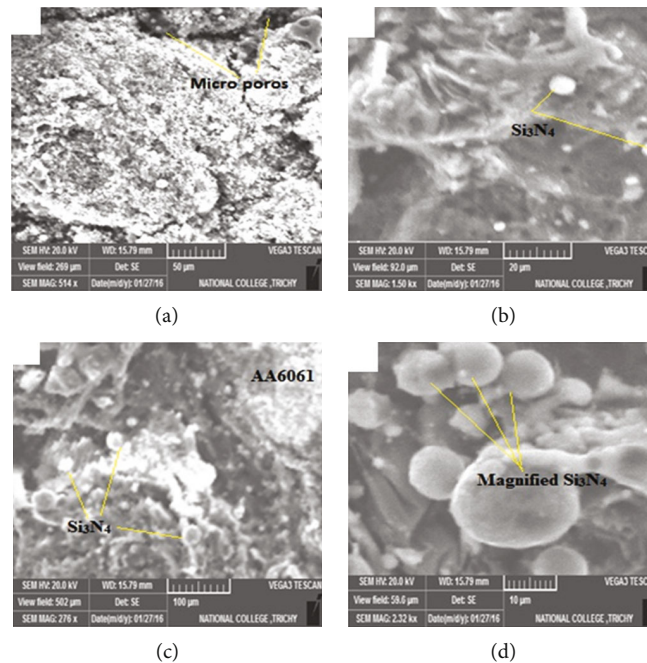
FIGURE 4: SEM image of AA6061 alloy nanocomposites (a) AA6061 alloy, (b) AA6061/4 wt% Si_3N_4, (c) AA6061/8 wt% Si_3N_4, and (d) AA6061/12 wt% Si_3N_4 nanocomposites.

was observed from Figures 5(a)–5(d) that the weight loss of both cast AA6061 alloy and its Si_3N_4-reinforced nanocomposites during the evaluation of a specific temperature range under a steady state heat flow rate of 27°C/min showed a downtrend. It was due to the effect of solubility on the AA6061 matrix at higher temperatures (more than 528°C). The different solubility phase transformation conditions are evidenced in Figure 2.

It was revealed in Figure 5(a) that the thermogravimetric analysis of unreinforced AA6061 alloy shows 45.12 ± 0.03 mg and was reduced to 6.2% compared to ambient temperature mass loss. It was varied due to the different phase temperatures, as evidenced in Figure 2. The incorporation of silicon nitrides into the AA6061 alloy matrix shows higher thermal stability (700°C) with reduced mass loss of 84.62 ± 0.51 mg. It is evidenced from Figures 5(b)–5(d) that the mass loss rate is directly proportional to the temperature, so the thermal performance of the nanocomposite is stable and the material savings is more than 15%. It helps to increase molten metal's fluidity during the composite's casting.

The thermogravimetric analysis helps to increase the material's thermal stability at high temperatures and plays a vital role during solid-to-liquid transition monitoring. Figure 4(d) illustrates that the AA6061 alloy nanocomposite, which contained 12 wt% of Si3N4, increases the temperature of the liquid and acts as a gathering of discontinuous secondary phase has a reduced weight fraction of 84.62 ± 0.51 mg at 700°C. Similarly, Fayomi et al. [18] studied the thermal, electrical, and corrosion characteristics of AA8011/ Si_3N_4 alloy composite and reported that silicon nitrides' presence enhances thermal stability at higher temperature and increase thermal conductivity.

2.7. Effect of Si_3N_4 on Heat Flow of $AA6061/Si_3N_4$ Nanocomposite. Differential thermal analysis for heat flow of aluminium alloy (AA6061) and its Si_3N_4 reinforced AA6061 nanocomposite is shown in Figure 6. The heat flow of AA6061 alloy nanocomposite gradually increases with an increase in the content of silicon nitrides then it was falling at an increased temperature range of 460°C. It is the evidence of heat flow thermometric features at 460°C, 470°C, 476°C, and 480°C on the intermetallic effect of AA6061 alloy during the solid-to-liquid phase transformation as proved in Figure 2 on different weight percentages of silicon nitrides. Arribas and Martín [19] studied and reported that the intermetallic compounds of the composites were located at ϕ-$CuAl_2$ and $Cu_2Mg_8Si_6Al_5$ under 535°C. It shows an Al liquid-phase and Si_3N_4 solid-phase bonded uniformly at 550°C. It is evidenced in Figure 4(d). One researcher used thermal-captured images for routine life prediction [20, 21]. The maximum heat flow of 9 mW was 12 wt% Si_3N_4-reinforced AA6061 nanocomposite. It was increased by 55% and located at 460°C compared to cast AA6061 alloy.

2.8. Effect of Si_3N_4 on the Hardness of $AA6061/Si_3N_4$ Nanocomposite. Figure 7 illustrates the histogram representation of Vickers (micro) hardness number (VHN) of $AA6061/Si_3N_4$ alloy nanocomposite. It is noted from Figure 7 that the VHN of AA6061 alloy is 29 ± 1.2 Hv, the additions of 4 wt%, 8 wt%, and 12 wt% of Si_3N_4 shows a 38 ± 1.13 Hv, 42 ± 0.78 Hv, and 46 ± 1.1 Hv, respectively. The maximum 46 ± 1.1 Hv is observed in 12 wt% Si3N4-reinforced AA6061 alloy nanocomposite due to the uniform distribution of reinforcement in the AA6061 matrix, as proved in Figure 4(d). It has increased by 40% as compared

(a)

(b)

(c)

(d)
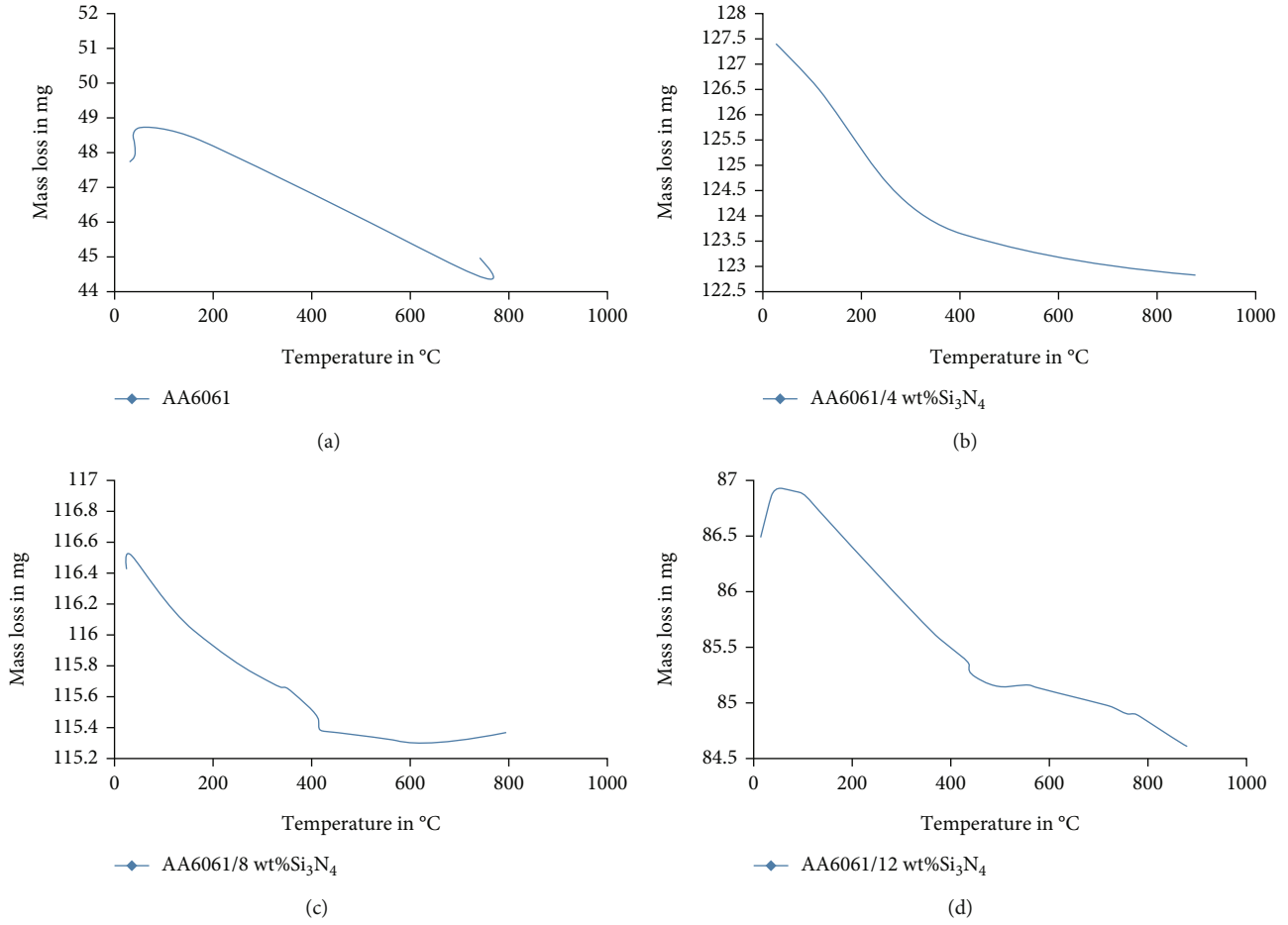
Figure 5: (a) Thermogravimetric analysis for AA6061/0 wt% Si_3N_4. (b) Thermogravimetric analysis for AA6061/4wt% Si_3N_4. (c) Thermogravimetric analysis for AA6061/8wt% Si_3N_4. (d) Thermogravimetric analysis for AA6061/12wt% Si_3N_4.
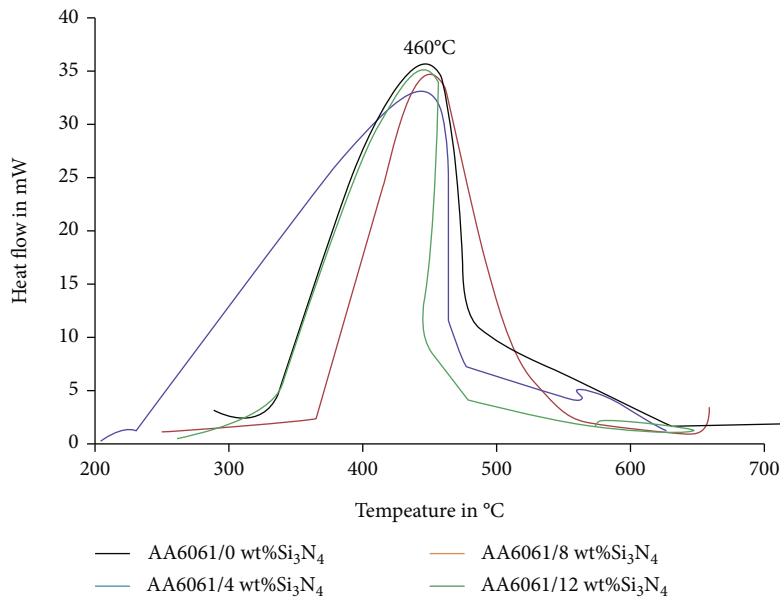
Figure 6: Heat flow analysis of AA6061/Si_3N_4 alloy nanocomposite.
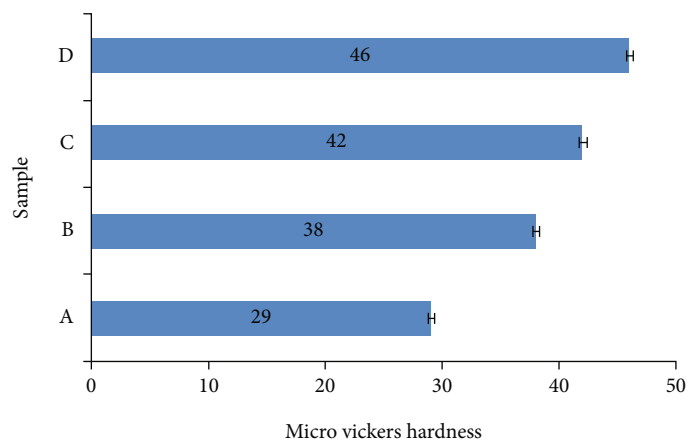
FIGURE 7: Micro Vickers hardness number of AA6061/Si$_3$N$_4$ alloy nanocomposite.
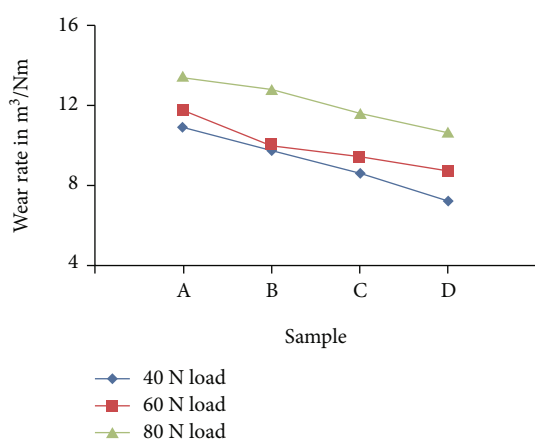
FIGURE 8: Dry-state wear rate of AA6061/Si$_3$N$_4$ alloy nanocomposite (sample A- AA6061/0 wt% Si$_3$N$_4$, B- AA6061/4 wt% Si$_3$N$_4$, AA6061/8 wt% Si$_3$N$_4$, and D- AA6061/12 wt% Si$_3$N$_4$).

to cast AA6061 alloy. The stirring speed of 600 rpm leads to an increase the particle distribution as well as an increased wettability. So the presence of Si3N4 in AA6061 alloy resisted the internal reimbursement during the dimple against the indenter and the dislocations of particles were limited by good bonding strength between the matrix and reinforcements.

2.9. Effect of Si$_3$N$_4$ on Wear Characteristics of AA6061/Si$_3$N$_4$ Nanocomposite. The dry-state wear performance of AA6061 alloy and AA6061/Si$_3$N$_4$ nanocomposites was tested by a pin-on-disc wear test machine attached with carbon steel disc (168 Hv) operated under the sliding velocity of 1.25 m/sec at an applied load 40 N, 60 N, and 80 N, respectively. It is seen from Figure 8 that the wear rate of the composite gradually increased with increasing the applied load under constant sliding velocity. However, increased content (4, 8, and 12 wt%) of Si$_3$N$_4$ in the AA6061 alloy matrix has reduced wear rates on 40, 60, and 80 N loads. The physical presence of nitride-based reinforcements withstands the high-friction load [15]. The least wear rate of 7.23 x 10^{-5} m^3/Nm is found on 12 wt% Si$_3$N$_4$-reinforced AA6061 nano-

composite under an applied load of 40 N at 1.25 m/sec sliding speed. However, the wear rate of nanocomposite is progressively increasing with the load from 40 N to 80 N.

3. Conclusions

The aluminium alloy nanocomposite contains different weight percentages of 0 wt%, 4 wt%, 8 wt%, and 12 wt% of silicon nitrides effectively developed by liquid state stir cat process with an applied stir speed of 600 rpm on the higher melting temperature of 750°C. The following experimental test results are concluded below.

(1) Rule of the mixture and Archimedes Principle studied the density and porosity of AA6061/ Si$_3$N$_4$ alloy nanocomposite, and the nanocomposite containing 12 wt% silicon nitrides found a low porosity level of 0.88% as compared to all other compositions

(2) The phase transformation of AA6061 alloy and the thermal adsorption effect of Si$_3$N$_4$ was plotted and explained. The various phases are illustrated in Figure 2

(3) AA6061/12 wt% Si$_3$N$_4$ alloy nanocomposite was found to have good thermal stability and minimum weight loss of 84.62 ± 0.51 mg at 700°C

(4) The sufficient heat adsorption of AA6061/12 wt% Si$_3$N$_4$ alloy nanocomposite was obtained as 9 mw at 480°C temperature. Its efficiency increased by 55% compared to unreinforced AA6061 alloy

(5) The hardness and wear resistance of AA6061/12 wt% Si$_3$N$_4$ alloy nanocomposite were enhanced to 37% and 20% compared to AA6061 alloy

(6) So, the composite containing 12 wt% of Si$_3$N$_4$ alloy nanocomposite is applied for the automobile—floor and rooftop applications

Data Availability

All the data required are available within the manuscript.

Conflicts of Interest

Authors declare no conflicts of interest.

References

[1] K. P. Rohatgi, P. Ajaykumar, N. M. Chelliahand, and T. P. D. Rajan, "Solidification processing of cast metal matrix composites over the last 50 years and opportunities for the future, the minerals, metals & materials society," *JOM*, vol. 72, no. 8, pp. 2912–2926, 2020.

[2] A. K. Sharma, A. Aherwar, and R. Rimasauskiene, "Matrix materials used in composites: A comprehensive study," *Materials Today: Proceedings*, vol. 21, pp. 1559–1562, 2020.

[3] E. A. M. Shalaby, A. Y. Churyumov, D. H. A. Besisa, A. Daoud, and M. T. Abou El-Khai, "A comparative study of thermal conductivity and tribological behavior of squeeze cast A359/AlN and A359/SiC composites," *Journal of Material Engineering and Performance*, vol. 26, no. 7, pp. 3079–3089, 2017.

[4] K. U. Kainer, "Metal matrix composites: custom-made materials for automotive and aerospace engineering," Wiley-VCH Verlag GmbH & Co. KGaA, Weinheim, 2006.

[5] D. J. Lloyd, "Particle reinforced aluminium and magnesium matrix composites," *International Materials Reviews*, vol. 39, no. 1, pp. 1–23, 1994.

[6] A. M. Cardinale, D. Macci, G. Luciano, E. Canepa, and P. Traverso, "Thermal and corrosion behaviour of as-cast Al-Si alloys with rare earth elements," *Journal of Alloy's Compounds*, vol. 695, pp. 2180–2189, 2017.

[7] S. Yashpal, C. S. Jawalkar, A. S. Verma, and N. M. Suri, "Fabrication of aluminium metal matrix composites with particulate reinforcement: a review," *Material Today Proceedings*, vol. 4, no. 2, pp. 2927–2936, 2017.

[8] N. Panwar and A. Chauhan, "Fabrication methods of particulate reinforced aluminium metal matrix composite-a review," *Material Today Proceedings*, vol. 5, no. 2, pp. 5933–5939, 2018.

[9] C. S. Ramesh, R. Keshavamurthy, and J. Madhusudhan, "Fatigue behavior of Ni-P coated Si_3N_4 reinforced Al6061 composites," *Procedia Materials Science*, vol. 6, pp. 1444–1454, 2014.

[10] C. S. Ramesh, R. Keshavamurthy, B. H. Channabasappa, and A. Ahmed, "Microstructure and mechanical properties of Ni-P coated Si_3N_4 reinforced Al6061 composites," *Material Science and Engineering Part A*, vol. 502, no. 1-2, pp. 99–106, 2009.

[11] X. Bai, C. Huang, J. Wang, B. Zou, and H. Liu, "Fabrication and characterization of Si_3N_4 reinforced Al_2O_3-based ceramic tool materials," *Ceramics International*, vol. 41, no. 10, pp. 12798–12804, 2015.

[12] J. Fayomi, A. P. I. Popoola, O. P. Oladijo, O. M. Popoola, and O. S. I. Fayomi, "Experimental study of ZrB_2-Si_3N_4 on the microstructure, mechanical and electrical properties of high grade AA8011 metal matrix composites," *Journal of Alloys and Compounds*, vol. 790, pp. 610–615, 2019.

[13] X. Zhu, Y. Zhou, and K. Hirao, "Effect of sintering additive composition on the processing and thermal conductivity of sintered reaction-bonded Si_3N_4," *Journal of American Ceramic Society*, vol. 87, no. 7, pp. 1398–1400, 2004.

[14] R. Karthik, K. Gopalakrishnan, R. Venkatesh, A. Mohana Krishnan, and S. Marimuthu, "Influence of stir casting parameters in mechanical strength analysis of aluminium metal matrix composites (AMMCs)," *Materials Today Proceedings*, vol. 62, no. 4, pp. 1965–1968, 2022.

[15] I. S. Han, D. W. Seo, S. Y. Kim, K. S. Hong, K. H. Guahk, and K. S. Lee, "Properties of silicon nitride for aluminum melts prepared by nitrided pressureless sintering," *Journal of the European Ceramic Society*, vol. 28, no. 5, pp. 1057–1063, 2008.

[16] M. O. Mazahery and M. O. Shabani, "Extruded AA6061 alloy matrix composites: the performance of multi-strategies to extend the searching area of the optimization algorithm," *Journal of Composite Materials*, vol. 48, no. 16, pp. 1927–1937, 2014.

[17] J. Chandradass, T. Thirugnanasambandham, P. Jawahar, and T. T. M. Kannan, "Effect of silicon carbide and silicon carbide/alumina reinforced aluminum alloy (AA6061) metal matrix composite," *Materials Today: Proceedings*, vol. 45, pp. 7147–7150, 2021.

[18] J. Fayomi, A. P. I. Popoola, O. M. Popoola, and O. S. I. Fayomi, "The appraisal of the thermal properties, electrical response, and corrosion resistance performance of AA8011 reinforced Nano Si_3N_4 for automobile application," *Journal of Alloys and Compounds*, vol. 850, article 156679, 2021.

[19] J. M. Arribas, F. C. Martín, and F. Castro, "The initial stage of liquid phase sintering for an Al-14Si-2.5Cu-0.5Mg (wt%) P/M alloy," *Material Science Engineering A*, vol. 527, no. 16-17, pp. 3949–3966, 2010.

[20] C. Ramesh Kannan, S. Manivannan, and M. Vivekanandan, "Synthesis and experimental investigations of tribological and corrosion performance of AZ61 magnesium alloy hybrid composites," *Journal of Nanomaterials*, vol. 2022, Article ID 6012518, 12 pages, 2022.

[21] A. Mohana Krishnan and M. Dineshkumar, "Evaluation of mechanical strength of the stir casted aluminium metal matrix composites (AMMCs) using Taguchi method," *Materials Today Proceedings*, vol. 62, no. 4, pp. 1943–1946, 2022.

Research Article

Influences of Various Thermal Cyclic Behaviours on Thermo Adsorption/Mechanical Characteristics of Epoxy Composite Enriched with Basalt Fiber

P. Karthikeyan,[1] L. Prabhu,[2] B. Bhuvaneswari,[3] K. Yokesvaran,[1] A. Jerin,[4] R. Saravanan,[5] S. Raghuvaran,[6] Kassu Negash [ID],[7] and Shubham Sharma[8]

[1]*Department of Aerospace Engineering, Agni College of Technology, Chennai, 600130 Tamilnadu, India*
[2]*Department of Mechanical Engineering, Aarupadai Veedu Institute of Technology, Chennai, 603104 Tamilnadu, India*
[3]*Department of Electronics and Communication Engineering, Panimalar Engineering College, Chennai, 600123 Tamilnadu, India*
[4]*Department of Mechanical Engineering, Vels Institute of Science Technology and Advanced Studies, Chennai, 600117 Tamilnadu, India*
[5]*Department of Mechanical Engineering, Saveetha School of Engineering, SIMATS, Chennai, 602105 Tamilnadu, India*
[6]*Department of Mechanical Engineering, K. Ramakrishnan College of Engineering, Trichy, 621112 Tamilnadu, India*
[7]*Department of Mechanical Engineering, Faculty of Manufacturing, Institute of Technology, Hawassa University, Ethiopia*
[8]*Department of Mechanical Engineering, University Centre for Research and Development, Chandigarh University, 140413 Mohali, Punjab, India*

Correspondence should be addressed to Kassu Negash; kassun@hu.edu.et

Exposure to advanced materials with unique thermomechanical characteristics has fulfilled the requirements of automotive, marine, and structural industries. The current research investigates the thermal adsorption and mechanical properties of epoxy composite enriched by basalt fiber via resin moulding technique with an applied pressure of 2 bar. Hydrophobic and dynamic analyzer tests developed composite's adsorption storage and loss modulus with 10, 30, 50, 70, 90, and 110 thermal cycles under 18°C to 150°C. ASTM test standards evaluated the effect of the thermal cyclic process on mechanical properties. The composite contained 45 vol% basalt fiber with 90 thermal cycles and found higher adsorption storage modulus, elasticity, tensile strength, and flexural strength of 9200 GPa, 80 GPa, 229 MPa, and 398 MPa, respectively. The thermal adsorption loss modulus was limited by 12% on 90 thermal cycles at 150°C compared to 10 thermal cycles.

1. Introduction

The utilization of polymer-based filler material was widely augmented in several applications due to their improved thermal stability, good mechanical characteristics, light weight, ability to make composite on compound phase, and durability [1–3]. The most common resin, epoxy, was bonded with different natural and synthetic fiber facilities with good mechanical and thermal characteristics [4–6]. Most researchers studied the performance of epoxy composite with natural fibers like jute fiber [7], aramid [8], basalt fiber [9], flax [10], glass, and carbon fiber [11] attained

enhanced thermomechanical characteristics. Along with the different filler (natural fiber) materials mentioned above, basalt fiber has excellent chemical and thermal stability with superior tensile strength [12]. Additionally, it is ecofriendly during preparation and easy to recycle [13, 14]. The absorption capability of hybrid composite with aramid/basalt fiber was evaluated and its result showed increased impact energy of composite [15]. The degradation properties of tensile strength of basalt fiber-reinforced polymer and fiber-reinforced polymer tendons for marine environment was investigated and compared [16]. The thermal performance of epoxy-developed composite with various weight

(a)

(b)

FIGURE 1: Main constitutions of epoxy composite (a) basalt fiber and (b) epoxy resin with hardener.

TABLE 1: Physical and mechanical properties of raw materials.

Materials/properties	Density (g/cc)	Elastic modulus (GPa)	Tensile strength (MPa)	Thermal conductivity (W/mK)	Coefficient of thermal expansion Per $°C \times 10^{-6}$
Epoxy	1.131	3.30	92.7	0.6	66
Basalt fiber	2.12	64	4537	0.0331	6

percentages of multiwalled nanotubes and micro-SiC was studied. It revealed that the composite containing 6 wt% multiwalled nanotubes showed 2.9 times higher thermal conductivity than unreinforced epoxy [17]. The properties of epoxy composite have been resolute by the behaviour of chemical action between matrix and fiber [18]. The mechanical performance of basalt fiber and glass fiber reinforced polymer composite fabricated by hand layup technique and studied its mechanical behaviour. The composite result found that basalt and glass fiber showed similar mechanical performance on applied high mechanical force [19].

The E-glass fiber/multiwalled carbon nanotubes reinforced epoxy composite was developed and studied by their thermomechanical properties. The physical presence of both E-glass fiber and multiwalled carbon nanotubes in epoxy composite has higher thermomechanical characteristics [20, 21]. The mechanical properties of basalt fiber reinforced polymer composites instead of the glass fiber composite structure were examined by SEM. The composite results showed maximum bending and tensile strength compared to the existing glass fiber composite structure. The physical presences of basalt fiber content on epoxy composite have high thermal performance [22, 23]. Based on the literature listed above, the basalt fiber reinforced epoxy composite per-

forms good thermomechanical characteristics compared to other fibers. So the present research investigation is to develop an epoxy composite containing 25 wt% of basalt fiber by resin mould technique. The developed composites are subjected to thermal adsorption and mechanical studies. The effect of thermal cycles on thermal adsorption storage modulus, modulus of elasticity, tensile strength, and flexural strength of the epoxy composite is tested by ASTM D3039 standards.

2. Materials and Method

2.1. Choice of Matrix and Reinforcement Materials. The epoxy resin and basalt fiber were chosen as the primary constitutions and reinforcement for the current research work. The epoxy resin is suitable for combination with nonreactive and reactive additives facilitating easy profile modification [24, 25]. Among the various fibers were referred from literature studies, basalt fiber has enhanced thermal and chemical stability, good tensile strength, and easy to recycle [12–14]. The basalt fiber and epoxy resin are illustrated in Figures 1(a) and 1(b). The physical and mechanical properties of both materials are detailed in Table 1.

(a) 0 degrees

(b) 90 degrees

(c) 2 × 2 texture design mat
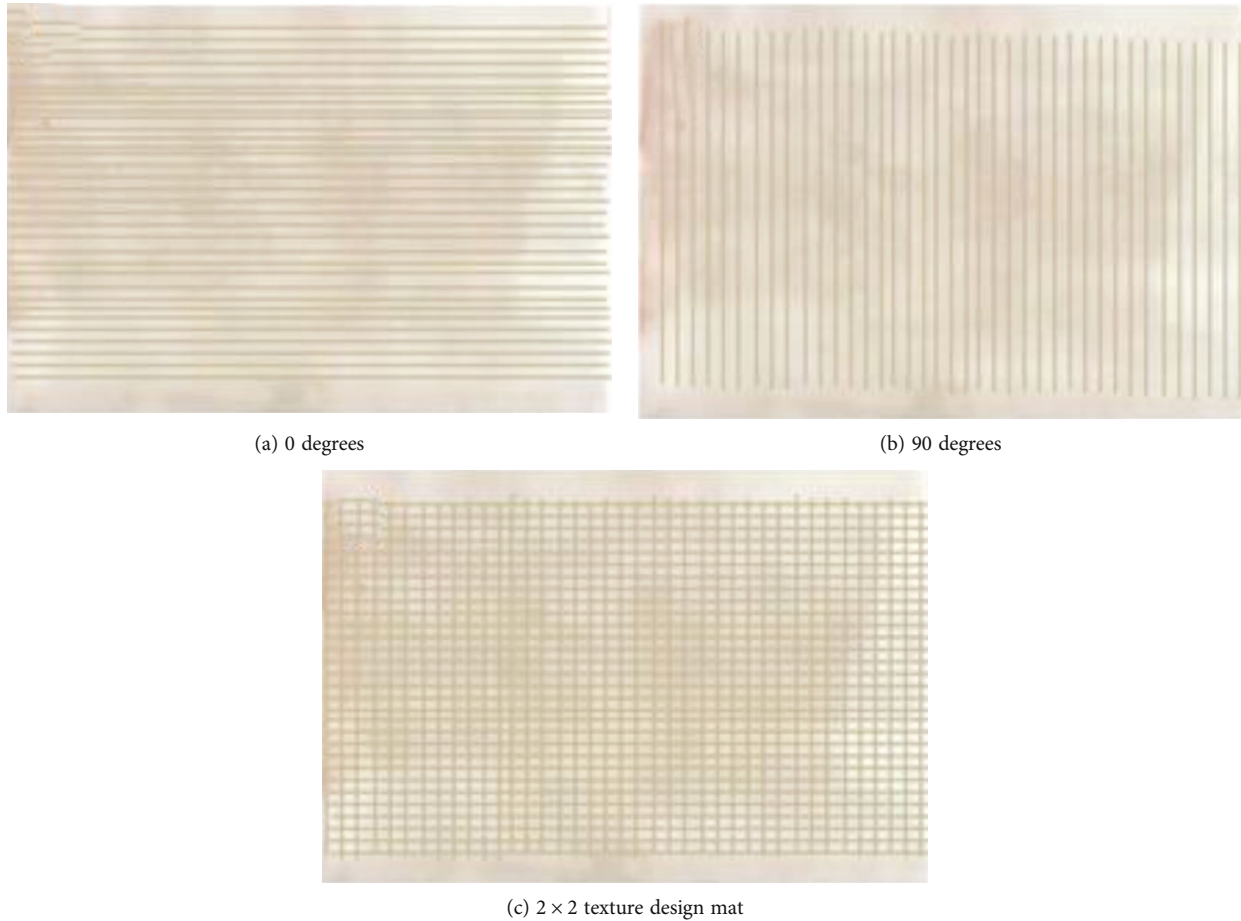
FIGURE 2: The epoxy composite texture layup design pattern with different orientations (a) 0 degrees, (b) 90 degrees, and (c) 2 × 2 texture design mat.
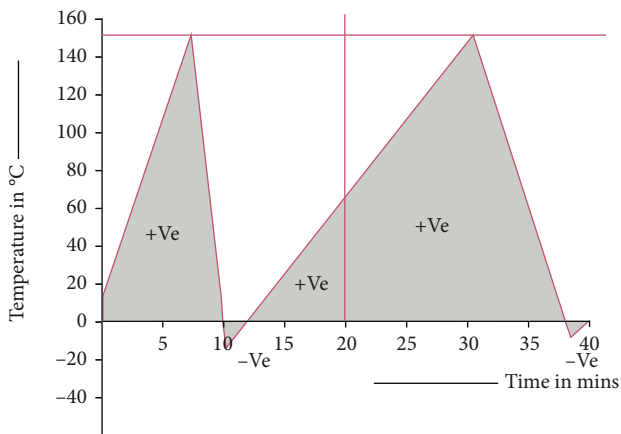
FIGURE 3: Thermal cyclic profile curve during various thermal cycles.

TABLE 2: Effect of damping factor and glass transition temperature effect on thermal adsorption of an epoxy composite.

Thermal cycle	d_{max}	GTT
10	0.3221	86.12
30	0.3144	86.21
50	0.3109	86.21
70	0.3094	86.23
90	0.3065	86.28
110	0.3038	86.29

2.2. Processing of Epoxy Composite.

Initially, the actual length of basalt fiber is waving with epoxy resin for the orientations of 0° and 90° parallel 2 × 2 texture design pattern as shown in Figure 2. The 45 vol% of basalt fiber is structured by epoxy resin as 2 × 2 texture design via hand-operated autowaving tool attached with resin mold. Meantime, the 55 vol% of epoxy is collected from a resin container with the help of a vacuum pump with a pressure of 2×10^5 pa, and then the collected epoxy is slowly layup on the above surface of 2 × 2 basalt mat, resulting in an even distribution of epoxy can able to make good interfacial bonding strength. Finally, bonded epoxy and basalt fiber layer is compacted with an applied pressure of 2 bar. The compressive force may enhance the interfacial bonding quality and resist the fiber movement between the interlayer during high tensile load. However various fabrication techniques are available for making PMC, but the resin mold technique is the most common and inexpensive method for developing PMC [24, 25]. Similarly, the second layer of epoxy composite is prepared and the final composite has a size of $100 \times 100 \times 3$
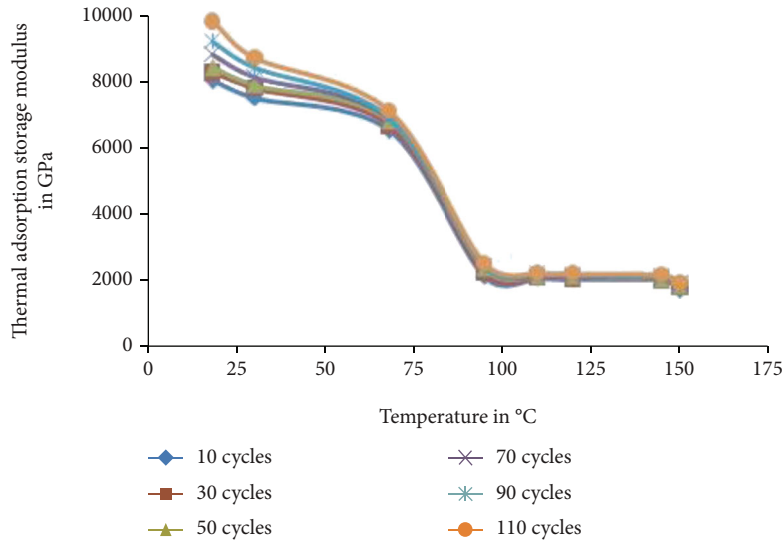
FIGURE 4: Thermal adsorption storage modulus of epoxy composites.
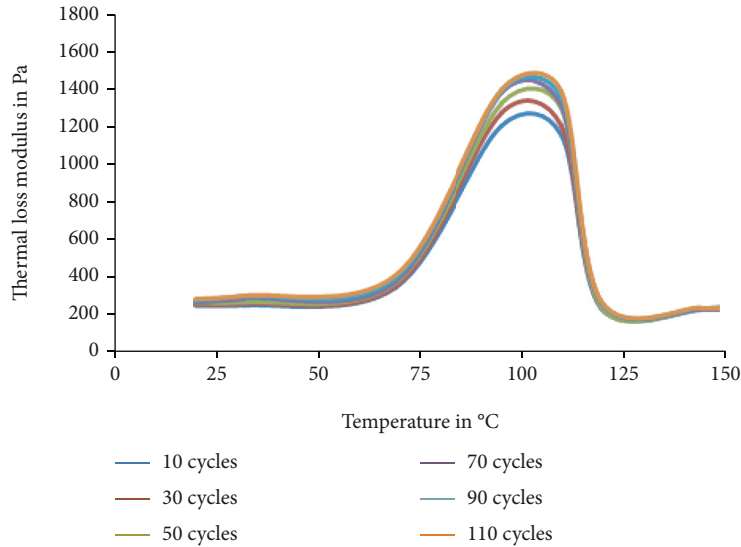
FIGURE 5: Thermal loss modulus of epoxy composites.

mm. The epoxy composite is shaped per ASTM test standards via a water jet machining process.

2.3. The Thermal Cyclic Design Process. It was considered different thermal cycle sequences of 10, 30, 50, 70, 90, and 110 cycles with increased temperatures of 18°C to 150°C. Then, it fell to -18°C. Each cycle has been defined with an interval sequence of 20 cycles; under the dwell time of 20 mins, thermal profile is shown in Figure 3. However, the cyclic thermal curve falls -18°C due to the solidification of basalt fiber after epoxy layup. The temperature was reduced to below the ambient temperature. It helps to increase the quality and a sufficient compact ratio is obtained during the final process. Similarly, the CFD technique observed the circular tube heat transfer with various thermal cycles [26].

3. Result and Discussions

3.1. Thermal Adsorption Storage Modulus. The Visco-Elastic thermal adsorption properties of the epoxy composite were evaluated by a dynamic analyzer with mechanical probe assembly. It was tested under the ASTM standard of D7028. The bonded structure of the epoxy composite was closely monitored into three different bending points on 1 Hz frequency at 18°C to 150° temperature under an applied load of 20 N associated with a 3°C/min heating rate.

The significance of glass transition temperature (GTT) and damping factor (dmax) for the epoxy composite was derived from digital analyzer trace points and its values were represented in Table 2. Figure 4 illustrates the Visco-Elastic thermal adsorption storage modulus of epoxy composite enriched with basalt fiber under different thermal cycles. It
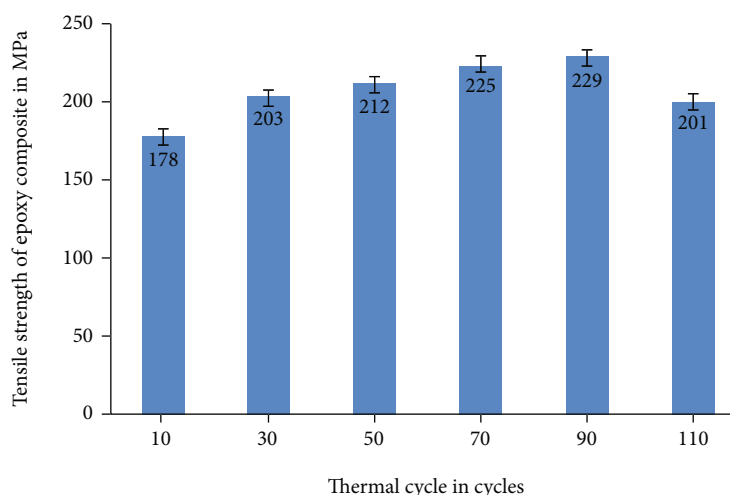
Figure 6: Tensile strength of epoxy composite with various thermal cycles.
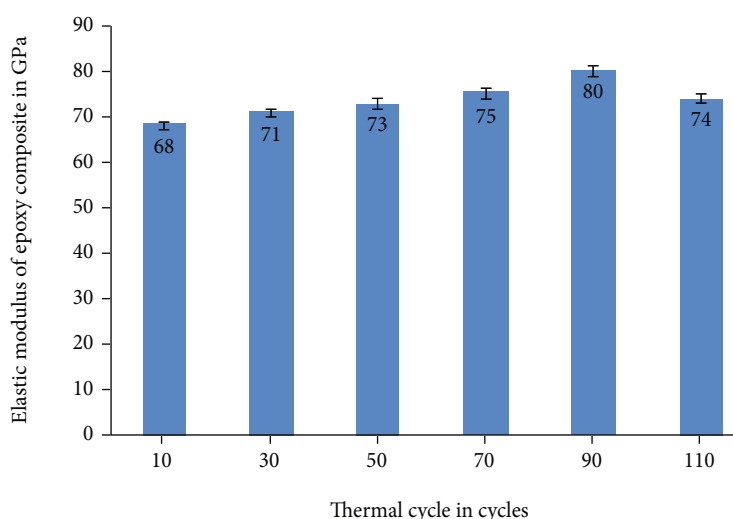
Figure 7: Elastic modulus of epoxy composite with various thermal cycles.

was noted from the above curve in Figure 4 that the thermal adsorption modulus of epoxy composites gradually decreased with an increase in temperature. But the composite that facilitates 110 cyles gained the maximum energy storage modulus of 9800 GPa. It was due to the glass transition temperature and cross-interface effect on a higher temperature. A similar trend was found in nylon copolymer/ EPDM rubber [27].

3.2. The Thermal Loss Modulus of an Epoxy Composite. Figure 5 represents the thermal loss modulus of an epoxy composite containing 45 vol% of basalt fiber evaluated by different thermal cycles. The composite facilitates three stages: rubbery, glass, and glass transition state. The rubbery state has no significant changes in thermal adsorption storage and loss modulus [27]. In the glass stage, the composite's structure was controlled on the most significant thermal storage modulus [26, 28]. At the same time, the GTT state thermal storage modulus has decreased progressively on the sensitivity of temperature changes. So the GTT state

has very important for deciding the properties of polymer composites.

As seen from Figure 5, the epoxy composite's thermal loss modulus gradually increased with temperature increase from 18°C to 75°C. Further increase in temperature showed the thermal loss modulus of composite has decreased. However, the thermal loss of epoxy composite may be varied due to the sensitivity of temperature, and a similar type of thermal profile was generated on various thermal cycles.

4. Mechanical Characteristics of Epoxy Composite on Different

4.1. Tensile Strength of Epoxy Composite. The tensile strength of the composite was evaluated by FIE make universal tensile machine with a capacity of 40 ton followed by ASTM D3039 standard with the dimensions of 250 × 150 × 25 mm, respectively. Figure 6 shows the tensile strength of epoxy composite with 10, 30, 50, 70, 90, and 110 thermal cycles.
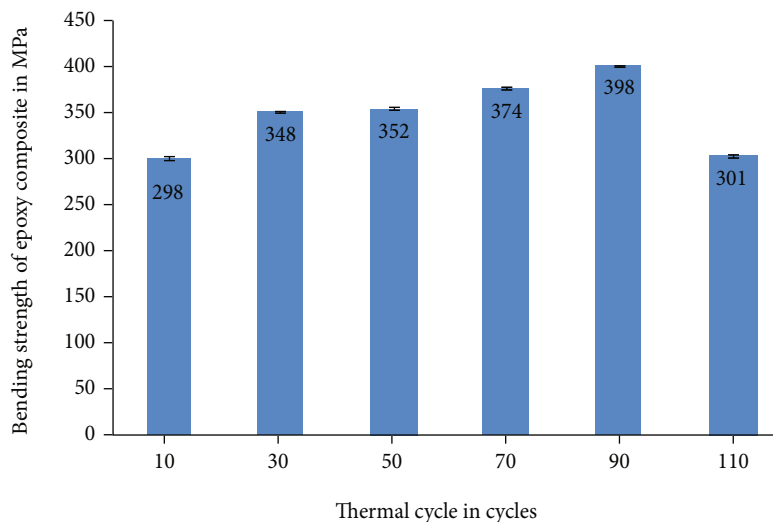
FIGURE 8: Bending strength of epoxy composite with different thermal cycles.

Figure 6 indicates basalt fiber's effect on the composite's tensile strength with varied thermal cyclic conditions. The tensile strength of the composite was gradually increased with the increase of the thermal cycle from 10 cyles to 90 cycles. Further increase in thermal cycle resulted in decreased tensile strength of 201 ± 2.1 MPa. It was due to the effect of thermal treatment and mismatched interlink connection of epoxy and basalt fiber. It was found that the composite has 90 thermal cycles and showed a maximum tensile strength of 229 ± 1.1 MPa. It increased by 28.65% as compared to 10 thermal cycles.

Similarly, the tensile strength of each cycle was increased by 14%, 19.1%, 26.4%, and 28.65%, respectively. It was because the effect of good chemical interface orientation on cyclic thermal action was insufficient to break. However, the treatment of thermal action may damage the polymer composite's chemical structure [9, 10].

4.2. Elastic Modulus of an Epoxy Composite. Figure 7 illustrates the modulus of elasticity of epoxy composite with different thermal cycles. The treatment of different thermal conditions was the most significant factor in improving mechanical properties. The epoxy composite's phenomenon was enhanced by the basalt fiber's orientation chemically bonded with resin resulting in high elastic modulus. It was observed from Figure 7 that the elastic modulus of the epoxy composite was progressively increased with increased thermal cycles of 90 nos.

The maximum elastic modulus of 80 GPa was identified as 90 thermal cycles. The characteristics investigation of the epoxy composite was enriched by basalt fiber act as superior strength at a higher temperature. However, further improvement in the thermal cycle of more than 90nos showed 74 GPa. It was due to the deviation of basalt fiber from resin.

4.3. Bending Strength of Epoxy Composite. The bending strength of epoxy composite with different thermal cyclic conditions is represented in Figure 8. It was increased 298 ± 2.1 MPa, 348 ± 0.91 MPa, 352 ± 3.2 MPa, 374 ± 1.8 *MPa*,

and 398 ± 0.71 MPa on 10, 30, 50, 70, and 90 thermal cycles. After 90 cycles, it reached 301 MPa due to the postcuring effect of strength between epoxy and basalt fiber. However, basalt fiber owed high thermal stability [12–14, 22]. The higher bending strength of 398 ± 0.71 *MPa* was observed in 90 cyles can withstand the higher temperature of 150°C. It was due to their highly effective bonding between epoxy and fiber, leading to resisting the high bending load without fracture or bulge of composite. The higher temperature was insufficient to damage the epoxy composite's chemical bonding [18, 27, 28].

5. Conclusions

The resin mould technique successfully developed the epoxy composite with an applied pressure of 2 bar. The mechanical properties like tensile, elastic modulus, and bending strength of composites were enriched by basalt fiber. A dynamic analyzer with a mechanical probe point investigated the effect of 10, 30, 50, 70, 90, and 110 cyclic thermal behaviour on thermal adsorption storage and loss modulus of the developed composite. The following results were made from the present research are mentioned below.

(1) The effect of thermal cycles on thermoadsorption/ mechanical characteristics of epoxy composite found superior thermal adsorption with high tensile and bending strength

(2) The composite contained 45 vol% of basalt fiber resulting in a higher thermal adsorption storage modulus of 9200 GPa under 150°C with a good glass transition temperature effect on 90 cycles

(3) Similarly, the epoxy composite's overall thermal adsorption loss modulus was limited by 12% on 150°C operated under 90 thermal cycles compared to 10 cycles

(4) Composite with 90 thermal cycles was found to have a superior tensile strength of 28.65% improvement compared to 10 cycles. Similarly, the bending strength of the composite showed 398 ± 0.71 MPa

(5) The elastic modulus of epoxy composite was estimated with different sequence thermal cycles, showing the parallel improvement and 90 cycles having a better elastic modulus of 80GPa. So, that epoxy composite with basalt fiber has good thermal adsorption modulus and superior mechanical properties

(6) The transportation of rooftop structure application utilized the superior properties of a developed best sample of the epoxy composite

Data Availability

All the data required are available within the manuscript.

Conflicts of Interest

The authors declare that there are no conflicts of interest regarding the publication of this paper.

References

[1] J. Andrzejewski, M. Szostak, M. Barczewski, and P. Luczak, "Cork-wood hybrid filler system for polypropylene and poly(lactic acid) based injection molded composites. Structure evaluation and mechanical performance," *Composite Part B Engineering*, vol. 163, pp. 655–668, 2019.

[2] N. Zareei, A. Geranmayeh, and R. Eslami-Farsani, "Interlaminar shear strength and tensile properties of environmentally-friendly fiber metal laminates reinforced by hybrid basalt and jute fibers," *Polymer Testing*, vol. 75, pp. 205–212, 2019.

[3] M. Kuranska, M. Barczewski, K. Uram, K. Lewandowski, A. Prociak, and S. Michałowski, "Basalt waste management in the production of highly effective porous polyurethane composites for thermal insulating applications," *Polymer Testing*, vol. 76, pp. 90–100, 2019.

[4] D. Matykiewicz, "Hybrid epoxy composites with both powder and fiber filler: a review of mechanical and thermomechanical properties," *Materials*, vol. 13, no. 8, p. 1802, 2020.

[5] S. Mahesh Babu and M. Venkateswara Rao, "Experimental studies on the effect of basalt powder inclusion on mechanical properties of hybrid epoxy and polyester composites reinforced with glass fiber," in *Advances in Manufacturing Technology*, pp. 25–31, Springer, Singapore, 2019.

[6] D. Matykiewicz, "Biochar as an effective filler of carbon fiber reinforced bio-epoxy composites," *Processes*, vol. 8, no. 6, p. 724, 2020.

[7] V. Gopalan, V. Suthenthiraveerappa, S. K. Tiwari, N. Mehta, and S. Shukla, "Dynamic characteristics of honeycomb sandwich beam made with jute/epoxy composite skin," *Emerging Material Research*, vol. 9, no. 1, pp. 1–12, 2020.

[8] M. Goodarz, S. H. Bahrami, M. Sadighi, and S. Saber-Samandari, "Low-velocity impact performance of nanofiber-interlayered aramid/epoxy nanocomposites," *Composite Part B Engineering*, vol. 173, article 106975, 2019.

[9] P. R. V. Doddi, R. Chanamala, and S. P. Dora, "Effect of fiber orientation on dynamic mechanical properties of PALF hybridized with basalt reinforced epoxy composites," *Material Research Express*, vol. 7, no. 1, article 015329, 2020.

[10] C. Wu, K. Yang, Y. Gu, J. Xu, R. O. Ritchie, and J. Guan, "Mechanical properties and impact performance of silk-epoxy resin composites modulated by flax fibres," *Part A Applied Science and Manufacturing*, vol. 117, pp. 357–368, 2019.

[11] P. Ghabezi and N. Harrison, "Mechanical behavior and long-term life prediction of carbon/epoxy and glass/epoxy composite laminates under artificial seawater environment," *Material Letter*, vol. 261, article 127091, 2020.

[12] V. Dhand, G. Mittal, K. Y. Rhee, S. J. Park, and D. A. Hui, "A short review on basalt fiber reinforced polymer composites, composite part B," *Engineering*, vol. 73, pp. 166–180, 2015.

[13] B. Wei, S. Song, and H. Cao, "Strengthening of basalt fibers with nano-SiO$_2$-epoxy composite coating," *Material Design*, vol. 32, no. 8-9, pp. 4180–4186, 2011.

[14] R. Venkatesh, N. Karthi, N. Kawin et al., "Synthesis and Adsorbent Performance of Modified Biochar with Ag/MgO Nanocomposites for Heat Storage Application," *Adsorption Science and Technology*, vol. 2022, Article ID 7423102, pp. 1–14, 2022.

[15] F. Sarasini, J. Tirillò, M. Valente et al., "Hybrid composites based on aramid and basalt woven fabrics: impact damage modes and residual flexural properties," *Material Design*, vol. 49, pp. 290–302, 2013.

[16] X. Wang, G. Wu, Z. Wu, Z. Dong, and Q. Xie, "Evaluation of prestressed basalt fiber and hybrid fiber reinforced polymer tendons under marine environment," *Material Design*, vol. 64, pp. 721–728, 2014.

[17] T. Zhou, X. Wang, X. Liu, and D. Xiong, "Improved thermal conductivity of epoxy composites using a hybrid multi-walled carbon nanotube/micro-SiC filler," *Carbon*, vol. 48, no. 4, pp. 1171–1176, 2010.

[18] N. Jain, V. K. Singh, and S. Chauhan, "Review on effect of chemical, thermal, additive treatment on mechanical properties of basalt fiber and their composites," *Journal of Mechanical Behaviour of Materials*, vol. 26, pp. 205–211, 2018.

[19] A. Mohana Krishnan, M. Dineshkumar, S. Marimuthu, N. Mohan, and R. Venkatesh, "Evaluation of mechanical strength of the stir casted aluminium metal matrix composites (AMMCs) using Taguchi method," *Materials Today: Proceedings*, vol. 62, no. 2022, pp. 1943–1946, 2022.

[20] M. M. Rahman, S. Zainuddin, M. V. Hosur et al., "Improvements in mechanical and thermo-mechanical properties of e-glass/epoxy composites using amino functionalized MWCNTs," *Composite Structures*, vol. 94, no. 8, pp. 2397–2406, 2012.

[21] V. Lopresto, C. Leone, and I. De Lorio, "Mechanical characterisation of basalt fibre reinforced plastic," *Composites Part B: Engineering*, vol. 42, no. 4, pp. 717–723, 2011.

[22] H. Kim, "Thermal characteristics of basalt fiber reinforced epoxy-benzoxazine composites," *Fibers and Polymers*, vol. 13, no. 6, pp. 762–768, 2012.

[23] H. Kim, "Effects of plies stacking sequence and fiber volume ratio on flexural properties of basalt fiber/nylon-epoxy hybrid composite," *Fibers and Polymers*, vol. 16, pp. 918–925, 2015.

[24] C. Ramesh Kannan, S. Manivannan, and M. Vivekanandan, "Synthesis and experimental investigations of tribological

and corrosion performance of AZ61 magnesium alloy hybrid composites," *Journal of Nanomaterials*, vol. 2022, Article ID 6012518, 12 pages, 2022.

[25] M. Zolghadr, M. J. Zohuriaan-Mehr, A. Shakeri, and A. Salimi, "Epoxy resin modification by reactive bio-based furan derivatives: curing kinetics and mechanical properties," *Thermochimica. Acta*, vol. 673, pp. 147–157, 2019.

[26] A. Natarajan, R. Venkatesh, S. Gopinath, L. Devakumar, and K. Gopalakrishnan, "CFD simulation of heat transfer enhancement in circular tube with twisted tape insert by using nanofluids," *Material Today Proceedings*, vol. 21, no. 1, pp. 572–577, 2020.

[27] K. E. George and C. Komalan, "Dynamic mechanical analysis of binary and ternary polymer blends based on nylon copolymer/EPDM rubber and EPM grafted maleic anhydride compatibilizer," *Express Polymer Letter*, vol. 10, pp. 641–653, 2007.

[28] Y. Chu, Q. Fu, H. Li, and K. Li, "Thermal fatigue behavior of C/C composites modified by SiC-MoSi$_2$-Crsi$_2$ coating," *Journal of Alloys and Compounds*, vol. 31, no. 4, pp. 8111–8115, 2011.

Research Article

Modelling and Deliberation of Multireinforcement Surface on Tribothermal Adsorption Performance of Nickel Alloy Matrix Hybrid Nanocomposite

G. Ramya Devi,[1] **C. B. Priya** [iD],[2] **C. Dineshbabu,**[3] **R. Karthick,**[4] **K. Thanigavelmurugan,**[5] **and Prabhu Paramasivam** [iD][6]

[1]Department of Mechanical Engineering, Saveetha School of Engineering, SIMATS, Chennai, 602105 Tamil Nadu, India
[2]Department of Production, National Institute of Technology, 620015, Trichy, Tamil Nadu, India
[3]Department of Mechanical Engineering, Kongunadu College of Engineering and Technology, Trichy, 621215 Tamil Nadu, India
[4]Department of Mechanical Engineering, M. Kumarasamy College of Engineering, Karur, 639113 Tamil Nadu, India
[5]Department of Mechanical Engineering, Loyola Institute of Technology, Chennai, 600123 Tamil Nadu, India
[6]Department of Mechanical Engineering, College of Engineering and Technology, Mattu University, 318, Ethiopia

Correspondence should be addressed to Prabhu Paramasivam; prabhuparamasivam21@gmail.com

The present research work is aimed at developing a nickel alloy (Ni-Cr) matrix hybrid nanocomposite comprising 5 wt%, 10 wt%, and 15 wt% of alumina nanoparticles (Al_2O_3) size of 50 nm with stable weight percentage (5 wt%) of titanium dioxide (TiO_2) nanoparticle via vacuum die casting process for an automobile brake pad application. The deliberation of multireinforcement surface on nickel alloy matrix tribological performance was evaluated by constant sliding distance (200 m) on dry sliding condition via rotating pin on disc apparatus with different loading conditions of 10 N, 30 N, 50 N, and 70 N under the sliding velocity of 0.25 m/sec, 0.5 m/sec, and 0.75 m/sec, respectively. The influences of alumina and titanium dioxide nanoparticles in the nickel alloy matrix resulted in the thermal conductivity increasing by 18% compared to unreinforced nickel alloy. After temperature drop, the coefficient of thermal expansion for nickel alloy hybrid composite decreases progressively with increased reinforcement content as 10 wt% Al_2O_3/5 wt% TiO_2. Further inclusion of both Al_2O_3 and TiO_2 in nickel alloy was increased nominally. The thermal adsorption characteristic on composites mass loss was decreased while temperature increased from 28°C to 1000°C.

1. Introduction

The innovative creation of conventional matrix materials (aluminium, magnesium, and titanium) was blended with organic/inorganic reinforcements to achieve specific characteristics such as high wear resistance [1]; good thermal stability on higher temperatures [2]; high tensile strength; and good corrosion resistance facilitates in a sports car, aviation, electrical contacts, and structural applications [3]. The incorporation of hard ceramic particles into metal matrix speaks with tremendous isotropic performance compared to conventional materials [4, 5]. Similarly, selecting matrix, reinforcement, and process parameters for composite fabrication was the most critical factor for deciding composite characteristics [6, 7]. Recently, most researchers referred to aluminium, magnesium, titanium, and their alloy matrix developed with organic/inorganic reinforcement [8] via conventional fabrication techniques such as solid and liquid state processing [9, 10]. Nickel and its alloy-based matrix materials have met the demand for high-temperature applications like automobile valves, brake pads, and siphon bodies [11]. In the past decades, various researches have been accomplished by tribomechanical performance studies on nickel-based alloy matrices such as nickel (Ni)/chromium

Table 1: Thermomechanical characteristics of matrix and reinforcements.

Descriptions	Materials/properties	Density g/cc	Hardness VHN	Modulus of elasticity GPa	Melting point °C	Thermal conductivity W/mK
Matrix	Ni-Cr alloy	7.75	204	110	1475	17
Reinforcements	Al_2O_3	3.96	1365	370	2054	30
	TiO_2	4.23	713	37.5	1843	0.62
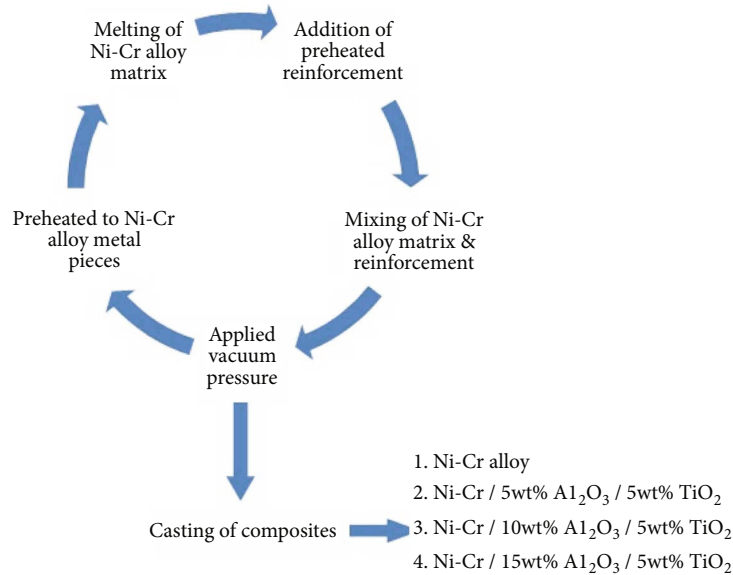
Figure 1: Schematic diagram for processing of Ni-Cr alloy matrix hybrid nanocomposite.

Table 2: Constitutions of Ni-Cr alloy matrix hybrid nanocomposite.

Sample	Weight percentage in %		
	Ni-Cr	Al_2O_3	TiC
1	100	0	0
2	90	5	5
3	85	10	5
4	80	15	5

(Cr)/zirconia matrix [12], Ni/Cr/M0S$_2$, nickel (Ni)/graphite (Gr)/titanium carbide (TiC), Ni/tungsten carbide (WC), Ni/titanium carbide (TiC), and Ni/cobalt (Co)/zirconia [13]. However, the properties of composite were integrated by ceramic phase (Si$_3$N$_4$, Al$_2$O$_3$, SiC, ZrO$_2$, etc.) [14], high-performance materials (Co, Fe, Ni, etc.) [15–17], and inter-metallic compounds alloys (Ti-Al, Fe-Al, Ni-Al, etc.) [18–20]. The tribological behaviour of Ni/Cr alloy was investigated at higher temperatures (20-600°C). It resulted in oxide sulfides during wear surface under reduced friction [21]. The Ni/TiC composite was developed through the Gr coating process. The Gr-coated layer in Ni/TiC composite has low wear loss and better coefficient friction than conventional Ni-Cr alloy [22]. Leech et al. [23] investigated the wear performance of Ni/TiC alloy composite by dry state pin on flat wear tester with a garnet abrasive wheel. They

found that the composite has superior wear performance on higher frictional temperature excavation on the constituent matrix. Incorporating TiC particles leads to resisting the depletion against the frictional temperature. The TiC-reinforced Ni-Cr alloy composite was produced by infiltration technique, and its electrical-thermal-wear characteristics were studied for high-temperature applications. TiC particles in the Ni matrix having good tribothermal behaviour resist the high frictional force during the evaluation of wear studies [24]. Srivastava et al. [25] studied the mechanical and chemical properties of zirconia bonded Ni-Co alloy composite. They found that the composite has good chemical and mechanical performance. Among the studies reported above, limited research is available on tribothermal adsorption on multiceramic reinforced nickel alloy hybrid nanocomposite. The present research is focused on developing a nickel alloy matrix bonded with various weight percentages of Al$_2$O$_3$ and stable weight percentages of TiO$_2$ via a vacuum die casting process. Finally, the developed composites' tribothermal performance was evaluated by ASTM test standards. The test results were compared to cast nickel alloy and recommended for brake pad applications.

2. Materials and Processing of Composites

2.1. Materials and Reinforcement. Ni-Cr alloy metals are pointed out for their superior tribomechanical characteristics
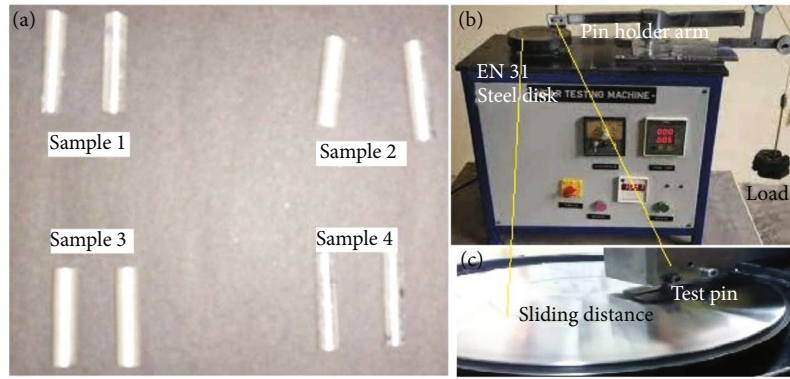
FIGURE 2: Dry state wear test apparatus setup: (a) test pin samples, (b) wear tester, and (c) enlarged view of test pin and rotating disk.

TABLE 3: Wear test input process parameters.

Parameters	Sliding distance	Sliding speed	Load
Unit	200 m	0.25, 0.5, and 0.75 m/sec	10, 30, 50, and 70 N
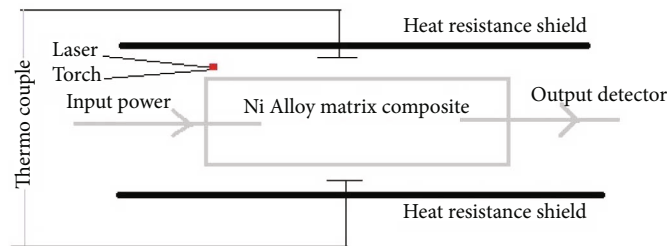
FIGURE 3: Block diagram for laser-based thermal conductivity evaluation.

TABLE 4: Wear performance Ni-Cr alloy matrix hybrid nanocomposite.

| Sample | Wear performance on 0.25 m/sec at 70 N load | | | |
	Wear rate $\times 10^{-3}$ mm^3/m	COF	Frictional force in N	Temperature in °C
1	26.12	0.29	58.12	57
2	23.81	0.37	62.17	59
3	23.12	0.39	67.43	64
4	21.98	0.41	69.43	68

and excellent corrosion resistance. So the nickel alloy was chosen as matrix material with 20% chromium [26]. The different weight percentages of 50 nm alumina (Al_2O_3) and stable weight percentage of TiO_2 nanoparticles were considered to reinforce the Ni-Cr alloy matrix. The Al_2O_3 has good wear resistance, the best electrical insulator, and high thermal stability. TiO_2 particles were one of the best complex reinforcements bonded to the Ni-Cr alloy matrix, resulting in good chemical stability and high thermal stability [27]. Table 1 indicates the thermomechanical properties of matrix and reinforcements.

2.2. Experimental Details for Processing and Testing of Ni-Cr Alloy Matrix Composites. The schematic diagram for pro-

cessing of Ni-Cr alloy matrix composite is represented in Figure 1. The different sized Ni-Cr alloy pieces are located in an electrical furnace configured with an induction coil with the capacity of 5 kg operated under a different temperature range of 27°C to 1700°C. The preheated temperature of Ni-Cr alloy is maintained at 400°C in stable condition on 15 min period [28]. Then, the furnace temperature is raised from 1200°C to 1500°C to melt the Ni-Cr alloy as molten (liquids) stage. Similarly, the reinforcements are preheated at 550°C to remove the moisture content and increase the wettability [29]. The externally preheated reinforcements are added into the semisolid stage (1100°C) Ni-Cr alloy, and both matrix and reinforcements are bonded with the help of stir action (400 rpm) for a 10 min period. The prepared Ni-Cr alloy matrix was poured into preheated (450°C) rectangular die sized on $100 \times 50 \times 20$ mm with an applied vacuum pressure of 2×10^5 Pa [29]. The developed Ni-Cr alloy matrix composites are cooled by natural ambient temperature without an external medium. Finally, the composites are sized by $30 \times 10 \times 10$ cm for tribological analysis. The constitutions of Ni-Cr alloy/reinforcements are mentioned in Table 2.

The dry state wear performance of unreinforced and reinforced Ni-Cr alloy composites (Figure 2(a)) was evaluated by ASTM G99-05 via pin-on-disk wear apparatus configured with EN31 steel counter disc is shown in Figure 2(b).
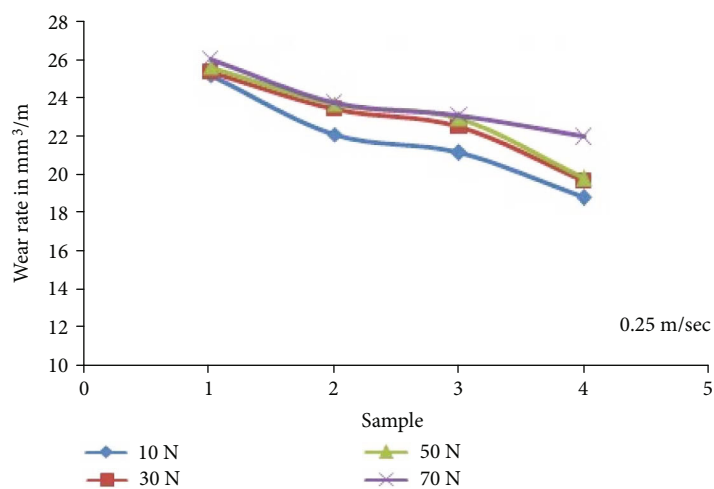
(a)
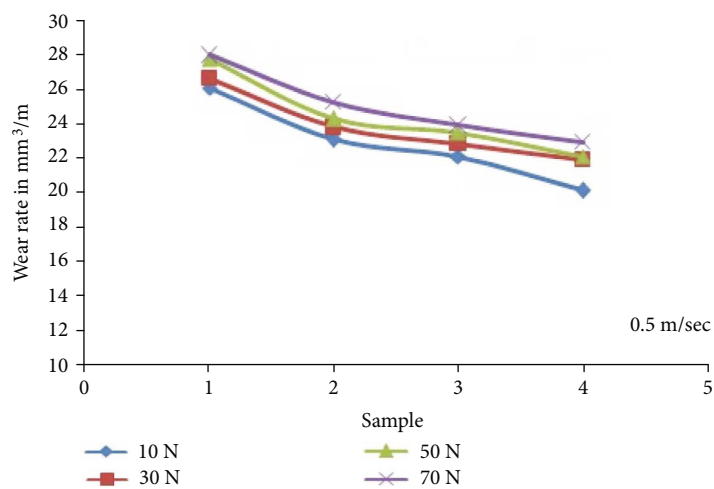
(b)
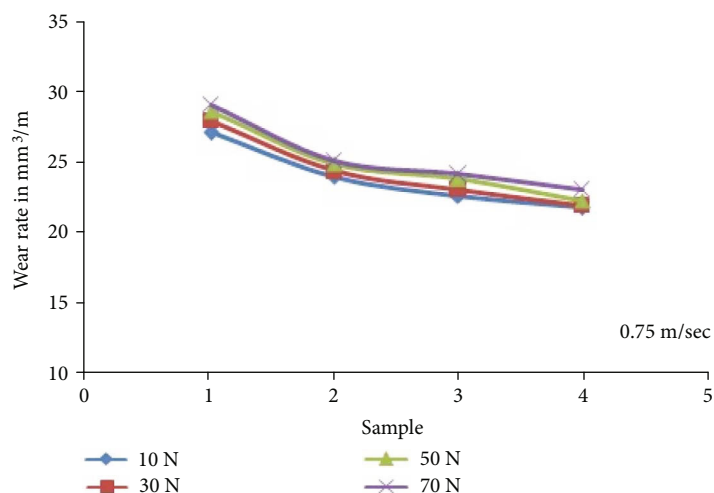
(c)

Figure 4: Continued.
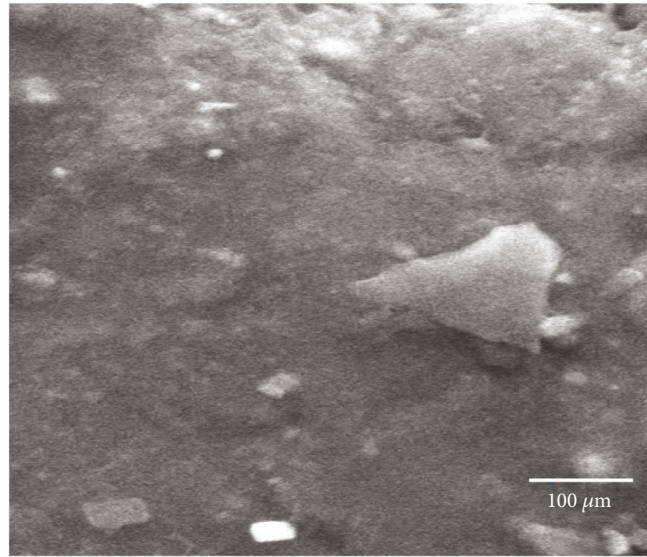
(d)

FIGURE 4: Wear rate of Ni-Cr alloy matrix composites (a) 0.25 m/sec, (b) 0.5 m/sec, and (c) 0.75 m/sec. (d) Optical micrograph of Ni-Cr/ 15 wt% Al_2O_3/5 wt% TiO_2 hybrid nanocomposite.

The wear test samples were sized by $30\,mm \times 10\,mm \times 10$ mm and held vertically into the pin holder arm, as shown in Figure 2(c). All the test samples were tested by test room conditions like $27°C$ temperature with 50-62% relative humidity maintained by a constant sliding distance of 200 m under different load and sliding speed conditions mentioned in Table 3.

Figure 3 illustrates the principle diagram for evaluating thermal conductivity on Ni-Cr alloy matrix composite ($10\,mm \times 50\,mm$) by laser beam source. The Jupiter STA 449/F3 model thermal analyzer was used to study the thermal behaviour of Ni-Cr alloy composites bonded with different reinforcements [29]. It was evaluated in an argon environment with a temperature range of $150°C$ to $2400°C$. The laser flash method is to be adopted for finding the thermal conductivity (ΛNi) of the Ni matrix body referred as

$$\Lambda Ni(T) = \rho(T) \times \alpha(T) \times Cp\,(T), \tag{1}$$

where Λ is the thermal conductivity, T is the temperature, ρ is the density of material, α is the thermal diffusivity, and Cp is the specific heat coefficient.

The linear thermal expansion of the Ni-Cr alloy matrix hybrid nanocomposite was estimated using NETZSCH make DIL 402C and LFA 427 model thermotester apparatus.

3. Results and Discussion

3.1. Effect Al_2O_3 and TiO_2 on Dry State Wear Performance of Ni-Cr Alloy Matrix Composite. Table 4 shows the wear test results on Ni-Cr alloy matrix hybrid nanocomposite tested by dry state condition with 0.25 m/sec, 0.5 m/sec, and 0.75 m/sec sliding speed under an applied load of 10 N, 30 N, 50 N, and 70 N, respectively.

It was observed from Figures 4(a)–4(c) that the wear rate of Ni-Cr alloy composite decreased gradually with the additions of Al_2O_3 and 5 wt% TiO_2. Figures 4(a)–4(c) illustrate the wear performance of Ni-Cr alloy containing 5 wt%, 10 wt%, and 15 wt% of Al_2O_3 with constant 5 wt% of TiO_2 hybrid nanocomposite evaluated by at 0.25 m/sec with different loading conditions like 10 N, 30 N, 50 N, and 70 N, respectively [30].

The composite having 15 wt% alumina nanoparticles with 5 wt% titanium dioxide particle shows an optimum wear resistance of $21.98\,mm^3$/m under high load 70 N. It was due to hard alumina's resistance to the deflection layer on the high frictional force. A similar trend was found during the wear evaluation of AZ61 magnesium alloy hybrid composites [7]. Figure 4(b) represents the wear rate of unreinforced and reinforced Ni-Cr alloy hybrid nanocomposite under 0.5 m/sec sliding velocity with varied load conditions of 10-70 N. It was clearly shown that the wear rate progressively increased with an increase in load condition at a constant sliding distance of 200 m [31]. Similar results were reported by León-Patiño et al. [24] during the evaluation of Ni/TiC composites. Figure 4(c) shows the variations of wear rate for Ni-Cr alloy hybrid nanocomposite estimated by a high sliding speed of 0.75 m/sec. It shows the wear rate of composite is $29.12\,mm^3$/m to $22.98\,mm^3$/m under 70 N applied load. However, the wear rate of the composite decreased with increased reinforcements. Good bonding strength between matrix and reinforcement is evidenced in Figure 4(d). However, interfacial bonding strength may be varied due to the choice of process (stir casting) parameter [5].

Figure 5 shows the coefficient of friction (COF) of Ni-Cr alloy and its hybrid nanocomposite estimated by 0.25 m/sec to 0.75 m/sec sliding velocity with varied load conditions of 10-70 N, respectively. Figure 5(a) illustrates that the
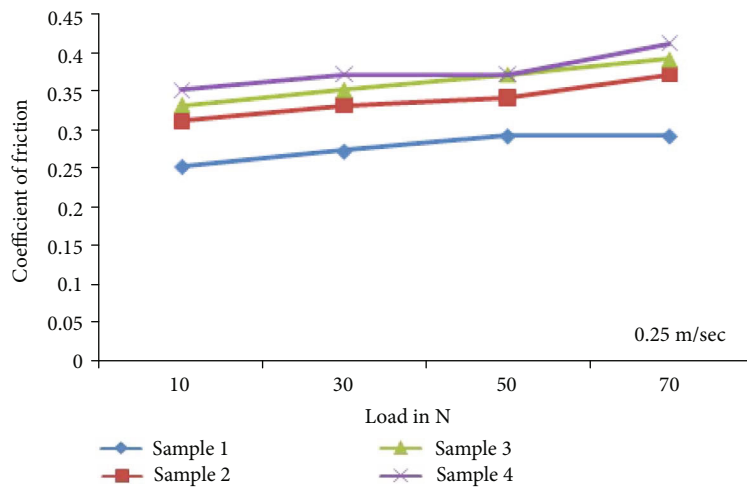
(a)
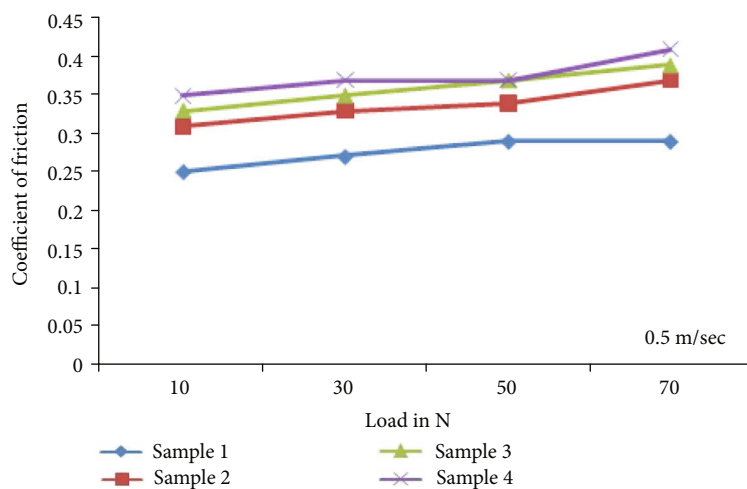
(b)
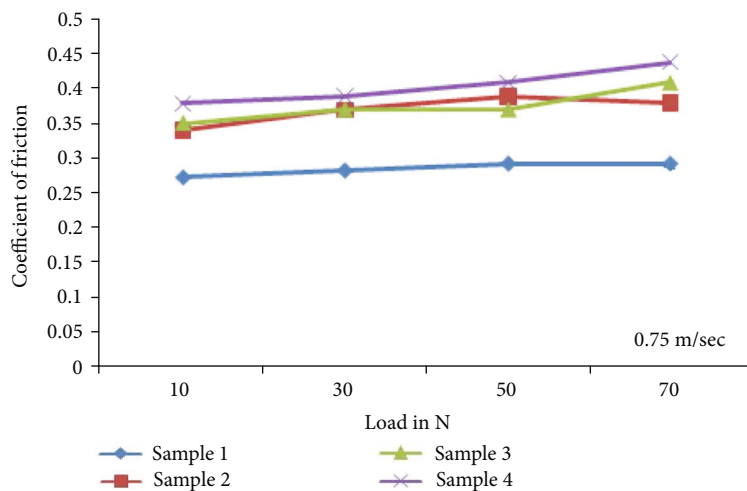
(c)

Figure 5: Continued.

(d)
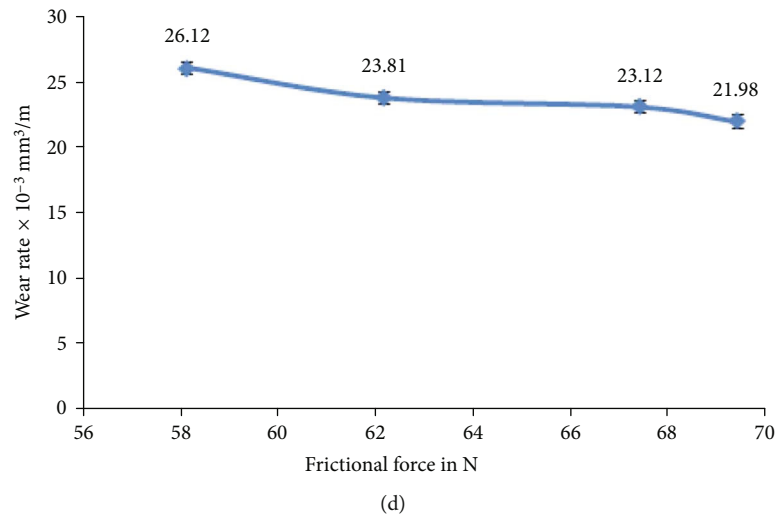
FIGURE 5: Coefficient of friction for Ni-Cr alloy matrix composites: (a) 0.25 m/sec, (b) 0.5 m/sec, and (c) 0.75 m/sec. (d) Effect of the frictional force on wear relation of Ni-Cr alloy hybrid nanocomposites.

coefficient of friction of unreinforced and reinforced Ni-Cr alloy composite varies from 0.25 to 0.41. The COF of composite has steadily increased with the additions of alumina nanoparticles and titanium dioxide particles. Figure 5(b) shows the COF of Ni-Cr alloy and its hybrid nanocomposite estimated by 0.5 m/sec sliding speed at different load conditions. The curve indicates that an upward slope varied from 0.34, 0.37, 0.39, and 0.41 on an applied load of 10 N, 30 N, 50 N, and 70 N, respectively. The improvement of COF was due to the presence of hard ceramist which leads to enhance the resistance of high frictional on the higher temperature of 57°C. The high sliding performance on COF of Ni-Cr alloy and its hybrid nanocomposite is shown in Figure 5(c). It was revealed from Figure 5(c) that the challenging ceramic plays a significant role in friction with a higher coefficient value of 0.44 under high load and sliding speed of 40 N and 0.75 m/sec with 73.6 N frictional force. However, the COF of the composite was increased progressively by adding reinforcement. The maximum COF is 0.44, found in sample 4. Its COF value increased 34% as compared to cast Ni-Cr alloy.

3.2. Effect of the Frictional Force on Wear Performance of Ni-Cr Alloy Matrix Composites. Figure 5(d) represents the relation of frictional force effect on wear behaviour of Ni-Cr alloy hybrid nanocomposite evaluated by 70 N load with the applied sliding speed of 0.25 m/sec.

It was revealed from Figure 5(d) that the composite's wear rate gradually decreased with an increased friction force of 58.12 N to 69.43 N. Sample 1 indicates that the wear rate of 26.12×10^{-3} mm^3/m on an applied load of 70 N showed that 58.12 N frictional force liberates the 57°C, while compared to reinforced hybrid nanocomposite, the wear rate of Ni-Cr alloy has high. The Ni-Cr/15 wt% Al$_2$O$_3$/5 wt% TiO$_2$ hybrid nanocomposite showed a minimum wear rate on high load under 0.25 m/sec sliding speed. The maximum frictional force of 69.43 N liberates the 68°C temperature and leads to abrasive wear, so the rigid reinforcements resist the

particle dislocation during high sliding force. So the wear rate of the composite was reduced, and the coefficient of friction was increased. Similarly, the past literature studies on the wear behaviour of Ni-Cr alloy showed an increased friction coefficient at high frictional temperatures.

3.3. Effect Al$_2$O$_3$ and TiO$_2$ on Thermal Adsorption Behaviour of Ni-Cr Alloy Matrix Composite. Table 5 represents the thermal adsorption behaviour of Ni-Cr alloy composite bonded with various weight percentages (5 wt%, 10 wt%, and 15 wt %) of Al$_2$O$_3$ and 5 wt% of TiO$_2$.

Figure 6 indicates that the thermal conductivity of Ni-Cr alloy contained 5, 10, and 15 wt% of alumina nanoparticle with stable 5 wt% of TiO$_2$. Both nanoparticles have enhanced the thermal performance of the composite.

The thermal conductivity of composite has varied from 33.918 W/m°C to 41.870 W/m°C due to the inclusion of hard ceramist. The cast Ni-Cr bonding has 33.918 W/m°C while adding 5 wt% of hybrid constitutions was 37.829 W/m°C. Generally, alumina and titanium dioxide have good thermal stability and high hardness compared to conventional reinforcements [4]. The maximum thermal conductivity of 41.870 W/m°C was found on a composite containing 15 wt% Al$_2$O$_3$/5 wt% TiO$_2$. It was due to the effect weight percentages and good isotropic properties of Ni-Cr alloy. However, the thermal conductivity of Ni-Cr alloy and its composites may vary due to input temperature conditioning. The influences of alumina and titanium dioxide nanoparticles in the nickel alloy matrix resulted in the thermal conductivity increasing by 18% compared to unreinforced nickel alloy.

The thermal dimension of temperature variations of Ni-Cr alloy and its hybrid nanocomposite coefficient of thermal expansion (CTE) is represented in Figure 7. It was closely observed by the thermal changes of Ni-Cr alloy hybrid nanocomposite which may be related to the bonding of matrix and reinforcement. The CTE of Ni-Cr alloy was 17 $\times 10^{-6}$ and adding 5 and 10 wt% Al$_2$O$_3$/5wt%TiO$_2$ was 15

TABLE 5: Thermal behaviour of Ni-Cr alloy composite.

| Sample/units | Constitutions | Thermal adsorption performance Ni-Cr alloy matrix hybrid nanocomposites | | |
		Thermal conductivity W/m°C	Coefficient of thermal expansion X10^{-6}	Wear loss on 1000°C mg
1	Ni-Cr alloy	33.918	17	9.78
2	Ni/5 wt% Al_2O_3/5 wt% TiO_2	37.829	15	34.78
3	Ni/10 wt% Al_2O_3/5 wt% TiO_2	39.619	13	54.32
4	Ni/15 wt% Al_2O_3/5 wt% TiO_2	41.870	15	40.71
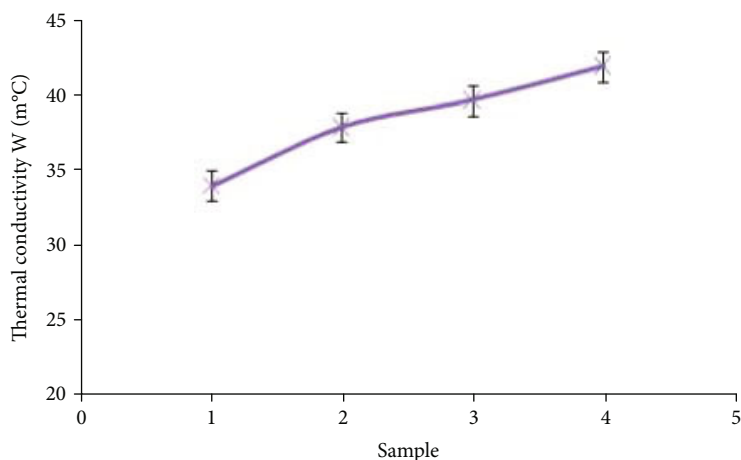
FIGURE 6: Thermal conductivity of Ni-Cr alloy matrix composites.
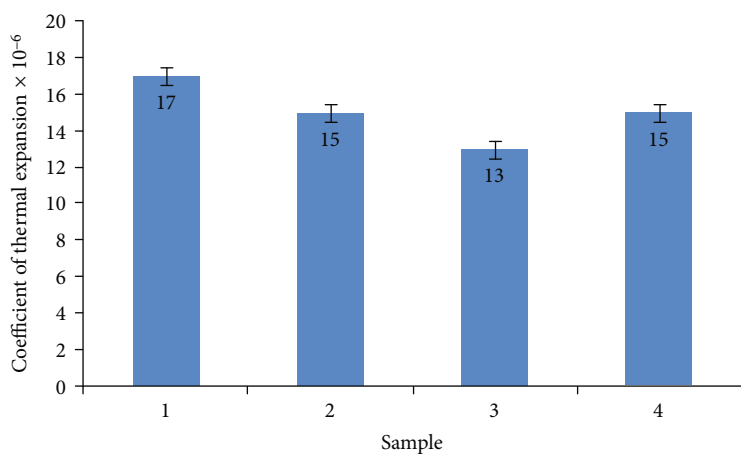
FIGURE 7: Coefficient of thermal expansion of Ni-Cr alloy matrix composites.

$\times 10^{-6}$ and 13×10^{-6}, respectively. It was due to the increased temperature of 30°C to 900°C. After that, the composite contained 15 wt% Al_2O_3/5wt% TiO_2 hybrid nanocomposite with a thermal growth of (15×10^{-6}). It happened due to its temperature drop from 900°C to 600°C. At this point, the thermal expansion was increased nominally. So, from the heating to cooling phase, the coefficient of thermal expansion for nickel alloy hybrid composite decreases progressively with increased reinforcement con-

tent as 10 wt% Al_2O_3/5 wt% TiO_2. Further inclusion of both Al_2O_3 and TiO_2 in nickel alloy was increased nominally.

3.4. *Thermal Adsorption Characteristics.* The thermal adsorption characteristics of mass loss of Ni-Cr alloy and its hybrid nanocomposites were evaluated by thermogravimetric apparatus configured with 0°C to 1500°C temperature span under a constant heat flow rate of 25°C/min as shown in Figures 8(a)–8(d). The wear loss of Ni-Cr alloy was found
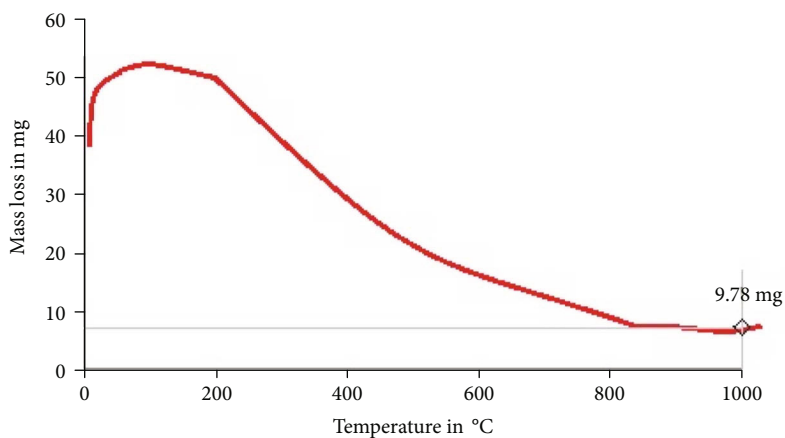
(a)
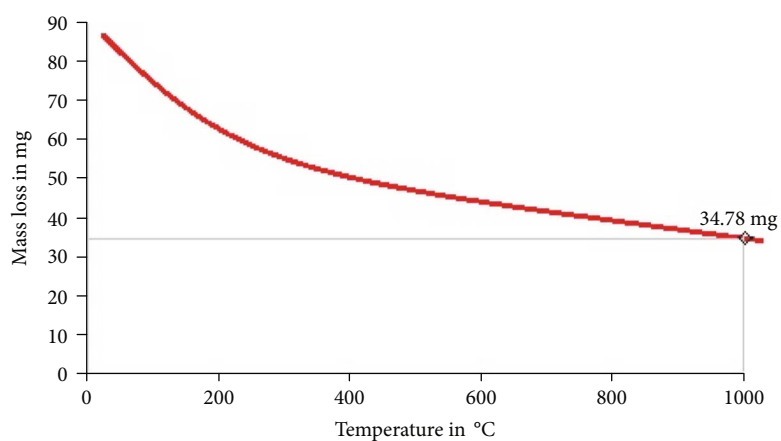
(b)
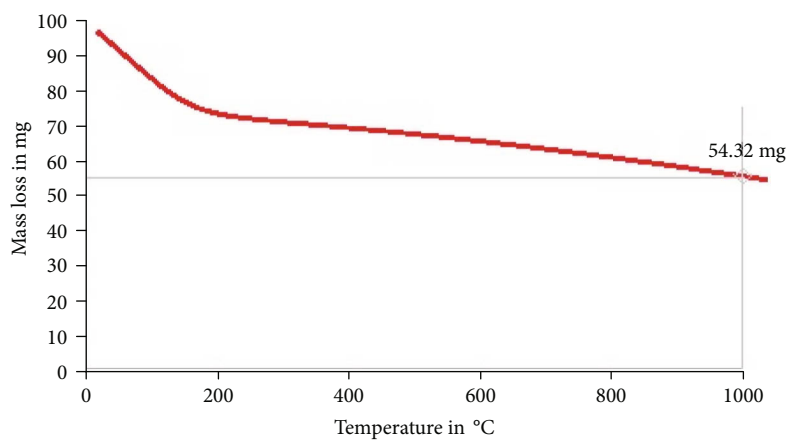
(c)

Figure 8: Continued.

(d)
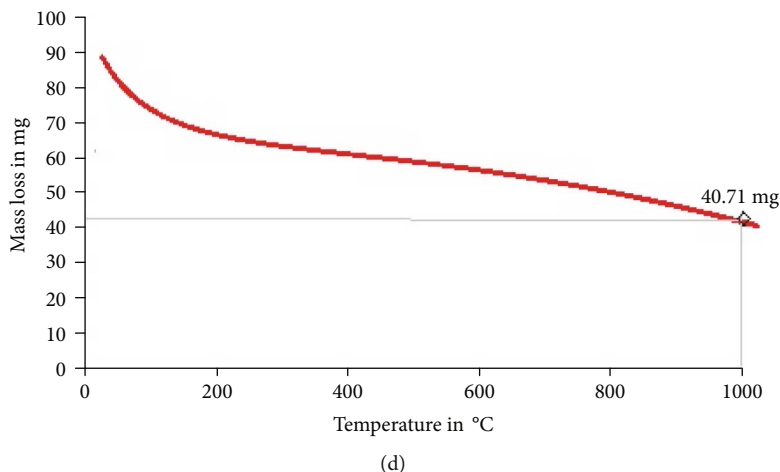
FIGURE 8: Thermal adsorption performance on wear loss of Ni-Cr alloy matrix composites: (a) cast Ni-Cr alloy, (b) Ni-Cr/5 wt% Al$_2$O$_3$/5 wt% TiO$_2$, (c) Ni-Cr/10 wt% Al$_2$O$_3$/5 wt% TiO$_2$, and (d) Ni-Cr/15 wt% Al$_2$O$_3$/5 wt% TiO$_2$.

at 9.78 mg on 1000°C under 25°C/min steady heat supply. At the same time, incorporating Al$_2$O$_3$ and 5 wt% of TiO$_2$ in the Ni-Cr matrix showed higher mass loss than Ni-Cr alloy. It was due to the effect of ceramic particles on different phases, like dislocation between the Ni-Cr layers. Figures 8(c) and 8(d) illustrate the effect of thermal adsorption on mass loss of hybrid nanocomposites containing 10 wt% and 15 wt% of alumina nanoparticles with stable 5 wt% of TiO$_2$ particle, resulting in a limited mass loss on a higher temperature. The curve of Figure 8(d) indicates the regular slope of 926°C. Further temperature increases showed a steady-state condition of mass loss. It happened due to the chain reaction of hard ceramic particles that can withstand the high temperature on 25°C/min heat flow.

The weight loss of the hybrid nanocomposite (Ni-Cr/15 wt% Al$_2$O$_3$/5 wt% TiO$_2$) was limited to 1.21 times of ambient temperature under the same heat flow of 25°C/min. However, the thermal adsorption on mass loss of composite is related to interfacial bonding strength between matrix and reinforcements of the hybrid nanocomposite.

4. Conclusions

The vacuum die casting process developed the nickel alloy (Ni-Cr) matrix hybrid nanocomposites. The developed composites were subjected to tribothermal characteristics studies. Based on this performance, the composite containing 15 wt% alumina nanoparticles with 5 wt% titanium nanoparticles was found to have optimum tribological-thermal properties compared to conventional cast Ni-Cr alloy. The wear resistance of sample 4 is increased by 16% compared to cast Ni-Cr alloy. The coefficient of friction of 0.44 is observed on Ni-Cr alloy/15 wt% alumina nanoparticle with 5 wt% titanium nanoparticle under high sliding speed and a load of 0.75 m/sec and 70 N. The thermal conductivity of Ni-Cr alloy/15 wt% Al$_2$O$_3$/5wt%TiO$_2$ hybrid nanocomposite found 18% increased conductivity compared to Ni-Cr alloy. However, the composite containing 15 wt% Al$_2$O$_3$/5wt% TiO$_2$ shows 15×10^{-6}, and its CTE decreased to 11% compared

to Ni-Cr alloy. It was due to the reason that decreased CTE was related to bonding strength between Ni-Cr alloy and ceramist. The thermal adsorption performance on weight loss of hybrid nanocomposite (Ni-Cr/15 wt% Al$_2$O$_3$/5 wt% TiO$_2$) was limited to 1.21 times ambient temperature under the heat flow rate of 25°C/min.

Data Availability

The data used to support the findings of this study are included within the article. Should further data or information be required, these are available from the corresponding author upon request.

Conflicts of Interest

The authors declare that there are no conflicts of interest regarding the publication of this paper.

References

[1] S. J. Komarneni, "Nanocomposites," *Journal of Materials Chemistry C, Materials for Optical and Electronic Devices*, vol. 2, no. 12, pp. 1219–1219, 1992.

[2] L. Natrayan and M. Senthil Kumar, "Influence of silicon carbide on tribological behaviour of AA2024/Al$_2$O$_3$/SiC/Gr hybrid metal matrix squeeze cast composite using Taguchi technique," *Materials Research Express*, vol. 6, no. 12, article 1265f9, 2019.

[3] D. S. Prasad and C. Shoba, "Hybrid composites - a better choice for high wear resistant materials," *Journal of Material Research Technology*, vol. 3, no. 2, pp. 172–178, 2014.

[4] F. Bauer, H. J. Gläsel, E. Hartmann, H. Langguth, and R. Hinterwaldner, "Functionalized inorganic/organic nanocomposites as new basic raw materials for adhesives and sealants," *International Journal of Adhesive and Adhesives*, vol. 24, no. 6, pp. 519–522, 2004.

[5] R. Karthik, K. Gopalakrishnan, R. Venkatesh, A. M. Krishnan, and S. Marimuthu, "Influence of stir casting parameters in mechanical strength analysis of aluminium metal matrix

composites (AMMCs)," *Material Today Proceeding*, vol. 62, Part 4, pp. 1965–1968, 2022.

[6] M. Senthil Kumar, L. Natrayan, R. D. Hemanth, K. Annamalai, and E. Karthick, "Experimental investigations on mechanical and microstructural properties of Al_2O_3/SiC reinforced hybrid metal matrix composite," *IOP Conference Series: Materials Science and Engineering*, vol. 402, no. 1, 2018.

[7] R. Venkatesh, C. R. Kannan, S. Manivannan et al., "Synthesis and experimental investigations of tribological and corrosion performance of AZ61 magnesium alloy hybrid composites," *Journal of Nanomaterials*, vol. 2022, Article ID 6012518, 12 pages, 2022.

[8] N. Verma and S. C. Vettivel, "Characterization and experimental analysis of boron carbide and rice husk ash reinforced AA7075 aluminium alloy hybrid composite," *Journal of Alloys and Compounds*, vol. 741, pp. 981–998, 2018.

[9] R. AM, M. Kaleemulla, S. Doddamani, and B. KN, "Material characterization of SiC and Al_2O_3–reinforced hybrid aluminum metal matrix composites on wear behavior," *Advanced Composite Letters*, vol. 28, 10 pages, 2019.

[10] L. Natrayan, M. Singh, and M. Senthil Kumar, "An experimental investigation on mechanical behaviour of SiCp reinforced Al 6061 MMC using squeeze casting process," *International Journal of Mechanical and Production Engineering Research and Development (IJMPERD)*, vol. 7, no. 6, pp. 663–668, 2017.

[11] D. Ulutan and T. Ozel, "Machining induced surface integrity in titanium and nickel alloys: a review," *International Journal of Machine Tools and Manufacture*, vol. 51, no. 3, pp. 250–280, 2011.

[12] Z. Fattahi, S. A. Sajjadi, A. Babakhani, and F. Saba, "Ni-Cr matrix composites reinforced with nano- and micron-sized surface- modified zirconia: synthesis, microstructure and mechanical properties," *Journal of Alloys and Compounds*, vol. 817, article 152755, 2020.

[13] L. Natrayan and M. Senthil Kumar, "Optimization of wear behaviour on AA6061/Al2O3/SiC metal matrix composite using squeeze casting technique–statistical analysis," *Materials Today: Proceedings*, vol. 27, Part 1, pp. 306–310, 2020.

[14] F. Li, S. Zhu, J. Cheng, Z. Qiao, and J. Yang, "Tribological properties of Mo and CaF_2 added SiC matrix composites at elevated temperatures," *Tribology International*, vol. 111, pp. 46–51, 2017.

[15] S. M. Sharma and A. Anand, "Friction and wear behaviour of Fe-Cu-C based self-lubricating material with CaF_2 as solid lubricant," *Industrial Lubrication and Tribology*, vol. 69, no. 5, pp. 715–722, 2017.

[16] F. Li, J. Cheng, S. Zhu, J. Hao, J. Yang, and W. Liu, "Microstructure and mechanical properties of Ni-based high temperature solid- lubricating composites," *Material Science and Engineering A*, vol. 682, pp. 475–481, 2017.

[17] J. M. Zhen, Y. Han, J. Chen et al., "Influence of Mo and Al elements on the vacuum high temperature tribological behavior of high strength nickel alloy matrix composites," *Tribology International*, vol. 131, pp. 702–709, 2019.

[18] L. Natrayan and M. Senthil Kumar, "An integrated artificial neural network and Taguchi approach to optimize the squeeze cast process parameters of AA6061/Al_2O_3/SiC/Gr hybrid composites prepared by novel encapsulation feeding technique," *Materials Today Communications*, vol. 25, article 101586, 2020.

[19] X. H. Zhang, J. Cheng, M. Niu, H. Tan, W. Liu, and J. Yang, "Microstructure and high temperature tribological behavior of Fe_3Al- $Ba_{0.25}Sr_{0.75}SO_4$ self-lubricating composites," *Tribology International*, vol. 101, pp. 81–87, 2016.

[20] B. Li, J. Jia, Y. Gao, M. Han, and W. Wang, "Microstructural and tribological characterization of NiAl matrix self- lubricating composite coatings by atmospheric plasma spraying," *Tribology International*, vol. 109, pp. 563–570, 2017.

[21] S. Yogeshwaran, R. Prabhu, L. Natrayan, and R. Murugan, "Mechanical properties of leaf ashes reinforced aluminum alloy metal matrix composites," *International Journal of Applied Engineering Research*, vol. 10, no. 13, pp. 11048–11052, 2015.

[22] C. A. I. Bin, Y. F. Tan, H. E. Long, T. A. N. Hua, and X. L. Wang, "Tribological properties of Ni-base alloy composite coating modified by both graphite and TiC particles," *Transactions of Nonferrous Metals Society of China*, vol. 21, no. 11, pp. 2426–2432, 2011.

[23] P. W. Leech, X. S. Li, and N. Alam, "Comparison of abrasive wear of a complex high alloy hardfacing deposit and WC- Ni based metal matrix composite," *Wear*, vol. 294-295, pp. 380–386, 2012.

[24] C. A. León-Patiño, M. Braulio-Sánchez, E. A. Aguilar-Reyes, E. Bedolla-Becerril, and A. Bedolla-Jacuinde, "Dry sliding wear behavior of infiltrated particulate reinforced Ni/TiC composites," *Wear*, vol. 426-427, pp. 989–995, 2019.

[25] M. Srivastava, V. K. Srinivasan, and W. Grips, "Influence of zirconia incorporation on the mechanical and chemical properties of Ni-Co alloys," *American Journal of Material Science*, vol. 1, no. 2, pp. 113–122, 2011.

[26] D. B. Miracle, "Metal matrix composites - from science to technological significance," *Composites Science and Technology*, vol. 65, no. 15–16, pp. 2526–2540, 2005.

[27] P. S. Bains, S. S. Sidhu, and H. S. Payal, "Fabrication and machining of metal matrix composites: a review," *Materials and Manufacturing Processes*, vol. 31, no. 5, pp. 553–573, 2015.

[28] K. Velavan, K. Palanikumar, E. Natarajan, and W. H. Lim, "Implications on the influence of mica on the mechanical properties of cast hybrid (Al+10%B_4C+Mica) metal matrix composite," *Journal of Materials Research and Technology*, vol. 10, pp. 99–109, 2021.

[29] C. H. Xu, G. Y. Wu, G. C. Xiao, and B. Fang, "Al_2O_3/(W,Ti)C/ CaF_2 multi-component graded self-lubricating ceramic cutting tool material," *International Journal of Refractory Metals and Hard Materials*, vol. 45, pp. 125–129, 2014.

[30] S. Y. Zhu, F. Li, J. Ma et al., "Tribological properties of Ni_3Al matrix composites with addition of silver and barium salt," *Tribology International*, vol. 84, pp. 118–123, 2015.

[31] D. S. Xiong, C. Q. Peng, and Q. Z. Huang, "Development of MoS_2- containing Ni-Cr based alloys and their high-temperature tribological properties," *Transactions of Nonferrous Metals Society of China*, vol. 8, no. 2, p. 2269, 1998.

SAGE Publishing

Research Article

Adsorption and Photocatalytic Degradation Properties of Bimetallic Ag/MgO/Biochar Nanocomposites

R. Venkatesh ,[1] P. Raja Sekaran,[2] K. Udayakumar,[2] D. Jagadeesh,[3] K. Raju ,[4] and Melkamu Beyene Bayu [5]

[1]*Department of Mechanical Engineering, Saveetha School of Engineering, SIMATS, Chennai, 602105 Tamil Nadu, India*
[2]*Department of Mechanical Engineering, Er. Perumal Manimekalai College of Engineering, Hosur, 635117 Tamil Nadu, India*
[3]*Department of Mechanical Engineering, Kongunadu College of Engineering and Technology, Trichy, 621215 Tamil Nadu, India*
[4]*Department of Mechanical Engineering, M. Kumarasamy College of Engineering, 639113 Tamil Nadu, India*
[5]*Department of Mechanical Engineering, Ambo Institute of Technology-19, Ambo University, Ambo, Ethiopia*

Correspondence should be addressed to R. Venkatesh; venkateshr.sse@saveetha.com
and Melkamu Beyene Bayu; melkamu.beyene@ambou.edu.et

The Ag/MgO/biochar nanostructures were fabricated using a solvent-free ball milling process as an effective adsorbent. Development of functional materials capable of completely removing organic pollutants from water and their adequate adsorption present challenges. The addition of MgO nanoparticles diffused equally on biochar surfaces in the biochar matrix, according to various characterization data. In decomposing biochar and compressing MgO, powdered metal enhanced mesopores and macropores of nanocomposites. XPS analysis indicates the potential synthesis of modified biochar nanocomposites. Adequate amounts of MgO added to biochar improved the ability of the nanocomposites to remove methylene blue (M.B.) through photosynthesis and adsorption. Photocatalytic analysis was carried out for the proposed novel composites to remove tetracycline (T.C.) subjected to different conditions. The photodegradation efficiency was found 80.26% for TC concentration, 50 ppm, H_2O_2 of 100 mM pH: 5-6 of Ag/MgO/biochar (0.01 g) at 25° temperature. Treatment of various organic wastewaters by metal oxide/biochar nanocomposites with strong adsorption and photocatalytic degradation capabilities is made possible by this research.

1. Introduction

Wastewater reclamation is required for various applications as a financially efficient and effective technologies for removing harmful contaminants [1, 2]. This approach is preferred in most countries based of water scarcity caused by fluctuating rainfall and inconsistent accessibility to other water sources, especially for cultivation [3, 4]. In terms of wastewater management, this strategy is a better option in light of the emergence of renewable initiatives.

The combined efficiency of adsorption and photocatalytic techniques dramatically increases the applications of biochar/meal oxide nanocomposites [5]. Pretreatment of the substrate with dissolved salts such as $MgCl_2$, $CaCl_2$, $FeCl_3$, and $ZnCl_2$ before pyrolysis is a common approach for producing metal

oxide-enhanced biochar [6]. In addition, metal oxides can be significantly reduced or precipitated on pure biochar surfaces. The main difference between the two fabrication techniques is whether or not the metal component is loaded before pyrolysis. Also, all species provide chemical solutions, which are dangerous to the ecosystem. In addition, asymmetric amounts of the two synthesized metal salts may lead to the accumulation of irregular dispersion of metal oxide nanoparticles on top of the biochar [7]. Consequently, developing simple and environmentally safe metal oxide/biochar nanocomposite formulations is necessary.

Ball milling is a solvent-free fabrication technique for synthesis of adsorbent nanocomposite materials due to easy process, environmentally accessibility, low cost, and high quality of materials [8]. Using ball milling techniques increases the

biochar particles' size and improves the biochar's absorbent properties by forming functional groups of the biochar [9]. To obtain the homogeneous distribution of metal oxide nanoparticles and propose the lattice defects for developing the photocatalytic execution [10], the results of this research suggest that ball milling is a quick and easy way to create a nanocomposite of metal oxide and biochar for enhanced high absorption and photocatalytic capabilities.

Over the past two decades, tetracycline (T.C.) has played a significant role due to its inhibitory antibacterial activity against the spread of coronavirus [11]. Tetracyclines (T.C.) are produced by modifying natural tetracycline to form many compounds that are widely antibacterial for humans and wildlife [12]. However, only a tiny portion of those tetracyclines is absorbed by human and animal organs, endangering both humans and the environment. Hence, a proper and effective treatment plan is essential [13].

Several experimental studies performed the determination and evaluation of materials for simultaneous absorption and photolysis of methylene blue (M.B.) from groundwater. This investigation used solvent-free ball milling fabrication techniques to fabricate Ag/MgO/biochar composites. The work has been followed to (i) conduct the XPS analysis for identifying the relation between biochar and their composites which was involved in ball milling techniques, (ii) investigate the performance of adsorption for removal of methylene blue, and (iii) analyze photocatalytic degradation of Ag/MgO/biochar for removal of tetracycline (T.C.) with different pH levels.

2. Materials and Methods

2.1. Preparation of Biochar.
The synthesis of Ag/MgO/biochar nanocomposites was prepared with the addition of silver nitrate ($AgNO_3$) -99.9% and magnesium chloride hexahydrate ($MgCl_2.6H_2O$) and methylene blue (M.B.). Chemicals are used correctly and are of diagnostic quality. Distilled water is used to produce organic matter.

2.2. Synthesis of Biochar Nanocomposites.
The modified Ag/MgO/biochar was synthesized using the high-energy ball milling method, as shown in Figure 1. At an Mg : Ag weight ratio of 1 : 1 and 2 : 1 wt% ratio of Ag : B.C. and Mg : B.C., 5 g of rice straw flour was mixed with 0.17 g of magnesium chloride hexahydrate ($MgCl_2.6H_2O$) and 0.08 and silver nitrate [14]. A planetary ball mill machine was used to grind 1.8 g of Pb and MgO mixtures at various volume ratios using 600 mL vials filled with 170 g agate balls of 6 mm diameter. The ball mill experiment is operated at 400 rpm for 12 hours with a 1-hour rotation change in direction.

2.3. Adsorption Performance of Ag/MgO/Biochar Nanocomposites.
The Ag/MgO/biochar nanocomposites of M.B. removal rate were identified with 30 mg of all combinations of specimen added to 200 mL of 200 mL M.B. solution. They were moved to the surface mixture and stirred for 24 h until equilibrium (25 2°C) was reached. M.B. adsorption on the sample gradually increased during the first 20 min due to the availability of multiple adsorption sites on the adsor-

bent material [15]. The kinetic adsorption process is enhanced by the functions of mesopores and macropores in Ag/MgO/biochar nanocomposites. The combinations were then passed through 0.22 μm nylon film filters, and the M.B. concentration of the extracted extract was determined using spectrophotometry with a wavelength of 665 nm. Mass balance analysis was used to estimate the amount of M.B. absorbed in the prepared MgO/biochar composites [16]. The adsorption process obtained measurements were simulated using adsorption kinetics and equilibrium adsorption models, and analytical expressions of the modelling techniques are presented in the Supplementary data.

2.4. Photocatalytic Analysis.
All samples dispersed in 100 mL of aqueous solution (160 mg/L) using a quartz beaker were subjected to photocatalytic analysis. Consequently, the stirring and irradiation were suspended suddenly under the 250 W LED lamp conditions. The measurement was taken at a particular time interval during the light irradiation for 2 mL of suspension [17]. The methylene blue (M.B.) removal rate was simulated and measured for 1st order and modified Elovich models during the light irradiation. The statistical value of all adsorbent and photocatalyst studies is used [18].

3. Results and Discussion

3.1. XPS Analysis of Ag/MgO/Biochar.
XPS analysis of robust surface techniques has been used to determine the ionic properties and interfacial bonding between biochar and their mixtures. Chemical compositions of Ag/MgO/biochar nanocomposites were compatible with the EDS spectrum. According to the results of the XPS examination, N1s, O1s, and C1s are encountered in this study with Ag/MgO/biochar nanocomposites as significant components, as shown in Figure 2. According to Figure 2, the highest peak intensities of C1s are 292.24 eV, 284.65 eV, and 282.45 eV, respectively, and are attributed to C=C, C–C, and C–O bonds. In addition, the C-O peak intensity from 289.57 eV to 292.24 eV changed significantly in the C1s of Ag/MgO@BC nanocomposites, and the C=C diffraction peak was observed from 294.02 eV to 288.24 eV [19]. Both of these changes indicate the conversion of Ag+ into AgNPs and the formation of MgONPs on the exterior of the customized biochar nanocomposites.

The biochar of O1s reaches different peak intensities depending on the binding energy at 535.21 eV, 538.16 eV, and 542.32 eV, respectively, attributed to metallic oxides by lattice oxygen subjected to surface oxygen-assessed functional group [20]. Similarly, O1s of Ag/MgO/biochar spectrum demonstrate that Mg-O bonding with change in intensity of peak at 539.21 eV, 540.26 eV, and 542.36 eV is partly related to change in the concentration of oxygen vacancy. In addition, the N1s spectra of biochar confirmed the existence of C-N at 399 and 403.25 eV, which is expanded to 401.45 and 405.26 eV in Ag/MgO@BC, indicating the synthesis of MgO and their potential interactions
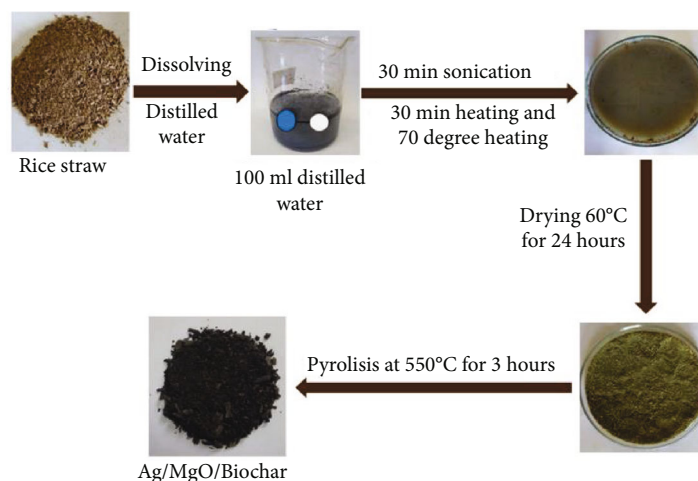
FIGURE 1: Synthesis of Ag/MgO/biochar.
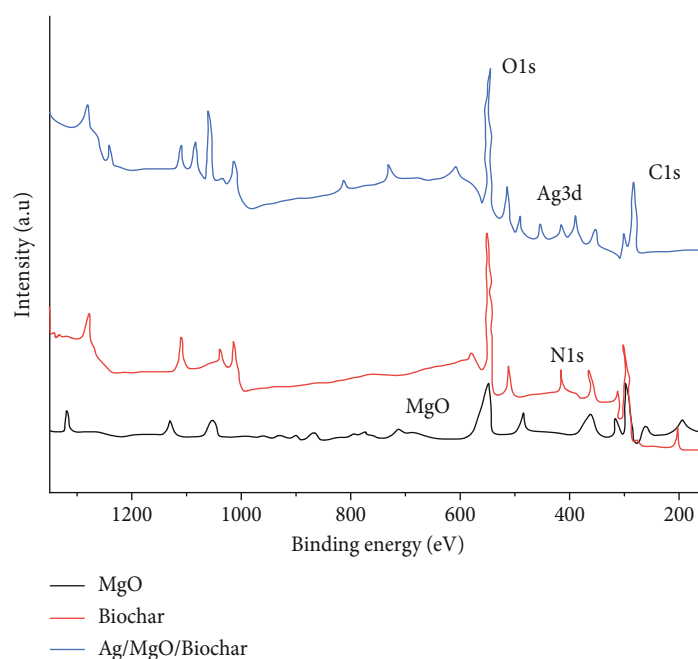
FIGURE 2: Ag/MgO/biochar XPS spectra.

with AgNPs and N interactions, as shown in Figures 3(a)–3(d).

Ball milling may cause chemical reactions among MgO and biochar in the composites, and the O1s spectra are supported by a slight change in the biochar and their composites (Figures 4(a) and 4(b)). Ball milling involves material interfaces sliding against each other in a friction-like manner, which converts a significant amount of mechanical energy into heat to produce larger parts on regional and macroscopic scales [21]. The extreme temperatures of available regions can cause localized changes and interactions of atoms to form nanocomposites.

Table 1 shows the quantitative analysis of the surface area that established the porous structure of MgO-biochar.

During ball milling, the biochar surface area Brunauer-Emmett Teller (BET) improved from $225.7 \, m^2/g$ to $280.65 \, m^2/g$, demonstrating that this technique can improve the surface area of biochar. The BET area of MgO is $4.3 \, m^2/g$ after the ball milling process when compared to without modified biochar. The specific surface area of Ag/MgO/biochar is $160.2 \, m^2/g$, equal to the definite standardized area. It suggests that high-intensity ball milling using MgO nanoparticles influenced the morphology and interfacial properties of the biochar matrix. In addition, a portion of the nanoparticles dissolved and incorporated into the bioreactor's permeate, reducing the nanocomposites' total active area. Both enlarged surface porous structures and cracks were observed as the biochar, and their blends were broken

(a)

(b)

Figure 3: Continued.

O1s of Ag/MgO/Biochar

(c)
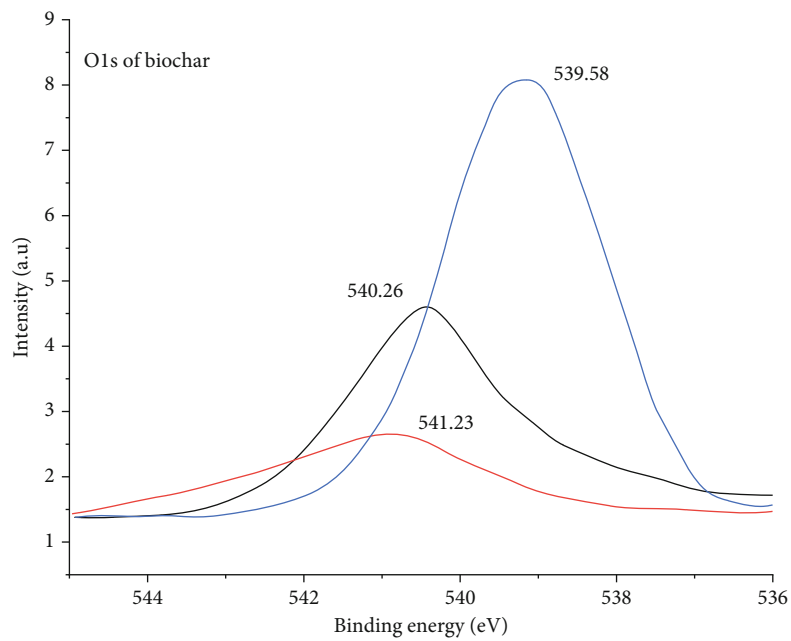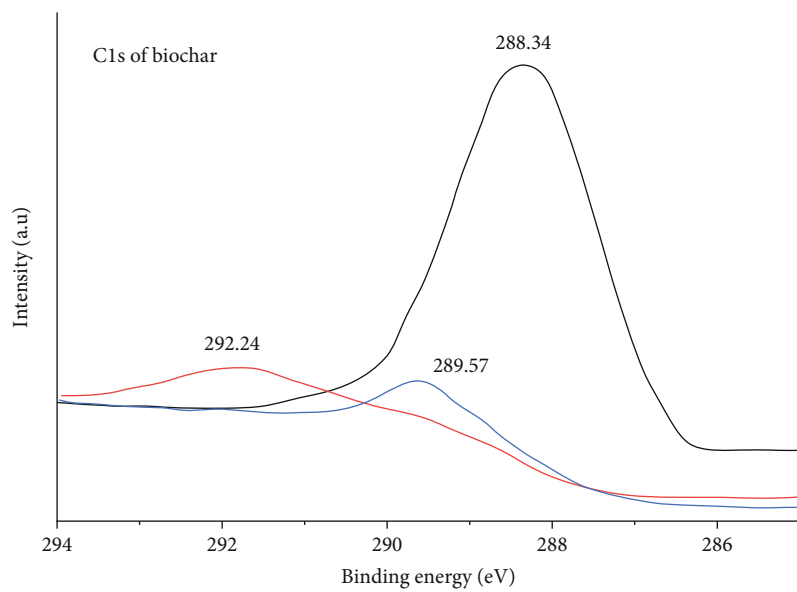
C1s of Ag/MgO/Biochar

(d)
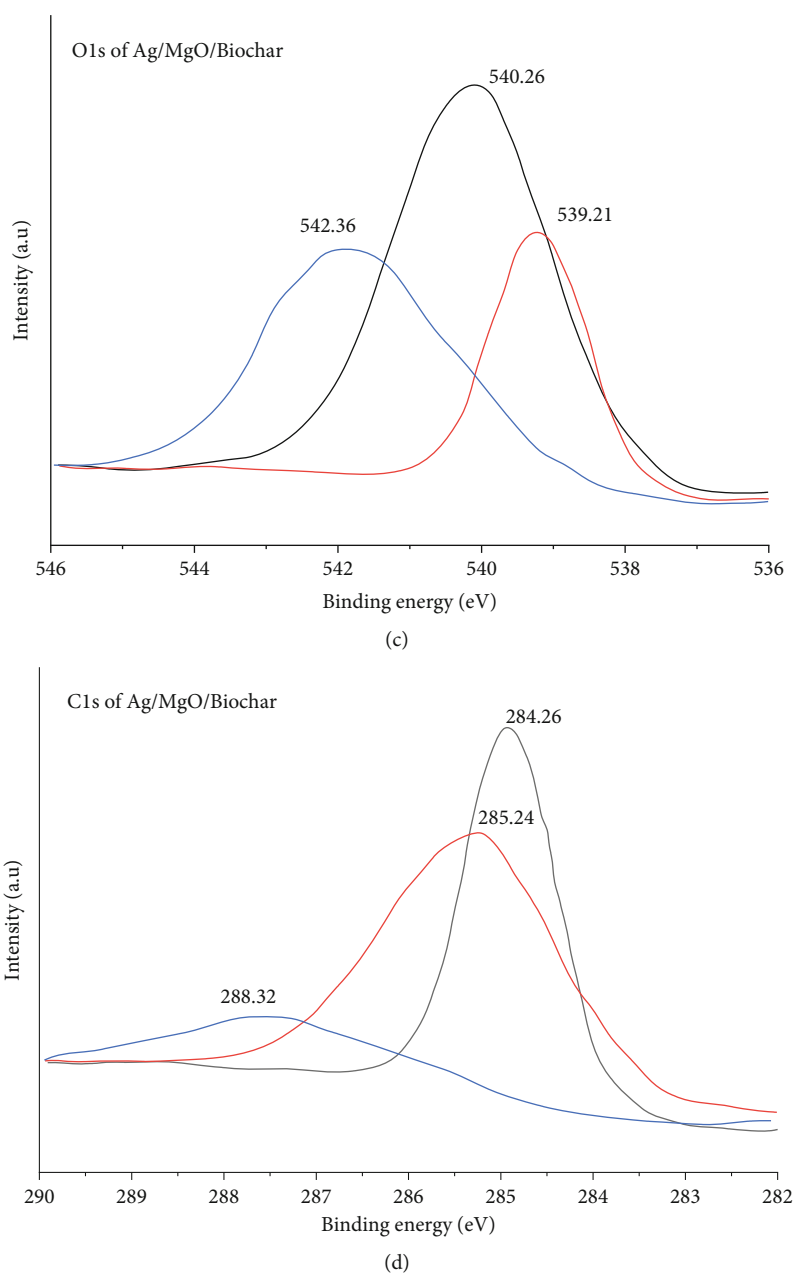
FIGURE 3: XPS analysis of biochar: (a) O1s biochar; (b) C1s of biochar; (c) O1s of Ag/MgO/biochar; (d) C1s of Ag/MgO/biochar.

into small-sized pieces during the ball milling process [22]. In the nanometre size range, MgO has a great propensity to extrude into the pores and fractures of biochar thermally. Mg_2p spectra of sample Ag/MgO/biochar are shown in Figure 5, with a characteristic peak at 51.46 eV for MgO. This Mg_2p spectrum showed a significant increase compared to BMmix, suggesting that the ball milling method may have had a more profound effect on the composition of the composites than easy mixing [23].

The sample N2 absorption spectra are all according to the classification of type I isotherms, confirming a large number of micropores, as shown in Figure 4. The N2 Adsorption Isotherm Decomposition compared to modified biochar shows apparent abrupt absorption at a relative pres-

sure of 1.0, demonstrating the formation of a significant number of macropores. The distribution of pore sizes in Table 1 shows the presence of numerous micropores, macropores, and micromesopores. MgO/Ag/biochar had a higher specific surface area and maximum pore size than other prepared samples. After the ball milling process significantly increases the macropores and mesopores ($V_{mes} + V_{mac}$), the squeeze of zinc oxide nanoparticles in biochar creates additional porosity and fractures and significantly expands the biochar, whereas grinding can break the biochar into smaller particles and increase the surface area.

3.2. Adsorption Mechanism of M.B. The adsorption process enhances adsorption kinetics due to the accessibility of

N1s of biochar

403.25

399.78

Intensity (a.u)

Binding energy (eV)

(a)

N1s of Ag/MgO/Biochar

401.45

405.26

Intensity (a.u)

Binding energy (eV)

(b)
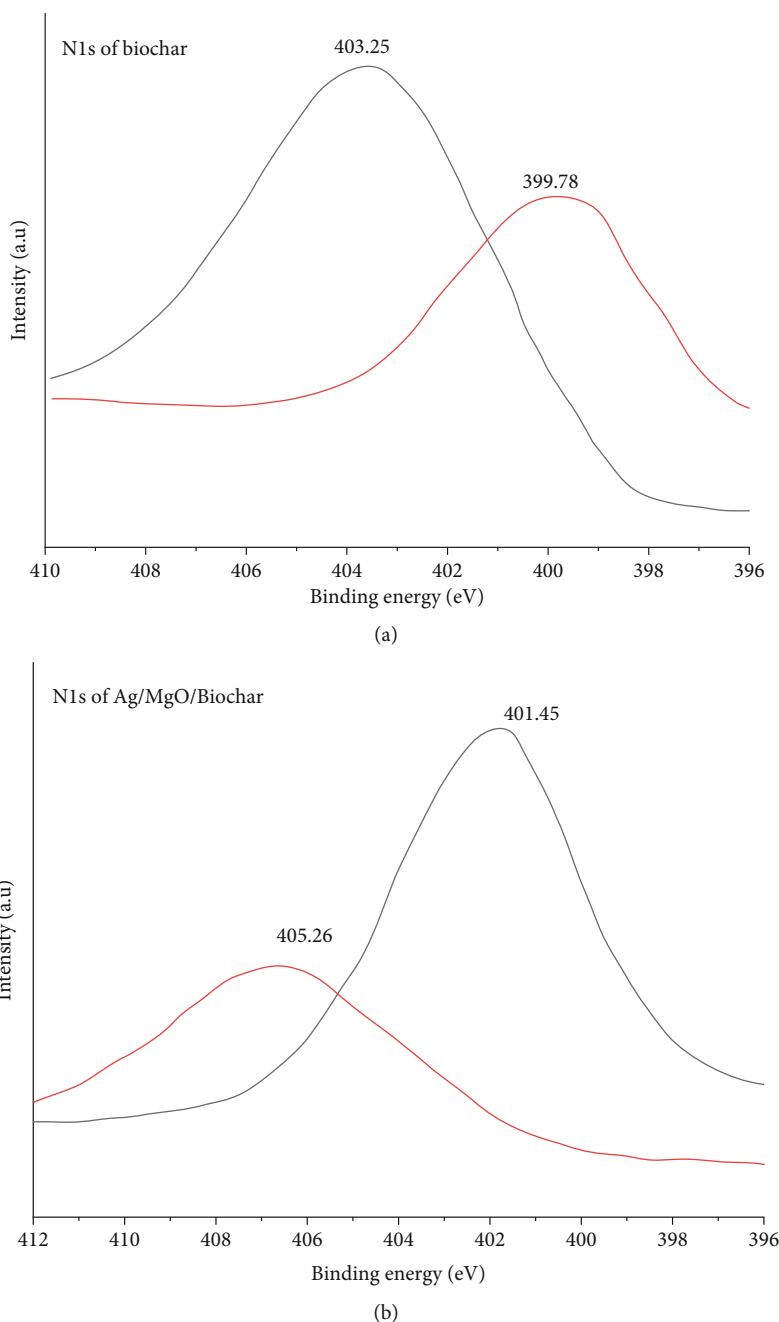
FIGURE 4: (a) N1s of biochar; (b) N1s of Ag/MgO/biochar.

TABLE 1: Ag/MgO/biochar physicochemical properties.

Materials	Average size of MgO (nm)	BTE (m^2/g)	BJH pore volume (cm^3/g)
MgO	102	10.52	—
Ag/MgO/biochar	25.6	160.2	0.95
H.C.	—	225.7	0.105
BMHC	—	280.65	0.132

mesopores and macropores. The absorption rate decreased until the absorption mechanism reached 256 min, as shown in Figure 6. The MB pseudosecond-order dynamic model of the adsorption process of nanocomposite membranes is better than the pseudofirst-order model coupled with a coefficient of determination, and also, Langmuir and Freundlich's best fit model is shown in Figure 7. It suggests that multiple processes may have been operating to regulate the adsorption of M.B. on MgO/biochar nanocomposites. The combinations of all nanocomposites had the highest M.B. adsorption, indicating that high MgO loading on biochar would reduce the adsorption capacity of Ag/MgO/biochar
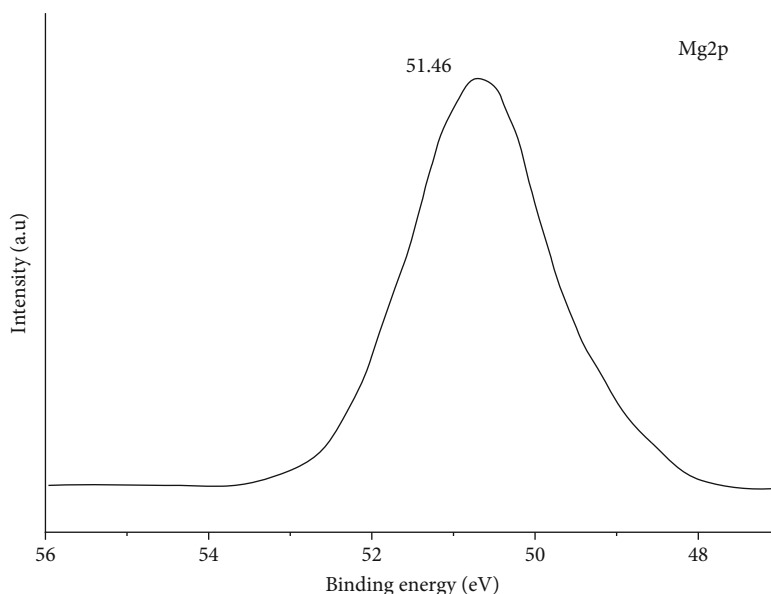
FIGURE 5: XPS spectra of Mg2p.
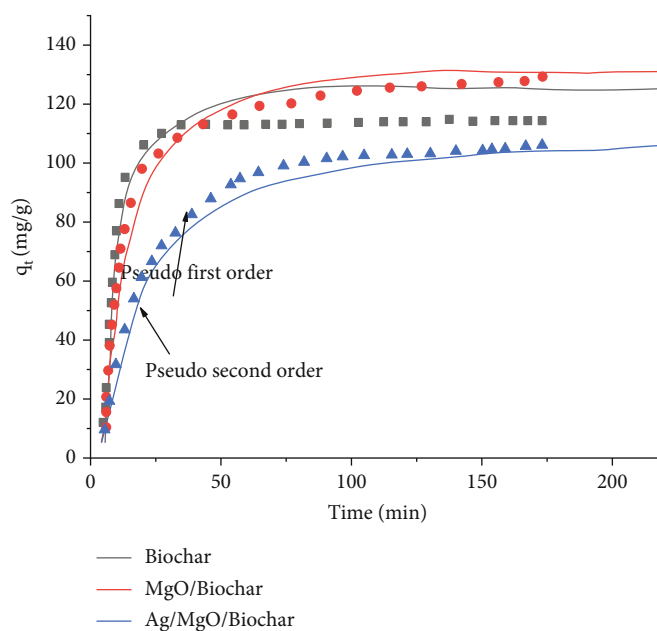
FIGURE 6: Adsorption kinetics.

composites. As shown in Table 2, adsorption kinetics of R^2 values of 0.991 and 0.925 were obtained for Ag/MgO/biochar for both first- and second-order mock samples, respectively. Table 3 shows the M.B. adsorption for Langmuir and Freundlich's best fit model.

3.3. Adsorption Isothermal of M.B. Recent research has demonstrated that M.B. adsorption in biochar-based nanocomposites can significantly affect electrostatic interactions (Zheng et al., [11]). Freundlich and Langmuir regression analysis was used to calculating the optimal efficiency of

M.B. adsorption isothermal. Although the different models, with R^2 values above 0.990, accurately characterized the isothermal models, they could not provide any light on the processes underlying M.B. adsorption on MgO/biochar nanocomposites, as shown in Table 4. All ball-milled samples in this investigation, whether they were MgO or not, had significantly more vital M.B. adsorption capacity than pure B.B. It is considered that adding nanoparticles to biochar throughout ball milling can expand the maximum adsorption areas and promote the electrostatic affinity of M.B. by improving the base equilibrium capacity of
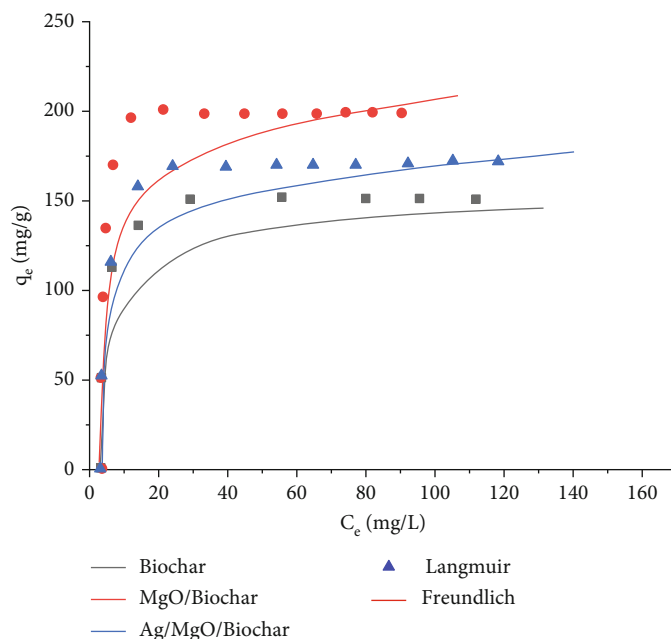
Figure 7: Adsorption kinetics M.B. on Langmuir and Freundlich model.

Table 2: M.B. adsorption pseudomodel fit analysis.

| Adsorbents | Pseudofirst-order model | | | Pseudosecond-order model | | |
	q_1 (mg/g)	K_1 (min^{-1})	R^2	q_2 (mg/g)	K_2 (min^{-1})	R^2
Biochar	120.65	0.254	0.982	118.56	0.0032	0.954
MgO/biochar	125.87	0.088	0.954	123.52	0.0025	0.895
Ag/MgO/biochar	98.54	0.045	0.991	86.54	0.0004	0.925

Table 3: Best fit analysis for Langmuir and Freundlich model adsorption kinetics.

| Adsorbents | Langmuir model | | | Freundlich model | | | q_e (mg/g) |
	q_1 (mg/g)	K_1 (min^{-1})	R^2	q_2 (mg/g)	K_2 (min^{-1})	R^2	
Biochar	126.45	25.4	0.952	105.78	0.115	0.936	132.62
MgO/biochar	132.57	13.26	0.924	118.65	0.123	0.974	145.69
Ag/MgO/biochar	102.32	5.32	0.961	65.65	0.975	0.962	122.58

Table 4: M.B. adsorption Langmuir model and Freundlich model.

| Adsorbents | Langmuir model | | | Freundlich model | | | q_{exp} (mg/g) |
	q_L (mg/g)	$K_{L(L/mg)}$	R^2	(mg/g)/(mg/L)^n	n	R^2	
Biochar	130.25	18.54	0.980	105.41	0.0625	0.954	132.65
MgO/biochar	148.25	2.542	0.965	132.65	0.0526	0.895	156.35
Ag/MgO/biochar	155.68	0.524	0.990	152.34	0.0449	0.925	165.32

nanocomposites. Conversely, insufficient loading may prime the combination of MgO nanoparticles on the exterior of the nanocomposites (Figure 8), limiting the surface area and closing the porosity to prevent M.B. adsorption.

3.4. Photocatalytic Degradation. Photocatalytic degradation of T.C. in Ag/MgO/biochar nanocomposites has been affected by different process parameters such as pH variations, T.C. concentration, Ag/MgO/biochar mixture ratio in percentage, temperature levels, and H_2O_2 conditions for removal of T.C. The pH was measured after photolysis of 100 ppm T.C. for 1 h, as it is considered to have a significant impact on the degradation as it affects the photocatalyst's surface possessions and capability to transfer electrons. The
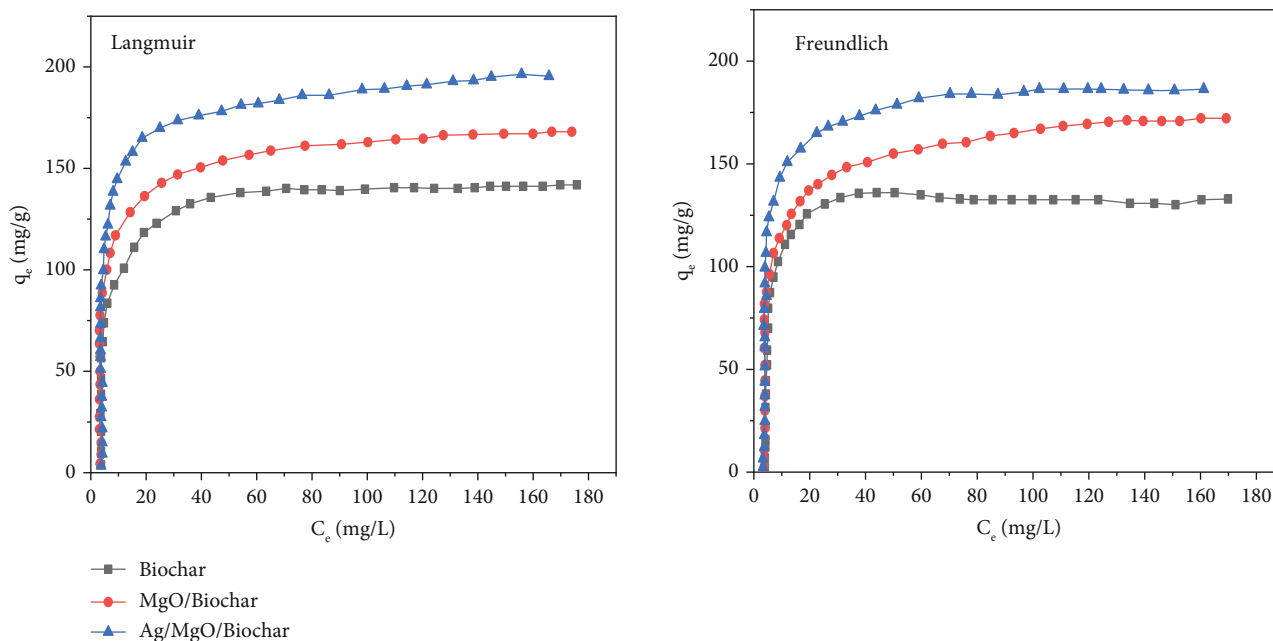
FIGURE 8: Adsorption isothermal.

T.C. removal efficiency for various pH levels of pH_2, pH_4, pH_6, and pH 8 is 28.13%, 32.15%, and 80.26%, respectively. At an acidic pH level (pH 8), it decreased to about 50.47%, which can be explained by the fact that H_2O_2 decomposes to O_2 rather than generating O.H. molecules, which are essential for the photosynthesis of T.C. It is important evident that Ag/MgO/biochar different proportions as a photocatalyst for degradation of T.C. for different pH levels accordingly shown in Figures 9(a) and 9(b).

Similarly, for all test conditions with initial T.C. concentration from 25 to 75 ppm, photocatalytic degradation efficiency was achieved to 80.24% for pH 6 at various times 30, 60, and 80 min for 25, 50, and 75 ppm, respectively. Figure 9(b) clearly shows the high efficiency of T.C.'s Ag/MgO/biochar removal under various concentrations. The objective of the present study was to investigate the effect of dosage variation of Ag/MgO@BC on the efficiency of T.C. removal by photocatalytic degradation of 50 ppm T.C. at pH 6 in 1 h (Figures 10(a) and 10(b)). The photocatalytic degradation efficiency increased from 47.68 to 62.88 and 80.24%, respectively, as the catalyst dosages increased from 0.005 to 0.0075 g and 0.01 g.

It can be concluded that the enhanced formation of hydroxyl free radicals causes faster photosynthetic degradation when the temperature is raised. Figure 11(a), depicting the effect of process temperature, demonstrates the efficiency of T.C. extraction at a heating rate of 10°C with a dose of 50 ppm in 1 h at pH 6. Whenever the temperature increased to 30°C, the efficiency increased and reached almost 80.2%. Also, at a significantly higher rate and an identical percentage of deterioration, the temperature reached 50°C. When the effect of temperature was studied in the absence of Ag/MgO@BC, the removal percentage was only about 14%, as shown in Figure 12, indicating that the minimum tempera-

ture had little effect on the T.C. decomposition rate. The remaining studies used moderate temperatures (25°C) to simulate actual conditions found in wastewater disposal operations.

During the T.C. photocatalytic degradation process, the H_2O_2 experiment was conducted for dissimilar absorptions 25, 50, 75, and 100 mM under pH 6 for 1 hour, as shown in Figures 11(a) and 11(b). The observed degradation rate was close to 52.25% at the lowest dose. When the amount of H_2O_2 was raised to 50, 75, and 100 mM, the degradation % suddenly increased to 54.24%, 66.24%, and 80.24%. The effect of H_2O_2 on the removal of T.C. is enhanced as it provides a photocatalytic degradation system with hydroxyls due to the widespread activity of hydroxyl families.

Furthermore, Ag/MgO/biochar recyclability and flexibility photocatalyst experimented for 1 hour under pH 6 for degradation of 50 ppm. The results show that the efficiency has reduced from 82.4% to 64.28% after a few usage cycles, indicating the reusability of Ag/MgO/biochar nanocomposites. It should be clarified that biochar accelerates the regeneration process of AgNPs and MgO N.P.s to achieve slow degradation efficiency for T.C. removal.

3.5. Future Scope and Recommendations. As a low-cost alternative to expensive activated charcoal, using biochar to remove pollutants from water is growing in significant importance. Future studies are needed to develop modified biochar, as the performance of this material varies depending on the type of raw materials used and the pyrolysis conditions. It may be possible to modify biochar properties to remove specific contaminants to increase their efficiency. Conservation of environmental research on bioenergy as a practical adsorbent for the removal of microbiological and metallic contaminants from water and gaseous particulate

(a)

(b)
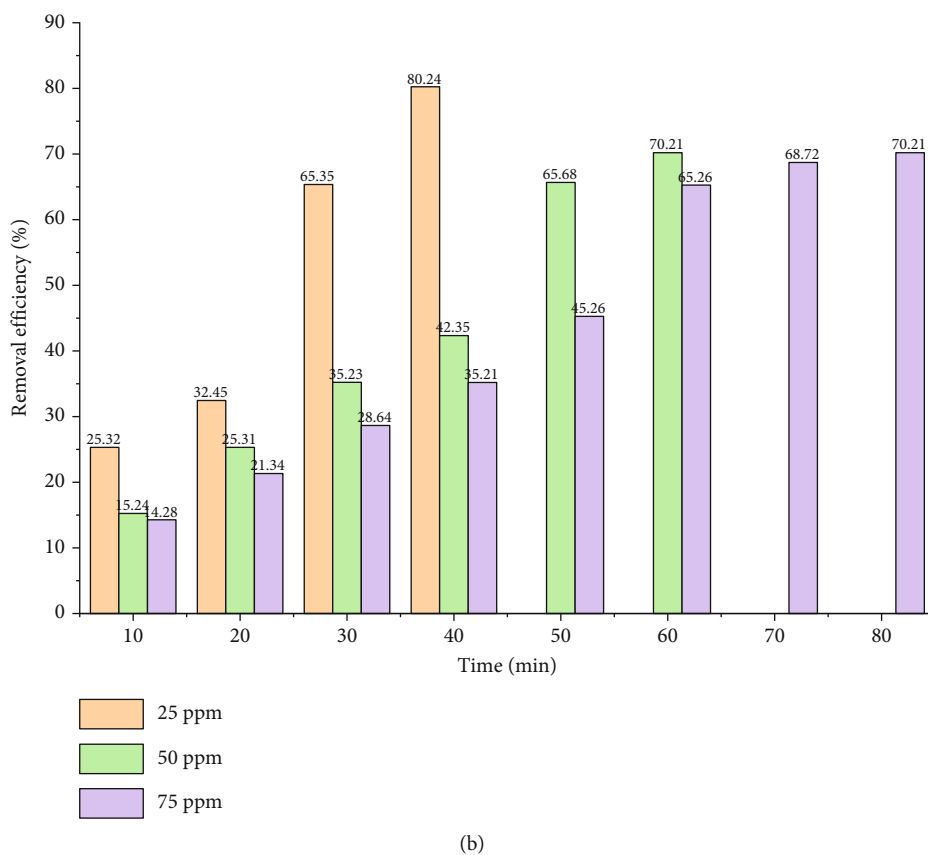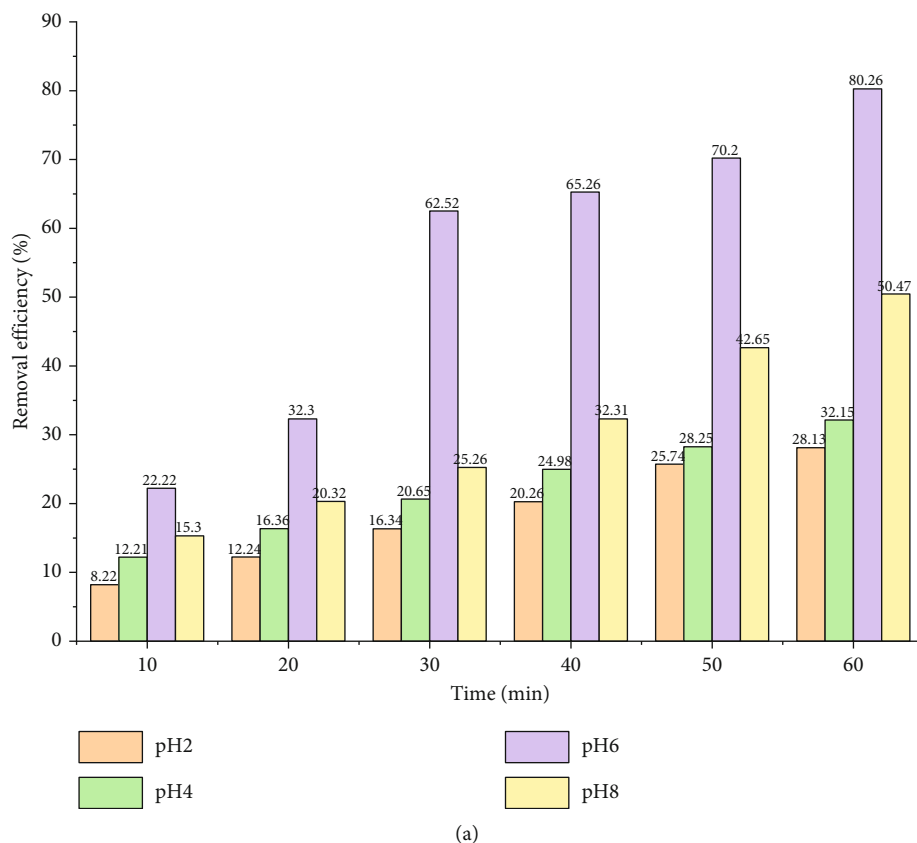
FIGURE 9: (a) Impact of pH on T.C. (b) Various ppm doses of Ag/MgO/biochar.
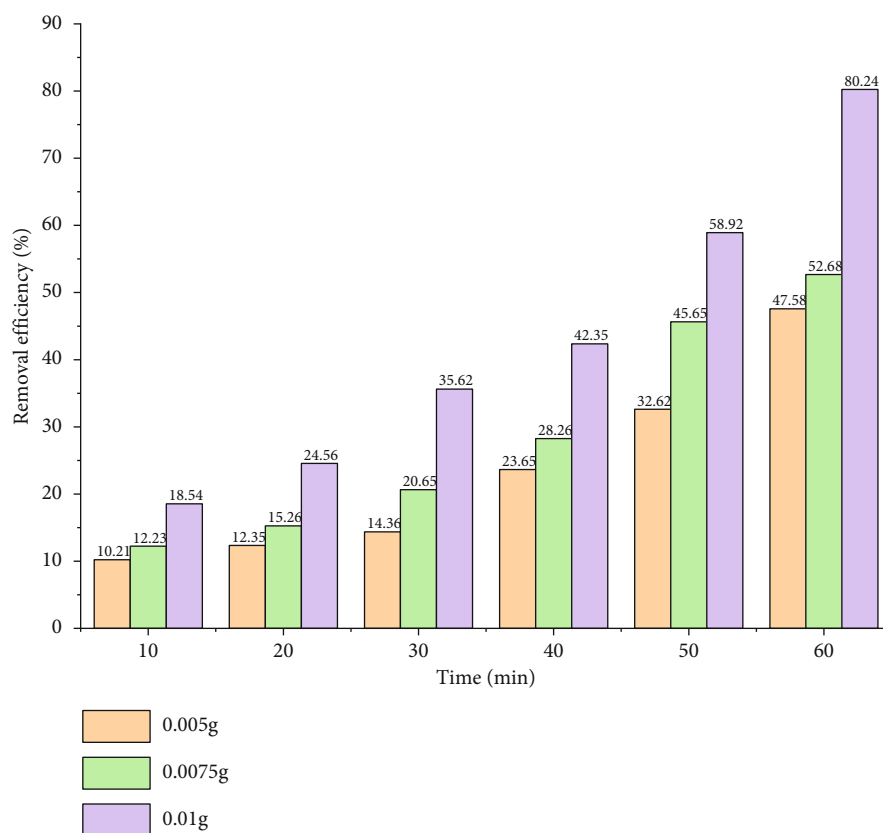
(a)
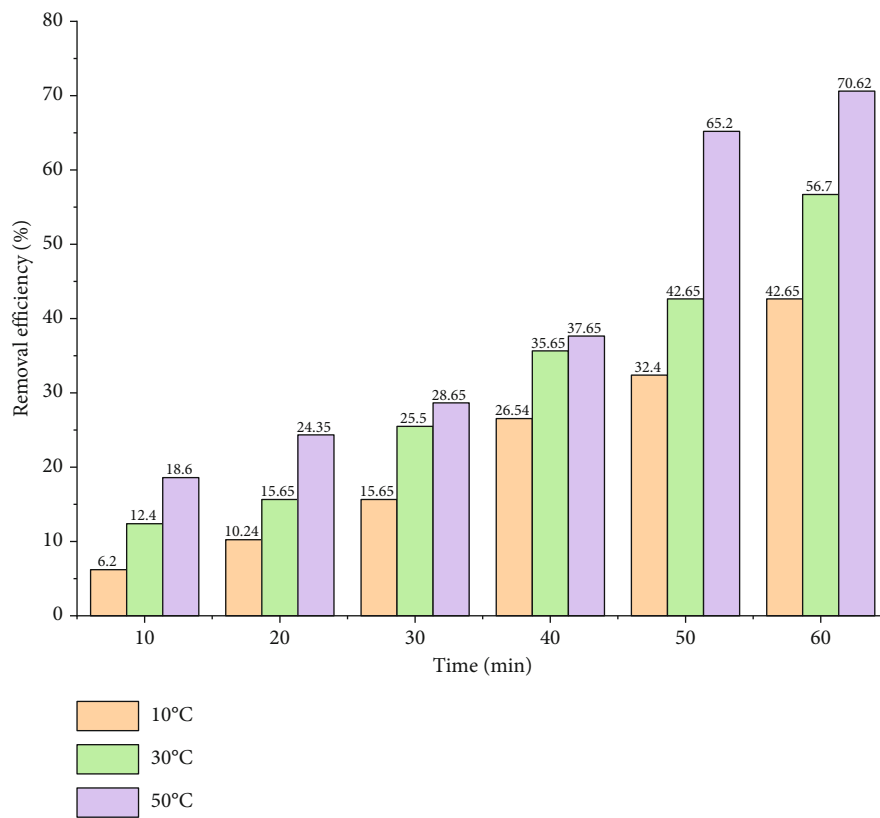
(b)

Figure 10: (a) Removal efficiency %. (b) Photocatalytic degradation temperature.

(a)

(b)
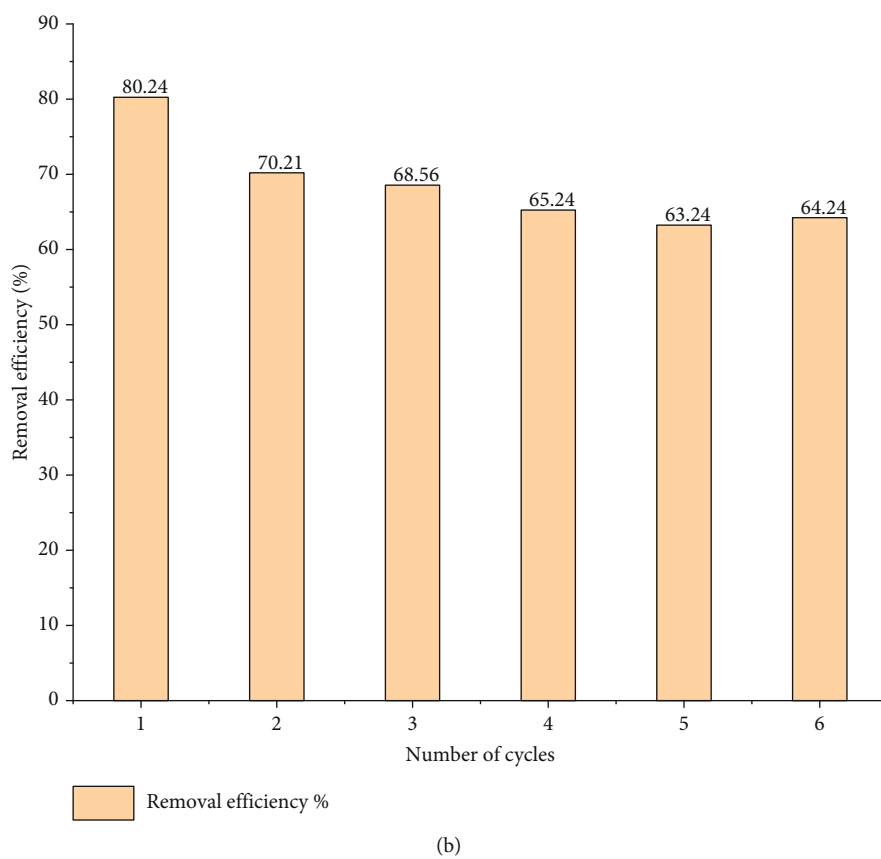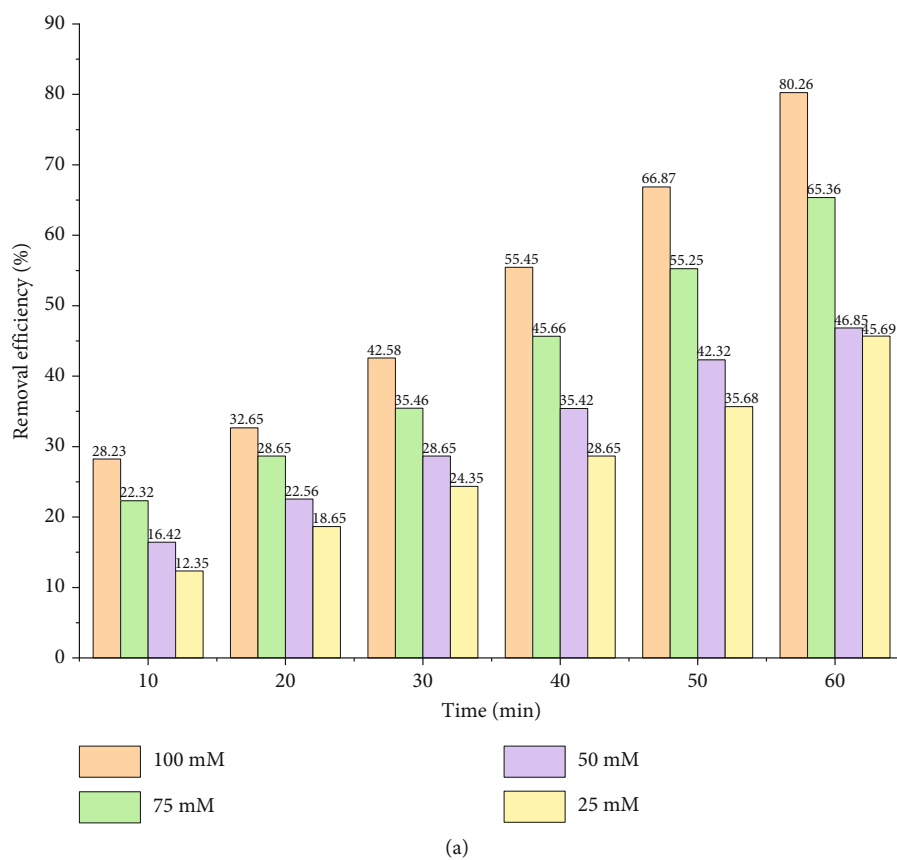
Figure 11: (a) Recyclability of Ag/MgO/biochar. (b) Photocatalytic degradation.
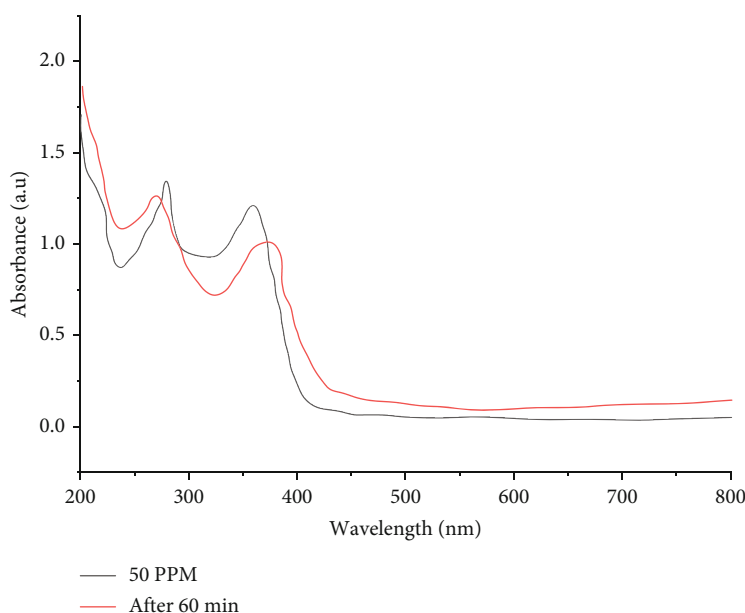
FIGURE 12: H_2O_2 removal efficiency.

pollution is extensive. Although the adsorption capacity of raw biochar is low, its physical and chemical properties are influenced by feed types and processing conditions.

4. Conclusions

The functional group of Ag/MgO/biochar nanocomposites was synthesized successfully by using solvent-free ball milling techniques for M.B. removal and photodegradation T.C. According to this investigation, the ball milling process provides greater flexibility and efficiency in a molecular and structural synthesis that can be used to remove natural and inorganic contaminants from the environment strategically. The successful synthesis of Ag/MgO/biochar nanostructures primarily removes M.B. by adsorption, which is controlled by an attractive electrostatic technique. Freundlich and Langmuir's features were used to match M.B. adsorption behaviour. Different models, with R^2 values above 0.91 and accurately characterizing isothermal, could not reveal any insight into the mechanisms underlying M.B. adsorption on MgO/biochar-nanostructured materials.

The results of this work show that ball-milled Ag/MgO/biochar nanocomposites are potential materials for removing dissolved organic substances from water. Adding MgO nanoparticles can efficiently generate the free radicals needed to break down highly concentrated M.B. in freshwater when exposed to light with the help of biochar. The Ag/MgO@BC exhibited significant performance under ideal process conditions, which included T.C. concentrations of 50 ppm, pH 6, Ag/MgO@BC dose of 0.01 g, the temperature of 25°C, and H2O2 concentration of 100 mM, Ag/ZnO@BC. The photocatalytic degradation of T.C. reaches 80.24%. Furthermore, the removal of M.B. from groundwater by nanocomposites depends on photosynthetic degradation.

Data Availability

The data used to support the findings of this study are included within the article.

Conflicts of Interest

The authors declare that there are no conflicts of interest regarding the publication of this paper.

References

[1] A. M. Omer, R. Dey, A. S. Eltaweil, E. M. Abd El-Monaem, and Z. M. Ziora, "Insights into recent advances of chitosan-based adsorbents for sustainable removal of heavy metals and anions," *Arabian Journal of Chemistry*, vol. 15, no. 2, article 103543, 2022.

[2] O. M. El-Borady, M. Fawzy, and M. Hosny, "Antioxidant, anticancer and enhanced photocatalytic potentials of gold nanoparticles biosynthesized by common reed leaf extract," *Applied Nanoscience*, vol. 1, pp. 1–12, 2021.

[3] M. Hosny, "Biogenic synthesis, characterization, antimicrobial, antioxidant, and catalytic applications of synthesized platinum nanoparticles (PtNPs) from Polygonum salicifolium leaves," *Journal of Environmental Chemical Engineering*, vol. 10, article 106806, 2022.

[4] E. M. Abd El-Monaem, "Sustainable adsorptive removal of antibiotic residues by chitosan composites: an insight into current developments and future recommendations," *Arabian Journal of Chemistry*, vol. 15, no. 5, article 103743, 2022.

[5] R. Li, J. J. Wang, B. Zhou et al., "Simultaneous capture removal of phosphate, ammonium and organic substances by MgO impregnated biochar and its potential use in swine wastewater treatment," *Journal of Cleaner Production*, vol. 147, pp. 96–107, 2017.

[6] R. Li, J. J. Wang, L. A. Gaston et al., "An overview of carbothermal synthesis of metal-biochar composites for the removal of

oxyanion contaminants from aqueous solution," *Carbon*, vol. 129, pp. 674–687, 2018.

[7] L. Natrayan, A. Merneedi, G. Bharathiraja, S. Kaliappan, D. Veeman, and P. Murugan, "Processing and characterization of carbon nanofibre composites for automotive applications," *Journal of Nanomaterials*, vol. 2021, Article ID 7323885, 7 pages, 2021.

[8] J. Shi, J. Wang, L. Liang et al., "Carbothermal synthesis of biochar-supported metallic silver for enhanced photocatalytic removal of methylene blue and antimicrobial efficacy," *Journal of Hazardous Materials*, vol. 401, article 123382, 2021.

[9] M. Kumar, X. Xiong, Z. Wan et al., "Ball milling as a mechanochemical technology for fabrication of novel biochar nanomaterials," *Bioresource Technology*, vol. 312, article 123613, 2020.

[10] D. Veeman, D. Dhamodharan, G. J. Surendhar, L. Natrayan, L. T. Jule, and R. Krishnaraj, "Systematic review on nine hallmarks of neurodegenerative disease," *Indian Journal of Biochemistry and Biophysics (IJBB)*, vol. 59, no. 3, pp. 249–257, 2022.

[11] Y. Zheng, Y. Wan, J. Chen, H. Chen, and B. Gao, "MgO modified biochar produced through ball milling: a dual-functional adsorbent for removal of different contaminants," *Chemosphere*, vol. 243, article 125344, 2020.

[12] C. A. Aggelopoulos, M. Dimitropoulos, A. Govatsi, L. Sygellou, C. D. Tsakiroglou, and S. N. Yannopoulos, "Influence of the surface-to-bulk defects ratio of ZnO and TiO_2 on their UV-mediated photocatalytic activity," *Applied Catalysis B: Environmental*, vol. 205, pp. 292–301, 2017.

[13] C. Ramesh, M. Vijayakumar, S. Alshahrani et al., "Performance enhancement of selective layer coated on solar absorber panel with reflector for water heater by response surface method: a case study," *Case Studies in Thermal Engineering*, vol. 36, article 102093, 2022.

[14] A. M. Omer, "Fabrication of easy separable and reusable MIL-125 (Ti)/MIL-53 (Fe) binary MOF/CNT/alginate composite microbeads for tetracycline removal from water bodies," *Scientific Reports*, vol. 11, pp. 1–14, 2021.

[15] J. Cao, L. Lai, B. Lai, G. Yao, X. Chen, and L. Song, "Degradation of tetracycline by peroxymonosulfate activated with zero-valent iron: performance, intermediates, toxicity and mechanism," *Chemical Engineering Journal*, vol. 364, pp. 45–56, 2019.

[16] Y. Chen, J. Q. Su, J. Zhang et al., "High-throughput profiling of antibiotic resistance gene dynamic in a drinking water river-reservoir system," *Water Research*, vol. 149, pp. 179–189, 2019.

[17] S. Palaniyappan, D. Veeman, S. Narain Kumar, G. J. Surendhar, and L. Natrayan, "Effect of printing characteristics for the incorporation of hexagonal-shaped lattice structure on the PLA polymeric material," *Journal of Thermoplastic Composite Materials*, vol. 1, no. article 08927057221089832, 2022.

[18] J. Dang, J. Guo, L. Wang et al., "Construction of Z-scheme Fe_3O_4/BiOCl/BiOI heterojunction with superior recyclability for improved photocatalytic activity towards tetracycline degradation," *Journal of Alloys and Compounds*, vol. 893, article 162251, 2022.

[19] Y. Luo, X. Wei, B. Gao et al., "Synergistic adsorption-photocatalysis processes of graphitic carbon nitrate (gC_3N_4) for contaminant removal: kinetics, models, and mechanisms," *Chemical Engineering Journal*, vol. 375, article 122019, 2019.

[20] S. L. James, C. J. Adams, C. Bolm et al., "Mechanochemistry: opportunities for new and cleaner synthesis," *Chemical Society Reviews*, vol. 41, no. 1, pp. 413–447, 2012.

[21] R. Venkatesh, C. Ramesh Kannan, S. Manivannan et al., "Synthesis and experimental investigations of tribological and corrosion performance of AZ61 magnesium alloy hybrid composites," *Journal of Nanomaterials*, vol. 2022, Article ID 6012518, 12 pages, 2022.

[22] M. M. Matheswaran, T. V. Arjunan, S. Muthusamy et al., "A case study on thermo-hydraulic performance of jet plate solar air heater using response surface methodology," *Case Studies in Thermal Engineering*, vol. 34, article 101983, 2022.

[23] C. Zhu, M. Takata, Y. Aoki, and H. Habazaki, "Nitrogen-doped porous carbon as-mediated by a facile solution combustion synthesis for supercapacitor and oxygen reduction electrocatalyst," *Chemical Engineering Journal*, vol. 350, pp. 278–289, 2018.

Retraction

Retracted: Implementation of Solar Heat Energy and Adsorption Cooling Mechanism for Milk Pasteurization Application

Adsorption Science and Technology

This article has been retracted by Hindawi following an investigation undertaken by the publisher [1]. This investigation has uncovered evidence of one or more of the following indicators of systematic manipulation of the publication process:

(1) Discrepancies in scope

(2) Discrepancies in the description of the research reported

(3) Discrepancies between the availability of data and the research described

(4) Inappropriate citations

(5) Incoherent, meaningless and/or irrelevant content included in the article

(6) Peer-review manipulation

The presence of these indicators undermines our confidence in the integrity of the article's content and we cannot, therefore, vouch for its reliability. Please note that this notice is intended solely to alert readers that the content of this article is unreliable. We have not investigated whether authors were aware of or involved in the systematic manipulation of the publication process.

Wiley and Hindawi regrets that the usual quality checks did not identify these issues before publication and have since put additional measures in place to safeguard research integrity.

We wish to credit our own Research Integrity and Research Publishing teams and anonymous and named external researchers and research integrity experts for contributing to this investigation.

The corresponding author, as the representative of all authors, has been given the opportunity to register their agreement or disagreement to this retraction. We have kept a record of any response received.

References

[1] G. Ramkumar, B. Arthi, S. D. S. Jebaseelan et al., "Implementation of Solar Heat Energy and Adsorption Cooling Mechanism for Milk Pasteurization Application," *Adsorption Science & Technology*, vol. 2022, Article ID 5125931, 13 pages, 2022.

Research Article

Implementation of Solar Heat Energy and Adsorption Cooling Mechanism for Milk Pasteurization Application

G. Ramkumar,[1] **B. Arthi,**[2] **S. D. Sundarsingh Jebaseelan,**[3] **M. Gopila,**[4] **P. Bhuvaneswari,**[5] **R. Radhika,**[6] **and Geremew Geidare Kailo** [7]

[1]*Department of Electronics and Communication Engineering, Saveetha School of Engineering, SIMATS, Chennai, 602105 Tamil Nadu, India*
[2]*Department of Computing Technologies, College of Engineering and Technology, Faculty of Engineering and Technology, SRM Institute of Science and Technology, SRM Nagar, Kattankulathur, Kanchipuram, Chennai, Tamil Nadu, India*
[3]*Department of Electrical and Electronics Engineering, Sathyabama Institute of Science and Technology, Chennai, Tamil Nadu, India*
[4]*Department of Electrical and Electronics Engineering, Sona College of Technology, Salem, 636005 Tamil Nadu, India*
[5]*Department of Electronics and Communication Engineering, Sri Venkateswara College of Engineering and Technology, Chittoor, Andhra Pradesh 517127, India*
[6]*Department of Electronics and Communication Engineering, S.A. Engineering College, Chennai, 600077 Tamil Nadu, India*
[7]*Department of Food Process Engineering, Ambo University, Ambo, Ethiopia*

Correspondence should be addressed to Geremew Geidare Kailo; kailo.geremew@ambou.edu.et

The use of renewable energy is crucial to the global growth of sustainability. Milk business amongst many other food industry divisions requires a significant amount of energy, making the meal processing business one of the most energy-intensive industries. As of right now, more than 30 percent of the dairy produced in India is processed. In distant parts of India, milk spoiling is more common due to the delay among milking and storing; as a result, facilities for quick pasteurization and storage are needed. Heated is necessary for pasteurization. Since for a long time, the Indian milk industry has relied on nonrenewable energy sources, that are not only becoming much more costly but are also to blame for significant environmental issues including greenhouse gases and health issues. Consequently, scientific communities, environmental and social organizations, and the governments have all pushed the use of green energy. Solar energy has been shown to be the most viable among various sustainable and renewable energies given the geographical position of India. Solar energy can be used to pasteurize milk because of the energy intensity and range of temperature requirements. Adsorbent refrigerator is recommended here since it is powered by waste/solar heat and can store (200 liters of milk) at low temperatures until it is distributed after the pasteurization process (easily available from farm waste). The solar collector of evacuated tube is used for minimizing heat loss and pasteurizing milk. The outcome demonstrates that milk can be simply pasteurized at 73°C for 25minutes at a flow rate of 5 liter per minutes. A solar energy adsorbent refrigeration system has been constructed and described for keeping 200 liters of milk at 10-15°C for 9–11 hours. Investigation findings indicate that the specific cooling power of the system is sufficient to store 200 liters of milk at 5.8 kW/kg and 5.5 kW/kg for 500 liter per hours hot water supplied at 92°C, 32°C condenser temperatures, and 5°C evaporator temperatures. The heat loss of evacuated tube collector is compared to solar concentrator. The study results provide evacuated tube collector is better for pasteurizing milk since to its highly efficient, longevity, and compactness.

1. Introduction

Every industry's and hence any nation's, economic progress depends on energy [1]. India is moving closer to being a developed country, and it has been noted that over the past 20 years, its energy usage has risen by around 6%. The requirement for easy accessibility of activities and commodities has made it difficult for business owners to meet customer demand. This holds true for all industrial sectors, such as the dairy sector. Presently, India produces 176.4 million tonnes of milk annually, or 7.8% of global milk output [2]. Due to the population boom, rising incomes, and more variety in milk products, it is anticipated that milk consumption would rise in the nearish term. The purchasing, marketing, and processing of dairy and milk products, as well as the representation of producers at the federal and state levels, are all major responsibilities of dairy cooperatives [3].

A healthy and balanced diet should include milk because of its highly nutritious qualities. Dairy is regarded as a complete food since it includes lactose and proteins in addition to all the other essential elements. Over than six billion people are consuming milk products and dairy globally. With an annual production of 187.7 MT and a daily supply of 394 grammes of milk per person, India is the world's leading producer [4]. Since Indian independence, small and marginal dairy farmers have generated 70% of the country's milk, and dairy has been a significant factor in the development of the regional economy and socioeconomic change. After the white revolution, India's milk supply rarely looked back, and it is now significantly contributes to the wellness of Indians. The recent analysis of FAO (Food and Agriculture Organization) statistics found that the globe produces approximately 804,887,098 tonnes of dairy annually. India is one of the world's emerging economies. In addition, it boasts the second-largest population in the world after China. Therefore, as the population grows, so does the demand for milk products. Additionally, India has roughly 5 lakhs of cattle from which milk may be obtained and subsequently given to the dairy facilities [5]. Hence, it is crucial for people's health to produce safer milk through the pasteurization procedure.

There are many renewable energy options including geothermal, solar, and wind. The energy collected from the sun is the most accessible and significant form of energy since it is renewable, nonpolluting, inexhaustible, and clean. Additionally, solar power contributes to pollution reduction and environmental stability [6, 7]. For various applications, the solar energy system has been developed as a nonconventional resource. It is often used for water purification and boiler feed in industrial operations. The system is used in dairy, food, textile, chemical agriculture, and beverage industries for various tasks including cleaning and sanitizing, water pumping, cooling, disinfection, filtration, drying, refrigeration, and air conditioning. Figure 1 depicts the solar usage in industrial applications. This is possible owing to the compactness layout of the equipment and high hotness.

India's increasing population has raised the demand for the food and dairy businesses. It did, however, typically rely on traditional energy sources. However, the governments
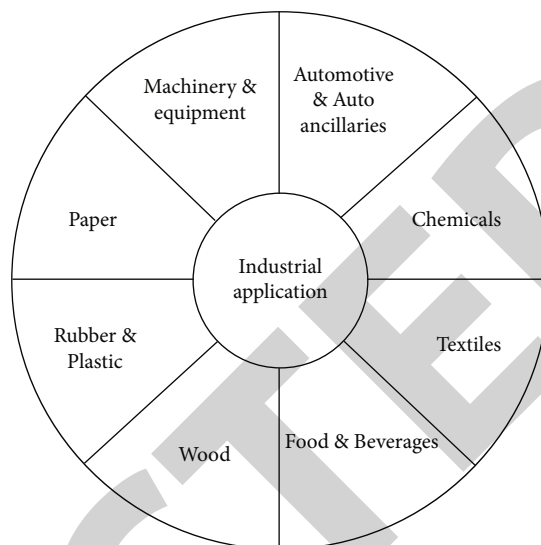
Figure 1: Solar usage in industrial.

and other industries are also looking for unconventional sources like wind, solar, and biomass owing to the acceleration of global warming. Solar collectors for dairy have been designed and developed with a lot of effort. Considering that solar energy is extensively available throughout the nation, its use is frequently promoted. The hot water required for cleaning, sterilizing bottles and cans, and pasteurizing milk can readily be produced by solar heaters. Various solar water heater designs were created and put to use in dairy [8]. Due to the need for thermal heating and cooling, the food industry, particularly the dairy industry, is highly sought after for solar energy applications. The dairy business uses 35 solar thermal systems, nine of which are located in European countries including France, Greece, Italy, and the Netherlands. The other three solar thermal systems use Fresnel reflectors and parabola through collectors to deliver steam at 140°C and 200°C and pressures between 4 and 12 bars. Three of the nine solar thermal systems use flat plate collectors to preheat and clean hot water to meet 20°C to 80°C ranges of temperature. Essential points of the solar power system that have already been employed in the pasteurized plan to reach operating temperatures ranging from 63°C to 72°C include solar collectors, heat exchangers, and water heating systems [9]. Figure 2 represents the various reasons for selecting the solar energy.

In France, the Louis Pasteur has established that heated wine at 55-65°C destroyed the spoilage organisms and assisted in its preserving; the word pasteurization was created. The use of this method gave rise to the word "pasteurization", that quickly gained popularity in technical jargon. Though Louis Pasteur was a pioneer in investigations on thermal treatment for preserving, several scientists may have contributed to the first sterilizing thermal treatment for dairy [10]. For different heat operations, the dairy business needs steam at a pressure of roughly 2 kg/cm2. The major heat operation, pasteurization (0.3 kg/l of milk), is one of many. Utilizing solar heated water, whether complete or partial, will lower fuel costs [11]. In the dairy sector, heating
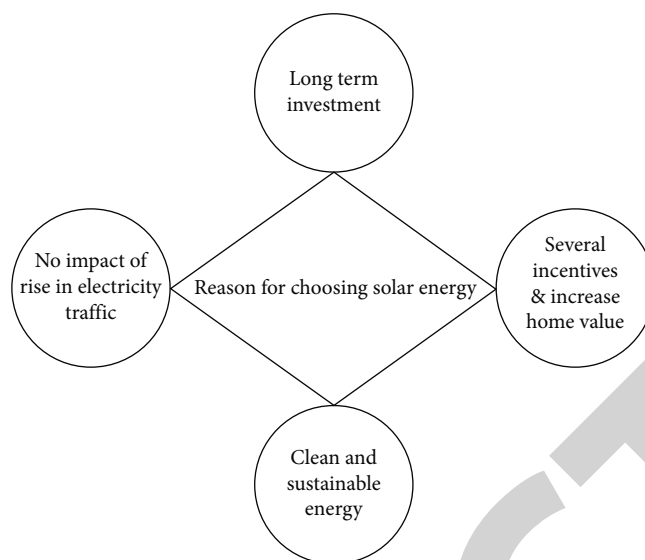
Figure 2: Various reason for selecting solar energy.

and cooling are frequent activities, and plates or tube heat transfer are typically utilized for these activities. One of the most well-known thermal treatments in a dairy processing center is pasteurization, that is carried out between 60 and 75°C depending on the process types [12]. The FSSAI defines "pasteurization" and "pasteurized" as the procedure of heating each substance of dairy of various sections to minimum 65°C and carrying at such temperature continued for at least 30 min or heating it to at least 72°C and carrying at certain temperature progressively for minimum 20 sec or another authorized time-temperature mixture that will give a negative test of phosphatase [13]. Solar pasteurization systems have been the focus of several international studies. Figure 3 depicts the pasteurization process in different temperature.

In the pasteurization process, hot water specifically provides the heat transfer, and the necessary energy is given by using various energy sources, including natural gas, coal, electricity, and renewable energy sources. In the modern world, growth in population and technology advances has both contributed to an increase in energy consumption. Moreover, since the Earth's fossil fuel supplies have been depleting, the use of renewable energy sources (such as solar, wind, and geothermal power,) has become more crucial for a sustainable society [14]. Geothermal energy is one of the renewable sources that has a wide range of uses, including both industrial and domestic heating and cooling in addition to electricity generation [15]. Figure 4 represents the various benefits for pasteurization process.

Geothermal power may be regarded as one of the finest possibilities as a renewable energy source for milk operations because the pasteurization of milk requires both heating and cooling operations concurrently. Typical vapor absorption techniques, which have fewer initial and continuing expenses than cooling towers, are the most used option for cooling purposes. Moreover, the chlorofluorocarbon refrigerants utilized in typical systems are not eco-friendly. In addition to being environmentally benign, the water ammo-

nia absorption cycle that uses water ammonia combination as a refrigerant also delivers the refrigerated temperature required for a milk operation [16]. On the other side, it would be more cost-effective if the water ammonia absorption cycle was driven by heat energy among 100 and 200°C. Consequently, geothermal energy is considered as a source of heat for water ammonia VAC systems (vapor absorption cycle). An absorbent, evaporation, a desorbed, a condenser, a heat exchanger, expanding valves, and a pump make up the absorption cycle. This system circulates ammonia (an absorber) and water (a refrigerator) to produce chilling [17].

Solar dairy pasteurization is the method of eliminating microorganisms from dairy and eradicating germs from it using the sun radiation [18]. With the aid of a solar vacuum tube collecting, that generates hot water at an extremely high temperature, the sun's beams are used to create steam [19]. Dairy is a naturally occurring liquids diet, and it is one of the most nutrient-dense diets. Whenever milk is handled poorly, the circumstances that the microorganisms create can spread. Antibiotic depositions in dairy brought on by the widespread use of antibiotics in animals used for food production are the alleged cause for both dairy production and consumer demand. A sufficient temperature and amount of time must be administered to kill the bacteria or microorganisms that grow slowly or produce holes [20]. Figure 5 depicts the various components for solar milk heater.

Since its operations need for more mild heat temperatures than those of other major industries, such as the chemical, textile, and paper industries, the dairy industry, along with other food industries, it has been singled out for its great potential for adopting solar technology [21]. The dairy must be chilled at 44°C or rising temperatures during farm production in order to meet the processing standards for dairy products, based on the national regulations of every nation. Based on product kind, the industrialized milk factories next perform various heat processes including
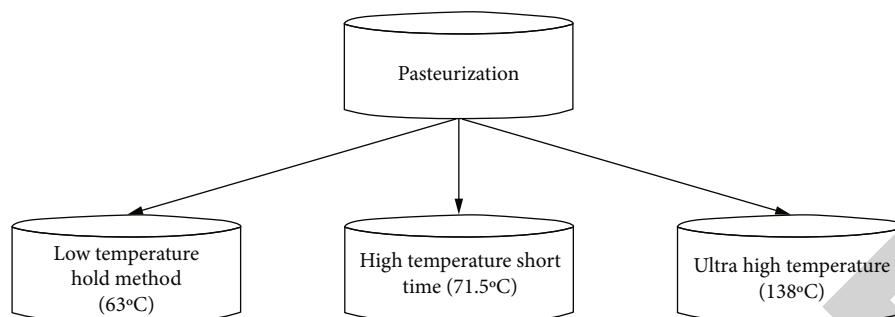
FIGURE 3: Pasteurization process in different temperature.
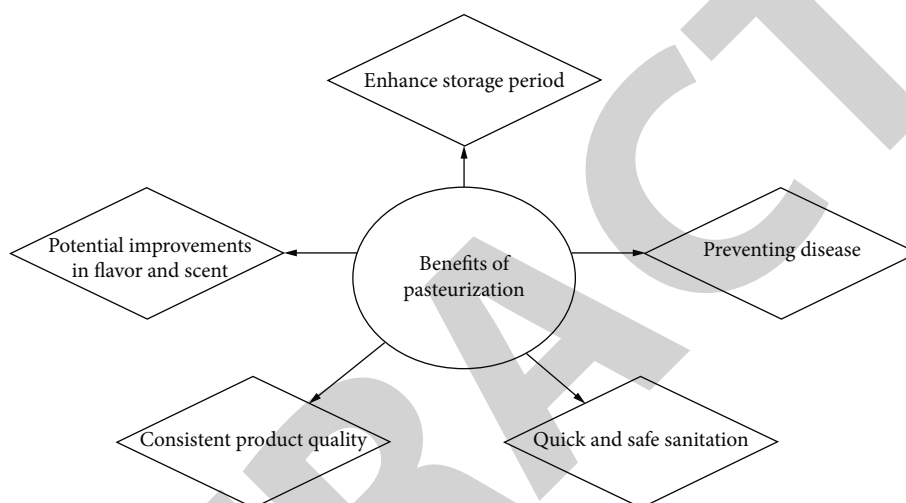
FIGURE 4: Various benefits for pasteurization.

pasteurization, sterilization, and ultrapasteurization. Presently, the worldwide dairy industry's output is made up of around 21% fluid milk usage [22]. Ultrapasteurization and pasteurization are the most used heat processes for fluid milk. This milk can be kept for five days after a standard pasteurization, but after receiving an ultrapasteurization process, it may be kept for three months. Whilst ultrapasteurization is the heat action that is most frequently used in established geographic regions, pasteurization is the thermal process that is regularly employed in emerging geographical area. Moreover, in industrialized regions, pasteurization is still employed to make a tiny amount of fluid milk with a short shelf life as well as other significant goods like cheese and yoghurt. The pasteurization of milk entails keeping the milk among 65 and 79°C for a predetermined amount of time, after which the milk must be quickly chilled to 4°C [23].

2. Related Works

One of the key dairy products, milk serves as a crucial component in the feed composition for infants and developing kids as well as adults. Moreover, the pasteurization framework's temperature has a significant impact on the final product performance. Hence, it is important to keep the ideal temperature throughout the pasteurization process since excessive heat destroys all of the vital nutrients present in the finished product, and minimum temperature is undesirable because the product will not have the appropriate nutrient value. As an outcome, a crucial prerequisite for pasteurizing dairy is the implementation of an ideal temperature control strategy. In light of the foregoing, this study present the application of a proportion (P), integrated (I), and derivatives (D), or PID, control for optimum control of temperature during the pasteurization of dairy. The first law of thermodynamics was used to simulate the milk pasteurization temperature, and three distinct tuning approaches, Zigler-Nichols (ZN), Cohen-Coon (CC), and Chien-Hrones-Reswick (CHR), were used to fine-tune the PID controller for the best pasteurization temperature management. The effectiveness of every tuned strategy was assessed using the rising time, settling time, peak amplitude, and overshoot. The control systems were modeled in MATLAB/Simulink. The outcomes demonstrated that the ZN tuned PID controller provided the settling time, minimum rising time, and peak amplitude of 0.34 s, 0.177 s, and 0.993, accordingly. ZN and CHR both achieved the lowest overrun of 0%. According to these findings, the CC tuned PID controller had a mild rising time of 1.02 seconds, settling time of 6.49 seconds, and an overshoot of 5.67 percent, suggesting that its effectiveness was relatively better than that of the other tuned strategies examined. The findings

FIGURE 5: Components for solar milk heater.

FIGURE 6: Process flow diagram for pasteurized milk.

tion range of 2 ng/mL and shows excellent dynamic linearity for SEA quantifiable identification from 3 to 160 ng/mL within 20 minutes of testing time, provided the 1030-fold improvements in the photoluminescence intensity of QB to the original quantum dot. With a low cross-reaction to typical analogues, such as E, D, C, and B, staphylococcal enterotoxins are suggested QB-ICA also exhibits strong selectivity to SEA identification. Additionally, by examining specimens of milk that had been enriched with SEA, the precision and accuracy of QB-ICA were evaluated. The coefficients of variation vary from 4.6 to 14.2 percent and the median recovery of intra- and interassays ranging from 85.5 to 128.1 percent, demonstrating a tolerable precision for the quantifiable determination of SEA in actual milk specimens. In conclusion, the work offers a potent and quick analytical technique for the proper supervision of SEA contamination in specimens of pasteurizing milk. For SEA quantified identification in actual milk samples, the suggested QB-ICA also shown acceptable specificity and acceptable accuracy. In pasteurized milk and other food ingredient, this investigation demonstrated a significant possibility for the on-site sensitivity identification of SEA contamination [25].

Dairy and milk products may be vulnerable to risks like aflatoxin M1 (AFM1). Aflatoxin generation has an impact by a quantity of variables, containing changes in the environment and an absence of sufficient substrates for feed healthier livestock. The study seeks to lower the toxicity level in pasteurizing milk to a value under that recommended by the European Codex Alimentarius Commission. In order to achieve this, the appropriate construction of the radioactive granite stone was first created as a minimum level gamma irradiation without interaction with pasteurizing milk. This milk comprising AFM1 that is positioned in this framework is evaluated, and the results comparing to the values of the control specimens utilizing AOAC technique. The LLGI dosing rates and the subsequent decrease in aflatoxin in the milk are then determined. With the use of the Monte Carlo N-Particle Transportation Protocol, the LLGI dosage rate is computed (MCNP). For modeling, the mass of every composition of pasteurizing milk and its constituent components is also estimated in additional to the spectra of gamma irradiation released by radioactivity granites. In comparison to the control specimen, the findings demonstrated a 51.5 percent drop in aflatoxin in pasteurizing milk

of this study have applications in the dairy industry since they provide light on how to best tune a PID controller for optimal control of temperature during milk pasteurization. This approach is not suitable because it causes steady-state error [24].

Given the right environment, Staphylococcus aureus can produce staphylococcal enterotoxin A (SEA), an essential biotoxin that frequently contaminates dairy and milk items. Herein, SEA protein was injected into BALB; the immune chromatographic assay (ICA) is generated and developed the anti-SEA monoclonal antibody utilizing extremely fluorescent quantum dot beads (QB) as a signal amplification assay for rapid and accurate detection of SEA in pasteurized milk. The suggested QB-ICA demonstrates superior SEA sensitivity identification in real milk specimens with a detec-

Figure 7: Schematic representation of pasteurized milk process.
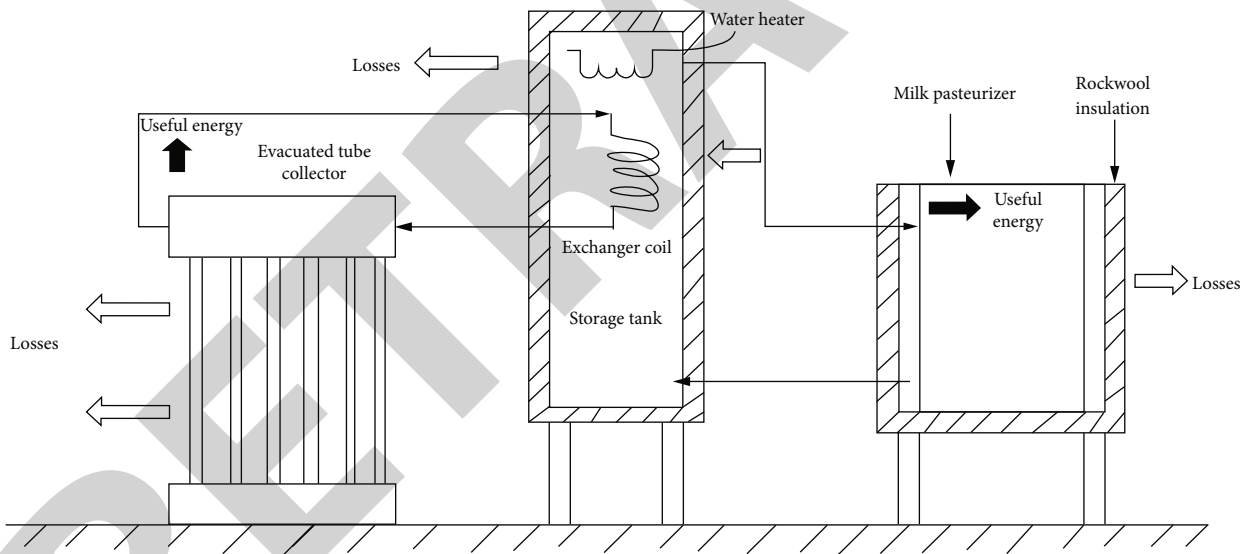
Figure 8: Milk pasteurization working process by using evacuated tube collector.

after 5 days, and a 99 percent reduction after 8 days. In dairy, the LLGI dosage level is 0.40 mGy per day. A global atomic energy agency research and prior findings indicate that this dosage rates level can increase milk's shelf life and improve safety without adversely affecting its chemical or sensory qualities. As a result, one of the acceptable strategies for lowering aflatoxin may be regarded to be the building built utilizing radioactive granite in this investigation [26].

Determining the heating process of milk is crucial since it is the greatest popular method for ensuring the microbial safety of dairy. Additionally, a rising issue in the dairy industry is the adulteration or mislabeling of pricey milk specimens like goat or sheep milk with cow's milk. Therefore, it is vital for both consumers and producers that milk speci-

mens' validity be determined. The study's objective was to distinguish between raw and pasteurized milk specimens utilizing partial least squared discriminant analysis (PLS-DA) and Raman spectroscopy first in terms of whether the dairy had been heated or not and then in terms of species (cow, goat, ewe, and mixed (adulterated)). Firstly, PLS-DA was utilized to distinguish between raw and pasteurized milk specimens. High specificity and sensitivity ratings were attained for pasteurized and raw milk samples in both calibrating and estimation techniques. Secondly, the suggested technique distinguished between pasteurized and raw milk specimens based on their species (cow, goat, sheep, and mixed). The specificity and sensitivity ratios were above 0.857 and 0.897 in the calibrating and forecasting

approaches, accordingly. Additionally, the precision scores exceeded 0.915. The findings demonstrate that the specimens were classified in a good and accurate manner. The findings indicate that milk samples may be effectively differentiated as per thermal treatment and species within 20 seconds per specimen using Raman spectroscopy in conjunction with PLS-DA. It was discovered that Raman spectra offer useful data that may be utilized, in particular, to distinguish between milk samples based on their origination [27].

The activated enzyme alkaline phosphatase (ALP) can be found in raw dairy. It is used as an indication to assess the effectiveness of the pasteurization process because to its distinctive heat-sensitive features. In the current work, a technique for measuring the activity of the ALP enzymes in pasteurized milk was devised using HPLC and a fluorescent detection. The process is focused on the identification and measurement of 4-methylumbelliferone (4MU), which is released when the dairy enzyme phosphatase reacts with the substrate 4-methylumbelliferyl phosphate (4MUP). Clarity, centrifuge, and solid phase extraction procedures were used to obtain and purify 4MU. With the use of a reversed-phase C18 column and gradients eluted made up of a binaries mobile phase comprising of HPLC grade methanol and water, the targeted component isolation was accomplished. The excitation and emission wavelengths of 365 and 460 nm, accordingly, were used to identify fluorescent. High specificity, strong linearity ($r2 > 0.9901$), minimal limits of identification (LOD, 0.349 mg/L), minimal limits of quantifying (LOQ, 0.432 mg/L), accuracy (> 100%), and accuracy (percent RSD 4.7652) were all demonstrated clearly in the technique evaluation studies. When compared to the Lovibond comparability approach, it was discovered that the HPLC method had the benefit of being able to identify contaminating of raw milk and ALP activation at extremely low levels. It is the first account of using an HPLC-fluorescence detection approach to find ALP at such low levels in dairy. The present standard techniques that use fluorometric technology for determining ALP activities in pasteurized milk might be regarded to be replaced by this novel chromatography approach. The quality assurance criteria now used in the dairy sector could benefit from this approach [28].

The ultrapasteurization and high-temperature short-time pasteurization (HTST) are two methods for pasteurizing fluid milk (UP). Although investigations have not conclusively shown it, the literature claims that UP enhances dairy astringency. Therefore, the goal of this research was to ascertain how milk's sensory and mechanical characteristics were affected by the pasteurization process, fat level, homogenized pressure, and storage period. Raw skim (0.3% fat), 3 percent, and 6 percent fat milk was homogenized at 20.7 MPa, pasteurizing in triplicate by indirect UP (150°C, 2.5 s) or by HTST (78°C, 16 s), and then kept at 4°C for 8 weeks. In addition, indirect UP was used to processing 2 percent fat milk, which was then homogenized at pressures of 13.8, 20.7, and 27.6 MPa and kept at 4°C for eight weeks. The milk was assessed for sensory profiled, instrumental viscosity, and frictional profiling at 25°C after

1, 4, and 8 weeks of storage. Protein structural changes in dairy at these times were examined using confocal laser scanning microscopy and sodium dodecyl sulphate polyacrylamide gel electrophoresis (PAGE). For eight week assessments, fresh HTST milk was analyzed at 7 weeks. Comparing to HTST pasteurization, ultrapasteurization enhanced the sensory and instrumental viscosity of milk. The fat content increased astringency and frictional profiles while decreasing sensory and instrumental viscosity. For UP vs. HTST, astringency, combined regimens frictional profiles, and perceived viscosity all enhanced. Increasing the storage period has no impact on the mechanical or sensory viscosity. Moreover, longer storing times typically led to higher astringency and frictional characteristics. When comparing to HTST milk, UP milk had more denatured whey protein, according to results from confocal laser scanning microscopy and sodium dodecyl sulphate PAGE. The rise in viscosity and frictional levels during storage was probably brought on by the aggregation or network these protein and casein micelles produced. The mechanical viscosity, astringency, or frictional behaviors were not substantially affected by the homogeneity force; moreover, specimens homogenized at 14 MPa as opposed to 21 and 28 MPa had greater sensory viscosity. In HTST milk and UP milk, astringency and frictional coefficients at 100 m/s slide speed were positively connected, while sensory viscosity and mechanical viscosity at a shearing rate of 50 s1 were strongly correlated ($r2 = 0.90$). Experimental assessment can therefore be utilized to identify specific milk sensory characteristics [29].

3. Methodology

3.1. Pasteurization of Milk Utilizing Solar Energy and Evacuated Tubes.
There are many other ways to combine different solar gatherers type, but the ETC was selected for pasteurizing milk since to its highly efficient, longevity, and compactness. It also does not require a monitoring system. Glass vacuum tubes with concentric twin tube geometry were made of chromium. The 0.8 W/m2 °C was the typical heat losing coefficients from tubes. Chromium steel tanks with a 200-liter storage capability were placed for the purpose of storing hot water. Up to 100+ °C may be attained with an evacuated tube solar collector. The following equations can be used to determine the evacuated tube collector area.

$$\text{Area}(a) = \left(\frac{W S_{hc} \nabla n}{T_i \tau \beta t \mu_{th}} \right), \tag{1}$$

where "W" stands for the weight of water (kg), "a" stands for the region of the absorber tube revealed to irradiation, "∇n" stands for the temperature change of the milk in the pasteurizer, "S_{hc}" stands for the particular warmth capability of the milk to be pasteurizing, "β" stands for evacuated tube collector inner absorber tubes absorption coefficient, "τ"stands for transmission coefficient of evacuated tube collector outer glass tubes, "η_{th}" is the efficiency of thermal for the entire solar milk pasteurizing scheme, and "t" is the time in second stands. This covers all heat-energy-transfer losses from the
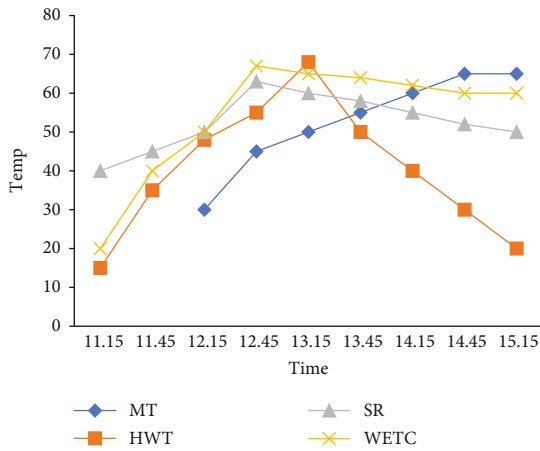
Figure 9: Performance evaluation of milk pasteurization by ETC (MT-milk temperature; HWT-hot water temperature; SR-solar radiation; WETC-water from ETC temperature).
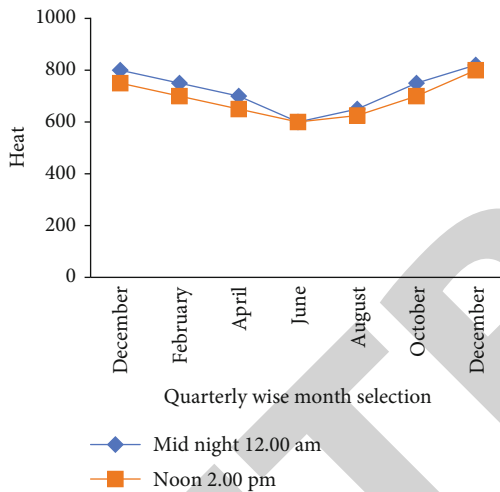
Figure 10: Solar irradiation absorption by ETC.
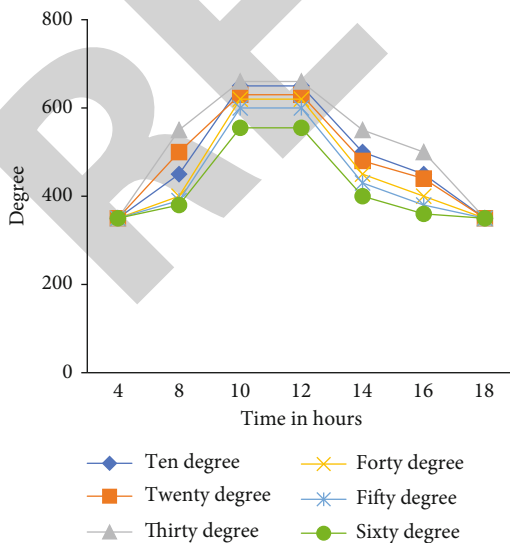
Figure 11: Absorption variance of solar radiation in various angles.

evacuated tube collector, milk pasteurizer, storage tank, and all associated pipe lines.

3.2. Design and Construction. Figure 6 depicts the process flow for a solar-powered milk pasteurizing technology. The unpasteurized milk storage tank is a cabinetry box shape chromium steel, with internal diameter of 2.20 m length, 2.20 m wide, and 0.90 m tall. This can hold around 200 L of milk daily basis. This can therefore encompass a limited milk-producing region. The provided milk is expected to be pasteurized among midnight twelve o'clock to two o'clock in the afternoon. The length of cylindrical parabolic concentrators for a continual flow process and focal length was identifying to be approximately 100 cm and 350 cm, correspondingly. An evacuated glass pipe has been installed near the sun's source of heat. The glass tube has a black coated to increase its ability to absorb solar infrared rays. The chromium tubes that run the whole height of the evacuation glass tube are within. The chromium tubes are 7 mm in diameter and 2.0 m in length. Whenever sunlight strikes the parabolic, it is reflecting off the surfaces and incidental light strikes the focal point where the glass tube is installed. The glass tube heats up as a result of this. Among the glass tube and the chromium tubing, there is a void.

The warming trend comes into effect, retaining the temperature inside the glass tube and causing the chromium tubes to heat up. This chromium tubes are heated to the necessary temperature as dairy is carried through them. The parabolic concentration is exposed to solar radiation. Estimated are the angles at which the rays strike the parabolic. Aluminum composite chromium evacuated tube was used to create the parabolic that was then welded to the framing component. The requisite heating of 73°C is reached at the parabola's output. It is then delivered to the cooling system from that. Thus, activated charcoal and methanol serve as the adsorbent operating pairings in an adsorbent cooler. The dairy is initially chilled to a minimum temperature of 5–6°C in the cooling unit. It is then transported to the last saving container, where it is kept refrigerated and in a controlled environment. A range of 15 and 20°C has been established as the storage condition. It is then delivered to the packaging facility where it is packaged before being delivered to the numerous places.

Figure 7 shows a diagrammatic representation of pasteurized milk process. The absorption chiller is heated by solar energy. Solar collectors are used for solar heating of flat surfaces. The functional counterparts of an absorption chiller are methanol and activated carbon, and the main components are an evaporator, desorber/adsorber, expansion valve, and condenser. The water jacket surrounds the adsorber/desorber bed and condenser, through which hot and cold water periodically flows through the mold. Porosity, the pores of activated charcoal, is occupied by methanol during decomposition. The temperature and pressure of the desorber bed is raised by hot water heated by the sun and circulated through it. With the help of a square pipe in the form of a spiral, the storage tank hot water is dispersed around the outside of the pasteurizer for efficient heat transfer to the milk filled inside. Moreover, in accordance with
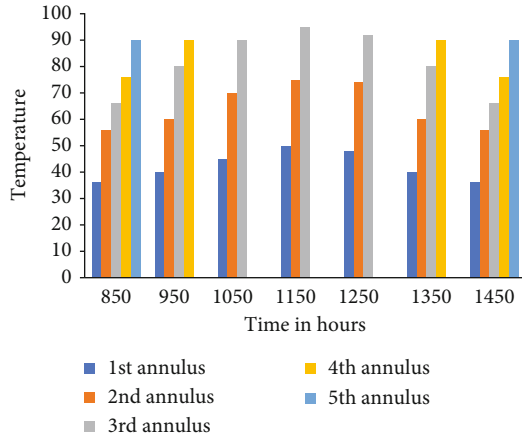
Figure 12: Need for evacuated tube collector in March 2021.
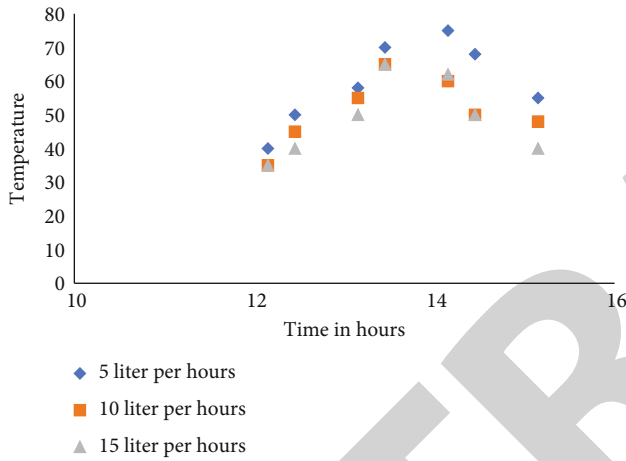
Figure 13: Various flow rates computation of milk temperature variation.

milk pasteurization regulations, the tank's materials are food-grade SS-304. Polyurethane insulates the pasteurizer's outside casing. For efficient pasteurization, the mechanical stirrer with a 58 rpm speed is fitted to disperse warmth evenly. Continually, lowering the milk's temperature, when the cooling procedure is carried out, is also beneficial. Within a GHI range of 600–800 W m2, it is simple to get temperatures exceeding 100°C.

The valves between the desorber and condenser are opened after the desorber bed reaches condensation pressure. The expelled methanol then goes to condensation. Methanol releases heat in the condenser during the condensation process, and the condensed methanol goes to the expansion device. The heat of the milk is then stored in receivers before moving to the evaporator, where it is cooled by methanol. The pressure and temperature of the desorber bed are reduced by the circulation of cold water. The valves between the evaporator and desorber are released, and the desorption process begins, when the pressure in the desorber bed drops below the desorber pressure.

3.3. Energy Used and Lost in Milk Pasteurizer. Equation (2) shows the usable value of warmth energy obtainable at the
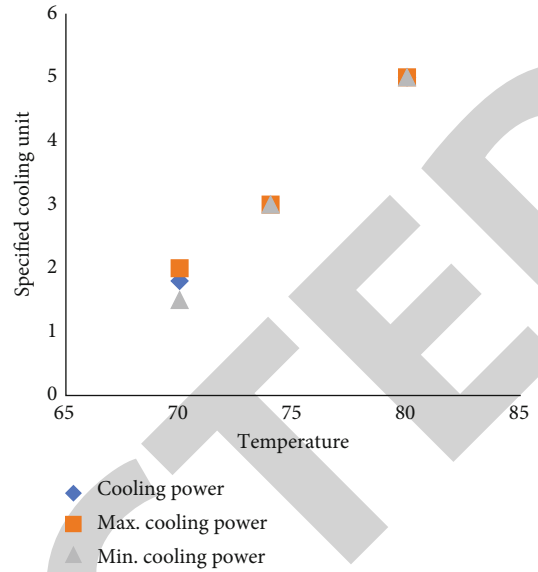
Figure 14: Various temperature cooling power uncertainty analysis.

tank of pasteurizer for pasteurizing milk.

$$E_p = E_r - E_{\text{pt}}, \tag{2}$$

where E_r stands for thermal and optical loss, and E_{pt} stands for thermal losses of receivers, convection, conduction, and radiation losses account for these losses. It is the tubular part of the pasteurizer is shielded with 45 mm rock wool insulating. By entering input data (bounding heat settings, material properties, shape, and features) into the algorithm created for milk pasteurizer, a full procedure was developed, and the outcome of thermal losses is determined. A 45 mm polyurethane insulating materials (the conductivity of thermal energy: 0.030 W m-1 k-1) was used to protect the bottom and side edges of the milk pasteurizer (432×559 mm). The inherent heat of vaporization of water was utilized to rapidly pasteurize milk at 65°C using wet steam from a steam receiver.

3.4. Calculation of Thermodynamic Losses of Steaming Receiver and Milk Pasteurizer. Ambient temperature and space temperature were taken as t_a and t_i, respectively, for all calculations. A cylindrical layer exposed to fluid convection on each side has the constant heat transfer which has denoted in Equation (3).

$$\varphi = \left(\frac{t_i - t_a}{r_{\text{cd}} + r_{\text{cn}}} \right). \tag{3}$$

While r_{cn} stands for convection resistance, and r_{cd} stands for conduction resistance, t_a is the ambient heat, and t_i is the temperature at the inner surface of the milk pasteurizer. In contrast, the following Equation (4) may be used to compute the heat conduction resistant from the

Table 1: Material properties utilized for evacuated tube collector.

Material	Characteristic	Rate
Wood	Heat conductance	0.15 W/m-K
	Density	16 mm
Aluminum	Heat conductance	190 W/m-K
	Thickness	4 mm
Air	Heat conductance	0.032 W/m-K
Polystyrene	Heat conductance	0.030 W/m-K
	Thickness	20 mm

Table 2: Processing attributes of investigational study.

Operational stipulation	Rate
Normal water inlet temperature	23°C–24°C
Flow rate mass of cold H2O	300 LPH
Boiling H2O inlet heat	85°C
Flow rate mass of hot H2O	500 LPH
Condensation temperature	35°C
Initial bed temperature	30°C–40°C
Maximum bed temperature	70°C–80°C

cylindrical section of the pasteurizer.

$$r_{cn} = \frac{\ln\left(R_e/R_i\right)}{2 \times 3.14 \times \lambda \times l}. \tag{4}$$

While l denotes the pasteurizer or receiver's lateral length, λ denotes the material's thermal conductivity, R_i denotes the pasteurizer or receiver's interior radius, and R_e denotes the pasteurizer's exterior radius. The following Equation (5) can be used to determine the conductivity resistant of the pasteurizer or receiver's round portion.

$$r_{cn} = \left(\frac{T}{a\lambda}\right), \tag{5}$$

where "a" denotes the cross-sectional region of the round unit of the bottom of the pasteurizer or steam receiver, and T is the wall thickest of the round unit of the receiver or pasteurizer. With this insulating, it is possible to compute the conductivity resistant for additional layers, planar walls, and cylindrical segment by summing the conducting resistant of all layers and generalizing as following Equation (6).

$$r_{cn} = \sum_{cn}^{i} r. \tag{6}$$

While i depicts the layer of chromium steel, insulating material also covers tubes with various thicknesses and thermal conductivities. Equation (7) may be used to compute

convective resistant.

$$r_{cn} = \left(\frac{1}{H_l s}\right). \tag{7}$$

Equation (8) may be used to determine thermal losses through irradiation.

$$R_{loss} = s\delta\xi(t_e - t_s). \tag{8}$$

While emissivity is denoted as ξ, the Stephen Boltzmann constant is denoted as δ, the space temperature is denoted as t_s, and t_e stands for exterior area temperature; it can be computed by using the following Equation (9).

$$t_e = t_a + \varphi r_{cn}. \tag{9}$$

Compute the overall heat losses through radiations by changing the value of t_e in Equation (8). The overall losses of the system may be estimated by aggregating all the losses.

3.5. Losses and Energy Availability Utilizing Evacuated Tube Collector. The following Equation (10) provides the energy input for an evacuated tube collector.

$$E_v = \left(\frac{S_t A_s}{1000}\right), \tag{10}$$

where A_s is the evacuated tube collector surface region, and S_t is derived by multiplying the effectively tube length (exposing to solar radiation) by the diameter (aperture) and quantity of tubes, and E_v is the rate of incident solar energy at collector (kW).

The heat performance of a solar evacuated tube collector can range from 70% to 80% depending on solar energy input, loss, and temperature transmitted to the working fluid. The primary goal of the research is to conduct a heat assessment of solar milk pasteurization. The water and glycol solution receives heat from the exhaust pipe collector header and is then utilized to warm the outer shell of the cylindrical pasteurizer in the hot water storage tank. Therefore, multiplying the flow rate mass by the fluid's heat and variation in temperature, it is possible to determine the quantity of heat energy (Q') transmitted to the functioning fluid before being transmitted to the dairy. A further advantage of this method is the thermal energy storing in the hot water tank that may be utilized to effectively pasteurize milk even when there is little sunlight.

The following equation may be used to determine how much energy is needed to heat 200 liters of storage tank water from room temperature (30°C) to nearly 95°C.

$$H_w = NS_{hc}\nabla t, \tag{11}$$

where N is the water mass, ∇t is its specific warmth capability, and H is the value at which warmth energy must be delivered to the water. Equivalent calculations may be used to determine how much energy is needed to heat 90 L of milk to a change in temperature of 40°C. Then the valuable

energy obtainable for milk pasteurized tank "H" and the overall useful energy obtained from ETC "H" are computed to be 5460 W and 4070W, accordingly. It is projected that the 18.8 m length of piping and fitting linking these 3 parts will result in total heat loss of 638 W. The pasteurizer and hot water tank both had estimated thermal losses of 116 and 90 W, accordingly. Figure 8 represents the milk pasteurization working process by using evacuated tube collector. Figure 9 depicts the performance evaluation of milk pasteurization by ETC.

4. Results and Discussion

Determining the median solar radiation (W-hr/m2) on an evacuated tube and the solar collector is crucial for sizing a solar adsorption process. There are certain days all year round with relatively little sun radiation. With clouds and wind, solar radiations vary. Therefore, it is crucial to understand solar radiation variations while designing heat storage systems of solar. The heating process for pasteurizing milk takes place from $11:00$ am to $2:00$ pm. Figure 10 depicts the typical solar radiation that evacuated tube collector in Pune, Maharashtra, India, which is located at geographic coordinates 18.5204 south and 73.8567 west, absorbs each month between $12:00$ am and $2:00$ pm. Despite the clear skies, the most solar radiation is attained in November and February (778 W hr/m2). Due to the wet period, irradiation is at its minimum in July and August (611 W hr/m2). On April 21, 2021, from 7 am to 4 pm, Figure 11 depicts the fluctuation in solar irradiance at the inclination angle ($10°-50°$). It demonstrates that in Figure 12, the $25°$ inclination angle produces the greatest results.

Solar heat is used as the system's input power for adsorbent refrigerated. The reflectance of the glass tube is taken into account as 0.2 while designing solar evacuated tube collector. The sun insolation that falls on the evacuated tube solar collectible surfaces is absorbed. Owing to sun insolation, the water temperature flowing inside the evacuated tube collectors rises. However, there are heat losses (the differences in temperature among the inside and the surrounding air) from the top, bottom, and side sections. In comparison to the side and bottom sections, loss of heat from the top via the glass cover is every time greater. Irradiation and convection from the absorbent tube to ambient are both taken into account when evaluating heat loss from the top.

For boiling fresh milk between midnight twelve o'clock and noon two o'clock, a tubular parabolic focusing gatherer has been created. The temperature of milk during heating is depicted in Figure 13 for various flow rates. The high liquid temperature for 5 LPH is 73°C at $2:00$ PM. In Figure 14, it can be seen how the system's highest temperature (T3) changes the system's particular cooling capacity. T3 was varied at various temperatures (70°C, 73°C, and 76°C), with no changes to the other variables listed in Table 1. Ordinary water is utilized to make chilled water. Table 2 provides information about the investigation's operational conditions. The change in specific cooling power (SCP) scores for three different desorber bed temperatures is shown in Figure 14. The highest SCP value for desorber bed temperature at 80°C ranges from 52 to 57 kW/kg. SCP values can vary by ± 4.15 percent for uncertainty analysis. The volume of desorbed methanol grows together with the heat of the desorber bed, increasing the SCP of the adsorbent refrigeration.

The planned work is anticipated to provide the following advantages. The pasteurization will be performed right after milking, which will slow the growth of psychotrophic bacteria. So, milk may be kept for a longer period of time. The milk may be kept by villagers for a very long period. The refrigerating scheme will be powered by biomass or solar heat to provide the heat needed for pasteurization and adsorbent. This will eliminate the need for energy, reduce operating costs, and reduce maintenance costs. CO2 production will decrease since there will be less spoiling. The factory will be environmentally beneficial since the pasteurizing procedure and storing will be powered by nonconventional resources.

Under real-world circumstances, the thermal energy needed to pasteurizing 200 liters of milk at a temperature differential of 70 to 78 degrees Celsius was measured to be 5.8 kWh and 5.5 kWh, accordingly. Solar concentrated and evacuated tube collector efficiency was determined to be 90.25 percent and 95.25 percent, accordingly, as expected. Solar concentration and evacuated tube collector efficiency values under field settings were discovered to be 90 and 95 percent, accordingly. The effectiveness of an evacuated tube collector is much better than that of a solar concentrator in both circumstances (theoretical and real). Because comparing to a solar concentrator, evacuated tube collectors have far lower thermal and optical losses. Additionally, optical losses were used to compute the losses of thermal energy per unit of time. Both systems can be used efficiently for pasteurizing milk, according to the study's findings, but the evacuated tube collector dependent solar milk pasteurizing method has proven to be more effective, inexpensive, steady, cost-effective, and compacted. It also offers better opportunities for milk processing decentralized.

4.1. Milk Pasteurizing in the Field with ETC. The temperatures of milk, water, glycol-water combination, and the sun's irradiation are all shown in Figure 9. The figure clearly shows that the solution of glycol temperature climbed quickly and reached its highest value of 95°C within the constant range of sun light, maintaining virtually at this heat throughout the investigation. Additionally, it is clear from Figure 9 that the storage tank hot water gradually warms up to a maximum temperature of 80°C. The net primary energy was calculated to be 6 kWh to attain the pasteurizing temperature in 85 minutes. The pasteurized process median GHI was observed to be 800 W/m^2; the median primary power on opening area (5.25 m2) of the evacuated tube collector was reported to be 4.5 kW. This test required 2.615 kW of power, using 3.91 kWh of energy overall over 1.5 hours. Under the current configuration of the milk pasteurization system operating on ETC, the effectiveness of the entire system was found to be 71.41 percent. Other trials produced similar findings.

5. Conclusions

In this research, the construction and effectiveness of a small milk storage system (200 liters capability) were examined. The pipes and containers are constructed of SS316. Solar thermal heating is employed for heating because it is readily accessible in India's rural areas, where power is scarce. An array of parabolic sun collectors has been used for heating. The outcome demonstrates that around 2:00 pm, the parabolic collectors produce the greatest outcomes. Milk can be held at a temperature of 73°C for 30 minutes while flowing at a rate of 5 LPH during that time. Thereafter, it is kept at 5 to 6°C in a chromium steel container for 30 minutes. Pasteurized milk is lastly kept in a finishing storage facility with regulated atmospheric conditions at a temperature between 15 and 20°C. Around 15 and 20°C has been chosen as the storage temperature. It is suggested to use an adsorbent refrigeration system for the cooling unit. Adsorbent cooling relies heavily on the choice of adsorbent pair. Activated carbon and methanol have been chosen and justified here after evaluating many academic works. Solar evacuated tube collectors are meant to power the adsorbent refrigeration unit. It is determined that 6 to 8 m^2 in size collectors are needed. Findings suggest that at a 25°C inclination angle, solar radiation collected by collectors was at its peak. Effectiveness of refrigeration systems had been estimated in terms of particular cooling energy. The highest specific cooling power value for desorber temperature at 78°C ranges from 50 to 60 kW/kg. Greater refrigerant is desorbed when the hot water temperature rises, raising the SCP as a result and raising the temperature of the bed. Both systems a solar concentrator and an evacuated tube collector may be used successfully for pasteurizing milk, but the system with the evacuated tube collector is more efficient, easier to build, and offers thermal storage so that the process can proceed in a variety of weather conditions. In the upcoming, this system may be powered by biogas that is readily accessible in rural regions from agricultural wastes.

Data Availability

The data used to support the findings of this study are included within the article. Should further data or information be required, these are available from the corresponding author upon request.

Conflicts of Interest

The authors declare that there are no conflicts of interest regarding the publication of this paper.

References

[1] K. Kapoor, K. K. Pandey, A. Jain, and A. Nandan, "Evolution of solar energy in India: a review," *Renewable and Sustainable Energy Reviews*, vol. 40, pp. 475–487, 2014.

[2] S. Dutta, "Traditional Indian Functional Foods," in *International Conference on Processed Foods and Beverages for Health: Beyond Basic Nutrition*, pp. 29-30, New Delhi, India, 2011.

[3] J. Fenoll, G. Jourquin, and J.-M. Kauffmann, "Fluorimetric determination of alkaline phosphatase in solid and fluid dairy products," *Talanta*, vol. 56, no. 6, pp. 1021–1026, 2002.

[4] V. Sivaprakash, L. Natrayan, R. Suryanarayanan, R. Narayanan, and P. Paramasivam, "Electrochemical anodic synthesis and analysis of TiO2 nanotubes for biomedical applications," *Journal of Nanomaterials*, vol. 2021, Article ID 9236530, 10 pages, 2021.

[5] H. Panchal, J. Patel, and S. Chaudhary, "A comprehensive review of solar milk pasteurization system," *Journal of Solar Energy Engineering*, vol. 140, no. 1, 2018.

[6] A. Merneedi, L. Natrayan, S. Kaliappan et al., "Experimental investigation on mechanical properties of carbon nanotube-reinforced epoxy composites for automobile application," *Journal of Nanomaterials*, vol. 2021, Article ID 4937059, 7 pages, 2021.

[7] L. Meunier-Goddik and S. Sandra, "Liquid milk products/pasteurized milk," in *Encyclopedia of dairy sciences*, vol. 3, pp. 1627–1632, Academic Press, Amsterdam, 2002.

[8] P. Walstra, P. Walstra, J. T. M. Wouters, and T. J. Geurts, *Dairy Science and Technology*, CRC Press, 2005.

[9] u. H. Israr, K. Muhammad, S. Muhammad et al., "Effect of heat treatments on sensory characteristics and shelf-life of skimmed milk," *African Journal of Food Science*, vol. 8, no. 2, pp. 75–79, 2014.

[10] H. Lund, "Renewable energy strategies for sustainable development," *Energy*, vol. 32, no. 6, pp. 912–919, 2007.

[11] N. Y. Ozcan and G. Gokcen, "Thermodynamic assessment of gas removal systems for single-flash geothermal power plants," *Applied Thermal Engineering*, vol. 29, no. 14–15, pp. 3246–3253, 2009.

[12] S. Yogeshwaran, R. Prabhu, L. Natrayan, and R. Murugan, "Mechanical properties of leaf ashes reinforced aluminum alloy metal matrix composites," *International Journal of Applied Engineering Research*, vol. 10, no. 13, pp. 11048–11052, 2015.

[13] H. N. Panchal and P. K. Shah, "Effect of varying glass cover thickness on performance of solar still: in a winter climate conditions," *International Journal of Renewable Energy Research*, vol. 1, no. 4, pp. 212–223, 2012.

[14] J. Aman, D.-K. Ting, and P. Henshaw, "Residential solar air conditioning: energy and exergy analyses of an ammonia-water absorption cooling system," *Applied Thermal Engineering*, vol. 62, no. 2, pp. 424–432, 2014.

[15] J. Kiruja, "Use of geothermal energy in dairy processing," *GRC Trans*, vol. 36, pp. 6–17, 2012.

[16] N. Safapour and R. H. Metcalf, "Enhancement of solar water pasteurization with reflectors," *Applied and Environmental Microbiology*, vol. 65, no. 2, pp. 859–861, 1999.

[17] F. O. Wayua, M. W. Okoth, and J. Wangoh, "Design and performance assessment of a flat-plate solar milk pasteurizer for arid pastoral areas of Kenya," *Journal of Food Processing & Preservation*, vol. 37, no. 2, pp. 120–125, 2013.

[18] M. Zorraquino, M. Roca, M. Castillo, R. Althaus, and M. Molina, "Effect of thermal treatments on the activity of quinolones in milk," *Milchwissenschaft*, vol. 63, no. 2, pp. 192–195, 2008.

[19] C. Vannoni, R. Battisti, and S. Drigo, "Potential for solar heat in industrial processes," *IEA SHC Task*, vol. 33, p. 174, 2008.

SAGE Publishing

Research Article

Comparative Study on EDM Parameter Optimization for Adsorbed Si$_3$N$_4$–TiN using TOPSIS and GRA Coupled with TLBO Algorithm

V. P. Srinivasan [ID],[1] **Ch. Sandeep** [ID],[2] **C. Shanthi** [ID],[3] **A. Bovas Herbert Bejaxhin** [ID],[4] **R. Anandan**,[5] **and M. Abisha Meji** [ID][6]

[1]Department of Mechanical Engineering, Sri Krishna College of Engineering and Technology, 641 008, Coimbatore, Tamil Nadu, India
[2]Department of Mechanical Engineering, Institute of Aeronautical Engineering, 500 043, Hyderabad, Telangana, India
[3]Department of Physics, Sona College of Technology, 636 005, Salem, Tamil Nadu, India
[4]Department of Mechanical Engineering, Saveetha School of Engineering, SIMATS, 602 105, Chennai, Tamil Nadu, India
[5]Department of Mechanical Engineering, Vinayaka Mission's Kirupananda Variyar Engineering College, Vinayaka Mission's Research Foundation, Deemed to be University, 636 308, Salem, Tamil Nadu, India
[6]School of Engineering and Applied Sciences, Kampala International University, Western Campus, Uganda

Correspondence should be addressed to V. P. Srinivasan; vpsrinivasa@gmail.com and M. Abisha Meji; abisha.meji@kiu.ac.ug

Electrical discharge machining is a thermo-physical-based material removal technique. 25 combinations of process variables were formulated with the aid of Taguchi technique for EDM of adsorbed Si$_3$N$_4$–TiN. Machining variables like pulse current, pulse-on time, pulse-off time, dielectric pressure, and spark gap voltage varied, and impact of each variables on the performance metrics (MRR, EWR, SR, ROC, θ, CIR, and CYL) was assessed. MCDM strategies like grey relational analysis and TOPSIS are utilized to find out the ideal arrangement of machining parameters to achieve most acute productivity of the multitude of reactions. Likewise, metaheuristic algorithm in particular GRA combined with teaching-learning-based optimization algorithm is utilized for getting global optimized input factors. Important factors like pulse current, pulse-on time, and spark gap voltage characteristically affect the outputs. It is recognized that the pulse-on time and the pulse current are the most significant input factors than others. The ideal machining parameters in view of GRA and TOPSIS techniques for acquiring better output factors are I, 12 amps; PON, 7 μsec; POFF, 4 μsec; DP, 12 kg/cm^2; and SV, 36 volts.

1. Introduction

Thermo-physical-based material removal technique named EDM is a modern machining methodology with phenomenal capacity of noncontact machining of profoundly hard and brittle workpieces with accurate three-dimensional complex shapes. Conceivably, surface attributes of the materials can be altered by the EDM process. The predominant problem associated with electrical discharge machining is a poor surface finish. By employing compacted electrodes, particles during the machining process will be settled on the material surface and limit the microcracks, voids, recast layer, and so forth [1–3]. The electrical discharge machining process guarantees legitimate carbonation and surface heat-treatment, and a superior material hardness was acquired with an elevated peak current and reduced duty factor [4]. The electrodischarge machining of each nonconductive workpiece relies upon large variables. Nickel and carbon intensify structure harmful mixtures like Ni (CN)$_2$ and (C$_5$H$_5$) NiNO. Nitrogen-containing ceramic materials (nitrides AlN, SiAlON, and Si$_3$N$_4$) are not being handled in hydrocarbons with a nickel holding assistive electrode

[5]. Material transmits by powder metallurgy electrodes and by powder particles suspended in the dielectric liquid; these two techniques offer practical option in contrast to the next right now utilized costly strategies for surface modifications like ion implantation and laser surface processing [6]. Both EDM and powder-mixed EDM can support the deposition of surface layers having novel trademark with unrivaled capability as far as mechanical, metallurgical, and tribological characteristics [7]. To accomplish green and healthy production, save resources, reduce the number of experimental trails, and improve the efficiency of experimental work, CuSn CLEs were employed [8]. Gap-active EDM is another methodology which gives a gap-detectable and automatic adjustable electrode retraction set up to facilitate improved textual attribute with reduced indentation, solidified-agglomerates, and crack [9]. Selecting permissible dielectric fluid is additionally indispensable in EDM since it has influence on the surface roughness. Using water as dielectric fluid advances a safe environment. Also, the electrode wear rate will be less, and surface finish will be better. On the other hand, hydrocarbon oil such as kerosene will break down and deliver harmful vapors like CO and CH_4 during EDM [10]. Also, vegetable oil-based dielectric liquids, namely, sunflower and jatropha oils, have homogeneous dielectric properties and erosion procedure when correlated with the traditional dielectric fluid. For sustainable manufacturing, biodegradable and ecofriendly vegetable oil-based dielectric liquid shall be selected [11]. TLBO algorithm is a novel population-based nature exhilarated breakthrough, and it has two stages specifically "teacher phase" and "learner phase." The modified TLBO technique also has two phases and exploits a new population class system into a traditional TLBO technique. The modified TLBO technique delineates an enhanced result quality and quick intermingling ratio than traditional TLBO. Statistical investigations on the trial results elucidated an extensive performance for proposed changes [12–14]. The TLBO algorithm has an extensive likely when contrasted with the combinatorial optimization complexity, like job-shop scheduling problems and flow-shop scheduling problems [15]. In joint optimization of TLBO, PSO, and GA, TLBO conferred impressive has surpassing amount of combination and within the fixed trails of iterations [16].

Square profiles in silicon nitride–titanium nitride are made using square tungsten-copper electrodes, and the machining input factors like I, PON, POFF, DP, and SV are optimized using various methodologies like GRA, TOP-SIS, and GRA coupled with TLBO algorithm [1]. Adsorbed silicon nitride–titanium nitride CMCs are best suited for high temperature applications because of their admirable properties. Contributions by numerous researchers in the area of mechanism of electrical discharge machining, influence of EDM parameters, selection of tool electrode, selection to dielectric fluid, influence of powder particles mixed with dielectric fluid, after machining surface morphology, etc., were considered for identifying the research gap in the previous work. In continuation to the previous work, currently circular profiles are made in silicon nitride–titanium nitride using cylindrical tungsten-copper electrodes,

and the machining input factors like I, PON, POFF, DP, and SV are optimized using joint optimization techniques. The response factors like MRR, EWR, SR, ROC, θ, CIR, and CYL are considered. The optimum electrical discharge machining ranges were attained by means of the Taguchi optimization technique for circular profiles. The optimal group of electrical discharge machining factors was attained through MCDM techniques like GRA and TOP-SIS. Also, global optimization approach GRA coupled with the TLBO algorithm was preferred. The optimal combination model bestows more prominent anticipated outcomes than estimated.

2. Experimental Procedure

Figure 1 depicts flawless exploration procedure of which the experimental work and electrical discharge machining parameter optimization are done. Commercially available silicon nitride–titanium nitride composites are used as workpiece material for the current research. Usually, silicon nitride–titanium nitride composites are fabricated by hot pressing and SPS process by mixing of Si_3N_4 and Ti powders at 1350°C temperature [17–19]. Si_3N_4–TiN has been selected because of its superior properties like high melting point, increased thermal shock resistance, high strength retention at elevated temperatures, excellent corrosion and wear resistance, improved surface hardness, and low density. It finds extensive applications in wear resistant parts, heat exchangers, gas turbines, extrusion dies, ball bearings, shot blast nozzle, level sensors in molten metal, and aircraft engines parts. In the Si_3N_4–TiN workpiece, electrical discharge machining is led utilizing electronic die-sinker (500×300 series) ED machine. Circular holes of 3 mm diameter are shaped on the Si_3N_4–TiN workpiece which is of 2 mm thickness and 50 mm diameter. The machining process was finished with tungsten-copper (W-Cu) material electrode of 3 mm diameter and 15 mm length. The Si_3N_4–TiN workpiece subsequent to the process is delineated in Figure 2. For every circular pocket, one new cylindrical-shaped electrode was chosen, and the tool electrodes before and after processing are shown in Figures 3(a) and 3(b), respectively. The deionized water is employed as dielectric liquid for safe environment [10].

2.1. Design of Experiments. The design of experiments is an organized way for regulating the correlation in dispersion through input factors impacting the process and output factors of that cycle. DOE facilitates to get convenient data around the process by directing least number of trails. The experimentations were accomplished using five input parameters differed at five positions as shown in Table 1. The DOE with 25 machining run order as obtained from the Taguchi methodology was produced using Minitab 19.0 statistical tool [1]. The order on which the experimental work is carried out and also the time taken for machining is shown in Table 2. The experimental results are portrayed in Table 3.
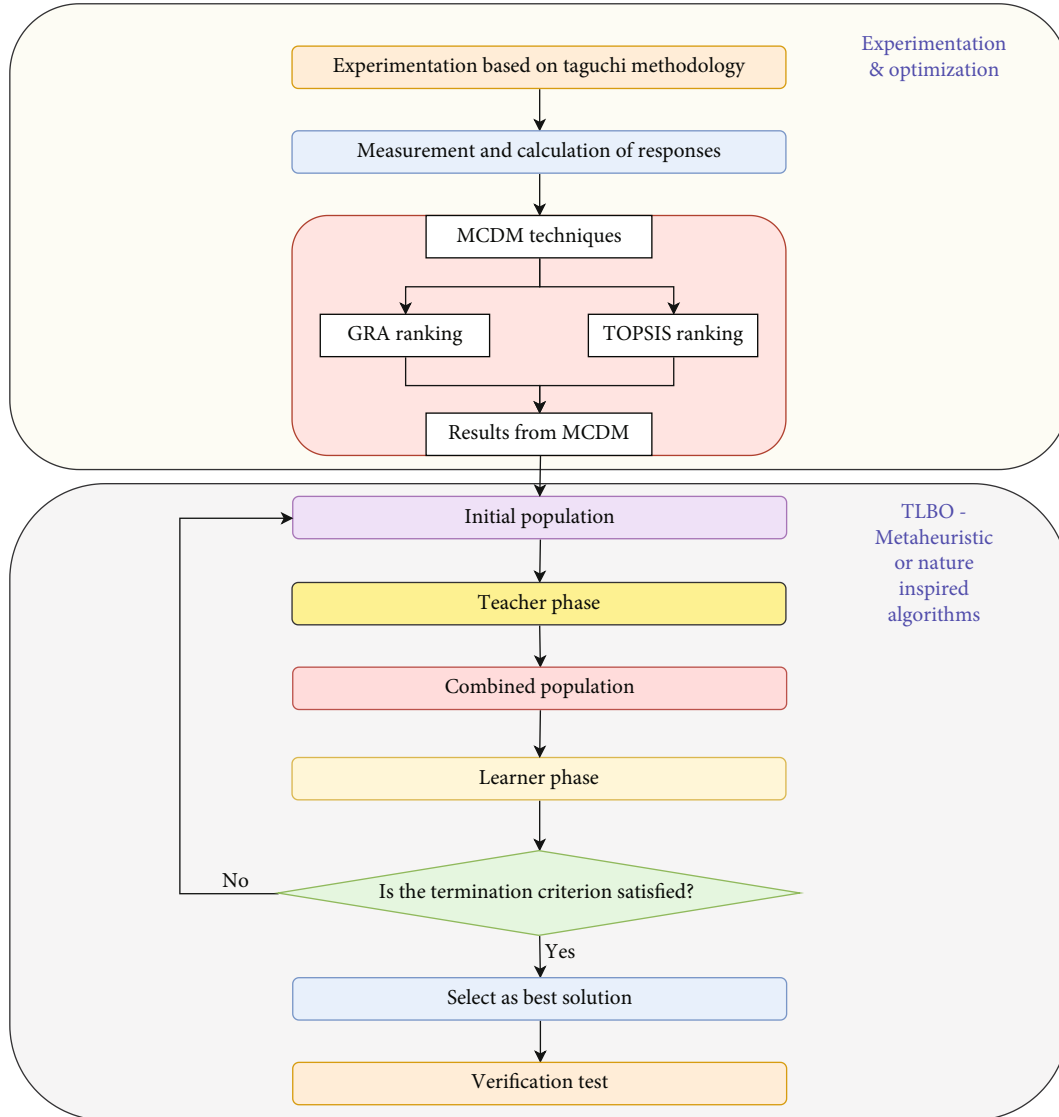
FIGURE 1: Proposed research plan (Srinivasan et al. [1]).

2.2. Measurements and Calculations of Response Factors. The MRR and the EWR were determined using Equation (1) and Equation (2), respectively. The radial overcut and taper angle were calculated using Equation (3) and Equation (4), respectively.

$$\text{Material removal rate, MRR} = \frac{W_{\text{initial}} - W_{\text{final}}}{\text{MT}} \ (\text{gm/min}), \tag{1}$$

$$\text{Electrode erosion rate, EWR} = \frac{W_{\text{BM}} - W_{\text{AM}}}{\text{MT}} \ (\text{gm/min}), \tag{2}$$

$$\text{Radial overcut, ROC (mm)} = \tan^{-1}\left\{\frac{\text{DT} - \text{DE}}{2}\right\}, \tag{3}$$

$$\text{Taper angle, } \theta \ (\text{deg}) = \tan^{-1}\left\{\frac{\text{DT} - \text{DB}}{2t}\right\}, \tag{4}$$

where W_{initial} and W_{final} are the weights of the workpiece before and after machining (g), W_{BM} and W_{AM} are the weights of the electrode before and after machining (g), MT is the time taken for machining (min), DT is the top diameter of drilled hole (mm), DB is the bottom diameter of drilled hole (mm), and DE is the diameter of electrode (mm).

The SR is measured using Mitutoyo (SURFTEST SJ-210) surface roughness tester. The geometrical tolerance results obtained from PC-DMIS metrology software are depicted in Figure 4 that is utilized to quantify the circularity and cylindricity for circular holes contrived in Si_3N_4–TiN workpiece.

3. Results and Discussions

3.1. Taguchi Methodology for Response Factors. In this investigation, negative polarity is selected as it increments the
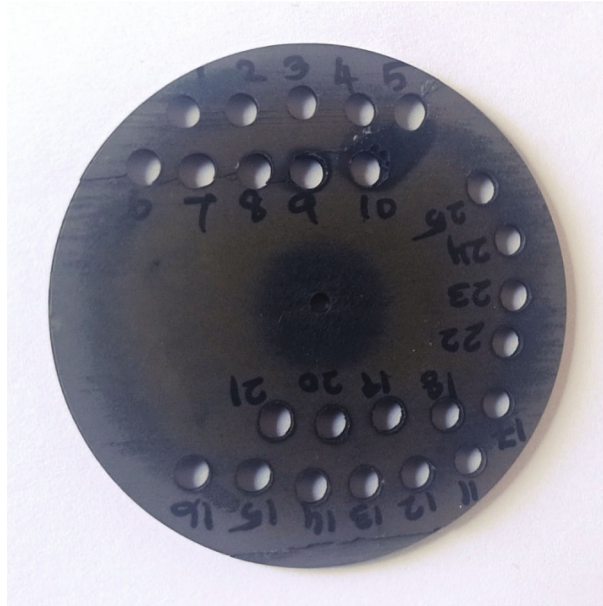
FIGURE 2: Machined Si_3N_4–TiN workpiece.

(a)

(b)
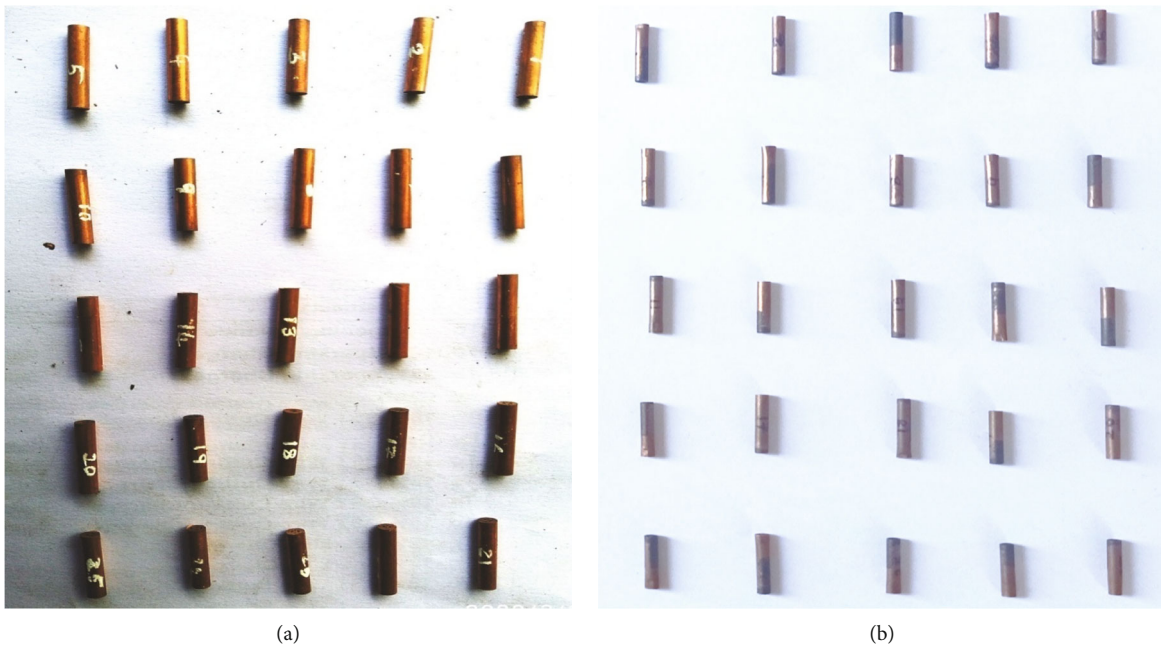
FIGURE 3: Cylindrical shaped electrodes: (a) before machining; (b) after machining.

MRR and reduces the EWR by bombarding the electrode by electrons present in the discharge section and workpiece by positive ions [1]. The MRR increases as the PON and the pulse current increments. It is ascertained that the dielectric pressure and the POFF does not impact mostly on the output factor and also the SV has average output factor. To get increased material removal rate, the pulse current and the PON should be increased. The EWR has effects similar to that of MRR. In this scenario also, as the PON and the pulse current increments, the electrode erosion rate reduces. It is noticed that the dielectric pressure and the POFF does

not impact much on the output factor and SV has average impact. To decrease the electrode erosion rate, moderate pulse-on time and pulse current are enforced. To achieve good surface, moderate pulse-on time and high gap voltage are enforced. From the main effect plot, it is evident that the surface quality decreases as the pulse current increments. The gap voltage increases the overall ROC, and the top radial would be reduced by employing lower discharge current and DP and higher SV. The θ could be reduced by decreasing pulse current and average DP. It is also observed that the low pulse current increases the taper angle

TABLE 1: Experimental input parameters.

Variables	Symbols	Units	Levels				
			1	2	3	4	5
Pulse current	I	amps	4	6	8	10	12
Pulse-on time	PON	μsec	5	6	7	8	9
Pulse-off time	POFF	μsec	2	4	6	8	10
Dielectric pressure	DP	kg/cm^2	12	14	16	18	20
Spark gap voltage	SV	Volts	28	30	32	34	36

drastically. To decrease the circularity, moderate discharge current and PON are employed, and the voltage should be maintained low. The effect of the DP and the POFF is high in circularity. The cylindricity is less at moderately high pulse current, and the main effect plot proves that decreasing pulse current increments the cylindricity profoundly. On the other hand, the lower PON increases the cylindricity, and SV should be continued low.

3.2. GRA Optimization. Grey relational analysis transforms the single-objective condition into an individual response optimization [1]. The GRA proceeds through the accompanying advances.

Step 1. Normalization is done for all the experimental output parameters by the successive equations.
    Normalization for higher-the-better,

$$x_i(k) = \frac{g_i(k) - \min g_i(k)}{\max g_i(k) - \min g_i(k)}. \tag{5}$$

Normalization for lower-the-better,

$$x_i(k) = \frac{\max g_i(k) - g_i(k)}{\max g_i(k) - \min g_i(k)}, \tag{6}$$

where $x_i(k)$ is normalized value for obtained response, min $g_i(k)$ is the least value of $g_i(k)$ for kth response, max $g_i(k)$ is the highest value of $g_i(k)$ for kth response, "i" is the experimental number, and "k" is the comparability sequence.

Step 2. Grey relational coefficient delineates the correlation among the desired and actual normalized experimental response. The GRC value is determined as follows:

$$\varphi_i(k) = \frac{\Delta_{\min} + \varphi\Delta_{\max}}{\Delta_{oi}(k) + \varphi\Delta_{\max}}, \tag{7}$$

where $\Delta(k)$ is a deviation sequence, i.e., $\Delta_{oi}(k) = |g_i(k) - x_i(k)|$; φ is a unique coefficient which sustains between 0 and 1 (usually assumed as $\varphi = 0.5$); k is a GRC; $\Delta_{\min}$ (least deviation sequence) is the lowest value of $\Delta(k)$; and $\Delta_{\max}$ (highest deviation sequence) is the highest value of $\Delta_{oi}(k)$.

TABLE 2: Table design and time taken for machining.

Run	Input machining factors					Machining time
	I	PON	POFF	DP	SV	(t) in min
1	4	5	2	12	28	29.09
2	4	6	4	14	30	27.33
3	4	7	6	16	32	24.45
4	4	8	8	18	34	21.36
5	4	9	10	20	36	19.53
6	6	5	4	16	34	30.29
7	6	6	6	18	36	28.04
8	6	7	8	20	28	26.25
9	6	8	10	12	30	23.47
10	6	9	2	14	32	20.25
11	8	5	6	20	30	32.25
12	8	6	8	12	32	30.12
13	8	7	10	14	34	25.43
14	8	8	2	16	36	23.45
15	8	9	4	18	28	19.23
16	10	5	8	14	36	28.29
17	10	6	10	16	28	26.32
18	10	7	2	18	30	24.11
19	10	8	4	20	32	21.35
20	10	9	6	12	34	18.25
21	12	5	10	18	32	31.23
22	12	6	2	20	34	27.25
23	12	7	4	12	36	23.45
24	12	8	6	14	28	19.58
25	12	9	8	16	30	17.45

Step 3. The grey relational grade is obtained from average value of GRC. The GRG is calculated as follows:

$$\theta_i = \frac{1}{n}\sum_{i=1}^{n}\varphi_i(k), \tag{8}$$

where θ_i is the GRG of ith trial, n is a number of trials, and $\varphi_i(k)$ is a GRC.

TABLE 3: Experimental results for responses after EDM.

Run	MRR (g/min)	EWR (g/min)	SR (μm)	ROC (mm)	θ (deg)	CIR (mm)	CYL (mm)
1	0.00298	0.00098	1.44	0.30	0.0488	0.0744	0.1282
2	0.00240	0.00032	0.71	0.24	0.0810	0.0491	0.0299
3	0.00172	0.00053	2.53	0.23	0.0985	0.0436	0.0545
4	0.00444	0.00111	0.56	0.18	0.0848	0.0525	0.0685
5	0.00220	0.00058	4.80	0.15	0.3140	0.0260	0.0272
6	0.00139	0.00065	0.87	0.38	0.0612	0.1752	0.1549
7	0.00280	0.00073	1.51	0.15	0.5622	0.0190	0.0094
8	0.00275	0.00083	2.87	0.19	0.3540	0.0376	0.0392
9	0.00409	0.00080	1.69	0.20	0.3667	0.0441	0.0748
10	0.00192	0.00069	0.92	0.16	0.0550	0.1465	0.0520
11	0.00198	0.00085	1.38	0.19	0.1229	0.0429	0.0763
12	0.00256	0.00079	3.99	0.20	0.0611	0.0320	0.0496
13	0.00204	0.00040	3.83	0.17	0.5150	0.1121	0.0973
14	0.00281	0.00116	1.27	0.21	0.0268	0.0509	0.0313
15	0.00312	0.00145	0.69	0.23	0.0893	0.0573	0.0818
16	0.00199	0.00059	3.26	0.20	0.0761	0.0205	0.0203
17	0.00151	0.00062	2.60	0.20	0.0871	0.0183	0.0320
18	0.00255	0.00123	1.15	0.12	0.0877	0.0303	0.0410
19	0.00207	0.00073	1.17	0.18	0.0951	0.0168	0.0277
20	0.00183	0.00029	2.52	0.19	0.0210	0.0473	0.0230
21	0.00117	0.00060	0.93	0.21	0.0244	0.0778	0.0307
22	0.00093	0.00079	0.65	0.06	0.0486	0.0557	0.0313
23	0.00219	0.00058	0.77	0.15	0.1098	0.0309	0.0120
24	0.00267	0.00040	1.42	0.24	0.2073	0.0137	0.0231
25	0.00186	0.00037	3.44	0.19	0.0355	0.0111	0.0216

In GRA, the GRG which is highest was given top ranking, and lower GRG is given last rank [1]. The calculated GRG for 25 experimental run orders is shown in Table 4. Figure 5 outlines the GRG for 25 experimental run orders, and Table 4 portrays the impact of input factor on the GRG. From Tables 4 and 5, it is evident that $A_5 B_3 C_2 D_1 E_5$ are the optimal input factor levels. Consequently, the 23rd experimental run order is the optimized group of input factors for best output response.

3.3. TOPSIS Optimization. Technique for order of preference by similarity to ideal solution is an ordinary MCDM optimization methodology that assists with selecting the better input factors among the enormous number of options which is having the shortest point from positive ideal solution and the largest point from negative ideal solution [1]. The MCDM using the TOPSIS methodology proceeds through the accompanying advances.

Step 1. First, all the information gathered from experimental run was utilized for developing decision matrix which comprises of n number of response factors which are complexions and m number of experimental runs that are the substitute result.

$$D_m = \begin{bmatrix} a_{11} & a_{12} & a_{13} & \cdots & \cdots & a_{1n} \\ a_{21} & a_{22} & a_{23} & \cdots & \cdots & a_{2n} \\ \vdots & \vdots & \vdots & \vdots & \vdots & \vdots \\ a_{m1} & a_{m2} & a_{m3} & \cdots & \cdots & a_{mn} \end{bmatrix}, \quad (9)$$

where a_{ij} is the measure of jth attribute to ith alternative.

Step 2. The accompanying condition gives the result for normalization of decision matrix.

$$\gamma_{ij} = \frac{a_{ij}}{\sqrt{\sum_{i=1}^{m} a_{ij}^2}}, \quad (10)$$

where γ_{ij} is normalized solution for $i = 1, 2, 3, \cdots, m$ and $j = 1, 2, 3, \cdots, n$.

Step 3. The weights of every characteristic are fixed, and for the whole attributes, the total sum of weightage should be
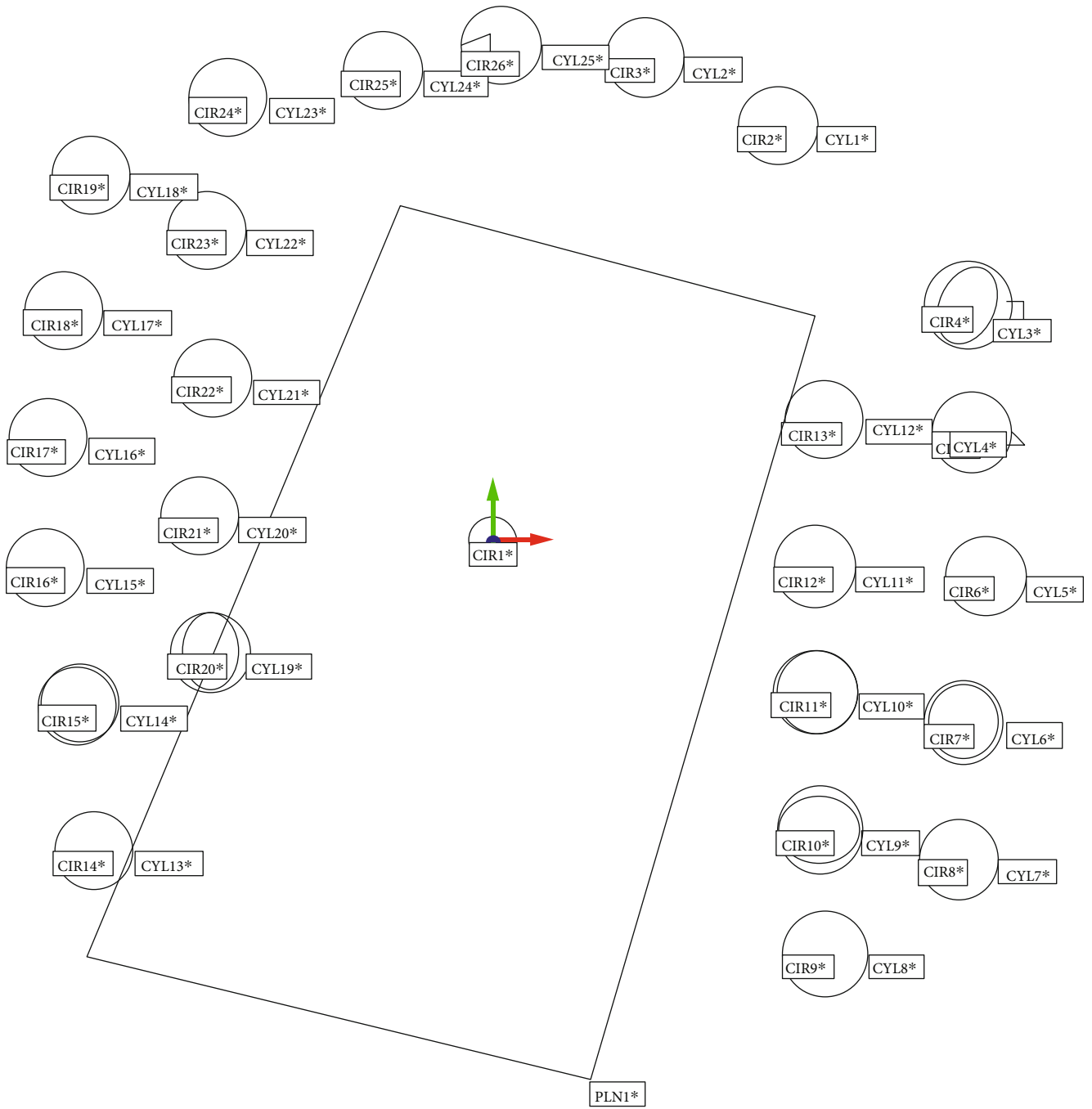
FIGURE 4: Circularity and cylindricity measurement.

equivalent to 1. By utilizing the accompanying condition, the weighted normalized decision matrix is determined.

$$\varphi_{ij} = w_j \gamma_{ij}, \qquad (11)$$

where $\sum_{j=1}^{n} w_j = 1$.

Step 4. The positive ideal solution (PIS) and negative ideal solution (NIS) can be determined by

$$\varphi^+ = (\varphi_1^+, \varphi_2^+, \cdots \varphi_n^+)$$
$$= \left\{ \left(\max \varphi_{ij} | j \in J_1 \right), \left(\min \varphi_{ij} | j \in J_2, i = 1, 2, \cdots n \right) \right\}, \qquad (12)$$

TABLE 4: Grey relational analysis.

Run	Normalization							Grey relational coefficient							GRG	Rank
	MRR (g/min)	EWR (g/min)	SR (μm)	ROC (mm)	θ (deg)	CIR (mm)	CYL (mm)	MRR (g/min)	EWR (g/min)	SR (μm)	ROC (mm)	θ (deg)	CIR (mm)	CYL (mm)		
1	0.10021	0.99889	0.70737	0.24714	0.94867	0.61426	0.90125	0.35720	0.99778	0.63081	0.39909	0.90689	0.56450	0.83507	0.67019	15
2	0.07176	0.99973	0.86105	0.43250	0.88917	0.76843	0.85911	0.35008	0.99945	0.78254	0.46838	0.81856	0.68347	0.78016	0.69752	10
3	0.03847	0.99946	0.47789	0.46339	0.85683	0.80195	0.69003	0.34211	0.99892	0.48919	0.48234	0.77740	0.71628	0.61731	0.63194	22
4	0.17148	0.99872	0.89263	0.61786	0.88215	0.74771	0.59381	0.37636	0.99745	0.82322	0.56680	0.80925	0.66464	0.55176	0.68421	14
5	0.06174	0.99939	0	0.71053	0.45863	0.90920	0.87766	0.34764	0.99879	0.33333	0.63334	0.48014	0.84631	0.80342	0.63471	21
6	1	0.99930	0.82737	0	0.92575	0	0	1	0.99861	0.74335	0.33333	0.87071	0.33333	0.33333	0.65895	16
7	0.09131	0.99921	0.69263	0.71053	0	0.95186	1	0.35494	0.99842	0.61930	0.63334	0.33333	0.91217	1	0.69307	12
8	0.08887	0.99908	0.40632	0.58696	0.38471	0.83851	0.79519	0.35433	0.99817	0.45717	0.54762	0.44832	0.75587	0.70941	0.61013	23
9	0.15437	0.99911	0.65474	0.55607	0.36125	0.79890	0.55052	0.37157	0.99823	0.59153	0.52970	0.43908	0.71317	0.52660	0.59570	24
10	0.04830	0.99926	0.81684	0.67964	0.93716	0.17489	0.70722	0.34442	0.99853	0.73190	0.60949	0.88835	0.37733	0.63069	0.65439	17
11	0.05123	0.99906	0.72000	0.58696	0.81174	0.80622	0.54021	0.34512	0.99811	0.64103	0.54762	0.72647	0.72069	0.52095	0.64286	20
12	0.07948	0.99913	0.17053	0.55607	0.92594	0.87264	0.72371	0.35198	0.99826	0.37609	0.52970	0.87099	0.79699	0.64409	0.65259	18
13	0.05436	1	0.20421	0.64875	0.08722	0.38452	0.39588	0.34587	1	0.38587	0.58737	0.35391	0.44824	0.45285	0.51059	25
14	0.09180	0.99866	0.74316	0.52518	0.98926	0.75746	0.84948	0.35506	0.99732	0.66064	0.51291	0.97898	0.67337	0.76862	0.70670	6
15	0.10696	0.99829	0.86526	0.46339	0.87383	0.71846	0.50241	0.35893	0.99660	0.78773	0.48234	0.79851	0.63977	0.50121	0.65215	19
16	0.05182	0.99938	0.32421	0.55607	0.89822	0.94272	0.92509	0.34526	0.99875	0.42525	0.52970	0.83087	0.89721	0.86970	0.69953	8
17	0.02826	0.99935	0.46316	0.55607	0.87795	0.95612	0.84467	0.33973	0.99870	0.48223	0.52970	0.80380	0.91933	0.76298	0.69092	13
18	0.07909	0.99857	0.76842	0.80321	0.87679	0.88300	0.78282	0.35189	0.99715	0.68345	0.71758	0.80229	0.81037	0.69717	0.72284	4
19	0.05578	0.99920	0.76421	0.61786	0.86321	0.96527	0.87423	0.34621	0.99840	0.67954	0.56680	0.78518	0.93504	0.79901	0.73003	2
20	0.04390	0.99976	0.48000	0.58696	1	0.77940	0.90653	0.34338	0.99951	0.49020	0.54762	1	0.69387	0.84250	0.70244	7
21	0.01164	0.99937	0.81474	0.52518	0.99375	0.59354	0.85361	0.33594	0.99875	0.72965	0.51291	0.98766	0.55160	0.77352	0.69858	9
22	0	0	1	1	0.94904	0.72821	0.84948	0.33333	0.33333	1	1	0.90750	0.64785	0.76862	0.71295	5
23	**0.06150**	**0.99940**	**0.84842**	**0.71053**	**0.83595**	**0.87934**	**0.98213**	**0.34758**	**0.99880**	**0.76737**	**0.63334**	**0.75296**	**0.80560**	**0.96549**	**0.75302**	**1**
24	0.08476	0.99963	0.71158	0.43250	0.65579	0.98416	0.90584	0.35330	0.99926	0.63418	0.46838	0.59227	0.96929	0.84153	0.69403	11
25	0.04537	0.99966	0.28632	0.58696	0.97324	1	0.91615	0.34373	0.99932	0.41197	0.54762	0.94921	1	0.85639	0.72975	3
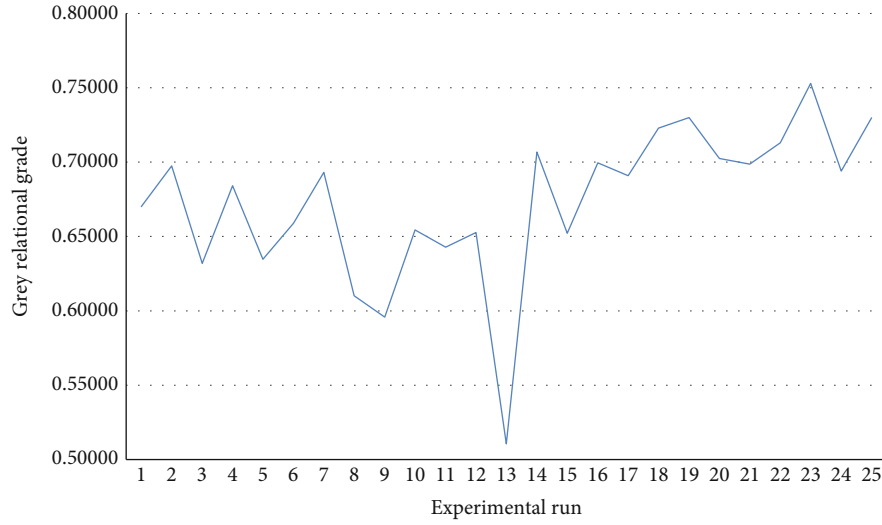
FIGURE 5: GRG for experimental run.

TABLE 5: Factor effect on GRG.

Parameter	Grey relational grade					Optimal level	Difference	Rank
	1	2	3	4	5			
I	0.66371	0.64245	0.63298	0.70915	**0.71766**	5	0.08469	1
PON	0.67402	0.68213	**0.68941**	0.64122	0.67469	3	0.04819	2
POFF	0.69341	**0.69833**	0.69287	0.67524	0.66610	2	0.03224	4
DP	**0.69017**	0.66121	0.67479	0.68365	0.66613	1	0.02896	5
SV	0.66349	0.67773	0.67350	0.65383	**0.69741**	5	0.03392	3

$$\varphi^{-} = (\varphi_1^{-}, \varphi_2^{-}, \cdots \varphi_n^{-})$$
$$= \left\{ \left(\min \varphi_{ij} | j \in J_1 \right), \left(\max \varphi_{ij} | j \in J_2, i = 1, 2, \cdots n \right) \right\}, \quad (13)$$

where J_1 and J_2 are sets of beneficial attribute and nonbeneficial attribute, respectively.

Step 5. Separation proportions of the entire options are determined from PIS and NIS

$$S_i^{+} = \sqrt{\sum_{j=1}^{n} \left(\varphi_{ij} - \varphi_i^{+} \right)^2}, \quad (14)$$

$$S_i^{-} = \sqrt{\sum_{j=1}^{n} \left(\varphi_{ij} - \varphi_i^{-} \right)^2}, \quad (15)$$

where $i = 1, 2, 3, \cdots, m$.

Step 6. The relative similarity index (SI) of every parameter is determined utilizing the accompanying equation

$$SI = \frac{S_i^{-}}{S_i^{+} - S_i^{-}}. \quad (16)$$

In TOPSIS, the first part is to change the outcomes to a decision matrix comprising of output responses (attributes) in columns and exploratory trials (alternatives) in rows as delineated in Equation (9). By utilizing Equation (10), the decision matrix is normalized, and relative weightage is doled to all entities. Then, equivalent relative weightage is fixed to entire seven responses, viz., material removal rate, electrode wear rate, surface roughness, radial overcut, taper angle, circularity, and cylindricity. The weighted normalization numbers were determined by using Equation (11). Using Equations (12) and (13), the positive ideal solution and negative ideal solution are obtained from the normalization matrix. Equations (14) and (15) are utilized to ascertain the separation measures of every alternative from PIS and NIS. Likewise, Equation (16) is employed to ascertain the similarity index for all the options by finding the separation measures [1].

Based on the TOPSIS optimization, the normalized matrix, weighted-normalized matrix, separation evaluated

TABLE 6: TOPSIS.

Run	Normalization							Weighted normalized matrix							Separation			Rank
	MRR (g/min)	EWR (g/min)	SR (μm)	ROC (mm)	θ (deg)	CIR (mm)	CYL (mm)	MRR (g/min)	EWR (g/min)	SR (μm)	ROC (mm)	θ (deg)	CIR (mm)	CYL (mm)	S⁺	S⁻	SI	
1	0.13596	0.28222	0.05264	0.16713	0.08112	0.14294	0.19924	0.01944	0.04036	0.00753	0.02390	0.01160	0.02044	0.02849	0.55500	4.84144	0.89715	23
2	0.12524	0.20437	0.15886	0.18570	0.35077	0.12007	0.21757	0.01791	0.02922	0.02272	0.02655	0.05016	0.01717	0.03111	0.53983	4.82192	0.89932	9
3	0.08427	0.23694	0.07426	0.04642	0.05385	0.13232	0.16201	0.01205	0.03388	0.01062	0.00664	0.00770	0.01892	0.02317	0.55256	4.84025	0.89754	21
4	0.08604	0.29544	0.11938	0.19498	0.02566	0.13858	0.09104	0.01230	0.04225	0.01707	0.02788	0.00367	0.01982	0.01302	0.54541	4.83305	0.89859	14
5	0.05879	0.17421	0.08648	0.14856	0.05264	0.39886	0.15125	0.00841	0.02491	0.01237	0.02124	0.00753	0.05704	0.02163	0.55111	4.83633	0.89770	20
6	0.06348	0.18665	0.10998	0.16713	0.09092	0.04574	0.08057	0.00908	0.02669	0.01573	0.02390	0.01300	0.00654	0.01152	0.54580	4.83398	0.89855	15
7	0.06063	0.21561	0.12972	0.17641	0.11756	0.11680	0.22193	0.00867	0.03083	0.01855	0.02523	0.01681	0.01670	0.03174	0.54352	4.82978	0.89885	11
8	0.09554	0.36867	0.06486	0.21355	0.08542	0.15601	0.23793	0.01366	0.05272	0.00927	0.03054	0.01222	0.02231	0.03402	0.55431	4.83905	0.89722	22
9	0.07349	0.08088	0.06674	0.22283	0.07748	0.13368	0.08697	0.01051	0.01157	0.00954	0.03187	0.01108	0.01912	0.01244	0.55111	4.83924	0.89776	19
10	0.09131	0.24891	0.13536	0.27854	0.04668	0.20256	0.37289	0.01306	0.03559	0.01936	0.03983	0.00668	0.02897	0.05332	0.54415	4.82824	0.89871	12
11	0.06706	0.14619	0.07238	0.13927	0.10503	0.08413	0.03490	0.00959	0.02091	0.01035	0.01992	0.01502	0.01203	0.00499	0.55104	4.83936	0.89777	18
12	0.07808	0.31273	0.10810	0.11142	0.08389	0.08249	0.11925	0.01117	0.04472	0.01546	0.01593	0.01200	0.01180	0.01705	0.54765	4.83475	0.89825	16
13	0.65497	0.16592	0.08178	0.35282	0.05854	0.47700	0.45055	0.09366	0.02373	0.01169	0.05045	0.00837	0.06821	0.06443	0.55909	4.83445	0.89633	25
14	0.08421	0.20976	0.26978	0.17641	0.33862	0.10237	0.11402	0.01204	0.03000	0.03858	0.02523	0.04842	0.01464	0.01630	0.52371	4.80696	0.90175	5
15	0.03583	0.15179	0.08742	0.19498	0.02334	0.21182	0.08930	0.00512	0.02171	0.01250	0.02788	0.00334	0.03029	0.01277	0.54916	4.83716	0.89805	17
16	0.05604	0.07462	0.23688	0.17641	0.02011	0.12878	0.06690	0.00801	0.01067	0.03387	0.02523	0.00288	0.01842	0.00957	0.52732	4.81669	0.90133	7
17	0.08574	0.18449	0.14194	0.13927	0.53778	0.05173	0.02734	0.01226	0.02638	0.02030	0.01992	0.07690	0.00740	0.00391	0.54420	4.82311	0.89861	13
18	0.06259	0.02588	0.36002	0.15784	0.49263	0.30520	0.28301	0.00895	0.00370	0.05148	0.02257	0.07045	0.04364	0.04047	0.51363	4.79046	0.90316	3
19	0.07833	0.20058	0.37506	0.18570	0.05845	0.08712	0.14427	0.01120	0.02868	0.05363	0.02655	0.00836	0.01246	0.02063	0.50810	4.79635	0.90421	2
20	0.04624	0.15649	0.24440	0.18570	0.08329	0.04982	0.09308	0.00661	0.02238	0.03495	0.02655	0.01191	0.00712	0.01331	0.52639	4.81479	0.90145	6
21	0.05264	0.13404	0.23782	0.21355	0.09422	0.11871	0.15852	0.00753	0.01917	0.03401	0.03054	0.01347	0.01697	0.02267	0.52711	4.81464	0.90132	8
22	0.06100	0.15108	0.30644	0.18570	0.07279	0.05581	0.05905	0.00872	0.02160	0.04382	0.02655	0.01041	0.00798	0.00844	0.51746	4.80630	0.90280	4
23	**0.06721**	**0.14790**	**0.45120**	**0.13927**	**0.30036**	**0.07079**	**0.07912**	**0.00961**	**0.02115**	**0.06452**	**0.01992**	**0.04295**	**0.01012**	**0.01131**	**0.49748**	**4.78251**	**0.90578**	**1**
24	0.08163	0.10071	0.13348	0.22283	0.19829	0.03730	0.06719	0.01167	0.01440	0.01909	0.03187	0.02836	0.00533	0.00961	0.54161	4.82841	0.89914	10
25	0.65497	0.16592	0.08178	0.35282	0.05854	0.47700	0.45055	0.09366	0.02373	0.01169	0.05045	0.00837	0.06821	0.06443	0.55909	4.83445	0.89634	24

TABLE 7: Mean similarity index of each parameter at entry level.

Parameter	Similarity index					Optimal level	Difference	Rank
	1	2	3	4	5			
I	0.89806	0.89722	0.89843	0.90108	**0.90175**	5	0.00453	1
PON	0.89922	0.89657	**0.90029**	0.90001	0.89845	3	0.00373	2
POFF	0.90072	**0.90118**	0.89895	0.89835	0.89835	2	0.00283	4
DP	**0.90008**	0.89897	0.89856	0.89999	0.89994	1	0.00111	5
SV	0.89803	0.89787	0.90001	0.89955	**0.90108**	5	0.00321	3

TABLE 8: Initial random population.

Run	Input parameter					Response								GRG	Rank
	I	PON	POFF	DP	SV	MRR	EWR	SR	ROC	θ	CIR	CYL			
1	4	5	2	12	28	0.00298	0.00098	1.44	0.30	0.0488	0.0744	0.1282		0.67019	15
2	4	6	4	14	30	0.00240	0.00032	0.71	0.24	0.0810	0.0491	0.0299		0.69752	10
3	4	7	6	16	32	0.00172	0.00053	2.53	0.23	0.0985	0.0436	0.0545		0.63194	22
4	4	8	8	18	34	0.00444	0.00111	0.56	0.18	0.0848	0.0525	0.0685		0.68421	14
5	4	9	10	20	36	0.00220	0.00058	4.80	0.15	0.3140	0.0260	0.0272		0.63471	21
6	6	5	4	16	34	0.02139	0.00065	0.87	0.38	0.0612	0.1752	0.1549		0.65895	16
7	6	6	6	18	36	0.00280	0.00073	1.51	0.15	0.5622	0.0190	0.0094		0.69307	12
8	6	7	8	20	28	0.00275	0.00083	2.87	0.19	0.3540	0.0376	0.0392		0.61013	23
9	6	8	10	12	30	0.00409	0.00080	1.69	0.20	0.3667	0.0441	0.0748		0.59570	24
10	6	9	2	14	32	0.00192	0.00069	0.92	0.16	0.0550	0.1465	0.0520		0.65439	17
11	8	5	6	20	30	0.00198	0.00085	1.38	0.19	0.1229	0.0429	0.0763		0.64286	20
12	8	6	8	12	32	0.00256	0.00079	3.99	0.20	0.0611	0.0320	0.0496		0.65259	18
13	8	7	10	14	34	0.00204	0.00010	3.83	0.17	0.5150	0.1121	0.0973		0.51059	25
14	8	8	2	16	36	0.00281	0.00116	1.27	0.21	0.0268	0.0509	0.0313		0.70670	6
15	8	9	4	18	28	0.00312	0.00145	0.69	0.23	0.0893	0.0573	0.0818		0.65215	19
16	10	5	8	14	36	0.00199	0.00059	3.26	0.20	0.0761	0.0205	0.0203		0.69953	8
17	10	6	10	16	28	0.00151	0.00062	2.60	0.20	0.0871	0.0183	0.0320		0.69092	13
18	10	7	2	18	30	0.00255	0.00123	1.15	0.12	0.0877	0.0303	0.0410		0.72284	4
19	10	8	4	20	32	0.00207	0.00073	1.17	0.18	0.0951	0.0168	0.0277		0.73003	2
20	10	9	6	12	34	0.00183	0.00029	2.52	0.19	0.0210	0.0473	0.0230		0.70244	7
21	12	5	10	18	32	0.00117	0.00060	0.93	0.21	0.0244	0.0778	0.0307		0.69858	9
22	12	6	2	20	34	0.00093	0.79000	0.05	0.06	0.0486	0.0557	0.0313		0.71295	5
23	**12**	**7**	**4**	**12**	**36**	**0.00219**	**0.00058**	**0.77**	**0.15**	**0.1098**	**0.0309**	**0.0120**		**0.75302**	**1**
24	12	8	6	14	28	0.00267	0.00040	1.42	0.24	0.2073	0.0137	0.0231		0.69403	11
25	12	9	8	16	30	0.00186	0.00037	3.44	0.19	0.0355	0.0111	0.0216		0.72975	3
Mean	8	7	6	16	32										

data, and SI of every option are delineated in Table 6. The alternative result with highest SI value is the predominant, and the trails are ranked depending upon the SI. The 23rd experimental run is the good run, and the 13th is the poor among every one of the other options. Table 7 displays the determined mean similarity index of all the input factors at all the levels.

3.4. TLBO Algorithms. TLBO algorithms depict the teaching, and learning phenomenon takes place in the classroom [1]. The current work was centered on maximization of material removal rate and minimization of electrode erosion rate, SR,

ROC, θ, circularity, and cylindricity, respectively. The regression equation for maximization and minimization of output factors is delineated in Equation (17) to Equation (23). Additionally, the parametric bounds are delineated in Equation (24) to Equation (28).

Maximization:

$$MRR = 0.00047 + 0.000367\,I + 0.000214\,PON$$
$$- 0.000039\,POFF - 0.000050\,DP - 0.000025\,SV.$$

$$(17)$$

Table 9: Teacher phase–updated process parameter and responses.

S. no	New input parameter					Bounded input parameter					New response								
	I	PON	POFF	DP	SV	I	PON	POFF	DP	SV	MRR	EWR	SR	ROC	θ	CIR	CYL	GRG	Rank
1	2.2	3.9	-0.6	9	24.6	4	3.9	2	12	28	0.00666	0.01322	0.56	0.31	0.0450	0.0950	0.1165	0.60515	23
2	2.2	5.45	2.7	12.5	28.3	4	5.45	2.7	12.5	28.3	0.00559	0.03850	0.93	0.29	0.0750	0.0858	0.1034	0.69752	10
3	2.2	7	6	16	32	4	7	6	16	32	0.00445	0.03060	2.02	0.22	0.2027	0.0672	0.0720	0.63194	21
4	2.2	8.55	9.3	19.5	35.7	4	8.55	9.3	19.5	35.7	0.00332	0.02270	3.12	0.16	0.3304	0.0486	0.0406	0.68421	14
5	2.2	10.1	12.6	23	39.4	4	9	10	20	36	0.00294	0.03060	3.35	0.15	0.3537	0.0439	0.0349	0.63471	20
6	5.1	3.9	2.7	16	35.7	5.1	3.9	2.7	16	35.7	0.00720	0.11713	0.84	0.23	0.1171	0.0921	0.0814	0.65895	15
7	5.1	5.45	6	19.5	39.4	5.1	5.45	6	19.5	36	0.00554	0.09817	1.78	0.19	0.2230	0.0682	0.0594	0.69307	12
8	5.1	7	9.3	23	24.6	5.1	7	9.3	20	28	0.00270	0.03376	2.49	0.21	0.2586	0.0373	0.0654	0.61013	22
9	5.1	8.55	12.6	9	28.3	5.1	8.55	10	9	28.3	0.00213	0.24074	3.51	0.27	0.2231	0.0516	0.0710	0.59570	24
10	5.1	10.1	-0.6	12.5	32	5.1	9	2	12.5	32	0.00371	0.03692	1.31	0.22	0.0887	0.0753	0.0641	0.65439	16
11	8	3.9	6	23	28.3	8	3.9	6	23	28.3	0.00432	0.11555	1.08	0.23	0.1253	0.0497	0.0740	0.64286	19
12	8	5.45	9.3	9	32	8	5.45	9.3	12	32	0.00370	0.05825	2.81	0.24	0.1874	0.0545	0.0614	0.65259	17
13	8	7	12.6	12.5	35.7	8	7	10	12.5	35.7	0.00316	0.05667	3.35	0.20	0.2392	0.0507	0.0388	0.51059	25
14	8	8.55	-0.6	16	39.4	8	8.55	2	16	36	0.00351	0.10291	1.12	0.16	0.0898	0.0646	0.0339	0.70670	6
15	8	10.1	2.7	19.5	24.6	8	9	2.7	19.5	28	0.00170	0.07684	0.81	0.18	0.0771	0.0407	0.0463	0.65215	18
16	10.9	3.9	9.3	12.5	39.4	10.9	3.9	9.3	12.5	36	0.00432	0.05156	2.66	0.21	0.1647	0.0543	0.0435	0.69953	8
17	10.9	5.45	12.6	16	24.6	10.9	5.45	10	16	28	0.00182	0.00811	2.48	0.21	0.1587	0.0260	0.0485	0.69092	13
18	10.9	7	-0.6	19.5	28.3	10.9	7	2	19.5	28.3	0.00217	0.16769	0.26	0.18	0.0092	0.0399	0.0436	0.72284	4
19	10.9	8.55	2.7	23	32	10.9	8.55	2.7	20	32	0.00163	0.16927	0.79	0.13	0.0610	0.0361	0.0211	0.73003	2
20	10.9	10.1	6	9	35.7	10.9	9	6	9	35.7	0.00183	0.03455	2.56	0.18	0.0993	0.0515	0.0207	0.70244	7
21	13.8	3.9	12.6	19.5	32	12	3.9	10	19.5	32	0.00290	0.13688	2.24	0.18	0.1789	0.0270	0.0359	0.69858	9
22	13.8	5.45	-0.6	23	35.7	12	5.45	2	20	35.7	0.00392	0.27592	0.34	0.14	0.0341	0.0523	0.0265	0.71295	5
23	**13.8**	7	2.7	9	39.4	12	7	2.7	9	36	0.00335	0.06894	1.36	0.19	0.0014	0.0667	0.0321	0.75302	1
24	13.8	8.55	6	12.5	24.6	12	8.55	6	12.5	28	0.00038	0.01559	1.91	0.20	0.0514	0.0297	0.0332	0.69403	11
25	13.8	10.1	9.3	16	28.3	12	9	9.3	16	28.3	0.00060	0.01717	2.70	0.17	0.1506	0.0101	0.0186	0.72975	3

TABLE 10: Combined population.

Run	Combined input parameter					New response							GRG	Rank
	I	PON	POFF	DP	SV	MRR	EWR	SR	ROC	θ	CIR	CYL		
1	4	5	2	12	28	0.00298	0.00098	1.44	0.30	0.0488	0.0744	0.1282	0.67019	49
2	4	6	4	14	30	0.00240	0.00032	0.71	0.24	0.0810	0.0491	0.0299	0.69752	21
3	4	7	6	16	32	0.00172	0.00053	2.53	0.23	0.0985	0.0436	0.0545	0.63194	46
4	4	8	8	18	34	0.00444	0.00111	0.56	0.18	0.0848	0.0525	0.0685	0.68421	23
5	4	9	10	20	36	0.00220	0.00058	4.80	0.15	0.3140	0.0260	0.0272	0.63471	38
6	6	5	4	16	34	0.02139	0.00065	0.87	0.38	0.0612	0.1752	0.1549	0.65895	19
7	6	6	6	18	36	0.00280	0.00073	1.51	0.15	0.5622	0.0190	0.0094	0.69307	6
8	6	7	8	20	28	0.00275	0.00083	2.87	0.19	0.3540	0.0376	0.0392	0.61013	40
9	6	8	10	12	30	0.00409	0.00080	1.69	0.20	0.3667	0.0441	0.0748	0.59570	44
10	6	9	2	14	32	0.00192	0.00069	0.92	0.16	0.0550	0.1465	0.0520	0.65439	24
11	8	5	6	20	30	0.00198	0.00085	1.38	0.19	0.1229	0.0429	0.0763	0.64286	41
12	8	6	8	12	32	0.00256	0.00079	3.99	0.20	0.0611	0.0320	0.0496	0.65259	47
13	8	7	10	14	34	0.00204	0.00010	3.83	0.17	0.5150	0.1121	0.0973	0.51059	48
14	8	8	2	16	36	0.00281	0.00116	1.27	0.21	0.0268	0.0509	0.0313	0.70670	27
15	8	9	4	18	28	0.00312	0.00145	0.69	0.23	0.0893	0.0573	0.0818	0.65215	37
16	10	5	8	14	36	0.00199	0.00059	3.26	0.20	0.0761	0.0205	0.0203	0.69953	34
17	10	6	10	16	28	0.00151	0.00062	2.60	0.20	0.0871	0.0183	0.0320	0.69092	39
18	10	7	2	18	30	0.00255	0.00123	1.15	0.12	0.0877	0.0303	0.0410	0.72284	16
19	10	8	4	20	32	0.00207	0.00073	1.17	0.18	0.0951	0.0168	0.0277	0.73003	20
20	10	9	6	12	34	0.00183	0.00029	2.52	0.19	0.0210	0.0473	0.0230	0.70244	31
21	12	5	10	18	32	0.00117	0.00060	0.93	0.21	0.0244	0.0778	0.0307	0.69858	22
22	12	6	2	20	34	0.00093	0.79000	0.05	0.06	0.0486	0.0557	0.0313	0.71295	17
23	12	7	4	12	36	0.00219	0.00058	0.77	0.15	0.1098	0.0309	0.0120	0.75302	2
24	12	8	6	14	28	0.00267	0.00040	1.42	0.24	0.2073	0.0137	0.0231	0.69403	25
25	12	9	8	16	30	0.00186	0.00037	3.44	0.19	0.0355	0.0111	0.0216	0.72975	36
26	4	3.9	2	12	28	0.00666	0.01322	0.56	0.31	0.0450	0.0950	0.1165	0.60515	43
27	4	5.45	2.7	12.5	28.3	0.00559	0.03850	0.93	0.29	0.0750	0.0858	0.1034	0.69752	12
28	4	7	6	16	32	0.00445	0.03060	2.02	0.22	0.2027	0.0672	0.0720	0.63194	35
29	4	8.55	9.3	19.5	35.7	0.00332	0.02270	3.12	0.16	0.3304	0.0486	0.0406	0.68421	18
30	4	9	10	20	36	0.00294	0.03060	3.35	0.15	0.3537	0.0439	0.0349	0.63471	33
31	5.1	3.9	2.7	16	35.7	0.00720	0.11713	0.84	0.23	0.1171	0.0921	0.0814	0.65895	26
32	5.1	5.45	6	19.5	36	0.00554	0.09817	1.78	0.19	0.2230	0.0682	0.0594	0.69307	14
33	5.1	7	9.3	20	28	0.00270	0.03376	2.49	0.21	0.2586	0.0373	0.0654	0.61013	42
34	5.1	8.55	10	9	28.3	0.00213	0.24074	3.51	0.27	0.2231	0.0516	0.0710	0.59570	45
35	5.1	9	2	12.5	32	0.00371	0.03692	1.31	0.22	0.0887	0.0753	0.0641	0.65439	28
36	8	3.9	6	20	28.3	0.00432	0.11555	1.08	0.23	0.1253	0.0497	0.0740	0.64286	32
37	8	5.45	9.3	12	32	0.00370	0.05825	2.81	0.24	0.1874	0.0545	0.0614	0.65259	29
38	8	7	10	12.5	35.7	0.00316	0.05667	3.35	0.20	0.2392	0.0507	0.0388	0.51059	50
39	8	8.55	2	16	36	0.00351	0.10291	1.12	0.16	0.0898	0.0646	0.0339	0.70670	8
40	8	9	2.7	19.5	28	0.00170	0.07684	0.81	0.18	0.0771	0.0407	0.0463	0.65215	30
41	10.9	3.9	9.3	12.5	36	0.00432	0.05156	2.66	0.21	0.1647	0.0543	0.0435	0.69953	10
42	10.9	5.45	10	16	28	0.00182	0.00811	2.48	0.21	0.1587	0.0260	0.0485	0.69092	15
43	10.9	7	2	19.5	28.3	0.00217	0.16769	0.26	0.18	0.0092	0.0399	0.0436	0.72284	5
44	10.9	8.55	2.7	20	32	0.00163	0.16927	0.79	0.13	0.0610	0.0361	0.0211	0.73003	3
45	10.9	9	6	9	35.7	0.00183	0.03455	2.56	0.18	0.0993	0.0515	0.0207	0.70244	9
46	12	3.9	10	19.5	32	0.00290	0.13688	2.24	0.18	0.1789	0.0270	0.0359	0.69858	11
47	12	5.45	2	20	35.7	0.00392	0.27592	0.34	0.14	0.0341	0.0523	0.0265	0.71295	7

TABLE 10: Continued.

Run	Combined input parameter					New response							GRG	Rank
	I	PON	POFF	DP	SV	MRR	EWR	SR	ROC	θ	CIR	CYL		
48	**12**	**7**	**2.7**	**9**	**36**	**0.00335**	**0.06894**	**1.36**	**0.19**	**0.0014**	**0.0667**	**0.0321**	**0.75302**	**1**
49	12	8.55	6	12.5	28	0.00038	0.01559	1.91	0.20	0.0514	0.0297	0.0332	0.69403	13
50	12	9	9.3	16	28.3	0.00060	0.01717	2.70	0.17	0.1506	0.0101	0.0186	0.72975	4

TABLE 11: Candidate solution based on the nondominance rank.

S. no	Combined input parameter					New response							GRG	Rank
	I	PON	POFF	DP	SV	MRR	EWR	SR	ROC	θ	CIR	CYL		
1	12	7	2.7	9	36	0.00658	0.00058	1.36	0.19	0.0014	0.0667	0.0321	0.75302	1
2	12	7	4	12	36	0.00219	0.00058	0.77	0.15	0.1098	0.0309	0.0120	0.74252	2
3	10.9	8.55	2.7	20	32	0.00573	0.00079	0.79	0.13	0.0610	0.0361	0.0211	0.73003	3
4	12	9	9.3	16	28.3	0.00610	0.00065	2.70	0.17	0.1506	0.0101	0.0186	0.72975	4
5	10.9	7	2	19.5	28.3	0.00542	0.00010	0.26	0.18	0.0092	0.0399	0.0436	0.72284	5
6	6	6	6	18	36	0.00280	0.00073	1.51	0.15	0.5622	0.0190	0.0094	0.72120	6
7	12	5.45	2	20	35.7	0.00530	0.00059	0.34	0.14	0.0341	0.0523	0.0265	0.71295	7
8	8	8.55	2	16	36	0.00502	0.00083	1.12	0.16	0.0898	0.0646	0.0339	0.70670	8
9	10.9	9	6	9	35.7	0.00648	0.00062	2.56	0.18	0.0993	0.0515	0.0207	0.70244	9
10	10.9	3.9	9.3	12.5	36	0.00450	0.00029	2.66	0.21	0.1647	0.0543	0.0435	0.69953	10
11	12	3.9	10	19.5	32	0.00430	0.00053	2.24	0.18	0.1789	0.0270	0.0359	0.69858	11
12	4	5.45	2.7	12.5	28.3	0.00295	0.00080	0.93	0.29	0.0750	0.0858	0.1034	0.69752	12
13	**12**	**8.55**	**6**	**12.5**	**28**	**0.00652**	**0.00040**	**1.91**	**0.20**	**0.0514**	**0.0297**	**0.0332**	**0.69403**	**13**
14	5.1	5.45	6	19.5	36	0.00248	0.00085	1.78	0.19	0.2230	0.0682	0.0594	0.69307	14
15	10.9	5.45	10	16	28	0.00464	0.00073	2.48	0.21	0.1587	0.0260	0.0485	0.69092	15
16	10	7	2	18	30	0.00255	0.00123	1.15	0.12	0.0877	0.0303	0.0410	0.68945	16
17	12	6	2	20	34	0.00093	0.79000	0.05	0.06	0.0486	0.0557	0.0313	0.68706	17
18	4	8.55	9.3	19.5	35.7	0.00268	0.00116	3.12	0.16	0.3304	0.0486	0.0406	0.68421	18
19	6	5	4	16	34	0.02139	0.00065	0.87	0.38	0.0612	0.1752	0.1549	0.68172	19
20	10	8	4	20	32	0.00207	0.00073	1.17	0.18	0.0951	0.0168	0.0277	0.67799	20
21	4	6	4	14	30	0.00240	0.00032	0.71	0.24	0.0810	0.0491	0.0299	0.67612	21
22	12	5	10	18	32	0.00117	0.00060	0.93	0.21	0.0244	0.0778	0.0307	0.67015	22
23	4	8	8	18	34	0.00444	0.00111	0.56	0.18	0.0848	0.0525	0.0685	0.66312	23
24	6	9	2	14	32	0.00192	0.00069	0.92	0.16	0.0550	0.1465	0.0520	0.66300	24
25	12	8	6	14	28	0.00267	0.00040	1.42	0.24	0.2073	0.0137	0.0231	0.65933	25

Minimization:

$$\text{EWR} = -0.000535 + 0.000106\,I + 0.000065\,\text{PON} \\ - 0.000014\,\text{POFF} - 0.000007\,\text{DP} + 0.000004\,\text{SV}, \tag{18}$$

$$\text{SR} = 0.35 - 0.0242\,I + 0.0076\,\text{PON} + 0.0660\,\text{POFF} \\ + 0.0492\,\text{DP} + 0.0029\,\text{SV}, \tag{19}$$

$$\text{ROC} = 0.118 - 0.00210\,I - 0.00200\,\text{PON} + 0.00010\,\text{POFF} \\ + 0.00320\,\text{DP} + 0.00180\,\text{SV}, \tag{20}$$

$$\theta = 0.367 - 0.03776\,I + 0.0086\,\text{PON} + 0.00444\,\text{POFF} \\ + 0.00327\,\text{DP} - 0.00182\,\text{SV}, \tag{21}$$

$$\text{CIR} = -0.090 + 0.00021\,I - 0.00397\,\text{PON} + 0.00182\,\text{POFF} \\ + 0.00060\,\text{DP} + 0.00459\,\text{SV}, \tag{22}$$

$$\text{CYL} = 0.003 - 0.00411\,I + 0.00295\,\text{PON} + 0.00159\,\text{POFF} \\ - 0.00010\,\text{DP} + 0.00163\,\text{SV}. \tag{23}$$

Table 12: Learner phase–new process variables and objective values after interaction.

| S.no	New input parameter					Bounded input parameter					New response							GRG	Rank	Interaction
	I	PON	POFF	DP	SV	I	PON	POFF	DP	SV	MRR	EWR	SR	ROC	θ	CIR	CYL			
1	12	6.75	1.545	6.75	40.4	12	6.75	2	12	36	0.00350	0.13135	0.96	0.18	0.0017	0.0639	0.0300	0.60641	14	1 and 25
2	12.72	6.56	4.66	11.12	38.2	12	6.56	4.66	12	36	0.00315	0.09232	1.68	0.18	0.0573	0.0558	0.0272	0.59075	19	2 and 24
3	11.728	8.671	0.951	20.88	30.9	11.728	8.671	2	20	30.9	0.00124	0.18281	0.53	0.13	0.0270	0.0329	0.0197	0.66722	6	3 and 23
4	12	9.88	9.069	15.12	26.265	12	9	9.069	15.12	28	0.00056	0.02956	2.67	0.17	0.1384	0.0122	0.0212	0.60127	17	4 and 22
5	11.728	7.22	1.34	21.92	27.365	11.728	7.22	2	20	28	0.00169	0.18283	0.21	0.17	0.0004	0.0342	0.0375	0.62493	11	5 and 21
6	5.52	5.56	6.66	17.12	38.2	5.52	5.56	6.66	17.12	36	0.00532	0.05504	2.09	0.20	0.2189	0.0687	0.0592	0.60589	15	6 and 20
7	12.72	5.549	1.34	21.76	36.635	12.72	5.549	2	20	36.635	0.00367	0.28810	0.34	0.13	0.0263	0.0495	0.0209	0.69926	3	7 and 19
8	8.48	8.55	-0.409	14.46	36.165	8.48	8.55	2	14.46	36	0.00342	0.08616	1.19	0.17	0.0741	0.0658	0.0337	0.61784	13	8 and 18
9	10.768	9.66	7.32	4.16	36.635	10.768	9	7.32	12	36	0.00155	0.00776	2.78	0.16	0.1501	0.0420	0.0138	0.67390	5	9 and 17
10	11.008	3.218	11.709	10.08	39.3	11.008	5	10	12	36	0.00349	0.01693	3.02	0.20	0.1828	0.0481	0.0353	0.59744	18	10 and 16
11	12.132	3.559	10	21.04	34.2	12.132	5	10	20	34.2	0.00249	0.14687	2.44	0.15	0.2007	0.0245	0.0209	0.58206	22	11 and 15
12	3.868	5.45	1.611	9.42	24.065	4	5.45	2	12	28	0.00569	0.03326	0.75	0.29	0.0544	0.0887	0.1061	0.63567	9	12 and 14
13	12	8.891	7.089	14.04	23.6	12	8.891	7.089	14.04	28	0.00576	0.00186	0.96	0.18	0.0869	0.0215	0.0167	0.73367	1	13 and 1
14	4.272	5.109	6.66	22.8	36	4.272	5.109	6.66	20	36	0.00588	0.08795	1.92	0.19	0.2506	0.0696	0.0646	0.62163	12	14 and 2
15	10.9	4.768	12.409	14.24	25.8	10.9	5	10	14.24	28	0.00217	0.01250	2.53	0.23	0.1459	0.0314	0.0544	0.54670	24	15 and 3
16	9.76	6.56	-0.409	18.88	30.935	9.76	6.56	2	18.88	30.935	0.00326	0.16765	0.41	0.18	0.0363	0.0517	0.0467	0.60428	16	16 and 4
17	12.132	5.78	2	20.22	37.135	12.132	5.78	2	20	36	0.00372	0.27516	0.39	0.13	0.0362	0.0510	0.0227	0.68916	4	17 and 5
18	8.5	9.111	10.389	20.16	35.535	8.5	9.111	10	20	35.535	0.00132	0.03507	3.16	0.12	0.2866	0.0246	0.0100	0.70768	2	18 and 6
19	5.28	4.901	4.66	14.24	33.065	5.28	5	4.66	14.24	33.065	0.00577	0.02300	1.49	0.24	0.1386	0.0799	0.0802	0.64285	8	19 and 7
20	10.24	7.879	4.66	21.76	29.8	10.24	7.879	4.66	20	29.8	0.00157	0.12110	1.18	0.16	0.0966	0.0315	0.0324	0.58418	21	20 and 8
21	3.172	5.34	3.34	16.2	26.865	4	5.34	3.34	16.2	28	0.00533	0.00922	0.88	0.27	0.1080	0.0761	0.0980	0.64698	7	21 and 9
22	12.132	5.242	10.231	20.42	29.8	12.132	5.242	10	20	29.8	0.00165	0.10828	2.27	0.17	0.1740	0.0166	0.0314	0.54200	25	22 and 10
23	3.04	8.902	7.34	17.34	35.1	4	8.902	7.34	17.34	35.1	0.00345	0.03616	2.70	0.18	0.2721	0.0572	0.0464	0.58076	23	23 and 11
24	6.24	9.781	1.769	14.66	34.035	6.24	9.781	2	14.66	34.035	0.00307	0.01896	1.33	0.18	0.1024	0.0663	0.0432	0.63513	10	24 and 12
25	12	7.879	6	14.66	28	12	7.879	6	14.66	28	0.00071	0.02914	1.70	0.19	0.0596	0.0280	0.0342	0.58480	20	25 and 13
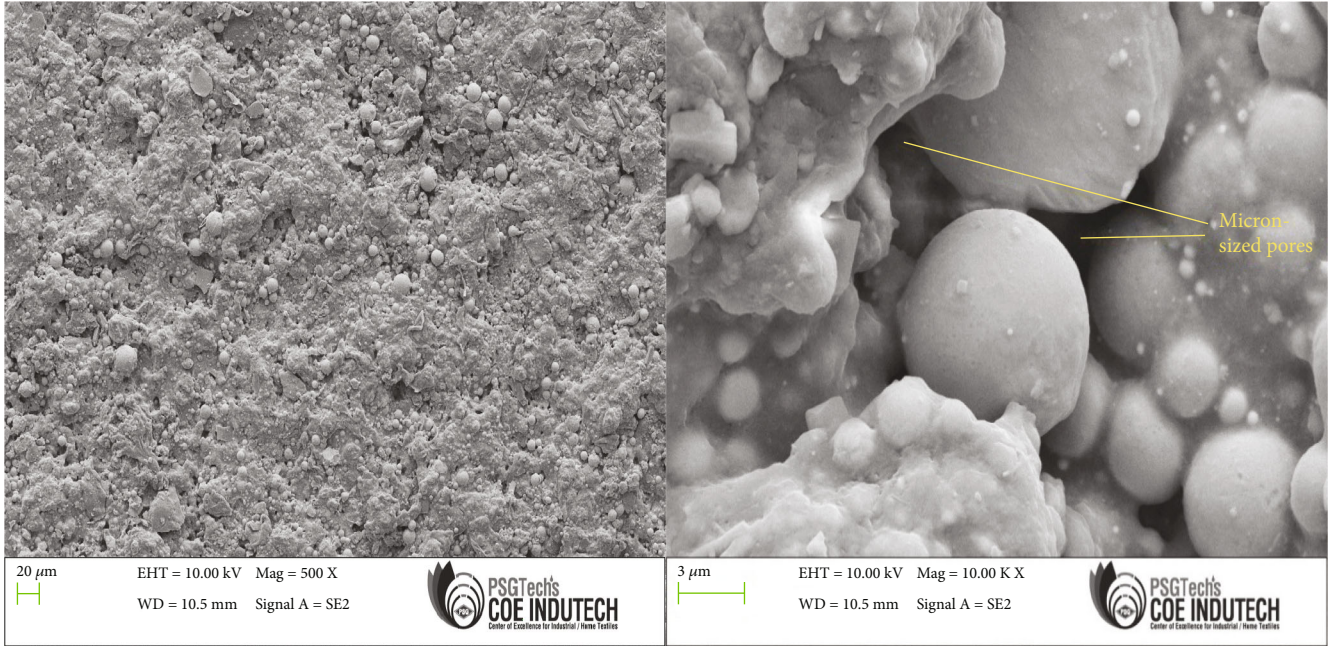
FIGURE 6: SEM micrographs of machined Si_3N_4–TiN.

TABLE 13: Comparison of various optimization techniques.

S. no	Output parameters	Taguchi	GRA	TOPSIS	TLBO
	GRG	—	0.75302	0.90578	0.73367
	Setting level	—	I: 12 amps PON: 7 μsec POFF: 4 μsec DP: 12 kg/cm^2 SV: 36 volts $(A_5B_3C_2D_1E_5)$	I: 12 amps PON: 7 μsec POFF: 4 μsec DP: 12 kg/cm^2 SV: 36 volts $(A_5B_3C_2D_1E_5)$	I: 12 amps PON: 8.89 μsec POFF: 7.09 μsec DP: 14.04 kg/cm^2 SV: 28 volts
1	MRR (g/min)	0.00440	0.00219	0.00219	0.00576
2	EWR (g/min)	0.00032	0.00058	0.00058	0.00186
3	SR (μm)	0.56	0.77	0.77	0.96
4	ROC (mm)	0.06	0.15	0.15	0.18
5	θ (deg)	0.0210	0.1098	0.1098	0.0869
6	CIR (mm)	0.0111	0.0309	0.0309	0.0215
7	CYL (mm)	0.0094	0.0120	0.0120	0.0167

Parameter bounds:

$$\text{Pulse current}: 4 \leq I \leq 12, \tag{24}$$

$$\text{Pulse-on time}: 5 \leq PON \leq 9, \tag{25}$$

$$\text{Pulse-off time}: 2 \leq POFF \leq 10, \tag{26}$$

$$\text{Dielectric pressure}: 12 \leq DP \leq 20, \tag{27}$$

$$\text{Spark gap voltage}: 28 \leq SV \leq 36. \tag{28}$$

The TLBO is carried through the accompanying advances.

Step 1. Set the population size, $N_p = 25$.

Step 2. Based on DOE, the design matrix is embraced, and the same is ranked utilizing the GRG as delineated in Table 8.

Step 3 (teacher phase). New solution is generated as delineated in Table 9.

$$X_{\text{new}} = X + r\left(X_{\text{best}} - T_f * X_{\text{mean}}\right), \tag{29}$$

where X_{new} is a recent solution, X is a current solution, r is a random value between 0 and 1, X_{best} is a teacher, T_f is a teaching entity either 1 or 2, and X_{mean} is a mean of the population.

TABLE 14: Comparison of verification test for various optimization techniques.

S.no	Output parameters		GRA	TOPSIS	TLBO
1	MRR (g/min)	Trial 1	0.00224	0.00199	0.00498
		Trial 2	0.00198	0.00221	0.00591
		Trial 3	0.00227	0.00230	0.00544
		Trial 4	0.00222	0.00204	0.00561
		Trial 5	0.00209	0.00219	0.00553
		Average	**0.00216**	**0.00215**	**0.00549**
2	EWR (g/min)	Trial 1	0.00055	0.00062	0.00092
		Trial 2	0.00061	0.00061	0.00190
		Trial 3	0.00057	0.00056	0.00181
		Trial 4	0.00061	0.00059	0.00199
		Trial 5	0.00062	0.00060	0.00177
		Average	**0.00059**	**0.00060**	**0.00168**
3	SR (μm)	Trial 1	0.77	0.79	0.82
		Trial 2	0.71	0.76	0.9
		Trial 3	0.8	0.81	0.89
		Trial 4	0.79	0.74	0.96
		Trial 5	0.75	0.78	0.95
		Average	**0.76**	**0.78**	**0.90**
4	ROC (mm)	Trial 1	0.14	0.15	0.16
		Trial 2	0.16	0.16	0.19
		Trial 3	0.17	0.16	0.14
		Trial 4	0.15	0.14	0.15
		Trial 5	0.15	0.13	0.19
		Average	**0.15**	**0.15**	**0.17**
5	θ (deg)	Trial 1	0.1089	0.1102	0.0910
		Trial 2	0.1099	0.1099	0.0891
		Trial 3	0.1101	0.1097	0.0852
		Trial 4	0.1089	0.1096	0.0888
		Trial 5	0.1095	0.1092	0.0869
		Average	**0.1095**	**0.1097**	**0.0882**
6	CIR (mm)	Trial 1	0.0308	0.0308	0.0301
		Trial 2	0.0281	0.0314	0.0210
		Trial 3	0.0313	0.0306	0.0202
		Trial 4	0.0304	0.0279	0.0289
		Trial 5	0.0335	0.0328	0.0221
		Average	**0.0308**	**0.0307**	**0.0245**
7	CYL (mm)	Trial 1	0.0121	0.0128	0.0152
		Trial 2	0.0132	0.0123	0.0159
		Trial 3	0.0129	0.0120	0.0182
		Trial 4	0.0115	0.0112	0.0181
		Trial 5	0.0122	0.0128	0.0170
		Average	**0.0124**	**0.0122**	**0.0169**

Step 4. Here, the bounded input factors are joined with the actual parameters taken from design of experiments. Table 10 delineates the combined population.

Step 5. Here, ranks 1 to 25 (50% of higher order rankings) are selected from the combined population table, and the same is optimized through the GRG. Ranks 1 to 25 acquired from the combined population are delineated in Table 11.

Step 6 (learner phase). Creation of new solution is developed by means of a partner response which is haphazardly chosen from the population is delineated in Table 12.

$$X_{\text{new}} = X + r\left(X - X_p\right), \tag{30}$$

where X_p is a partner solution.

Based on the TLBO technique, the global optimal values were identified. The optimal set of input factors are acquired from the learner phase based on the top ranking [1]. This ranking is produced after interaction between parameters as displayed in Table 12. The SEM images of the hole made using optimal machining parameters are delineated in Figure 6. From the micrograph, it is evident that the machined area of the Si_3N_4–TiN ceramic matrix composite workpiece exhibits good surface finish.

3.5. Verification Test. The GRG for different optimization methods is calculated for electrodischarge machining of Si_3N_4–TiN ceramic matrix composite workpiece. A point by point correlation is made for the GRG acquired from joint optimization techniques and is outlined in Table 13. Finally, a confirmatory experiment was done for the final TLBO optimized values, and the outcomes are great in contention. Table 14 portrays the outcomes obtained for optimal input machining factors.

4. Conclusions

The input factors influencing electrodischarge machining of adsorbed Si_3N_4–TiN workpiece using cylindrical-shaped W-Cu electrode were examined. The experimental runs for directing the experiments were arranged utilizing statistical tool by design of experiments methodology. The disparate mixture of input factors like I, PON, POFF, DP, and SV is chosen in this research. The outputs like MRR, EWR, SR, ROC, θ, CIR, and CYL are determined. Here, various optimization methodologies like Taguchi methodology, grey relational analysis, TOPSIS, and TLBO are engaged to obtain the combination of optimized factors to increase material removal rate and to decrease EWR, SR, taper angle, ROC, circularity, and cylindricity. From the experimental results and calculations, the accompanying conclusions were obtained:

(i) The outcomes determined for grey relational analysis and TOPSIS are comparative. The best output factors are obtained for I = 12 amps, PON = 7 μsec, POFF = 4 μsec, DP = 12 kg/cm^2, and SV = 36 volts ($A_5B_3C_2D_1E_5$).

(ii) The execution of GRA coupled with TLBO a global optimization technique gave the preferred outcomes over that of other methodologies. The accompanying

combination was achieved from GRA coupled with TLBO algorithm $I = 12$ amps, $PON = 8.89\,\mu sec$, $POFF = 7.09\,\mu sec$, $DP = 14.04\,kg/cm^2$, and $SV = 28$ volts.

4.1. Future Scopes of the Research

(i) This study can be further extended for nanocomposites and microstructure studies on machined surface of adsorbed Si_3N_4–TiN composites.

(ii) Other shape of electrodes like rectangle, hexagon, and octagon can be employed.

(iii) Furthermore, in the future, different electrode materials can be employed to characterize the surface integrity, fatigue performance, and dry sliding wear behaviour of adsorbed Si_3N_4–TiN. Also, different polishing methods can be imparted for better surface finish and fatigue life, higher wear resistance, and microhardness.

(iv) Optimization techniques like genetic algorithm, simulated annealing, particle swarm optimization, and ant bee colony optimization can be employed to find out significant parameters.

Nomenclature

CIR:	Circularity
CLE:	Composite laminated electrode
CYL:	Cylindricity
DOE:	Design of experiments
DP:	Dielectric pressure
EDM:	Electrical discharge machining
EWR:	Electrode wear rate/electrode erosion rate
GA:	Genetic algorithm
GRA:	Grey relational analysis
GRC:	Grey relational coefficient
GRG:	Grey relational grade
I:	Pulse current
MCDM:	Multicriteria decision-making
MRR:	Material removal rate
POFF:	Pulse-off time
PON:	Pulse-on time
PSO:	Particle swarm optimization
ROC:	Radial overcut
Si_3N_4–TiN:	Silicon nitride–titanium nitride
SI:	Similarity index
SR:	Surface roughness
SV:	Spark gap voltage
TLBO:	Teaching-learning-based optimization
TOPSIS:	Technique for order of preference by similarity to ideal solution
θ:	Taper angle.

Data Availability

The data were within this article.

Conflicts of Interest

The authors declare that they have no conflict of interest.

References

[1] V. P. Srinivasan, P. K. Palani, and S. Balamurugan, "Experimental investigation on EDM of Si_3N_4-TiN using grey relational analysis coupled with teaching-learning-based optimization algorithm," *Ceramics International*, vol. 47, no. 13, pp. 19153–19168, 2021.

[2] Z. Zhang, Y. Zhang, W. Ming, Y. Zhang, C. Cao, and G. Zhang, "A review on magnetic field assisted electrical discharge machining," *Journal of Manufacturing Processes*, vol. 64, pp. 694–722, 2021.

[3] S. Suresh Kumar, T. Varol, A. Canakci, S. Thirumalai Kumaran, and M. Uthayakumar, "A review on the performance of the materials by surface modification through EDM," *International Journal of Lightweight Materials and Manufacture*, vol. 4, no. 1, pp. 127–144, 2021.

[4] S. Dasa, U. Acharya, S. V. V. N. Siva Rao, S. Paul, and B. S. Roy, "Assessment of the surface characteristics of aerospace grade AA6092/17.5 SiCp-T6 composite processed through EDM," *CIRP Journal of Manufacturing Science and Technology*, vol. 33, pp. 123–132, 2021.

[5] S. N. Grigoriev, K. Hamdy, M. A. Volosova, A. A. Okunkov, and S. V. Fedorov, "Electrical discharge machining of oxide and nitride ceramics: a review," *Materials & Design*, vol. 209, article 109965, 2021.

[6] S. Kumar, R. Singh, T. P. Singh, and B. L. Sethi, "Surface modification by electrical discharge machining: a review," *Journal of Materials Processing Technology*, vol. 209, no. 8, pp. 3675–3687, 2009.

[7] J. T. Philip, J. Mathew, and B. Kuriachen, "Transition from EDM to PMEDM - impact of suspended particulates in the dielectric on Ti6Al4V and other distinct material surfaces: a review," *Journal of Manufacturing Processes*, vol. 64, pp. 1105–1142, 2021.

[8] K. Jiang, W. Xiaoyu, J. Lei et al., "Investigation on the geometric evolution of microstructures in EDM with a composite laminated electrode," *Journal of Cleaner Production*, vol. 298, article 126765, 2021.

[9] S. Das, S. Paul, and B. Doloi, "A gap-active electrical discharge machining (GA-EDM) to rectify the textural defects of the processed surface," *Journal of Manufacturing Processes*, vol. 64, pp. 594–605, 2021.

[10] S. Chakraborty, V. Dey, and S. K. Ghosh, "A review on the use of dielectric fluids and their effects in electrical discharge machining characteristics," *Precision Engineering*, vol. 40, pp. 1–6, 2014.

[11] B. Singaravel, K. C. Shekar, G. G. Reddy, and S. D. Prasad, "Experimental investigation of vegetable oil as dielectric fluid in Electric discharge machining of Ti-6Al-4V," *Ain Shams Engineering Journal*, vol. 11, no. 1, pp. 143–147, 2020.

[12] R. V. Rao, V. J. Savsani, and D. P. Vakharia, "Teaching-learning-based optimization: a novel method for constrained mechanical design optimization problems," *Computer-Aided Design*, vol. 43, no. 3, pp. 303–315, 2011.

[13] Y. Ma, X. Zhang, J. Song, and L. Chen, "A modified teaching-learning-based optimization algorithm for solving optimization problem," *Knowledge-Based Systems*, vol. 212, no. 5, article 106599, 2021.

[14] S. Vitayasak and P. Pongcharoen, "Performance improvement of teaching-learning-based optimisation for robust machine layout design," *Expert Systems with Applications*, vol. 98, pp. 129–152, 2018.

[15] A. Baykasoğlu, A. Hamzadayi, and S. Y. Köse, "Testing the performance of teaching-learning based optimization (TLBO) algorithm on combinatorial problems: flow shop and job shop scheduling cases," *Information Sciences*, vol. 276, pp. 204–218, 2014.

[16] A. Semnani, M. Ostadhassan, X. Yungui, M. Sharifi, and B. Liu, "Joint optimization of constrained well placement and control parameters using teaching-learning based optimization and an inter-distance algorithm," *Journal of Petroleum Science and Engineering*, vol. 203, article 108652, 2021.

[17] N. Ahmad and H. Sueyoshi, "Properties of Si_3N_4-TiN composites fabricated by spark plasma sintering by using a mixture of Si_3N_4 and Ti powders," *Ceramics International*, vol. 36, no. 2, pp. 491–496, 2010.

[18] N. Ahmad and H. Sueyoshi, "Microstructure and mechanical properties of silicon nitride-titanium nitride composites prepared by spark plasma sintering," *Materials Research Bulletin*, vol. 46, no. 3, pp. 460–463, 2011.

[19] N. Ahmad and H. Sueyoshi, "Densification and mechanical properties of electroconductive Si_3N_4–based composites prepared by spark plasma sintering," *Sains Malaysiana*, vol. 41, no. 8, pp. 1005–1009, 2012.

§SAGE
Publishing

Research Article

Synthesis and Adsorbent Performance of Modified Biochar with Ag/MgO Nanocomposites for Heat Storage Application

R. Venkatesh ⓘ,[1] **N. Karthi,**[2] **N. Kawin,**[3] **T. Prakash** ⓘ,[4] **C. Ramesh Kannan,**[5] **M. Karthigairajan,**[6] **and Ketema Bobe** ⓘ[7]

[1]*Department of Mechanical Engineering, Saveetha School of Engineering, SIMATS, Chennai, 602105 Tamil Nadu, India*
[2]*Department of Mechatronics Engineering, SNS College of Technology, Coimbatore, 641035 Tamil Nadu, India*
[3]*Department of Mechanical Engineering, Kongunadu College of Engineering and Technology, Trichy, 621215 Tamil Nadu, India*
[4]*Department of Mechanical Engineering, SNS College of Technology, Coimbatore, 641035 Tamil Nadu, India*
[5]*Department of Mechanical Engineering, Dr. Navalar Nedunchezhiyan College of Engineering, Tholudur, 606303, Tamil Nadu, India*
[6]*Department of Mechanical Engineering, Gojan School of Business and Technology, Chennai, 600052 Tamil Nadu, India*
[7]*Department of Mechanical Engineering, Ambo University, Ambo, Ethiopia*

Correspondence should be addressed to Ketema Bobe; ketema.bobe@ambou.edu.et

Heat storage is a major problem in the world. Many research is going on the heat storage application. This research investigates the novel Ag/MgO/biochar nanocomposites for heat storage. Ag/MgO/biochar nanocomposites were fabricated using solvent-free ball milling techniques. According to several analytical measurements, the Ag/MgO nanoparticles in biochar are uniformly dispersed across the carbon interface. This type of adsorbent material has been characterized by different techniques such as X-ray diffraction pattern analysis (XRD), FTIR analysis, scanning electron microscope (SEM), and transmission electron microscope (TEM) as all indicate the surface morphology and successful ball milling synthesis of Ag/MgO nanocomposites. The UV visible spectroscopy wavelength range of AgNPs and MgONPs is 330 nm and 470 nm, respectively. FTIR analysis revealed that different functional groups of modified biochar nanocomposites such as O-H group are 3728 cm^{-1} and for C-H bond is 932 cm^{-1}, C-O group is 1420 cm^{-1}, and C=O is 1785 cm^{-1}, respectively. Adsorption tests showed that 1.0 gL^{-1} dosage with 60% phosphate removal, an ion, and 0.2 gL^{-1} of dosages that had 85% methylene blue decomposition, a charged synthetic dye, were the lowest absorption levels. This research suggests that ball milling offers the advantages of stabilization and chemical adaptability for customized remediation of different atmospheric contaminants. Ball milling is a facile and feasible process to fabricate carbon-metal-oxide nanomaterials.

1. Introduction

Due to its low cost, high efficiency, and ease of implementation, the adsorption technique is one of the most effective techniques for removing organic dyes from water [1]. Recent research has extensively investigated the effects of adsorption and photocatalytic techniques on metal oxide/biochar nanocomposites [2]. Water pollution is one of the main causes of eutrophication, environmental threats, human welfare, and animal planet. Wastewater reclamation is required for various applications as a financially sustainable and effective technologies for removing unwanted contaminants. In terms of wastewater generation, this strategy is a better option in light of the emergence of renewable techniques [3, 4]. This approach has gained importance among most of the country's population due to the groundwater issues crisis due to fluctuating precipitation and uneven access to many freshwater resources, particularly for farming. Adsorption process, catalysis, improved oxidative degradation, electrochemical analysis, and microbial degradation are among a few of the remediation techniques invented to reduce the hazards brought on by natural dyes.

Depending on the pH value, phosphorus in different forms of the critical nutrients PO43-, H2PO4-, and HPO42 enhances aquatic plants growth [5–7]. In general, biochar (BC) has low adsorption capacity due to restricted adsorption location, low area of surface impact, and negatively discharged surface on phosphorus [8, 9]. Solid BC is produced by biomass using the pyrolysis method under low oxygen (no oxygen) environmental conditions at high temperatures. To develop the adsorption, modification of BC with various MO, such as La2O3, CaO, and MgO, is of great importance. Biochar surface modification is performed by impregnation fabrication techniques, which have high adsorption capacity and high phosphorus removal from various water resources. For biomedical applications, excellent features such as ease of fabrication, recyclability, and surface functionalization have allowed biochar to be used in various industries. Several studies have revealed that MgO exhibits effective adsorption measurements for decreasing PO_4^{3-} from water. The maximum absorption coefficient was obtained at $121.25 \, mgg^{-1}$ for MgO modified biochar using the impregnation technique investigated by Li et al. [7, 8]. Rather than standard impregnation, the emerging ball milling approach is a solvent-free modification technique that requires adding oxides to the modified biochar surface [10, 11].

The synthesis of nanocomposites through ball milling approaches is the most widely recognized technique that improves the physical and chemical properties of metal oxide with biochar nanocomposites [12, 13]. The physical properties of the nanomaterials can be enhanced by ball milling the composites into nanoparticles, which will improve the overall ability to adsorption capability [13, 14]. The modified biochar composites (CuO, MgO, and Fe_3O_4) with different metal oxides were fabricated through ball milling for disposal of methylene blue from the water content [15]. According to the observations of those investigations, ball milling provides a large surface area and chemical bonding of the biochar [16, 17], which allows the nanocomposite produced from biochar-containing metal oxides to have better removal efficiency than pure biochar.

For the first time, Persicaria salicifolia biomass was investigated to support less harmful chemical compounds as natural and eco-friendly chemicals for phytofabrication of zinc oxide-silver sponsored activated carbon nanocomposite (Ag/ZnO@BC). About 20 nm in diameter and spread evenly on the surface of the biochar substrate, MgO nanoparticles were used in the nanocomposite to create nanoscaled geometries and microporous structures, according to the physicochemical parameters of the prepared nanostructured materials. MgO/biochar nanomaterials were prepared using a simple ball milling technique to provide dual adsorption. At moderate adsorbent concentrations of $1.0 \, gL^{-1}$ and $0.2 \, gL^{-1}$, adsorption tests showed 62.9% removal of phosphorus, 87.5% removal of methylene blue, and charged molecular dye. Desorption capacity of this novel nanocomposite as photocatalysts in various systems revealed its strong photodegradation efficiency, which reached 70.3% under optimal process parameters: 50 ppm of TC, pH 6, 0.01 g of Ag/ZnO@BC, 25°C temperature, and 100 mM H_2O_2 relative to parameters.

The synthesis of MgO nanoparticles with Ag is the preparation of modified biochar materials through solvent-free ball milling techniques, which is the main innovation of this investigation. In this study, inspired by the research above, modified Ag/MgO/biochar nanocomposites were fabricated by ball milling process followed by ball milling techniques and phosphorus elimination from pollutant water. Subsequently, the experimental study aimed to investigate (i) the properties of modified Ag/MgO/biochar nanocomposites, (ii) effect of AgNPs and MgONPs on Escherichia coli pneumonia, including S. aureus and E. coli species of antibacterial activity, (iii) scanning electron microscope (SEM) and transmission electron microscope (TEM) studies reveal the surface morphological changes on biochar nanocomposites, and (iv) adsorption performance of removal of methylene blue (MB) and phosphates by using Ag/MgO/biochar nanocomposites.

2. Materials and Methods

2.1. Materials. Silver nitrate ($AgNO_3$) -99.9% and magnesium chloride hexahydrate ($MgCl_2.6H_2O$) synthesized the Ag/MgO biochar nanocomposites.

2.2. Synthesis of Biochar Ag/MgO Biochar. 5 g of rice straw powder was mixed with 0.175 g of magnesium chloride hexahydrate ($MgCl_2.6H_2O$) and 0.08 g of $Ag.NO_3$ for Mg : Ag weight ratio is 1 : 1 and 3 : 1 wt% ratio for Ag : BC and Mg : BC, respectively. This solution was then mixed with 100 mL of deionized water, and the samples were diluted for approximately 30 minutes, stirred for an additional 30 minutes, and heated to 70°C. The mixture was further dried completely at 60°C. Dry rice straw powder was oxidized in an electric furnace at 600°C for three hours to convert MgO and Ag ions into MgONPs and AgNPs. This produced the biochar element, which was used to create unique biocomposites (Ag/MgO@BC), which were finally obtained. Figure 1 shows the detailed flow chart for synthesising modified biochar nanocomposites.

2.3. Characterization of Modified Ag/MgO Biochar. The photosynthesis of Ag/MgO with biochar absorption quantitative measurement was confirmed by UV-visible spectroscopy (IG-28 ms). The wavelength range for UV analysis is 665 nm was followed. Furthermore, the elemental compositions of modified biochar surfaces were analyzed by energy-dispersive spectroscopy (EDS). These XRD patterns reveal the crystalline structure of nanocomposites under Cu kα radiation ($\lambda = 0.154 \, nm$), which functioned at 40 kV to 40 mA. SEM and TEM performed at 5.0 kV and 80 kV were used to study the surface morphology, chemical compositions, and elemental analysis of the proposed biochar samples. FT-IR measurements were obtained using TENSOR-5, Bruker FTIR spectroscopy in the spectrum range of 4000-400 cm^{-1}. TGA experiment was completed with the help of Pyris-1, Diamond TG/DTA PerkinElmer analyzer. Zeta PALS, Brookhaven, was used to measure the zeta potentials of the prepared materials to evaluate their surface properties and sustainability.

FIGURE 1: Fabrication of Ag/MgO/biochar nanocomposites.

2.4. *Heat Storage Adsorption Mechanism.* Dissolving K_2HPO_4 (potassium phosphate) and $NaNo_3$ (sodium nitrate) in 100 ml distilled water to prepare the nitrate and phosphate solutions, respectively. Also, the adsorption of phosphate to nanomaterials was evaluated by measuring the phosphorus concentration of 50 mg of each sample in 20 mg L-1 solution (B). The feedstock 1800 ml/L P and 40 mg/LN was prepared for the adsorption experiment and carried out at room temperature (220 C) using 65 mL digestion vessels. During the filtration process, excitation-correlated ionized atomic emission spectroscopy was used to determine P levels. The solutions were finally passed through 0.25 μm nylon membrane, and the MB dosage of the filtrates was determined using UV–visible spectroscopy with a frequency range of 700 nm. Also, MB and P were used as treatments for adsorption experiments, which were carried out in similar conditions. Summary statistics from each experiment were presented after repeated runs. New tests were performed each time there was a measurement variation of 5%.

3. Results and Discussion

3.1. *UV Visible Spectroscopy.* The surface plasmonic resonance (SPR) of Ag/MgO/biochar excited by a light source at specific wavelengths was recorded using wavelength-distinct UV-visible spectroscopy as shown in Figures 2(a) and 2(b). SPR peak intensities determine morphological changes through the shape and size of nanoparticles. The SPR spectra reveal that no band is identified in the modified biochar. The UV visible range of AgNPs and MgONPs is 330 nm and 470 nm, respectively, representing the surface decrease of silver ions and magnesium oxide in BC and the formation of biochar nanocomposites. The measured AgNPs SPR band was consistent with a previous study aimed at developing silver nanoparticle-based nanocomposites [18]. In addition, as can be seen in Figure 2(c), the energy band gap energy (Eg) of Ag/MgO with BC was determined using the Tauc plot and 3.4 eV-3.12 eV. According to Saedi et al., the energy band gap became very narrow due to the addition of MgO and Ag nanoparticles in the nanostructure [19]. Due to the synthesis of Ag-C compounds, the precipitation of

MgONPs and AgNPs on the biochar surface narrows the frequency wavelength energy band gap of specific BC. It accelerates the development of stable energy levels in Ag/MgO/BC, as a result of the interface of AgNPs through the carbon in the biochar [20].

3.2. *FT-IR Analysis.* The functional group found by the oxidation and normalisation of photocatalyzed nanoparticles is revealed by FTIR analysis. From the analysis, three kinds of functional group were observed in modified biochar such as O-H group is 3728 cm-1, the C-O bond is 932 cm-1, the C-O group is 1420 cm^{-1}, and C=O is 1785 cm^{-1}, respectively. Zheng et al. [21] have achieved that the biochar produced spectra comparable to Ag/MgO biochar and demonstrated that adding MgO nanoparticles to the composites did not affect the functional groups of the biochar. These patterns, which also appeared in the Ag/biochar and MgO/biochar spectra with various strengths, decreased both AgNPs and MgONPs on the biochar surface. Additionally, a novel MgO maximum intensity was detected in the MgO/biochar composite at 632 cm^{-1}, demonstrating the production of MgO nanoparticles [22]. Due to the interfacial bonding between Ag, MgO, and biochar, as shown in Figure 3, these all-organic molecules occurred in Ag/MgO@BC spectra, although with varying intensities. The result concluded that preparation of biochar with rice straw is entirely accountable for the AgNPs and MgONPs of reduction and stabilization on the surface of the modified biochar. The results clearly show the formation of Ag/MgO/biochar nanocomposites.

3.3. *Zeta Potential.* Zeta potential analysis is an important technique for analysing the surface morphological changes and stability of aqueous materials [21]. Charging variation on material surfaces can be affected by energy measurements. Often in micromolar strength, depending on the scale used for analysis, it is a very precise method for studying nanomaterials. It was observed from the Z potential results that the pure biochar nanocomposites had the highest concentration of bioactive ingredients at 28.4 mV, which is shown in Figure 4. After adding Ag/MgO to form the modified biochar composites, the zeta potential value changed to 29.2 mV, demonstrating that the MgO and Ag

Biochar

(a)

MgO
330 nm

Ag
470 nm

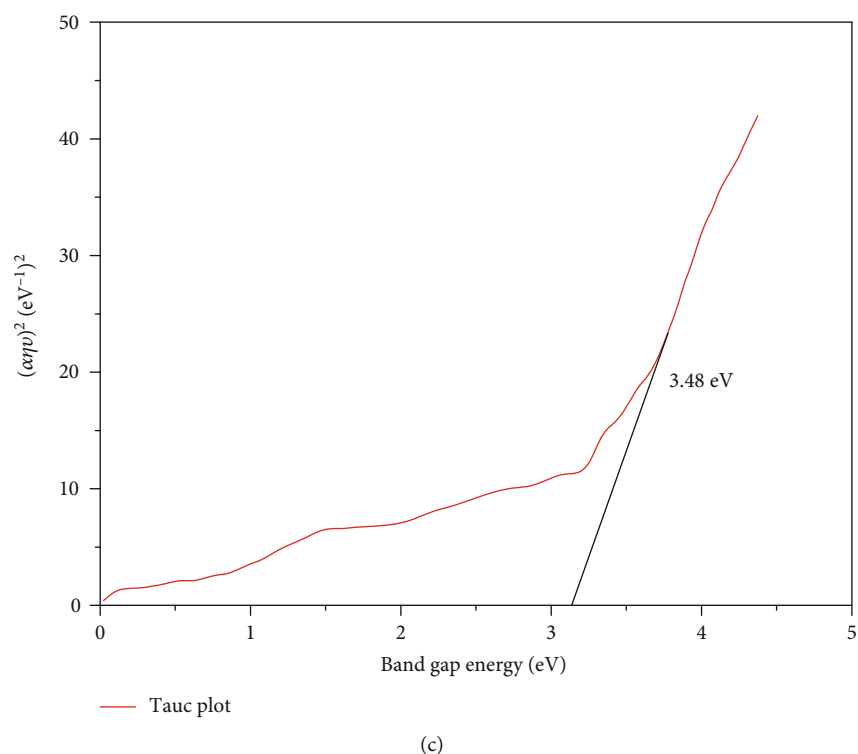Ag/MgO/Biochar

(b)

Figure 2: Continued.

(c)
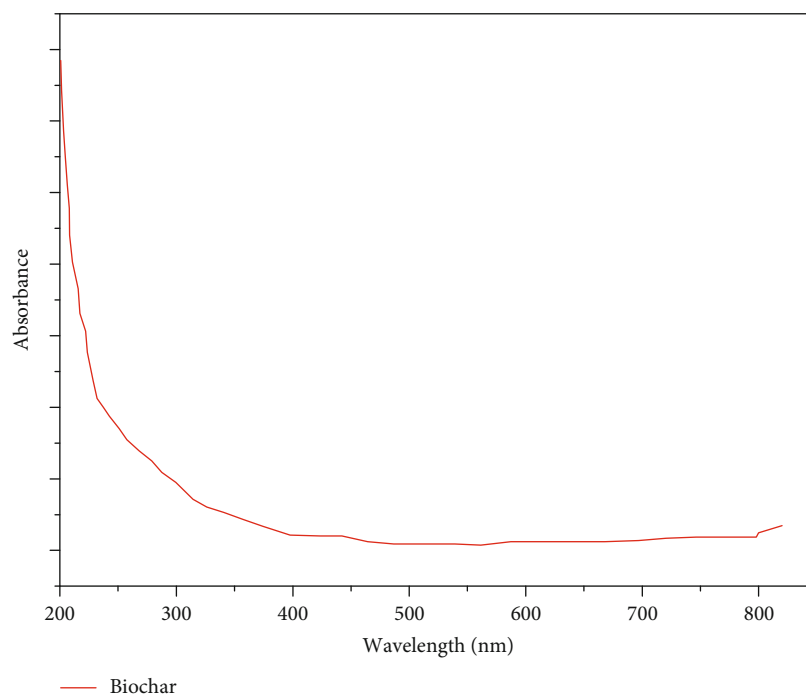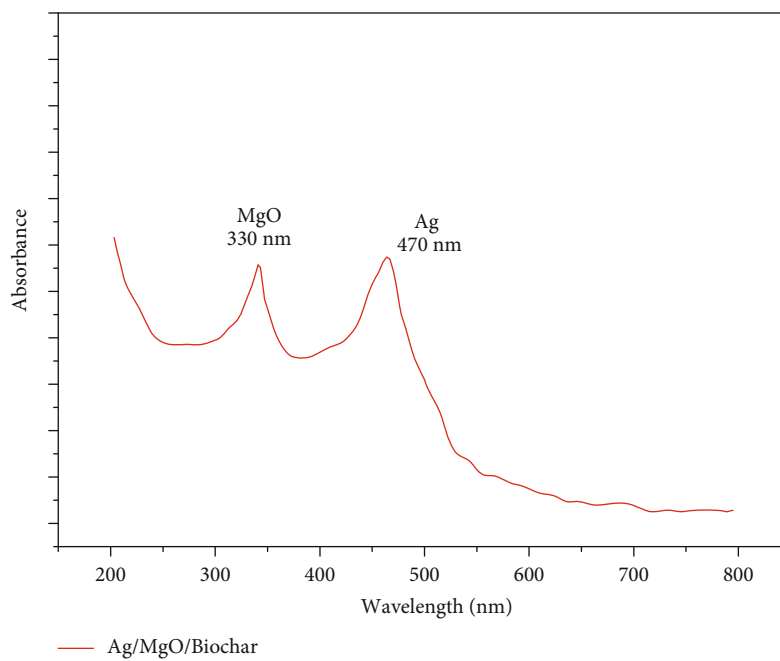
FIGURE 2: FTIR spectroscopy. (a) Biochar. (b) Ag/MgO/biochar. (c) Tauc Ag/MgO/biochar.
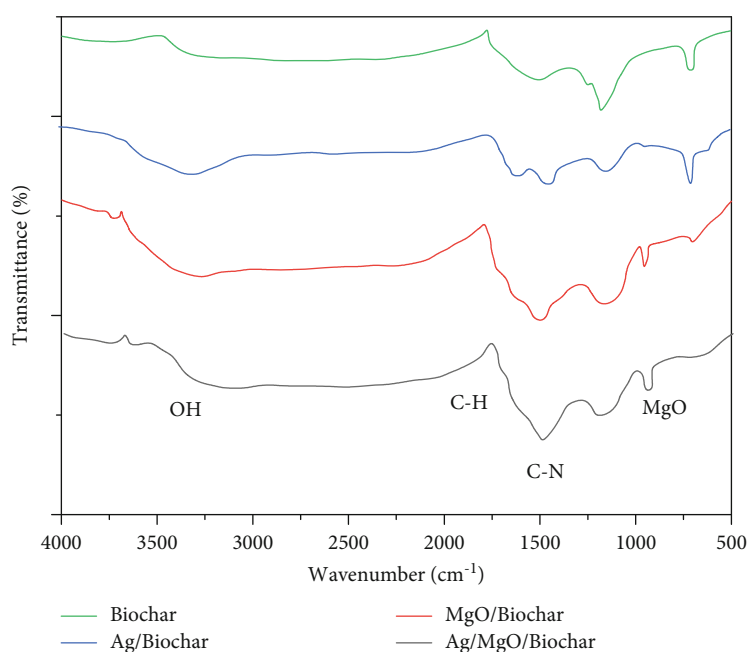

FIGURE 3: FTIR spectra.

nanoparticles on the biochar surface were activated successfully. The observed negative electrostatic potential can infer the stability of Ag/MgO@BC due to repulsive interactions between weakly charged ions [23].

3.4. SEM. The elemental presence of carbon especially develops with higher reaction temperature. EDX spectrum

determined the different chemical constituents presented in biochar and their modified biochar nanocomposites. As shown in Figure 5, the EDX spectrum of pure biochar consists of elements C and O, which are anticipated the main components for typical biochar materials. Various elements considered major constituents of nanocomposites were also found in varying amounts, including C, Mg, Si, O, N, and
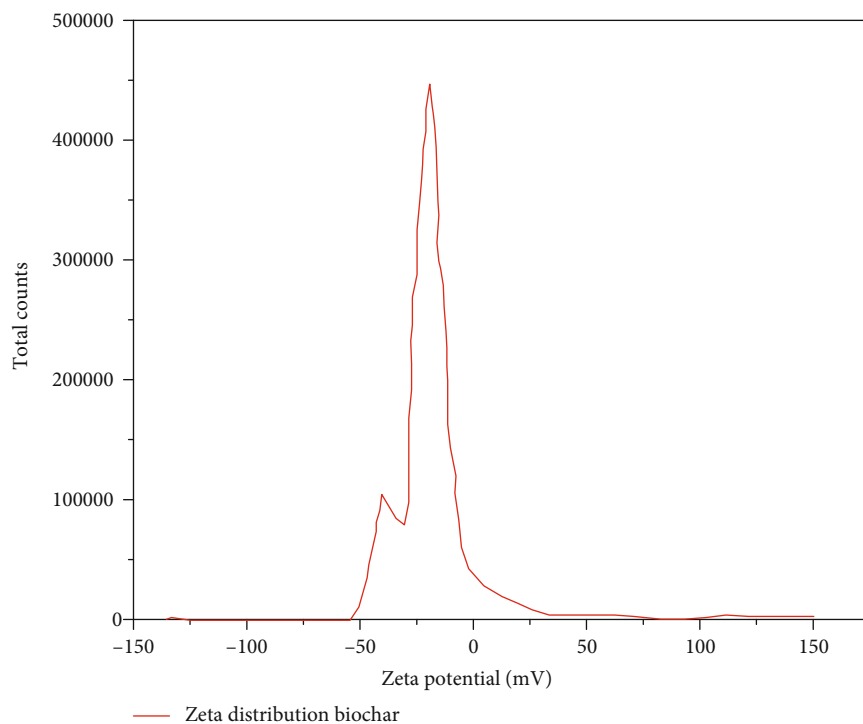
(a)
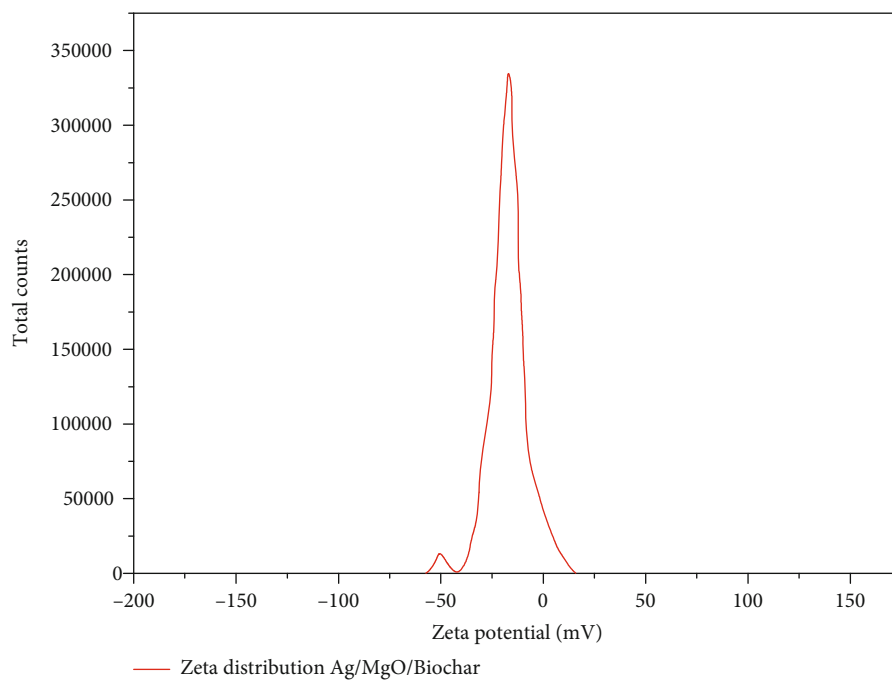
(b)

FIGURE 4: Zeta potential. (a) Biochar. (b) Ag/MgO/biochar.

k. Figures 5(a) and 5(b) show the EDS spectrum of all chemical elements available in Ag/MgO@BC nanocomposites [24]. Additionally, Mg-characteristic signals were observed in the same curve at energies of 0.9, 8.65, and 9.6 keV. These characteristics were determined according to Shaban et al. demonstrating the production of Ag/ MgO@BC. Figure 5(b) shows the surface chemical composition of this biochar, which is 60.52% C, 2.15% Mg, 16.24.8% O, Ag 2.52%, and a small quantity of Si (0.7%). The lowest Ag % was 2.41%, and the essential MgO was 1.37%, corresponding to the proportion of magnesium oxide and silver ions (2%) according to EDX analysis of
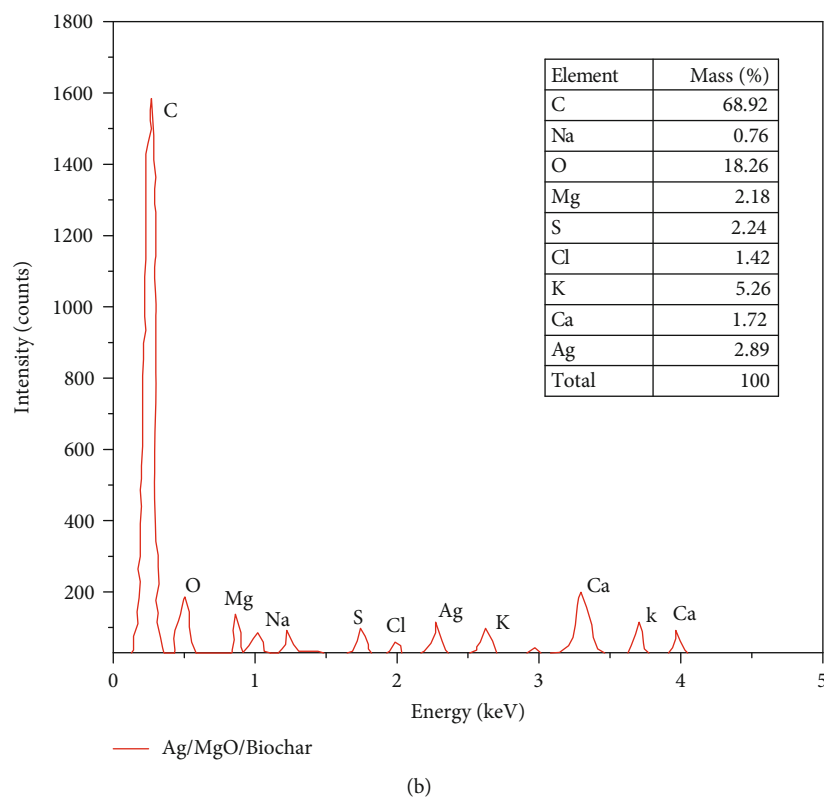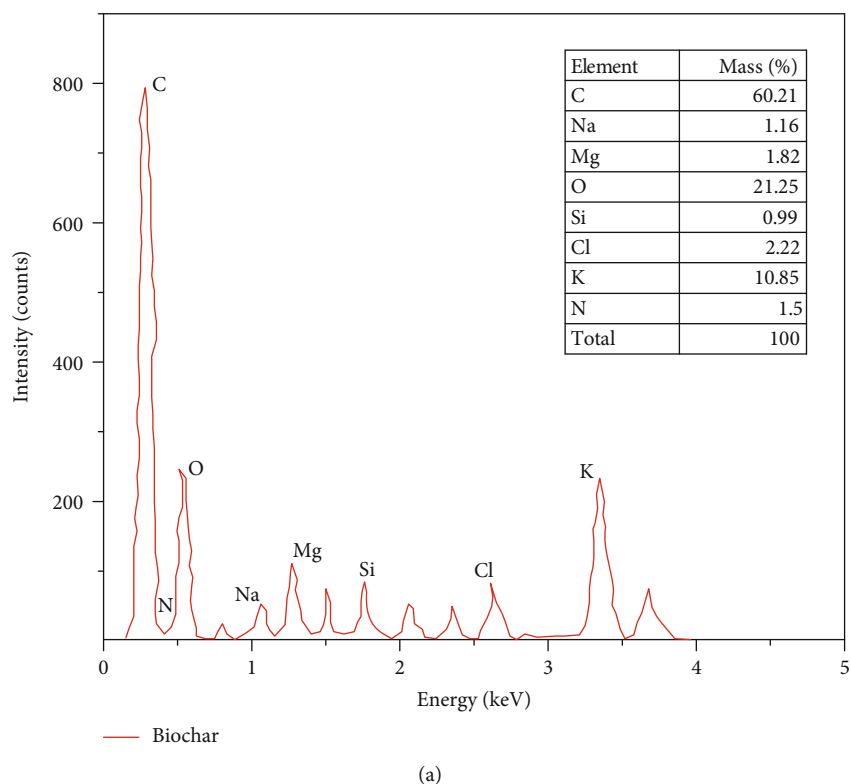
Element	Mass (%)
C	60.21
Na	1.16
Mg	1.82
O	21.25
Si	0.99
Cl	2.22
K	10.85
N	1.5
Total	100

(a)

Element	Mass (%)
C	68.92
Na	0.76
O	18.26
Mg	2.18
S	2.24
Cl	1.42
K	5.26
Ca	1.72
Ag	2.89
Total	100

(b)

FIGURE 5: EDS spectrum of (a) biochar and (b) Ag/Mg/biochar.

the Ag/MgO @BCs surface. Biochar was initially applied to the surface to demonstrate the superior performance of rice straw extract in reducing zinc and silver ions.

The morphological changes and chemical % of elements of pure biochar and their Ag/MgO/biochar nanocomposites were characterized by using scanning electron microscope

(a)

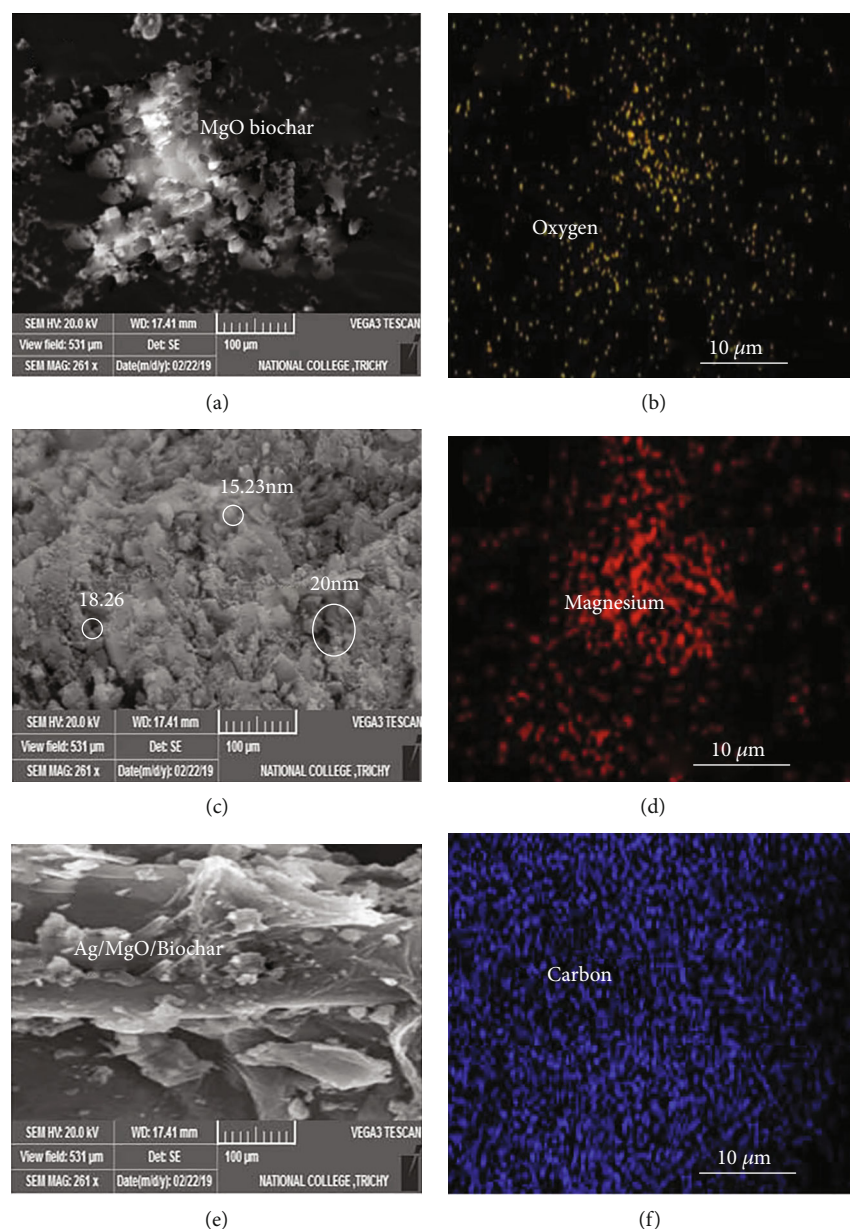

(b)

(c)

(d)

(e)

(f)

FIGURE 6: (a) MgO biochar. (b) Oxygen. (c) Ag/MgO/biochar. (d) Magnesium. (e) Ag/MgO/biochar. (f) Carbon.

(SEM) and energy dispersive spectrum (EDS), respectively. SEM is only useful for gathering information about surface morphology, but when combined with EDX, can be utilized to identify and quantify adherent nanoparticles. Figure 6(a) shows the MgO biochar elements in SEM. In this SEM, results revealed a pore structure during the thermal transesterification reaction, as porosity is widely believed to be caused by the emission of fine organic matter such as H_2O, CO_2, CH_4, and CO. This analysis also reveals the effect of AgNPs and MgONPs on biochar surface, porosity, size, and shape of the nanoparticles seen in Figure 6(b). The broad concentration of white nanoparticles on Ag/MgO@BC shown in Figures 6(c) and 6(d), which are not truly missing in biochar, suggests that MgONPs and AgNPs on the biochar surface were successfully ball milled (Figure 6(a)). Presence

of Ag/MgO/biochar and carbon elements has been showed in Figures 6(e) and 6(f).

3.5. TEM Analysis. In this investigation, the size and morphology of photosynthesized AgNPs and MgONPs on activated carbon surfaces were examined using TEM analysis, frequently used to detect structural changes in prepared biochar nanoparticles. Figure 7(a) shows the TEM image of AgNPs and MgONPs on the biochar surface. TEM analysis clearly shows that the spherical shape of AgNPs and MgONPs was obtained up to 25 nm by using higher scales. The particle size obtained from TEM analysis agreed with SEM measurement, confirming effective ball milling synthesis techniques and determining the potential capability of different applications due to nanoparticle
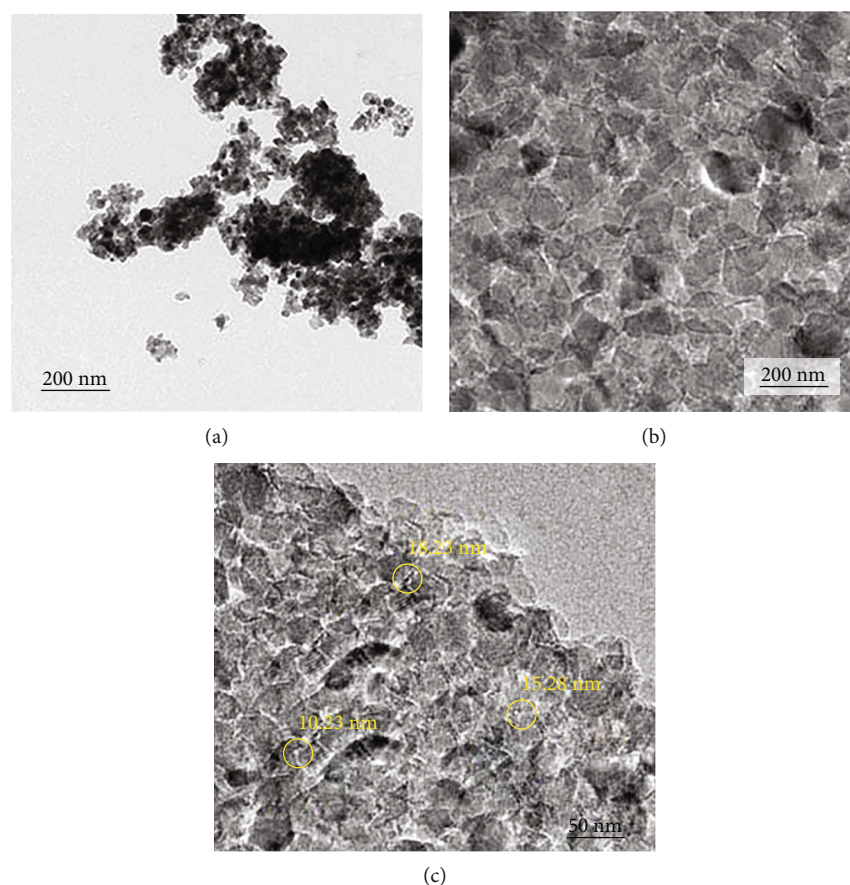
(a)

(b)

(c)

FIGURE 7: TEM images of Ag/MgO/biochar composites. (a) 200 nm. (b) MgONPs. (c) 100 nm modified biochar.

formation (Figure 7(b)). Figure 7(c) shows that the structure of MgO nanoparticles consists of nanostructures with random shapes and sizes of approximately 30 nm. Consistent with the results of Zheng et al. [21], they noted similar structures for Ag-composites with sizes ranging from 10 to 40 nm.

3.6. Thermal Gravity Analysis (TGA). Figure 8 shows pure biochar's thermal gravity analysis (TGA) and their reinforcement Ag/MgO/biochar nanocomposites. It exhibited a first continuous phase with a 10% weight loss up to 170°C, but the BC-prepared specimens showed an 8% weight loss, which could be attributed to moisture loss. Therefore, the temperature for biochar and Ag/MgO/biochar nanocomposites is 280°C and 352°, respectively. Significant weight loss between 320 and 460°C for Ag/MgO@BC sample and 330 and 450°C for BC nanocomposites can be attributed to the decomposition of major chemical elements. In conclusion, both samples experienced moderate weight loss up to 600°C, which may be due to the degrading lattice structure, although pure biochar weight loss was significant. However, Ag/MgO/BC experienced less overall weight loss than biochar, which may be attributed to the MgO NPs and AgNPs to withstand thermal degradation.

3.7. XRD Analysis. Figure 9 shows the XRD diffraction pattern of peak components of biochar and their nanocompos-ites. The XRD spectrum of silver nanoparticles shows the different peak intensities at 35^0, 42.65^0, 52.86^0, and 66.28^0 that are referenced from (111), (200), (220), and (311) planes subjected to face centred cubic (FCC) good agreed with the JCPDS file number 04-0783. The XRD diffraction patterns of Ag/MgO/biochar 32^0, 38.42^0, 45.32^0, and 52.18^0 have many characteristic patterns attributable to the (111), (200), (220), (311), and (222) plane crystalline structure that is identical to the peak of pure magnesium oxide nanoparti-cles according to JCPDS no. 87-0653. In addition, the (111) orientation is related to the formation orientation for ball-milled AgNPs at the interface of Ag/MgO/BC composites, in agreement with several other experimental works. The average crystalline size of nanoparticles was calculated by using the Debye Scherrer equation. The research showed that the MgO size of nanoparticles was reduced from 70 nm to 17 nm by ball milling with biochar. The MgO crystal structure produced from this investigation is comparable to the MgO improved biochar produced using the pyrolysis process. However, the results show that all AgNPs and MgONPs were successfully synthesized by ball milling on the biochar surface, yielding Ag/Mg/BC composites.

3.8. Antibacterial Activity. Bacteria Gram-positive and Gram-negative strain suppression abilities of Ag and MgO nanoparticles have been used in a spectrum of pharmacolog-ical activities. The antimicrobial potential of implanted
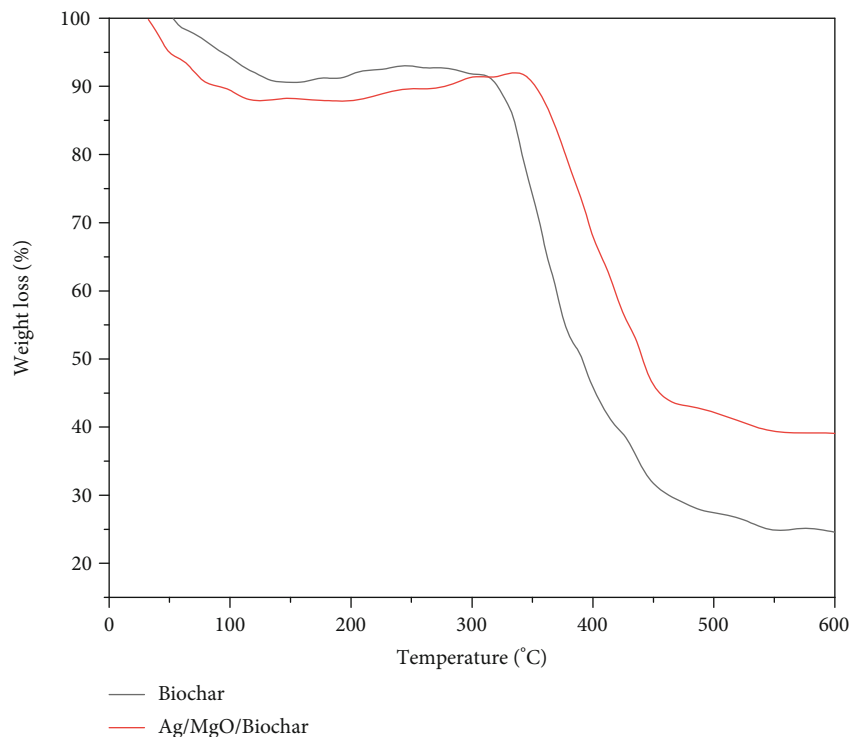
FIGURE 8: Thermal gravity analysis (TGA) of biochar and Ag/MgO/biochar nanocomposites.
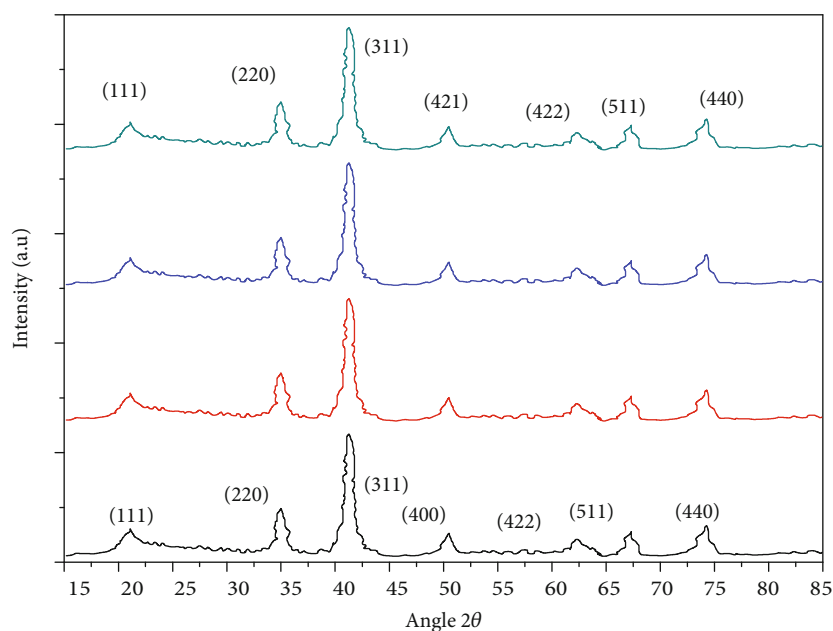

FIGURE 9: XRD diffraction pattern.

nanotechnology is thought to work in 2 phases: first, they inactivate thiol compounds in enzymes, and then, attach to the microbial chromosome, shorten it, and prevent DNA replication causing death [25]. The antibacterial activity of Ag/MgO@BC prepared nanocomposites throughout this research was then evaluated against a variety of Gram-positive and Gram-negative bacteria [26], including Escherichia coli pneumonia including S. aureus and E. coli species as shown in Figure 10. Research revealed that Ag/MgO@BC was a good antimicrobial treatment against pneumonia as it inhibited its growth at a large scale ($1x10^8$ CFU/mL) compared to other incorporated AgNPs and MgO/biochar nanocomposites. Figure 11 shows the zone of inhibition for both S. aureus and E. coli species of Ag/MgO@BC nanocomposites.
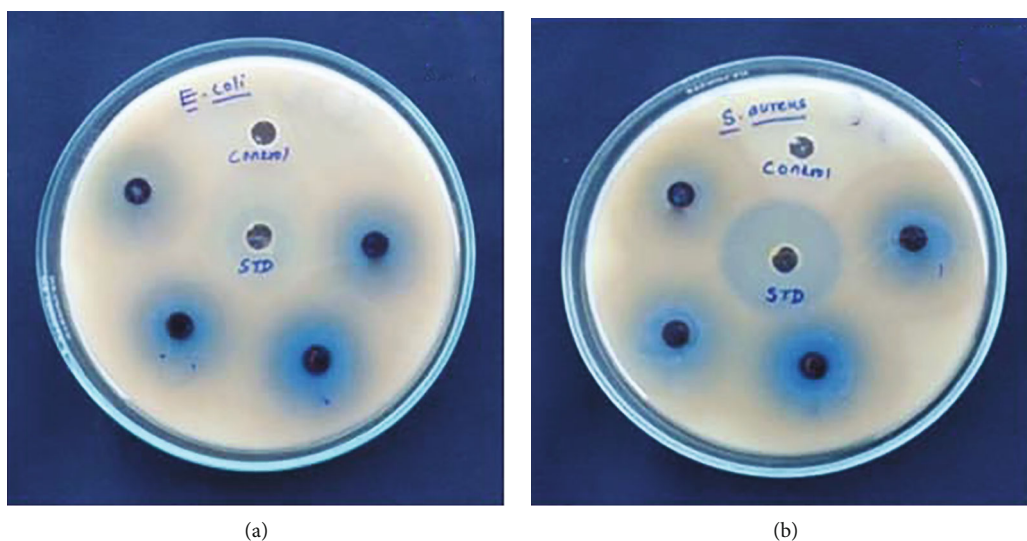
(a) (b)

FIGURE 10: Antibacterial activity Gram-positive and Gram-negative.
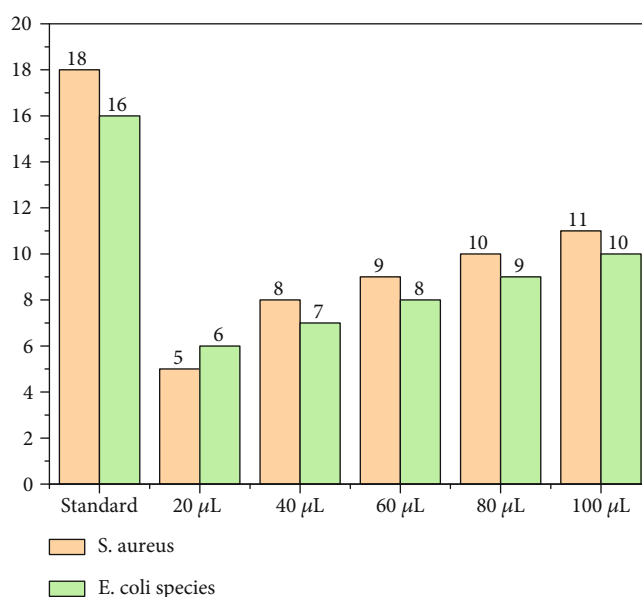

FIGURE 11: Zone of inhibition in mm antibacterial activity for Ag/MgO/biochar.

3.9. Adsorption Performance of Ag/MgO/Biochar Nanocomposites.

Figures 12 and 13 show the adsorption performance of Ag/MgO/biochar nanocomposites. As small amounts of Mg/biochar were released from themselves, the aged biochar had limited MB and negative P adsorption. The P adsorption performance of Ag/MgO/Biochar was not affected by the ball-milling process, but the adsorption of MB was improved almost 8.4 times, which may be a result of higher surface area and pore size. The resulting Ag/MgO/biochar nanomaterials showed significantly enhanced adsorption of both P and MB. Strong Mg-P and Ag-P interfacial bonding and strong interaction between anionic P and electrically charged biochar surface during experimental parameters are responsible for enhanced P adsorption efficiency. The absorp-

tion properties of P removal have increased due to adding MgO to biochar composites. According to experimental results, Ag/MgO/biochar nanocomposites had charged positively membrane characteristics that aided in magnetic attractions and interfacial deposition of P ion species, which facilitated adsorption [27]. The MgO/biochar nanomaterials had MB absorption of 61.5 and 108.8% greater than pure biochar adsorption. The enhanced base neutralization ability of the biochar matrix [26], which is beneficial for removing ionic MB and attractive electrostatic stress at elevated pH levels, can be considered from the perspective of enhanced MB adsorption with Ag/MgO addition [25]. In the MgO/biochar nanocomposites specimens, MB sorption was initially enhanced and then diminished with MgO and concluded that there
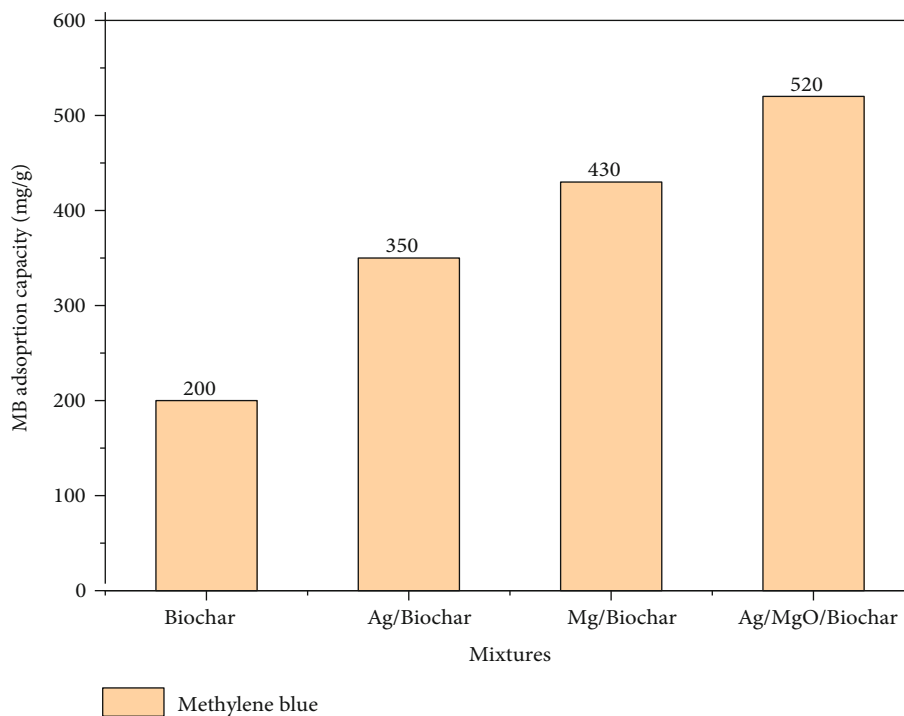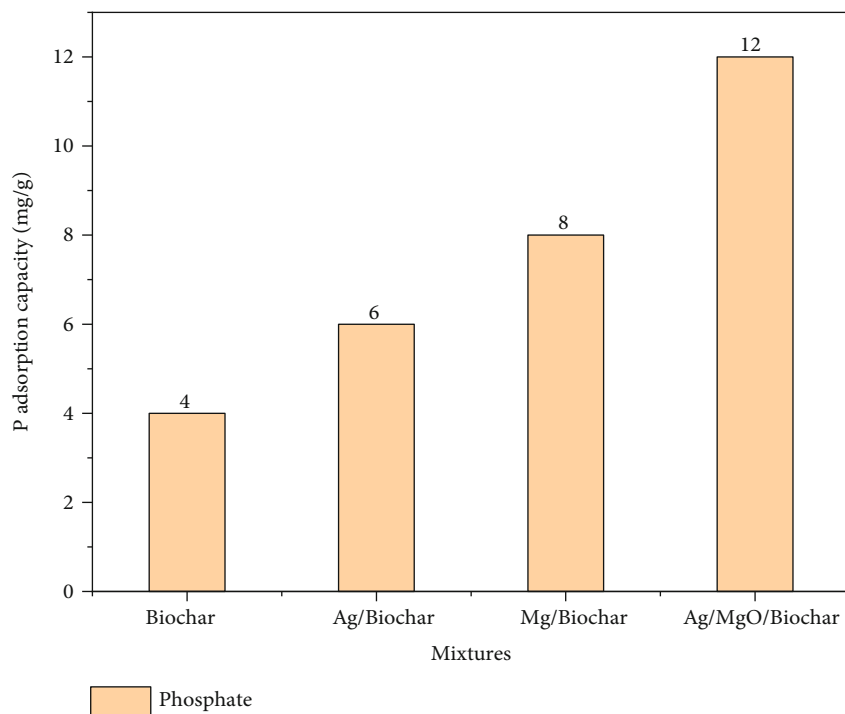
FIGURE 12: Removal of methylene blue.

FIGURE 13: Removal of phosphate.

may be a perfect balance among MgO and biochar for removing contaminants [28]. Ag/MgO/biochar at 1 : 1 ratio of composites had the best P removal effectiveness in this work, combined with acceptable large efficiency for MB sorption [29].

3.10. Future Scope and Recommendations. Using biochar to remove contaminants from water is gaining significant popularity as an affordable alternative to expensive activated carbon [30]. Future research is needed to develop modified biochar to improve biochar quality, and its

performance varies depending on feedstock type and pyrolysis conditions [31]. It might be possible to modify biochar's characteristics to remove particular impurities to make it more efficient. Biochar has also been thoroughly explored as a cost-effective adsorbent for removing biological and metal pollutants from aqueous and gaseous atmospheric pollutants in environmental protection [32]. Although fresh biochar has a small adsorption capacity, different feed types and process conditions affect its physical and chemical properties (active adsorption sites, size distribution, and charge density) [33]. Consequently, it is necessary to develop techniques designed to regulate the concentration of biochar detection to improve its binding capacity to a range of environmental pollutants.

4. Conclusion

Synthesis of Ag/MgO@BC composites using rice straw biomass has been established for the first time in the present work using a scalable, cost-effective ball-milling method. This research demonstrates that the ball milling technique is a viable way to produce nanocomposite of metal oxides and biochar for wastewater treatment. The MgO was added into the biochar and uniformly dispersed, which improved the ability of the nanocomposites to bind MB and provide them with photocatalytic properties. According to experimental results, the ball-milling process provides more adaptability with efficiency on modified absorptions as well as structural modification achieved by synthesis techniques that strategically remove all biological and elemental contaminates. MB and PO_4^{3-} were successfully and synergistically removed from aqueous systems using Ag-added MgO-biochar nanocomposites.

FTIR analysis results found that MgO/biochar mixture also shows a unique MgO maximum intensity at $632\,cm^{-1}$, proving the synthesis of MgO nanoparticles. According to JCPDS no. 87-0653, the XRD diffraction patterns of Ag/MgO/Biochar 32^0, 38.42^0, 45.32^0, and 52.18^0 have numerous distinctive patterns that can be attributed to the crystal lattice of the (111), (200), (220), (311), and (222) planes, which is exactly equivalent to the peak of pure magnesium oxide nanoparticles. EDX analysis reveals that O, C, Mg, and Ag surface element content of 18.26%, 68.92%, 2.18%, and 2.89%, respectively. The elemental analysis of Ag/MgO@BC observed that the percentage of Ag is 2.89% and Mg is 2.18%, which is close to the percentage of MgO and silver ions. Most ball-milled nanoparticles have 10 to 40 nm on the spherical surface of Ag/MgO@BC nanocomposites. Zeta potential of 28.4 mV has been used to indicate sustainability, and Ag/ZnO@BC showed high efficiency. When compared to other integrated AgNPs and MgO/Biochar nanocomposites, the analysis revealed that Ag/MgO@BC prevented the development of pneumonia at a high scale (1×10^8 CFU/mL).

Modified biochar Ag/ZnO@BC exhibited significant antibacterial activity towards S. aureus and E. coli species bacteria, with high productivity of 40% at the highest concentration (100 g/mL). Evaluation of some alternative green-synthesized AgNPs, MgONPs, and their nanostructured materials revealed that Ag/MgO@BC is a potent antibacterial agent against gram-positive and gram-negative because of a large dosage (2×10^8 CFU/mL). Consequently, the zone of inhibition was 11 mm against S. aureus and 10 mm for E. coli antibacterial activity. Combining Ag/MgO@BC is a unique nanocomposite that can be effectively used for a wide range of environmental and therapeutic applications.

Data Availability

The data used to support the findings of this study are included within the article. Should further data or information be required, these are available from the corresponding author upon request.

Conflicts of Interest

The authors declare that there are no conflicts of interest regarding the publication of this paper.

References

[1] Y. Xiao, H. Lyu, J. Tang, K. Wang, and H. Sun, "Effects of ball milling on the photochemistry of biochar: enrofloxacin degradation and possible mechanisms," *Chemical Engineering Journal*, vol. 384, article 123311, 2020.

[2] R. Li, J. J. Wang, L. A. Gaston et al., "An overview of carbothermal synthesis of metal-biochar composites for the removal of oxyanion contaminants from aqueous solution," *Carbon*, vol. 129, pp. 674–687, 2018.

[3] M. Hosny, "Biogenic synthesis, characterization, antimicrobial, antioxidant, and catalytic applications of synthesized platinum nanoparticles (PtNPs) from Polygonum salicifolium leaves," *Journal of Environmental Chemical Engineering*, vol. 10, article 106806, 2022.

[4] E. M. Abd El-Monaem, A. S. Eltaweil, H. M. Elshishini et al., "Sustainable adsorptive removal of antibiotic residues by chitosan composites: an insight into current developments and future recommendations," *Arabian Journal of Chemistry*, vol. 15, no. 5, article 103743, 2022.

[5] J. Kruse, M. Abraham, W. Amelung et al., "Innovative methods in soil phosphorus research: a review," *Journal of Plant Nutrition and Soil Science*, vol. 178, no. 1, pp. 43–88, 2015.

[6] C. Tarayre, L. De Clercq, R. Charlier et al., "New perspectives for the design of sustainable bioprocesses for phosphorus recovery from waste," *Bioresource Technology*, vol. 206, pp. 264–274, 2016.

[7] R. Li, J. J. Wang, B. Zhou et al., "Recovery of phosphate from aqueous solution by magnesium oxide decorated magnetic biochar and its potential as phosphate-based fertilizer substitute," *Bioresource Technology*, vol. 215, pp. 209–214, 2016.

[8] R. Li, J. J. Wang, B. Zhou et al., "Enhancing phosphate adsorption by Mg/Al layered double hydroxide functionalized biochar with different Mg/Al ratios," *Science of the Total Environment*, vol. 559, pp. 121–129, 2016.

[9] T. T. Li, Z. H. Tong, B. Gao, Y. C. C. Li, A. Smyth, and H. K. Bayabil, "Polyethyleneimine-modified biochar for enhanced phosphate adsorption," *Environmental Science and Pollution Research*, vol. 27, no. 7, pp. 7420–7429, 2020.

[10] F. Yu, F. Y. Tian, H. W. Zou et al., "ZnO/biochar nanocomposites via solvent free ball milling for enhanced adsorption and photocatalytic degradation of methylene blue," *Journal of Hazardous Materials*, vol. 415, article 125511, 2021.

[11] X. Zhang, K. Ren, Y. T. Wang, B. X. Shen, F. Shen, and Y. Shang, "Solvent-free synthesis of MnOx-FeOx/biochar for Hg0ando-xylene removal from flue gas," *Energy & Fuels*, vol. 35, no. 19, pp. 15969–15977, 2021.

[12] M. Kumar, X. Xiong, Z. Wan et al., "Ball milling as a mechanochemical technology for fabrication of novel biochar nanomaterials," *Bioresource Technology*, vol. 312, article 123613, 2020.

[13] S. O. Amusat, T. G. Kebede, S. Dube, and M. M. Nindi, "Ball-milling synthesis of biochar and biochar-based nanocomposites and prospects for removal of emerging contaminants: a review," *ournal of Water Process Engineering*, vol. 41, article 101993, 2021.

[14] B. Wang, B. Gao, and Y. S. Wan, "Entrapment of ball-milled biochar in Ca-alginate beads for the removal of aqueous Cd(II)," *Journal of Industrial and Engineering Chemistry*, vol. 61, pp. 161–168, 2018.

[15] Y. F. Li, A. R. Zimmerman, F. He et al., "Solvent-free synthesis of magnetic biochar and activated carbon through ball- mill extrusion with Fe_3O_4 nanoparticles for enhancing adsorption of methylene blue," *Science of The Total Environment*, vol. 722, article 137972, 2020.

[16] X. Xu, Y. Zheng, B. Gao, and X. Cao, "N-doped biochar synthesized by a facile ball-milling method for enhanced sorption of CO_2 and reactive red," *Chemical Engineering Journal*, vol. 368, pp. 564–572, 2019.

[17] D. Liu, G. Li, J. Liu, and Y. Yi, "Organic-inorganic hybrid mesoporous titanium silica material as bi-functional heterogeneous catalyst for the CO_2 cycloaddition," *Fuel*, vol. 244, pp. 196–206, 2019.

[18] P. S. Kumar, R. N. Kamath, P. Boyapati, P. J. Josephson, L. Natrayan, and F. D. Shadrach, "IoT battery management system in electric vehicle based on LR parameter estimation and ORMeshNet gateway topology," *Sustainable Energy Technologies and Assessments*, vol. 53, article 102696, 2022.

[19] S. Saedi, M. Shokri, J. T. Kim, and G. H. Shin, "Semi-transparent regenerated cellulose/ZnONP nanocomposite film as a potential antimicrobial food packaging material," *Journal of Food Engineering*, vol. 307, article 110665, 2021.

[20] E. Gurgur, S. Oluyamo, A. Adetuyi, O. Omotunde, and A. Okoronkwo, "Green synthesis of zinc oxide nanoparticles and zinc oxide–silver, zinc oxide–copper nanocomposites using Bridelia ferruginea as bio template," *SN Applied Sciences*, vol. 2, pp. 1–12, 2020.

[21] Y. Zheng, Y. Yang, Y. Zhang et al., "Facile one-step synthesis of graphitic carbon nitride-modified biochar for the removal of reactive red 120 through adsorption and photocatalytic degradation," *Biochar*, vol. 1, no. 1, pp. 89–96, 2019.

[22] M. Ponnusamy, L. Natrayan, P. P. Patil, G. Velmurugan, and Y. T. Keno, "Statistical analysis on interlaminar shear strength of nanosilica addition with woven dharbai/epoxy hybrid nanocomposites under cryogenic environment by Taguchi technique," *Adsorption Science & Technology*, vol. 2022, article 6571515, 9 pages, 2022.

[23] T. Bhuyan, K. Mishra, M. Khanuja, R. Prasad, and A. Varma, "Biosynthesis of zinc oxide nanoparticles from *Azadirachta indica* for antibacterial and photocatalytic applications," *Materials Science in Semiconductor Processing*, vol. 32, pp. 55–61, 2015.

[24] Y. Khimsuriya, D. K. Patel, Z. Said et al., "Artificially roughened solar air heating technology - a comprehensive review," *Applied Thermal Engineering*, vol. 214, article 118817, 2022.

[25] A. Z. Hassan, A. W. M. Mahmoud, G. M. Turky, and G. Safwat, "Rice husk derived biochar as smart material loading nano nutrients and microorganisms," *Bulgarian Journal of Agricultural Science*, vol. 26, pp. 309–322, 2020.

[26] M. M. Matheswaran, T. V. Arjunan, S. Muthusamy et al., "A case study on thermo-hydraulic performance of jet plate solar air heater using response surface methodology," *Thermal Engineering*, vol. 34, article 101983, 2022.

[27] A. S. Eltaweil, A. M. Abdelfatah, M. Hosny, and M. Fawzy, "Novel biogenic synthesis of a Ag@biochar nanocomposite as an antimicrobial agent and photocatalyst for methylene blue degradation," *ACS Omega*, vol. 7, no. 9, pp. 8046–8059, 2022.

[28] Z. Ma, J. Liu, Y. Liu, X. Zheng, and K. Tang, "Green synthesis of silver nanoparticles using soluble soybean polysaccharide and their application in antibacterial coatings," *International Journal of Biological Macromolecules*, vol. 166, pp. 567–577, 2021.

[29] L. Natrayan, D. Veeman, P. P. Patil, V. S. Nadh, P. Balamurugan, and M. D. Chewaka, "Surface state treatment of carbon dots using sulphur dioxide isotherm," *Adsorption Science & Technology*, vol. 2022, article 7387409, 9 pages, 2022.

[30] Y. Yao, B. Gao, J. Chen, and L. Yang, "Engineered biochar reclaiming phosphate from aqueous solutions: mechanisms and potential application as a slow-release fertilizer," *Environmental Science & Technology*, vol. 47, no. 15, pp. 8700–8708, 2013.

[31] M. Hosny, M. Fawzy, and A. S. Eltaweil, "Green synthesis of bimetallic Ag/ZnO@Biohar nanocomposite for photocatalytic degradation of tetracycline, antibacterial and antioxidant activities," *Scientific Reports*, vol. 12, no. 1, pp. 1–17, 2022.

[32] M. Ponnusamy, L. Natrayan, P. P. Patil, G. Velmurugan, and S. Thanappan, "Multiresponse optimization of mechanical behaviour of Calotropis gigantea/nano-silicon-based hybrid nanocomposites under cryogenic environment," *Adsorption Science & Technology*, vol. 2022, article 4138179, 14 pages, 2022.

[33] S. Lokina, A. Stephen, V. Kaviyarasan, C. Arulvasu, and V. Narayanan, "Cytotoxicity and antimicrobial activities of green synthesized silver nanoparticles," *European Journal of Medicinal Chemistry*, vol. 76, pp. 256–263, 2014.

SAGE
Publishing

Research Article

Finite Element Method-Based Spherical Indentation Analysis of Jute/Sisal/Banana-Polypropylene Fiber-Reinforced Composites

Nitish Kaushik,[1] **Ch. Sandeep,**[2] **P. Jayaraman,**[3] **J. Justin Maria Hillary,**[4] **V. P. Srinivasan** ⓘ**,**[5] **and M. Abisha Meji** ⓘ[6]

[1]*Department of Production and Industrial Engineering, Birla Institute of Technology, Mesra, 835215, Ranchi, Jharkhand, India*
[2]*Department of Mechanical Engineering, Institute of Aeronautical Engineering, 500043, Hyderabad, Telangana, India*
[3]*Department of Mechanical Engineering, Prathyusha Engineering College, 602025, Thiruvallur, Tamil Nadu, India*
[4]*Department of Mechatronics Engineering, Sri Krishna College of Engineering and Technology, 641008, Coimbatore, Tamil Nadu, India*
[5]*Department of Mechanical Engineering, Sri Krishna College of Engineering and Technology, 641008, Coimbatore, Tamil Nadu, India*
[6]*Department of Physics, School of Engineering and Applied Sciences, Kampala International University, Western Campus, Uganda*

Correspondence should be addressed to M. Abisha Meji; abisha.meji@kiu.ac.ug

Material hardness of natural fiber composites depends upon the orientation of fibers, ratio of fiber to matrix, and their mechanical and physical properties. Experimentally finding the material hardness of composites is an involved task. The present work attempts to explore the deformation mechanism of natural fiber composites subjected to post-yield indentation by a spherical indenter through a two-dimensional finite element analysis. In the present work, jute-polypropylene, sisal-polypropylene, and banana-polypropylene composites are considered. The analysis is attempted by varying the properties of Young's modulus of fiber and matrix, diameter of fiber, and horizontal and vertical center distance between the fibers. The analyses results showed that as the distance between the fiber's center increases, the bearing load capacity of all composite increases nonlinearly. The jute fiber composite shows predominate load-carrying capacity compared to other composites at all L/D ratios and interference ratios. The influence of subsurface stress in lateral direction is minimal and gets reduced as the distance between the fiber centers increases. The variation in diameter of fiber influences significantly, i.e., beyond the L/D ratio of 1.0; for the same contact load ratio, the bearing area support is double for jute-polypropylene composite compared to sisal-polypropylene composite. Compared to the sisal-polypropylene composite, for the same interference ratio, the load-carrying capacity is two times high for banana-polypropylene composite, whereas four times high for jute-polypropylene composite, but this effect decreases as the L/D ratio decreases. In all the composites, the subsurface stress gets distributed as the L/D ratio increases. The ratio of fibers center distance to diameter of fiber influences marginally on the contact load and contact area and significantly on the contact stress for all the fiber-reinforced composites.

1. Introduction

Natural fibers are extensively used in the preparation of composites due to their low cost, low density, and biodegradable. The properties of natural fiber composite depend on source of fiber, fiber extraction, fiber preparation, fiber property, matrix preparation, matrix property, and fabrication process like hand molding, compression molding, injection molding, continuous pultrusion, and extrusion molding and their process parameters. Verma et al. [1] fabricated the alkali-treated sisal reinforced with starch and epoxy matrix biocomposites and investigated their mechanical and microstructure characteristics. The results revealed that epoxy-coated fiber composite showed improved property. Verma et al. [2] fabricated and
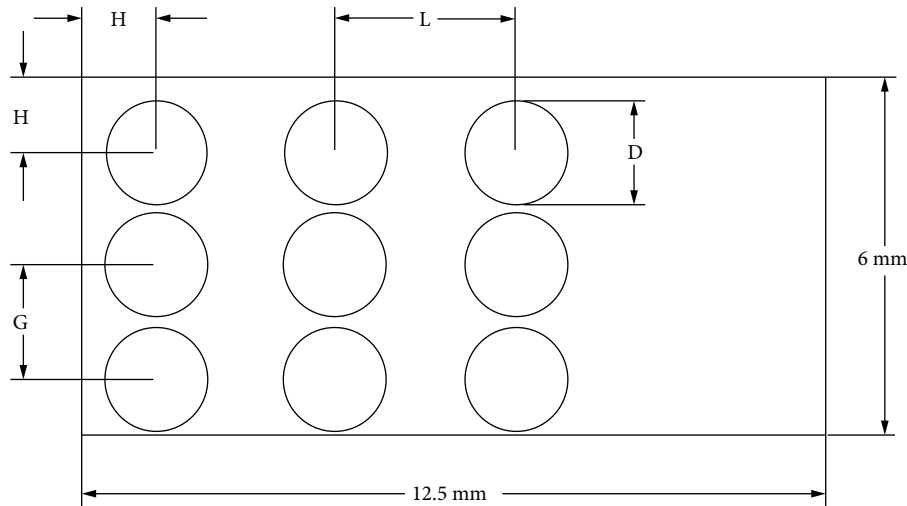
FIGURE 1: Geometrical modeling parameter.

experimentally characterized the jute and starch hybrid bio-composites. They concluded that water absorption significantly affected the mechanical properties of the composites. Verma et al. [3] investigated the mechanical and physical behavior of soy protein and sisal fiber-reinforced green composites. Vijay et al. [4] experimentally studied the raw and alkali-treated tridax procumbens fiber composites. The alkali-treated fiber-based composites showed improved thermal stability, tensile, and crystallinity. Dinesh et al. [5] investigated the influence of wood dust as fillers in the mechanical and thermal properties of jute –epoxy fiber composites. The results showed that padauk wood dust embedded composite improved the mechanical property, whereas rosewood dust enhanced the thermal stability of the composite. Jothibabu et al. [6] attempted to evaluate the hybridization effect on mechanical property through the different stacking sequence of areca sheath fiber/jute fiber/glass fabric fiber composites. Vijay et al. [7] examined the thermo-mechanical characteristics of Azadirachta indica seed powder and Camellia sinensis powder filled jute epoxy composites. Vijay et al. [8] studied the physical, chemical, thermal, mechanical, and morphological characteristics of treated and untreated Leucas aspera fibers. Vijay et al. [9] examined the physical and chemical properties of Vachellia farnesiana fibers. Sathish Kumar and Nivedhitha [10] studied the different weight fraction-based chemically modified kenaf fiber-epoxy composites. The results showed that 6% NaOH treated 40% weight fraction fiber composite showed improved mechanical property compared to others. The above natural fiber composites are fabricated with different orientation of fibers and ratio of fiber to matrix so finding their mechanical properties is an involved task. If a model or method is developed to find the mechanical properties in advance that may reduce cost and time incurred to fabricate the materials with required properties. Generally, the hardness values for the metallic materials are well known and are available in ASTM standard format, but the hardness values for natural fiber composites are unknown in most of the circumferences. Indentation-based hardness has direction benefits in different engineering applications like load-bearing mechanical elements and contact effects at different length scales in micro, meso, and macro applications. The pioneered indentation of metals was approached by Tabor [11]. The followers attempted in numerical, semianalytical, and analytical methods using different shapes of indenters indenting infinite half space to explore the plasticity role. Ishlinsky [12] attempted indentation of rigid perfectly plastic half space against a rigid sphere using the slip-line theory of plasticity and concluded that indentation hardness is three times of material yield strength, whereas Hill et al. [13] used flow theory for the same. Johnson [14] stated that indentation behavior of elastic perfectly materials against rigid indenter can be explored in deformation order of elastic, elastoplastic, and fully plastic deformations. Samuels and Mulhearn [15] explored the deformation behavior of half space against a blunt indenter and observed that subsurface deformation is in radial direction under the contact zone. The pioneer finite element method-based study was attempted by Hardy et al. [16], who detected that contact pressure changes from elliptical to rectangular and also observed that contact stress in axis symmetry is constant as the applied load increases. Follansbee et al. [17] compared their elastic-plastic indentation numerical results with the Hertz elastic solution and shallow and deep indentations experimental results and found good agreement with them. Giannakopoulos et al. [18] found constitutive relations for applied normal load and indentation interference using finite element method for elastic and elastic-plastic material against a Vickers indenter. Komvopoulos and Ye [19] observed the behavior rigid sphere indentation against an elastic perfectly plastic half-space through the finite element study. The developed constitutive equations showed good agreement with Johnson [14] and concluded that material hardness is three times the yield strength of indented material. Park and Pharr [20] explored the elastic and plastic dominant regimes in elastic-plastic indentation. Mesarovic et al. [21] detected a decreasing trend in mean contact pressure for larger indentation which leads to the failure. Bhattacharya et al. [22] studied the elastic and plastic behavior with finite element approach at submicrometer scale and compared with experimental results. They said that continuum-
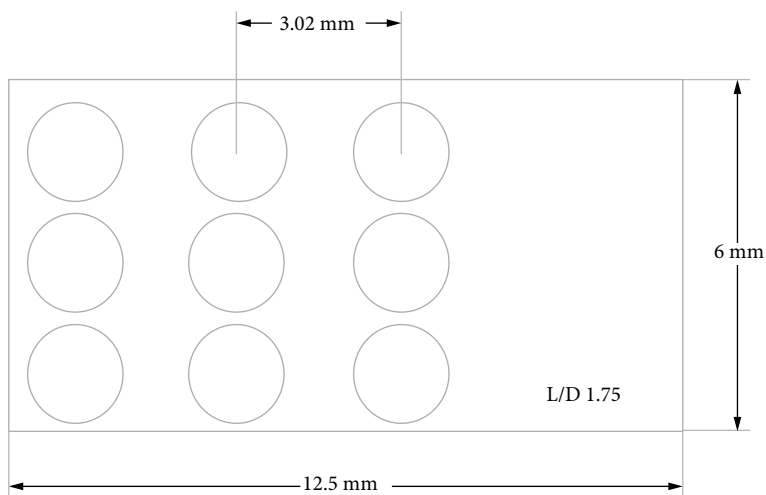
(a)
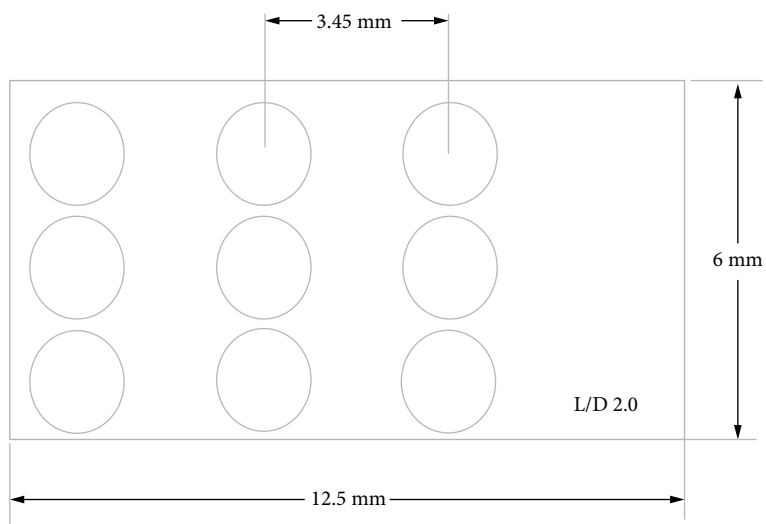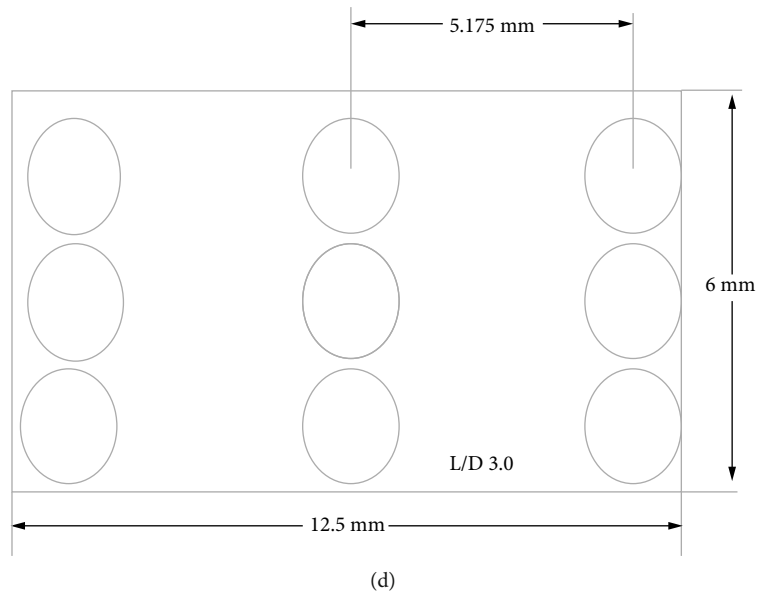

(b)
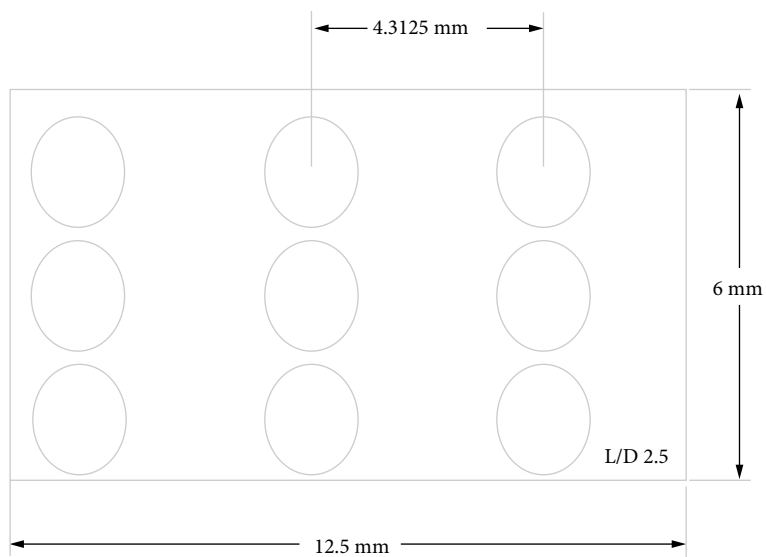
(c)

FIGURE 2: Continued.

(d)

FIGURE 2: Models with different *L/D* ratios (by varying the distance between fiber centers).
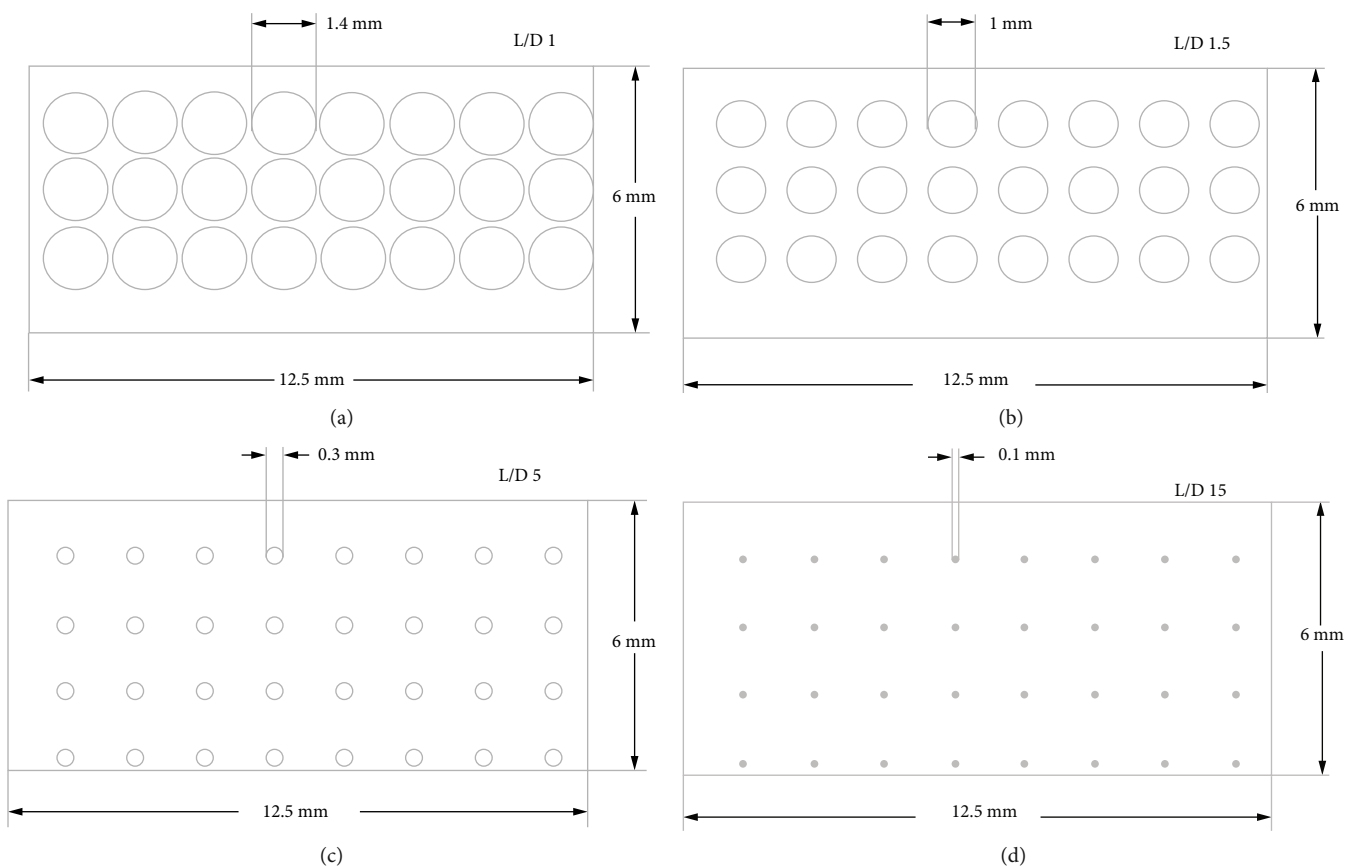

(a)

(b)

(c)

(d)

FIGURE 3: Models with different *L/D* ratios (by changing the fiber diameter).

based finite element approach can relate load and indentation at submicrometer scale in a well manner, and Knapp et al. [23] developed finite element approach-based nanoindentation method to expose the elastic modulus and hardness of layered medium.

Apart from the indentation models, flattening models are also approach by different researchers. Kogut et al. [24] analyzed deformation of a sphere asperity against a rigid flat through finite element approach and deduced empirical relations for contact parameters with
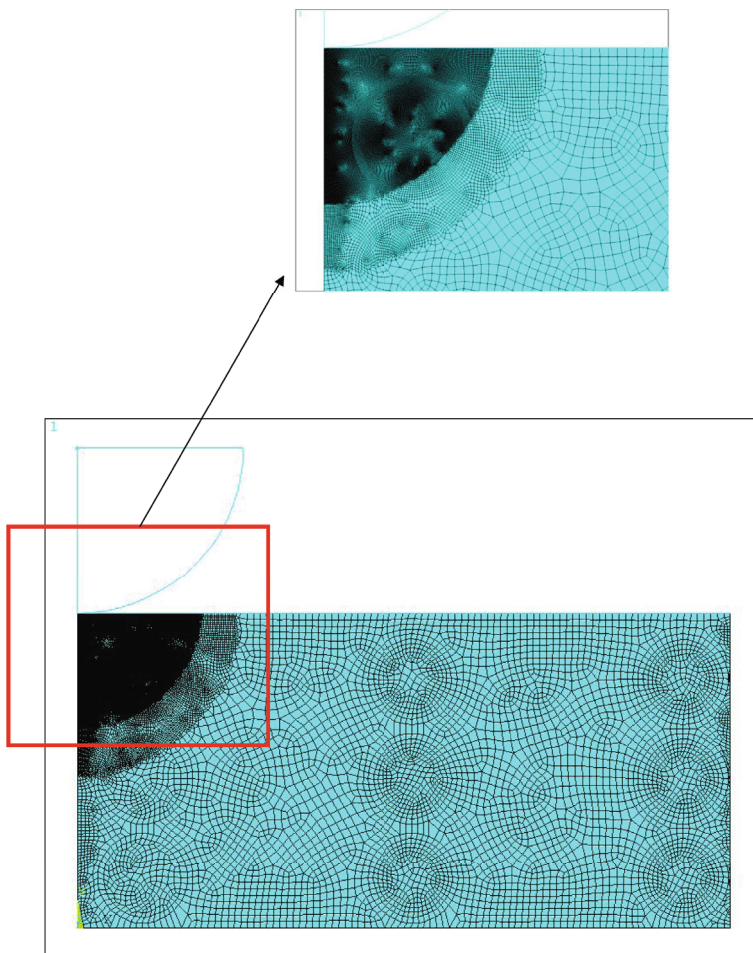
Figure 4: Meshed model of L/D 3.0.
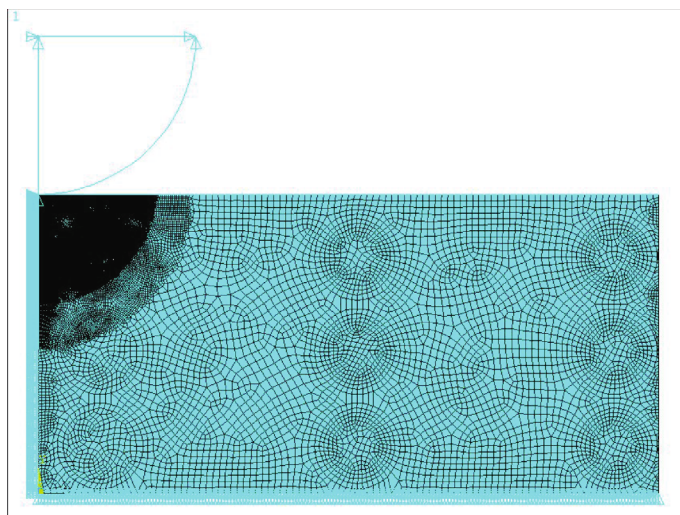
Figure 5: Finite element model of L/D 3.0 with boundary conditions.

interference as variable. Chang et al. [25] called as CEB model assumed volume conservation at the tip of spherical asperity and offered a simplified analytical contact area and contact load solution for the elastic-plastic contact deformation behavior similarly Thornton et al. [26] who provided a simplified analytical solution based on elastic perfectly plastic collision of spheres with truncated Hertz contact pressure distribution.

Figure 6: Validation of present model with Yanping Cao et al. [38] model.

Table 1: Physio-mechanical properties of fibers and matrix.
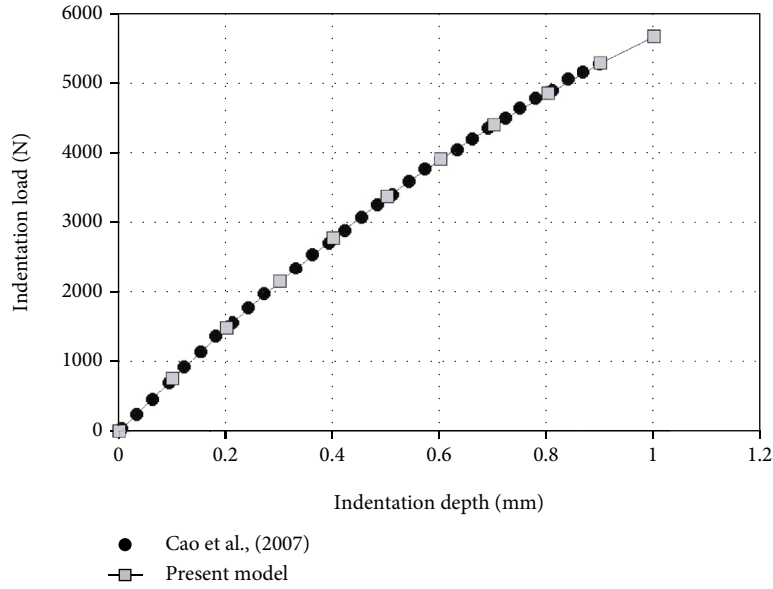
Fiber/matrix	Density (g/cm³)	Tensile strength-Y (MPa)	Tensile modulus-E (MPa)	Poisson's ratio	Reference
Banana	1.35	600	17.85	0.30	[39]
Sisal	1.45	567	10.4	0.32	[39]
Jute	1.3-1.45	393-800	13-26.5	0.31	[40]
Polypropylene	0.9	27	0.8	0.41	[41]

Kocharski et al. [27] and Vu-Quoc et al. [28] provided more accurate finite element solutions with realistic elastic plastic deformation of spherical asperity during its loading, but they did not provide common solution for the global contact parameters. Kogut et al. [29] carried out a finite element-based loading and unloading of rigid sphere indentation in a half space for elastic-plastic materials. Meanwhile, Quicksall et al. [30] explored the effect of Young's modulus and yield strength properties impact on single asperity flattening model. Jackson et al. [31] extended the Kogut et al. [24] model for low to high E/Y values and developed empirical expressions for contact parameters with the variation of H/Y against the deforming contact geometry.

Brizmer et al. [32] explored the contact condition effects with the study of ductile and brittle materials with their respective failure criterions. Ovcharenko et al. [33] experimented with copper, stainless steel spheres, and sapphire flat and observed good agreement with the existing contact models. Jackson et al. [34] compared their results with the spherical indentation models of Komvopoulos et al. [19] and Kogut and Komvopoulos et al. [35]. Recently, Wagh et al. [36] analyzed the composite laminates with finite thickness using spherical indenter. Lei Zhou et al. [37] explored the influence of eccentricity and indentation modulus for an anisotropic elastic half space indented by a spherical rigid indenter.

The above-mentioned literature explored the different metallic materials' elastic-plastic indentation and flattening

behavior, but the natural fiber composite materials indentation behavior is not explored in detail. The objective of the present work is to explore the indentation characteristics of elastic–plastic behavior of natural fiber composite materials for mostly using fibers and matrixes, and the present work attempted to develop an empirical relation to calculate material hardness of natural fiber composites when subjected to post-yield indentation through finite element analysis, by accounting the properties of matrix and fibers such as diameter of fiber, horizontal and vertical center distance between the fibers, and Young's modulus of fiber and matrix.

2. Modeling and Analysis Details

Mostly hardness of composite materials is found using ASTM D785 standard. In order to explain the effect of fiber and matrix properties, two-dimensional model is considered here, and the geometrical and modeling content are discussed in the below section.

2.1. Modeling Details. For the two-dimensional indentation analysis, a model having 12.5×6 mm and a spherical indenter of 3.175 mm radius as per the ASTM D785 standard are considered. The geometrical parameters for modeling are shown in Figure 1. The horizontal and vertical distance from the top of the specimen is (H), the horizontal distance between fiber centers is (L), the vertical
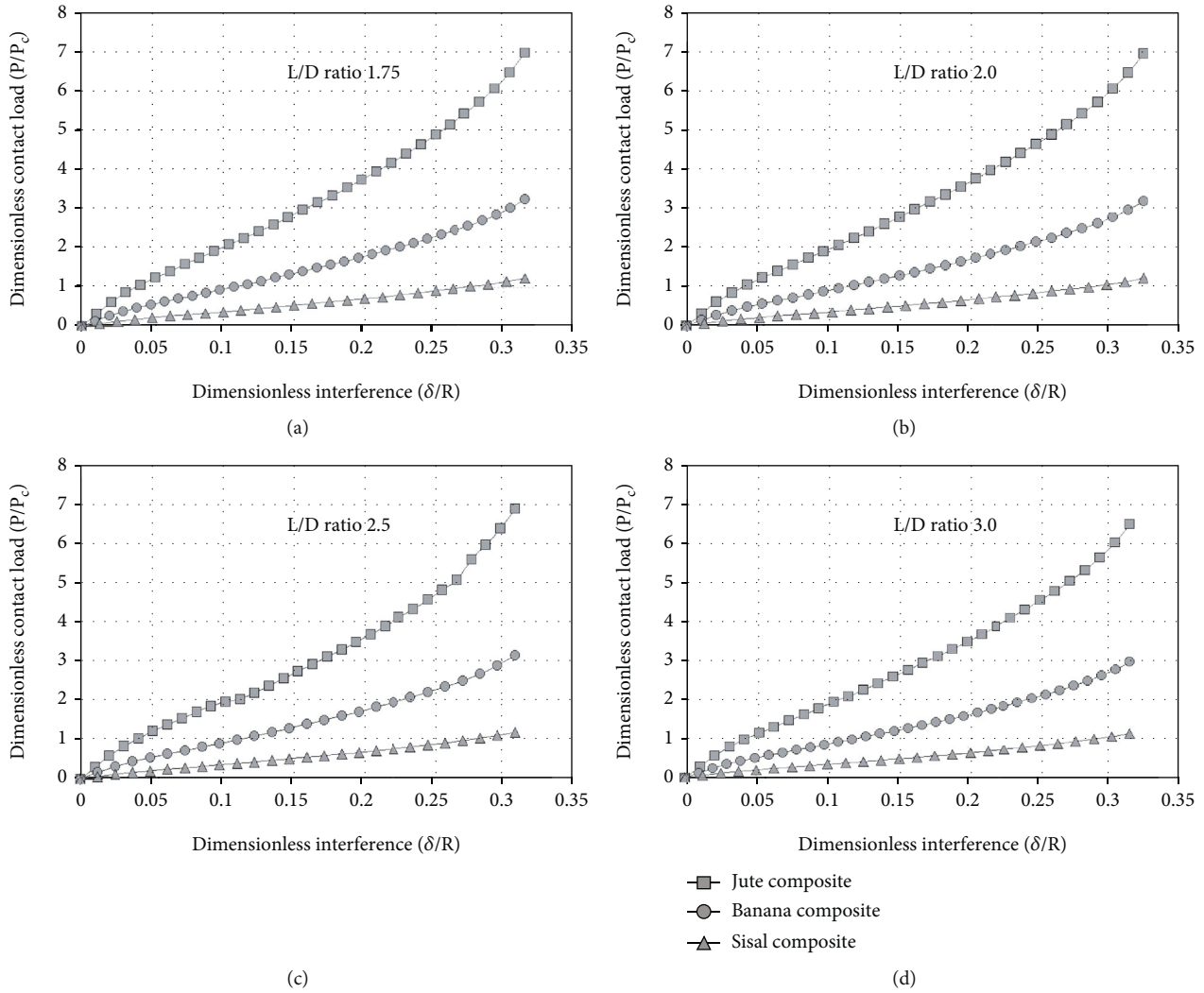
(a)

(b)

(c)

(d)

Figure 7: Contact load ratio for various L/D ratios.

distance between fiber centers is (G) and the diameter of the fiber is (D).

The distance between the fiber's center and the fiber diameter are most geometrically affecting parameters of the material hardness apart from the orientation of the fibers, so the distance between the fiber's center and the fiber diameter is taken as varying parameters of the present work. The different L/D ratios such as 1.75, 2.0, 2.5, and 3.0 are obtained by changing the distance between fibers center (http://i.e.by changing the horizontal length between fiber centers only), and the resultant models for different L/D ratios by changing the fiber diameter are given below in Figures 2(a)–2(d) and 3(a)–3(d), respectively.

2.2. Analysis Details. The finite element approach based ANSYS® package is employed in indentation analysis of natural fiber-reinforced composites. In order to mesh the above models, 8-noded 2D element (PLANE 183) is taken. The meshed model of L/D 3.0 is shown in Figure 4. It consists of 73,698 elements in which more than 60% of elements are occupied in the expected contact zone. A rigid spherical indenter is placed on the model. The surface contact pair

between the rigid indenter and the model is established with frictionless condition. The top surface of the model consists of contact element (CONTA172), and the rigid indenter holds non-flexible elements (TARGE169). The nodes on the planar symmetry of the meshed model are constrained in horizontal direction, and the nodes on the bottom of the meshed model are constrained in all directions. The resultant finite element model having L/D 3.0 is shown in Figure 5. Similarly, all other models having different L/D ratios are modeled and meshed. The indentation is done by applying the displacement incrementally to the indenter with incremental substeps of maximum 8,000, and then, the contact parameters are extracted from each analysis results.

2.3. Validation of Present Model. The present finite element model is validated with Yanping Cao et al. [38] model, and the result shows a variation less than 1%. The indentation depth is given up to 1 mm in the present model. Figure 6 shows the indentation load versus indentation depth for the present model which shows the same behavior as Yanping Cao et al. [38] model.
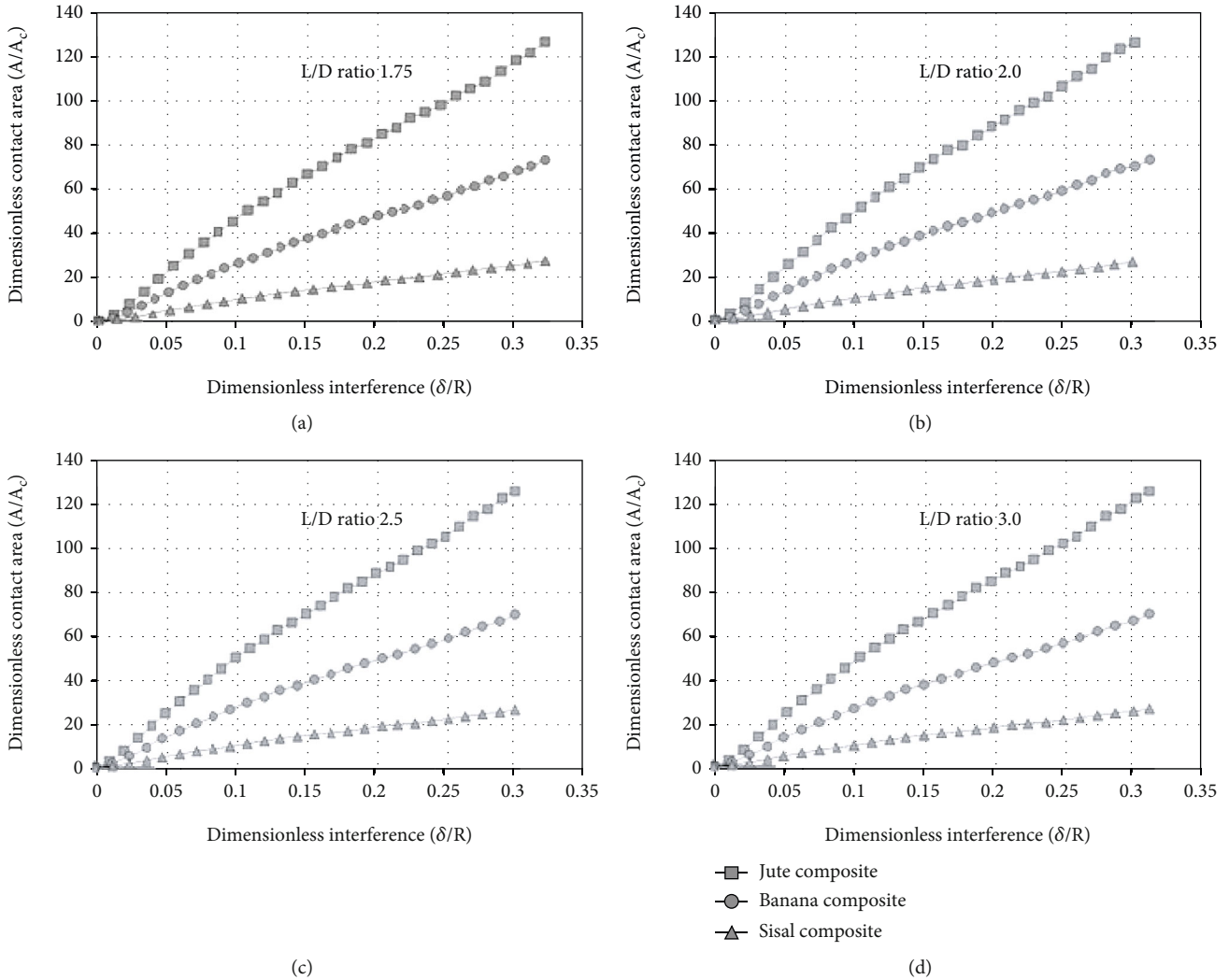
(a)

(b)

(c)

(d)

Figure 8: Variation of contact area ratio for various L/D ratios.

3. Results and Discussion

For the present indentation analysis, the most commonly using natural fibers and matrix are utilized which is given in Table 1 where the natural fiber-reinforced composite's E/Y ratio varies in the range of 18 to 40. The contact parameters are observed for every small step of the indentation to enumerate the influence of distance between fiber centers and fiber diameter.

3.1. Influence of Distance between Fiber Centers on Contact Parameters. The contact loads for every step are extracted from the analysis results.

3.1.1. Influence of Contact Load. The response of contact load ratio against interference ratio for the L/D ratios of 1.75, 2.0, 2.5, and 3.0 is shown in Figures 7(a)–7(d).

In Figure 7, as the dimensionless interference increases, the load-bearing capacity increases for all the fiber composites nonlinearly, but the trend looks similarly. The deviation among the load-carrying capacity increases as the interference ratio increases. For the same interference ratio, the jute

fiber-based composite shows very high load-bearing capacity compared to all other composites. The sisal fiber-based composite shows very less load-carrying capacity, whereas the banana fiber-based composite behavior is intermediate so, for the increasing E/Y ratio, load-carrying capacity also increases. At the same interference ratio, as the L/D ratio increases, the load-bearing capacity increases marginally which is less than 3% for all composites.

3.1.2. Effect of Contact Area. The contact areas for every step are extracted from the analysis results. The contact area ratio against the interference ratio for the L/D ratios of 1.75, 2.0, 2.5, and 3.0 is shown in Figures 8(a)–8(d).

From the Figure 8, as the dimensionless interference increases, the contact area ratio increases for all the fiber composites, and the deviation among them also increases. Compared to sisal fiber composite, the jute fiber composite shows five times high bearing area ratio, whereas the banana fiber-based composite shows two times high bearing area ratio. In each composite, for the same interference ratio, as the L/D ratio increases, the contact area ratio marginally increases as like contact load ratio.
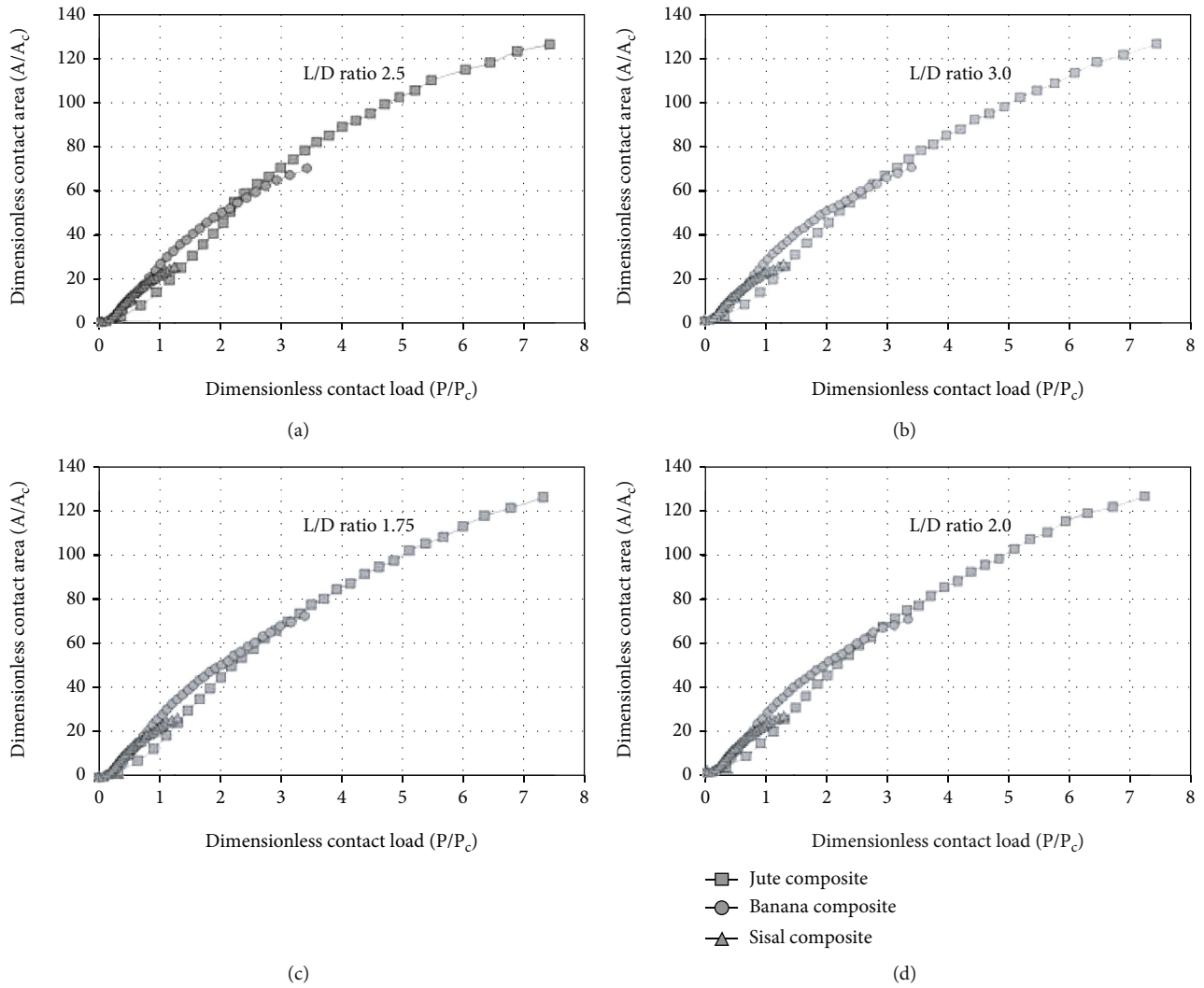
(a)

(b)

(c)

(d)

Figure 9: Response of contact area ratio vs contact load ratio for various L/D ratios.

3.1.3. Effect of E/Y Ratio on Contact Load and Area. Figures 9(a) and 9(b) shown below show the response of contact area ratio against contact load ratio for various L/D ratios. As contact load ratio increases, the contact area ratio also increases. For the same indentation depth, the jute fiber-reinforced composites have very high dimensionless contact area when compared to banana and sisal fiber-reinforced composites.

3.1.4. Effect of L/D Ratio on Contact Load and Area. Figure 10 shows the influence of L/D ratios on the contact area ratio with contact load ratio.

The influence of L/D ratios on all the composites is similar, but for the same contact load ratio, the bearing area is large for banana composite, and it is less for the jute composite and intermediate for sisal composite.

3.1.5. Effect of E/Y Ratio and L/D Ratio on Von Mises Stress Distribution. The three modes of deformation of polypropylene such as elastic, elastic-plastic, and plastic deformations are extracted from the analysis results. The Von Mises stress plots of the three mode of deformation are shown in

Figures 11(a)–11(c). The Von Mises stress distribution is used to identify the areas in which the equivalent stress is maximum and minimum and its distribution pattern and also it is used to predict failure of the material.

The resultant Von Mises stress plots for jute-polypropylene composite at δ/R of 0.31496 for different L/D ratios are shown in Figures 12(a)–12(d). The influence of distance between the fiber centers on stress distribution is less.

Figures 13(a)–13(d) show the stress distribution in the banana-polypropylene composites of increasing L/D ratio at δ/R of 0.31496.The influence of increase in L/D ratio on stress distribution is marginal.

When compared to jute and banana fiber-reinforced composites, the stress distribution in sisal-polypropylene composite is significant. The resultant Von Mises stress plots for sisal-polypropylene composite at δ/R of 0.31496 for different L/D ratios are shown in Figures 14(a)–14(d).

3.2. Influence of Fiber Diameter on Contact Parameters. The contact loads for every step are extracted from the analysis results by accounting the influence of fiber diameter.
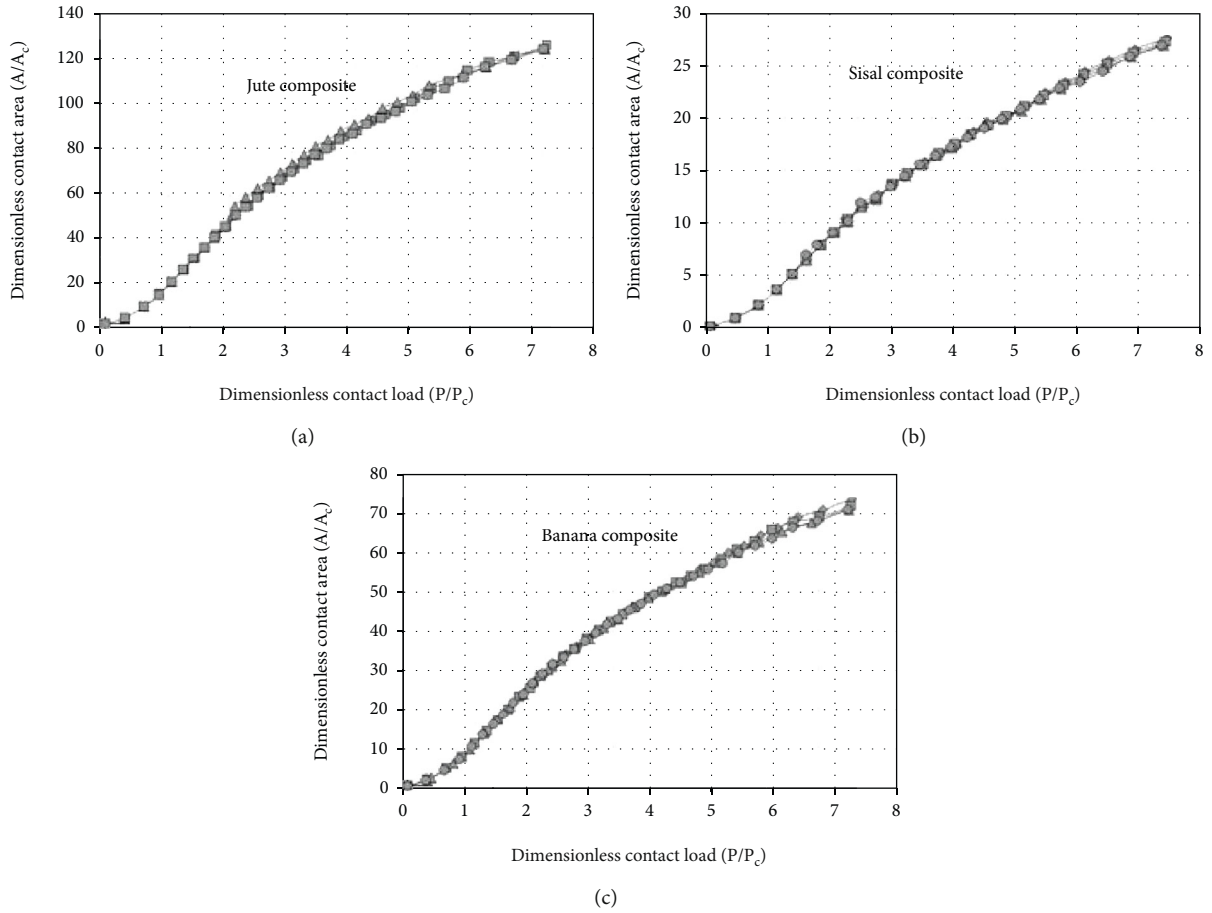
(a)

(b)

(c)

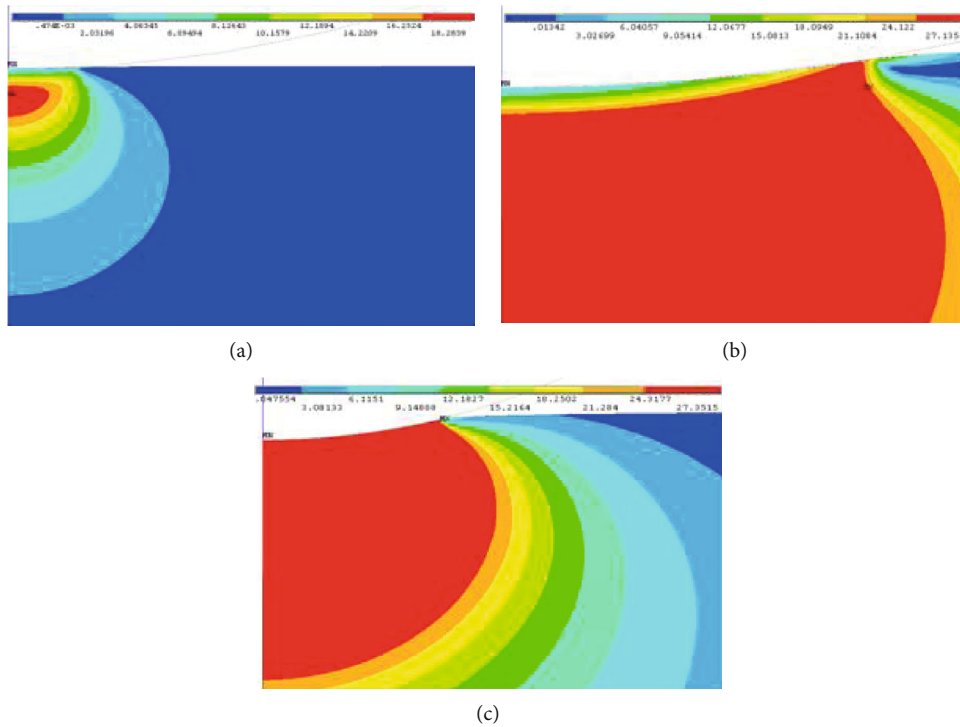Figure 10: Response of contact area ratio vs contact load ratio for different composite.

(a)

(b)

(c)

Figure 11: Von Mises stress plot for three modes of deformation of polypropylene matrix.

L/D 1.75   L/D 2

(a)   (b)

L/D 2.5   L/D 3

(c)   (d)

Figure 12: Von Mises stress plot for jute-polypropylene composite for various L/D ratios.

L/D 1.75   L/D 2

(a)   (b)

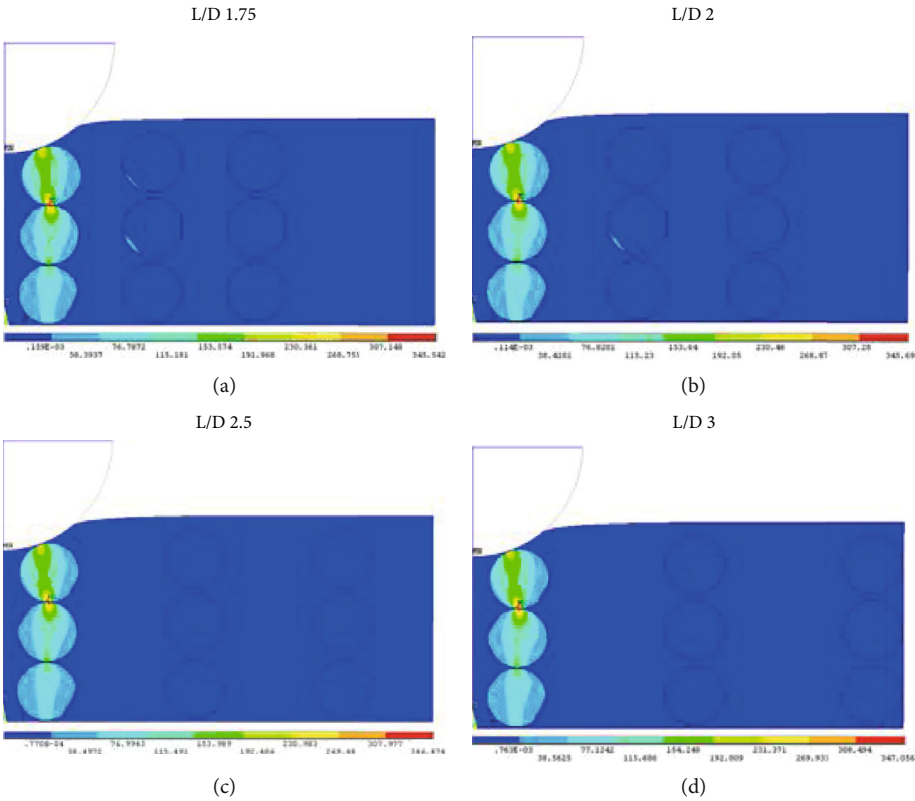L/D 2.5   L/D 3

(c)   (d)
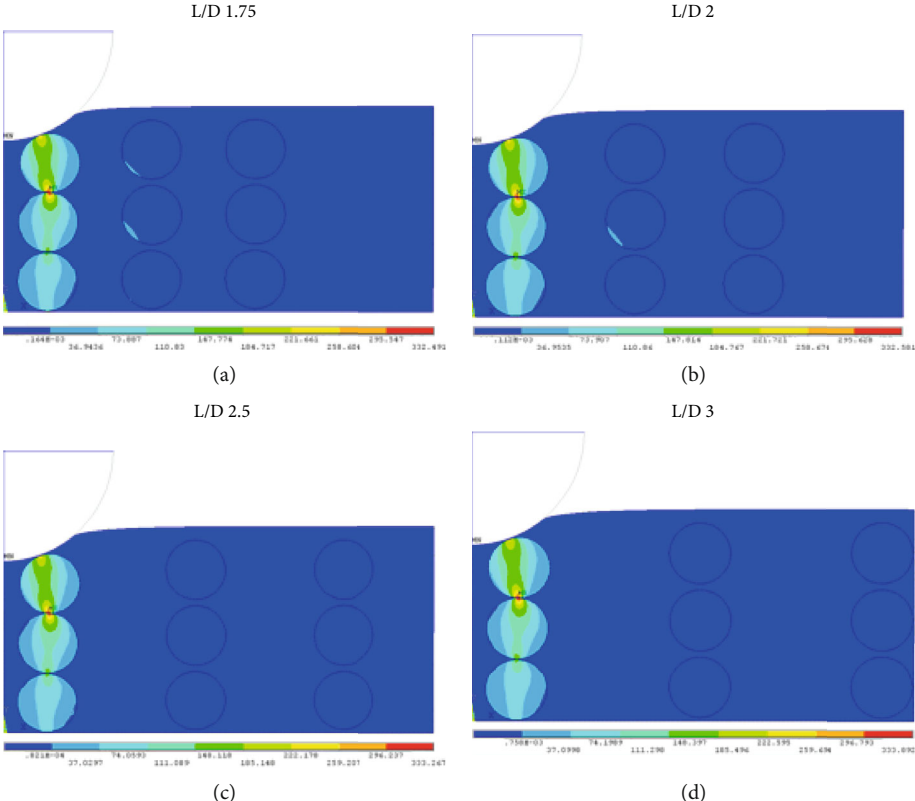
Figure 13: Von Mises stress plot for banana-polypropylene composite for various L/D ratios.

L/D 1.75

L/D 2

(a)

(b)

L/D 2.5

L/D 3

(c)

(d)
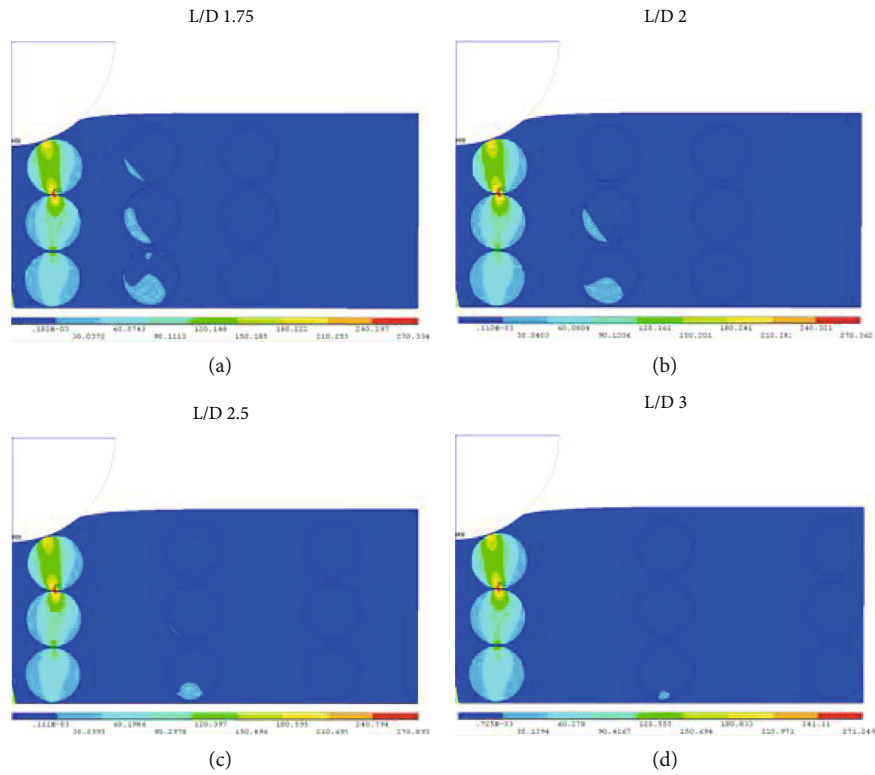
FIGURE 14: Von Mises stress plot for sisal-polypropylene composite for various L/D ratios.
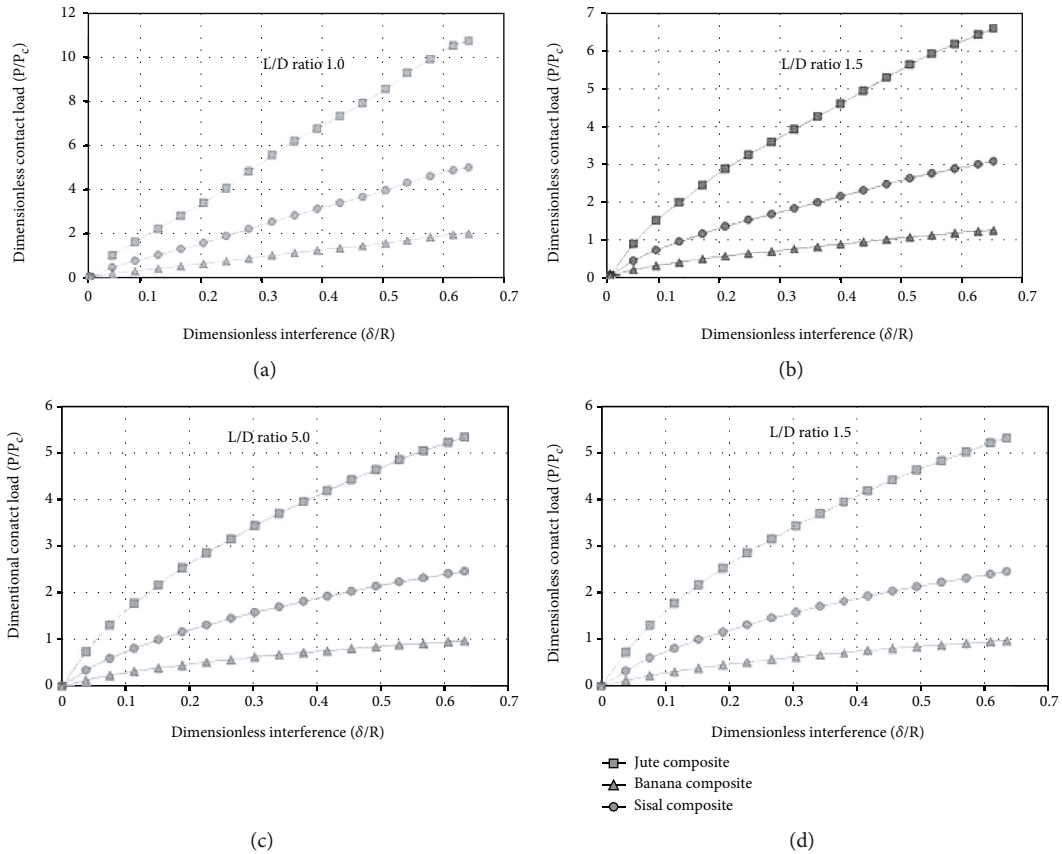

(a)

(b)

(c)

(d)

FIGURE 15: Response of contact load ratio vs interference ratio for various L/D ratios.
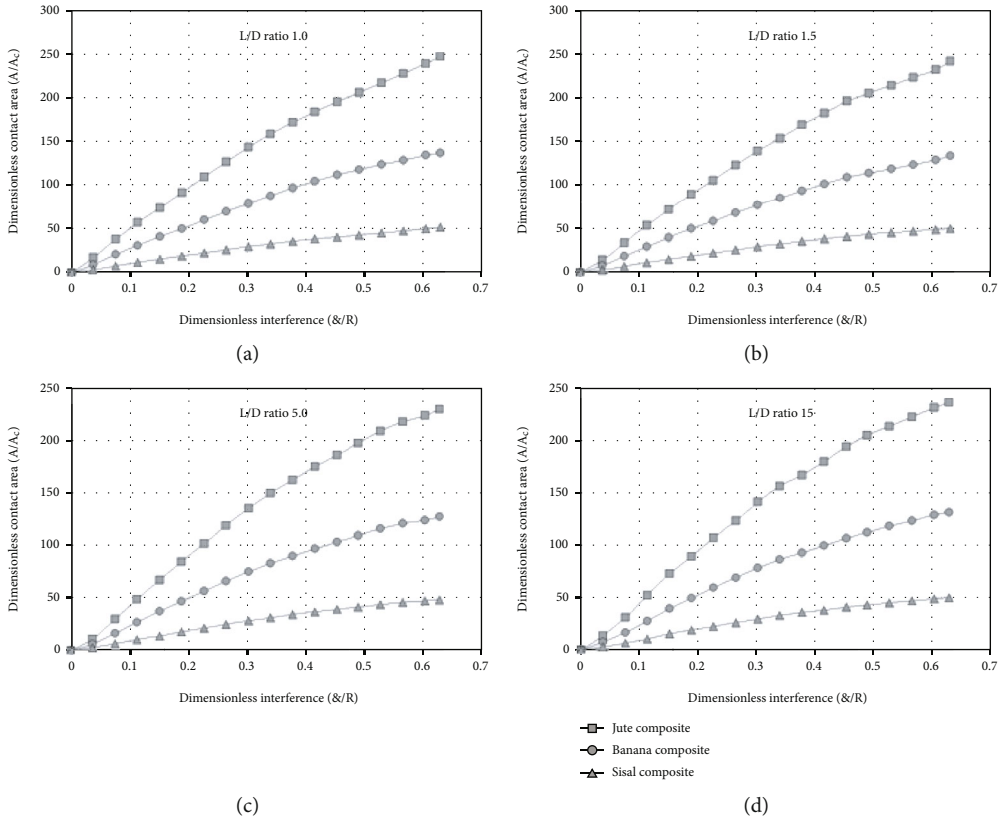
FIGURE 16: Response of contact area ratio vs interference ratio for various *L/D* ratios.
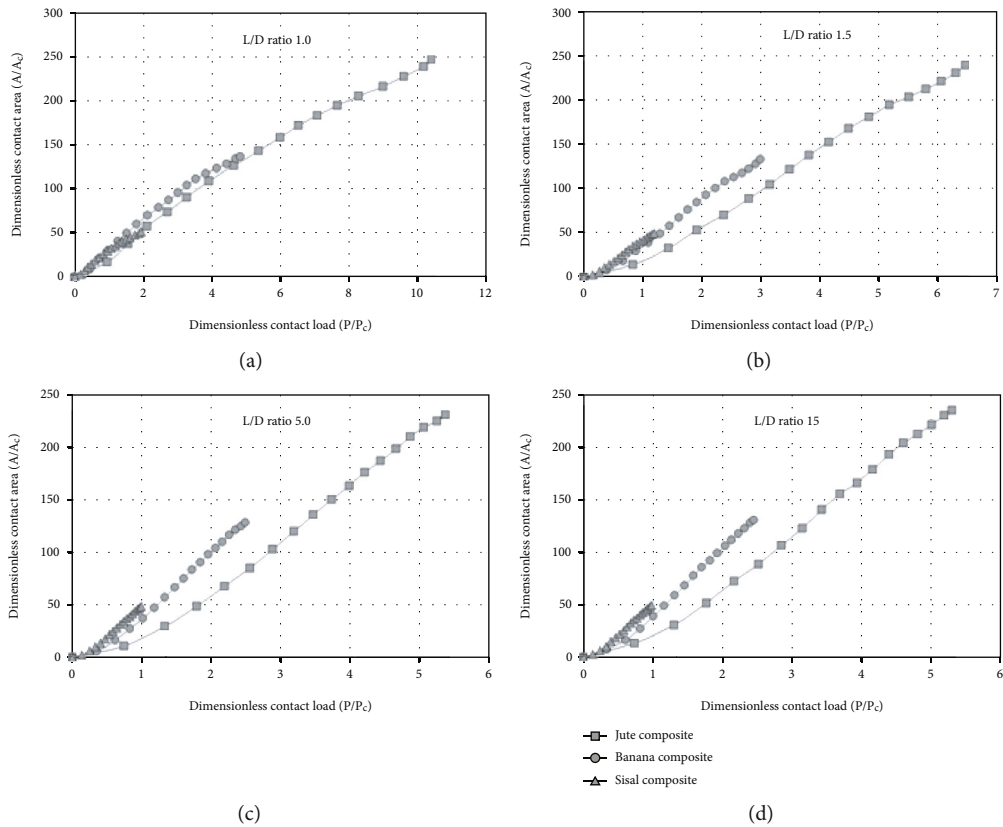

FIGURE 17: Response of contact area ratio vs contact load ratio for various *L/D* ratios.
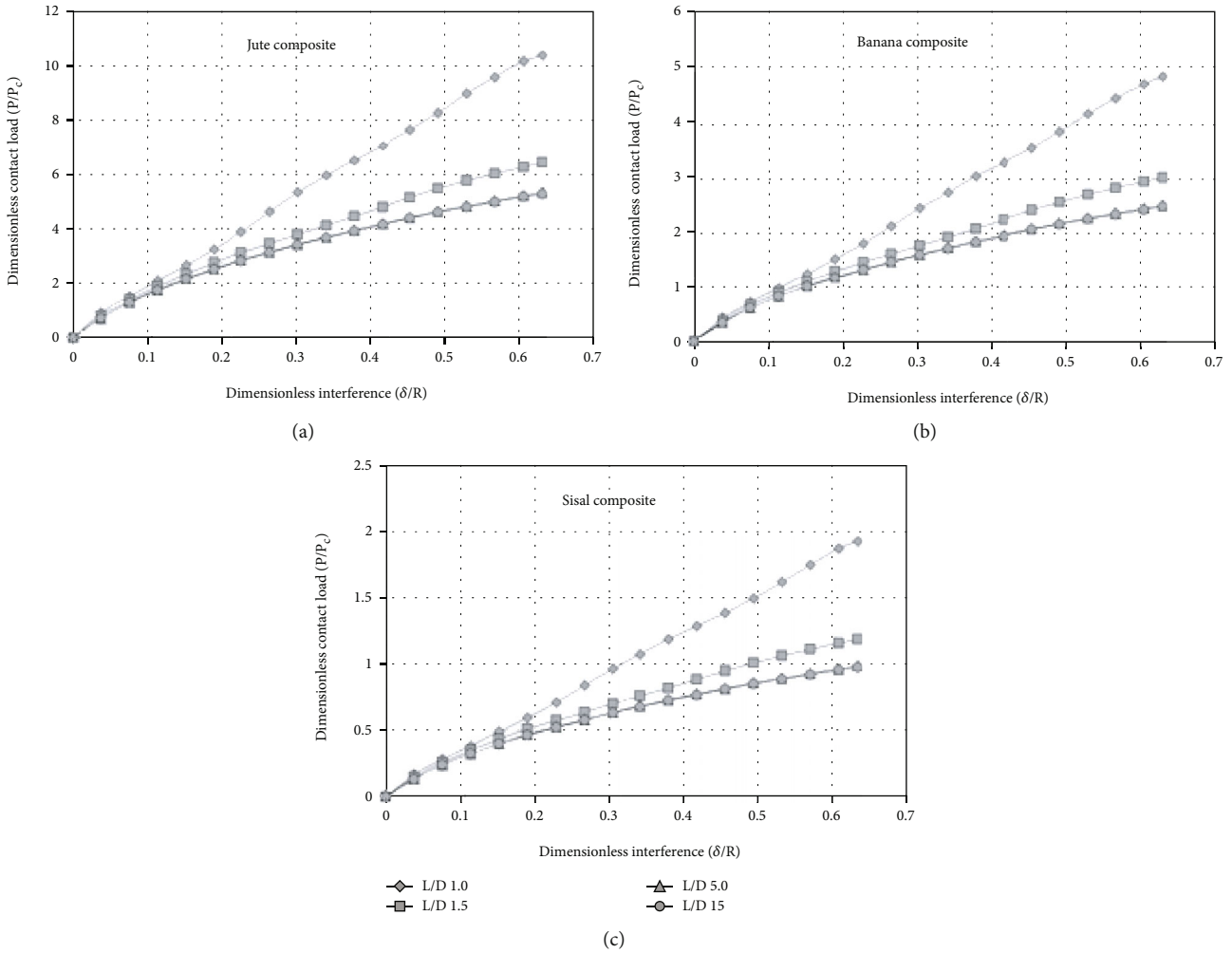
(a)

(b)

(c)

FIGURE 18: Response of contact load ratio vs interference ratio for various L/D ratios of composites.

3.2.1. Effect of Contact Load. The response of contact load ratio against the interference ratio for the L/D ratios of 1.0, 1.5, 5.0, and 15 is shown in Figures 15(a)–15(d).

As the interference ratio increases the contact load ratio increases for all fiber-reinforced composites. The load-bearing capacity of all the composites decreases with increase in L/D ratio. The jute fiber-reinforced composite shows high load-carrying capacity compared to all other fiber-reinforced composites. The sisal fiber-reinforced composite has low load-carrying capacity and the banana fiber-reinforced composites shows an intermediate behavior as L/D ratio increases.

3.2.2. Effect of Contact Area. From the analysis results, the contact area for every step is calculated. The response of the contact area ratio against the interference ratio for the L/D ratios of 1.0, 1.5, 5.0, and 15 is shown in Figures 16(a)–16(d). The response of the contact area ratio against the contact load ratio for various L/D ratios of 1.0, 1.5, 5.0, and 15 is shown in Figures 17(a)–17(d).

As the interference ratio increases, the contact area ratio increases nonlinearly for all fiber-reinforced composites. The

jute fiber-reinforced composite shows large load-bearing area compared to all other fiber-reinforced composites. As the L/D ratio increases, the load-bearing area slightly decreases for all the composites.

3.2.3. Effect of E/Y Ratio on Contact Area against Contact Load. As the contact load ratio increases, the contact area ratio also increases linearly, but on the other hand as the L/D ratio increases, the load-bearing area also increases for increasing dimensionless load in all the composites due to the variation in E/Y ratio.

3.2.4. Effect of L/D Ratio on Contact Load against Interference. The influence of the L/D ratio on the contact load ratio against the interference ratio and dimensionless contact area shows significant difference in all the composites.

In Figure 18, the load-bearing capacity is high for jute composite, for sisal composite is low and intermediate for banana composite, but as the dimensionless interference increases, the load-bearing capacity decreases for increasing L/D ratio.

In Figures 19(a)–19(c), for the high L/D ratio, the load-bearing area is high only at low load ratio, but for high load
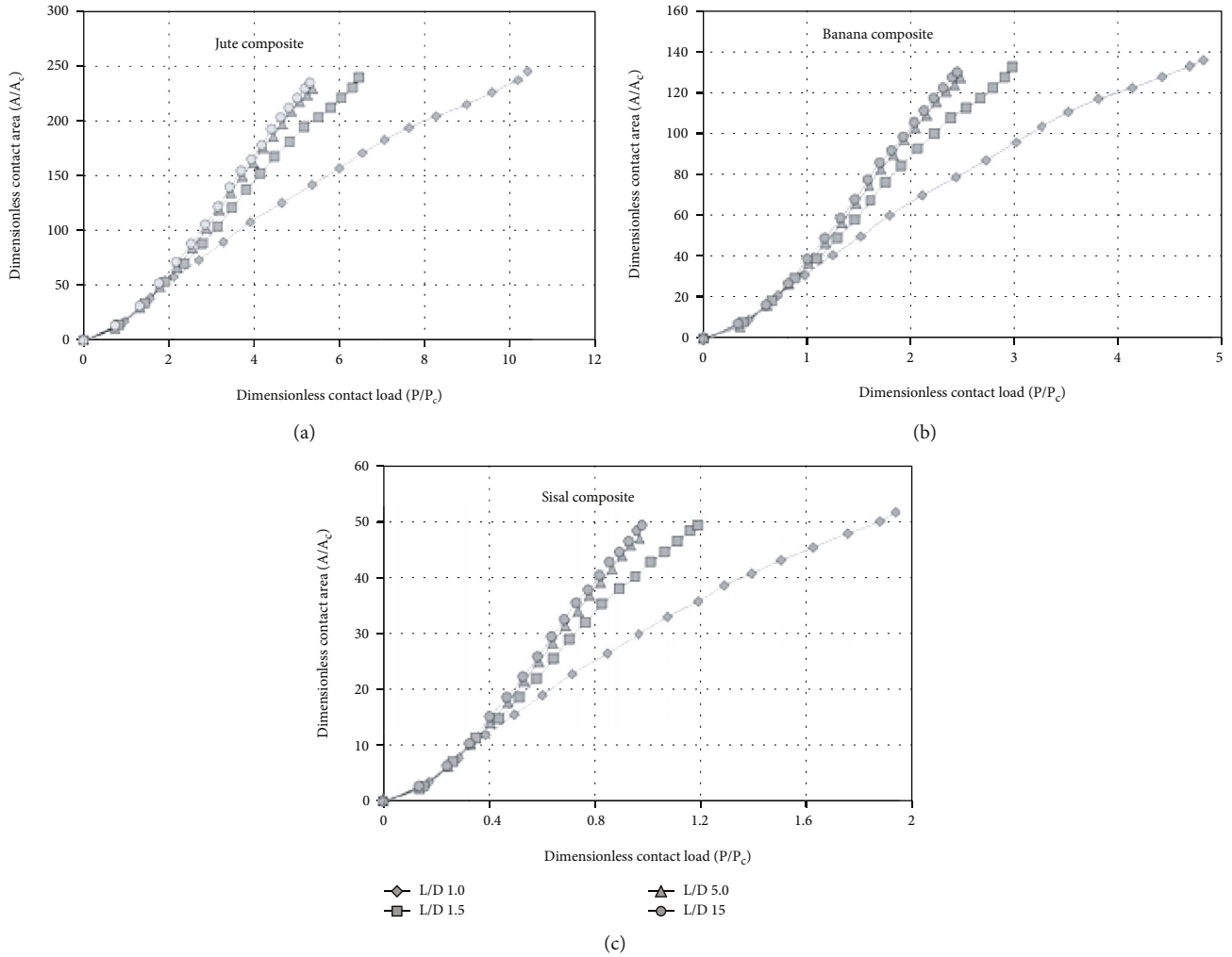
(a)

(b)

(c)

FIGURE 19: Response of contact area ratio against contact load ratio for various L/D ratios of composites.

ratio, the load-bearing area increases for smaller L/D ratio, and similar behaviors are observed in banana and sisal composites, but their load-bearing area and load-carrying capacity are less.

3.2.5. Effect of L/D Ratio on Von Mises Stress Distribution.
The resultant Von Mises stress plots for jute-polypropylene composite at δ/R of 0.529133 for different L/D ratios are shown in Figures 20(a)–20(d). As the L/D ratio increases the maximum stress decreases.

The resultant Von Mises stress plots for banana-polypropylene composite at δ/R of 0.529133 for different L/D ratios are shown in Figures 21(a)–21(d). As the L/D ratio increases the maximum stress decreases.

The resultant Von Mises stress plots for sisal-polypropylene composite at δ/R of 0.529133 for different L/D ratios are shown in Figures 22(a)–22(d). As the L/D ratio increases, the maximum stress decreases.

Empirical relations are developed for contact parameters with variables as dimensionless interference and ratio of dis-

tance between fiber centers to diameter of fiber:

$$
\begin{aligned}
\frac{P}{P_c} =\ & -3966.91 + 3966.0027\,\frac{\delta}{R} - 303.25\left(\frac{\delta}{R}\right)^{1.5} \\
& - 1767.20\ \left(\frac{\delta}{R}\right)^2 - \frac{193.79\delta/R}{\ln \delta/R} + 3956.94\left(-193.79^{-\delta/R}\right) \\
& - 2.07\left(\frac{L}{D}\right) - 13.020\left(\frac{L}{D}\right)\ln\left(\frac{L}{D}\right) + 11.366\left(\frac{L}{D}\right)^{1.5},
\end{aligned}
$$

$$
\begin{aligned}
\frac{A}{A_c} =\ & -412.85 + 267.56\,\frac{\delta}{R} + 1664.56\left(\frac{\delta}{R}\right)^2 - 18099.34\left(\frac{\delta}{R}\right)^3 \\
& + 64608.36\left(\frac{\delta}{R}\right)^4 - 77774.008\left(\frac{\delta}{R}\right)^5 + 729.37\left(\frac{L}{D}\right) \\
& - 478.78\left(\frac{L}{D}\right)^2 + 138.04\left(\frac{L}{D}\right)^3 - 14.75\left(\frac{L}{D}\right)^4.
\end{aligned}
$$

$$(1)$$

L/D 1

L/D 1.5

(a)

(b)

L/D 5

L/D 15

(c)

(d)
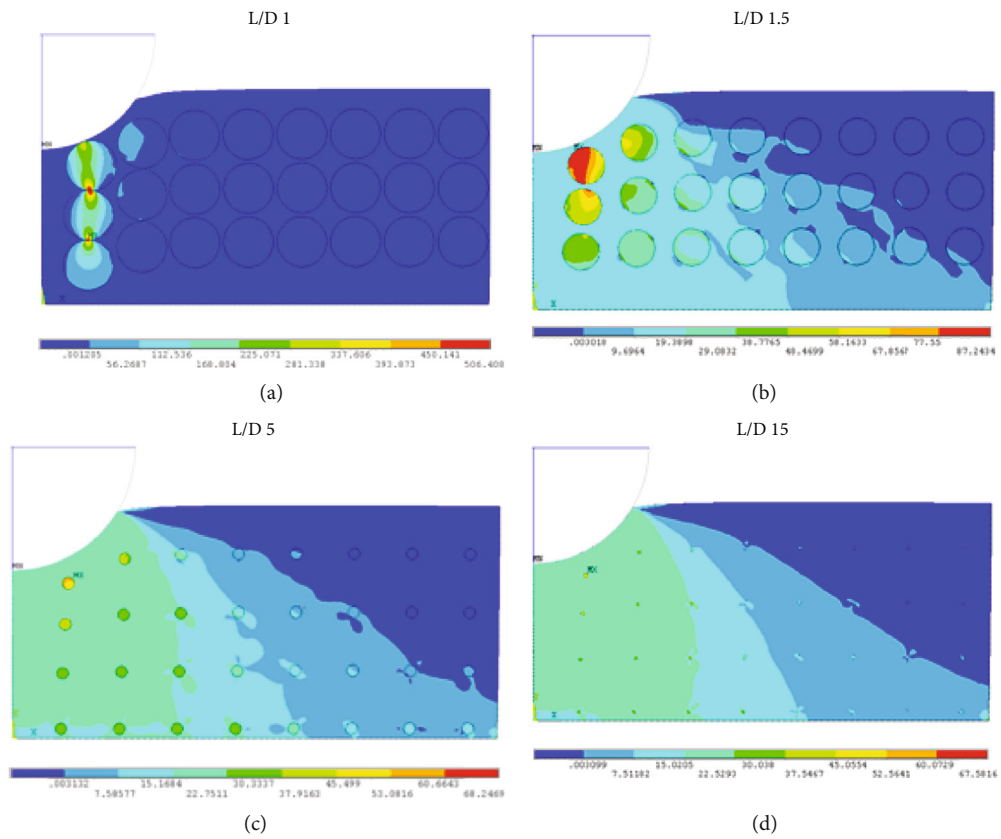
Figure 20: Von Mises stress plot for jute-polypropylene composite for various *L/D* ratios.

L/D 1

L/D 1.5

(a)

(b)

L/D 5

L/D 1.5

(c)

(d)
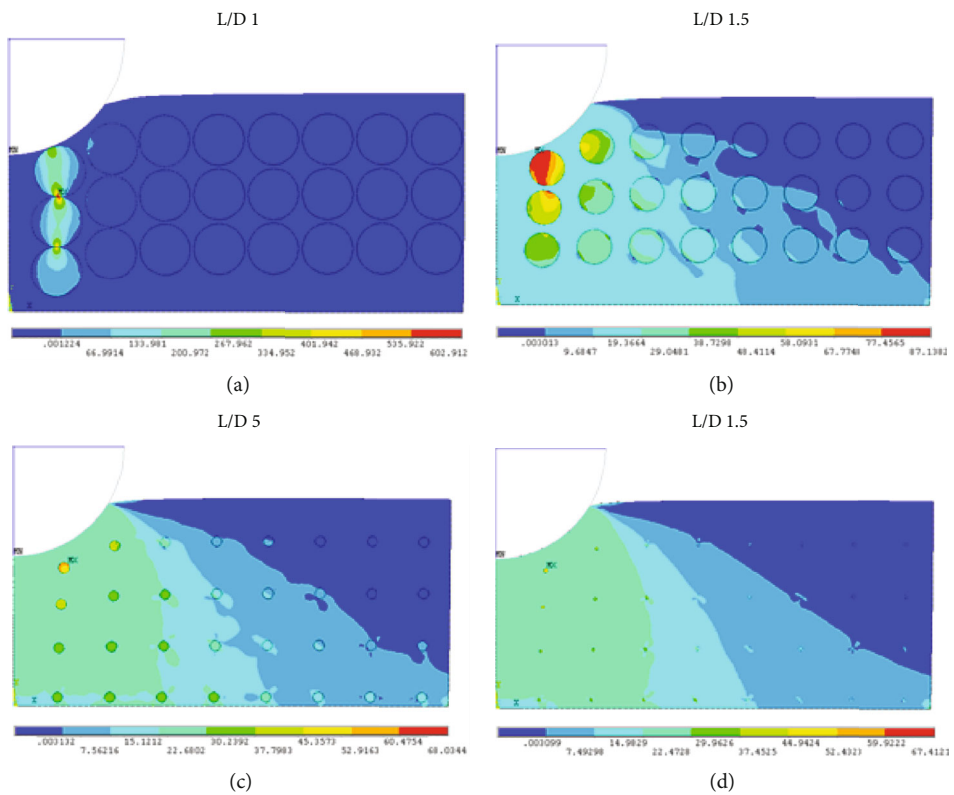
Figure 21: Von Mises stress plot for banana-polypropylene composite for various *L/D* ratios.

L/D 1

L/D 1.5

(a)
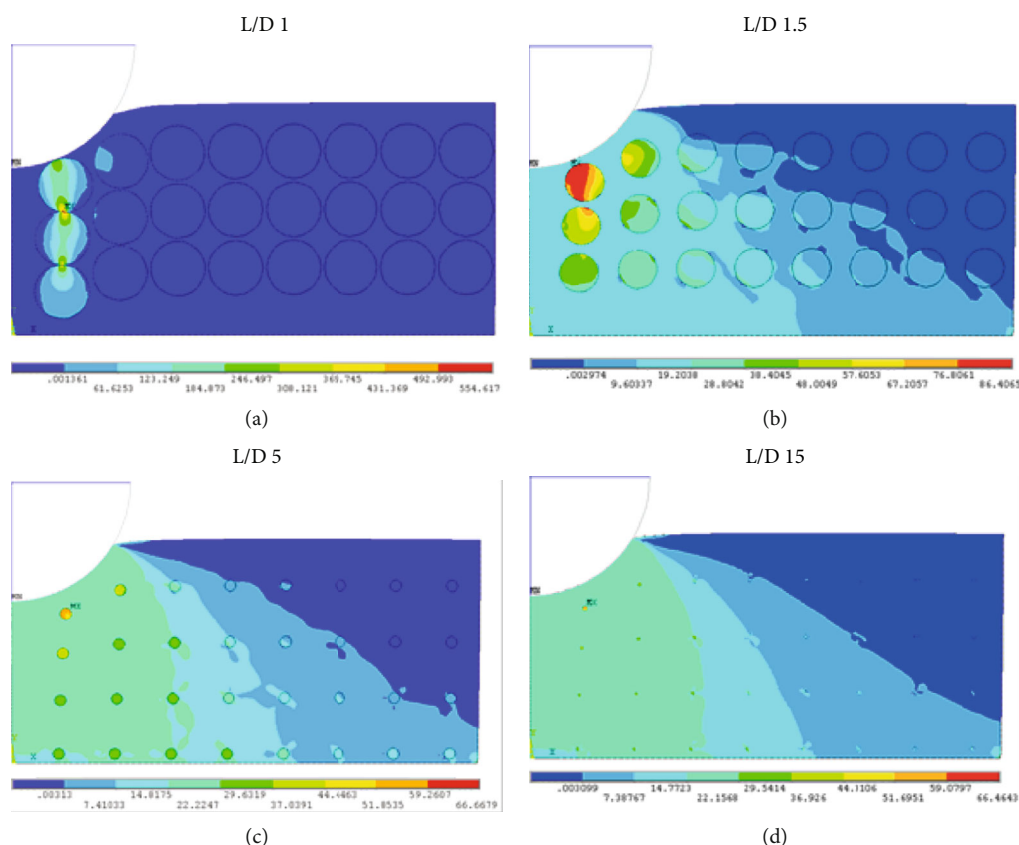
(b)

L/D 5

L/D 15

(c)

(d)

Figure 22: Von Mises stress plot for sisal-polypropylene composite for various L/D ratios.

4. Conclusion

Indentation analyses are carried on sisal-polypropylene, jute-polypropylene, and banana-polypropylene natural composites through finite element method. The results revealed that the neat polypropylene undergone three different modes of (elastic, elastoplastic, and full plastic) deformation regimes, but the indentation of the sisal-polypropylene, jute-polypropylene, and banana-polypropylene composites exposed only elastic deformation and stayed away from the elastic-plastic and plastic deformations.

As the distance between fiber centers increases, the contact load ratio increases nonlinearly for all composites. The load-carrying capacity of jute fiber composite is six times, and the bearing area ratio is five times greater than sisal fiber composite at maximum interference ratio. The impact of subsurface stress gets reduced as the distance between fiber centers increases. Compared to varying the distance between the fiber's center, the variation in diameter of fiber influences significantly. After the L/D ratio of 1.0, for the same contact load ratio, the bearing area support is double for jute-polypropylene composite compared to sisal-polypropylene composite. Compared to the sisal-polypropylene composite, for the same interference ratio, the load-carrying capacity is two times high for banana-polypropylene composite, whereas four times high for jute-polypropylene composite compared to sisal-polypropylene composite, but this effect decreases as the L/D ratio decreases. The subsurface stress

gets distributed in all composites as the L/D ratio increases. In overall, the jute-polypropylene composite shows a high load-carrying capacity than other composites so this can be utilized in high load-carrying applications.

Generalized empirical relations are developed to appropriately calculate contact load, contact area with variables as interference ratio, and ratio of distance between the fiber centers and diameter of fiber.

Data Availability

The data are made available within this article.

Conflicts of Interest

The authors declare that they have no conflict of interest.

References

[1] A. Verma, A. Gaur, and V. K. Singh, "Mechanical properties and microstructure of starch and sisal fiber biocomposite modified with epoxy resin," *Materials Performance and Characterization*, vol. 6, no. 1, pp. 20170069–20170520, 2017.

[2] A. Verma, K. Joshi, A. Gaur, and V. K. Singh, "Starch-jute fiber hybrid biocomposite modified with an epoxy resin coating: fabrication and experimental characterization," *Journal of the Mechanical Behavior of Materials*, vol. 27, no. 5-6, 2018.

[3] A. Verma, C. Singh, V. K. Singh, and N. Jain, "Fabrication and characterization of chitosan-coated sisal fiber–phytagel

modified soy protein-based green composite," *Journal of Composite Materials*, vol. 53, no. 18, pp. 2481–2504, 2019.

[4] R. Vijay, D. Lenin Singaravelu, A. Vinod et al., "Characterization of raw and alkali treated new natural cellulosic fibers from _Tridax procumbens_," *International Journal of Biological Macromolecules*, vol. 125, pp. 99–108, 2019.

[5] S. Dinesh, P. Kumaran, S. Mohanamurugan et al., "Influence of wood dust fillers on the mechanical, thermal, water absorption and biodegradation characteristics of jute fiber epoxy composites," *Journal of Polymer Research*, vol. 27, no. 1, p. 9, 2020.

[6] S. Jothibasu, S. Mohanamurugan, R. Vijay, D. Lenin Singaravelu, A. Vinod, and M. R. Sanjay, "Investigation on the mechanical behavior of areca sheath fibers/jute fibers/glass fabrics reinforced hybrid composite for light weight applications," *Journal of Industrial Textiles*, vol. 49, no. 8, pp. 1036–1060, 2020.

[7] R. Vijay, A. Vinod, R. Kathiravan, S. Siengchin, and S. D. Lenin, "Evaluation of Azadirachta indica seed/spent Camellia sinensis bio-filler based jute fabrics-epoxy composites: experimental and numerical studies," *Journal of Industrial Textiles*, vol. 49, no. 9, pp. 1252–1277, 2020.

[8] R. Vijay, S. Manoharan, S. Arjun, A. Vinod, and D. Lenin Singaravelu, "Characterization of silane-treated and untreated natural fibers from stem of Leucas Aspera," *Journal of Natural Fibers*, vol. 18, no. 12, pp. 1957–1973, 2021.

[9] R. Vijay, J. D. James Dhilip, S. Gowtham et al., "Characterization of natural cellulose fiber from barks of Vachellia farnesiana," *Journal of Natural fibers*, vol. 19, no. 4, pp. 1343–1352, 2022.

[10] R. Sathish Kumar and D. M. Nivedhitha, "Mechanical characteristics study of chemically modified kenaf fiber reinforced epoxy Composites," *Journal of Natural Fibers*, vol. 19, no. 7, pp. 2457–2467, 2022.

[11] D. Tabor, *The Hardness of Metals*, Clarendon Press, Oxford, England, 1951.

[12] A. Y. Ishlinsky, "Axially symmetric problem in plasticity and Brinell's hardness test," *Journal of Applied Mathematics and Mechanics (Russian Translation is Prikladnaya Matematika i Mekhanika)*, vol. 8, pp. 201–224, 1994.

[13] R. Hill, *The Mathematical Theory of Plasticity*, Oxford University Press, London, 1967.

[14] K. L. Johnson, *Contact Mechanics*, Cambridge University Press, Cambridge, England, 2012.

[15] L. E. Samuels and T. O. Mulhearn, "An experimental investigation of the deformed zone associated with indentation hardness impressions," *Journal of the Mechanics and Physics of Solids*, vol. 5, no. 2, pp. 125–134, 1957.

[16] C. C. Hardy, C. N. Baronet, and G. V. Tordion, "The elasto-plastic indentation of a half-space by a rigid sphere," *International Journal for numerical methods in engineering*, vol. 3, no. 4, pp. 451–462, 1971.

[17] P. S. Follansbee and G. B. Sinclair, "Quasi-static normal indentation of an elasto-plastic half-space by a rigid sphere-I. Analysis," *International journal of solids and structures*, vol. 20, no. 1, pp. 81–91, 1984.

[18] A. E. Giannakopoulos, P. L. Larsson, and R. Vestergaard, "Analysis of vickers indentation," *International Journal of Solids and Structures*, vol. 31, no. 19, pp. 2679–2708, 1994.

[19] K. Komvopoulos and N. Ye, "Three-dimensional contact analysis of elastic-plastic layered media with fractal surface topog-

[20] Y. J. Park and G. M. Pharr, "Nanoindentation with spherical indenters: finite element studies of deformation in the elastic-plastic transition regime," *Thin Solid Films*, vol. 447, pp. 246–250, 2004.

[21] S. D. Mesarovic and N. A. Fleck, "Spherical indentation of elastic-plastic solids," *Proceedings of the Royal Society of London. Series A: Mathematical, Physical and Engineering Sciences*, vol. A455, pp. 2707–2728, 1999.

[22] A. K. Bhattacharya and W. D. Nix, "Finite element simulation of indentation experiments," *International Journal of Solids and Structures*, vol. 24, no. 9, pp. 881–891, 1988.

[23] J. A. Knapp, D. M. Follstaedt, S. M. Myers, J. C. Barbour, and T. A. Friedmann, "Finite-element modeling of nanoindentation," *Journal of Applied Physics*, vol. 85, no. 3, pp. 1460–1474, 1999.

[24] R. L. Jackson and I. Green, "A finite element study of elasto-plastic hemispherical contact," in *Proceedings of the STLE/ASME 2003 International Joint Tribology Conference. Contact Mechanics*, pp. 65–72, Ponte Vedra Beach, Florida, USA, October 2003.

[25] W. R. Chang, I. Etsion, and D. B. Bogy, "An elastic-plastic model for the contact of rough surfaces," *The Journal of Tribology*, vol. 109, no. 2, pp. 257–263, 1987.

[26] C. Thornton, "Coefficient of restitution for collinear collisions of elastic perfectly plastic spheres," *Journal of Applied Mechanics*, vol. 64, no. 2, pp. 383–386, 1997.

[27] S. Kocharski, T. Klimczak, A. Polijaniuk, and J. Kaczmarek, "Finite-elements model for the contact of rough surfaces," *Wear*, vol. 177, no. 1, pp. 1–13, 1994.

[28] L. Vu-Quoc, X. Zhang, and L. Lesburg, "A normal force-displacement model for contacting spheres accounting for plastic deformation: force-driven formulation," *Journal of Applied Mechanics*, vol. 67, no. 2, pp. 363–371, 2000.

[29] L. Kogut and I. Etsion, "Elastic-plastic contact analysis of a sphere and a rigid flat," *Journal of Applied Mechanics*, vol. 69, no. 5, pp. 657–662, 2002.

[30] J. J. Quicksall, R. L. Jackson, and I. Green, "Elasto-plastic hemispherical contact models for various mechanical properties," *Proceedings of the Institution of Mechanical Engineers, Part J: Journal of Engineering Tribology*, vol. 218, no. 4, pp. 313–322, 2004.

[31] R. L. Jackson and I. Green, "A finite element study of elasto-plastic hemispherical contact against a rigid flat," *Journal of Tribology*, vol. 127, no. 2, pp. 343–354, 2005.

[32] V. Brizmer, Y. Kligerman, and I. Etsion, "The effect of contact conditions and material properties on the elasticity terminus of a spherical contact," *International Journal of Solids and Structures*, vol. 43, no. 18-19, pp. 5736–5749, 2006.

[33] A. Ovcharenko, G. Halperin, G. Verberne, and I. Etsion, "In situ investigation of the contact area in elastic-plastic spherical contact during loading-unloading," *Tribology Letters*, vol. 25, no. 2, pp. 153–160, 2007.

[34] R. L. Jackson and L. Kogut, "A comparison of flattening and indentation approaches for contact mechanics modeling of single asperity contacts," *Journal of Tribology*, vol. 128, no. 1, pp. 209–212, 2006.

[35] L. Kogut and K. Komvopoulos, "Analysis of the spherical indentation cycle for elastic-perfectly plastic solids," *Journal of Materials Research*, vol. 19, no. 12, pp. 3641–3653, 2004.

raphies," *Journal of Tribology*, vol. 123, no. 3, pp. 632–640, 2001.

[36] A. Wagh, P. Maimi, N. Blanco, and D. Trias, "Predictive model for the spherical indentation of composite laminates with finite thickness," *Composite Structures*, vol. 153, pp. 468–477, 2016.

[37] L. Zhou, S. Wang, L. Li, H. Wei, and A. Dai, "An approximate solution of the spherical indentation on a generally anisotropic elastic half-space," *International Journal of Solids and Structures*, vol. 161, pp. 174–181, 2019.

[38] Y. Cao, X. Qian, and N. Huber, "Spherical indentation into elastoplastic materials: Indentation-response based definitions of the representative strain," *Materials Science and Engineering: A*, vol. 454-455, pp. 1–13, 2007.

[39] N. Venkateshwaran and A. Elayaperumal, "Banana fiber reinforced polymer composites-a review," *Journal of Reinforced Plastics and Composites*, vol. 29, no. 15, pp. 2387–2396, 2010.

[40] M. Haque, S. Islam, S. Islam, N. Islam, M. Huque, and M. Hasan, "Physicomechanical properties of chemically treated palm fiber reinforced polypropylene composites," *Journal of Reinforced Plastics and Composites*, vol. 29, no. 11, pp. 1734–1742, 2010.

[41] T. H. Quazi, A. K. Shubhra, M. M. Alam, and M. A. Quaiyyum, "Mechanical properties of polypropylene composites: a review," *Journal of Thermoplastic Composite Materials*, vol. 26, no. 3, pp. 362–391, 2013.

♦SAGE
Publishing

Research Article

Garlic Peel Surface Modification and Fixed-Bed Column Investigations towards Crystal Violet Dye

E. Pravin Raaj,[1] K. Bhuvaneshwari,[1] R. Lakshmipathy ⓘ,[2] V. Vandhana Devi,[1] and Ivan Leandro Rodriguez Rico ⓘ[3]

[1]*Department of Civil Engineering, KCG College of Technology, Karapakkam, Chennai 600097, India*
[2]*Department of Chemistry, KCG College of Technology, Karapakkam, Chennai, 600097, India*
[3]*Faculty of Chemical and Pharmacy, Department of Chemical Engineering, Central University "Marta Abreu" of Las Villas, Cuba*

Correspondence should be addressed to R. Lakshmipathy; lakshmipathy.che@kcgcollege.com
and Ivan Leandro Rodriguez Rico; ivanl@uclv.edu.cu

Garlic peel, a low-cost agro-waste, was explored as an adsorbent for the remediation of wastewater containing the crystal violet (CV) cationic dye. The garlic peel was treated with NaOH at $1:1.5$ ratios in order to modify the surface and increase its porosity. The surface-modified garlic peel was ground to a smaller size in order to increase its surface area and used as an adsorbent in the continuous column investigations. Column parameters such as bed height, flow rate, and initial concentration were optimised and found that optimal removal efficiency was achieved at 3 ml rate of flow, 3 cm column depth, and $100\,\text{mg}\,\text{l}^{-1}$ initial concentration. The surface-modified garlic peel exhibited a higher loading capacity of $99.9\,\text{mg}\,\text{g}^{-1}$ towards CV at optimised conditions. SEM investigations confirmed the surface modification and increase in porosity of the garlic peel. The column data was tending to fit well with Thomas and Yoon-Nelson's models suggesting the scalability to an industrial level. Regeneration of MGP was successful with 0.01 M HCl solution. These results conclude that garlic peel is a potential agro-waste material that can be used to mitigate water pollution.

1. Introduction

Environmental pollution is considered to be one of the biggest threats to human and animal life and number of mortalities reported due to environmental pollution is rising year by year [1]. Industrial revolutions in developed and developing countries are one major source for environmental pollution. Textile and dyeing industries are inevitable part of our life and these industries utilise various dyes for manufacturing and the effluents released from these industries are not fit for use in any forms. Hence, it is highly desirable to treat the effluents from textile and dyeing industries prior to its release or reuse. Treatments techniques include chemical oxidation [2], photodegradation [3], biological process [4], and adsorption [5].

All the treatment techniques have their own merits and demerits; however, adsorption is a powerful and dominant technique compared to other techniques that are used in treatment process. Various adsorbents such as activated carbon [6], zeolites [7], agro-wastes [8], nanomaterials [9], and composites [10] are successfully demonstrated for the treatments of coloured water especially dye-loaded wastewaters. Agro-wastes find special applications in adsorption due to their cost and eco-friendly nature and their availability. Several agro-wastes have been reported in the literature to date for the remediation of cationic and anionic dyes from wastewater. Untreated agro-wastes suffer from poor adsorption capacity due to low porosity and presence of cations. The adsorption capacity of agro-wastes can be improvised to a greater extent by surface modification and chemical treatments [11]. Inline to the modifications, this study aims at use of a surface-modified agro-waste as an adsorbent for the elimination of synthetic dyes from aqueous solution.

Garlic is a common and key ingredient used in several recipes prepared all over the world and the peel waste is usually discarded due to its unpleasant taste. The garlic peel (GP) waste usually contributes for 16-20% mass of the garlic which amounts to approximately 3 million tons per year [12]. The peels are rich in nutrients and often used in composting and it can be effectively utilised as adsorbents. Hameed and Ahmed proposed garlic peel as an adsorbent for the methylene blue removal from aqueous solution in batch process [13]. Liang et al. suggested the use of garlic peel for the elimination of multi-metal ions from wastewater [14]. Asfaram et al. highlighted the use of garlic peel in removal of direct red 12B as an economical adsorbent [15]. In another study, Liu et al. reported the comparative investigation of native and mercerised garlic peel for the removal of Pb ions [16]. Yanjun et al. chemically modified the garlic peel as used in the adsorption of quinolone antibiotics [17]. In spite of its abundant availability and tendency, the garlic peels are less explored and their ability towards organic contaminants remediation must be established.

This study aims at surface modifications of garlic peels with caustic and further investigates its efficiency towards crystal violet removal in continuous process. The novelty of this investigation is the surface modification of low-cost adsorbent such as garlic peel with economical reagent such as NaOH and employing it in fixed-bed column investigations.

2. Materials and Methods

2.1. Garlic Peel Adsorbent Preparation. Garlic peels (GP) were collected from local agro industry and the peels were washed with tap water to remove any dirt and dust. The water-washed peels were dried under sunlight for four days and later it was ground to small pieces. For surface modifications, garlic peel and sodium hydroxide were mixed in 1 : 1.5 ratios and heated at 100°C for 120 min in a hot air oven. Post heat treatment, the peels were washed with excess water to remove the sodium hydroxide and bring it to neutral pH. The water-washed peel samples were once again dried in oven at 100°C for 120 min and dry samples were kept named as modified garlic peels (MGP) and stored in containers for further use.

2.2. Stock Solution. The stock solution was made by dispersing exactly 1 g of crystal violet dye in 1 L of distilled water. Later, appropriate lower dilutions were made depending on the requirements.

2.3. Fixed-Bed Studies. Fixed-bed studies are considered to be one of the important and prominent investigations in the case of real-time water treatment at industry level. Since the preliminary data obtained can be scaled up to industrial scale level, these studies find unique attention among the community. Investigations were performed for the elimination of crystal violet dye from synthetic solutions with MGP as an adsorbent. The MGP (approximately $0.862\,\mathrm{g\,cm^{-1}}$) was packed in a pencil column of 20 cm height with an internal diameter of 2 cm. The CV stock was allowed from the top of the column at a fixed rate controlled with a peristaltic
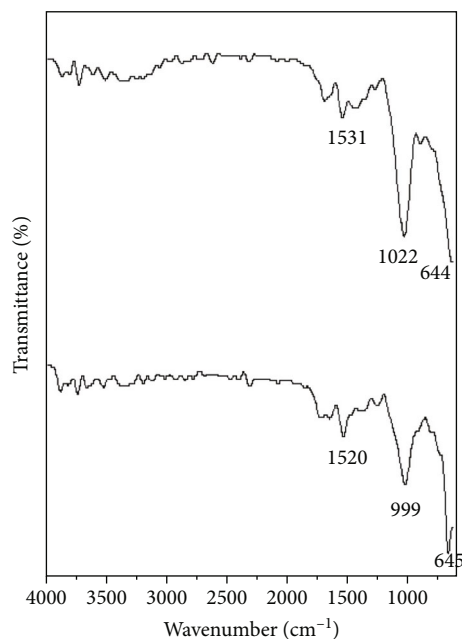

FIGURE 1: FTIR spectra of modified and unmodified garlic peels.

pump. Column parameters such as flow rate, bed height, and initial concentration were tested and optimised. Each parameter under investigation was varied while keeping the other parameters constant. The flow rate was investigated between 3 and 7 ml, bed height at 1, 2, and 3 cm, and initial concentrations between 100 and 300 ppm. The inlet of CV solution was continued until the concentration of input and output remains the same considering the column is saturated [18]. All the samples collected were subjected to UV-visible spectrophotometer to determine the residual concentration of CV at 590 nm.

2.4. Data Analysis. The output of any fixed-bed columns is generally expressed as breakthrough curves and the dynamic behaviour of the columns can be understood by the curve shapes which is considered to be crucial characteristic [19]. The S form curves obtained in breakthrough curves are examined when the output concentration of column reached 0.1% of input concentration and the same is considered to be saturated when the concentration reached 95% of influent. Finally, the volume of effluent (V_{eff}), amount of CV uptake (D_{ad}), absolute quantity of CV dye (D_{total}), and removal % of CV can be determined by the following equations:

$$V_{\mathrm{eff}} = Q t_{\mathrm{total}}, \tag{1}$$

where the volumetric flow rate is denoted with V_{eff} and the total flow time with t_{total}.

$$D_{\mathrm{ad}} = \frac{Q}{1000} \int_{t=0}^{t=\mathrm{total}} C_{\mathrm{ad}} dt, \tag{2}$$

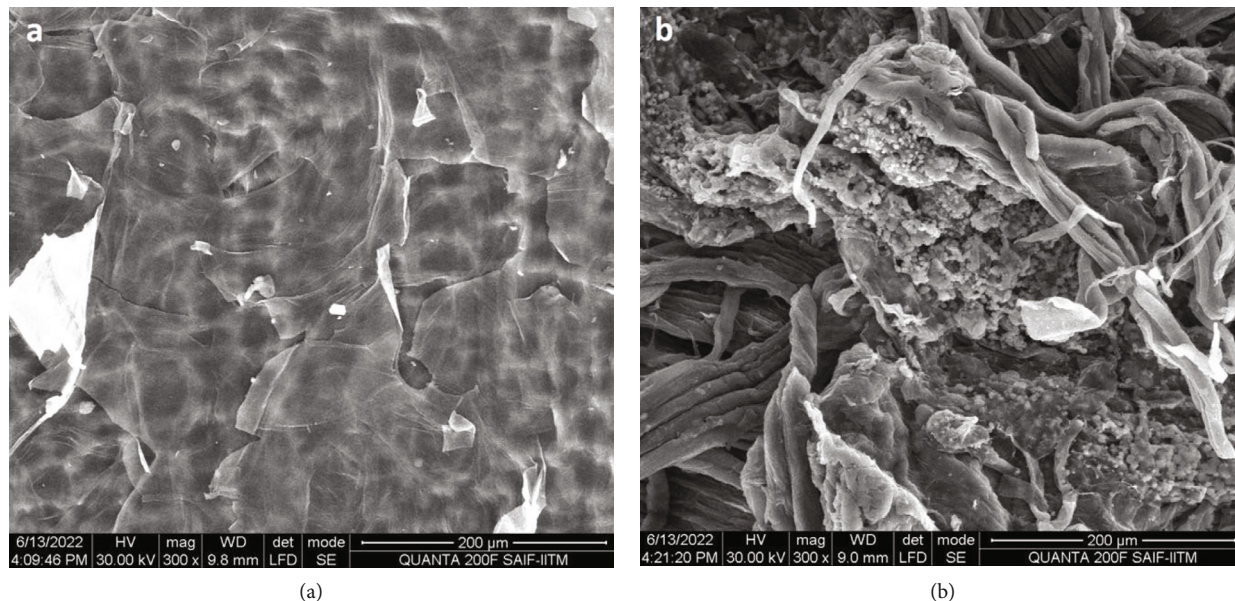where C_{ad} is the quantity of CV removed.

FIGURE 2: SEM image of (a) unmodified GP and (b) modified GP.

$$D_{\text{total}} = \frac{C_0 Qt_{\text{total}}}{1000}, \qquad (3)$$

$$R\,(\%) = \frac{D_{\text{ad}}}{D_{\text{total}}}\,x100, \qquad (4)$$

where $R\,(\%)$ is the removal percentage.

2.5. Adsorbent Characterisation. The surface-modified garlic peel was characterised with Fourier Transform Infrared (FTIR), Scanning Electron Microscope (SEM), and Energy Dispersive X-ray (EDX) techniques to understand the changes and modifications. The FTIR analysis was carried out between 4000 and 400 cm^{-1} in Thermo Nicolet Avater 360 equipment. The SEM images of unmodified and modified garlic peels were captured with Quanta 200F FEI instrument equipped with EDX detector. The elemental composition of the garlic peel was obtained from EDX detector of SEM instrument.

3. Results and Discussion

The modified garlic peel (MGP) was subjected to FTIR, SEM, and EDX analyses in order to determine the surface functional groups, porosity, and elemental changes in comparison to the unmodified garlic peel.

The FTIR spectra of modified and unmodified garlic peels are shown in Figure 1. The FTIR spectra displayed were few intense peaks for unmodified garlic peel. A weak peak at 1720 cm^{-1} corresponding to stretching vibrations of carbonyl group (C=O) and a sharp medium peak at 1531 cm^{-1} corresponding to stretching vibrations C-C ring were observed. A strong sharp peak at 1022 corresponds to C-C bending vibrations of esters. A strong sharp peak at 645 corresponds to the metal-oxide bond vibration which is attributed to Ca-O bond since the presence of calcium in

garlic peels is evident from EDX patterns. It is observed that the functional groups and peaks remain unchanged even after surface modification with NaOH suggesting that the surface modification has not impacted the functional groups present on the garlic peels.

The SEM images of unmodified and modified garlic peels are represented in Figure 2. The surface of unmodified garlic peel is smooth with no evidence of porosity (Figure 2(a)). In the case of modified garlic peel, the surface is not smooth as seen in the unmodified garlic peel and the surface looks completely distorted during the treatment with NaOH (Figure 2(b)). The fibres of garlic peel are exposed and look porous in nature. These observations suggest that the surface modification is successfully achieved with NaOH.

The EDX patterns of the modified and unmodified garlic peels are represented in Figure 3. It is noticed that the unmodified garlic peel contains various minerals such as Ca, Mg, K, and Cl (Figure 3(a)). After surface treatment with NaOH, the elements such as Mg and K disappeared and these might have leached out during the treatment process (Figure 3(b)). Na element peak suggests the incorporation of Na ions on the surface during the treatment step. Additional elements observed in the modified GP might be due to surface contaminations.

3.1. Optimization of pH of the Solution. The presence of hydronium ion greatly influences any sorption process and system and it is imperative to optimise the H$^+$ concentration of the solution before the fixed-bed column studies are embarked. To understand the optimum pH of the solution; investigations were performed in batch process to optimise the H$^+$ concentration of the solution. The pH was varied between pH 2 and 10 by fixing the other variables such as dose, time, and concentration. The results of the investigation are shown in Figure 4 and it can be noticed that with
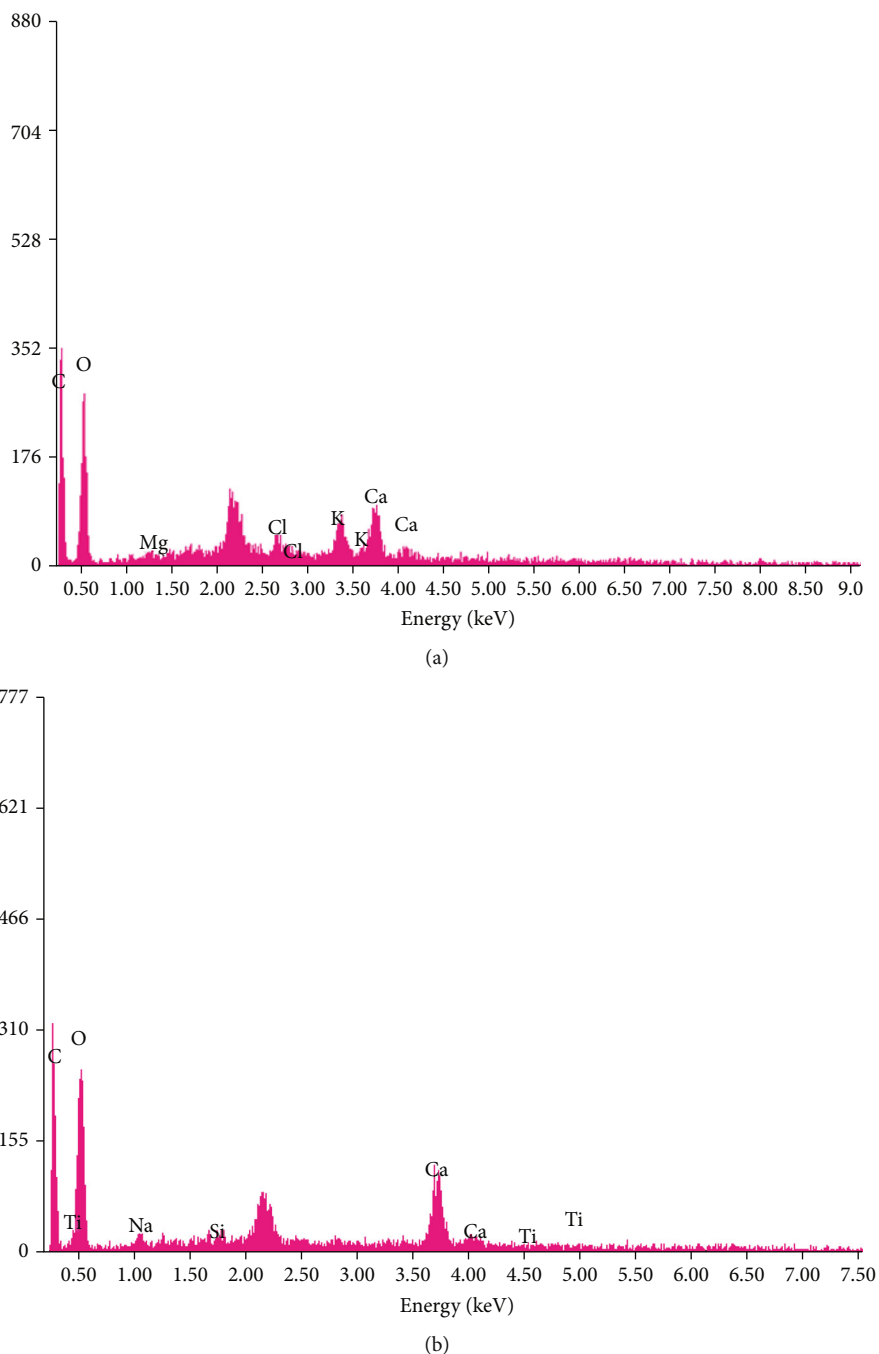
(a)

(b)

Figure 3: EDX patterns of (a) unmodified GP and (b) modified GP.

surging pH, the removal efficiency increased and reached peak at pH 6. Further increase in pH resulted in decrease of the removal efficiency. The increase in efficiency with respect to surging pH is due to reduction in H^+ ions concentration and competitive sorption for sites of active on MGP surface. The decrease in efficiency beyond pH 6 is due to surface of the garlic peel turning positive which could repel the adsorption of cationic dyes. This is successfully explained by the point zero charge of the adsorbent being at pH 5.7. Thus, pH 6 was fixed and set as optimum pH for the fixed-bed investigations of CV removal by MGP.

3.2. Fixed-Bed Column Investigations. The continuous investigations are carried out in a glass column packed with MGP by varying the key parameters of the column and the date obtained are represented in Table 1.

3.2.1. Flow Rate. The rate of flow in the continuous process greatly influences the rate of adsorption and it is considered a crucial parameter to be optimised prior to any scale-up process. Hence, the rate of flow of CV solution into the MGP packed column was investigated by changing the rate of flow and the data and BTC obtained are shown in
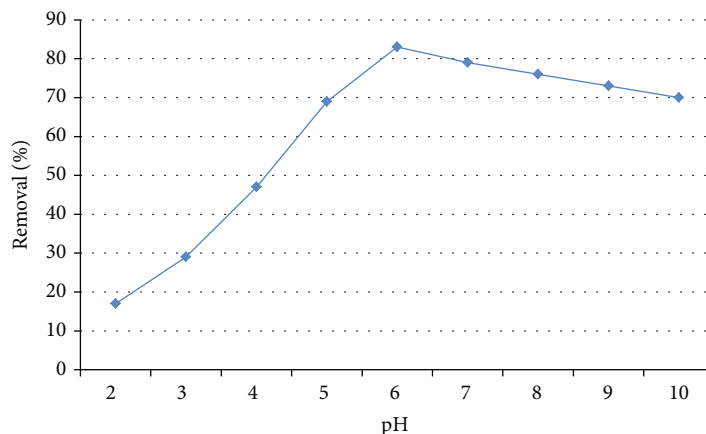
FIGURE 4: Optimization graph for pH for the removal of CV by MGP.

TABLE 1: Continuous column parameters for the removal of CV by MGP.

C_0 (mg l^{-1})	Q (ml min^{-1})	H (cm)	D_{ad} (mg)	D_{total} (mg)	R (%)	EBCT (min)
100	3	1	18.08	45	45.1	1.57
100	5	1	14.4	55	26.3	1.17
100	7	1	7.2	52.5	13.7	0.15
100	3	2	51.4	105	48.9	2.38
100	3	3	99.9	169.5	58.9	3.56
200	3	3	59.6	225	26.4	—
300	3	3	41.4	216	19.1	—

Table 1 and Figure 5. It is seen that with increasing flow rate, the removal percentage and dye adsorption capacity plunged to lower values. The removal percentage decreased from 45.1% to 13.7% suggesting that lower flow rates are desirable. Similarly, the dye adsorption capacities decreased from 18.0 to 7.2 mg g^{-1} suggesting that slower rate of flow increases the rate of adsorption. At low flow rates, the time of residence of CV molecules is high and hence, they have sufficed time to interact with the surface of the MGP to get adsorbed, while increasing the rate of flow decreases the residence time of CV molecules and thus the time of interaction with the surface decreases. Similar trend was reported for methyl green dye by mesoporous materials in continuous process [20].

3.2.2. Bed Height. Bed height is one another crucial parameter of fixed-bed analysis that can decide the economic feasibility of the continuous process. In view of the above, the bed height investigations were performed at different heights and the data and breakthrough curves obtained are summarised and represented in Table 1 and Figure 6. The data interestingly indicates that the percentage removal and loading capacity of MGP towards CV molecules surged with augmented bed heights. As seen from Table 1, the removal percentage increased from 45.1 to 58.9% and the loading capacity also improved significantly from 18.0 to 99.9 mg g^{-1}. The significant loading capacity observed is due to greater mass transfer zone due to increased bed depth of column.
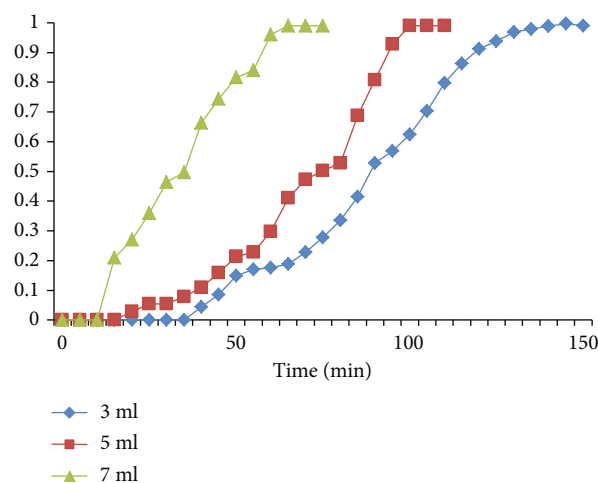
FIGURE 5: Breakthrough curves of variation of flow rate.

The column exhibits more adsorption sites at higher bed heights and thus greater is the adsorption capacity. Similar trend was observed and reported for the CV removal by activated carbon from bamboo leaves [21].

3.2.3. Initial Concentration. The initial concentration of CV solution finds a pivotal role in determining the efficiency and effectiveness of the fixed-bed columns. In order to know the influence of initial concentrations on the continuous

FIGURE 6: Breakthrough curves of variation of bed height.

FIGURE 7: Breakthrough curves of variation of initial concentration.

process, experiments were run on varying the initial concentration of CV solution and the data and breakthrough curves are shown in Figure 7 and Table 1. It is noticed that with increasing initial concentrations, the breakthro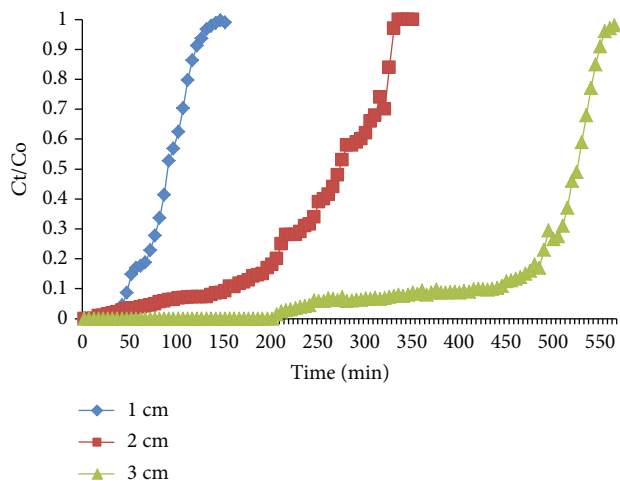ugh points started appearing early and in addition to that, the removal efficiency was significantly plunged to lower values. Following the trend, the loading capacity also went down from $99.9 \, \text{mg} \, \text{g}^{-1}$ to $41.4 \, \text{mg} \, \text{g}^{-1}$. This is due to the competitive adsorption among the CV molecules at high concentrations and lack of surface active sites for adsorption. Similar trend was reported for CV removal by *Citrullus Lanatus* Rind in continuous studies [22].

3.3. *Mathematical Models.* Mathematical models play a crucial role in predicting the data and breakthrough curves obtained from continuous process and it is also handy in scaling up the bench scale process to industrial systems for real-time applications. In view of the above, various mathematical models and equations were developed for the purpose and in this study, most widely used models such as Adams-Bohart, Thomas, and Yoon-Nelson equations were adopted and applied for the data obtained.

3.3.1. *Adams-Bohart Model.* Continuous column data and the breakthrough curves are generally predicted with the Adams-Bohart model due to its ease of application and information obtained [23]. This model is helpful in predicting the initial breakthrough curves of the sorption system and suggests that the fraction of adsorbate coming is proportional to adsorption rate. The equation is given as

$$\ln \frac{C_t}{C_0} = k_{\text{AB}} C_0 t - k_{\text{AB}} N_0 \frac{z}{U_0}. \qquad (5)$$

A graph of ($\ln C_0/C_t$) vs t was plotted and the values of t were considered up to 0.5 of C_0/C_t from breakthrough curves and the constants such as K_{AB} and N_0 were determined from the slope and intercept of the liner plots obtained from equation (5) and summarised in Table 2. The K_{AB} values found to decrease with increasing rate of
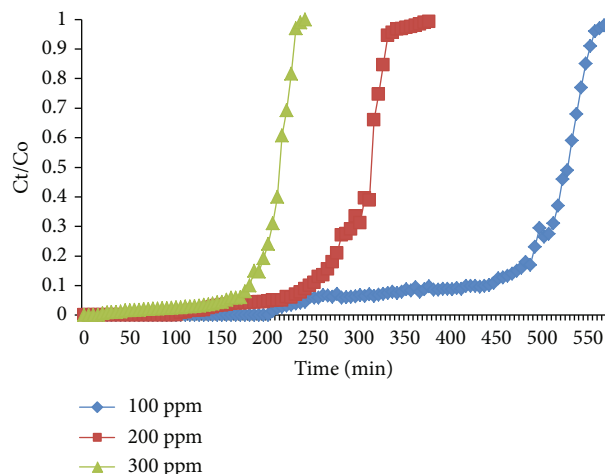
flow and initial concentration and increases with augmenting bed heights. The correlation coefficients were also found to be moderately high indicating the applicability of the model for the initial part of the BCT's. The trend observed depicts that the external mass transfer is the dominating mechanism of the present system [7].

3.3.2. *Thomas Model.* The Thomas model is one of the realistic models that can describe the achievements of breakthrough curves perfectly [24]. This model can also estimate the loading capacity of the CV onto MGP from the liner plots. The formula/equation for the Thomas model is given as

$$\ln \left(\frac{C_0}{C_t} - 1 \right) = \frac{k_{\text{Th}} q_0 m}{Q} - k_{\text{Th}} C_0 t. \qquad (6)$$

The linear plots of the Thomas model provided the constants from the slope and intercept and the values are summarised in Table 3. It is observed that the K_{Th} values increase with increasing flow rates and preliminary concentration and decrease with augmenting bed heights. In the case of q_0, the trend was observed to be quite opposite to that of K_{Th}. The maximum loading capacity was estimated to be $97.4 \, \text{mg} \, \text{g}^{-1}$ which is very close to the experimental value $99.9 \, \text{mg} \, \text{g}^{-1}$ indicating the suitability of the model. The correlation coefficients support the better applicability of the model to the present CV removal onto MGP surface.

3.3.3. *Yoon-Nelson Model.* Another simplest model that can precisely explain the breakthrough curves is the Yoon-Nelson model which was originally developed to describe the gas phase molecule adsorption on to activated carbon [25]. The general expression is given as

$$\ln \left(\frac{C_t}{C_0 - C_t} \right) = k_{\text{YN}} t - \tau k_{\text{YN}}. \qquad (7)$$

The constants of the Yoon-Nelson model derived from the linear plots are summarised in Table 4. It is observed that

TABLE 2: Parameters and constants of the Adams-Bohart model for the removal of CV by MGP.

Parameter		K_{AB} (l/mg min)	N_0 (mg/l)	R^2
	3	1.4×10^{-5}	11345	0.932
Flow rate of solution (ml/min)	5	1.1×10^{-5}	13657	0.919
	7	1.0×10^{-5}	15098	0.904
	1	1.4×10^{-5}	11345	0.932
Adsorbent depth (cm)	2	1.7×10^{-5}	10105	0.941
	3	2.3×10^{-5}	9087	0.949
	100	2.3×10^{-5}	9087	0.949
Preliminary concentration (mg l^{-1})	200	2.0×10^{-5}	11732	0.934
	300	1.8×10^{-5}	12897	0.907

TABLE 3: Parameters and constants of the Thomas model for the removal of CV by MGP.

Parameter		K_{Th} (ml/min mg)	q_0 (mg/g)	R^2
	3	2.1×10^{-3}	45.7	0.989
Flow rate of solution (ml/min)	5	2.4×10^{-3}	32.8	0.979
	7	2.6×10^{-3}	29.7	0.971
	1	2.1×10^{-3}	45.7	0.989
Adsorbent depth (cm)	2	1.9×10^{-3}	69.9	0.991
	3	1.6×10^{-3}	97.4	0.993
	100	1.6×10^{-3}	97.4	0.993
Preliminary concentration (mg l^{-1})	200	1.9×10^{-3}	77.5	0.981
	300	2.6×10^{-4}	58.8	0.975

TABLE 4: Parameters and constants of the Yoon-Nelson model for the removal of CV by MGP.

Parameter		K_{YN} (min^{-1})	τ (min)	R^2
	3	0.932	199.9	0.990
Flow rate of solution (ml/min)	5	0.918	173.0	0.985
	7	0.909	123.8	0.978
	1	0.932	199.9	0.990
Adsorbent depth (cm)	2	0.956	279.2	0.978
	3	0.977	323.8	0.963
	100	0.977	323.8	0.963
Preliminary concentration (mg l^{-1})	200	0.963	239.7	0.954
	300	0.953	207.4	0.939

the K_{YN} and τ values decrease with increasing flow rate and preliminary concentrations and increase with increasing bed depths. The correlation coefficients obtained for the CV removal by MGP from Yoon-Nelson plots are high suggesting the applicability of this model as well to the present sorption system. The τ values found to be high for highest bed depths suggesting that the time for 50% exhaustion of column is high compared to other conditions.

3.4. Regeneration of MGP.
Regeneration is an imperative step in adsorption process since it decides the economic via-

bility of the adsorbent and scale up for industrial process. Further disposal of CV-loaded MGP is not safe since it might contaminate the disposal sites. Keeping this in mind, investigations were performed to regenerate the MGP and recover the CV. To regenerate the MGP, various desorbing or regeneration agents were utilised such as 0.01 M HCl, 0.01 M NaOH, 0.01 M NaCl, and H_2O. It was found that regeneration of 0.01 M HCl exhibited highest regeneration efficiency compared to the other reagents selected in this study. The greater efficiency exhibited by the HCl is due to the competitive adsorption exhibited by the hydronium ions

on to the surface active sites. The regeneration efficiency was found to be in the following order HCl > NaOH > NaCl > H_2O. End of the investigation, concentrated CV solution was obtained and this can be reused in the dyeing industry with modifications in pH or recovered as solid by evaporation method.

4. Conclusion

The present investigation outlined the surface modification of garlic peel with NaOH and its applications in removal of crystal violet in continuous column mode. The analytical characterizations such as SEM and EDX confirmed the surface modification and porosity of the surface. The fixed-bed column investigations were performed at varying bed heights, flow rates, and initial concentrations and found that lower flow rates and initial concentrations with higher bed depths are desirable for optimum performance of the column. The mathematical methods were used for the column data and Thomas and Yoon-Nelson models explained the breakthrough patterns satisfactorily and can be used in scaling up the process for industrial applications. The regeneration efficiency showcased the reusability potential of the MGP. These results concluded that low-cost agro-waste such as garlic peel can be a prolific adsorbent for the remediation of crystal violet from wastewaters.

Data Availability

All the data required are available within the manuscript.

Conflicts of Interest

The authors declare no conflicts of interest.

References

[1] https://gahp.net/pollution-and-health-metrics/.

[2] S. Şahinkaya, "COD and color removal from synthetic textile wastewater by ultrasound assisted electro-Fenton oxidation process," *Journal of Industrial and Engineering Chemistry*, vol. 19, no. 2, pp. 601–605, 2013.

[3] R. Lakshmipathy, M. K. Kesarla, A. R. Nimmala et al., "ZnS nanoparticles capped with watermelon rind extract and their potential application in dye degradation," *Research on Chemical Intermediates*, vol. 43, no. 3, pp. 1329–1339, 2017.

[4] P. Ghosh, Swati, and I. S. Thakur, "Enhanced removal of COD and color from landfill leachate in a sequential bioreactor," *Bioresource Technology*, vol. 170, pp. 10–19, 2014.

[5] R. Jayachandra, S. Rajasekhara Reddy, and R. Lakshmipathy, "D-Galactose based hydrophobic ionic liquid: a new adsorbent for the removal of Cd2+ ions from aqueous solution," *Environmental Progress & Sustainable Energy*, vol. 38, no. S1, pp. S139–S145, 2019.

[6] P. Samiyammal, A. Kokila, L. Arul Pragasan et al., "Adsorption of brilliant green dye onto activated carbon prepared from cashew nut shell by KOH activation: studies on equilibrium isotherm," *Environmental Research*, vol. 212, p. 113497, 2022.

[7] R. Lakshmipathy, G. L. Balaji, and I. L. R. Rico, "Removal of Pb2+ ions by ZSM-5/AC composite in a fixed-bed bench scale

[8] R. Biswas, S. N. Patra, A. K. Dalai, and V. Meda, "Taguchi-based process optimization for activation of agro-food waste biochar and performance test for dye adsorption," *Chemosphere*, vol. 285, p. 131531, 2021.

[9] C. H. Nguyen, "Efficient removal of cationic dyes from water by a combined adsorption- photocatalysis process using platinum-doped titanate nanomaterials," *Journal of the Taiwan Institute of Chemical Engineers*, vol. 99, pp. 166–179, 2019.

[10] C.-Y. Chen and W. J. Tseng, "Preparation of TiN-WN composite particles for selective adsorption of methylene blue dyes in water," *Advanced Powder Technology*, vol. 33, no. 2, p. 103423, 2022.

[11] M. B. Surafel, V. P. Sundaramurthy, A. A. Temesgen, and C. Gomadurai, "A statistical modelling and optimization for Cr (VI) adsorption from aqueous media via Teff straw-based activated carbon: isotherm, kinetic and thermodynamic studies," *Adsorption Science and Technology*, vol. 2022, article 7998069, p. 16, 2022.

[12] E. A. Kotenkova and N. V. Kupaeva, "Comparative antioxidant study of onion and garlic waste and bulbs," *IOP Conference Series: Earth and Environmental Science*, vol. 333, p. 012031, 2019.

[13] B. H. Hameed and A. A. Ahmad, "Batch adsorption of methylene blue from aqueous solution by garlic peel, an agricultural waste biomass," *Journal of Hazardous Materials*, vol. 164, no. 2-3, pp. 870–875, 2009.

[14] S. Liang, X. Guo, and Q. Tian, "Adsorption of Pb^{2+}, Cu^{2+} and Ni^{2+} from aqueous solutions by novel garlic peel adsorbent," *Desalination and Water Treatment*, vol. 51, no. 37-39, pp. 7166–7171, 2013.

[15] A. Asfaram, M. R. Fathi, S. Khodadoust, and M. Naraki, "Removal of Direct Red 12B by garlic peel as a cheap adsorbent: kinetics, thermodynamic and equilibrium isotherms study of removal," *Spectrochimica Acta Part A: Molecular and Biomolecular Spectroscopy*, vol. 127, pp. 415–421, 2014.

[16] W. Liu, Y. Liu, Y. Tao, Y. Yu, H. Jiang, and H. Lian, "Comparative study of adsorption of Pb(II) on native garlic peel and mercerized garlic peel," *Environmental Science and Pollution Research*, vol. 21, no. 3, pp. 2054–2063, 2014.

[17] Y. Zhao, W. Li, J. Liu et al., "Modification of garlic peel by nitric acid and its application as a novel adsorbent for solid-phase extraction of quinolone antibiotics," *Chemical Engineering Journal*, vol. 326, pp. 745–755, 2017.

[18] S. S. Baral, N. Das, T. S. Ramulu, S. K. Sahoo, S. N. Das, and G. R. Chaudhury, "Removal of Cr(VI) by thermally activated weed Salvinia cucullata in a fixed- bed column," *Journal of Hazardous Materials*, vol. 161, no. 2-3, pp. 1427–1435, 2009.

[19] A. A. Ahmad and B. H. Hameed, "Fixed-bed adsorption of reactive azo dye onto granular activated carbon prepared from waste," *Journal of Hazardous Materials*, vol. 175, no. 1-3, pp. 298–303, 2010.

[20] S. M. Alardhi, T. M. Albayati, and J. M. Alrubaye, "Adsorption of the methyl green dye pollutant from aqueous solution using mesoporous materials MCM-41 in a fixed-bed column," *Heliyon*, vol. 6, no. 1, p. e03253, 2020.

[21] S. K. Ghosh, A. K. Hajra, and A. Bandyopadhyay, "Air agitated tapered bubble column adsorber for hazardous dye (crystal violet) removal onto activated ($ZnCl_2$) carbon prepared from

bamboo leaves," *Journal of Molecular Liquids*, vol. 240, pp. 313–321, 2017.

[22] K. S. Bharathi and S. P. T. Ramesh, "Fixed-bed column studies on biosorption of crystal violet from aqueous solution by Citrullus lanatus rind and Cyperus rotundus," *Applied Water Science*, vol. 3, no. 4, pp. 673–687, 2013.

[23] G. Bohart and E. Q. Adams, "Some aspects of the behavior of charcoal with respect to CHLORINE.1," *Journal of American Chemical Society*, vol. 42, no. 3, pp. 523–544, 1920.

[24] H. C. Thomas, "Heterogeneous ion exchange in a flowing system," *Journal of American Chemical Society*, vol. 66, no. 10, pp. 1664–1666, 1944.

[25] Y. H. Yoon and J. H. Nelson, "Application of gas adsorption kinetics I. A theorical model for respirator cartridge service life," *American Industrial Hygiene Association Journal*, vol. 45, no. 8, pp. 509–516, 1984.